The generation of internal gravity waves by an oscillating wing moving in a pycnocline.

A thesis submitted to the University of Manchester for the degree of Doctor of Philosophy in the Faculty of Science and Engineering.

August 2000

Po Koon Huang

Faculty of Science and Engineering

School of Engineering

Division of Aerospace Engineering

To my family

Table of Contents

List of Figures

List of Tables

Abstract

Internal waves around an oscillating source moving in a pycnocline are studied using small amplitude theory. The pycnocline dispersion relation is used with ray theory to produce the plan-view phase configurations. When the mean velocity of the source is small and the oscillatory frequency is low, internal waves move ahead of the body. A streamlined body moving and oscillating in a pycnocline, produced in a laboratory tank of stratified brine, together with a schlieren system are used to observe the plan-view shape of the waves. The theoretical and experimental wave systems compare well. The theory is also extended to produce the phase configuration for an accelerating and decelerating source.

The dispersion relation for surface gravity waves including surface tension effects is used to produce phase configurations of surface and capillary waves and these are compared with experiments in the laboratory.

The forces on a NACA 0012 wing with aspect ratio of 1.7, oscillating about its quarter chord and moving in a pycnocline, are compared with that of the wing in a homogeneous fluid. A semi-conductor type balance capable of measuring forces to one hundredth of a Newton has been designed and built for this purpose. When compared with a homogeneous fluid the average lift coefficients are lower in the pycnocline while the mean drag coefficients are higher.

Pycnocline waves around a moving wing in a wide pycnocline are studied experimentally. Both side-view and plan-view schlieren images of the waves are observed. The theory derived using the dispersion relation for stratified waves is used to explain the physics of the observed wave system.

Plan-view schlieren images of the pycnocline waves around the oscillating wing when the wing is at a fixed position in the pycnocline still show waves propagating away from the trailing edge even when the oscillatory frequency is higher than the natural frequency at the centre of the pycnocline. This is found to be due to the flow induced by the oscillation of the wing.

The behaviour of the wing tip vortices are studied experimentally using the schlieren system. The development of a vortex dipole due to the horizontal movement of the wing is also studied using dye visualisation. More flow visualisation of internal waves and the vortices around a wing are provided on the enclosed CD-ROM.

Declaration

No portion of the work referred to in the thesis has been submitted in support of an application for another degree or qualification of this or any other university or other institute of learning.

Copyright

Acknowledgements

The author would like to express his sincere gratitude to Dr. T. N. Stevenson for his guidance and advice throughout the period of research.

The author would also like to thank Dr. J. A. G. Aston of Defence Evaluation and Research Agency (DERA), Haslar, for instigating this research.

The advice and help from Dr. David Smith, the staff and the technicians at the Goldstein Aeronautical Research Laboratory in designing and manufacturing of the equipment for the experiments is deeply appreciated.

The discussions with Dr. A. K. O. Law have been very useful in the understanding of the research. Dr. Law has provided information from his research which is supported by Defence Evaluation and Research Agency (DERA), Farnborough.

The author would also like to acknowledge the Overseas Research Studentship from the Committee of Vice-Chancellors and Principals of the Universities of the United Kingdom (CVCP), the Postgraduate Research Scholarship from the University of Manchester and other financial support secured by Dr. T. N. Stevenson.

This research has been funded by the Defence Evaluation and Research Agency (DERA) and their support is gratefully acknowledged.

Preface

The author graduated with a First Class B.Eng. Honours degree in Aerospace Engineering at the University of Manchester in July 1995. He started this Ph.D. research program with the School of Engineering, Aerospace Division from September 1995.

List of Symbols

α	Incidence angle of the wing
β	Non-dimensional frequency of wave energy
β_f	Non-dimensional oscillatory frequency
$\Delta\rho$	Density difference across the pycnocline
Δt	Time interval between data points
ε	Thickness of pycnocline
ε_x	Strain of material
ϕ	Phase of the wave energy
Φ	Equals to $(\phi - \phi_0)$ or $(\phi_2 - \phi_0 + \omega_f t)$ where ϕ_0 is the initial phase and it is a constant
ϕ_r	Phase shift of the wave energy at the caustic
γ	Defined as ± 1
λ	Wavelength
λ_{cw}	Wavelength of capillary waves
λ_{gw}	Wavelength of gravity waves
λ_{mws}	Wavelength corresponding to minimum wave speed
λ_s	The second coefficient of viscosity
μ	Viscosity of fluid
μ_s	Background fluid viscosity + perturbation
θ	The angle, measured anticlockwise from the positive x-direction, that the ray path makes with the horizontal
ρ	Density of fluid
ρ	Density perturbation
ρ_1	Fluid with lower density, the upper layer of a pycnocline
ρ_2	Fluid with higher density, the bottom layer of a pycnocline
ρ_c	Density at the centre of pycnocline
ρ_{cw}	Density of the fluid at the level of the wing in a pycnocline
ρ_o	Undisturbed background density
ρ_s	Background fluid density ρ_o + density perturbation ρ
σ	Frequency parameter defined as $U\omega_f/g'$
τ	Surface tension
ς	A unit vector vertically upwards
ω	Frequency of wave energy
Ω	ω/N_c
ω_f	Oscillatory frequency
ω_r	Frequency of fluid relative to background for stratified wave theory
ω_{rh}	Frequency of fluid relative to background for pycnocline wave theory
ψ	Stream function
ψ	The angle between the energy path and the positive x-direction in x-y plane.
a	Acceleration of the source
b_1	Gradient of the curve for q_o vs q_i
b_2	Value of q_o when $q_i = 0$
c	Chord length of the wing

c	Phase velocity for surface waves
c_{cw}	Phase velocity for capillary waves
C_D	Drag coefficient
c_{gw}	Phase velocity for gravity waves
C_L	Lift coefficient
d	Deceleration of the source
D	Drag
E	Non-dimensional parameter, defined as ε/c
E	Young's Modulus of the material
E_a	Limit of possible error
$E_{a\,rss}$	Probable error
f_{Ny}	Nyquist frequency defined as half the sampling rate
Fr	Froude number
Fr_i	Internal Froude number
g	Acceleration due to gravity
G	Non-dimensional parameter, defined as $\varepsilon N_c^2/2g$
g'	Effective acceleration due to gravity
GF	Gauge factor or sensitivity of the strain gauge
h	Distance below the centre of pycnocline
h	Depth of water
I	Second moment of area of the cross-section
J	Defined as $1-\left(\gamma\omega_f/N\lvert\sin\theta\rvert\right)$
K	Magnitude of wavenumber
K	Non-dimensional wavenumber
k	Wavenumber
k	x-component of wavenumber **k**
K_1	Value of the x-component of non-dimensional wavenumber K
K_1	Magnitude of the x-component of wavenumber **k**
K_2	Value of the y-component of non-dimensional wavenumber K
K_2	Magnitude of the y-component of wavenumber **k**
K_f	Reduced frequency
l	y-component of wavenumber **k**
L	Lift
m	Equals to 2n + 1
m	z-component of wavenumber **k**.
M	Non-dimensional parameter, defined as $\varepsilon N_c/U$
M_X	Bending moment
N	Local natural frequency
n	Mode of pycnocline oscillation, defined by the number of times a vertical velocity profile changes sign
N_c	Frequency at the centre of the pycnocline
N_{cp}	Number of calibration points
p	Pressure of fluid
p_o	Undisturbed background pressure
p_s	Background fluid pressure p_o + pressure perturbation p
Q	Velocity of source
q_i	True value

q_o	Indicated value
$R_{1,2}$	Distance from the origin
$R_{1,2,3,4}$	Resistance of each arm of the Wheatstone bridge circuit
Re	Reynolds number
s	Span of the wing
S_{qi}	Standard deviation of true value
St	Strouhal number
t	Time
T	Non-dimensional time t
t_a	Time at which constant acceleration ends
TCR	Temperature coefficient of resistance, defined as the percentage change in resistance of a strain gauge per 100 °F
t_d	Time when constant deceleration starts
U	Speed of source
u	x-component of velocity **V**
U_{bg}	Background velocity near to the trailing edge of the wing
U_c	Constant speed
U_f	Final speed
$\mathbf{u}_g$	Group velocity
U_g	Horizontal group velocity
u_g	x-component of group velocity $\mathbf{u}_g$
$\mathbf{u}_{gr}$	Group velocity relative to the background flow
U_{gr}	Magnitude of $\mathbf{u}_{gr}$
u_{gr}	x-component of group velocity $\mathbf{u}_{gr}$
U_i	Initial speed
U_{max}	Maximum speed
V	Velocity of fluid
v	y-component of velocity **V**
V_g	Non-dimensional group velocity
v_g	y-component of group velocity $\mathbf{u}_g$
V_{in}	Input voltage
V_{out}	Output voltage
V_p	Phase velocity of pycnocline waves
V_{Pr}	Phase velocity of pycnocline waves relative to background fluid
w	z-component of velocity **V**
w_g	z-component of group velocity $\mathbf{u}_g$
w_{gr}	z-component of group velocity $\mathbf{u}_{gr}$
X	Non-dimensional x
Y	Non-dimensional y

CHAPTER 1

INTRODUCTION

1.1 General Overview

This thesis considers stably stratified fluids where the background density decreases with an increase of altitude. When a fluid element is displaced vertically it tries to return to its equilibrium position, overshoots and an oscillation is started. This oscillation translates into waves and the energy propagates away from the source of the disturbance. There are numerous studies of internal waves generated by a disturbance in different background stratifications. For two layers of fluid, there is a step change of density at the interface on which waves behave similarly to surface gravity waves. As the interface widens by diffusion or mixing, it becomes a pycnocline where the density distribution can be defined by a hyperbolic function. As the pycnocline continues to widen, after a long time, the distribution can approach a linear stratification.

The object of the research is to study the behaviour of the vortices and internal gravity waves produced by the motion of an oscillating, lifting wing moving in a pycnocline. Changes of incidence of the wing and accelerations of the wing in different stratifications with pycnoclines will be considered. The motion of the wing produces internal waves and the far field wave system can be modelled by a moving oscillating point source. The turbulent wake, the collapse of the turbulent wake and the trailing vortices can also produce internal waves.

If the incidence of a horizontal finite wing, which is not moving forward, is increased and decreased continuously in a homogeneous media then vortices are

produced. The work done in changing the incidence of the aerofoil produces the energy within the vortices and the energy decays by viscous dissipation. If the fluid is stably stratified then vortices will again be generated but will soon collapse to produce a mixed turbulent region that will spread out at its equilibrium level producing internal waves in the process. Some of the energy decays by viscous dissipation within the collapsed turbulent region but the internal waves will carry energy to the far field before the waves themselves are dissipated by viscous effect. However there is a further important feature. The oscillating aerofoil will produce oscillatory waves moving out from the aerofoil, taking away energy that has to be provided by the mechanism which is changing the incidence of the aerofoil. If the wing oscillates about the ¼ chord position, this results in a small flow moving out from the trailing edge. Because of the Doppler effect this means that internal waves can take energy away from the aerofoil even if the oscillation frequency is above the natural frequency.

If the aerofoil moves at fixed incidence in a pycnocline, internal waves are generated by the collapsing trailing vortices and by the motion of the wing. The waves will move with the aerofoil's body generated waves, and will remain in a wedge shaped region behind the aerofoil. If the aerofoil incidence is varying then two sets of oscillatory internal waves are generated which take energy to the far field. These oscillatory waves are not steady relative to the body and are from (a) the collapsing vortices and from (b) the oscillating pressure field. The force to change the incidence of the aerofoil would be expected to be higher in the stratified fluid because it is feeding energy into the waves of type (b) but it is not obvious that the type (a) waves will increase the force. However the drag of a moving body producing wave energy in a stratified fluid is not necessarily higher than that of the same body moving in a homogeneous fluid. The drag of a horizontal circular cylinder can be less in a stratified fluid. This is a result of the wave system modifying the flow around the cylinder so that the boundary layer separation is delayed, resulting in a thinner wake with a lower base drag. So that, even though it is losing energy in producing a wave system the work done to move the body can be lower (Law 1999).

Impulsive movements of a body in a pycnocline will generate energy which propagates in all horizontal directions with a phase configuration, which in the plan-view, consists of concentric circles. A small amplitude theory for the phase configuration has been developed. In the limit of the pycnocline becoming infinitely

thin, the mode zero pycnocline waves should become the deep water surface waves. This is certainly the case for the steady part of the wave system as these produce Kelvin ship waves in the limit. The impulsive and oscillatory waves spread out way beyond the narrow wedge shaped steady wave system.

1.2 Introduction to the research work

The present work investigates several aspects of internal waves produced by a wing moving within a pycnocline. They will be discussed mainly in chapters, 3, 4 and 5. Chapter 2 reviews some of the important theories and previous work done by other authors.

In chapter 3, the pycnocline waves generated by an oscillating and moving body will be modelled as a point source. A pycnocline dispersion relation and ray theory will be used to plot two-dimensional plan-view wave systems. A vertical schlieren system has been set up to visualise the plan-view phase configuration of the waves. A slender body was used to generate internal waves in a thin pycnocline. The theoretical plots compare well with the experimental results. This theory is also extended to an accelerating and decelerating source. In the limit of a vanishingly thin pycnocline the theory produces interfacial gravity waves.

At a very high oscillatory frequency and relatively low velocity, surface tension waves can be observed experimentally on the free surface by the schlieren system. With surface tension included in the theory the agreement between theory and experiment is very good.

When a wing moves and oscillates in a pycnocline, the lift and drag forces acting on the wing are different from those of the wing in a constant density media. This is due to the presence of internal waves and the effects of stratification on the wing and on the trailing vortices generated. Chapter 4 describes how these forces are measured. A strain gauge balance attached to an oscillatory mechanism was designed. The voltage outputs from the strain gauges were fed into an analogue to digital converter and they are plotted onto the screen of a computer. The system is capable of measuring forces to a small fraction of a Newton. Due to the sensitivity of the gauges, signal processing using Matlab was used to filter off the electronic noise. A set of non-dimensional parameters is introduced so that the results can be presented in a meaningful way.

In chapter 5, a smaller NACA 0012 wing was manufactured to study the fluid motion and the internal waves generated when the wing moves horizontally and oscillates in a pycnocline. The way in which the vortices collapse to produce internal waves under these varying conditions is studied. Both horizontal and vertical schlieren systems were set-up so that both the plan-view and side-view waves could be seen simultaneously. One limitation is that the side-view schlieren can only be produced when the pycnocline is very wide or the density gradient is small. The images of internal waves produced by a wing fixed at an incidence angle will be shown. Near to the wing, the shapes of the waves are affected by the geometry of the wing. In the far field, these waves transform to the herring bone structure similar to the Kelvin ship waves except that the cusps along the path of the source do not finish at the source. The wing is also allowed to oscillate about its quarter chord with and without a forward velocity. For a stationary oscillating wing, in the near field, the side-view energy resembles that of a St. Andrew cross-wave centred at the trailing edge of the wing if the oscillatory frequency is less than the background natural frequency. The arms of the waves are curved due to the nonlinear background density. The plan-view consists of circular waves. Above the natural frequency, waves can still be seen emerging from the trailing edge of the wing.

The present study focuses on the waves generated by an oscillating moving source. Schlieren images are produced with the wing moving at different velocities and frequencies. Wavenumber surfaces are presented to predict any forward moving waves. For thin pycnoclines, only the plan-view schlieren images can be produced.

There is also a brief attempt to study both wing tip and trailing edge vortices in the stratified fluid by using the schlieren system and coloured dye. The vortices can be seen collapsing, creating internal waves. A vortex dipole due to the movement of the wing is also made visible using the dye. The data for the experimental images which are provided on the enclosed CD-ROM are given in table 5.6.

This work was financed by a DERA, Haslar Agreement to look for an instability in the flow which would reduce the drag of the oscillating wing. The total drag on a wing in stratified fluid has components such as profile drag, wave drag, viscous drag and induced drag. A paper by Gaponov-Grekhov et al (1983) indicates that at a high Froude number, gravity waves can help to reduce the drag. The paper considers an interface with two layers of fluid at different densities and the oscillating body is

travelling horizontally at a vertical distance below the interface. This work was clarified by Peake (1996) and by Dr. J. A. G. Aston of DERA Haslar who instigated this research. A graph of Froude number against a frequency parameter σ has been provided to identify the unstable region where there is a possibility of a reduction in drag. This will be discussed in chapter 4.

In the next two sections, the fundamental equations, the assumptions and terms used throughout the thesis will be discussed.

1.3 The Vaisala-Brunt frequency

The Vaisala-Brunt frequency, N, is the frequency of a vertical harmonic motion of a fluid particle. It is also known as the buoyancy or natural frequency.

In an incompressible fluid, a fluid particle of density ρ_o which is initially in equilibrium is lifted vertically a distance z. The background density at the new height is $\rho_o + z\frac{d\rho_o}{dz}$, where z is measured vertically upwards. The subscript o refers to the undisturbed background and $\frac{d\rho_o}{dz}$ is negative. The restoring force is,

$$z\frac{d\rho_o}{dz} \times \text{Volume} \times g$$

and results in a (mass × acceleration) term,

$$\rho_o \times \text{Volume} \times \frac{d^2z}{dt^2}.$$

Thus $$\frac{d^2z}{dt^2} = \frac{g}{\rho_o}\frac{d\rho_o}{dz}z.$$

This is a simple harmonic motion with oscillatory frequency

$$N = \sqrt{-\frac{g}{\rho_o}\frac{d\rho_o}{dz}}. \qquad (1.1)$$

1.4 The equations

The flows are assumed to be on a sufficiently small scale that the effects of the earth's rotation can be neglected. The equation of motion is

$$\rho_s \frac{D\mathbf{V}}{Dt} = \rho_s\left(\frac{\partial}{\partial t} + \mathbf{V}.\nabla\right)\mathbf{V} = -\nabla p_s - \nabla \wedge (\mu_s \nabla \wedge \mathbf{V}) + \nabla((2\mu_s + \lambda_s)\nabla \cdot \mathbf{V}) - g\varsigma\rho_s \qquad (1.2)$$

where $\frac{D}{Dt} = \frac{\partial}{\partial t} + u\frac{\partial}{\partial x} + v\frac{\partial}{\partial y} + w\frac{\partial}{\partial z}$, ρ_s is the density, $\mathbf{V}$ is the velocity, t is the time, p_s the pressure, μ_s the viscosity, λ_s the second coefficient of viscosity, g is the gravitational acceleration and ς is a unit vector vertically upwards. The last term is the buoyancy force per unit volume.

The continuity equation is

$$\frac{D\rho_s}{Dt} + \rho_s \nabla \cdot \mathbf{V} = 0. \qquad (1.3)$$

For an incompressible flow $\nabla \cdot \mathbf{V} = 0$ and equation (1.3) reduces $\frac{D\rho_s}{Dt} = 0$, i.e. there is no change in density along a particle path.

CHAPTER 2

REVIEW OF PREVIOUS WORK

2.1 Introduction

In this chapter, the theory for both stratified waves and pycnocline waves will be revisited. Here *stratified wave theory* refers to the internal waves represented by a dispersion relation in the vertical x-z plane while *pycnocline wave theory* refers to the dispersion relation for pycnocline waves in the horizontal x-y plane. In section 2.2 stratified wave theory results in the St. Andrews cross-wave which is a building block for the wave systems around moving bodies. Section 2.3 consists of a bibliographical review on stratified waves. The theory will be discussed again in chapter 5 together with the experimental results from an oscillating wing moving horizontally in a pycnocline. The theory and review of previous work on pycnocline waves is in section 2.4 and 2.5 respectively. The ray theory by Stevenson (1973) outlined in section 2.6 will be used extensively with the pycnocline dispersion relation in chapter 3. Other dispersion relations related to surface gravity waves are discussed in section 2.7. They will also be applied with the ray theory to produce the phase configurations for both deep water surface waves and capillary waves in chapter 3.

Previous work on an oscillating wing will be reviewed in section 2.8. Most of the discussion will be on the various flows and vortices around a wing. This section will be relevant to chapter 4 when the forces on an oscillating wing in stratified fluid will be compared to those in a constant density fluid. There appears to be no previous published literature on the forces on wings in a stratified fluid. However some new

unpublished finite difference results of Law (1999) will be compared with the experiments in chapter 4.

2.2 Stratified wave theory

A horizontal cylinder oscillating with frequency ω in an incompressible, inviscid and non-diffusive stratified fluid with a background natural frequency N will produce a St. Andrew's cross-wave. The wave energy is confined to the four arms which are beams of energy inclined at angles of $\theta = \pm \sin^{-1}(\omega/N)$ to the horizontal.

The equations are for a stationary fluid without background flow. The Boussinesq approximation will be used which neglects changes in the background density in the momentum equations except when multiplied by a gravity term. For an incompressible flow without solute diffusion there will be no change in density along a particle path and the continuity equation reduces to $\nabla \cdot \mathbf{V} = 0$. The momentum equation (1.2) reduces to

$$\rho_s\left(\frac{\partial \mathbf{V}}{\partial t}\right) = -\nabla p_s - g\varsigma\rho_s .$$

After subtracting the background hydrostatic relations, and writing the pressure and density perturbations as $p = p_s - p_o$ and $\rho = \rho_s - \rho_o$, the momentum equation for a two-dimensional flow in the x and vertical z directions becomes

$$\rho_o \frac{\partial u}{\partial t} = -\frac{\partial p}{\partial x}$$

and

$$\rho_o \frac{\partial w}{\partial t} = -\frac{\partial p}{\partial z} - \rho g .$$

The subscript o refers to the unperturbed background conditions. The continuity equation is

$$\frac{\partial u}{\partial x} + \frac{\partial w}{\partial z} = 0 .$$

The incompressibility equation $\frac{D\rho_s}{Dt} = 0$ reduces to

$$\frac{\partial \rho}{\partial t} + w\frac{d\rho_o}{dz} = 0 .$$

A stream function ψ is introduced, $u = \frac{\partial \psi}{\partial z}$ and $w = -\frac{\partial \psi}{\partial x}$ which satisfy the continuity equation. After the pressure and density gradient terms are eliminated, the momentum equation becomes

$$\nabla^2 \frac{\partial^2 \psi}{\partial t^2} + N^2 \frac{\partial^2 \psi}{\partial x^2} = 0 .$$

A plane wave solution of the form $\psi = \psi_o e^{i(kx+mz-\omega t)}$ is sought so that the dispersion relation takes the form

$$\omega^2 = N^2 \left(\frac{k^2}{k^2 + m^2} \right) \qquad (2.1)$$

or $\omega = \pm N \sin\theta ,$

where θ is the angle between the wave number vector and the vertical. The energy propagates at the group velocity, $\left[\frac{\partial \omega}{\partial k}, \frac{\partial \omega}{\partial m} \right] = \left[u_g, w_g \right]$, and forms a St. Andrew's cross whose arms are inclined at θ to the horizontal.

When there is a background flow with a velocity distribution of [U, 0], then the velocity u is not necessarily small and is written as $u = U + u'$ where u' is the velocity perturbation in the x-direction. The products of terms involving velocity u must therefore be retained in the momentum, the incompressibility and the continuity equations. The analysis follows that above and the dispersion relation becomes

$$(\omega_f + Uk)^2 = N^2 \left(\frac{k^2}{k^2 + m^2} \right)$$

This is the same result as that obtained by using the Doppler relation with the original dispersion relation (2.1).

Nicolaou (1987) described how the three-dimensional dispersion relation with a vertically sheared background flow could be derived from the momentum equation to give

$$\omega = kU_{bg} + lV_{bg} + \gamma N \left(\frac{k^2 + l^2}{k^2 + l^2 + m^2} \right)^{1/2} \quad \text{where } \gamma = \pm 1.$$

The two-dimensional version of this equation is used in section 5.3.

In a pycnocline where the natural frequency N varies with height, the energy does not travel in straight lines and reflections occur at a level where N = ω. A pycnocline can be represented by the exp-tanh density profile

$$\rho(z) = \rho_c \exp\left(-\frac{\Delta\rho}{2\rho_c}\tanh\left(\frac{2z}{\varepsilon}\right)\right) \qquad (2.2)$$

where ρ(z) is the density distribution, z is measured vertically upwards from the centre of the pycnocline where the conditions are denoted by the subscript c. ρ_c is the density at the centre of the pycnocline, Δρ is the maximum density difference across the pycnocline and ε is the pycnocline thickness. The background natural frequency can be expressed as

$$N(z) = \left(-\frac{g}{\rho_o(z)}\frac{d\rho_o(z)}{dz}\right)^{1/2} = N_c \operatorname{sech}\left(\frac{2z}{\varepsilon}\right), \qquad (2.3)$$

where $N_c = \left(\frac{g\Delta\rho}{\varepsilon\rho_c}\right)^{1/2}$.

The dispersion relation in equation (2.1) becomes

$$\omega^2 = \frac{(N(z))^2 k^2}{k^2 + (m(z))^2} = (N(z))^2 \sin^2(\theta(z)) \qquad (2.4)$$

with $\mathbf{k} = [k, m(z)]$ and θ(z)is the angle that the ray path makes with the horizontal in a frame of reference fixed in the background. θ(z) is measured anticlockwise from the positive x-direction.

2.3 Review of works on stratified flow

Mowbray & Rarity (1967) demonstrated that when a horizontal cylinder oscillates in a stable stratified fluid, a St Andrew's cross-wave with the cylinder at its centre is produced. The visualisation of the internal wave pattern used a Toepler-schlieren system. The system produces a two-dimensional image and waves are represented by dark and light bands. Linear theory, which was outlined in the previous section, predicts the angle of the waves, but there is no width to the arms of the cross. By satisfying the boundary conditions around a finite sized cylinder, Hurley (1969) introduced an inviscid theory which produced arms of constant width. However this does not agree with the experimental image which shows the arms widening away from

the source. A viscous similarity solution was introduced by Thomas (1971) which shows that the waves spread and the velocities are attenuated away from the forcing region.

Using Lighthill's theory for dispersive waves, Stevenson (1968) described the internal waves generated by a travelling cylinder in a linearly stratified salt solution. Stevenson (1969) extended the experiments and theory to an oscillating body moving vertically through the solution. Later in that year, Stevenson & Thomas (1969) produced further results of the oscillating cylinder moving both horizontally and also at an angle to the horizontal. Stevenson (1973) introduced the ray theory that produced the phase configuration for a point source or a two-dimensional source moving in an arbitrary path with arbitrary speed using any dispersion relation. This theory will be discussed again in section 2.6.

Voisin (1994) applied the Green's function to the generation of internal waves by a moving point source. Dupont and Voisin (1996) extended the theory to internal waves generated by a translating and oscillating sphere in a fluid with constant natural frequency.

When a horizontal cylinder is oscillating in a pycnocline, internal waves similar to the St Andrew's cross-wave are formed, except that the arms bend towards the vertical as the background natural frequency decreases or increases. Reflections occur at the caustics where the natural frequency is equal to the wave frequency. Ray theory breaks down at the caustics but the problem can be solved by introducing an Airy function which shows that a phase shift occurs (Lighthill 1967). Internal waves generated by a moving horizontal cylinder in a pycnocline are discussed by Stevenson et al (1986). Away from the source, Nicolaou et al (1993) showed how the trapped internal waves developed into pycnocline waves. The work was further complicated by the introduction of background shear and arbitrary stratification, Nicolaou & Stevenson (1997).

2.4 Pycnocline wave theory

Stratified wave theory follows the energy as it moves through the pycnocline reflecting at the upper and lower caustics.

These waves may be studied using the dispersion relation

$$\frac{\omega^2}{N^2(z)} = \frac{k^2 + l^2}{k^2 + l^2 + m^2(z)} \qquad (2.5)$$

where z is measured vertically upwards, N(z) is the natural frequency distribution and [k, l, m] are the [x, y, z] components of the wavenumber **k**, Bretherton (1966). This involves following the ray paths as they curve towards the caustics and reflect back towards the centre of the pycnocline. The horizontal wavenumbers, k and l, are constants and the vertical wavenumber m is a function of z, Bretherton (1966). Alternatively the dispersion relation of Groen (1948) and Krauss (1966) can be used with the pycnocline density distribution of equation (2.2) and the expressions for the natural frequency, equation (2.3).

The pycnocline theory implicitly selects the dominant wave numbers during the derivation of a dispersion relation and effectively averages all the phase changes at the caustics which occur in the stratified wave theory. The incompressible, inviscid, equation for the vertical velocity perturbation w(z) together with the boundary conditions form a Stürm-Liouville system whose solution is in terms of eigenfunctions. Krauss (1966) and Thorpe (1971) derived solutions for w in terms of hypergeometric functions using the boundary conditions that $\omega \to 0$ as $z \to \pm\infty$. Solutions represent trapped internal waves moving out horizontally and are valid for positive horizontal wavenumber K which satisfies the dispersion relation

$$\varepsilon^2\left(N_c^2 - \omega^2\right)K^2 - 2m\varepsilon\omega^2 K - \left(m^2 - 1\right)\omega^2 = 0, \qquad (2.6)$$

where ω is the wave frequency, $m = (2n + 1)$ and the oscillation modes, n, are defined by the number of times a vertical velocity profile changes sign. The expression can be rewritten as

$$K\varepsilon = \frac{\Omega}{\left(1-\Omega^2\right)}\left\{m\Omega \pm \left(\Omega^2 + m^2 - 1\right)^{1/2}\right\} \qquad \text{where } \Omega = \frac{\omega}{N_c}. \qquad (2.7)$$

Both ω and K remain constant along a horizontal wave path. The mode zero wave, $n = 0$, in the limit of the pycnocline becoming infinitely thin becomes an interfacial wave; all other modes have no meaning in this limit. The dispersion relation was

derived for two-dimensional waves stretching horizontally from $-\infty$ to $+\infty$. It will now be used to describe the way in which energy disperses in any horizontal direction in a pycnocline. The group speed in any horizontal direction from the point disturbance is

$$\frac{U_g}{\varepsilon N_c} = \frac{mK\varepsilon + m^2 - 1}{(K\varepsilon)^3}\Omega^3 \qquad (2.8)$$

with K being the wave number in that direction.

2.5 Pycnocline waves around a moving point disturbance

When a pressure disturbance moves close to the interface between two layers of fluid with different densities, interfacial waves are generated. Experiments by Ekman (1904) showed that these waves which are responsible for the 'dead water' phenomenon can slow down ships. Hudimac (1961) considered a two layer fluid with a free surface. The free surface was represented by a solid boundary. He evaluated the wave drag by using a source distribution moving at a constant depth. Crapper (1967) used a pressure point moving over a fluid surface in a two layer fluid analysis. Both of them had shown that when a body moves in a two layer system the internal wave energy is confined to a V-shaped wedge behind the body. The total included angle of the wedge is $\theta = \sin^{-1}(1/Fr)$ where Fr is a Froude number. Many of the studies involving internal waves created by moving disturbances with constant horizontal motion assumed an inviscid incompressible Boussinesq fluid with diffusion neglected.

Sturova (1978) considered a two layer system with one of the layers stratified. Arshanaya & Stetsenko (1988) experimentally included a powered body under the stratified layer. The wave amplitudes in the stratified layer due to the disturbance in the constant density layer increased as the density step between the two layers was increased.

Over time, the step change in density across an interface will diffuse to form a pycnocline which will act as a waveguide that traps internal waves. Aksenov et al (1985) and Dokuchayev & Dolina (1977) studied trapped waves in a fluid with a constant natural frequency, N, bounded by solid horizontal boundaries. This is similar to three layers of fluid with a constant N centre layer bounded by constant density layers.

As the pycnocline thickness approaches zero, the zeroth mode solutions approach interfacial waves. This has been shown by Aksenov et al (1987, 1989), Dysthe & Trulsen (1989). Miles (1971) and Holliday (1981) use Green's functions to study the three-dimensional waves from a moving body. Miles produced a far field solution for the dominant mode when the body is within the pycnocline and Holliday produced a solution when the body is at the edge of the pycnocline. When the source is within the pycnocline region the disturbances are the strongest. Internal waves of the lowest mode tend to dominate the centre while higher modes dominate towards the outer edges (Sturova & Sukharev 1981, 1983). Keller & Munk (1970) applied a linear asymptotic theory to produce the modes 0 and 1 wave shapes around a moving body but there are no transverse waves in their solutions.

Using the ray theory of Stevenson (1973) and the dispersion relation for pycnocline waves (equation 2.7), Nicolaou et al (1995) derived the plan-view phase configuration for internal waves generated by an accelerating body. This will be extended to an oscillating body in chapter 3.

2.6 Ray theory for a moving point source

Ray theory will be used to determine the waves from an impulsively started accelerating source in a pycnocline. Ray theory is a far field theory and is therefore limited to regions away from the source where non-linear effects are insignificant. However, in stratified internal wave problems, where comparisons have been made between ray theory solutions and experiments, good agreement was shown over the whole field except in the region very close to the body, typically to within three to four body lengths.

The theory for moving oscillating waves was provided by Stevenson (1973). This is now applied to the waves within a pycnocline.

The dispersion relation relating the frequency to the wavenumber components is $\omega = \omega(k, l, m)$ where ω is the frequency of oscillation of the fluid, not of the source. The group velocity $\mathbf{u_g}$ is $\left[\frac{\partial\omega}{\partial k}, \frac{\partial\omega}{\partial l}, \frac{\partial\omega}{\partial m}\right]$.

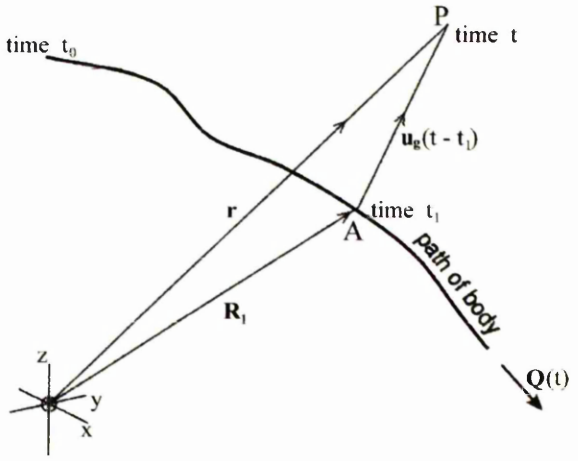

Figure 2.1 Co-ordinate system for ray theory.

Referring to figure 2.1, a body starts to accelerate with velocity $\mathbf{Q}(t)$ at time t_0. At time t_1, the body will be at position A with velocity $\mathbf{Q_1}$. The energy of frequency ω leaves A with group velocity $\mathbf{u_g}$. At a later time, t, the energy will be at position P. The distance of position P from the origin is given by $\mathbf{r} = \mathbf{R_1} + \mathbf{u_g}(t - t_1)$.

If ω_f is a source frequency associated with forced oscillations of the body or vortex shedding from the body, then the frequency of oscillation of the fluid is given by the Doppler relation $\omega = \omega_f + \mathbf{Q_1}\cdot\mathbf{k}$. The subscript, refers to time t_1, and the phase ϕ of the energy at position P is given by $\phi = (\mathbf{k}\cdot\mathbf{u_g} + \omega_f - \omega)(t - t_1) - \omega_f t + \phi_0$ where $\mathbf{k}$ is the wave number vector and ϕ_0 is a constant. This is rearranged to give

$$t - t_1 = \frac{\Phi}{\mathbf{k}\cdot\mathbf{u_g} - \omega + \omega_f} \qquad (2.9)$$

where $\Phi = (\phi - \phi_0 + \omega_f t)$ is a constant and the phase configuration is given by

$$\mathbf{r} = \mathbf{R_1} + \frac{\Phi\mathbf{u_g}}{\mathbf{k}\cdot\mathbf{u_g} - \omega + \omega_f} \qquad (2.10)$$

where Φ varies by 2π between successive crests or troughs. The equation for the phase configuration may be evaluated once the dispersion relation, group velocity and $\mathbf{Q}(t)$ are known. The radiation condition requires that $t - t_1 > 0$. If the body experiences more than one frequency, then the overall wave system is obtained by superimposing the wave system due to each individual value of ω_f together with the wave system when $\omega_f = 0$.

2.7 Surface waves

The dispersion relation for surface waves is (Lamb, 1932)

$$\omega^2 = gK\left(1+\frac{\tau K^2}{\rho g}\right)\tanh(Kh), \qquad (2.11)$$

where τ is the surface tension and h is the depth of water of density ρ.

Deep water waves

When $\tau = 0$ and $Kh \to \infty$ the deep water dispersion relation is obtained, $\omega^2 = gK$ and the group speed is, $U_g = \frac{d\omega}{dK} = \frac{g}{2\omega}$.

Shallow water waves

When $\tau = 0$ and $Kh \to 0$ the shallow water dispersion relation is $\omega^2 = ghK^2$ and $U_g = \frac{d\omega}{dK} = \frac{ghK}{\omega}$.

Capillary waves

For short wavelengths, less than about 20 mm, gravity may be neglected and with $Kh \to \infty$, $\omega^2 = \frac{\tau}{\rho}K^3$ and $U_g = \frac{d\omega}{dK} = \frac{3\tau K^2}{2\omega\rho}$.

Woodhead (1983) presented phase configurations of waves from these dispersion relations for an accelerating body using the ray tracing method.

2.8 Flow over a finite span wing

There have been experimental, theoretical and numerical studies of unsteady flow over an oscillating wing, many of which are related to dynamic stall where the wing's incidence is beyond the stalling angle. The experiments were usually conducted in a constant density water tunnel or in a wind tunnel. Various methods were used to visualise the flow around the wing. Among them Kim & Park (1988) and Park et al (1990) performed smoke wire visualisation of unsteady separation over an oscillating aerofoil in a wind tunnel.

Koochesfahani (1989) investigated the vortical patterns in the wake of an oscillating aerofoil. Both sinusoidal and non-sinusoidal oscillations were considered. The velocity profiles in the wake were used to study the oscillation amplitude, frequency and the drag or thrust of the wing. He concluded that the pitching aerofoil can produce thrust at high frequency. The critical frequency at which an oscillating aerofoil will have no drag depends on the amplitude of the oscillation. The detail formation of vortices in the wake of a pitching aerofoil has also been studied by Wilder et al (1996) by measuring the wake of a NACA 0012 aerofoil in a water tunnel using a laser-Doppler velocimetry method.

McAlister & Carr (1979) have included a NACA 0012 wing oscillating between 0 and 5 degrees in their hydrogen bubble visualisation experiments. They concluded that the laminar boundary layer in the dynamic case is thinner than the steady case where the wing's incidence was fixed at 5 degrees. From the wake structure, the vortices are more pronounced in the dynamic case, indicating an increase in lift. Another related work on more advanced aerofoil sections was carried out by McCroskey et al (1981). Selected experimental results were further analysed and discussed by McCroskey & Pucci (1982). McCroskey (1982) included a general theoretical discussion on unsteady aerofoils.

Gad-el-Hak (1986) studied the unsteady flow around an oscillating wing in a towing tank using the dye-layer technique, which requires the fluid to be slightly stratified such that the layers of dye can stay stable. The wing was made to oscillate between 0 and 30 degrees. Rectangular, swept and delta wings, having sharp or blunt leading edges were used to study the unsteady flow field. For a NACA 0012 rectangular wing, the leading edge separation vortex rolls along the chord and the flow stays close to the wing surface. He also studied the effects of frequency on the interaction between the leading edge and the trailing edge vortices.

DeLaurier & Harris (1982) have studied oscillating wing propulsion over a Reynolds number range of 25,000 to 40,000 in a wind tunnel. The wing had a NACA 0012 section and was pivoted at mid chord and was oscillated between -30 and 30 degrees incidence. The single component balance was measuring only thrust using a parallelogram-beam strain gauge load cell which can be reoriented to measure lift. This arrangement is similar to the balance 2 in chapter 4 of this thesis. The effect of inertial force due to the pitching of the wing in their experiments appeared to be negligible. The

experiments show that the average thrust may increase considerably with pitch amplitude and frequency.

There are some numerical and theoretical approaches carried out by other authors. Soviero & Bortolus (1992) introduced a vortex lattice method to calculate the unsteady pressure distribution on oscillating rectangular lifting surfaces in subsonic flow. Laha (1993) extended the vortex lattice method to several wings in small-amplitude oscillations. However both the works are primarily to find the pressure distribution on the wing. Mook & Dong (1994) have used panel methods to simulate wakes and blade-vortex interaction. This study also included fully attached flow past an oscillating two-dimensional NACA 0012 wing. The generated vortices in the wake are similar to those produced experimentally by Koochesfahani (1989).

In chapter 4, the work involving the forces on an oscillating wing in a pycnocline are primarily experimental. No other similar experimental data has so far been found. When a wing moves in a pycnocline, waves are generated by both the body and the wake. Sarpkaya (1983) conducted experiments to compare trailing vortices in homogeneous and stratified fluids. The results indicated that the vortices in stratified fluid rise only to a finite height. They soon decay into turbulence.

CHAPTER 3

WAVES FROM AN OSCILLATING AND MOVING BODY

3.1 Introduction

The ray theory discussed in section 2.6 will now be implemented throughout this chapter. Several computer programs were written to plot the phase configurations of pycnocline waves and surface waves by incorporating their dispersion relations with the ray tracing method. The various dispersion relations are given in section 2.4 and 2.7. The theory and its implementation will be discussed fully in section 3.4 and 3.5. Section 3.6 presents pycnocline waves obtained using a vertical schlieren system. This optical system, which is sensitive to density gradients, will record the waves as dark and bright bands. The details of the experimental set-up and the schlieren system will be described in section 3.2 and 3.3. The theoretical waves, plotted as dots, will be superimposed on the experimental schlieren photographs.

Lighthill (1978), has shown how the shapes of deep water gravity waves produced by a point source can be deduced from their wavenumber surfaces. This approach will now be extended to pycnocline waves in section 3.7. A new set of non-dimensional parameters will be introduced. In the limit where the pycnocline thickness approaches zero for the zeroth mode, the wavenumber surfaces will be the same as those of Lighthill. Lighthill did not evaluate the shape of the surface waves.

In section 3.8, one of the computer programs will also plot the phase configurations of an accelerating and decelerating source. The plots will be based on

two of the experimental images in section 3.6. These comparisons will enable us to see how the phase configurations change by varying the acceleration or deceleration of the source.

The vertical schlieren was also used to visualise surface waves where surface tension is a dominant restoring force. These images will be compared with the theoretical phase configurations in section 3.9. Finally in section 3.10, the effects of increasing the source speed on the phase configurations of surface waves will be investigated. At low source speed, the wave system is dominated by ripples with extremely short wavelengths known as capillary waves. However at higher velocities, gravity waves with longer wavelengths will be seen to emerge. Capillary waves are also present at higher velocities. Surface tension is the main restoring force for waves with short wavelengths; longer waves are primarily gravity waves.

3.2 The experimental set-up

The model is a perspex slender body with a maximum width of 10 mm and a length of 27 mm. This streamlined model reduces the vortex shedding from the boundary layers. The experiments were in a towing tank of length 4.53 m, width 0.7m and depth 0.5m. In chapter 4, this tank will be used again for force measurement over a low aspect ratio wing. Both the experimental set-ups share the same oscillatory mechanism and trolley. A bent strut linked the model to a mechanism which oscillates the model vertically with a total distance of 5 mm. The whole mechanism rests on a trolley which runs on two polished metal rails. The trolley is driven by a motor via a belt and pulley system and its speed can be varied by a speed controller. The controller was calibrated by measuring the time taken for the trolley to move a fixed distance.

Flow visualisations were made using two schlieren systems through the perspex sections of the tank. These two systems will be described in section 3.3 although only the vertical schlieren system was used to produce the images in this chapter. Still images produced by the horizontal schlieren system will be shown in chapter 5 where some MPEG video clips of the motion of the waves provided by the enclosed CD-ROM will be discussed.

3.3 Schlieren system

The schlieren system is the primary visualisation method for stratified flow because of its sensitivity to density changes. Mowbray used the technique to investigate the wave configurations of two-dimensional oscillatory and moving disturbances in linearly stratified brine, (Mowbray & Rarity 1967) and (Mowbray 1967). This method is now being used for unsteady waves around an oscillating body moving in a pycnocline. The steady motion is in a horizontal plane and the oscillation is superimposed on this. The two schlieren systems allow the plan-view and side-view images to be observed simultaneously.

Video cameras were preferred over still cameras because of their ability to demonstrate the motion of the unsteady waves relative to the source. However a 35mm still camera would have offered a much better image resolution. The video cameras used have a standard PAL resolution of 576 × 768 pixels per frame. Examples from the videos are on the enclosed CD-ROM but at a lower resolution.

A 'C' computer program, which uses the Mil graphic library supplied by Matrox, was written to capture the images via a video capture card installed in a computer. The program will allow nine frames to be captured each time at a resolution of 576 × 768 pixels per frame.

3.3.1 Vertical schlieren

The video images in this chapter were obtained with a vertical schlieren system which shows plan-views of the waves. Figure 3.1 illustrates the arrangement of the system. From the bottom of the figure, a convex lens is used to condense the light from a halogen lamp. Filters must be used to reduce the intensity of the light beam in order to prevent the photo-sensitive cell in the video camera from 'burning out'. A concave mirror with diameter 0.305 m and focal length 3.05 m reflects the light as a parallel beam. The mirror is front silvered to prevent double reflections. The parallel beam of light is then reflected upward through the perspex working section by a plane mirror with a thickness of 6.4 mm and dimensions of 0.46 m by 0.46 m. Another identical plane mirror, placed directly above, reflects the beam to a similar concave mirror which then brings the beam to focus on a vertical knife edge. The beam passes straight and parallel through the working section. Half the light forming the image on the knife edge

is cut off and the rest enters the video camera which is focused on the working section of the tank. Any disturbance to the fluid will cause the beam to deflect either onto or away from the knife edge and change the illumination of the image of the working section. The system will be sensitive to a disturbance which causes the light to bend in the directions normal to the knife edge. In the images, waves moving along the path of the body are more apparent. Video clip 48 in the CD-ROM shows a streamlined body with zero speed oscillating at 6.33 rad/s, circular waves were produced. With a vertical knife edge the waves of the same phase moving in opposite directions along the centreline of the tank appear opposite in tone. However if the knife edge is horizontal, then the waves moving across the tank in opposite directions will appear in opposite tone.

The strut that holds the model will produce waves on the free surface between the air and the water. Depending on the speed of the strut, either surface gravity waves or capillary waves will be produced. The parallel beam that passes through the working section will be deflected by both the internal waves and the waves on the free surface. The resulting image will have the free surface waves superimposed on the internal waves which is undesirable. In order to overcome the problem, a flat piece of perpex was positioned on the free surface over an area larger than the frame of observation. This eliminates any free surface waves from the image and allows only the internal waves to be recorded. If the perspex is not perpendicular to the light beam, then the beam can be refracted. The perspex is levelled using a spirit level placed on its surface. The struts have to be bent to bring the model below the perspex. The strut is streamlined to reduce its disturbance; the vertical portion of the strut will not cause much disturbance unless the speed is high enough for vortex shedding to occur. These vortices tend to spread horizontally in a stratified flow and on the schlieren they will be superimposed vertically along the whole vertical portion of the strut and will therefore appear strongly. Video clip 64 shows an example of the vortex shedding from the strut. The angle of the bend must be small to cause as little disturbance as possible to the stratified layers. The horizontal section tends to produce more disturbance to the fluid. However once the pycnocline becomes wide, the bent portion of the strut will produce internal waves. Examples of these are shown in video clips 50, 51,52, 53, 56 and 57. The schlieren experiments are thus limited to low speed and relatively thin pycnoclines.

3.3.2 Horizontal schlieren

The pictures in chapter 5 were produced using the horizontal schlieren system which will show the side-view of the waves. The horizontal schlieren system was more difficult to set up due to the uneven bending of the light rays through the pycnocline.

Figure 3.2 shows the arrangement of the horizontal schlieren system. Like the vertical system, a convex lens is used to condense the light from a halogen vapour lamp onto a flat mirror. The image of the light source on the mirror should be about the same size as the filament of the lamp. This image will then act as a single source at the focal point of a concave mirror with diameter 0.203 m and focal length 1.83 m which reflects the light as a parallel beam. The parallel beam of light passes through the working section and is received by another similar concave mirror at the other side of the tank. Both mirrors are front silvered to prevent double reflections. If the fluid is linearly stratified, then the undisturbed density distribution will deflect the light rays downward by the same angle and a parallel beam will emerge. However with a pycnocline, the rays are deflected by different angles and this will distort the image. The problem can be solved by having a very thin working section or a weak pycnocline. The latter approach was adopted and it is common to wait for around three weeks for the pycnocline to widen. The waiting time can be reduced by having a smaller density difference between the top and bottom layers of the pycnocline when filling the tank. The distortion of the images during the experiments were minimal and this can be verified from the video clip 140s on the CD-ROM supplied. The second concave mirror has to be lowered and tilted to accept the beam. The beam is reflected to another plane mirror which then brings the beam to focus on a vertical knife edge. This plane mirror is needed due to the constraints on space in the laboratory. Like the vertical schlieren system, a vertical knife edge was used and half the light on the knife edge is cut off from the camera which is focused on the working section of the tank. Any disturbances within the working section will bend the light rays from their undisturbed positions and change the illumination of the image. This system is also more sensitive to waves travelling in the direction of the model motion. The waves of the same phase moving in opposite directions horizontally will appear opposite in tone.

3.4 Theory

The dispersion relation for a pycnocline is given by equation (2.6) as

$$\varepsilon^2\left(N_c^2-\omega^2\right)K^2-2m\varepsilon\omega^2K-\left(m^2-1\right)\omega^2=0$$

where $m = 2n + 1$ and n is the mode of oscillation. This is rearranged as

$$\omega^2=\frac{(\varepsilon N_c K)^2}{(\varepsilon K)^2+2m\varepsilon K+\left(m^2-1\right)} \tag{3.1}$$

and the horizontal group speed U_g is

$$\frac{\partial\omega}{\partial K}=\frac{\omega^3}{K^3N_c^2}\left(\frac{m^2-1}{\varepsilon^2}+\frac{mK}{\varepsilon}\right). \tag{3.2}$$

When considering a moving body it is assumed that energy propagates from a point with velocity $\mathbf{u_g}=[u_g,v_g]$ and wavenumber $\mathbf{k}=[k,l]$ with $K=\left(k^2+l^2\right)^{1/2}$. From Doppler relation, $\omega = \omega_f + U_1K\cos\psi$, it is possible for ω to be negative when $\cos\psi$ is negative.

The co-ordinate system adopted for the phase configurations involves a body moving in a straight horizontal path as shown in figure 3.3a. At time t = 0 the body starts to move from point A with an initial speed U_i in the x-direction. The origin is at the centre of the body and the body moves in a horizontal plane[x , y]. At point B, energy of frequency ω, radiated from the source travelling at speed U_1, satisfies the Doppler relation $\omega = \omega_f + U_1K\cos\psi$. From point B, this energy travelling with $\mathbf{u_g}$, reaches point C at time t_2 and the phase at C is given by

$$\phi_2=\phi_0+(KU_g-\omega)(t_2-t_1)-\omega_f t_1.$$

$\phi_0 - \omega_f t_1$ is the phase of energy as it leaves the source at B and $(KU_g - \omega)(t_2 - t_1)$ is the change of phase over this period. This is rearranged as

$$\phi_2=\phi_0+(KU_g-\omega+\omega_f)(t_2-t_1)-\omega_f t_2$$

and the time taken to travel from point B to C is given by

$$t_2-t_1=\frac{\phi_2-\phi_0+\omega_f t_2}{KU_g-\omega+\omega_f}. \tag{3.3}$$

The co-ordinates of C are given by

$$[x,y]=\left[\frac{(\Phi+\omega_f t_2)U_g\cos\psi}{KU_g+\omega_f-\omega}-\int_{t_1}^{t_2}U(t)dt\ ,\ \pm\frac{(\Phi+\omega_f t_2)U_g\sin\psi}{KU_g+\omega_f-\omega}\right] \tag{3.4}$$

where $\Phi = (\phi_2 - \phi_0)$ varies by 2π between successive crests or troughs. The radiation condition implies that from equation (3.3),

$$t_2 - t_1 = \frac{\Phi + \omega_f t_2}{KU_g - \omega + \omega_f} > 0.$$

The $\omega_f t_2$ has been retained so that at a later stage the Cauchy-Poisson waves can be made consistent with these waves. Referring to figure 3.3b, the speed of the body, U(t), and its distance travelled are evaluated during three different stages, (a) during a constant acceleration, a, (b) with constant speed, U_c and (c) with a constant deceleration, d.

(a) At t = 0, the body moves from origin A with initial velocity U_i, accelerates constantly to U_c in time t_a. After time t_1, when $0 < t_1 < t_a$, the velocity $U(t_1)$ and distance R_1 from the A is given by

$$U(t_1) = (U_i + at_1) \quad , \quad R_1 = \left(U_i t_1 + \frac{1}{2} a t_1^2\right) \text{ where } R_1 = \text{length AB.}$$

(b) During the constant speed stage, when $t_a < t_1 < t_d$,

$$U(t_1) = U_c = (U_i + at_a) \quad , \quad R_1 = \left(\frac{1}{2} t_a (U_c + u_i) + U_c (t_1 - t_a)\right).$$

(c) When the body is decelerating, $t_d < t_1 < t_2$,

$$U(t_1) = (U_c + d(t_1 - t_d)),$$

$$R_1 = \frac{1}{2} t_a (U_c + U_i) + U_c (t_d - t_a) + \frac{1}{2} (t_1 - t_d)(2U_c + d(t_1 - t_d))$$

where the deceleration d takes a negative value. At time = t_2, the body reaches the final velocity U_f. The distance of the body from the starting point is

$$R_2 = \frac{1}{2} t_a (U_c + U_i) + U_c (t_d - t_a) + \frac{1}{2} (t_2 - t_d)(U_c + U_f)$$

where U_c, U_i, U_f, a, d, t_2, are known. The time at which the acceleration ends is $t_a = \frac{U_c - U_i}{a}$ and the time when the deceleration starts is $t_d = \frac{U_c - U_f + t_2 d}{d}$. The input values of a and d must not be 0 to avoid any singularity. R_1 is the distance of the body from the starting point at time t_1, i.e. $R_1 = \int_0^{t_1} U(t)dt$ and similarly $R_2 = \int_0^{t_2} U(t)dt$.

Thus the integral in equation (3.4) is R_2–R_1.

If the body starts impulsively, $a \to \infty$ and $t_a \to 0$. For $t_a < t_1 < t_d$,

$$U(t_1) = U_c \quad , \quad R_1 = U_c t_1$$

and for $t_d < t_1 < t_2$,

$$U(t_1) = (U_c + d(t_1 - t_d)),$$

$$R_1 = U_c t_d + \frac{1}{2}(t_1 - t_d)(2U_c + d(t_1 - t_d)).$$

If the body does not decelerate, i.e. $U_f = U_c$, $t_d = t_2$ and $d \to 0$ then $U(t_1) = U_c$ and $R_1 = U_c t_1$.

If the source starts impulsively from rest, then Cauchy-Poisson waves are also generated. These waves satisfy the dispersion relation, the group velocity equation, the radiation relation and are independent of ω_f, however they do not need to satisfy the Doppler relation. Impulsive waves are evaluated with $t_1 = 0$ and after time t_2, the phase is given by $\phi = \phi_0 + (KU_g - \omega)t_2$. The waves are circular waves with the centre at point A where the source moves impulsively. The radius is given by

$$U_g t_2 = \frac{\phi - \phi_0 + \omega t_2}{K} = \frac{(\phi - \phi_0)U_g}{KU_g - \omega}.$$

The phase configuration for Cauchy-Poisson waves is given by

$$[x, y] = \left[\frac{\Phi U_g \cos\psi_A}{KU_g - \omega} - \int_0^{t_2} U(t)dt \ , \ \pm \frac{\Phi U_g \sin\psi_A}{KU_g - \omega} \right] \qquad (3.5)$$

where $\Phi = \phi - \phi_0$ varies by 2π between successive crests and ψ_A is the angle at point A measured anti-clockwise from the x-axis. Equation (3.5) can also be expressed as

$$\left(x + \int_0^{t_2} U(t)dt, \right)^2 + y^2 = \left(\frac{\Phi U_g}{KU_g - \omega} \right)^2. \qquad (3.6)$$

3.5 Implementation of the theory

The dispersion relations of equation (2.6) together with those for surface waves in section 2.7 were used to write computer programs in 'C' using the ray tracing method. These programs allow the wave configurations of the oscillating moving body to be plotted and they produce graphic files in tagged image file format (tif), which can be edited using any image editor software. All the graphic functions are provided by the Matrox Mil graphics library.

Figure 3.4 shows the flow chart for the input parameters of one of the programs. The programs can plot deep and shallow water waves with or without considering the effects of surface tension, pycnocline waves or capillary waves. Further wave systems such as interfacial waves can be included as long as the dispersion relations are known. However this may increase the number of input parameters. The background is divided into 768 by 576 pixels with the origin at the top left hand corner of the window. The scale of the waves has to be adjusted accordingly for each kind of wave. The capillary waves will have the smallest wavelength, followed by surface and pycnocline waves. It follows that the wavenumbers for capillary waves will be much higher than pycnocline and surface gravity waves. The difference in wavelengths will make it difficult to see the capillary waves if they are plotted onto the same scale as the surface gravity waves. This problem will be addressed in section 3.10.

Figures 3.5a to 3.5c show the flow charts involving the iterative processes. The program will plot oscillatory or non-oscillatory waves or both by altering the values in the ω_f loop. The iteration for the magnitude of the wavenumber, K, form the main loop where the frequency of the fluid, ω, and the magnitude of the group velocity, U_g, are calculated from equations (3.1) and (3.2). The solutions for the pycnocline waves have $K > 0$. This condition arises during the derivation of the dispersion relation as already stated. For surface waves the condition is $K \neq 0$.

The next loop is for phase which is set to iterate from -600π to 600π with steps of 2π for pycnocline waves. This range may be much higher for capillary waves. Within this loop, Cauchy-Poisson waves are calculated from equation (3.5). They do not need to satisfy the Doppler relation and are only calculated once when $\omega_f = 0$ to prevent repetition.

Several statements are included in the program to avoid singularities. Such statements include $\omega \neq 0$, $U_g \neq 0$ and $(KU_g - \omega + \omega_f) \neq 0$. The last statement is necessary in calculations from equation (3.3).

The radiation condition implies that, from equation (3.3), $(t_2 - t_1) > 0$ and $t_1 > 0$. If this is not applied, waves will be evaluated corresponding to energy travelling towards the source from infinity. The Doppler relation, $\omega = \omega_f + U_1 K \cos\psi$, gives the angle, ψ, between the group velocity vector and the body path. This allows the co-ordinates of the energy to be obtained from equation (3.4). These co-ordinates will then have to be translated to screen position with the origin at the top left of the window. Any dots that are plotted outside the window will be discarded.

The pycnocline waves can have many different modes of oscillation as mentioned in section 2.4 while there are only mode 0 surface waves.

3.6 Comparison between experimental and theoretical phase configurations of pycnocline waves

The density and natural frequency distributions for the pycnocline are shown in figure 3.17. The body is at the centre of the pycnocline. The properties were measured at the beginning of the experiments and they will vary slightly over a period of time during the experiments. The experiments were all done within the same day. As the pycnocline thickness increases, the time taken for the transition from 'stratified waves' to 'pycnoclines waves' will be increased. The theory uses only the two-dimensional horizontal pycnocline dispersion relation, therefore the theoretical and the experimental results will agree better if the thickness of the pycnocline remains as small as possible.

Figures 3.6 to 3.21 show the theoretical phase configurations of pycnocline waves superimposed onto the experimental images, obtained from the vertical schlieren system described in section 3.3.1. These images are plan-views of an oscillating streamlined body moving in a pycnocline. The direction of travel is from left to right as indicated by the arrow. The position from which the body starts is shown by the yellow outline of the streamline body on the left of each picture. The green represents the oscillatory waves and the red are the non-oscillatory waves. Impulsive waves are represented by the blue circular waves centred at the point from which the body starts. The yellow represents the energy along the body path where the green oscillatory waves

and the red non-oscillatory waves are superimposed on each other. A vertical knife edge was used in the schlieren system, so that if the waves moving towards the right appear dark then the waves of similar phase moving to the left will be of light tone. All the waves in the experiment appear to be mode 0 pycnocline waves.

The still images in the figures 3.6 to 3.21 are obtained from videos which have been converted to MPEG video files stored on the enclosed CD-ROM. These video clips show the directions and speeds of the waves but are of a lower resolution than the original videos. A full list of the video clips is provided in section 5.10. The video clips from which the experimental images were captured, are listed in the table 3.1.

Figure number	Video clip number
3.6	66
3.7	67
3.8	61
3.9	62
3.11	63
3.12	68
3.13	69
3.14	70
3.15	71
3.18	75
3.19	76

Table 3.1 The video clips corresponding to figures 3.6 to 3.19.

A typical characteristic of oscillatory pycnocline waves is that the green 'herring bone' waves are seen moving towards the body for most body velocities and frequencies. When one of them reaches the body it opens out as an oval shaped wave which grows away from the body. Depending on the speed of the source, some of them can move ahead of the source, which means the magnitude of the group velocity is higher than the speed of the source in the same direction.

The distance between each phase agrees well with the linear theory. The theory is for a point source and so the source position relative to the finite body is indeterminate. Moreover, near to the body, there will be vortex shedding and turbulent mixing. The theory is only valid in the 'far field' but there is certainly a similarity with the experimental waves quite close in to the body.

The 'steady wave' system is stationary relative to the body and they are hardly visible in most of the pictures. In some of the pictures such as figures 3.10 and 3.11, the body reached a speed where some pseudo-steady waves can just be seen. These waves are not steady during acceleration. At this speed vortex shedding and turbulent mixing in the wake of the body will start to become prominent. To the left of the source another wave system, not accountable by the theory, can be seen in figure 3.18. These waves with smaller wavelengths are believed to be oscillatory waves generated by the vortices. They are relatively weak waves and are not visible in other figures. Some steady wave systems are presented on the CD-ROM but the steady case was studied extensively by Paonessa (1992).

The green oscillatory waves terminate as tangents to the circular impulsive start waves at two points. Transverse waves can be found between the two points replacing the impulsive waves. If the body had been travelling for an infinite time then the green oscillatory waves instead of terminating would continue out to infinity, except where transverse waves are present. One example of this is figure 3.6 where the body was given an impulsive start and moved for a relatively long time at a low speed.

The impulsive start waves are very weak and they are only just visible in some of the figures such as 3.11, 3.19 and 3.20. There is always a strong bow wave in the experiments which is not given by the small amplitude theory. The bow wave happens to be of the same shape as the first wave discarded by the radiation condition.

The pycnocline dispersion relation

$$\varepsilon^2\left(N_c^2-\omega^2\right)K^2-2m\varepsilon\omega^2K-\left(m^2-1\right)\omega^2=0$$

can be rearranged as

$$K=m\left(\Omega^{-2}-1\right)^{-1}\left\{1\pm\left(m^{-2}+\left(1-m^{-2}\right)\Omega^{-2}\right)^{1/2}\right\}$$

where $\Omega=\frac{\omega}{N_c}$ and $K=K\varepsilon$. Nicolaou et al (1995) used this relation to produce the phase configurations for a body accelerating in a pycnocline but neglected the negative sign because this corresponds to $K<0$. There will be solutions for K when Ω is both negative and positive. In the phase configurations generated by the 'C' program, the solutions generated by the negative Ω will appear mostly in yellow because of the superposition of the green oscillatory and red non-oscillatory waves. Most of the green oscillatory waves have positive Ω. The solutions from the negative part are confined to

the narrow wake along the path of the body and the corresponding wavenumbers are much higher. In practice, these waves are not visible in the experiments because they were destroyed by the wake of the source which is dominated by vortex shedding and turbulent mixing. In section 3.7, another set of non-dimensional parameters will be used to produce the wavenumber surfaces of the waves and their corresponding phase configurations.

3.7 Wavenumber surfaces and phase configurations

The equations in section 3.4 may be written in another set of non-dimensional quantities which will be used to produce wavenumber surfaces and phase configurations for pycnocline waves as well as surface waves and interfacial waves. The dispersion relation, equation (3.1), can be written as

$$K = \frac{\beta^2}{1-(M\beta)^2}\left\{m \pm \left[1+\frac{m^2-1}{\beta^2 M^2}\right]^{1/2}\right\} \qquad (3.7)$$

where $K=\frac{U^2K}{\varepsilon N_c^2}$, $\beta=\frac{U\omega}{\varepsilon N_c^2}$, $M=\frac{\varepsilon N_c}{U}$, $\beta=\beta_f+K_1$ and $K^2=K_1^2+K_2^2$ where K_1 and K_2 are non-dimensional wavenumbers in the x and y directions respectively. T will be used for dimensionless time, $T=\frac{t\varepsilon N_c^2}{U}$. Equation (3.7) will be used to plot the wavenumber surfaces with $\beta_f=\frac{U\omega_f}{\varepsilon N_c^2}$. The value of the non-dimensional group velocity becomes

$$V_g=\left(\frac{mKM^2+m^2-1}{K^3M^2}\right)\beta^3 \qquad (3.8)$$

where $V_g=\frac{U_g}{U}$.

Equation (3.3) becomes $T_2 - T_1 = \frac{\Phi}{KV_g-K_1}$ and the radiation condition requires $T_2-T_1 > 0$ where $\Phi = \phi_2 - \phi_0 + \beta_f T$. If the body has been travelling for an infinite time at speed U the phase configuration, from equation (3.4), takes the form

$$X=\left(V_g\frac{K_1}{K}-1\right)\frac{\Phi}{KV_g-K_1} \qquad (3.9)$$

and

$$Y=V_g\frac{K_2}{K}\frac{\Phi}{KV_g-K_1} \qquad (3.10)$$

where X and Y have the body as origin and have been made non-dimensional with the length $\frac{U^2}{\varepsilon N_c^2}$.

The wavenumber surfaces for some of the experimental images in section 3.6 are shown in figures 3.22 to 3.25. These wavenumber surfaces correspond to plan-view pycnocline waves produced by a body travelling from left to right. The surfaces represent only the top half of the wavenumber surfaces. There are at least two surfaces for each value of the frequency ratio β_f corresponding to the $\pm\beta$. Some smaller values of β_f have extra oval surfaces near to the origin where the wavenumbers are small. These surfaces are part of the solutions with positive β. The legends show the value of β_f. The branches on the right hand side of the figures have positive β and those on the left hand side have negative β. The regions where energy is to be found are given by Lighthill (1978). At a particular value of K, the normal to the dispersion relation wavenumber surface pointing towards higher β_f, corresponds to the direction from the body at which that value of K is to be found. All the normals toward higher β_f point from right to left except in a region close to the origin where some curves have a component left to right. This indicates that there are waves forward of the body; within that closed region, on the K_1 axis, the wavenumber surface gives waves directly ahead of the body on the x-axis.

The steady wave system has $\beta_f = 0$. In this case the two surfaces are symmetrical about the K_2 axis. Both surfaces give the same phase configurations which are stationary relative to the body. When β_f is not zero the two signs in the dispersion relation produce unsteady waves of different shapes which are superimposed on the steady wave system. The points of inflexion on the curves represent the cusps of the waves. Figures 3.26 to 3.28 showing phase configurations have the bodies travelling for a long time. The branches on the left with negative β have narrower wedges of waves behind the body. These waves become smaller with increasing M and β_f. When the phases are negative, there is no wave for negative β because the radiation condition, $T - T_1 > 0$, has not been satisfied.

The figures 3.22 to 3.25 are arranged in the order of increasing values of M. In the limit when M approaches zero, the wavenumber surface will be that of the deep water waves. The value of M is affected by the thickness of the pycnocline, the natural

frequency at the centre of the pycnocline and the speed of the body. In all the cases shown here, the values of M are changed only by the speed of the source.

The range of K_1 can be established from the condition $K > 0$. If $m = 1$ (n = 0), equation (3.7) becomes $K = \frac{2\beta^2}{1-(M\beta)^2} > 0$, hence $\beta \neq 0$ and $1 - (M\beta)^2 > 0$. The Doppler relation gives $\beta = \beta_f + K_1$ and $\beta_f > 0$. From $1 - (M\beta)^2 > 0$, K_1 is given by $-\left(\frac{1}{M}+\beta_f\right) < K_1 < \left(\frac{1}{M}-\beta_f\right)$. For $\beta < 0$, $\beta_f + K_1 < 0$ and $K_1 < -\beta_f$. Similarly for $\beta > 0$, $K_1 > -\beta_f$. Therefore the range of K_1 when $\beta < 0$ is $-\left(\frac{1}{M}+\beta_f\right) < K_1 < -\beta_f$ and for $\beta >$ 0, the range is $-\beta_f < K_1 < \left(\frac{1}{M}-\beta_f\right)$. Given that $K^2 = K_1^2 + K_2^2$, a range of values for K_1 is used to obtain K_2.

3.7.1 Wavenumber surfaces and phase configurations (M = 0)

The wavenumber surfaces for a surface gravity wave generated by a source moving and oscillating are given by Lighthill (1978). These have been reproduced using the non-dimensional terms $K = \frac{U^2K}{\varepsilon N_c^2}$, $\beta = \frac{U\omega}{\varepsilon N_c^2}$ and M = 0. In the limit where the thickness of the pycnocline, $\varepsilon \to 0$, $N_c \to \infty$ and $\varepsilon N_c^2 \to 2g$. Hence $M \to 0$ and for the n = 0 mode, the non-dimensional dispersion relation, equation (3.7), with $m = 1$ reduces to $K = 2\beta^2$ or $K = 0$. For $K = 2\beta^2$, $\omega^2 = \frac{K\varepsilon N_c^2}{2} = Kg$ which is the deep water dispersion relation. In the definitions of the present non-dimensional wavenumber, $K = \frac{U^2K}{2g}$, and the frequency ratio, $\beta = \frac{U\omega}{2g}$, there is a factor of two difference compared to Lighthill's definitions of $\frac{U^2k}{g}$ and $\frac{U\omega}{g}$ respectively.

The natural frequency at the centre of the pycnocline is

$$N_c^2 = \frac{g\Delta\rho}{\rho_c\varepsilon}.$$

Given $\rho_c = \frac{\rho_2+\rho_1}{2}$ and $\Delta\rho = \rho_2 - \rho_1$,

$$N_c^2 = \frac{2g(\rho_2 - \rho_1)}{\varepsilon(\rho_2 + \rho_1)}.$$

Substitute this into $\omega^2 = \frac{K\varepsilon N_c^2}{2}$ to give

$$\omega^2 = gK\frac{(\rho_2 - \rho_1)}{(\rho_2 + \rho_1)}$$

which is the dispersion relation for interfacial waves Lamb (1932).

Figure 3.22 shows the wavenumber surfaces for a body travelling from left to right (in Lighthill's book, the body is travelling from right to left). Lighthill does not show the shape of the waves. The phase configuration for the case when $\beta_f = 0.125$ is shown in figure 3.26a and b. Only 5 phases are shown and their values are shown in the legends. Broken oval waves with phases 2π, 4π and 6π can be seen around the body in the far field and they belong to the branches on the right hand side of the wavenumber surfaces with positive β and V_g. These waves, where energy is spread around the source, have high group velocity and large wavelengths. In the near field, there are two wedges where two sets of waves are contained. The waves within the larger wedge, with phases -4π and -2π, belong to the branch on the right hand side of the wavenumber surfaces with positive β and V_g. Waves within the smaller wedge, with phases 2π, 4π and 6π, are from the left branch with negative β and V_g. There is no solution for phases -4π and -2π with negative β and V_g because the radiation condition has not been satisfied. At higher wavenumbers, the Kelvin ship waves for all phases end at the source.

3.7.2 Wavenumber surfaces and phase configurations (M = 14.49)

Figure 3.27a and b show the far and near field phase configurations for the case when M = 14.46 and $\beta_f = 0.02$. The wavenumber surfaces for this value of M are shown in figure 3.23. The surfaces on the left have negative K_1. They have large values of K that form a narrower wedge with tiny waves. These waves are shown in figure 3.27b and they have negative β and V_g. At higher values of β_f, these waves would have almost disappeared. The angle of this narrow wedge can be verified from the left wavenumber branch, which is almost perpendicular to the K_1 axis, with its normal at the

point of inflexion virtually parallel to the K_1 axis. Again for this branch, there is no solution for waves with negative phases because the radiation condition is not fulfilled.

The waves within the larger wedge belong to the right branch with positive K_1 and smaller values of K. They have negative phases but positive β and V_g. The positive phases form fast propagating long oval waves all around the source as shown in figure 3.27a. They belong to the solutions with small values of K very near to the origin in the wavenumber plot.

At the critical value of $\beta_f = 3.96\times10^{-2}$, the curve crosses itself and above this value there are only two branches. There will not be any waves found ahead of the source for $\beta_f > 4.15\times10^{-2}$.

The non-dimensional approach will allow the solutions with negative β to be seen more clearly by looking at the near field. As the values of β_f increase, the waves associated with the branches on the left fill a narrower wedge relative to the wedge formed by the waves associated with the surfaces on the right. Figure 3.28a and b show the phase configuration for the case of $\beta_f = 4.5\times10^{-2}$. Comparing figure 3.28a with figure 3.27a, the oval waves have broken up. In the near field, figure 3.27b and 3.28b show that with increasing β_f the relative angle of the two wedges formed by the right and left branches is now more prominent. In figure 3.28b, the tiny waves of herring bone structure can just be seen behind the source.

Figure 3.28 and figure 3.20 have the same values of M and β_f, except that the body in figure 3.28 has been travelling for a long time and the transverse waves are missing. Figure 3.28 and figure 3.26 represent an increase in the value of M from 0 to 14.47. Notice how the relative angle of the wedges formed by the two branches with $\pm\beta$ has become significant with increasing M.

3.7.3 Wavenumber surfaces (M = 39.47 and 73.64)

Figure 3.24 and 3.25 are the wavenumber surfaces for M = 39.47 and M = 73.64 respectively. The range of values of wavenumber, K, for oval branches become smaller with increasing M. This indicates that the general wavelengths for these fast propagating oval waves increase with M. As the value of M increases, the branches for the same values of β_f are displaced nearer to the K_2 axis.

3.7.4 Wavenumber surfaces and phase configurations (M = 0.75)

A typical pycnocline in the ocean has a thickness of 100 m and a natural frequency at the centre of 0.015 rad/s. If a symmetrical body moves along the centre of a pycnocline then mode 1 steady waves are produced. However if a body oscillates in a vertical plane and moves at a horizontal speed of 2 m/s, then mode 0 pycnocline waves could be produced. If $\beta_f \leq 0.125$, then some of the waves will have a component in the direction where the body travels. Figure 3.29 shows the wavenumber surfaces for each of the cases. Above the critical value of 0.121 for β_f, only two branches exist. The points of inflection on the curves represent the cusps of the waves (Lighthill 1978). It can be seen that the angles of the wedges associated with the left curves become smaller with increasing β_f. The angles are also smaller than the wedges associated with the curves on the right, except when $\beta_f = 0$ where the curves are symmetrical and the waves are superimposed on each other.

The phase configuration of the waves produced with the body oscillating at increasing β_f are shown in figures 3.31. The body has been travelling for a long time with its direction of travel indicated by the arrow. The distance across each frame is 20 km. The blue dots are the steady waves and the red dots are the oscillatory waves.

Figure 3.30 shows the wavenumber surfaces for n = 1. No waves are expected to be ahead of the body. The branches for the case of $\beta_f = 0$ is symmetrical about the K_2 axis and the branches for higher values of β_f appear to be nearly symmetrical about the other smaller values of K_1. The normals at the points of inflection indicate that the angle of the wedge formed by the two branches are about the same. An example of the kind of waves produced with the body oscillating at $\beta_f = 0.125$ are shown in figure 3.32a and b, which confirm the analysis of the wavenumber surfaces.

3.8 Phase configurations of an accelerating and decelerating source

If the body accelerates slowly, then the pseudo-steady and oscillatory waves may be complete waves and not finish tangential to the impulsive waves. The impulsive waves can move ahead of the transverse waves. Nicolaou et al (1995) showed how the transverse waves developed relative to an accelerating body. However their analysis does not include any waves from an oscillating body.

The body starts from rest with a constant acceleration of $a = \frac{U_c}{t_a}$ and reaches a maximum constant speed of U_c or U_{max} in time t_a. Similarly, if the body is travelling at U_c, before decelerating to rest after time, t_d, then $d = -\frac{U_c}{t_d}$. The non-dimensional acceleration of the body is $\frac{a}{\varepsilon N_c^2}$, and d is negative.

The condition for the impulsive waves to move ahead of the transverse waves, if present, can be established by referring back to figure 3.3. The origin from which the impulsive waves spread out is moved to A with the positive x and y directions remaining the same as before. Given that equation (3.4) has $\cos\psi = 1$ and $\sin\psi = 0$, with the Doppler relation $\omega_f - \omega = -U_1K$, the energy of the transverse waves along the body path can be found at

$$[x,y]_A = \left[\frac{(\Phi + \omega_f t_2)U_g}{K(U_g - U_1)} + \int_0^{t_1} U(t)dt \ , \ 0\right]$$

at time = t_2. The impulsive waves along the body path, from equation (3.5) with $\cos\psi_A = \pm 1$ are given by

$$[x,y]_A = \left[\pm\frac{\Phi U_g}{KU_g - \omega} \ , \ 0\right].$$

The condition for the impulsive waves to move farther in the positive x-direction from point A than the transverse waves is

$$\frac{(\Phi + \omega_f t_2)U_g}{K(U_g - U_1)} + \int_0^{t_1} U(t)dt \ < \ \frac{\Phi U_g}{KU_g - \omega}$$

and $\cos\psi_A = 1$. The value of Φ is in multiples of 2π.

The circular impulsive waves are more likely to move ahead of the transverse waves at a low body speed and frequency of oscillation, ω_f. Figure 3.33 shows a body accelerating from rest to $U_{max} = 2.16\times10^{-3}$ m/s having travelled for a distance of 104 mm. There should be no impulsive wave for slow acceleration, however the impulsive waves are included so that the relative positions of the transverse waves can be seen. This kind of situation can happen when there is a jerk before the body starts to accelerate. This figure should be compared with the impulsive start case shown in figure 3.6 where no transverse waves are observed. The impulsive waves are seen to move ahead of the transverse waves at the early stage of the acceleration. Figure 3.34

shows the case for a body which starts impulsively to $U_{max} = 2.16\times10^{-3}$ m/s and decelerates to rest. The cusps of the waves are seen to be closer together; the circular wave near to the body has phase 2π, produced by the body when $U_f \rightarrow 0$ m/s. Note that no transverse waves are present for a decelerating body. Two further slightly different cases are shown in figures 3.35 and 3.36. In figure 3.35, a body starts impulsively from rest to $U_{max} = 2.16\times10^{-3}$ m/s and then decelerates to $\frac{1}{3}$ of its maximum speed. Figure 3.36 shows a body accelerating to $U_{max} = 2.16\times10^{-3}$ m/s, travelling at U_{max} for 16.9 s and then decelerating to $\frac{U_c}{2}$. Both the features associated with acceleration and deceleration can be seen. Figure 3.37 and 3.38 has the body accelerating from rest to U_{max} and then decelerating to rest again. In figure 3.37, the body has a higher acceleration and a lower deceleration while the opposite case is shown in figure 3.38. The total distance travelled and U_{max} remain the same for figures 3.33 to 3.38.

Figure 3.39 shows a body accelerating slowly to $U_{max} = 1.1\times10^{-3}$ m/s in 19.9 s and figure 3.40 is the decelerating case with the body starting impulsively to 1.1×10^{-3} m/s and then decelerating to rest in the same time. These figures should be compared to figure 3.10 where over the same distance and maximum speed, the body took 3.5 s to accelerate from rest. Figure 3.41 shows a body starting impulsively to U_{max} and then decelerating to $\frac{U_{max}}{3}$ in a total of 14.9 s. Figure 3.42 shows the case for a body taking 4 s to accelerate to U_{max}, travels at U_{max} for 3.5s and then decelerates to $\frac{U_{max}}{2}$ in 6 s.

3.9 Waves due to surface tension

The 'C' program used to produce the plan-view phase configuration of pycnocline waves using the ray tracing method (Stevenson, 1973) can also be used to produce ripples, shallow water waves, deep water waves and any other wave system provided the dispersion relation is known. Ripples are produced when surface tension is more significant than gravity in restoring the flatness of the water surface. They are defined as waves with wavelength less than 0.07 m. The ripples with even shorter wavelength of less than 4 mm are known as capillary waves. These waves can be

excited with frequencies of more than 70Hz but are often difficult to see. They have extremely high wave speed and suffer rapid attenuation.

Experiments involving ripples produced by an oscillating and moving body are presented in figures 3.43 to 3.47. The ripples were generated by a vibrating thin steel wire positioned just touching the surface of the water. For experiments involving a lower frequency of oscillation, a slender body on the water surface was attached to the end of the wire so that waves of larger wavelength could easily be produced. The wire was linked to a 15 watt speaker which was attached to the trolley that moves on two metal rails above the tank. This tank is the same tank as that described in section 3.2 for the visualisation of pycnocline waves. The oscillatory mechanism previously used to generate pycnocline waves was replaced by a frequency generator (TWG 501). The generator is capable of generating square, sine and saw-tooth signals, and it has a range of 0.01 to 10^7 Hz. Only sine wave oscillations were used in the experiments. The signals from the generator were also fed into a Hewlett Parkard digital oscilloscope in order to monitor the actual frequency and the stability of the sine wave patterns. It was often more difficult to generate a stable low frequency sine signal due to the frequency response of the speaker. However this was later achieved by attaching a heavier body to the end of the wire or adding mass such as plasticine to the wire. There was no problem achieving frequencies higher than 15 Hz but frequencies close to those associated with the movement of the trolley should be avoided to prevent any resonance.

The same vertical schlieren system as described in section 3.3.1, for the visualisation of pycnocline waves, was used to observe the ripples. The only modification was to remove the piece of perspex, which previously eliminated the surface waves.

The phase configurations generated by the program are shown next to each individual experimental image. The distance horizontally across each frame is 0.222 m. The total time in seconds, as an input to the program, is 35 × final speed of the source in m/s. The source took just 15% of the total time to accelerate constantly to its final speed. The depth of the tank is 0.46 m and the density of the water is 998 kg/m^3. Surface tension for pure water should be 0.074 N/m, but during the experiments, it was found that surface contamination has lowered this value considerably. The estimated value of the surface tension is 0.048 N/m for figures 3.43 and 3.44. For figures 3.45 to 3.47, the surface tension is lower at 0.045 N/m.

The ripples shown in all figures are not pure surface tension waves. The dispersion relation used to produce the ripples is for surface waves on water of arbitrary but uniform depth. This equation is shown in section 2.7 as

$$\omega^2 = gK\left(1+\frac{\tau K^2}{\rho g}\right)\tanh(Kh)$$

where τ is the surface tension, ρ is the equilibrium density, K is the magnitude of the wavenumber, ω is the frequency experienced by the fluid, g is the acceleration due to gravity and h is the height of the tank. For most of the range of wavenumbers encountered, $Kh \to \infty$ and $\tanh(Kh) \to 1$. The wave speed, $\frac{\omega}{K} = \sqrt{\frac{g}{K}+\frac{\tau K}{\rho}}$. Lighthill (1978) has illustrated the existence of a minimum wave speed during the transition between capillary waves and gravity waves. Given that the wavelength, $\lambda = \frac{2\pi}{K}$, it can be shown that the minimum wave speed occurs when $\lambda_{mws} = 2\pi\left(\frac{\tau}{\rho g}\right)^{1/2}$. The subscript 'mws' stands for minimum wave speed. For pure surface tension waves, the wavelength λ must be small compared to λ_{mws}. For pure gravity waves λ has to be large compared with λ_{mws}. For surface tension of 0.048 N/m and 0.045 N/m, the corresponding λ_{mws} are 13.9 mm and 13.5 mm respectively. In all of the figures, a wide range of wavelengths is observed. This means that the experimental phase configurations cannot be accurately reproduced by using either the dispersion relation for capillary waves or deep water waves alone. Indeed, the range of wavelengths seen is around the transition between waves dominated by surface tension and gravity.

The assumption is that the experimental images consist of waves where surface tension is the main restoring force, but gravity cannot be totally ignored. This analysis has yielded remarkable agreement between the experimental images and the theoretical phase configurations. It is now interesting to see how the wave system progressively changes from a system dominated by surface tension to waves due to gravity. The next section will discuss how the waves produced by a body change with increasing speed; they change from capillary waves to surface gravity waves.

3.10 Surface waves produced by a moving body

When analysing surface waves or interfacial waves, gravity is commonly seen as the only restoring force for the fluid elements to return to their equilibrium positions. With the addition of surface tension, the deep water dispersion relation is altered and waves of very short wavelength known as 'ripples' are produced. In fact, the addition of surface tension has a similar effect to increasing the acceleration due to gravity. In this section, the wave systems of a moving body will be produced by using the following two dispersion relations given in section 2.7:

$$\omega^2 = \left(g + \frac{\tau K^2}{\rho} \right) K$$

for deep water waves with surface tension

and $\omega^2 = gK$

for deep water waves without surface tension.

From the dispersion relation without surface tension, the group velocity, $\frac{\partial \omega}{\partial K}$, is half the magnitude of the phase velocity, $c = \frac{\omega}{K}$. The group velocity for capillary waves is 1.5 times its wave speed. For a steady moving source without oscillation, the pure gravity wave crests can move at the maximum speed, equal to the speed of the source, if they are moving along the same path as the source. Otherwise the wave speed is given by $U\cos\psi$ where ψ is the angle between the direction of propagation of the wave and the direction of the source moving at speed U. This means that there can be no pure gravity waves ahead of the source. The shortest capillary waves near the body path can be moving ahead of the source. It is interesting to note that the fastest moving gravity waves have the longest wavelengths while the fastest capillary waves have the shortest wavelengths. This implies that for waves with wavelengths somewhere between that of pure gravity and capillary waves, there is a wavelength which corresponds to a minimum wave speed. The expressions for the wavelengths of gravity waves and capillary waves are $\lambda_{gw} = \frac{2\pi}{g} c_{gw}^2$ and $\lambda_{cw} = \frac{2\pi\tau}{\rho c_{cw}^2}$ respectively. The subscripts 'gw' stands for gravity waves and 'cw' means capillary waves. From the Doppler relation, $\frac{\omega}{K} = U\cos\psi$, and increasing the source speed will increase the maximum wave speed.

Putting this together with the equations for wavelengths, it can be seen that the wavelengths of the gravity waves will become longer while the wavelengths for capillary waves will become shorter with increasing source speed.

With the help of the computer program, it is now convenient to investigate the significance of the two restoring forces on the wave systems produced by a moving source. Wave systems for an oscillating and moving source will also be shown. These will differ slightly from the above discussion due to the frequency term in the Doppler relation.

The depth considered is 1000 m and the surface tension, when applicable, is 0.074 N/m. The total time of travel is (4×body speed) seconds and the distance in metres across each frame is 1.2 × body speed(m/s) × total time(s). The acceleration takes up $\frac{1}{4}$ of the total time and is given by $\frac{4\times\text{body speed}}{\text{total time}}$ m/s^2. Figure 3.48a to c show the steady wave systems produced by a point source moving with a speed of 0.5 m/s. The directions of travel for all figures are indicated by the arrows. Only the first 20 waves are shown in 3.48a and b. Figure 3.48a includes the effect of surface tension whereas in figure 3.48b, the surface tension is excluded. At this speed, the wave system is dominated by ripples and therefore figure 3.48b is an unrealistic representation. As the ripples can be very close together for higher wavenumbers, it is necessary to plot only one wave out of every 20 waves up to the 400th wave in figure 3.48c to show the overall shapes clearly.

When the body speed is increased to 1 m/s, comparing figure 3.49a and 3.49b, this reveals a transition of ripples to Kelvin ship waves, at least for the first 7 waves. Figure 3.49c show that the ripples exist for the next 1000 waves, but note that there are now 50 waves between every 2 drawn. In figure 3.50a, the waves can be easily identified with the Kelvin ship waves shown in figure 3.50b. In figure 3.50b, the waves are expected to finish at the source, while in figure 3.50a they are not likely to do so. This is not obvious as the ripples are superimposed onto the longer waves, but the same effect can be easily seen by comparing figures 3.49a and b. In figure 3.50c, each ripple now has 500 waves between them. At 5 m/s, figure 3.51a shows almost identical Kelvin ship waves as in figure 3.51b, except for the extra wedge shaped waves near the body path which is due to the surface tension effect. Figure 3.51c shows that ripples still dominate at higher phases, but they are now more swept back. Figures 3.52a to c

show the similar cases for U = 15m/s. From figures 3.50 to 3.52, the gravity waves are restricted to the first few phases of the wave system.

Impulsive waves are not shown here because the waves are too close together near the starting point and cannot be clearly presented using the same scale. The transverse waves are superimposed onto the impulsive waves, at least at the early stage of the acceleration. If the body starts impulsively, then the steady waves finish at the tangent to the circular impulsive waves.

The surface wave systems of an oscillating and moving body differ from the steady wave system by the addition of a frequency term in the Doppler relation, $\omega = \omega_f + UK\cos\psi$. The wave speed is $c = \frac{\omega}{K} = \frac{\omega_f}{K} + U\cos\psi$ and now depends on the wavenumber, frequency of oscillation and the speed of the source. For lower values of $\frac{\omega_f}{K}$, the wave system will look like the steady wave system. The group velocity for gravity waves, as mentioned before, is half that of the wave speed. For any gravity waves to be ahead of the source, the magnitude of the group velocity must be greater than the source speed. This is equivalent to $U_g = \frac{1}{2}\left(\frac{\omega_f}{K} + U\cos\psi\right) > U$, hence $\frac{\omega_f}{K} > (2 - \cos\psi)U$, and along the body path, the condition becomes $\frac{\omega_f}{K} > U$. This is only possible for very low values of K which correspond to very long waves. Examples of this kind of wave are the oval waves around the source as seen in figure 3.26a. The group velocity of capillary waves is 1.5 times the wave velocity, and the corresponding condition for any waves ahead of the source is $\frac{\omega_f}{K} > -\frac{U}{3}$ which will be satisfied at all positive K.

Figures 3.53 to 3.57 show the oscillatory waves with the same range of velocities as in figures 3.48 to 3.52. The frequency of oscillation is 2 Hz and for each phase there appear to be two waves as clearly shown in figure 3.53b and c. This suggests that if wavenumber surfaces are to be plotted, there should be two branches for each value of ω_f and the source speed. Notice that each set of two capillary waves of the same phase ahead of the source is closer together as compared to those behind the source. As the speed of the source increases, the two waves appear to be superimposed onto one

another and the capillary waves look almost identical to those of the steady capillary wave system at the same speed. This phenomenon can be explained from the dispersion relation $c = \frac{\omega}{K} = \frac{\omega_f}{K} + U\cos\psi$. As the waves ahead of the source are waves of very high wavenumber, the $\frac{\omega_f}{K}$ term becomes very small, hence the capillary wave system will look similar to that of the steady wave system. For waves with smaller wavenumbers, especially those that are affected more by gravity than surface tension, each phase gives two completely different waves. The wavenumber surfaces for deep water gravity waves are shown in figure 3.22. They are the solutions for the pure gravity waves shown in figures 3.53b to 3.57b. As the speed of the source increases, pure gravity waves with larger wavelengths and pure capillary waves with very short wavelengths are produced. This has a de-coupling effect which differentiates the two wave systems as seen in figures 3.55a to 3.57a.

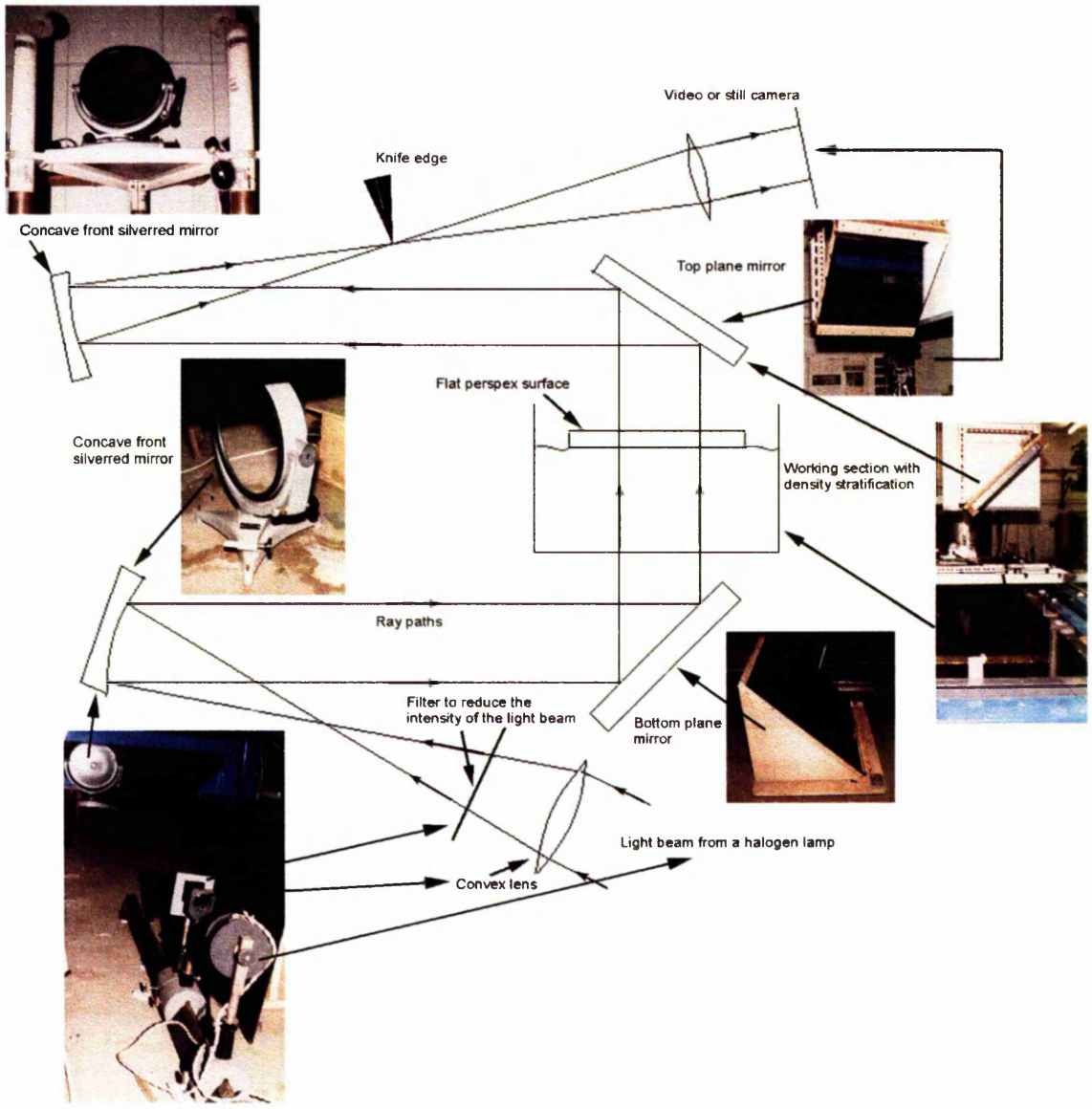

Figure 3.1 Vertical schlieren system.

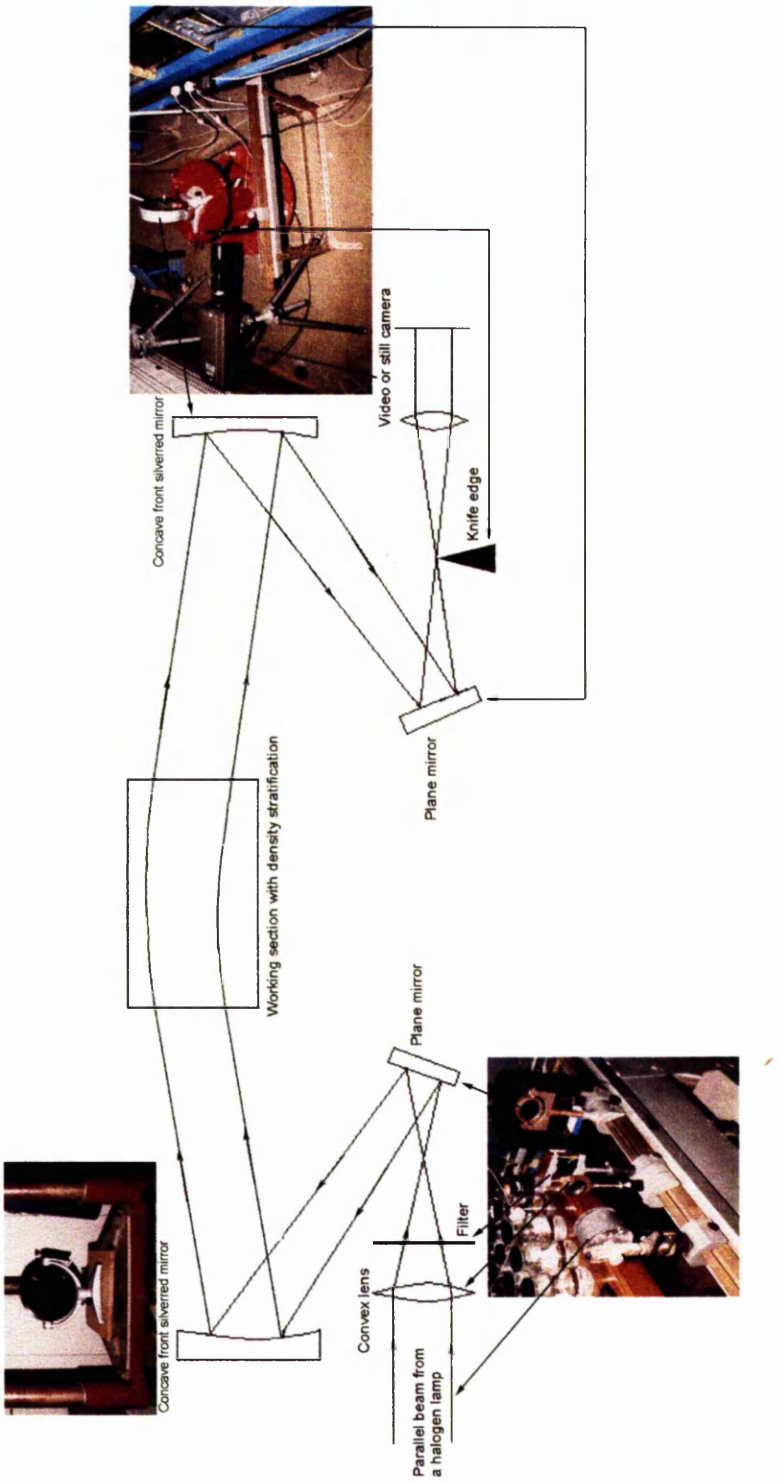

Figure 3.2 Horizontal schlieren system.

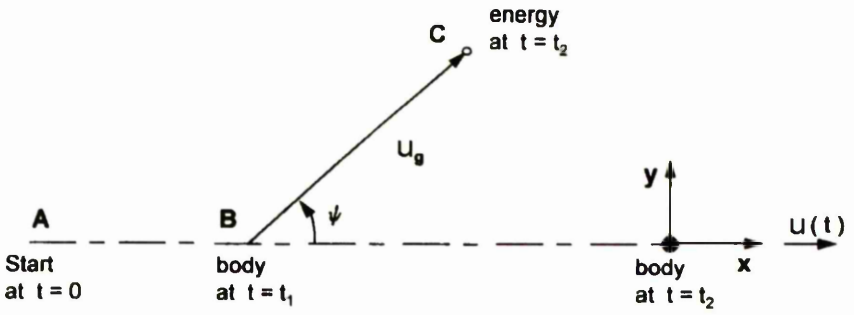

Figure 3.3a Co-ordinate system for a body moving in a straight horizontal path.

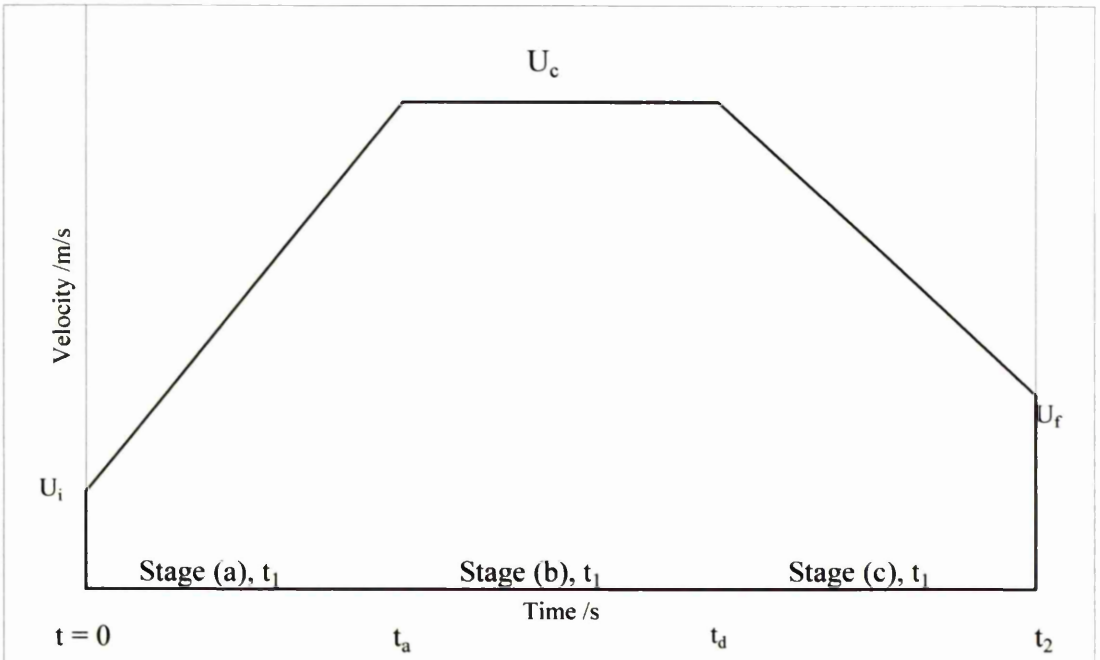

Figure 3.3b Evaluation of $U(t_1)$ and R_1 for an accelerating and decelerating body

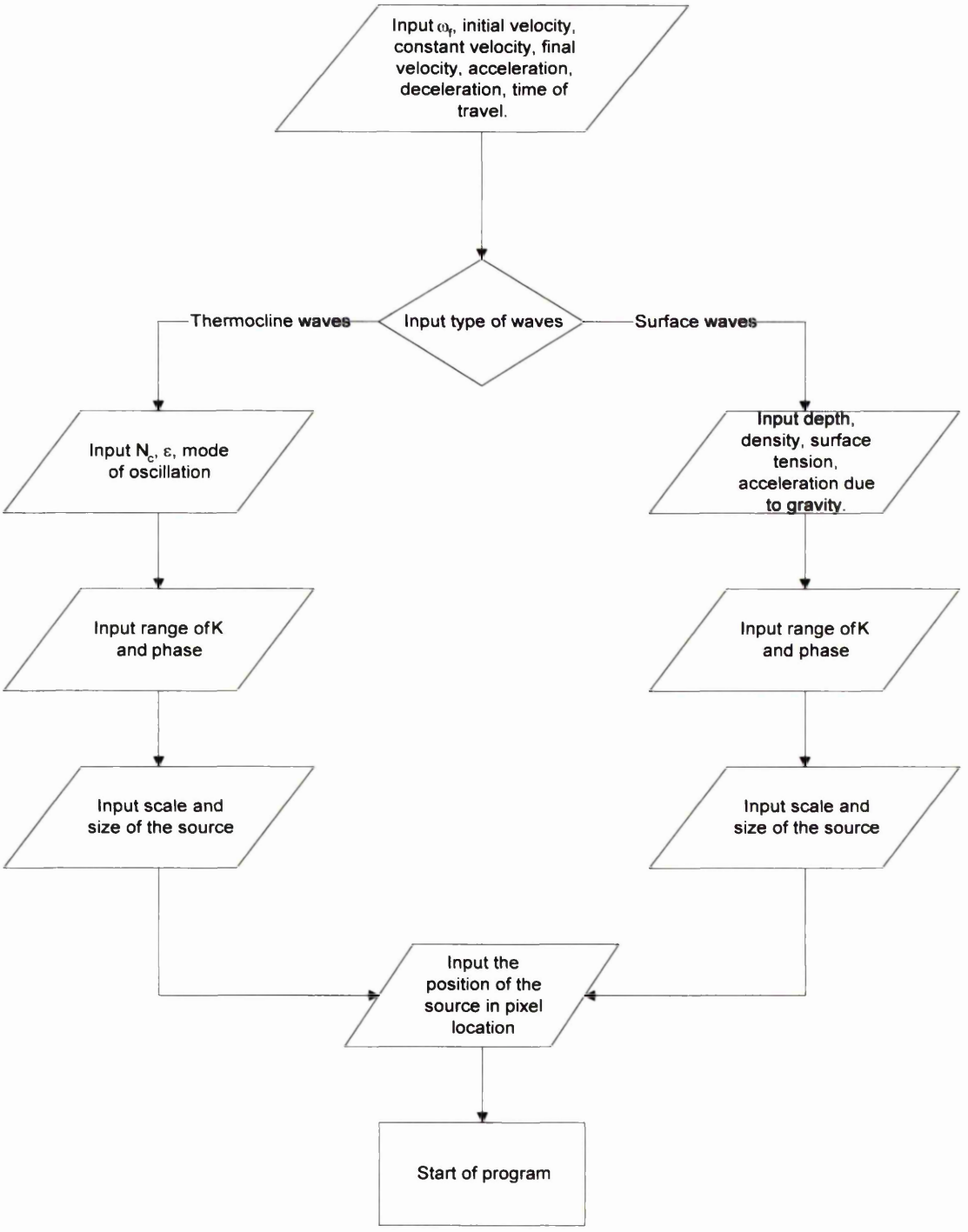

Figure 3.4 Flow chart for input parameters.

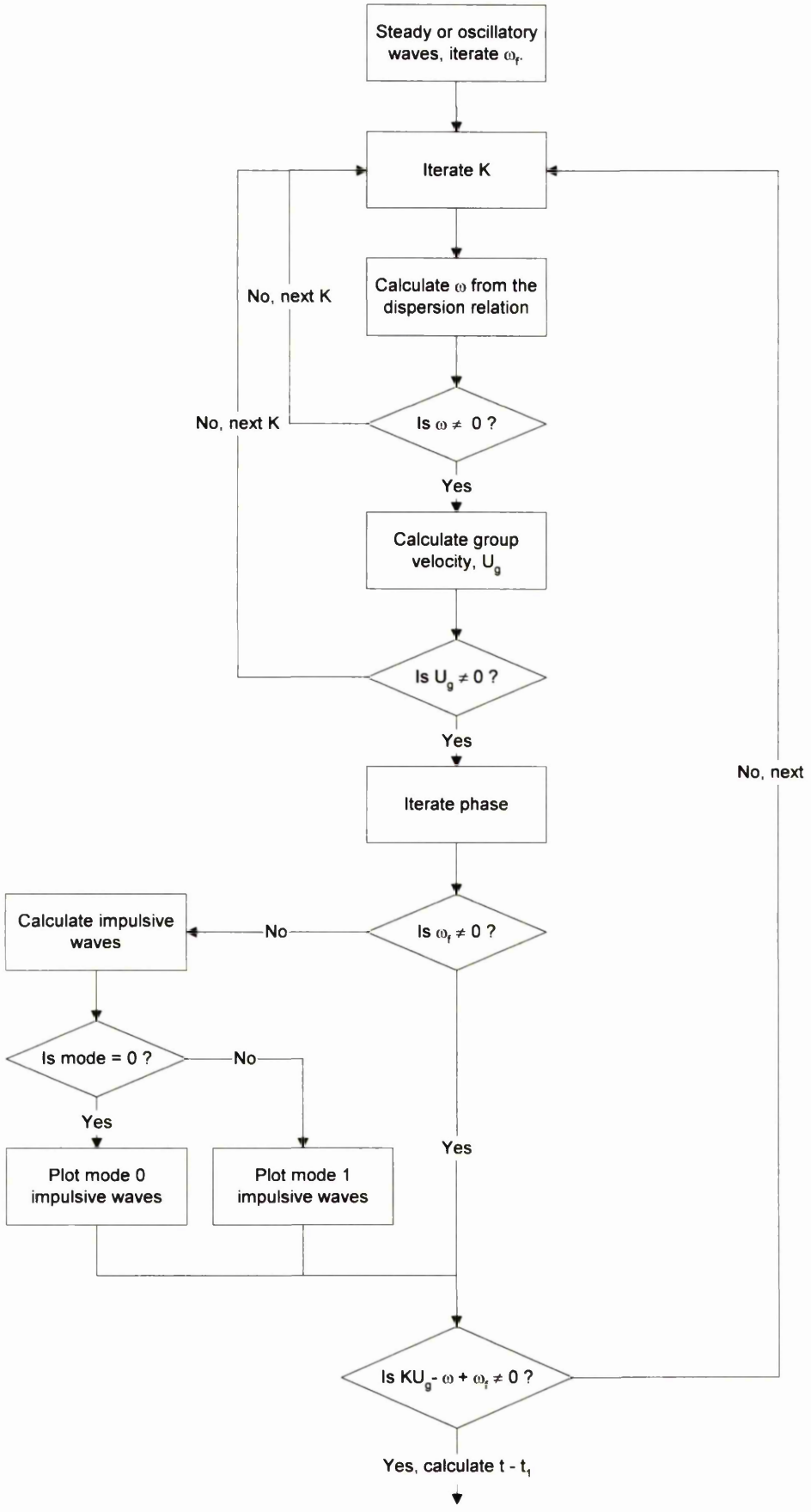

Figure 3.5a Flow chart for the main program.

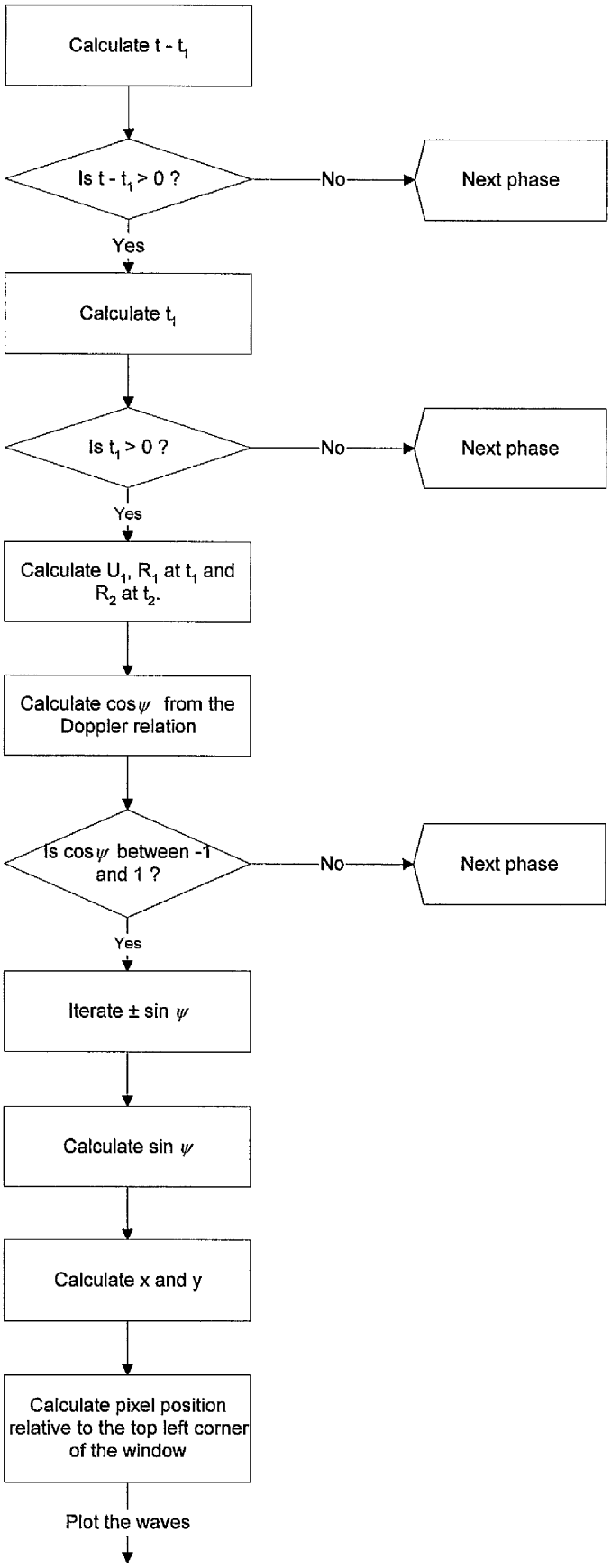

Figure 3.5b Flow chart for the main program.

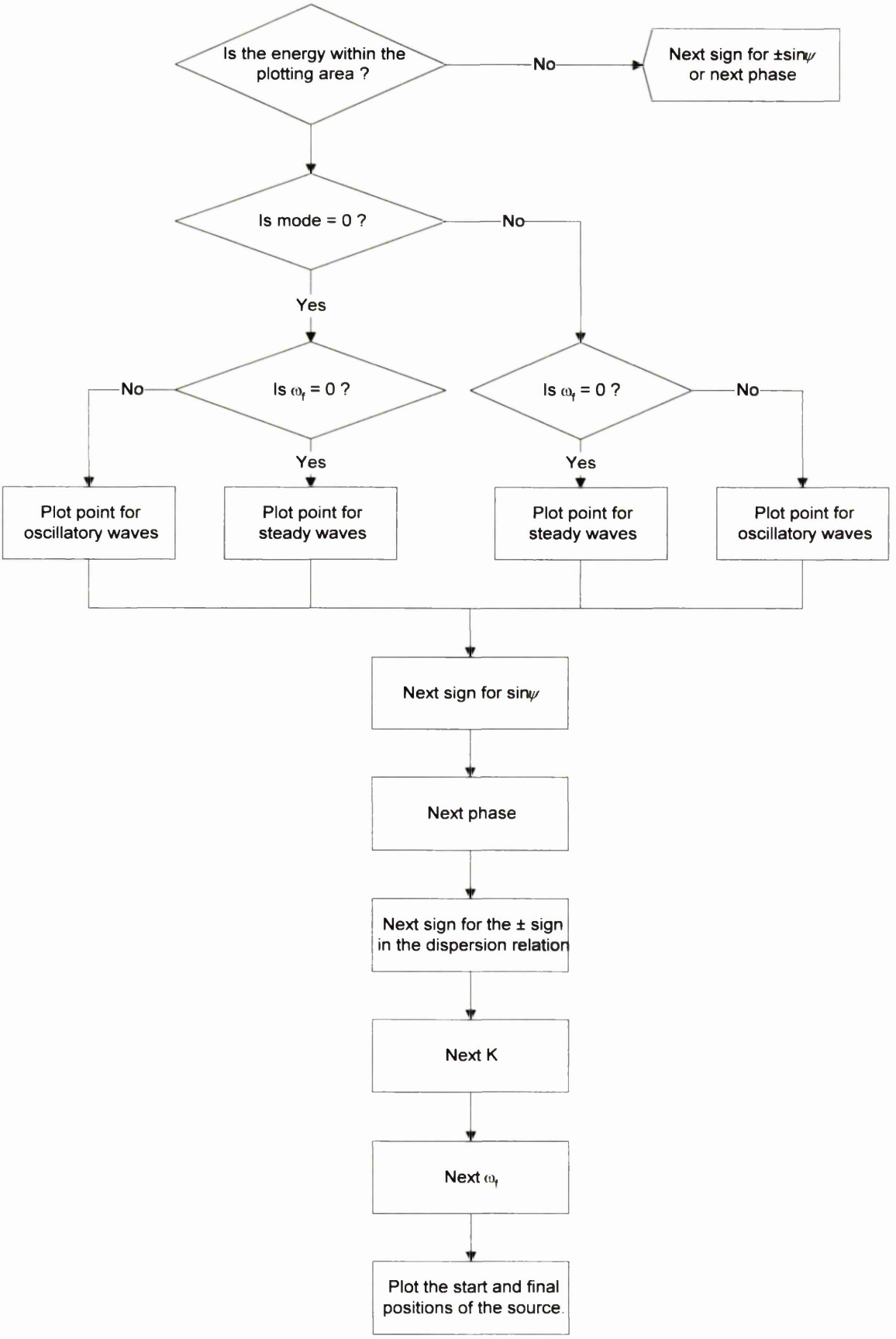

Figure 3.5c Flow chart for the main program.

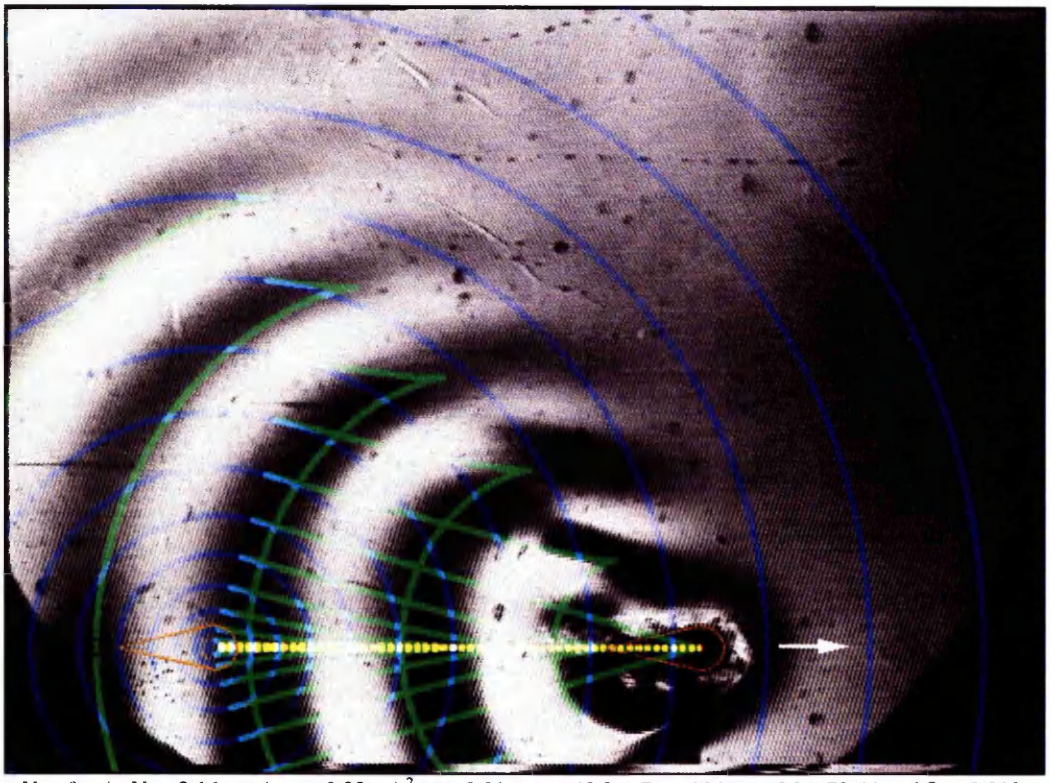

$U_i = 0$ m/s, $U_f = 2.16$ mm/s, $a = 0.22$ m/s^2, $t_a = 0.01$ s, $t_2 = 48.2$ s, $R_2 = 104$ mm, $M = 73.64$ and $\beta_f = 0.012$.

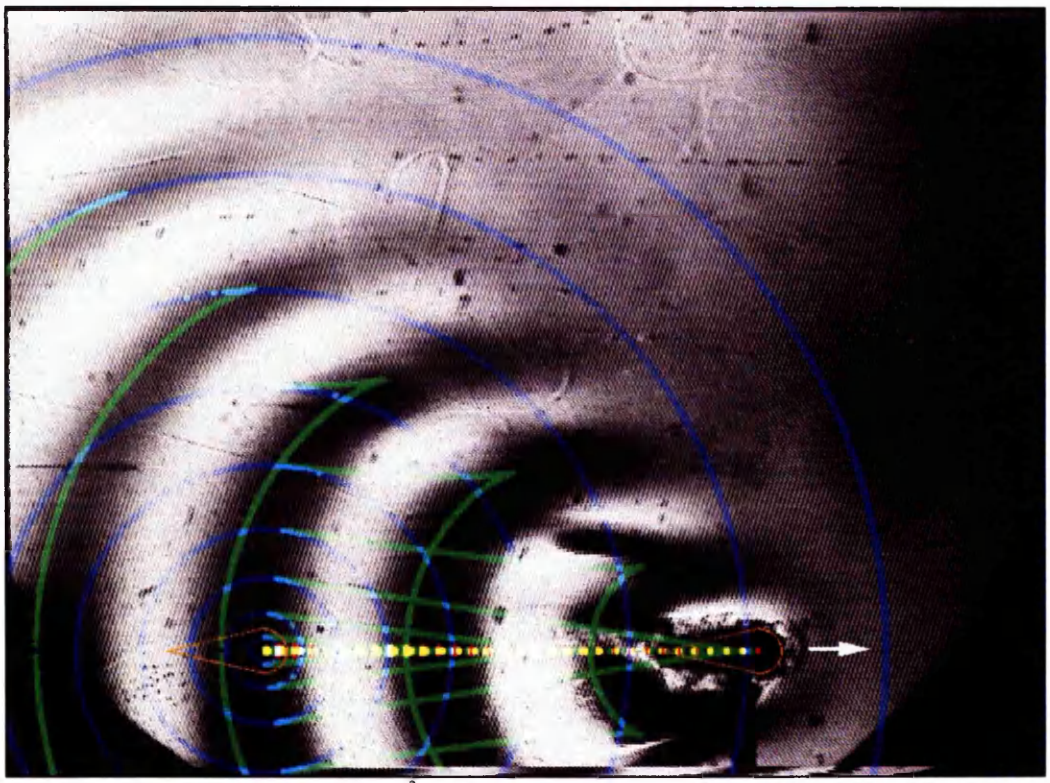

$U_i = 0$ m/s, $U_f = 3.85$ mm/s, $a = 0.38$ m/s^2, $t_a = 0.01$s, $t_2 = 28.4$ s, $R_2 = 106$ mm, $M = 41.31$ and $\beta_f = 0.021$.

Figures 3.6 and 3.7. Plan-view mode 0 waves produced by an oscillating body moving horizontally in a pycnocline. Both pictures show impulsive starts from rest. The blue lines are impulsive waves, green lines are oscillatory waves and red & yellow lines are steady waves. $N_c = 7.23$ rad/s, $\varepsilon = 0.022$ m, $\omega_f = 6.38$ rad/s.

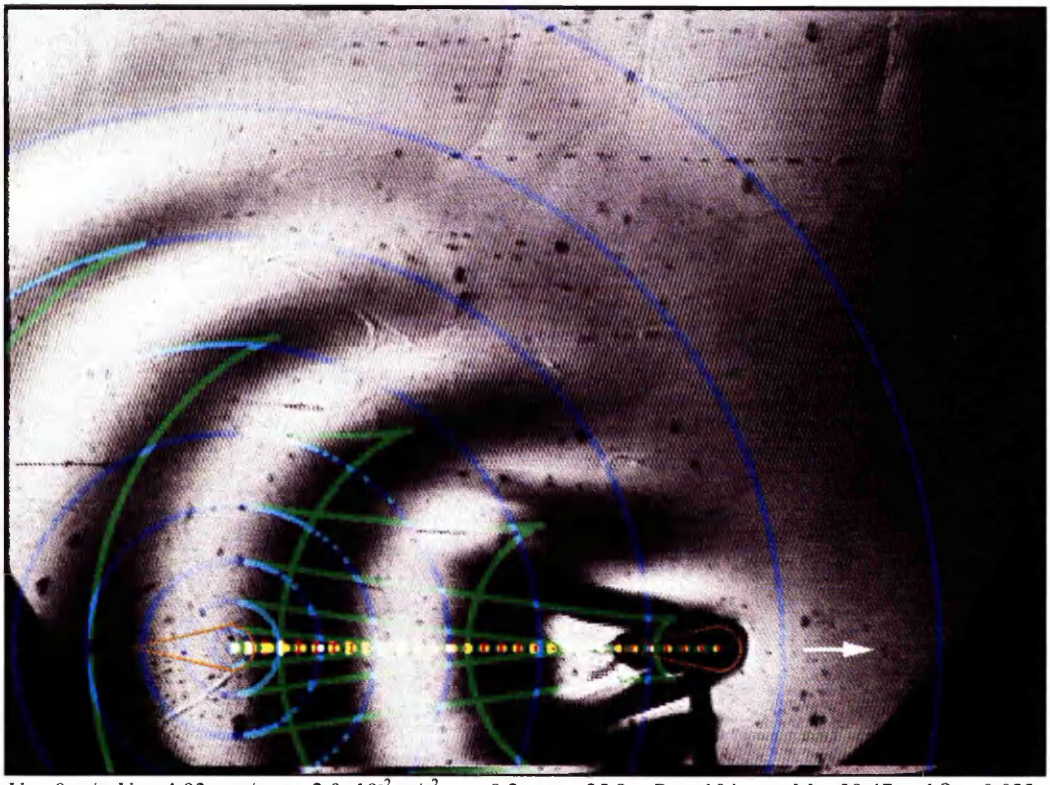

$U_i = 0$ m/s, $U_f = 4.03$ mm/s, $a = 2.0\times10^{-2}$ m/s^2, $t_a = 0.2$ s, $t_2 = 25.9$ s, $R_2 = 104$ mm, $M = 39.47$ and $\beta_f = 0.022$.

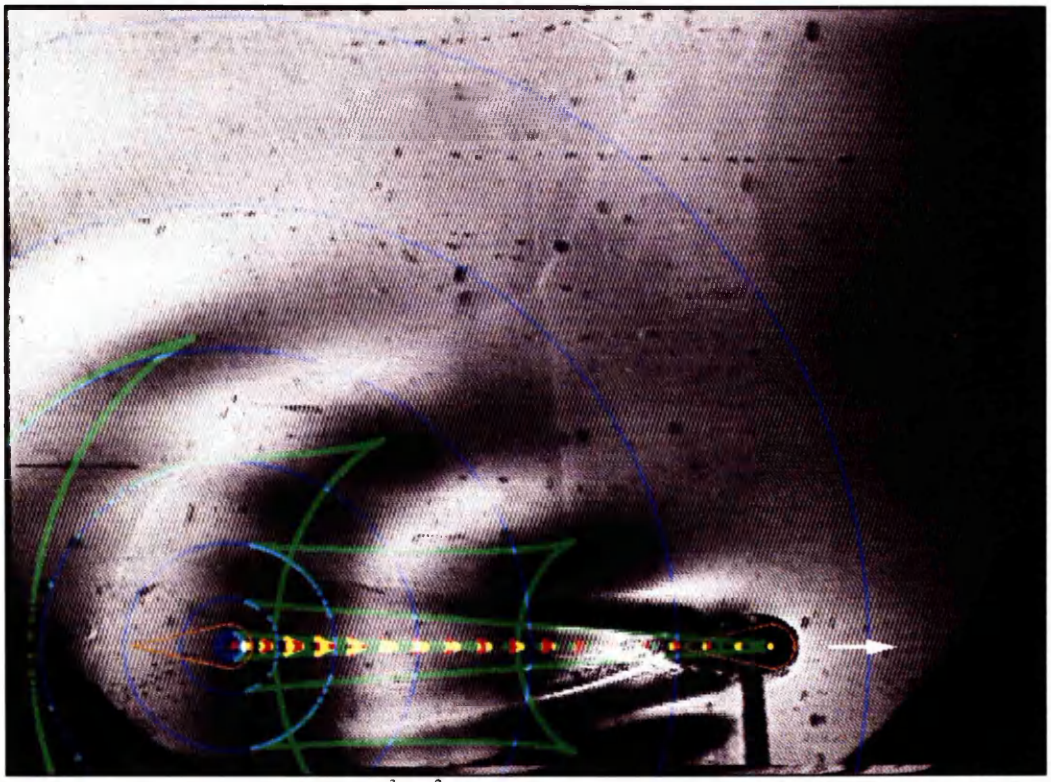

$U_i = 0$ m/s, $U_f = 7.6$ mm/s, $a = 2.5\times10^{-3}$ m/s^2, $t_a = 3$ s, $t_2 = 16.8$ s, $R_2 = 116$ mm, $M = 20.93$ and $\beta_f = 0.042$.

Figures 3.8 and 3.9. Plan-view mode 0 waves produced by an oscillating body moving horizontally in a pycnocline. The blue lines are impulsive waves, green lines are oscillatory waves. The red lines for figure 3.8 are steady waves but in figure 3.9, they are pseudo-steady due to acceleration. $N_c = 7.23$ rad/s, $\varepsilon = 0.022$ m, $\omega_f = 6.38$ rad/s.

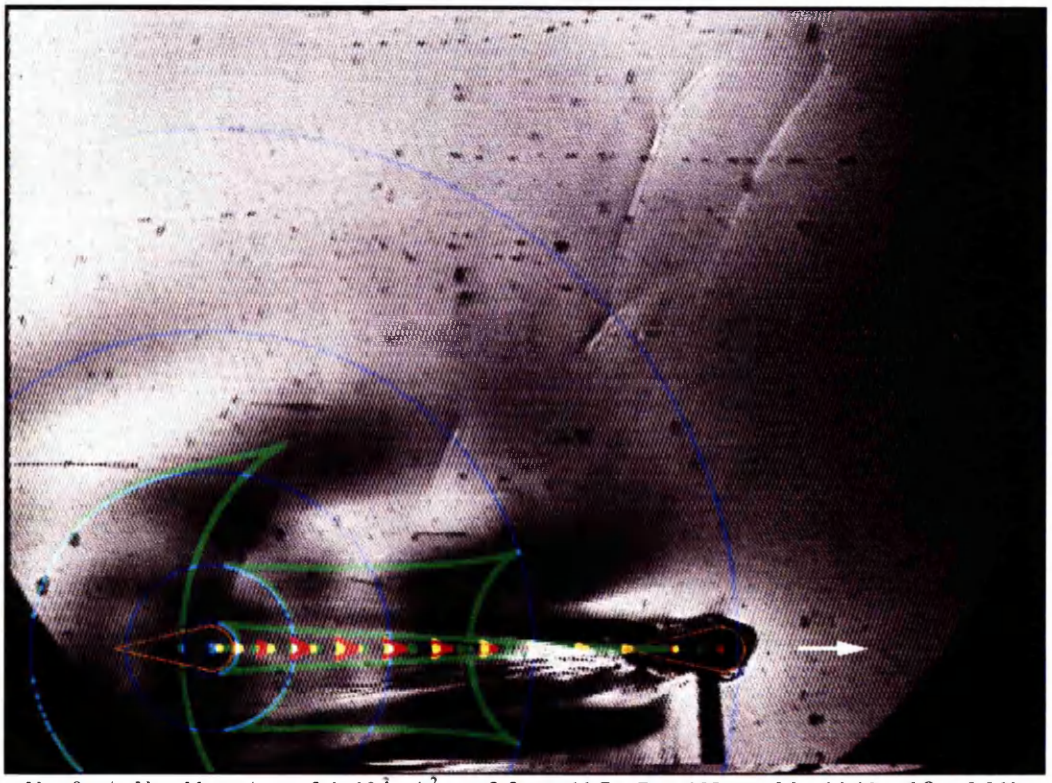

$U_i = 0$ m/s, $U_f = 11$ mm/s, $a = 3.1\times10^{-3}$ m/s^2, $t_a = 3.5$, $t_2 = 11.7$ s, $R_2 = 109$ mm, $M = 14.46$ and $\beta_f = 0.061$.

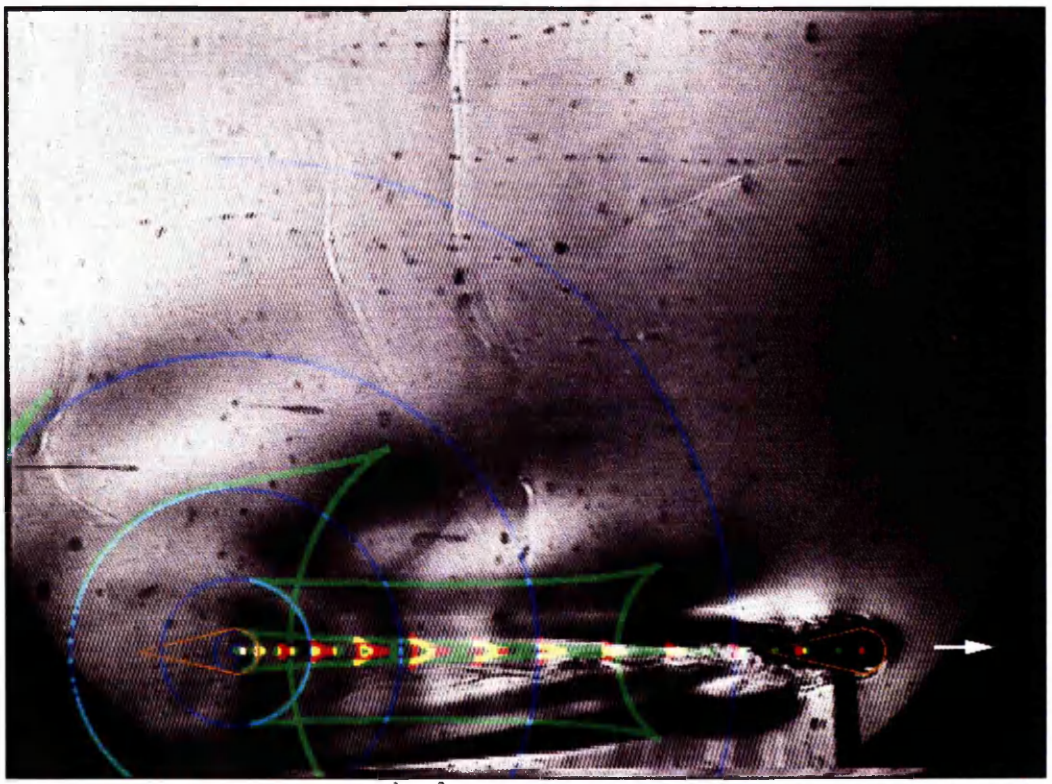

$U_i = 0$ m/s, $U_f = 14.4$ mm/s, $a = 3.2\times10^{-3}$ m/s^2, $t_a = 4.5$ s, $t_2 = 11.6$ s, $R_2 = 134$ mm, $M = 11.05$ and $\beta_f = 0.08$.

Figures 3.10 and 3.11. Plan-view mode 0 waves produced by an oscillating body moving horizontally in a pycnocline. The blue lines are impulsive waves, green lines are oscillatory waves and red lines are pseudo-steady waves because of acceleration. The arrow shows the direction of travel. $N_c = 7.23$ rad/s, $\varepsilon = 0.022$ m, $\omega_f = 6.38$ rad/s.

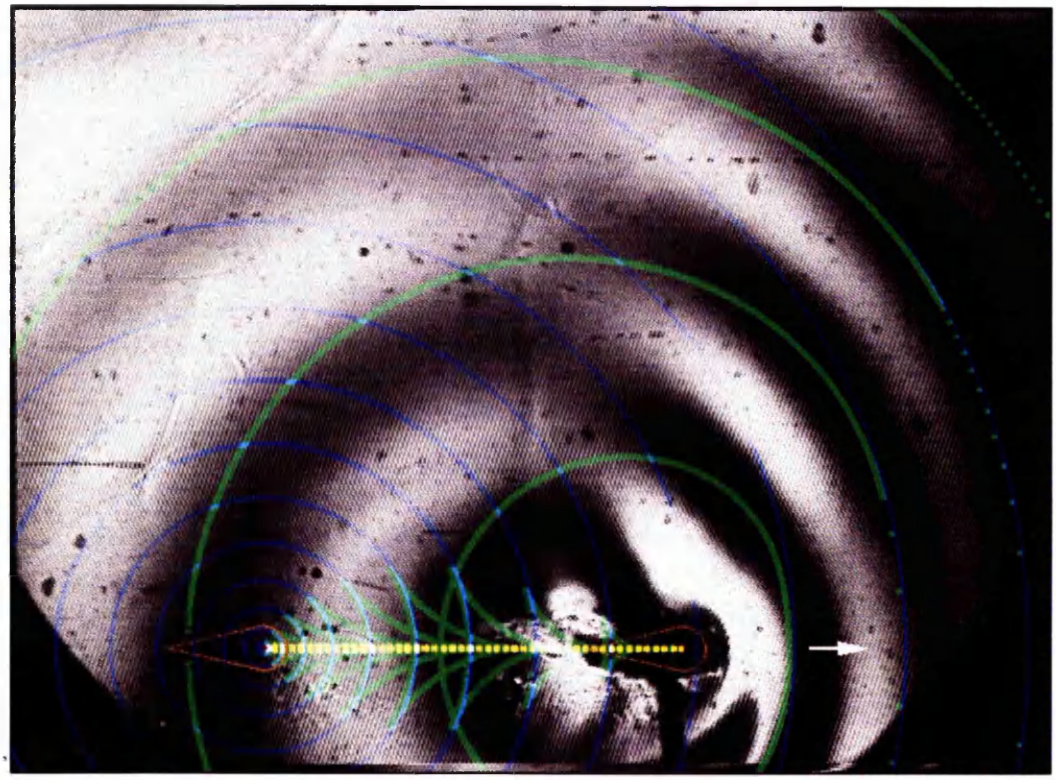

$U_i = 0$ m/s, $U_f = 2.16$ mm/s, $a = 2.0\times10^{-3}$ m/s^2, $t_a = 1.1$ s, $t_2 = 42.1$ s, $R_2 = 90$ mm, $M = 73.64$ and $\beta_f = 1.065\times10^{-2}$.

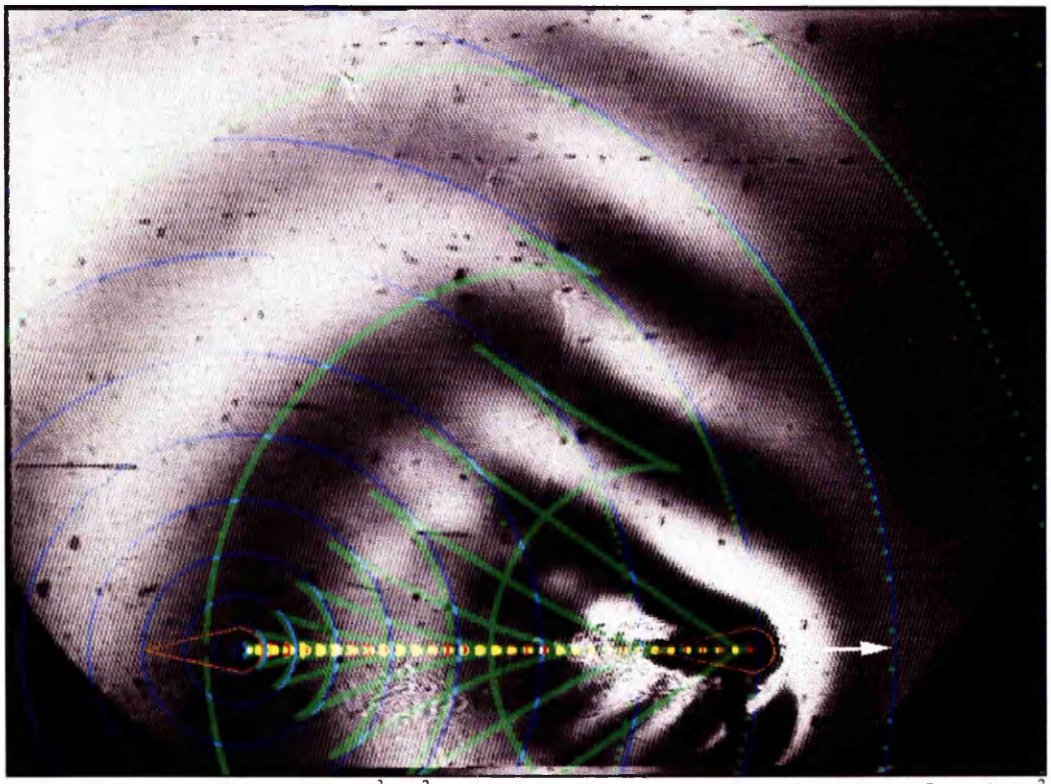

$U_i = 0$ m/s, $U_f = 3.85$ mm/s, $a = 1.3\times10^{-3}$ m/s^2, $t_a = 2.9$s, $t_2 = 29.8$ s, $R_2 = 109$ mm, $M = 41.31$ and $\beta_f = 1.9\times10^{-2}$.

Figures 3.12 and 3.13. Plan-view mode 0 waves produced by an oscillating body moving horizontally in a pycnocline. The blue lines are impulsive waves, green lines are oscillatory waves. The red lines for figure 3.12 are steady waves but they are pseudo-steady in figure 3.13. $N_c = 7.23$ rad/s, $\varepsilon = 0.022$ m, $\omega_f = 5.67$ rad/s.

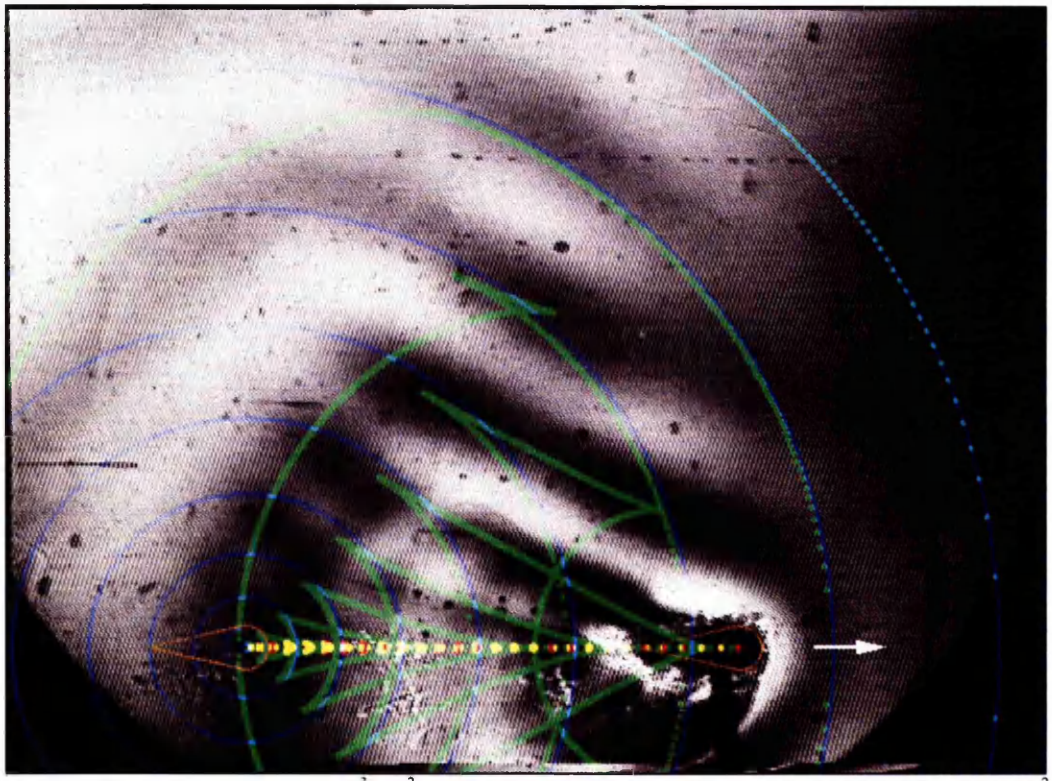

$U_i = 0$ m/s, $U_f = 4.5$ mm/s, $a = 2.1\times10^{-3}$ m/s^2, $t_a = 2.2$ s, $t_2 = 25.1$ s, $R_2 = 108$ mm, $M = 35.35$ and $\beta_f = 2.22\times10^{-2}$.

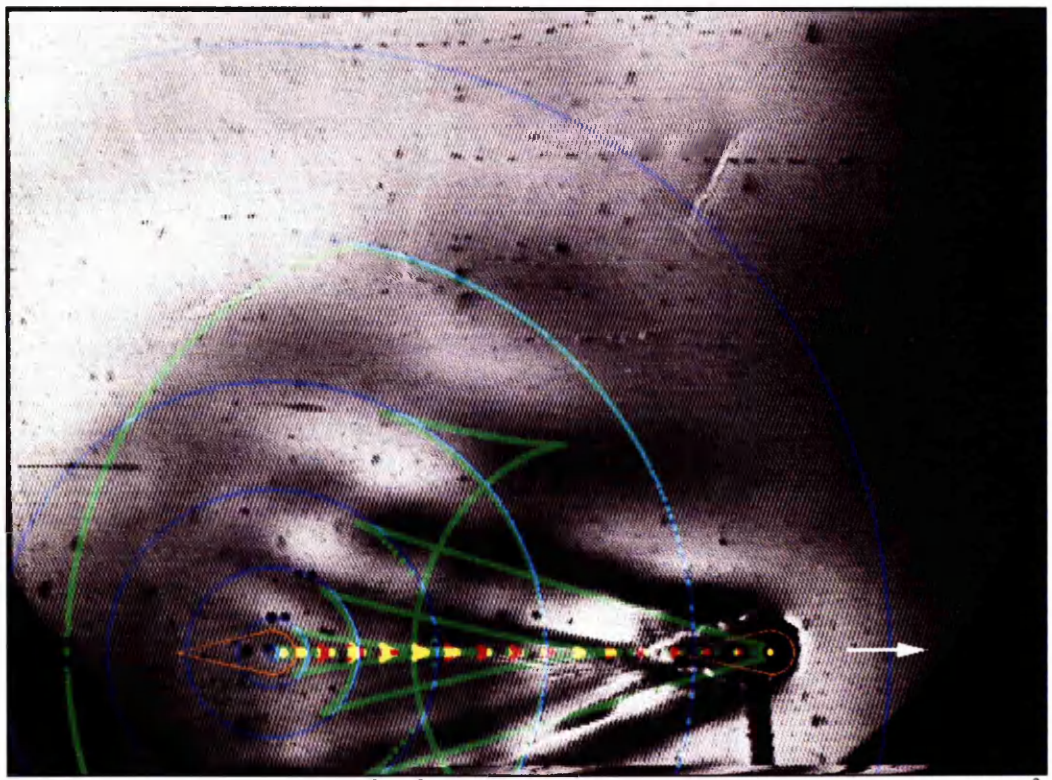

$U_i = 0$ m/s, $U_f = 7.6$ mm/s, $a = 2.5\times10^{-3}$ m/s^2, $t_a = 3$ s, $t_2 = 15.6$ s, $R_2 = 107$ mm, $M = 20.93$ and $\beta_f = 3.75\times10^{-2}$.

Figures 3.14 and 3.15. Plan-view mode 0 waves produced by an oscillating body moving horizontally in a pycnocline. The blue lines are impulsive waves, green lines are oscillatory waves and red lines are pseudo-steady waves. The arrow shows the direction of travel. $N_c = 7.23$ rad/s, $\varepsilon = 0.022$ m, $\omega_f = 5.67$ rad/s.

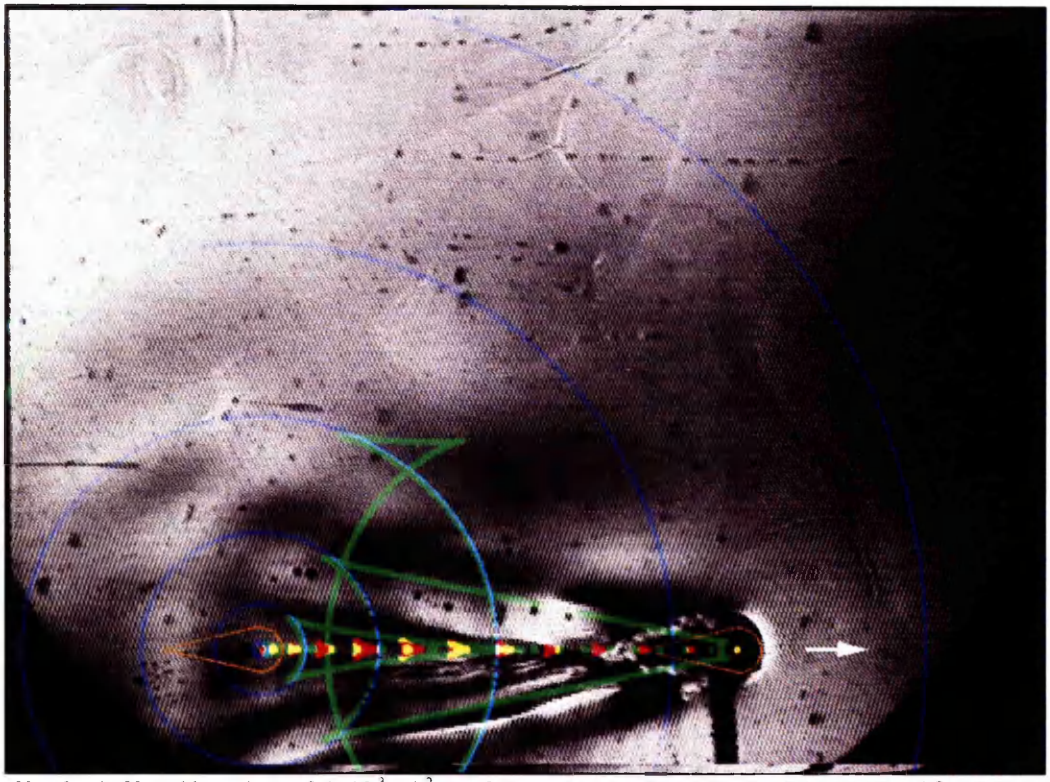

$U_i = 0$ m/s, $U_f = 11$ mm/s, $a = 3.1\times10^{-3}$ m/s^2, $t_a = 3.6$ s, $t_2 = 11.1$ s, $R_2 = 103$ mm, $M = 14.46$ and $\beta_f = 0.054$.

Figure 3.16. Plan-view mode 0 waves produced by an oscillating body moving horizontally in a pycnocline. The blue lines are impulsive waves, green lines are oscillatory waves and red lines are pseudo-steady waves. The arrow shows the direction of travel. $N_c = 7.23$ rad/s, $\varepsilon = 0.022$ m, $\omega_f = 5.67$ rad/s.

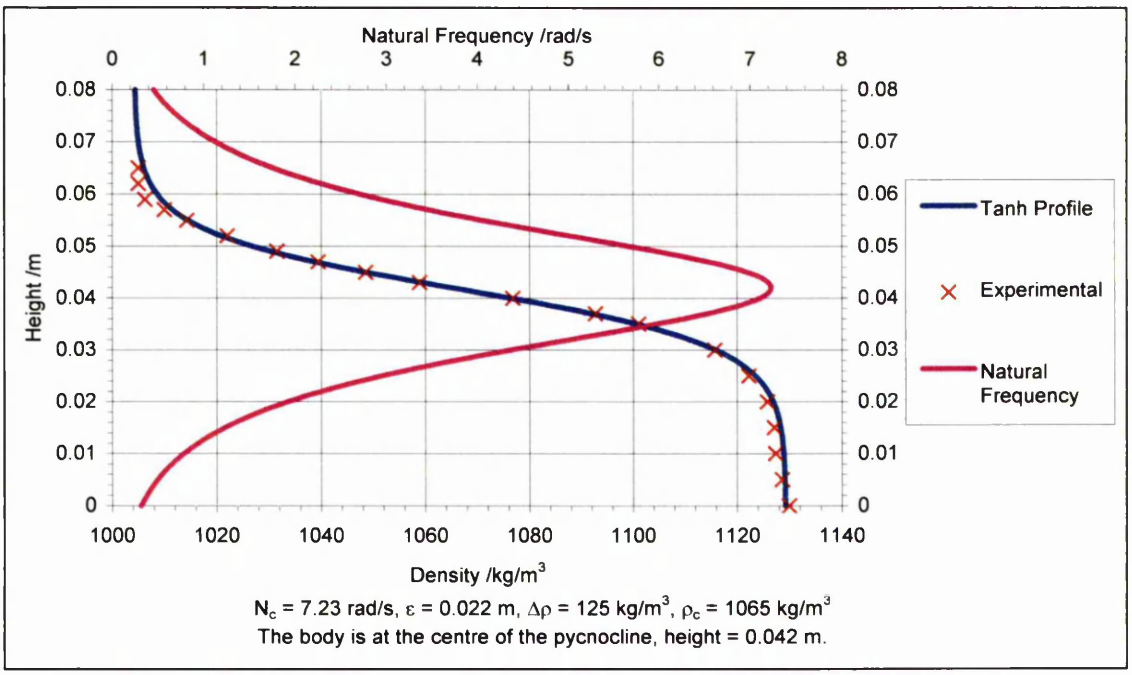

Figure 3.17 Density and frequency distributions of a pycnocline.

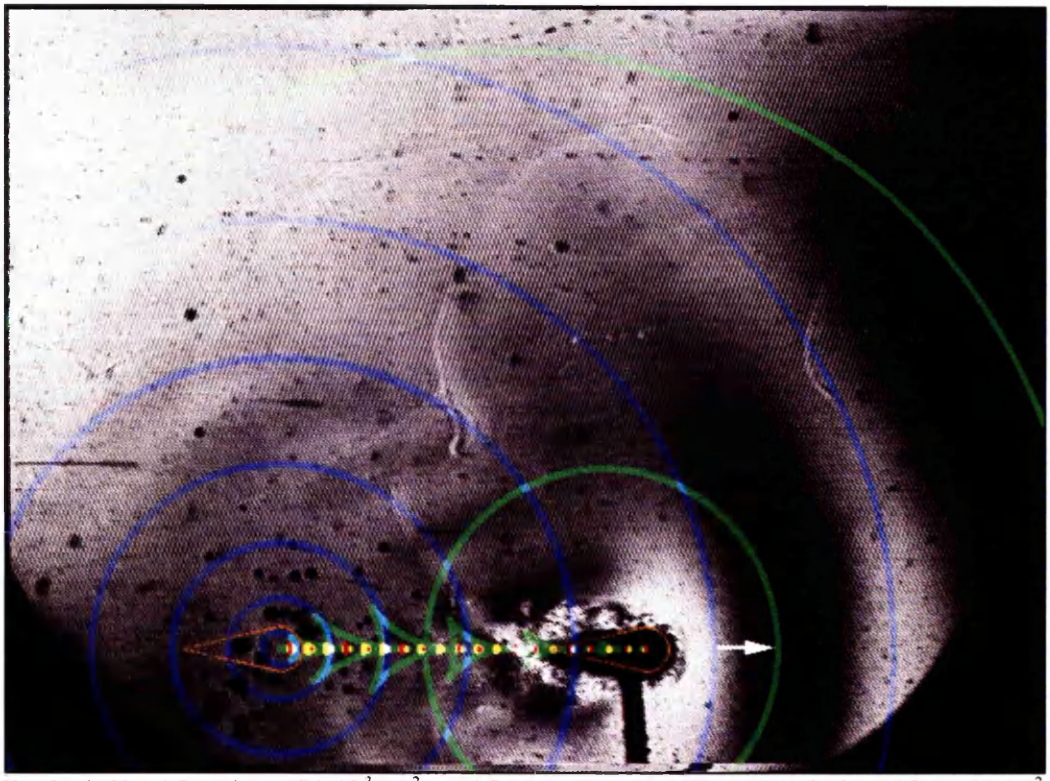

$U_i = 0$ m/s, $U_f = 4.5$ mm/s, $a = 6.4\times10^{-3}$ m/s^2, $t_a = 0.7$ s, $t_2 = 17.8$ s, $R_2 = 79$ mm, $M = 35.35$ and $\beta_f = 1.86\times10^{-2}$.

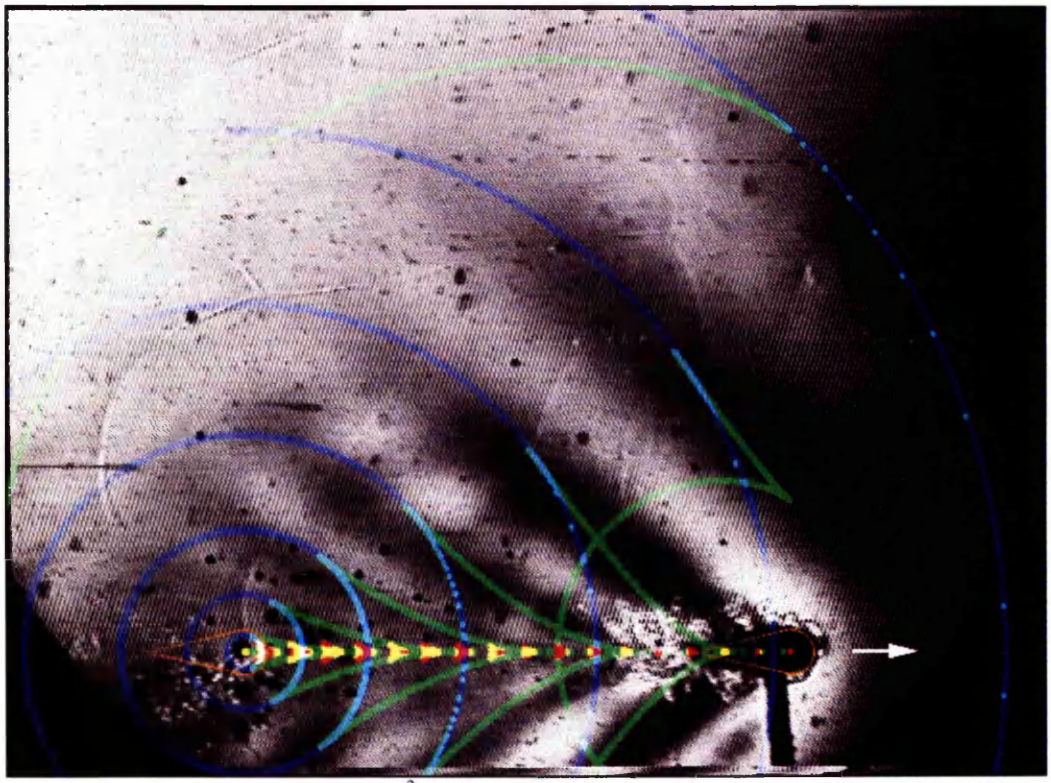

$U_i = 0$ m/s, $U_f = 7.8$ mm/s, $a = 0.39$ m/s^2, $t_a = 0.2$ s, $t_2 = 15.1$ s, $R_2 = 117$ mm, $M = 20.39$ and $\beta_f = 0.032$.

Figures 3.18 and 3.19. Plan-view mode 0 waves produced by an oscillating body moving horizontally in a pycnocline. The blue lines are impulsive waves, green lines are oscillatory waves and red lines are steady waves. The arrow shows the direction of travel. $N_c = 7.23$ rad/s, $\varepsilon = 0.022$ m, $\omega_f = 4.75$ rad/s.

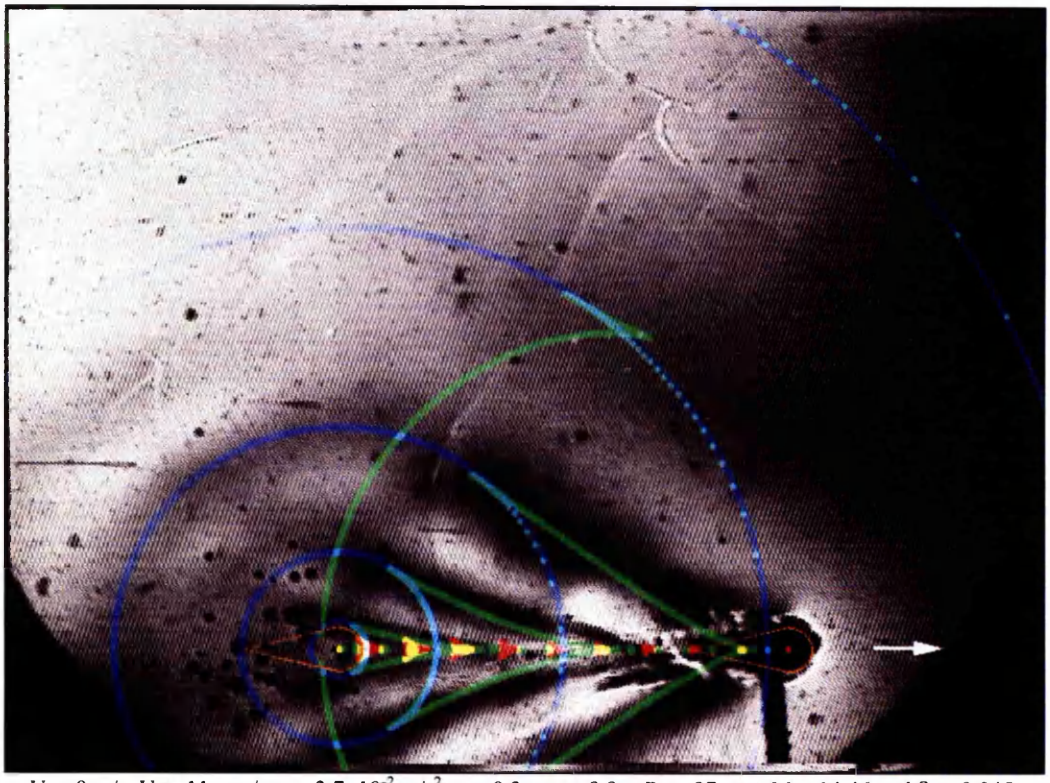

$U_i = 0$ m/s, $U_f = 11$ mm/s, $a = 3.7\times10^{-2}$ m/s^2, $t_a = 0.3$ s, $t_2 = 8.9$ s, $R_2 = 97$ mm, $M = 14.46$ and $\beta_f = 0.045$.

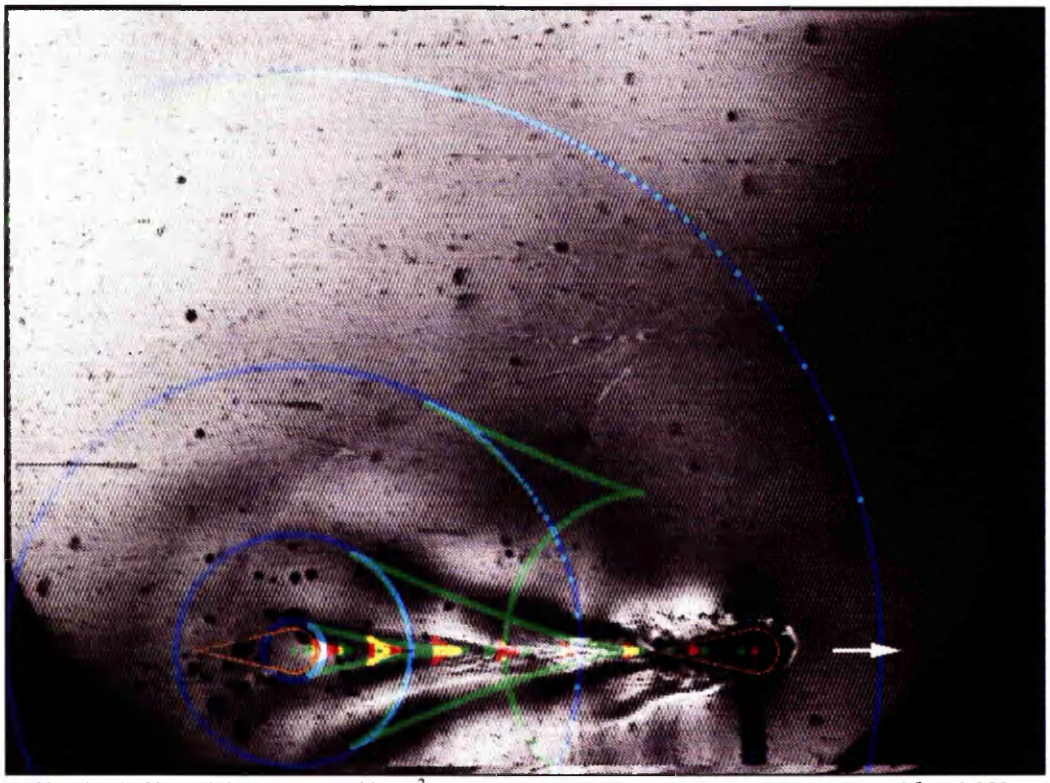

$U_i = 0$ m/s, $U_f = 14.4$ mm/s, $a = 0.32$ m/s^2, $t_a = 0.45$ s, $t_2 = 7.1$ s, $R_2 = 99$ mm, $M = 11.05$ and $\beta_f = 0.059$.

Figures 3.20 and 3.21. Plan-view mode 0 waves produced by an oscillating body moving horizontally in a pycnocline. The blue lines are impulsive waves, green lines are oscillatory waves and red lines are steady waves. The arrow shows the direction of travel. $N_c = 7.23$ rad/s, $\varepsilon = 0.022$ m, $\omega_f = 4.75$ rad/s.

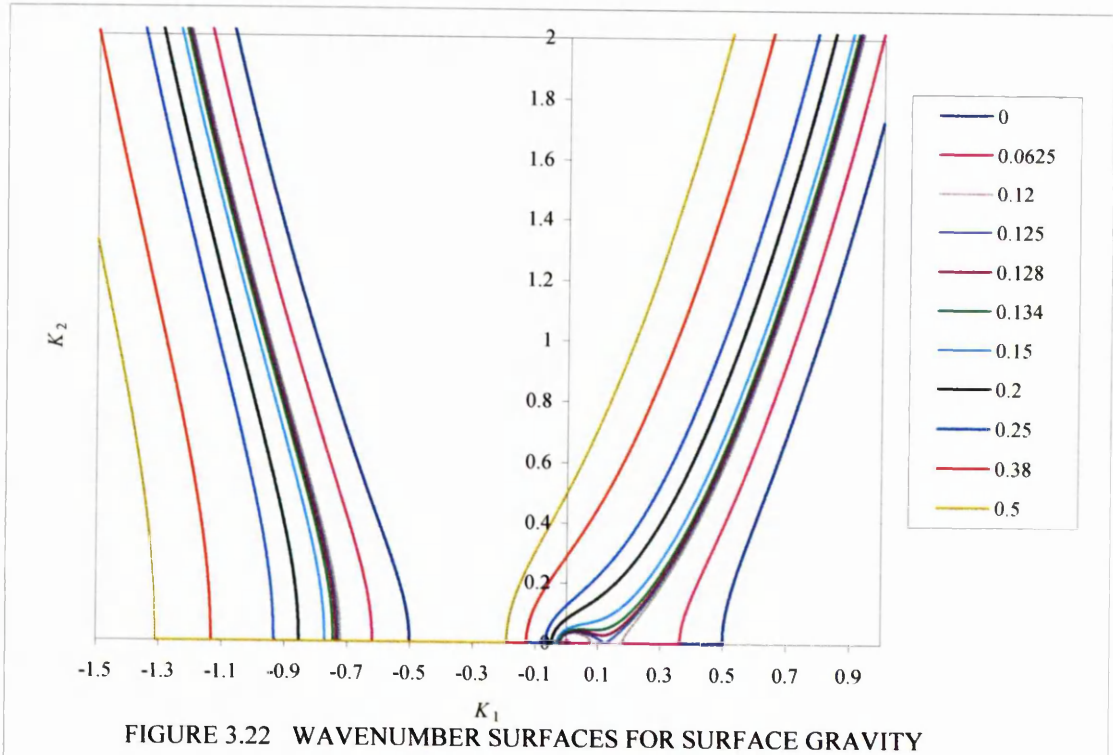

FIGURE 3.22 WAVENUMBER SURFACES FOR SURFACE GRAVITY WAVES

$M \to 0$, $n = 0$, $\varepsilon N_c^2 = 2g$, $\varepsilon \to 0$ and $N_c \to \infty$.

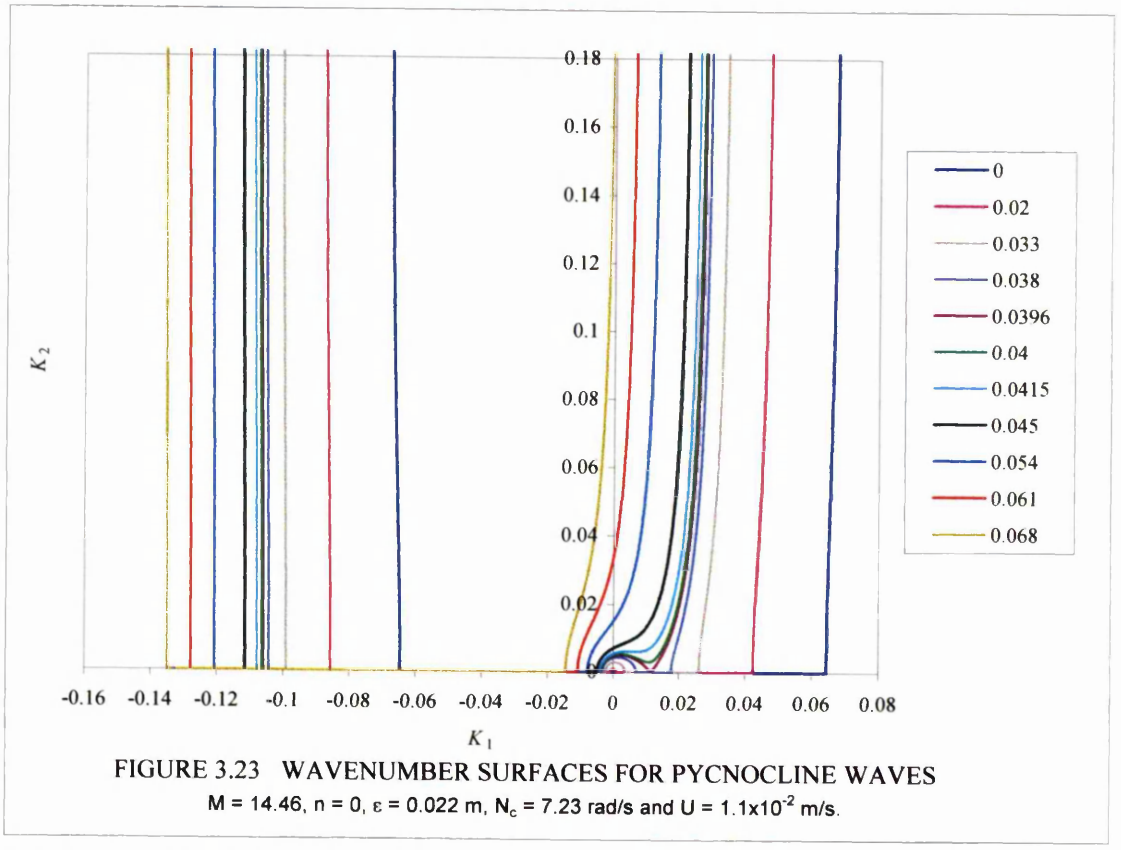

FIGURE 3.23 WAVENUMBER SURFACES FOR PYCNOCLINE WAVES

$M = 14.46$, $n = 0$, $\varepsilon = 0.022$ m, $N_c = 7.23$ rad/s and $U = 1.1 \times 10^{-2}$ m/s.

The legend shows the values of β_f.

Each value of β_f produces two curves, the right curve has $+\beta$ while the left curve has $-\beta$.

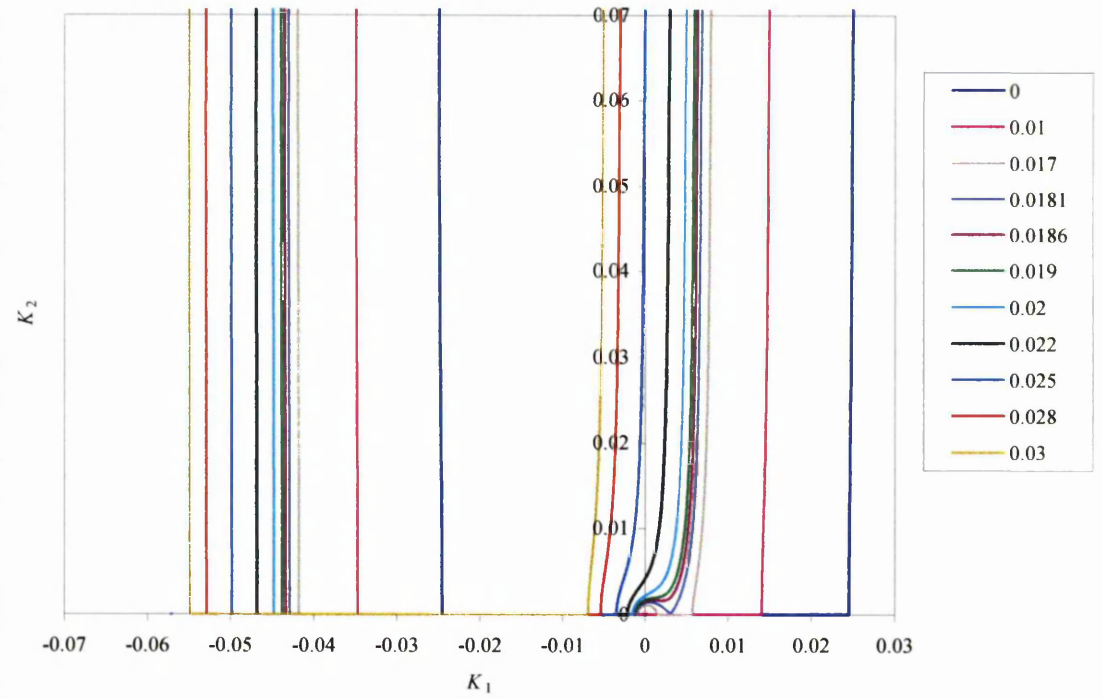

FIGURE 3.24 WAVENUMBER SURFACES FOR PYCNOCLINE WAVES

M = 39.47, n = 0, ε = 0.022 m, N_c = 7.23 rad/s and U = 4.03x10^{-3} m/s.

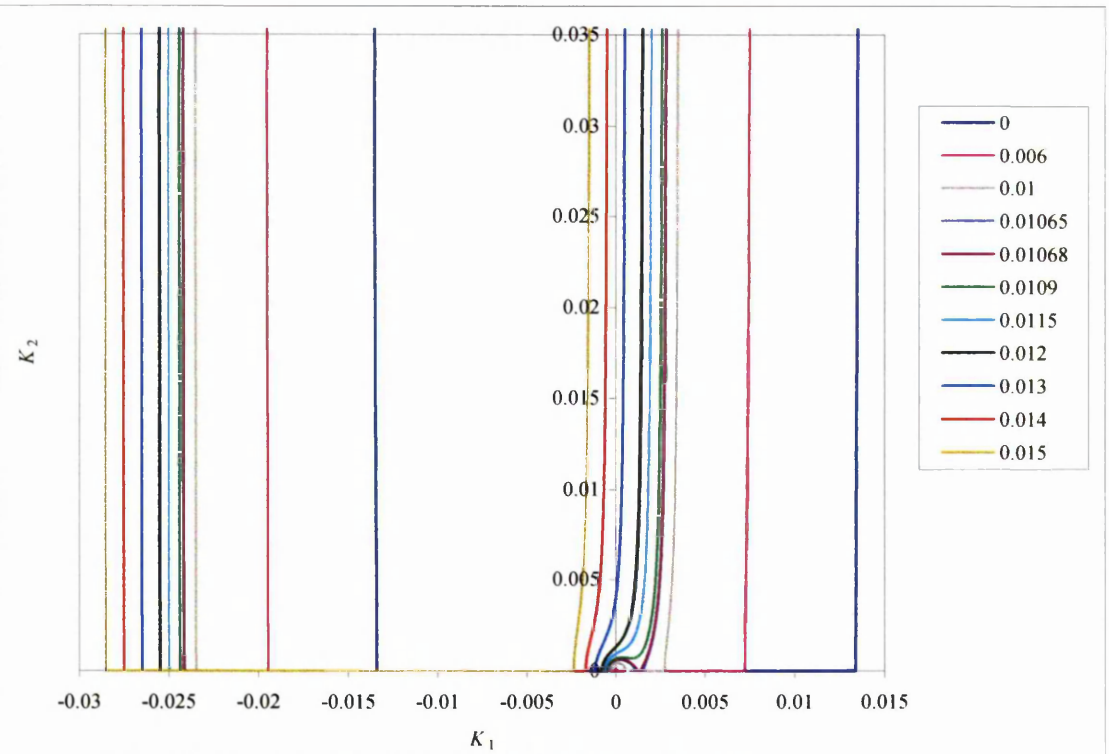

FIGURE 3.25 WAVENUMBER SURFACES FOR PYCNOCLINE WAVES

M = 73.64, n = 0, ε = 0.022 m, N_c = 7.23 rad/s and U = 2.16x10^{-3} m/s.

The legends show the values of β_f.

Each value of β_f produces two curves, the right curve has $+\beta$ while the left curve has $-\beta$.

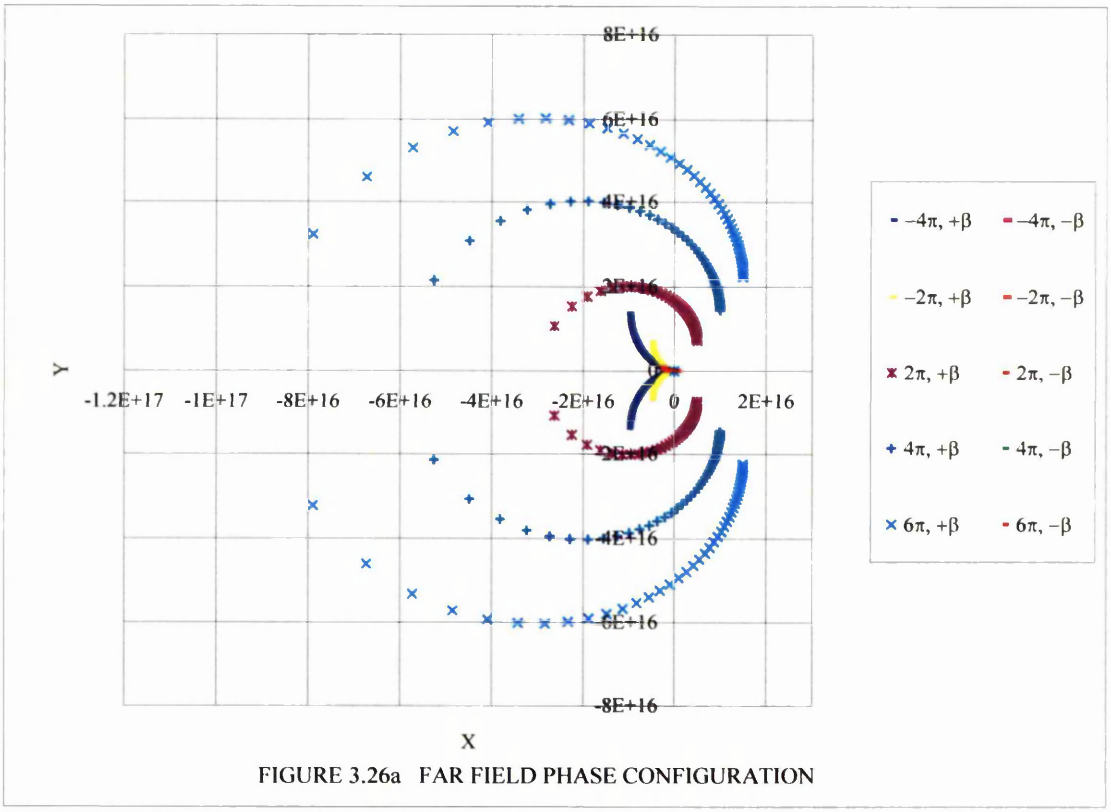

FIGURE 3.26a FAR FIELD PHASE CONFIGURATION

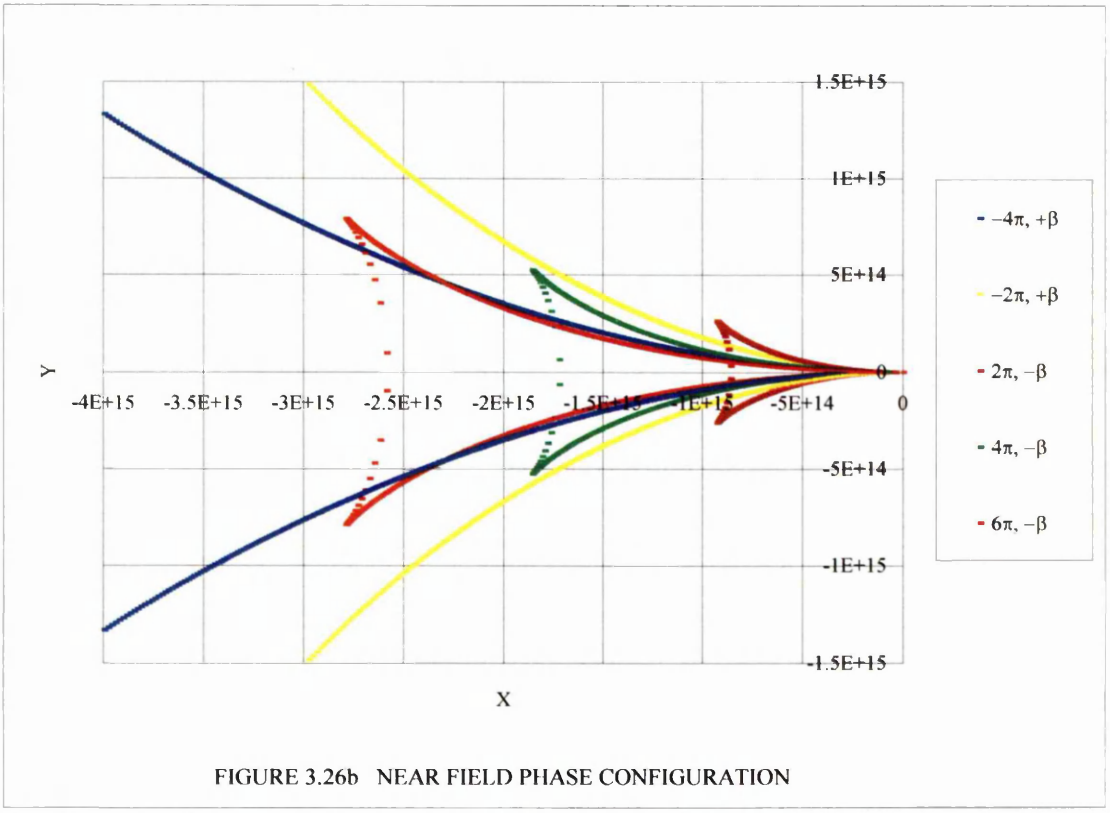

FIGURE 3.26b NEAR FIELD PHASE CONFIGURATION

Oscillatory surface gravity waves produced by an oscillating and moving body.
The legends show the phases and the sign of β. The right branch of the 2 wavenumber surfaces has +β and the left branch has -β.
M = 0, β_f = 0.125, εN_c^2 = 2g m/s^2, U = 1 m/s, ω_f = 2.54 rad/s and n = 0.

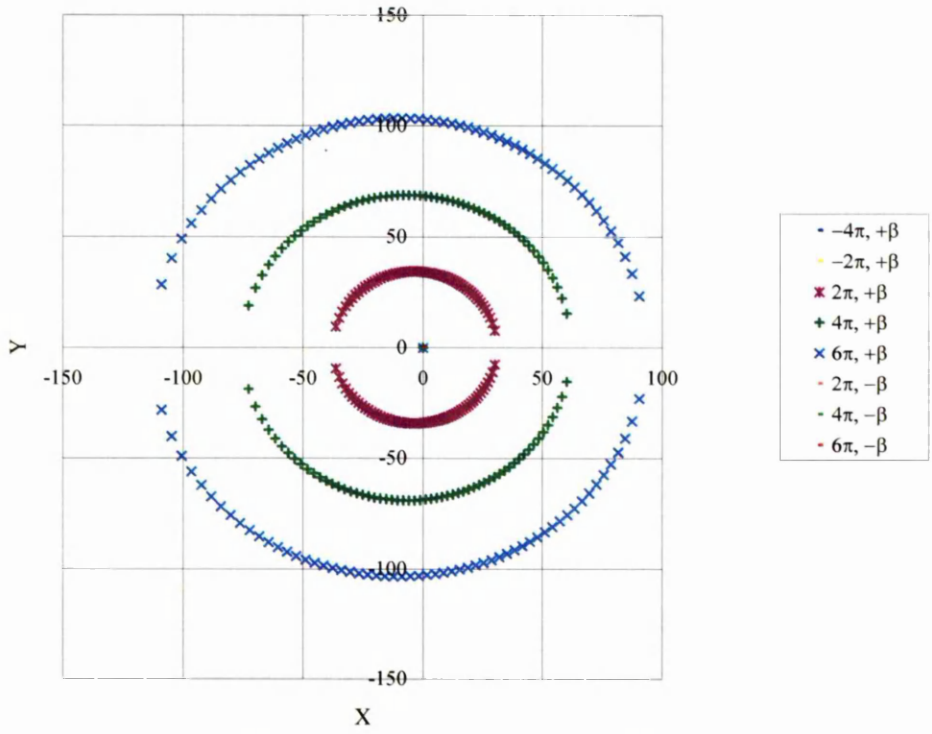

FIGURE 3.27a FAR FIELD PHASE CONFIGURATION

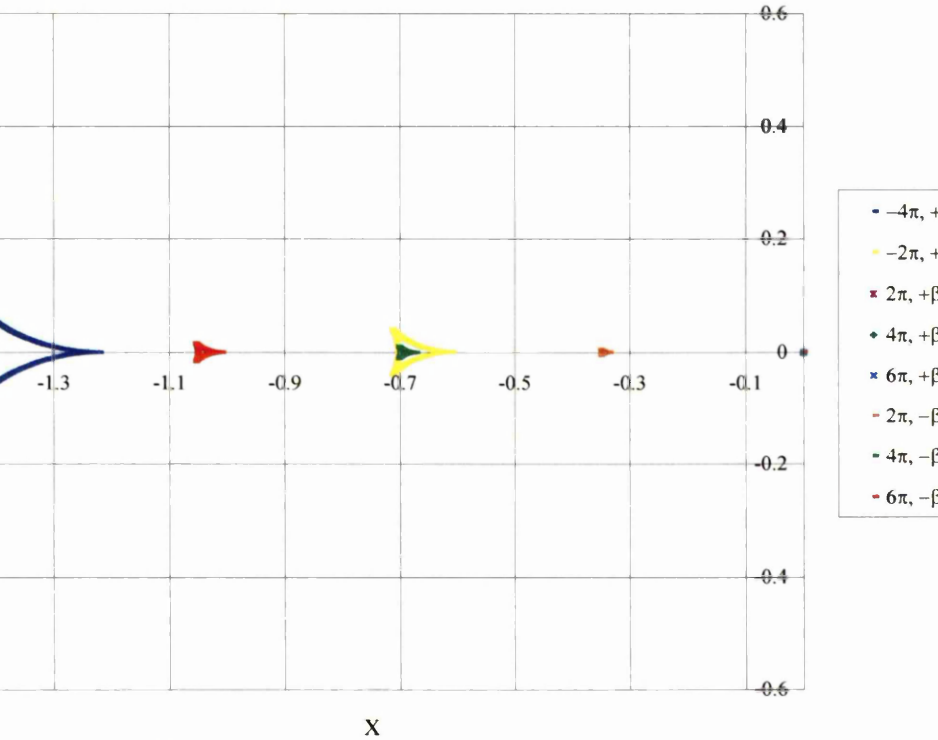

FIGURE 3.27b NEAR FIELD PHASE CONFIGURATION

Oscillatory pycnocline waves produced by an oscillating and moving body.
The legends show the phases and the sign of β. The right branch of the 2 wavenumber surfaces has +β and the left branch has -β.
M= 14.46, β_f = 0.02, ε = 0.022 m, N_c = 7.23 rad/s, U = 0.011 m/s, ω_f = 2.09 rad/s and n= 0.

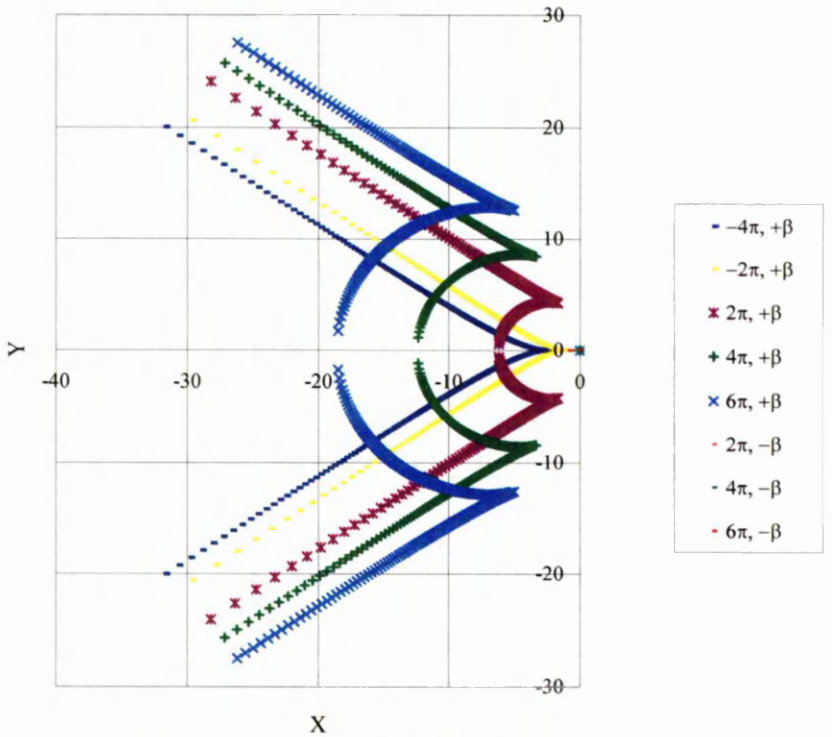

FIGURE 3.28a FAR FIELD PHASE CONFIGURATION

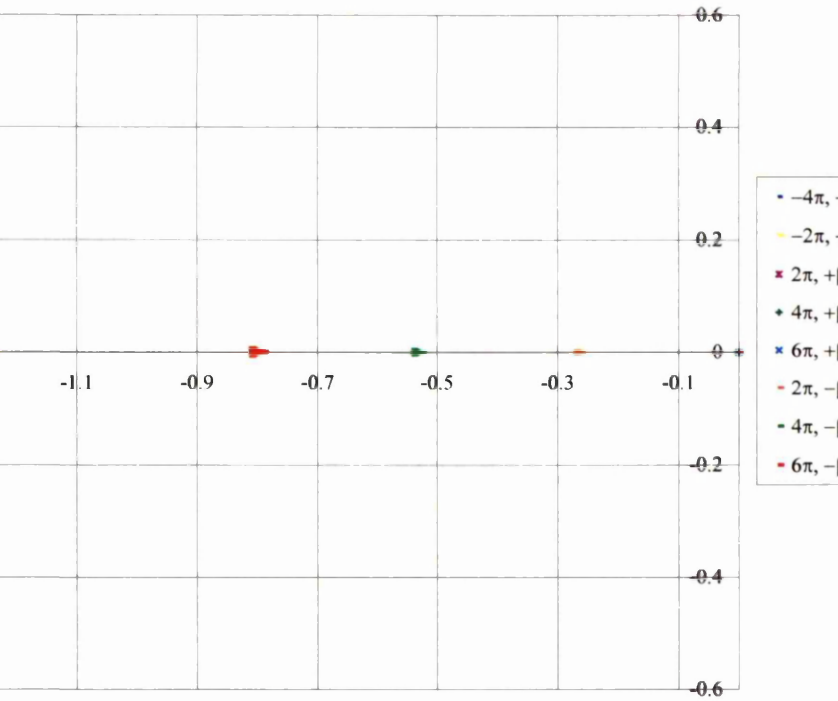

FIGURE 3.28b NEAR FIELD PHASE CONFIGURATION

Oscillatory pycnocline waves produced by an oscillating and moving body.
The legends show the phases and the sign of β. The right branch of the 2 wavenumber surfaces has +β and the left branch has -β.
M= 14.46, β_f = 0.045, ε= 0.022 m, N_c = 7.23 rad/s, U= 0.011 m/s, ω_f = 4.75 rad/s and n = 0.

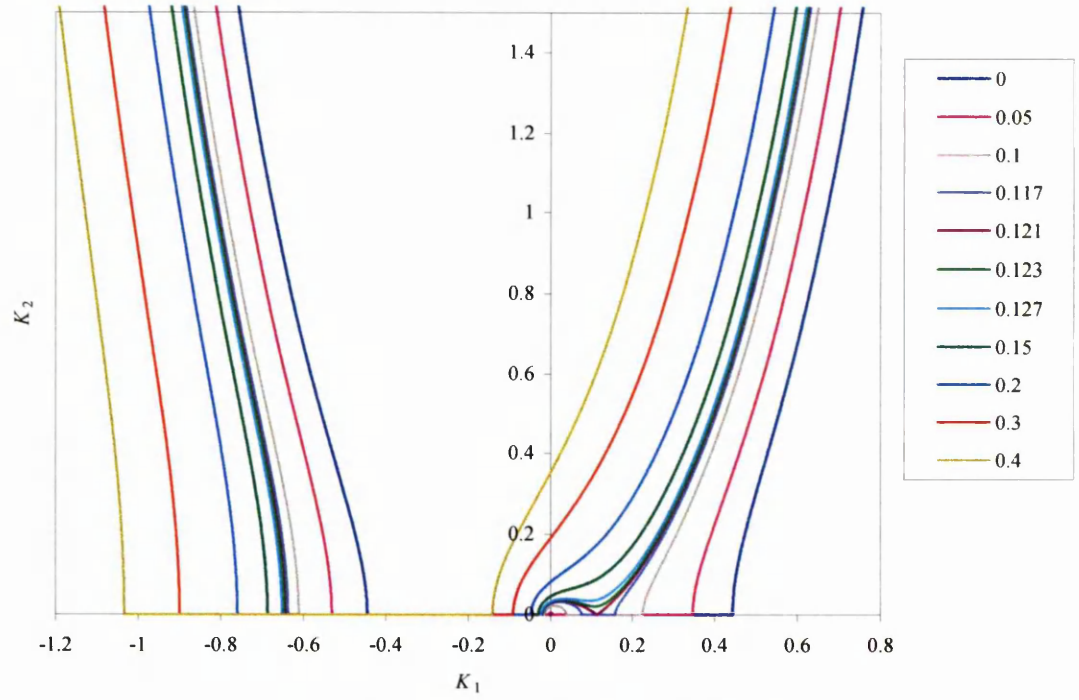

FIGURE 3.29 WAVENUMBER SURFACES FOR PYCNOCLINE WAVES
M = 0.75, n = 0, ε = 100 m, N_c = 0.015 rad/s and U = 2 m/s.

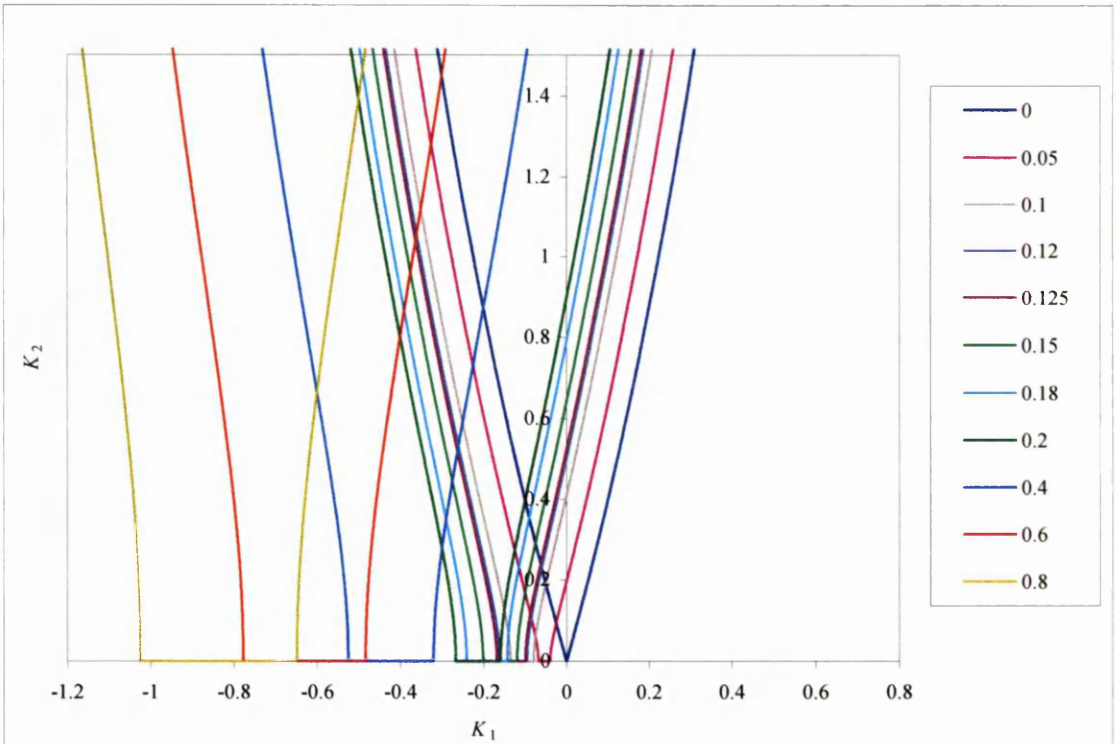

FIGURE 3.30 WAVENUMBER SURFACES FOR PYCNOCLINE WAVES
M = 0.75, n = 1, ε = 100 m, N_c = 0.015 rad/s and U = 2 m/s.

The legend shows the values of β_f.

Each value of β_f produces two curves, the right curve has $+\beta$ while the left curve has $-\beta$.

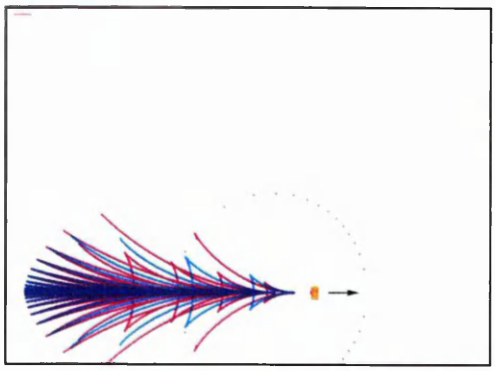

$\omega_f = 1.125\times10^{-3}$ rad/s, $\beta_f = 0.1$.

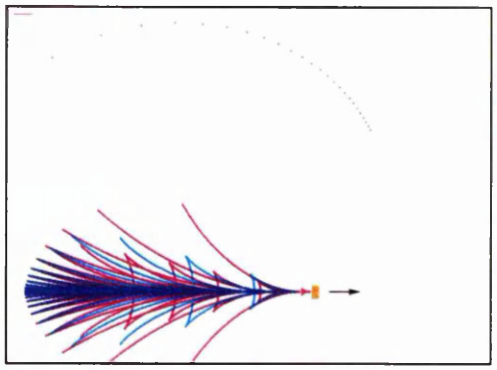

$\omega_f = 1.361\times10^{-3}$ rad/s, $\beta_f = 0.121$.

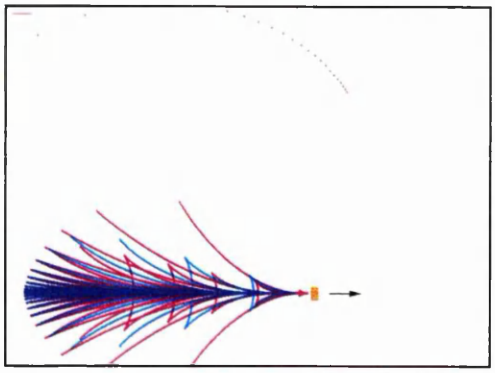

$\omega_f = 1.406\times10^{-3}$ rad/s, $\beta_f = 0.125$.

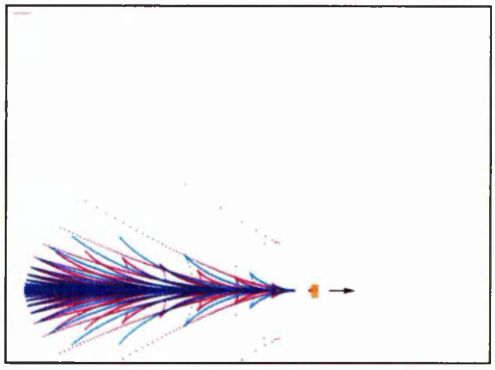

$\omega_f = 2.25\times10^{-3}$ rad/s, $\beta_f = 0.2$.

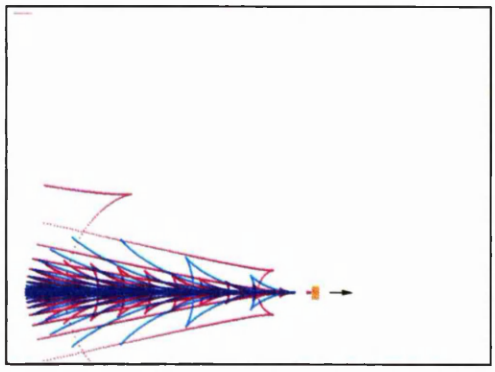

$\omega_f = 4.5\times10^{-3}$ rad/s, $\beta_f = 0.4$.

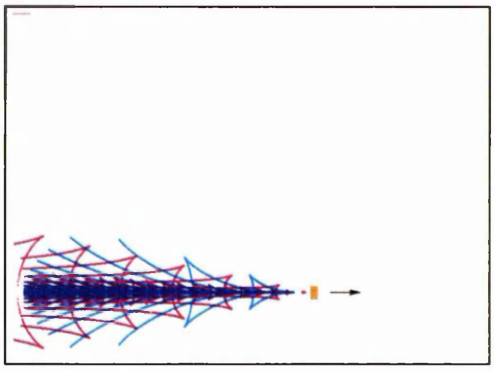

$\omega_f = 1.125\times10^{-2}$ rad/s, $\beta_f = 1.0$.

Figure 3.31 Pycnocline waves in the ocean.

$U = 2$ m/s, $t = 6000$ s, $n = 0$.
$N_c = 0.015$ rad/s, $\varepsilon = 100$ m.
β_f is defined as $\frac{U\omega_f}{\varepsilon N_c^2}$ and $M = \frac{\varepsilon N_c}{U} = 0.75$.

The distance across each frame is 20,000 m. The blue dots are the steady waves and the pink dots are the oscillatory waves. The arrow shows the direction of travel. Impulsive waves are not shown.

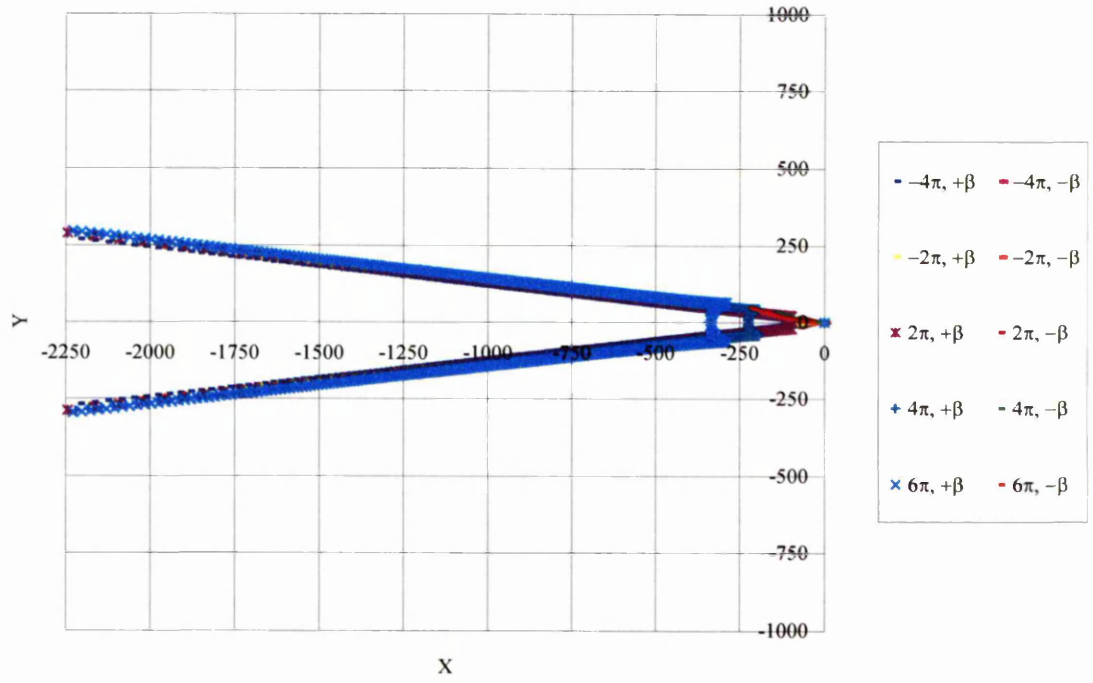

FIGURE 3.32a FAR FIELD PHASE CONFIGURATION

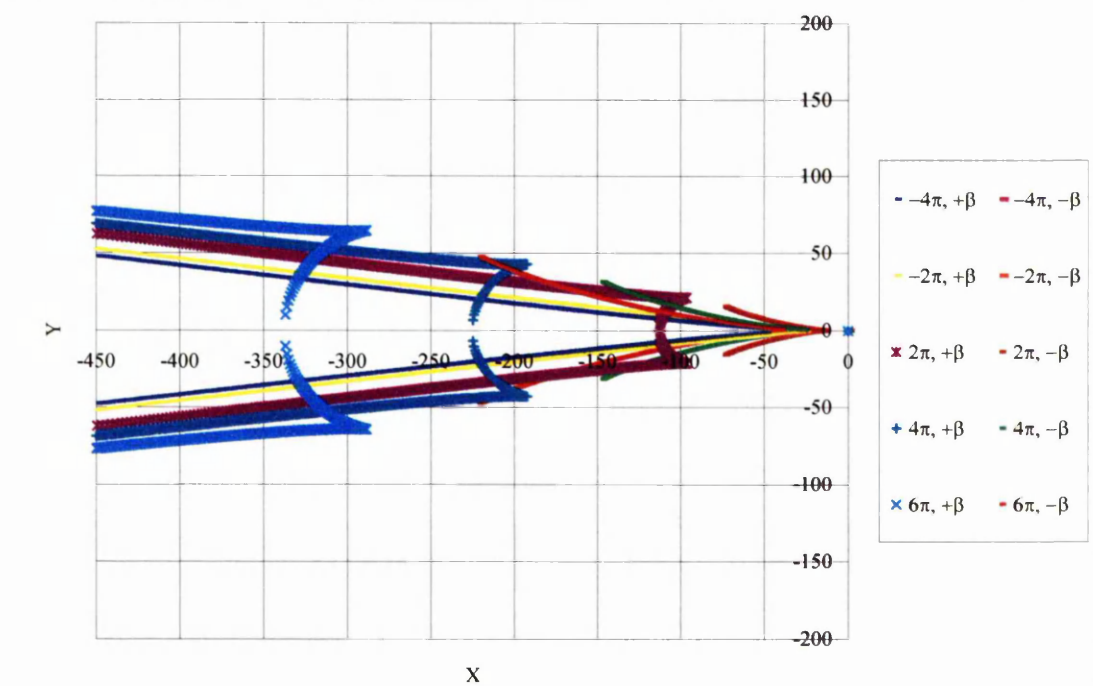

FIGURE 3.32b NEAR FIELD PHASE CONFIGURATION

Oscillatory pycnocline waves produced by an oscillating and moving body.
The legends show the phases and the sign of β_f. The right branch of the 2 wavenumber surfaces has $+\beta$ and the left branch has $-\beta$.
M = 0.75, β_f = 0.125, N_c = 0.015 rad/s, ε = 100 m, U = 2 m/s, $\omega_f = 1.4 \times 10^{-3}$ rad/s and n = 1.

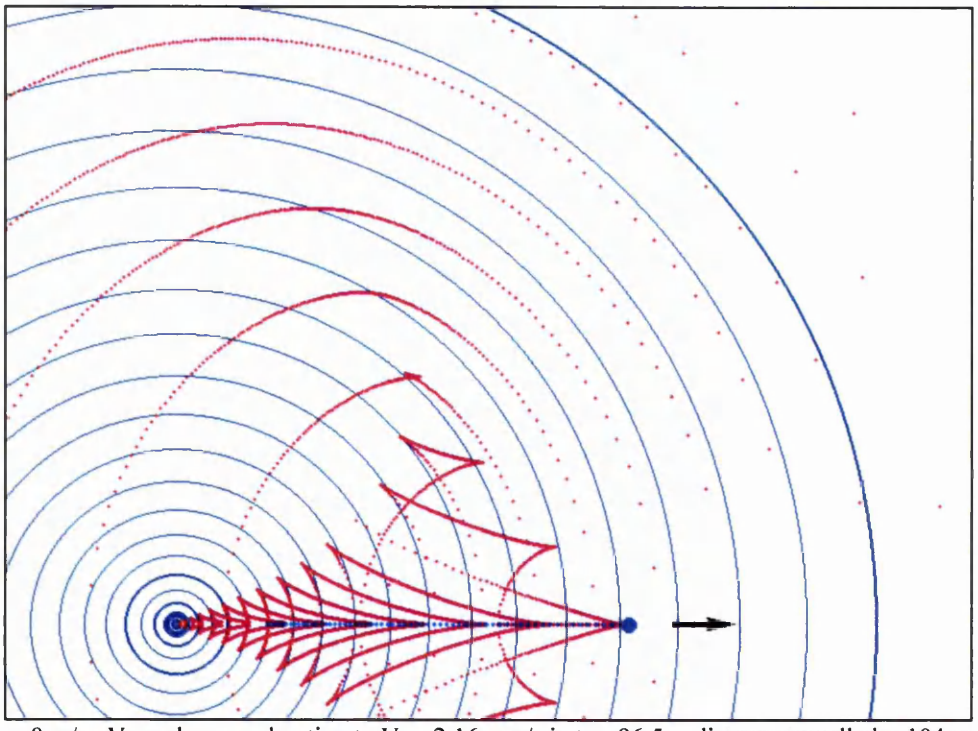

U_i = 0 m/s. Very slow acceleration to U_f = 2.16 mm/s in t_a = 96.5 s, distance travelled = 104 mm.

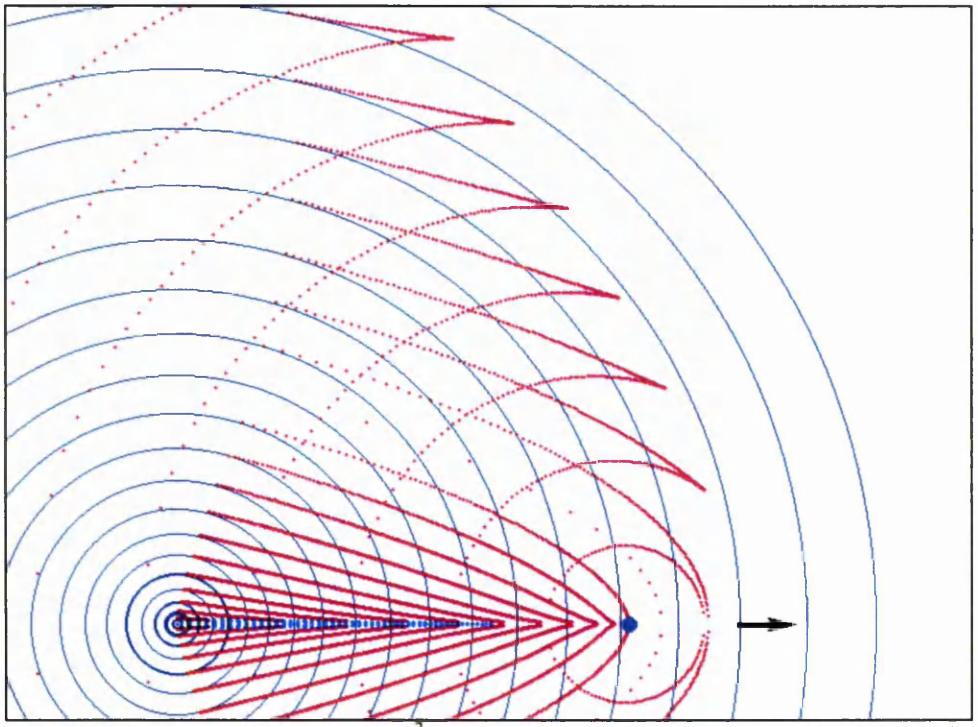

U_i = 0 m/s. Impulsive start with a = 2.24 m/s^2 to U_{max} = 2.16 mm/s, slow constant deceleration for 96.5 s to U_f = 0 m/s. Total time = 96.5 s, distance travelled = 104 mm.

Figures 3.33 and 3.34. Mode 0 pycnocline waves from an oscillating point source travelling horizontally in a pycnocline. The top figure shows an accelerating source and the bottom figure shows the decelerating case for the same distance travelled. The blue circles are the impulsive waves, the pink dots are the oscillatory waves and the pale blue dots are the non-oscillatory waves. N_c = 7.23 rad/s, ε = 0.022 m, ω_f = 6.38 rad/s.

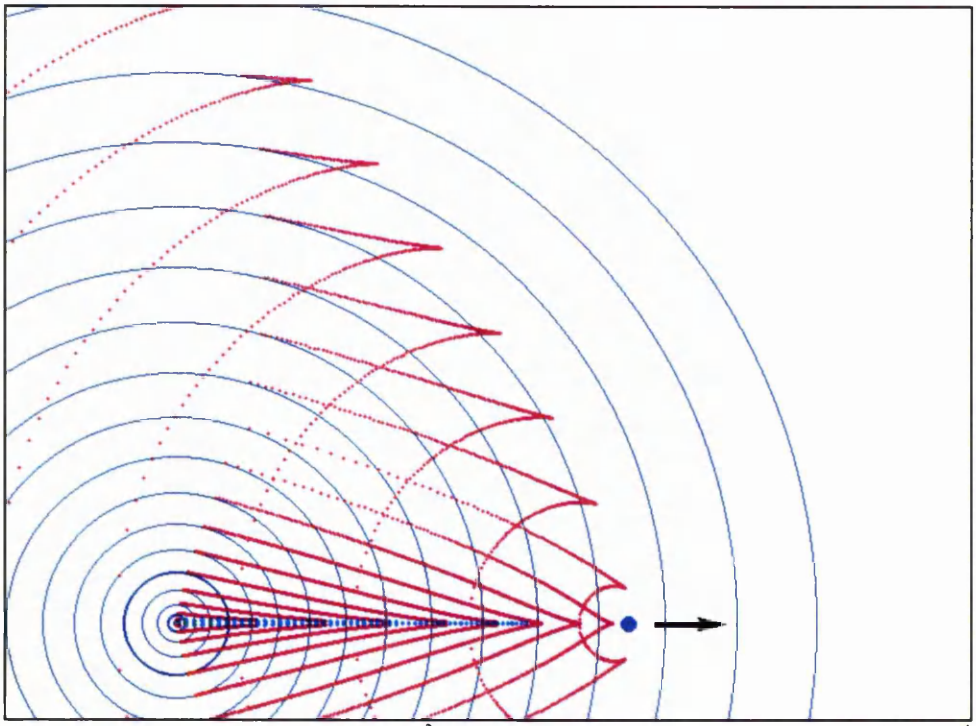

U_i = 0 m/s. Impulsive start with a = 2.24 m/s^2 to U_{max} = 2.16 mm/s, decelerates to $U_f = 7.2\times10^{-4}$ m/s in 72.4 s. Total time =72.4 s, distance travelled = 104 mm.

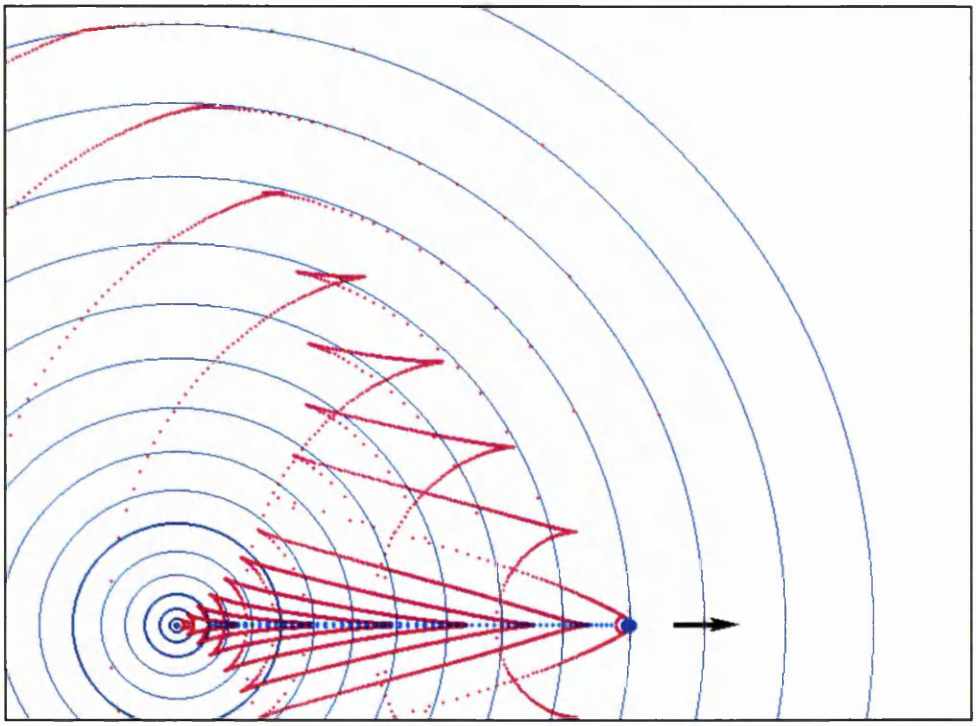

U_i = 0 m/s. Accelerates for 19.3 s to constant U_{max} = 2.16 mm/s, travels at U_{max} for 16.9 s, slow constant deceleration for 28.9 s to $U_f = 1.08\times10^{-3}$ m/s. Total time = 65.1 s, distance travelled = 104 mm.

Figures 3.35 and 3.36. Mode 0 pycnocline waves from an oscillating point source travelling horizontally in a pycnocline. The top figure shows an impulsive start to U_{max} and then decelerates to U_f. The bottom figure shows a constant acceleration to U_{max}, stays at U_{max}, and then decelerates to U_f. N_c = 7.23 rad/s, ε = 0.022 m and ω_f = 6.38 rad/s.

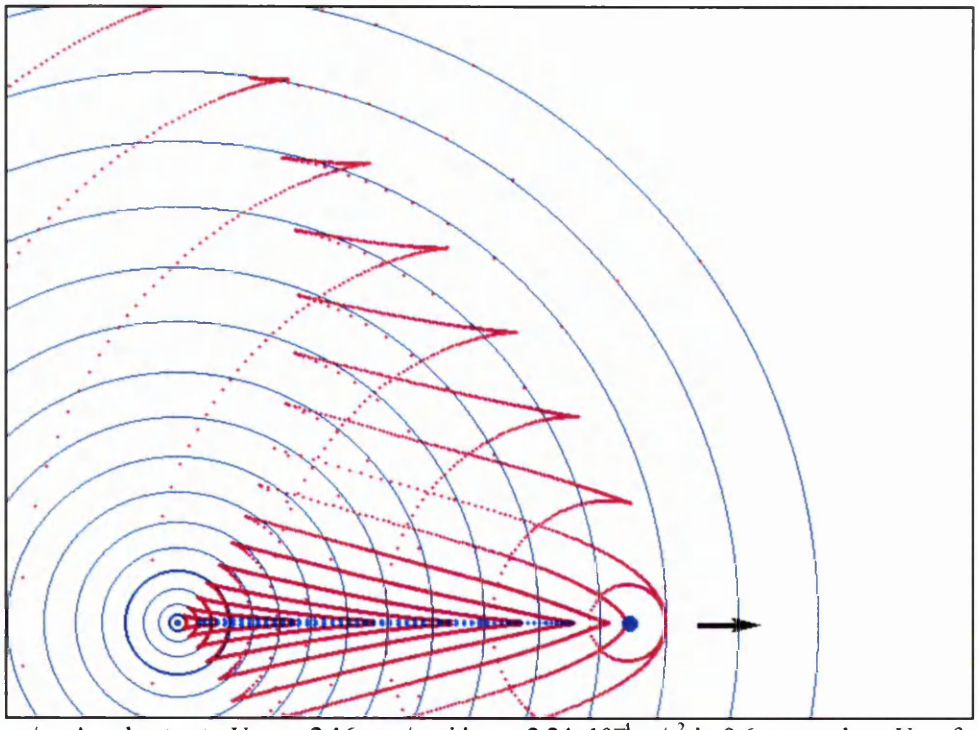

U_i = 0 m/s. Accelerates to U_{max} = 2.16 mm/s with a = 2.24×10^{-4} m/s^2 in 9.6 s, travels at U_{max} for 24.1s and decelerates to U_f =0 m/s in 38.6 s. Total time =72.3 s, distance travelled = 104 mm.

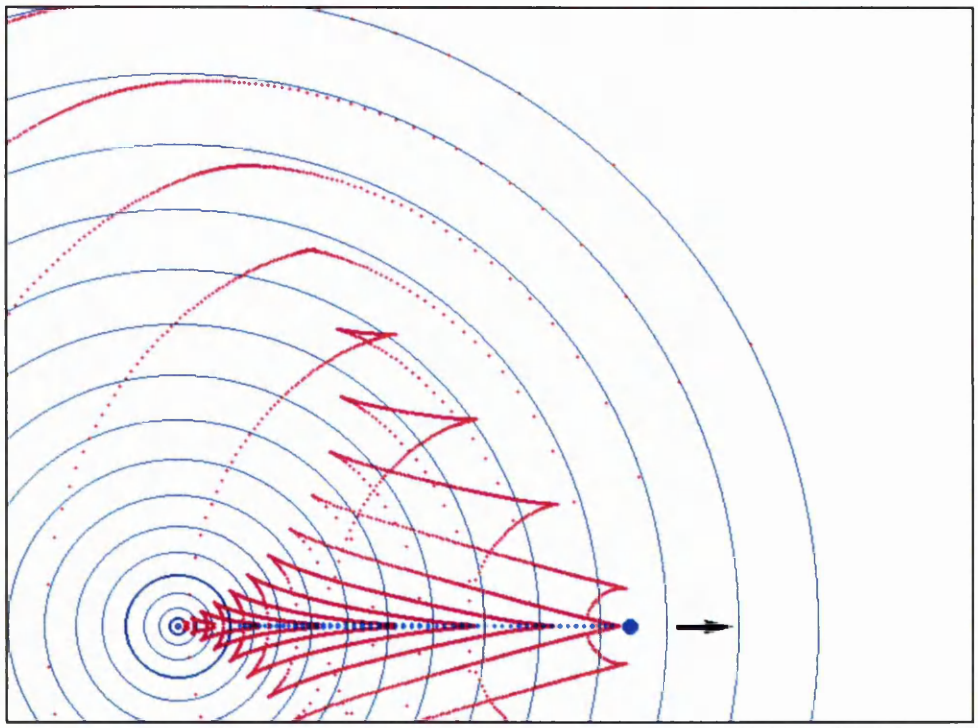

U_i = 0 m/s. Accelerates to U_{max} = 2.16 mm/s in 38.6 s, travelled at U_{max} for 24.1 s and decelerates in 9.6 s to U_f = 0 m/s. Total time = 72.3 s, distance travelled = 104 mm.

Figures 3.37 and 3.38. Both figures show a source accelerating to U_{max}, staying at U_{max} and then decelerating to U_f. The time taken for each stage is different. Blue circles are the impulsive waves, the pink dots are the oscillatory waves and the pale blue dots are the non-oscillatory waves. N_c = 7.23 rad/s, ε = 0.022 m, ω_f = 6.38 rad/s.

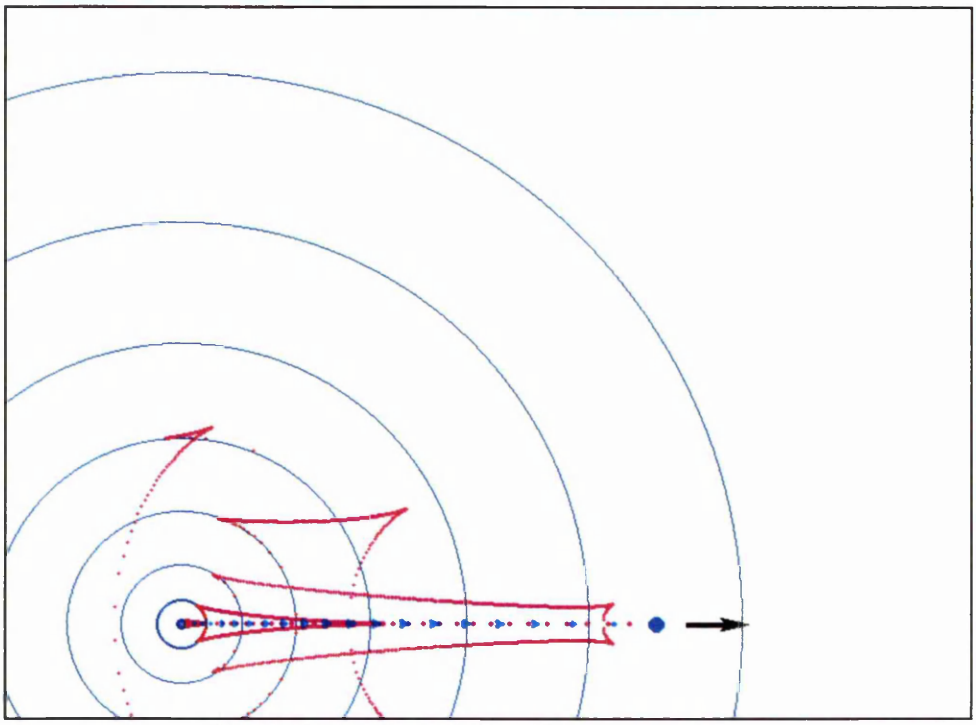

$U_i = 0$ m/s, accelerates to $U_f = 11$ mm/s in $t_a = 19.9$ s.

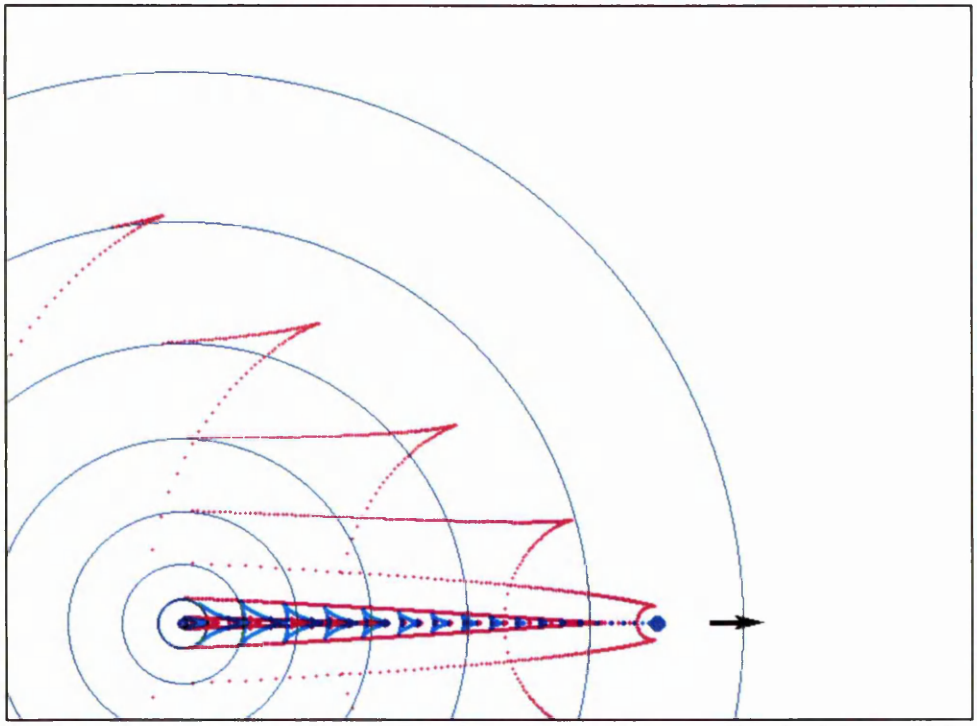

$U_i = 0$ m/s, impulsive start to $U_{max} = 11$ mm/s and then decelerates to $U_f = 0$ m/s in $t_d = 19.9$ s.

Figures 3.39 and 3.40. Mode 0 pycnocline waves from an oscillating point source travelling horizontally in a pycnocline. The top figure shows an accelerating body and the bottom figure shows the decelerating case for the same distance travelled. The blue circles are the impulsive waves, the pink dots are the oscillatory waves and the pale blue dots are the non-oscillatory waves. $N_c = 7.23$ rad/s, $\varepsilon = 0.022$ m, total distance travelled = 109 mm, $\omega_f = 6.38$ rad/s.

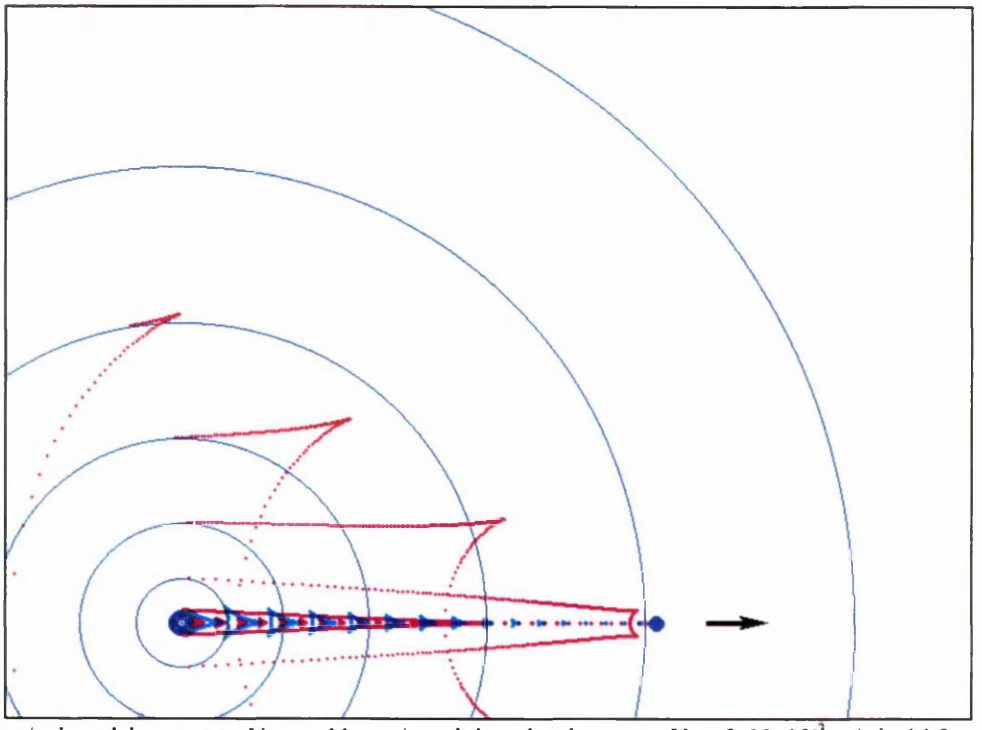

U_i = 0 m/s, impulsive start to U_{max} = 11 mm/s and then decelerates to $U_f = 3.66\times10^{-3}$ m/s in 14.9 s. Total distance travelled = 109 mm.

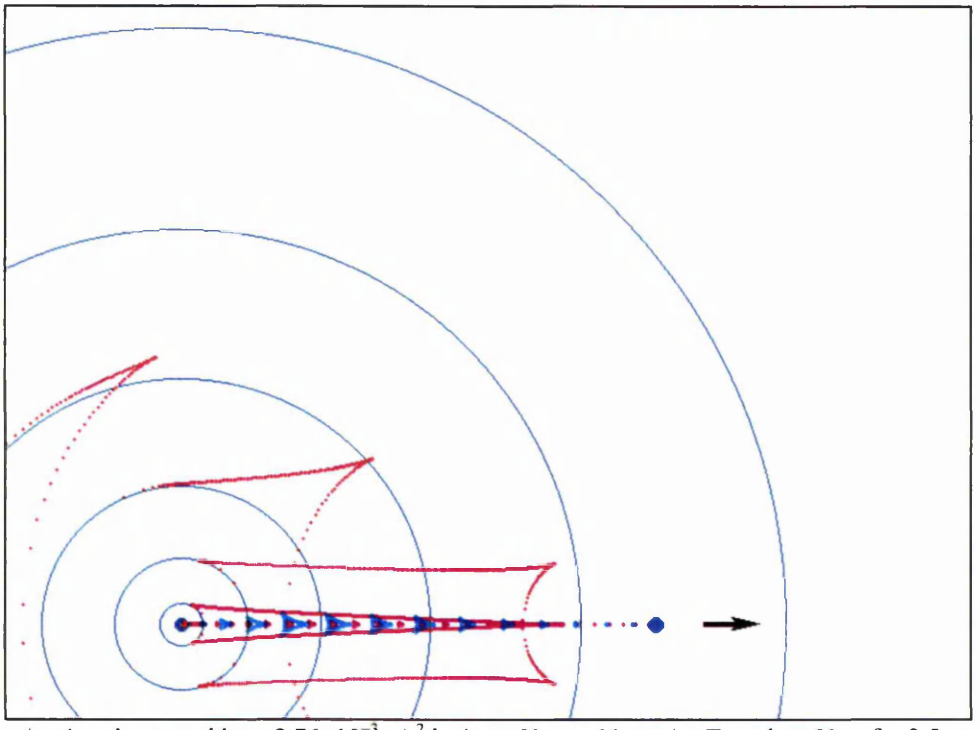

U_i = 0 m/s. Accelerates with $a = 2.76\times10^{-3}$ m/s^2 in 4 s to U_{max} = 11 mm/s. Travels at U_{max} for 3.5s, and decelerates with $d = -9.2\times10^{-4}$ m/s^2 in 6 s to $U_f = 5.49\times10^{-3}$ m/s. Total time = 13.5s, distance travelled = 109 mm.

Figures 3.41 and 3.42. Top figure shows a decelerating body and the bottom figure shows a body accelerating, travelling at a constant velocity and then decelerating to U_f. The blue circles are the impulsive waves, the pink dots are the oscillatory waves and the pale blue dots are the non-oscillatory waves. N_c= 7.23 rad/s, ε= 0.022 m, ω_f= 6.38 rad/s.

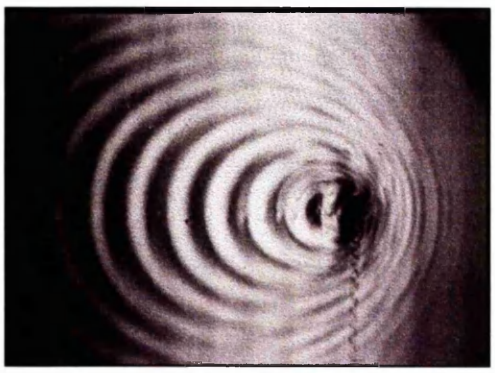

Figure 3.43a

Plan-view experimental image of surface waves produced by an oscillating moving point source.
U = 0.198 m/s, ω_f = 20 Hz.

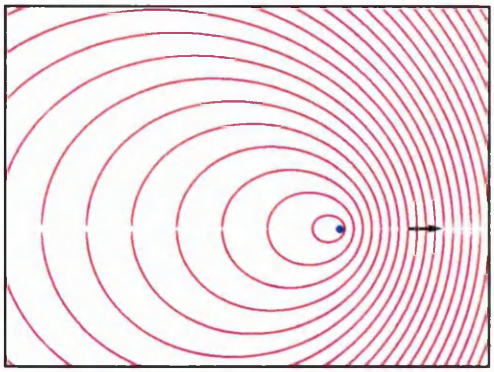

Figure 3.43b

Plan-view theoretical phase configuration of surface waves with surface tension produced by an oscillating moving point source.
U = 0.198 m/s, ω_f = 20 Hz.

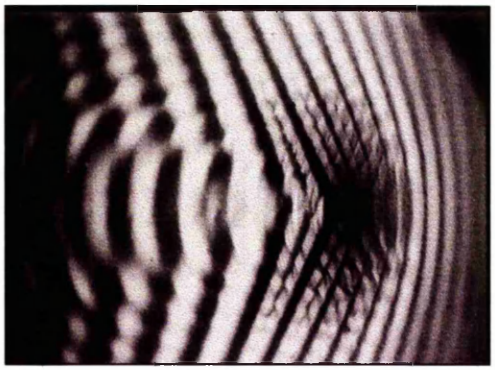

Figure 3.44a

Plan-view experimental image of surface waves produced by an oscillating moving point source.
U = 0.227 m/s, ω_f = 20 Hz.

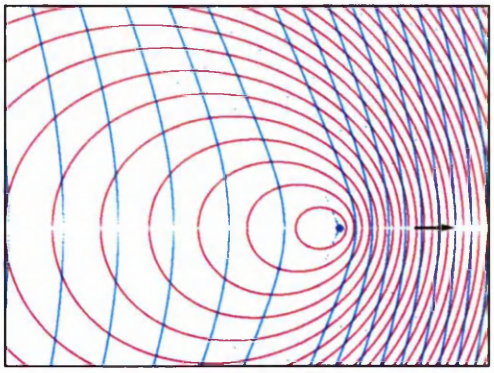

Figure 3.44b

Plan-view theoretical phase configuration of surface waves with surface tension produced by an oscillating moving point source.
U = 0.227 m/s, ω_f = 20 Hz.

U is the speed of the source in m/s, ω_f is the frequency of oscillation in Hz.

The direction of travel is from left to right as indicated by the arrow.

Distance horizontally across each frame is 0.222 m.

The common input parameters for each case are as followed, (with U in m/s)

Depth of the tank = 0.46 m.
The total time, t = 35 × U seconds.
Acceleration, a = U/(0.15 × t) m/s^2
The surface tension, τ = 0.048 N/m.
Density, ρ = 998 kg/m^3.

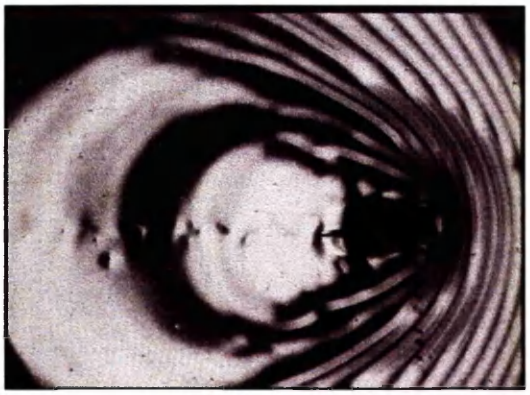

Figure 3.45a U = 0.195 m/s, ω_f = 5.88Hz.

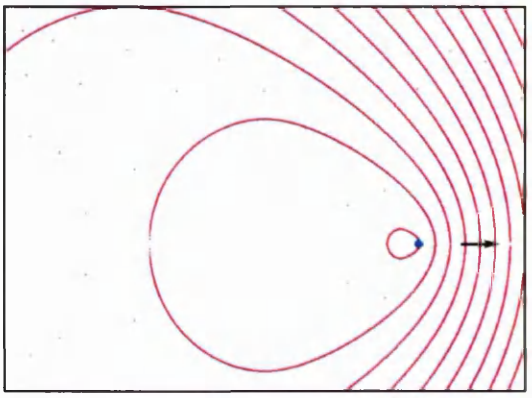

Figure 3.45b U = 0.195 m/s, ω_f = 5.88Hz.

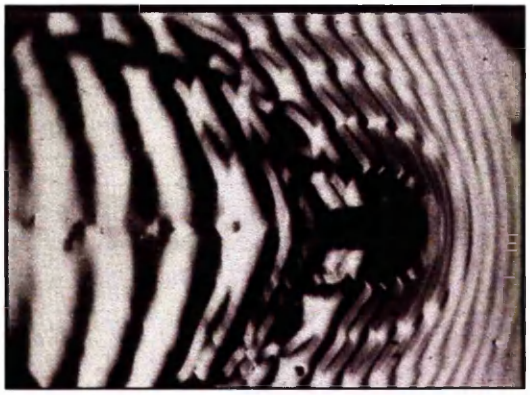

Figure 3.46a U = 0.228 m/s, ω_f = 5.88Hz.

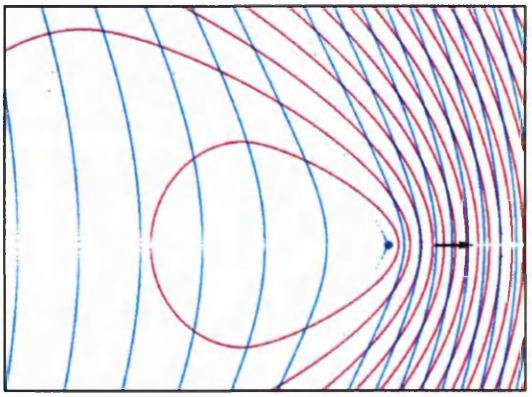

Figure 3.46b U = 0.228 m/s, ω_f = 5.88Hz.

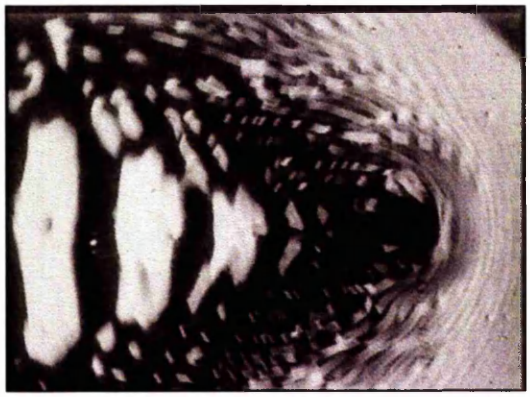

Figure 3.47a U = 0.261 m/s, ω_f = 5.88Hz.

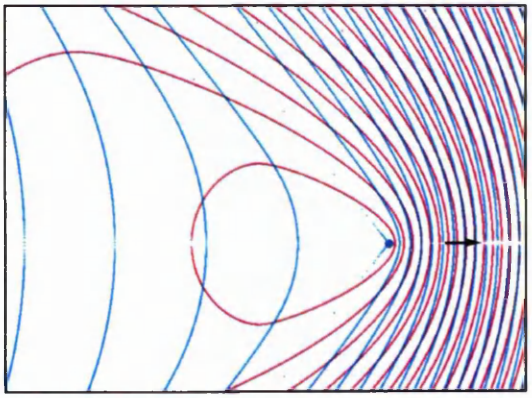

Figure 3.47b U = 0.261 m/s, ω_f = 5.88Hz.

Plan-view experimental images of surface waves produced by an oscillating and moving body.

U is the speed of the body in m/s, ω_f is the frequency of oscillation in Hz.
The direction of travel is from left to right as indicated by the arrow.
Distance horizontally across each frame is 0.222 m.

Plan-view theoretical phase configurations of surface waves with surface tension.

The common input parameters are:
(with U in m/s)
Depth of tank = 0.46 m.
Surface tension, τ = 0.045 N/m.
Density, ρ = 998 kg/m^3.
Total time taken, t = 35 × U seconds.
Acceleration, a = U/(0.15 × t) m/s^2.

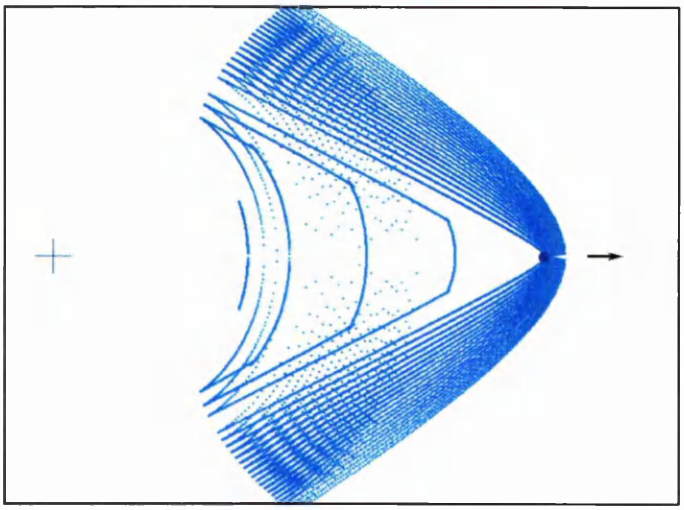

Figure 3.48a.

U = 0.5 m/s.
Including surface tension effect.

The figure shows the first 20 waves.

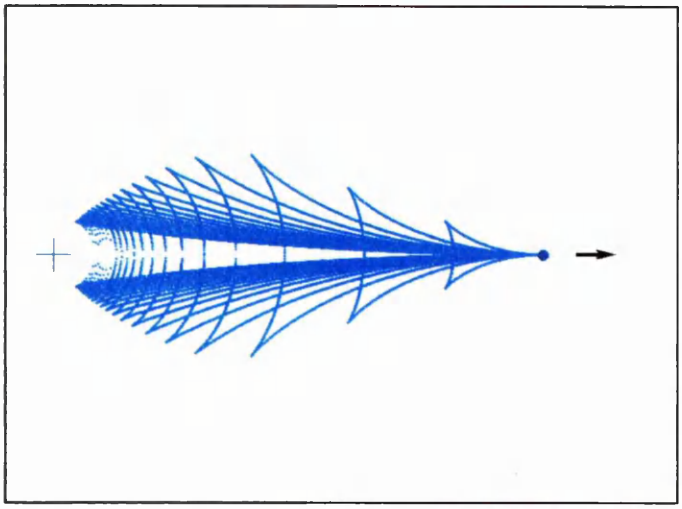

Figure 3.48b.

U = 0.5 m/s.
Excluding surface tension effect.

The figure shows the first 20 waves.

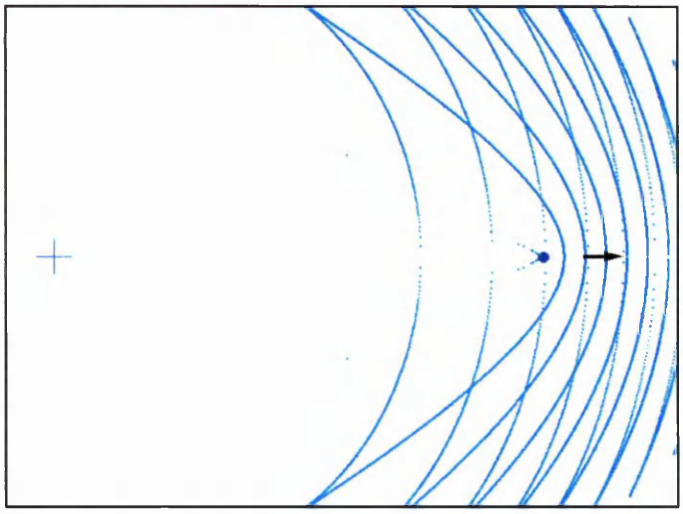

Figure 3.48c.

U = 0.5 m/s.
Including surface tension effect.

The figure shows every 20 waves up to 400 waves.

Steady deep water surface waves. The source moves from rest with constant acceleration to the velocity specified. Total time of travel, t = 4×U seconds with U in m/s. The acceleration, a, is given by (4 × U) / t m/s^2 and the distance across each frame is (1.2 × U × t) m.

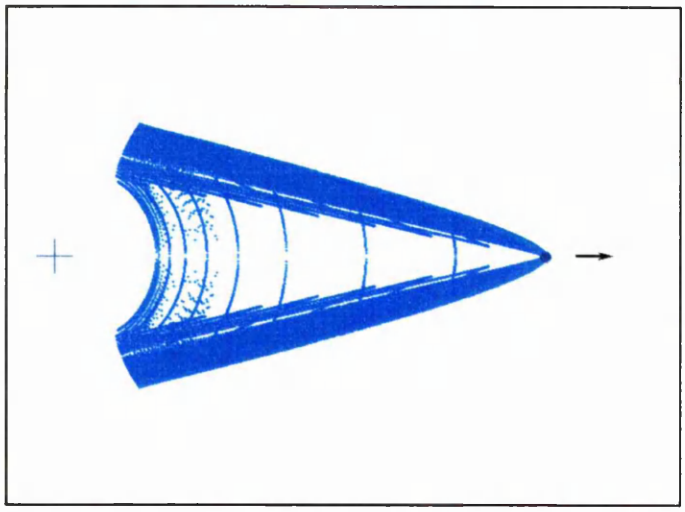

Figure 3.49a.

U = 1.0 m/s.
Including surface tension effect.

The figure shows the first 20 waves.

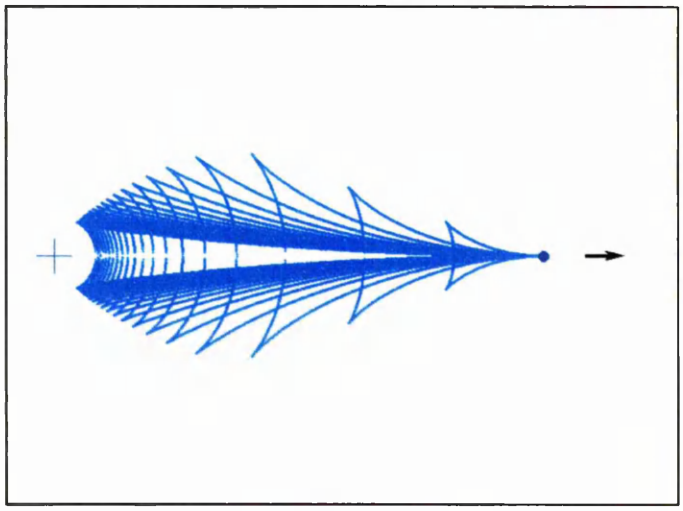

Figure 3.49b.

U = 1.0 m/s.
Excluding surface tension effect.

The figure shows the first 20 waves.

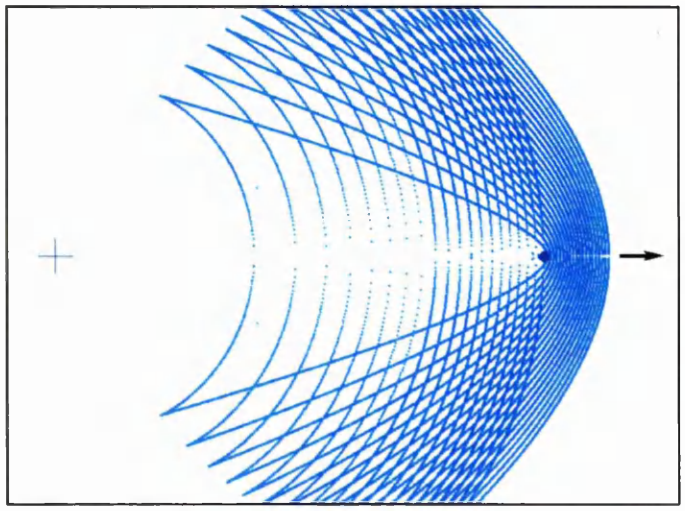

Figure 3.49c.

U = 1.0 m/s.
Including surface tension effect.

The figure shows every 50 waves up to 1,000 waves.

Steady deep water surface waves. The source moves from rest with constant acceleration to the speed specified. Total time of travel, t = 4×U seconds with U in m/s. The acceleration, a, is given by (4 × U) / t m/s^2 and the distance across each frame is (1.2 × U × t) m.

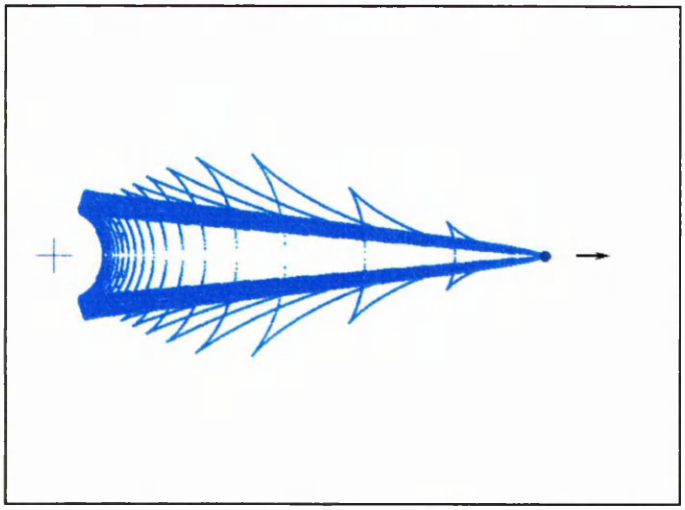

Figure 3.50a.

U = 2.0 m/s.
Including surface tension effect.

The figure shows the first 20 waves.

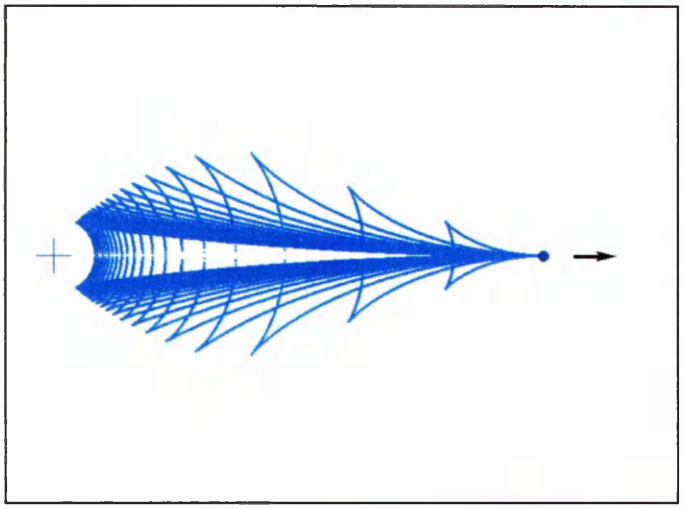

Figure 3.50b.

U = 2.0 m/s.
Excluding surface tension effect.

The figure shows the first 20 waves.

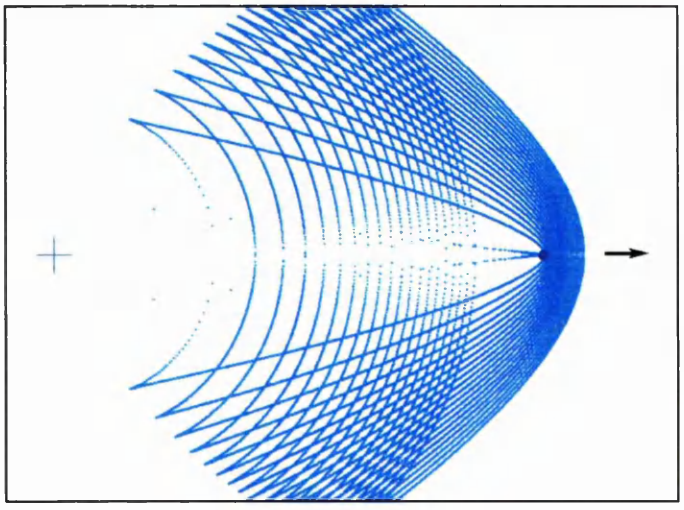

Figure 3.50c.

U = 2.0 m/s.
Including surface tension effect.

The figure shows every 500 waves up to 10,000 waves.

Steady deep water surface waves. The source moves from rest with constant acceleration to the speed specified. Total time of travel, t = 4×U seconds with U in m/s. The acceleration, a, is given by (4 × U) / t m/s^2 and the distance across each frame is (1.2 × U × t) m.

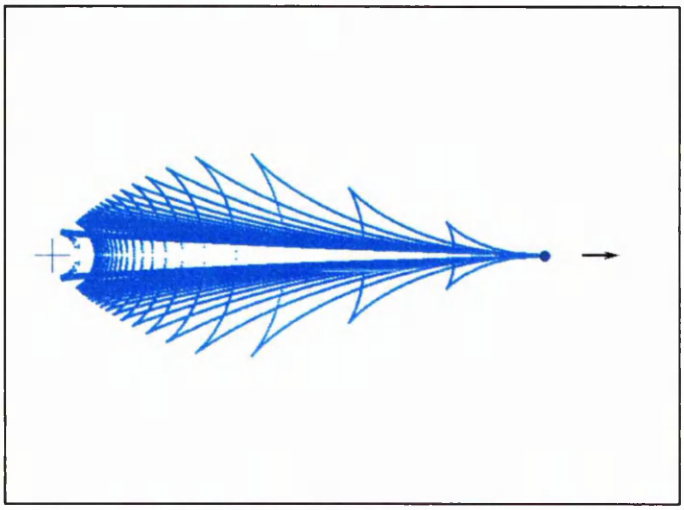

Figure 3.51a.

U = 5.0 m/s.
Including surface tension effect.

The figure shows the first 20 waves.

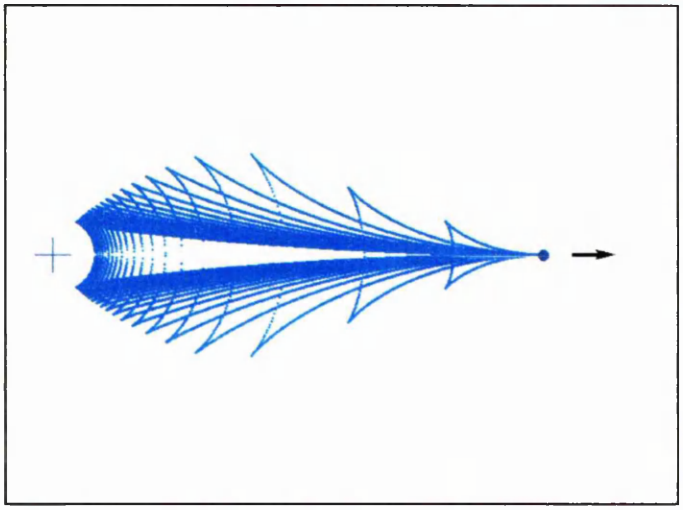

Figure 3.51b.

U = 5.0 m/s.
Excluding surface tension effect.

The figure shows the first 20 waves.

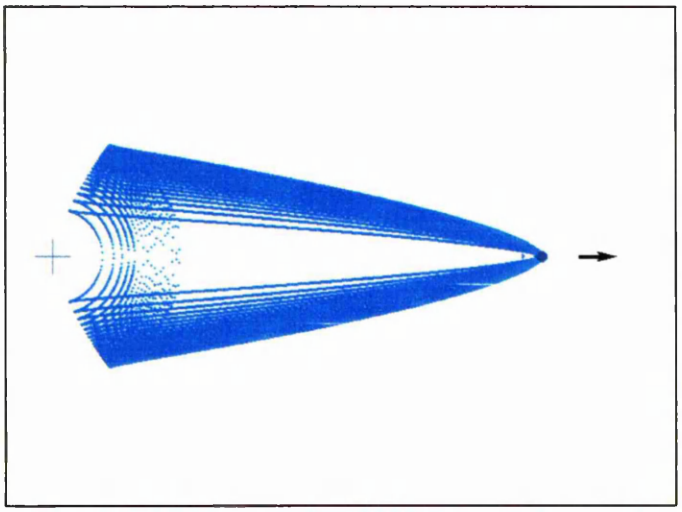

Figure 3.51c.

U = 5.0 m/s.
Including surface tension effect.

The figure shows every 500 waves up to 10,000 waves.

Steady deep water surface waves. The source moves from rest with constant acceleration to the speed specified. Total time of travel, $t = 4 \times U$ seconds with U in m/s. The acceleration, a, is given by $(4 \times U) / t$ m/s^2 and the distance across each frame is $(1.2 \times U \times t)$ m.

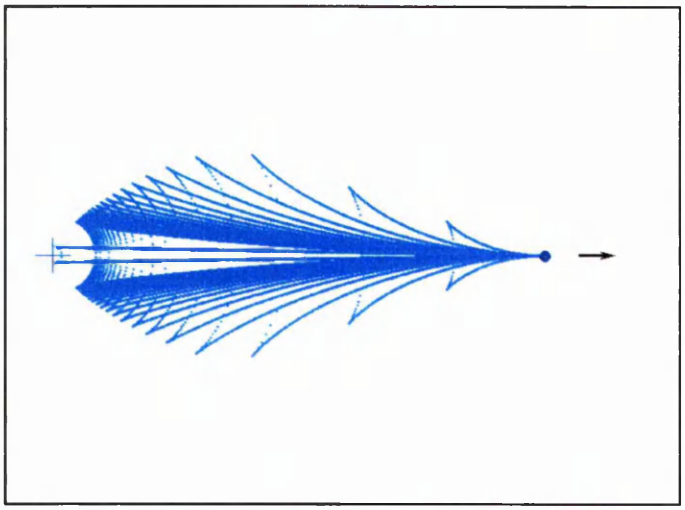

Figure 3.52a.

U = 15.0 m/s.
Including surface tension effect.

The figure shows the first 20 waves.

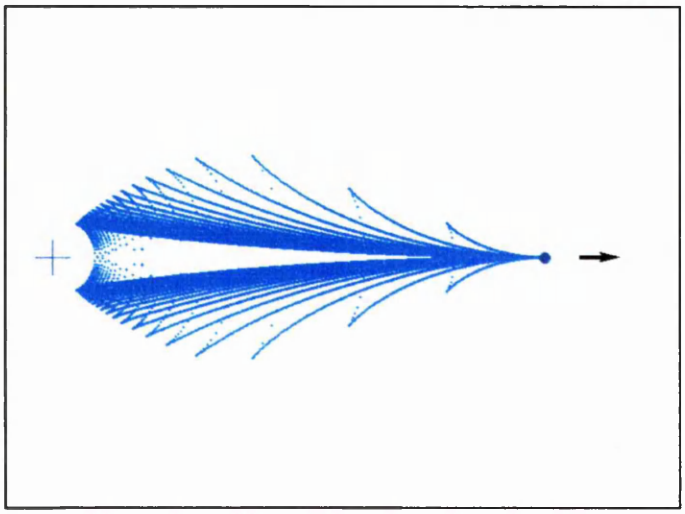

Figure 3.52b.

U = 15.0 m/s.
Excluding surface tension effect.

The figure shows the first 20 waves.

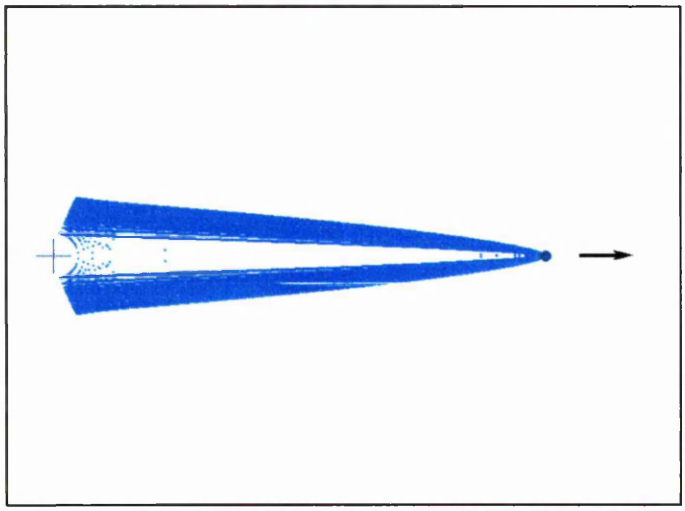

Figure 3.52c.

U = 15.0 m/s.
Including surface tension effect.

The figure shows every 5,000 waves up to 100,000 waves.

Steady deep water surface waves. The source moves from rest with constant acceleration to the speed specified. Total time of travel, $t = 4 \times U$ seconds with U in m/s. The acceleration, a, is given by $(4 \times U) / t$ m/s^2 and the distance across each frame is $(1.2 \times U \times t)$ m.

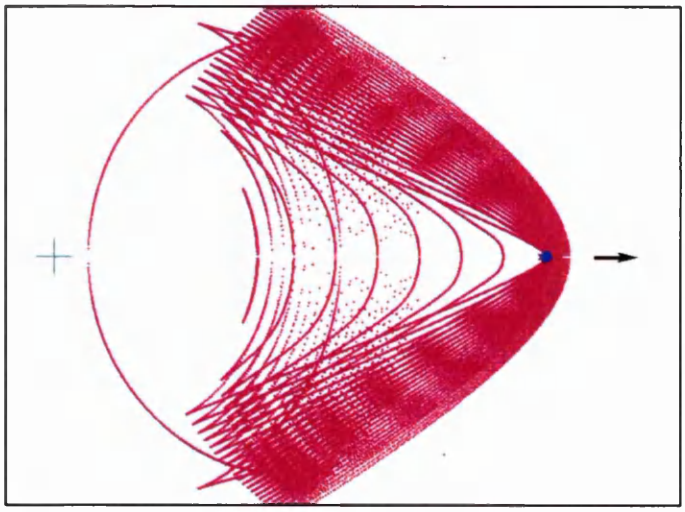

Figure 3.53a.

U = 0.5 m/s.
ω_f = 12.57 rad/s

Including surface tension effect.

The figure plots waves with phases from $-20 \times 2\pi$ to $+20 \times 2\pi$ in steps of 2π.

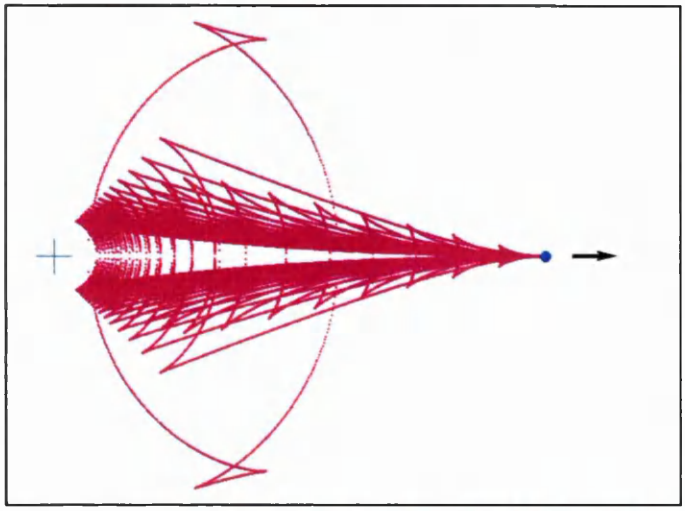

Figure 3.53b.

U = 0.5 m/s.
ω_f = 12.57 rad/s

Excluding surface tension effect.

The figure plots waves with phases from $-20 \times 2\pi$ to $+20 \times 2\pi$ in steps of 2π.

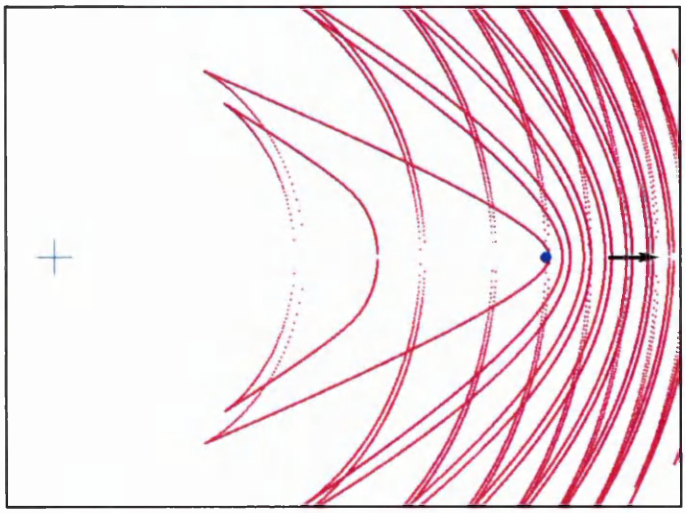

Figure 3.53c.

U = 0.5 m/s.
ω_f = 12.57 rad/s

Including surface tension effect.

The figure plots waves with phases from $-400 \times 2\pi$ to $+400 \times 2\pi$ in steps of $20 \times 2\pi$.

Oscillatory deep water surface waves. The oscillating source moves from rest with constant acceleration to the speed specified. Total time of travel, $t = 4 \times U$ seconds with U in m/s. The acceleration, a, is given by $(4 \times U) / t$ m/s^2 and the distance across each frame is $(1.2 \times U \times t)$ m.

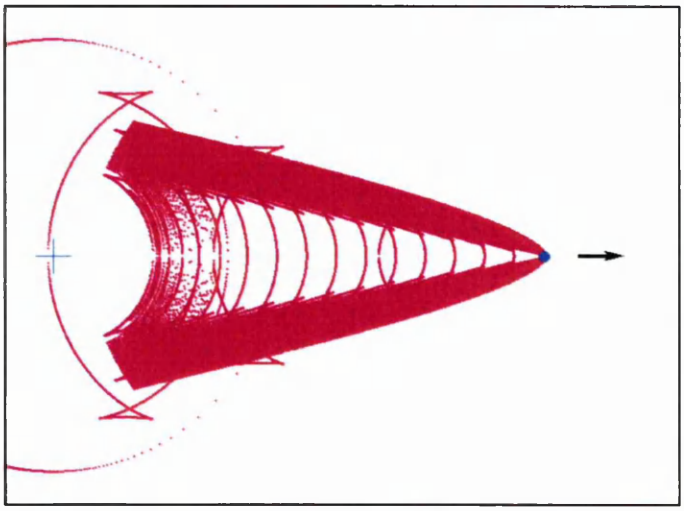

Figure 3.54a.

U = 1.0 m/s.
ω_f = 12.57 rad/s

Including surface tension effect.

The figure plots waves with phases from $-20 \times 2\pi$ to $+20 \times 2\pi$ in steps of 2π.

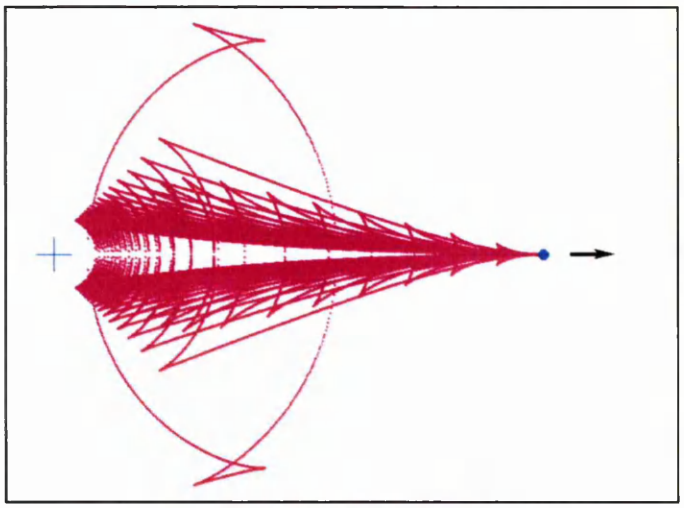

Figure 3.54b.

U = 1.0 m/s.
ω_f = 12.57 rad/s

Excluding surface tension effect.

The figure plots waves with phases from $-20 \times 2\pi$ to $+20 \times 2\pi$ in steps of 2π.

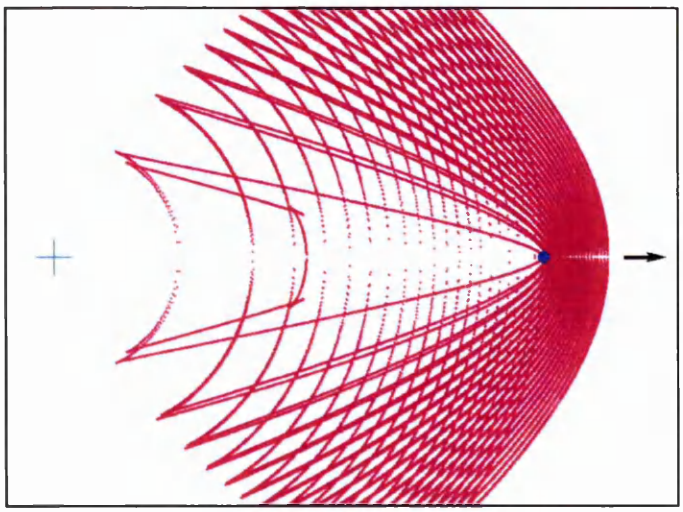

Figure 3.54c.

U = 1.0 m/s.
ω_f = 12.57 rad/s

Including surface tension effect.

The figure plots waves with phases from $-1{,}000 \times 2\pi$ to $+1{,}000 \times 2\pi$ in steps of $50 \times 2\pi$.

Oscillatory deep water surface waves. The oscillating source moves from rest with constant acceleration to the speed specified. Total time of travel, t = 4×U seconds with U in m/s. The acceleration, a, is given by (4 × U) / t m/s^2 and the distance across each frame is (1.2 × U × t) m.

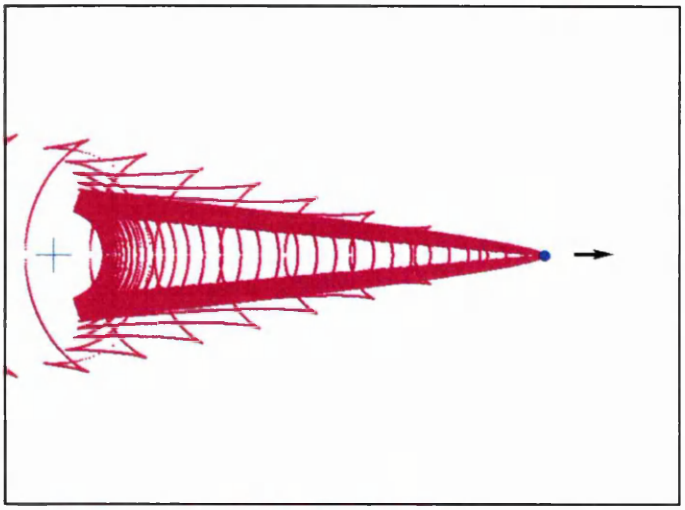

Figure 3.55a.

U = 2.0 m/s.
ω_f = 12.57 rad/s

Including surface tension effect.

The figure plots waves with phases from $-20 \times 2\pi$ to $+20 \times 2\pi$ in steps of 2π.

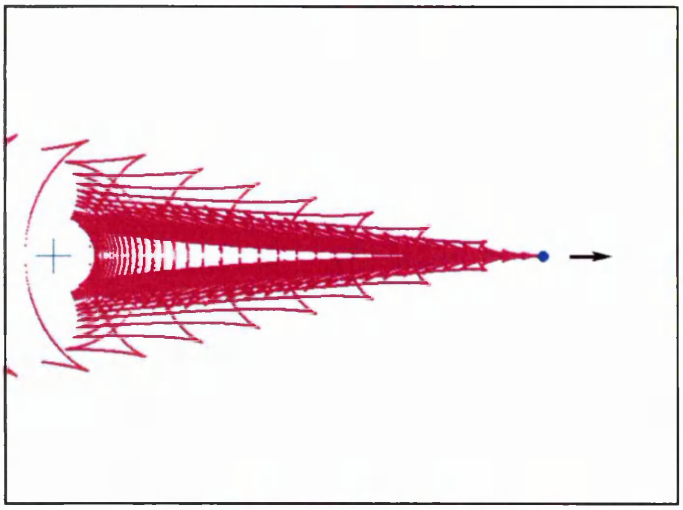

Figure 3.55b.

U = 2.0 m/s.
ω_f = 12.57 rad/s

Excluding surface tension effect.

The figure plots waves with phases from $-20 \times 2\pi$ to $+20 \times 2\pi$ in steps of 2π.

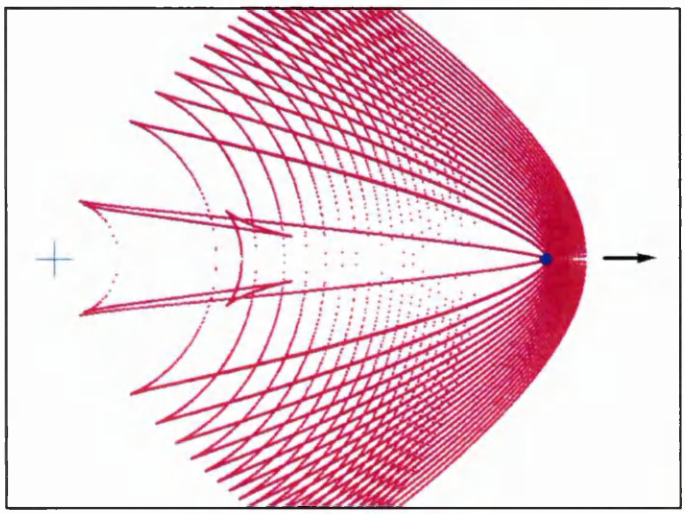

Figure 3.55c.

U = 2.0 m/s.
ω_f = 12.57 rad/s

Including surface tension effect.

The figure plots waves with phases from $-10{,}000 \times 2\pi$ to $+10{,}000 \times 2\pi$ in steps of $500 \times 2\pi$.

Oscillatory deep water surface waves. The oscillating source moves from rest with constant acceleration to the speed specified. Total time of travel, $t = 4 \times U$ seconds with U in m/s. The acceleration, a, is given by $(4 \times U) / t$ m/s^2 and the distance across each frame is $(1.2 \times U \times t)$ m.

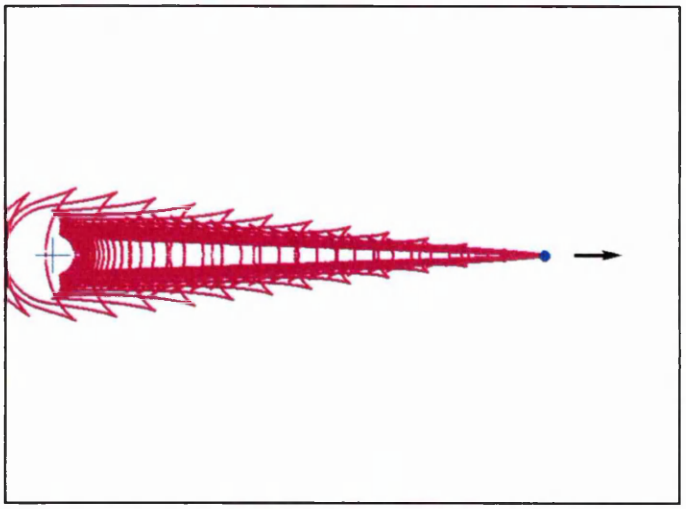

Figure 3.56a.

U = 5.0 m/s.
ω_f = 12.57 rad/s

Including surface tension effect.

The figure plots waves with phases from $-40 \times 2\pi$ to $+40 \times 2\pi$ in steps of $2 \times 2\pi$.

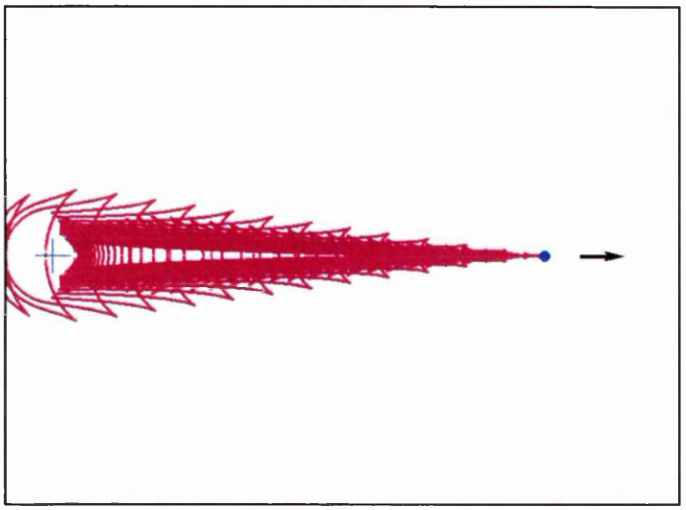

Figure 3.56b.

U = 5.0 m/s.
ω_f = 12.57 rad/s

Excluding surface tension effect.

The figure plots waves with phases from $-40 \times 2\pi$ to $+40 \times 2\pi$ in steps of $2 \times 2\pi$.

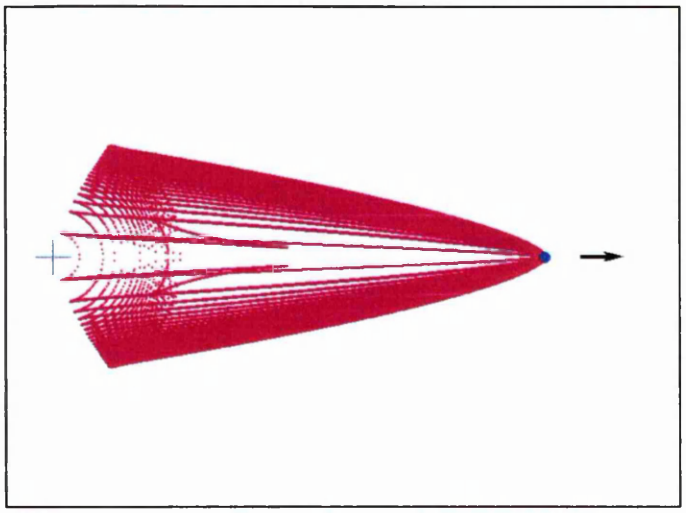

Figure 3.56c.

U = 5.0 m/s.
ω_f = 12.57 rad/s

Including surface tension effect.

The figure plots waves with phases from $-10{,}000 \times 2\pi$ to $+10{,}000 \times 2\pi$ in steps of $500 \times 2\pi$.

Oscillatory deep water surface waves. The oscillating source moves from rest with constant acceleration to the speed specified. Total time of travel, t = 4×U seconds with U in m/s. The acceleration, a, is given by (4 × U) / t m/s^2 and the distance across each frame is (1.2 × U × t) m.

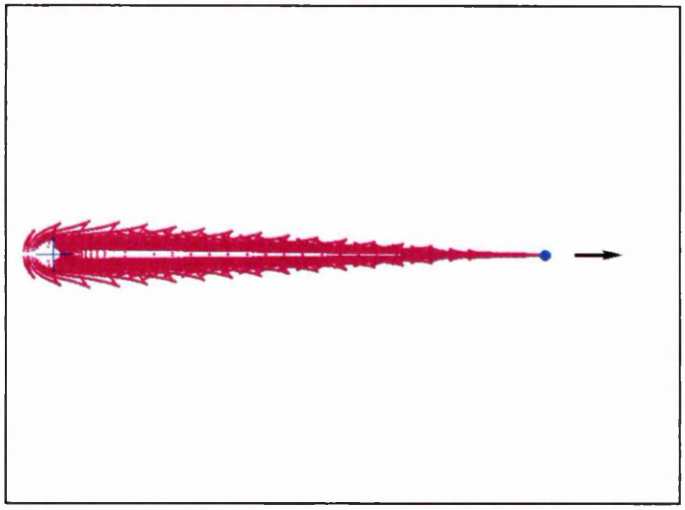

Figure 3.57a.

U = 15.0 m/s.
ω_f = 12.57 rad/s

Including surface tension effect.

The figure plots waves with phases from $-100 \times 2\pi$ to $+100 \times 2\pi$ in steps of $5 \times 2\pi$.

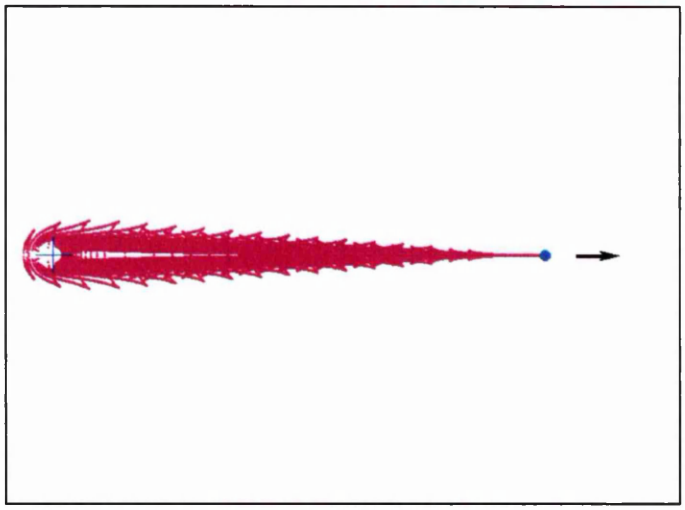

Figure 3.57b.

U = 15.0 m/s.
ω_f = 12.57 rad/s

Excluding surface tension effect.

The figure plots waves with phases from $-100 \times 2\pi$ to $+100 \times 2\pi$ in steps of $5 \times 2\pi$.

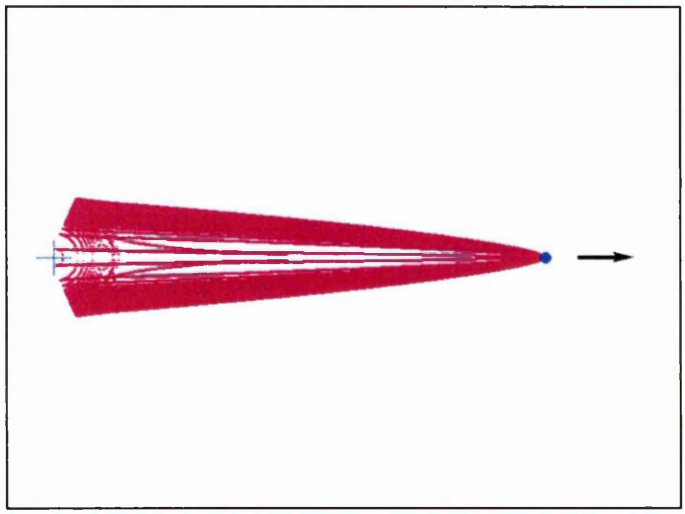

Figure 3.57c.

U = 15.0 m/s.
ω_f = 12.57 rad/s

Including surface tension effect.

The figure plots waves with phases from $-100{,}000 \times 2\pi$ to $+100{,}000 \times 2\pi$ in steps of $5{,}000 \times 2\pi$.

Oscillatory deep water surface waves. The oscillating source moves from rest with constant acceleration to the speed specified. Total time of travel, t = 4×U seconds with U in m/s. The acceleration, a, is given by $(4 \times U) / t$ m/s^2 and the distance across each frame is $(1.2 \times U \times t)$ m.

CHAPTER 4

MEASUREMENT OF FORCES ON AN OSCILLATING WING MOVING IN A PYCNOCLINE

4.1 Introduction

The behaviour of vortices and their effect on a lifting wing when the wing is moving through a constant density fluid have been well researched. However if the wing is moving through a pycnocline with a density gradient, it generates vortices which tend to collapse. As the vortices collapse and fluid returns to its original level or mixes due to turbulence and spreads at its new density level, the flow over the wing is expected to change significantly. It is therefore interesting to know how the forces on the wing moving through a pycnocline differ from those of a wing in a constant density media.

In section 4.2, the set-up for the experiments measuring forces on a low aspect ratio NACA 0012 wing, moving through both constant density and stratified fluid, will be discussed. The wing will be allowed to oscillate about its quarter chord. Sections 4.3 to 4.6 will discuss the force transducers and their electrical circuits used for the force measurements. Semiconductor strain gauges, which are more sensitive than the conventional metallic gauges, were used so that the difference between the wing in a constant density media and a stratified fluid can be detected. Noise reduction by signal processing will be discussed in section 4.7.

A dimensional analysis is discussed in section 4.8 and the experimental results are presented in section 4.9 and 4.10.

4.2 The experimental set-up

The experiments were in the same towing tank as that for the schlieren experiments i.e. length 4.53 m, width 0.7m and depth 0.5m. Figure 4.1 shows a view of the tank, looking down along the length. The tank is supported by 12 tyres that isolate it from any ground vibrations. The working section is made of perspex through which the position of the wing in the pycnocline can be seen. A trolley which runs on two polished metal rails was driven by a motor via a belt and pulley system. These rails are built on a separate support from the tank and the movement of the trolley does not disturb the fluid in the tank. Figures 4.2 and 4.3 show how the belt is linked to the motor by two pulleys at each end of the tank. The tension in the belt can be adjusted. To measure the velocity of the trolley, a black disc is attached to the pulley and has reflective tapes arranged in a cross. A light source, placed at about 30 mm from the disc, has its beam directed perpendicular to the disc at about 45 mm from the centre of the disc. The light beam will be reflected 4 times per revolution to a sensor next to the source. The signal is fed to a revolution counter which gives the angular velocity of the disc in reflections per minute. The diameter of the pulley is 90 mm and the trolley velocity in metres per second can be given from the following equation,

$$\text{Trolley Velocity} = \frac{\text{Reflections/min}}{(\text{Reflections/revolution}) \times 60} \times 2\pi \times \frac{0.09}{2}$$

The accuracy of the system increases as the number of reflections per revolution increases. The velocity can also be measured directly from the time taken for the trolley to move a fixed distance. A gearbox is used to slow down the rotation speed of the motor. The motor and gearbox are bolted to an independent support so that the fluid in the tank is isolated from any vibrations. The switches for the oscillatory mechanism and the motor for trolley movement are located near to each other so that both switches can be switched on at the same time. A speed controller allows the velocity of the trolley to be varied. The speed controller has a marked dial of 0 to 10 that varies linearly with trolley velocity; figure 4.4 shows the calibration.

The model is a perspex wing with a chord length of 0.09 m and an aspect ratio of 1.7. The profile is that of a NACA 0012 aerofoil. This gives a wing span of 0.153 m

compared to the tank width of 0.7 m so that the effects of the wall on the model will be minimal. Trip wires with a diameter of 0.404 mm are located 5 mm from the leading edge on both top and bottom surfaces. The wing is attached to a strain gauge balance so that the forces on the wing can be measured. There are two different balances, one which can only measure the forces when the wing's incidence is fixed while the other is also capable of measuring the forces when the wing is oscillating. The way in which the balances are attached to the trolley and the model depends on which of the two balances is used. The two balances share the same force transducer module which is interchangeble. The designs of the two balances will be described in detail in sections 4.5 and 4.6.

4.2.1 The oscillatory mechanism

The sinusoidal pitching motion of the wing is provided by the mechanism shown in figure 4.5. The angular velocity of the motor is being slowed down by 2 gearboxes linked by belts and pulleys. The final pulley is linked to a flywheel that transforms the circular motion into a vertical motion. The oscillation frequency of the wing can be controlled by a dial located on the green gearbox in figure 4.6. The vertical distance travelled is 5 mm which will cause the wing to oscillate between 0 and 4.8 degrees.

A slotted opto-switch is used to determine the angle and the oscillation frequency of the wing. It is powered by three 1.5 volt batteries. An infra-red beam is passed across the slot from the source to a photodetector. The thin aluminium piece breaks the beam and causes a voltage drop each time the wing's incidence is at 4.8 degree.

4.2.1.1 Vibration control of the oscillatory mechanism

The motor was initially bolted onto a plate which also houses the rest of the oscillatory mechanism including the gearboxes. A spectrum analysis was made to identify the electric noise due to the oscillatory mechanism which was believed to come mostly from the motor and gearboxes. The frequency of the noise originating from the motor is very high and it can be easily filtered off. The gearboxes create noise which is closer to the frequencies of interest. The amplitude of this noise is however much lower than that produced by the motor. The system as a whole produced an unacceptable level of noise.

The objective was then to isolate the motor and the gearboxes since they produced most of the noise. Ideally each of the moving parts should be treated independently since they move at different frequencies. The motor and gearboxes were each attached to a spring and damper system and they were linked by rubber belts. Several combinations of spring and dampers were used and the results indicate that the use of relatively soft springs alone was most effective. This is due to the high frequency of the motor being much higher than the natural frequency of the system. The springs used must also be large enough to prevent the moving parts from moving sideways as the trolley accelerates. Extra low frequencies were also experienced due to the way in which each moving part was inter-linked by the rubber belts. This is undesirable since the frequencies may be too near the intended frequencies of oscillation. In order to overcome this, the motor and gearboxes were mounted onto a common platform which rest on eight springs. This is shown in figure 4.6. The approach has proved to be functional although not ideal, the final reduction of noise has still to be done by signal processing which will be discussed in section 4.7.

4.2.2 Creation and measurement of density stratification

The density stratification is first produced as a two layer system with fresh water above salt water. The density step across the interface quickly becomes a narrow pycnocline and the thickness increases with time through salt diffusion. Once the experiments start, there will be some mixing which will further change the density distribution in the pycnocline. It is possible to use oil and water to produce a two layer system, however the difference in viscosity will cause problems. There will also be a problem of surface tension between the two layers. The results of the stability analysis of Gapanov-Grekhov et al (see Peake 1996) is for an interface and there are several attempts to obtain narrower pycnoclines in order to compare the theory with the experimental results. Naturally the experiments must be carried out immediately after filling the tank with two layers of fluid and the number of runs made will be limited to ensure that the pycnocline remains thin. Experiments involving wider pycnoclines can start after a few days.

The pycnocline can be produced by several methods. The first method involved filling the towing tank with fresh water to a predetermined height. The salt water is then fed slowly into the bottom of the tank, displacing the fresh water upwards until the

overall height is 0.46m from the bottom. The salt solution of a certain density is first prepared in a mixing tank. The solution is then sent to two tanks located in the temperature controlled laboratory as shown in figure 4.7. Both the tanks have a depth of 1.22 m, the tank labelled salt has a diameter of 0.88 m while the tank labelled water has a diameter of 0.81 m. In practice, it is necessary to use both tanks to contain the salt solution in order to generate the necessary capacity. The fresh water is left in the towing tank and the salt water is stored in the two tanks for at least 3 days so that the temperatures will converge to the laboratory temperature. The process can be speeded up by pumping the salt solution between the two tanks or by using a heater. The salt water is sent to the towing tank to complete the filling process. The interface quickly diffuses to form a pycnocline. The filling process took about 4 hours and immediately after the fill, the pycnocline thickness was around 20 mm. Using this method, it was often difficult to initially determine exactly the level of the centre of the pycnocline relative to the wing.

An alternative method is to have the towing tank partly filled with salt water. Fresh water was then filled horizontally onto the surface via a hose and a piece of plywood floating on the surface. The two tanks shown in figure 4.7 now contain water, which must be at the correct temperature before it is sent to the towing tank. The initial level of the interface relative to the wing can be better determined in this way. The minimum pycnocline thickness achieved was more than 20 mm. To reduce the thickness, fluid was syphoned from the centre of the pycnocline (Gilreath, 1983) but this tended to produce an asymmetrical profile.

The next method used a plastic sheet to separate the brine and the fresh water as the tank was being filled, by running water onto the sheet. It was not necessary to run the fresh water slowly onto the sheet, in fact the water was allowed to run at full speed. Almost the whole tank was covered with the plastic sheet and the velocity of the fresh water had slowed down significantly by the time it reached the edges of the sheet. The sheet was then withdrawn. This reduced the filling time to less than an hour without causing much disturbance to the interface. The result was a much thinner pycnocline which was less than 20 mm. The original plan was to have the plastic at the interface in order to slow the diffusion process. If the sheet were to be held in position by rollers at both ends of the tank, this system would probably have worked even better.

A conductivity probe was used to measure the density distribution of the pycnocline. The electrodes are made of platinum and they have to be platinised before

use. When using the probe, it is essential to make sure that there are no air bubbles between the plates causing excessive resistance. The probe has to be calibrated before each set of experiments. The process involves dipping the probe into containers of salt solutions at different densities as shown in figure 4.8. The probe forms an arm of a Wheatstone bridge circuit and the voltage output can be read from either a digital oscilloscope or a voltmeter. Figure 4.9 shows a box consisting of 6 Wheatstone bridge circuits labelled 6 to 12. Channel 12 has a different gain value from the rest and is used exclusively for density measurement. Figure 4.10 shows a typical calibration chart and curve fittings are used for each range of voltages. The measured density distributions of the pycnoclines are shown in figures 4.99 to 4.103.

4.3 Basic Wheatstone bridge circuits for strain gauges

4.3.1 Normal force measurement

By considering the equilibrium of an element with length δx within a cantilever flexible beam or a flexure, the two fundamental equations necessary to derive the shear force are:

$$\frac{\partial(\text{shear force})}{\partial x} = 0$$

and

$$\frac{\partial(\text{bending moment})}{\partial x} = \text{shear force.}$$

The first equation shows that the shear force is constant provided the vertical force acts outside the element considered. The second equation indicates that at any section in the beam the slope of the moment distribution is equal to the shear. Figure 4.11 shows the positions of the strain gauges relative to the forces. The '–' labelled N1 to N4 are the gauges measuring normal forces. Those labelled M1 to M4 measure the pitching moment. The strain, $\varepsilon_x = \frac{My}{EI}$ where I is the second moment of area of the cross-section where the strain gauge is mounted, E is the Young's modulus of the material which in this case is stainless steel, M is the bending moment of the material at the position where the strain gauge is mounted and y is the distance of the strain gauge to the neutral axis of the bending moment which is half the thickness of the cross-section of the flexure.

With the Wheatstone bridge arrangement shown in figure 4.12,

$$V_{out} = \frac{1}{4} \times GF \times V_{in} \times (\varepsilon_1 - \varepsilon_2 + \varepsilon_3 - \varepsilon_4), \qquad (4.1)$$

Ringel & Levin (1985). $\varepsilon_1 - \varepsilon_2 + \varepsilon_3 - \varepsilon_4$ is the total strain in all four arms of the bridge. The subscripts 1 to 4 correspond to the positions of the gauges on the bridge. GF is the gauge factor, also known as the sensitivity of the strain gauge. This becomes

$$V_{out} = \frac{1}{4} \times GF \times V_{in} \times \frac{y}{EI} \times (M_{N1} - M_{N2} + M_{N3} - M_{N4}),$$

where M_{Nx} is the bending moments at the positions where the gauges are mounted. Given that M_a and M_b are bending moments at horizontal distances x_a and x_b from the wing's centre of pressure as shown in figure 4.11. $M_{N1} = -M_a$, $M_{N2} = -M_b$, $M_{N3} = M_b$ and $M_{N4} = M_a$ for a vertical upward force, the minus and plus are the compressions and tensions.

$$V_{out} = \frac{1}{4} \times GF \times V_{in} \times \frac{y}{EI} \times 2(M_b - M_a).$$

This shows that $V_{out} \propto M_b - M_a$, and

$$\text{shear force} = \frac{\partial M}{\partial x} = \frac{M_b - M_a}{|x_b - x_a|}.$$

For a particular installation the distance $x_b - x_a$ will be fixed so that the shear force is proportional to V_{out}.

Ideally, this arrangement should give a voltage output that is proportional to the force acting perpendicular to the line joining the two stations even though the point of application does not remain fixed. This allows the lift of the wing to be measured without having to find the pitching moment. Changes due to temperature or axial load will cause equal changes in resistance in both sign and magnitude for all the four strain gauges, resulting in zero bridge output.

4.3.2 Moment measurement

The arrangement of the strain gauges on the flexible beams in order to measure the pitching moment is basically similar except they are placed close to the centre of the beams. Figure 4.11 shows the positions of the strain gauges labelled M1 to M4 for measuring moments on the flexures. The idea is to measure the bending moment of a point in the middle of the two stations with distances x_c and x_d from the centre of pressure. Figure 4.13 shows the Wheatstone bridge arrangement. The resulting bridge output is proportional to the sum of the bending moments. Given

4. Measurement of forces on an oscillating wing moving in a pycnocline

$$V_{out} = \frac{1}{4} \times GF \times V_{in} \times (\varepsilon_4 - \varepsilon_1 + \varepsilon_3 - \varepsilon_2)$$

from equation (4.1) for a the standard Wheatstone bridge, the output voltage in terms of bending moments is

$$V_{out} = \frac{1}{4} \times GF \times V_{in} \times \frac{y}{EI} \times (M_{M4} - M_{M1} + M_{M3} - M_{M2}).$$

M_{Mx} are the bending moments at the positions where the gauges are mounted. It is assumed that M_c is the bending moment experienced by strain gauges M_{M1} and M_{M4}, and M_d is the bending moment experienced by strain gauges M_{M2} and M_{M3}. If the transducer experiences a positive upward force, $M_{M1} = -M_c$, $M_{M2} = -M_d$, $M_{M3} = M_d$ and $M_{M4} = M_c$. Hence,

$$V_{out} = \frac{1}{4} \times GF \times V_{in} \times \frac{y}{EI} \times 2(M_c + M_d)$$

and V_{out} is proportional to the average of the bending moments at the two sections where the gauges are mounted. The distance between the two stations should be as small as possible. Again the resistance change due to axial loads and temperature are cancelled out.

4.3.3 Axial force measurement

Two strain gauges in adjacent arms of a bridge will be used to measure the drag and they will be positioned as shown in figure 4.14 and 4.18. The positions of the strain gauges are similar to having the gauges on the top and bottom of a cantilever beam with a force acting perpendicular to the beam. The strain gauges should be near to the root of the beam where the bending moment is a maximum. The thickness of the flexible beams for drag are crucial as they have to be sufficiently rigid to minimise the interaction effects due to the pitching moment and at the same time thin enough so that the strain gauge output is sensitive to the small axial force. There is only enough space for two strain gauges and thus only a half-bridge circuit can be used. Figure 4.15 shows the Wheatstone bridge circuit. This arrangement differs from that of the normal force measurement in that the voltage output will be proportional to the drag provided that the point of force application remains unchanged. From equation (4.1) with only two strain gauges,

$$V_{out} = \frac{1}{4} \times GF \times V_{in} \times (\varepsilon_1 - \varepsilon_2).$$

The output voltage in terms of bending moments becomes

$$V_{out} = \frac{1}{4} \times GF \times V_{in} \times \frac{y}{EI} \times 2M_a$$

if the strain gauge labelled A1 experiences a tension and A2 experiences a compression for a drag as shown in figure 4.14. V_{out} is proportional to the bending moment M_a, but the sensitivity is half that of a full-bridge circuit.

Again, as long as both the strain gauges are subjected to the same strains, either temperature or vertical force, the Wheatstone bridge circuit will compensate for the errors. However, the moment can instigate strains similar to that of the axial force causing a significant output. This can be corrected during the calibration process.

4.3.4 Alternative Wheatstone bridge arrangements

The arrangements of the strain gauges within the Wheatstone bridge circuit for measuring normal forces and moments described so far are principally for balance 1 which will be discussed in section 4.5. For balance 2 where the location of the application of the force with respect to the location of the strain gauges is known, the strain gauge arrangement for normal force measurement can be used to measure moment. The design of balance 2 will be discussed in section 4.6.

Alternative arrangements can also be useful if one or two of the strain gauges in any of the four arms fails. Under this situation, only two strain gauges can be used and the arrangement depends on which of the strain gauges fail. For example if strain gauge N_3 for normal force measurement in figure 4.12 fails, then N_4 will have to be discarded and both the arms are replaced by two 5.1 kΩ resistors as shown in figure 4.16. Given that N_1 and N_2 experience bending moments of $-M_a$ and $-M_b$ respectively for an upward force, the voltage output becomes

$$V_{out} = \frac{1}{4} \times GF \times V_{in} \times \frac{y}{EI} \times (M_b - M_a),$$

which is half the previous magnitude. V_{out} remains proportional to the difference between the moments at the 2 stations. The input voltage to the Wheatstone bridge can be increased to compensate for the reduction, however it must not exceed the limit of 30 volt which can cause failure of the strain gauges. Section 4.4.4 will discuss the range of values of input voltage for null stability.

If strain gauge M_2 in figure 4.13 fails, then there is a choice of discarding either strain gauge M_3 or M_1. Figure 4.17a shows the circuit if M_3 is replaced while figure

4.17b shows the case if M_1 is removed. Given that $M_{M1} = -M_c$, $M_{M3} = M_d$ and $M_{M4} = M_c$ for a vertical upward force, the voltage outputs for the two circuits become

$$V_{out} = \frac{1}{4} \times GF \times V_{in} \times \frac{y}{EI} \times 2M_c \qquad \text{for figure 4.17a}$$

and

$$V_{out} = \frac{1}{4} \times GF \times V_{in} \times \frac{y}{EI} \times (M_c + M_d) \qquad \text{for figure 4.17b.}$$

Figure 4.17a has an arrangement similar to that of the axial force measurement. It is preferred over the arrangement in figure 4.17b due to its ability to compensate for any strains due to temperature.

4.4 Design of a force transducer module

Prior to finalising the strain gauge balance design, a rough estimation of the lift and drag was made using finite wing theory based on properties of symmetrical wing sections using vortex sheet thin aerofoil theory. Elliptical and Fourier representations of the circulation distribution for a symmetrical wing were assumed.

Two types of balances are considered and they both use the force transducer module as shown it figure 4.18. The concept of the design was taken from Bradshaw (1970) and a NASA designed three-component internal strain gauge balance as described by Pope (1984). The NASA design is however intended for an internal balance where the transducer is inside a model. With the strain gauges placed in positions as shown, this transducer has the ability to measure the normal, axial forces and the moment about a point in a vertical plane. Forces perpendicular to the axis of the transducer will be termed normal and forces acting along the axis will be the axial forces. The forces on the model will be called lift and drag. The concept for the design of the drag member is taken from Pope (1965) and it is built separately from the transducer and has two thin webs through which all forces are transmitted. These two thin webs each have strain gauges installed on the surfaces which will have tension and compression stresses. The drag unit is not only sensitive to axial force but also to moment. It is therefore important for it to be located as close to the model as possible to reduce the interaction effect of the moment. With this arrangement, an adequate strain can be experienced by the gauges on the flexures of the parallel-flexure linkage without large displacements due to the normal force. The flexures will extend or compress under the normal force with the axial force producing a bending moment. The horizontal beams of the drag member are thick to minimise the interaction effects from

the normal force. The force member is assembled with the forward and aft portions of the transducer body in such a way as to maintain a stiff cross-section for bending moments in the normal force and side force planes. One of the critical considerations in the design is the method of attachment of the member to the balance body. To overcome slippage, a large number of screws or pins are used so that the force holding the parts together will be high.

The whole force transducer module is made of stainless steel to withstand the corrosive action of brine and to provide enough stiffness to minimise the interactions on each of the components. Stainless steel also has an excellent fatigue life. However the manufacturing process will be more difficult due to the hardness of the material and the requirement for the precise thickness of the flexures.

4.4.1 Selection of strain gauges

The most important factors being considered when selecting strain gauges for the balance are size and sensitivity. Metallic strain gauges have gauge factors that typically range from 2 to 3.2 as compared to 55 to 225 for the range of semiconductor gauges available. The gauge factor is the strain sensitivity of the strain gauge. Naturally, since the forces to be measured are small, semiconductor type gauges are the only option. Both the companies Kyowa and Kulite offer strain gauges that are suitable. Kyowa's KSP-2-1000-E4 gauge has a gauge factor of 160 and a resistance of 1000 ohms with an encapsulated size of 7.5 mm by 4.0 mm. This is compared to Kulite's UHP-5000-060 (0.76 mm by 0.51 mm) and S/UHP-5000-060 (encapsulated 6.4 mm by 3.6 mm) which have a gauge factor of 175 and a resistance of 5000 ohms. The encapsulated gauges have the strain sensitive element sandwiched between layers of epoxy-impregnated glass paper. Kulite's gauges were selected due to their small size, higher gauge factors, higher resistance and much lower cost. High resistance allows higher output signals with less power dissipation. The Kulite strain gauge has a resistance of 5000 ohms and hence a higher input voltage can be used for the Wheatstone bridge circuit to obtain higher sensitivity without overheating. The non-encapsulated or bare gauges are required for the drag member of the force transducer. None of the encapsulated gauges reviewed are small enough to position the gauges onto the axial force flexures, and still leave room for water-proofing. The encapsulated gauges are for the normal force and moment member and there is just enough space for

them on the double cantilever beams of the force transducer. In most cases, the encapsulated gauge is preferred due to the ease of installation. The installation procedures will be discussed in section 4.4.4.

Like most semiconductor type gauges, Kulite's strain gauges are also sensitive to temperature change. The strain gauges were selected based on the requirement of balance 1 where the gauges are submerged in water and temperature variation is small. The temperature in the laboratory is controlled and there is temperature compensation in the arrangement of the strain gauges within the Wheatstone bridge circuits. Balance 2 was later required to measure the forces on the oscillating wing. This balance has two force transducers above the water. Further temperature compensation is thus needed and this will be discussed in sections 4.4.2 and 4.4.3.

4.4.2 Temperature compensation

Semiconductor strain gauges are generally more sensitive to temperature than metallic strain gauges. The resistance of a strain gauge increases with temperature and the gauge factor decreases with temperature. Generally the process involves two kinds of compensation. The span compensation tackles the drift of gauge factor due to temperature. The bridge null and null shift compensations deal with the change of gauge resistance due to temperature. The operating temperature in the laboratory is controlled and it varies slightly between 19 degree and 21.5 degree Celsius. Throughout a typical day the temperature stays stable. As the gauge factor remains relatively constant within the range of temperature, the focus is to compensate for the change of resistance due to temperature.

4.4.3 Bridge null and null shift compensation

The basic arrangements for a Wheatstone bridge with 4 strain gauges are discussed in section 4.3. In figure 4.12, the output voltage will be zero provided that the bridge is exactly balanced, this implies $R_2R_4 = R_1R_3$. R is the resistance in each of the arms denoted by the subscript. However, it is not possible to ensure that the nominal resistance of each strain gauge is the same. The null will also shift with temperature unless the effective TCR of each arm is identical. The TCR is the temperature coefficient of resistance and is defined as the percentage change in resistance of a strain gauge per 100 °F. Furthermore the resistance and the TCR of each strain gauge will

change again once it is bonded to the material. In reality, the voltage output will always display a non-zero null and a null shift which can be of either positive or negative sign. This problem can be solved by having a shunt resistor and a series resistor in one of the arms. These resistors have very low TCR and are independent of temperature change within the range of temperature experienced. The shunt resistor effectively reduces the resistance and the TCR of that arm while the series resistor will compensate for the loss of resistance.

The values of the resistance for the shunt and parallel resistors are determined by the following procedures. The temperature of the force module is lowered to a temperature slightly below laboratory temperature by placing the module on the surface of a flat metal container in which is cold water. The voltage output, V_0 and the input resistance, R_{i0} are measured. This process is repeated by placing the module on the surface of a conventional electric heater with a temperature above the laboratory temperature. The voltage output is V_T, the input resistance is R_{iT} and $T = T_0 + \Delta T$ where ΔT is the difference between the highest and lowest temperature. These values are then used to calculate the required single parallel resistor and a single series resistor needed to be placed in one of the arms. In practice the series resistor is replaced by a potentiometer of a suitable range of resistance to fine tune the null of the Wheatstone bridge. The details and the equations needed for the calculations are supplied by the Kulite semiconductor strain gauge manual. The balance condition will be achieved at both the temperatures. Provided that the uncompensated null shift is linear with temperature, the voltage output will be zero in any temperature within the range. Initial concern was that the presence of a parallel resistor will cause the output to be non-linear. This was proved unfounded as the value of the shunt resistors are all relatively large compared to the resistance of the strain gauge. The calibration chart also shows that the outputs are linear with the forces. Figure 4.19 shows the actual arrangement of the Wheatstone bridge circuits used for the two force transducers.

4.4.4 Strain gauge installation and performance test

Epoxy cement M-Bond 610 from Micro-Measurements is recommended by Kulite for the installation of its strain gauges. The cement has an operating temperature range of –269 °C to +260 °C. It's low viscosity means than the glue-lines can be extremely thin at less than 0.005 mm, and upon curing they become hard and void-free.

Glue-lines are the thin adhesive between the strain gauge and the surface on which it is mounted. This reduces creep, hysteresis and linearity problems. The curing agent and the resin of the adhesive can be kept separately for 9 months. After mixing the adhesive it has to be used within 12 weeks before it becomes too viscous. Micro Measurements also produces M-Bond 43-B and the viscosity is as low as the M-Bond 610. It is a single component and has a storage life of 9 months.

The gauges were installed strictly according to the instructions supplied by Micro Measurements instruction bulletin B-130-14. The procedure consists of surface preparation, surface cleaning, gauge positioning, adhesive application, clamping, curing and post-curing for extra stability. Isopropyl alcohol was used to degrease the surface and surface abrasion was done using fine 240 grit emery paper. The cramping pressure should be around 105 kN/m^2 to maintain thin glue-lines and control the bonded resistance of the gauges. The installation was cured at a temperature of 100 °C for 4 hours. For stress relaxation, the clamps were removed and the installation was post cured at 140 °C for 2 hours.

After the installation, the resistance of each gauge was tested. The gauges should be completely insulated from the surface. The gauges were connected as a Wheatstone bridge circuit as described in section 4.3 and 4.4, and together with the analogue to digital converter and the power supply, the system was monitored. The input voltage was kept constant at 12 volt and the current at 2 mA. Normally the system is left overnight and once there is no null shift, the transducer is loaded to check for creep and hysteresis. If the voltage output remains constant throughout the period of loading, and, once the load is removed, it returns to its pre-loaded value, then the installation is considered successful.

Each strain gauge can sustain power dissipation levels of 10 to 25 mW with acceptable null stability, and up to 50mW without damage. In a typical Wheatstone bridge with 4 strain gauges shown in section 4.3, the maximum input voltage will be about 30 volts without damaging the gauges. It is normally not necessary to have large input voltages due to the high gauge factor associated with the semi-conductor type gauge. To ensure null stability, the input voltage should be kept below 21 volts which corresponds to a power dissipation of 25mW per gauge assuming a bonded resistance of 4.5 kΩ per gauge. Throughout the experiments the input voltage has been kept at 12

volts and the system is stable after the warming up time of 12 hours. Typically the system is on for 3 days before the experiments are started.

4.5 Design of balance 1

The first design shown in figure 4.20 has the transducer arranged as a 'sting' supporting the model. One force transducer is used and the wing is attached to the forward section of the transducer. The aft section is attached to the trolley by a vertical streamlined strut. This design is only capable of measuring forces on the wing at a fixed incidence. During calibration, the wing will be replaced by a calibration bar with notches to allow different moments to be applied.

4.5.1 Water proofing and protection against the effects of salt

The performance of the semiconductor type strain gauge can be easily degraded by the effects of moisture. The gauge or bare wires will have to be replaced once in contact with brine. Balance 1 is totally submerged in the fluid, thus it is necessary to waterproof the whole force transducer module. The materials are supplied by Micro Measurements Group and most of the application instructions were carried out according to the instruction bulletins. However, due to the space constraint, it was impossible to follow the procedures strictly. Several combinations of the suggested methods were tried, and a water proofing method was finally adopted. The sensitivity of the force transducer is reduced due to the extra coatings needed.

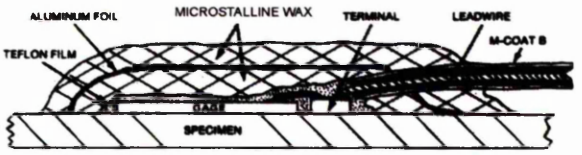

Figure 4.21 First layer of water-immersion coating.

The area around the strain gauges is first cleaned thoroughly with pure isopropyl alcohol. The wires leading to the strain gauges are primed with a layer of M-Coat B and allowed to air-dry. This coat of M-Coat B will improve bonding ability to other coatings. Teflon tape is then carefully placed onto the strain gauges and lead connections. This will prevent the strain gauges and any exposed wire from getting in

contact with the coatings. M-Coat W-1 which is a soft microcrystalline wax is heated and allowed to drip onto the Teflon tape. A brush or a spatula is used to spread the wax while it is still in its semi-liquid state. As soon as the wax hardened, aluminium sticky tape was pressed on to prevent moisture from penetrating. This is followed by another layer of wax which together acts as the first layer of the water-immersion coating. Figure 4.21 shows the cross section of the first coat. The next coat is M-Coat J which is a two-part polysulfide liquid polymer compound. This coat acts as the barrier against brine and it also protects installations from mechanical damage. Almost the whole force transducer will be covered with M-Coat J with special attention paid to ensure the wires which are previously primed with M-Coat B, are fully surrounding with M-Coat J. The full procedures for the application of M-Coat J protective coating can be obtained from Measurement Group instruction bulletin B-147-4. To further prevent brine from attacking the bonding between the stainless steel material and the coatings, a rubber balloon covering the whole force transducer is glued to the hardened M-Coat-J coating with silicon rubber. The wires should be secured and prevented from moving while waiting for each coating to harden. The most common places for the fluid or moisture to penetrate are gaps around the wire and the weak bonding of the coatings to the stainless steel material. These areas must be checked at every stage.

4.5.2 Calibration

The calibration procedure for balance 1 will differ slightly from balance 2. The exact positions of the lift and drag on the model are not known and the calibration of the moment will require the normal force to act at several positions away from the strain gauges.

The balance has to be mounted on a calibration rig which ensures that the transducer is either horizontal or vertical. It is then loaded with the expected range of known forces and moments. The Wheatstone bridge outputs of each loading are recorded and these results are used in the calibration equations.

The calibration of balance 1 was done with the balance submerged in the water and also outside the water. This is to ensure that the strain gauges are subjected to the same operating conditions as the actual experiments. However the calibration with the transducer outside the water showed little difference. A calibration bar is attached to the balance in place of the model so that suitable loads can be applied. Precisely located

circular notches are cut into the surface for positioning the calibration weights. Successive notches allow variations of moment while the normal force is held constant. Another horizontal bar is attached perpendicular to the calibration bar to facilitate the drag force calibration.

The deflections of the balance due to loading are small and the balance can be assumed to be horizontal with the loads applied perpendicular to the balance. The compensation for interactions is based on a calibration process that forms simultaneous equations. The equations are linear which means that the interactions involving terms higher than second order do not exist. Figure 4.22a shows the voltage outputs from the moment circuit of the force transducer due to normal force loading at several distances from a reference point on the calibration bar. Several weights are used and the graphs are extrapolated to locate the zero voltage point when the moment is zero. This point should be on the flexures where the strain gauges measuring moment are mounted. The distance of this point to the applied normal loads will give the applied moment. Figure 4.22b shows the results in terms of the moments applied in a clockwise direction about the zero-voltage point. The normal circuit output was designed to be insensitive to the variation of the position where the normal forces act. Figure 4.23a shows that this is true for small normal force loadings. With a 50g load, the normal circuit output appears to vary slightly with its position from the reference point. This could be due to the deflection of the balance at larger loads. Figure 4.23b shows the normal and moment circuit outputs due to the normal force loading at the reference point. Figure 4.24a shows the voltage outputs from the axial force circuit due to the normal force acting at different distance from the zero-voltage point. This represents the interaction of the normal force on the axial circuit outputs. Figure 4.24b shows the axial circuit output due to axial force loading. The relative inconsistency of the points is due to the thick water proofing material. The equations yield the following 3 × 3 matrix from which the drag, lift and moment can be obtained.

$$\begin{bmatrix} V_A \\ V_N \\ V_M \end{bmatrix} = \begin{bmatrix} 12.527 & 0 & 228.69 \\ 0 & 39.547 & 0 \\ 0 & 0 & 629.24 \end{bmatrix} \begin{bmatrix} D \\ L \\ M \end{bmatrix}$$

and

$$\begin{bmatrix} D \\ L \\ M \end{bmatrix} = \begin{bmatrix} 12.527 & 0 & 228.69 \\ 0 & 39.547 & 0 \\ 0 & 0 & 629.24 \end{bmatrix}^{-1} \begin{bmatrix} V_A \\ V_N \\ V_M \end{bmatrix}.$$

V_A, V_N, V_M are the voltage outputs from the axial, normal and moment circuits respectively in mV. D, L, M are the drag, lift and the moment. The position of the centre of pressure on the model can be found after the drag, lift and moment are known. From figure 4.11, h = zsinθ, d1 = zcosθ and $(D \times h) + L(d1 + d2) = M$. Since θ and d2 are also known, z can be found and the position of the centre of pressure can then be determined.

There are several problems encountered when using balance 1. The water-proofing material needed can be thick and hard so that the drag measurement can be inconsistent. This can be overcome by having a thinner waterproofing material but the balance must be removed from the brine after every experiment. Checks must also be done to ensure that there are no gaps in the material. It is also prudent to replace the coatings after several experiments. Each time when the waterproofing coatings are replaced the balance must be re-calibrated. The coatings will also take sometime to harden and thus there can be slight variation in the calibration initially. The forces acting on the wing are too far from the transducer which results in too large an interaction on the axial circuit output. The distance has since been reduced by having a shorter joint between the model and the forward section of the transducer.

4.6 Design of balance 2

The second design uses two of the force transducers with three struts supporting the model. The front two struts support the wing at the quarter chord where the lift is expected to be the greatest, while the back strut controls the angle of incidence from the trailing edge. Figures 4.25a and b and figure 4.29a show the schematic arrangement and photographs of the balance. Balance 2 allows the forces on an oscillating wing to be measured.

The front transducer holds the two struts via a ball bearing so that there is no moment about that point. The other ends of the two struts hold the model via a pin joint at the quarter chord so that the wing can swing freely. Since the struts are linked to the force transducer at a fixed location, the strain gauges are used to measure the front lift of the wing. A third strut pin jointed at 82.5 mm from the leading edge is connected to the second transducer that measures the drag of the wing.

During oscillation, the output from the axial component of the back force transducer will consist of contributions from both the back lift and the input force necessary to oscillate the wing. The back lift is expected to be small.

The distance along the chord between the position where the front two struts and the back hold the wing is 60 mm. The angle of incidence was varied by lowering the drag transducer and the back strut from a reference point where the incidence angle of the wing is zero.

4.6.1 Water proofing and protection against the effect of salt

Design 2 has both of the force transducers outside the water and it is only necessary to splash proof the strain gauges. Therefore only a layer of Teflon tape followed by a layer of crystalline wax (M-Coat B) are needed to protect the installations. The wire must be tightly secured to the transducer as the wax offers little mechanical protection. This arrangement has proved to be effective, and since there is less coating, the force transducer is far more sensitive than the first balance.

In the actual balance arrangement, the force transducer measuring drag uses the above protection coatings. However, the force transducer from balance 1 is used as the transducer measuring lift in balance 2 as they are interchangeable. The lift force is large enough to overcome the extra layers of protective coatings.

4.6.2 Calibration

The calibration procedures for the two force transducers used in balance 2 are simpler than for balance 1. This is because the forces to be measured are all at fixed positions from the transducers. The force transducer measuring lift was calibrated with different weights acting at the position where the transducer is connected to the front two struts of the balance. The force transducer measuring drag was connected to the back strut and it was calibrated with different weights acting on the point where the back strut holds the model with a pin joint. Figures 4.26 and 4.27 show the calibration charts.

4.6.3 Inertia of the balance

The force modules will record voltage outputs due to the movement of the model and the transducers themselves. When a wing oscillates, the front 2 struts, the back strut and the drag transducer will all be subjected to movements and some small voltage outputs from both the lift and drag transducers will be expected. When the trolley moves, the transducers will be expected to respond to the translation, especially the drag transducer which is sensitive to horizontal force. The voltage outputs due to these movements must be corrected if they are significant relative to the forces on the model.

It is not easy to account for the inertia of the balance and model during oscillation. If the wing is oscillating and not moving forwards the strain gauges will be recording the forces due to the flow around the wing. Measurements will have to be made when the wing is oscillating in air and in the fluid. Theoretical calculations were done to access the magnitude of the inertia forces and they are found to be small. Figure 4.28 shows the force diagram used to calculate the inertia forces.

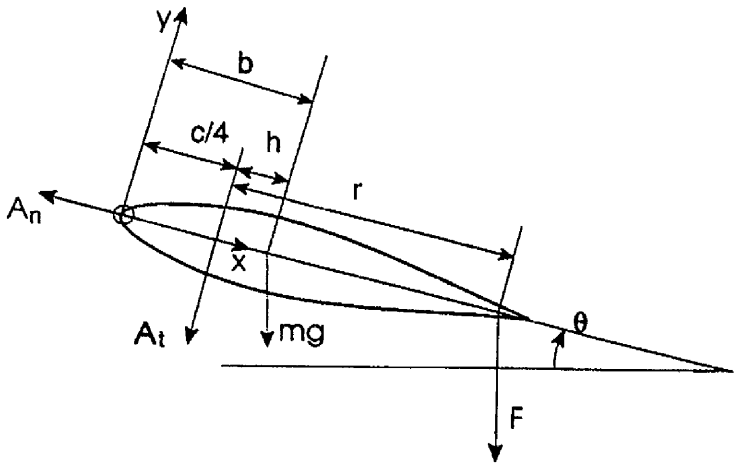

Figure 4.28 Force diagram for inertia force calculation.

The mass moment of inertia of a thin vertical rectangular solid element of mass δm about an axis through the centroid of the element is

$$I_{element} = \frac{1}{12}\,\delta m(\text{height of element})^2.$$

By the parallel axis theorem, the moment of inertia of that element about an axis through the quarter chord is

$$(I_{c/4})_{element} = I_{element} + \delta m(\text{distance of centroid of the element to } \frac{1}{4} \text{ chord of wing})^2.$$

The total moment of inertia of the wing about an axis along the quarter chord is then

$$(I_{c/4})_{wing} = \int (I_{c/4})_{element}\, \partial x.$$

This gives a value of $I_{c/4} = 8.54 \times 10^{-5}$ kgm^2 for the wing with a chord length of 0.09 m and an aspect ratio of 1.7. Using the NACA sectional profile equation, the centre of gravity of the wing is at 1.522×10^{-2} m after the quarter chord. The total cross-sectional area of the 12% thickness perspex wing is 6.635×10^{-4} m^2, the volume is 1.015×10^{-4} m^3 and the mass is 0.127 kg.

The force equations are:

$$A_n - mg\sin\theta - F\sin\theta = m\dot{\theta}^2 h$$

$$A_t - mg\sin\theta - F\sin\theta = m\ddot{\theta}h$$

$$hmg\cos\theta - rF\cos\theta = I_{c/4}\ddot{\theta}$$

where A_t, A_n are the forces at the quarter chord position where the aerofoil is pivoted and F is the applied force required to oscillate the aerofoil.

The lift error is $A_n \sin\theta - A_t \cos\theta - mg - F$ and the drag error is $-A_n \cos\theta - A_t \sin\theta$. For an oscillation of $\theta = 0$ to 4.8 degree with $\omega_f = 1.02$ rad/s the forces are given in tables 4.1 and 4.2. All are in S.I. units.

$\omega_f t$	F/N	A_n/N	A_t/N	L_{error}/N	D_{error}/N
0.000E+00	-3.160E-01	3.878E-02	-9.290E-01	1.459E-07	-3.495E-06
6.409E-01	-3.160E-01	6.193E-02	-9.277E-01	5.018E-05	1.097E-06
1.282E+00	-3.160E-01	7.587E-02	-9.267E-01	8.013E-05	6.276E-06
1.923E+00	-3.160E-01	7.511E-02	-9.267E-01	7.849E-05	5.945E-06
2.564E+00	-3.160E-01	5.994E-02	-9.278E-01	4.588E-05	5.050E-07
3.204E+00	-3.160E-01	3.634E-02	-9.291E-01	-5.125E-06	-3.687E-06
3.845E+00	-3.159E-01	1.369E-02	-9.296E-01	-5.422E-05	-2.832E-06
4.486E+00	-3.159E-01	9.882E-04	-9.297E-01	-8.172E-05	-2.628E-07
5.127E+00	-3.159E-01	3.288E-03	-9.297E-01	-7.675E-05	-8.392E-07
5.768E+00	-3.159E-01	1.968E-02	-9.295E-01	-4.125E-05	-3.522E-06
6.409E+00	-3.160E-01	4.363E-02	-9.287E-01	1.066E-05	-2.946E-06

Table 4.1 Inertia forces of aerofoil oscillating in air (aerofoil mass = 0.127 kg).

$\omega_f t$	F/N	A_n/N	A_t/N	L_{error}/N	D_{error}/N
0.000E+00	-4.817E-02	5.912E-03	-1.416E-01	2.224E-08	-5.328E-07
6.409E-01	-4.821E-02	9.439E-03	-1.414E-01	7.650E-06	1.672E-07
1.282E+00	-4.823E-02	1.156E-02	-1.412E-01	1.222E-05	9.569E-07
1.923E+00	-4.823E-02	1.145E-02	-1.412E-01	1.197E-05	9.064E-07
2.564E+00	-4.821E-02	9.136E-03	-1.414E-01	6.995E-06	7.699E-08
3.204E+00	-4.817E-02	5.541E-03	-1.416E-01	-7.814E-07	-5.622E-07
3.845E+00	-4.813E-02	2.088E-03	-1.418E-01	-8.267E-06	-4.318E-07
4.486E+00	-4.811E-02	1.507E-04	-1.418E-01	-1.246E-05	-4.006E-08
5.127E+00	-4.812E-02	5.015E-04	-1.418E-01	-1.170E-05	-1.279E-07
5.768E+00	-4.814E-02	3.000E-03	-1.417E-01	-6.289E-06	-5.370E-07
6.409E+00	-4.818E-02	6.652E-03	-1.416E-01	1.625E-06	-4.492E-07

Table 4.2 Inertia forces of aerofoil oscillating in water (aerofoil mass = 0.019 kg).

Table 4.1 shows the forces if the aerofoil were oscillated in air. The inertia term in the equations has a negligible effect; most of the force is due to the 'mg' term. Increasing the inertia by two orders of magnitude does not change the forces significantly. Table 4.2 shows the inertia forces when the aerofoil weight was reduced in the fluid; the weight of the perspex model is almost that of the salt solution it displaces. The weight is retained in the inertia term.

The effect of the aerofoil's inertia is insignificant. However it remains to check if oscillations of the aft support affect the lift. It should have no effect on the drag. Finally the inertia effects in the balance will have to be checked.

4.6.4 Inertia of the back strut on the drag module voltage output

The wing and the front 2 struts were removed with only the back strut connected to the drag force module. The tank was filled with water up to 0.46 m. With the trolley stationary, the back strut is made to oscillate at a frequency of 2.57 rad/s. This is to assess the effect of the oscillation of the drag module and the back strut on the drag module voltage outputs. The drag output recorded was negligible. The trolley was then made to travel at 0.131 m/s with the strut at a position corresponding to zero wing incidence, had the wing been fitted. This is to assess the response of the force outputs due to the horizontal trolley movement. Finally in order to find the combined effects, the trolley was allowed to travel at 0.131 m/s with the strut oscillating at 2.567 rad/s. The drag output is entirely due to the movement of the trolley and the surface wave drag of the back strut, the correction for this will be discussed in 4.6.6.

4.6.5 Inertia of balance with a T-structure replacing the wing

The wing was replaced by a T-structure as shown in figure 4.29b. The tank was filled with water to a depth of 0.46 m. This T-structure has a mass of a mere 1.95 g in air which is much less than the wing's 127 g. The wing has a mass of 19 g in water. The T-structure was made to oscillate at 7.18 rad/s with the trolley stationary. Since the T-structure is much lighter compared to the wing, the inertia of the system should be much less than the system with the wing. It is likely that the inertia will be dominated by the inertia of the struts since the mass of the T-structure is less than the struts. The back strut is expected to contribute most of the inertia force since both the mass and distance from the line of rotation are large. The front two struts, although having greater combined mass, will have negligible inertia force since the movement relative to the line of rotation is minute. The T-structure has much lower mass but the centre of gravity is at some distance from the line of rotation. Figure 4.31 shows the lift and drag outputs. The magnitude of the force, including friction in the system and the vortices generated by the T-structure, is in the order of the low frequency noise that passes filtering.

The trolley was then allowed to move at 0.227 m/s. The drag of the system minus the drag of the T-structure and the three struts will give the effects of the inertia of the system on the drag module outputs. The outputs appear to be dominated by the effect of horizontal trolley movement and this will be discussed in section 4.6.6. This analysis is also applied to the lift module outputs and they are insignificant.

4.6.6 Voltage outputs due to movement of trolley

The effects of the trolley movement were investigated in a number of ways. The trolley was made to move at several velocities with the force modules connected to the three struts holding the wing in both water and air. In the presence of the water, viscous drag of both the struts and wing, and drag due to the surface wave produced by the struts increase the voltage outputs from the drag measurements. The struts are designed to produce a purely horizontal flow in the stratified fluid and will not produce significant internal waves. The experiments were repeated with the three struts and the T-structure, the back strut alone and the back strut with the T-structure. The trolley was also allowed to travel at several velocities with the force modules not connecting to any struts and models.

It was found that the moment of the trolley caused reductions in the voltage outputs of the drag even without the model and the struts. The lift outputs were unaffected. It is therefore apparent that the strain gauges measuring drag are picking up the effect of the horizontal acceleration of the trolley. Since these effects vary with time, it is not sufficient to take time averages of the drag of the struts and the T-structure. This is particularly true in the case of an oscillating wing as the drag of the model also varies with time. Since the sampling rate of the analogue to digital converter is fixed, point by point evaluations at each time interval for each stage will be a more accurate method. This method is illustrated in figure 4.30. The key in this figure shows which voltage outputs correspond to the curves. They are, in order, (1) the wing alone which was evaluated from other curves, (2) the output with the three struts and the trolley movement after subtracting the effect of the separating structure, (3) the output of the T-structure after subtracting the effect of back strut and the trolley movement, (4)* the T-structure, trolley movement and three struts, (5)* the back strut, trolley movement and T-structure, (6)* the back strut and trolley movement, (7)* the wing with the three struts and trolley movement during an oscillation. The starred results are direct measurements and the others are evaluated from these. The x-axis shows the time after the initial acceleration.

4.6.7 Uncertainty analysis

The previous analysis concerns the dynamic characteristics of the system, the static performance will now be studied. The equations from this section can be obtained from Doebelin (1990). Consider the drag coefficient which is a function of the drag force D, velocity of the wing U, density of the fluid ρ, span of the wing s and chord of the wing c. The uncertainty of C_D consists of possible errors from each of the components. The direct errors consist of reading the density from the hydrometer, the length for s, c, distance travelled by trolley, the time from the stopwatch, voltage reading from digital oscilloscope or voltmeter and the force measurements using dead weights. These errors are given in table 4.3.

There are errors associated with reading the calibration charts for D, U and ρ due to curve fitting. The standard deviation, S_{qi}, from the true value can be obtained the following equation,

4. Measurement of forces on an oscillating wing moving in a pycnocline

$$S_{qi}^2 = \frac{1}{N_{cp}} \Sigma \left(\frac{q_o - b_2}{b_1} - q_i \right)^2$$

where N_{cp} is the number of calibration points, q_o is indicated value, q_i is the true value. Assuming that q_o and q_i are related by a linear function $q_o = b_1 q_i + b_2$, b_1 is the gradient of the curve and b_2 is the value of q_o when $q_i = 0$. The information needed to derive the standard deviations from the true values of ρ, U and D can be obtained from figures 4.4, 4.10, 4.26 and 4.27. They are listed in errors 6 to 9 in table 4.3 with other possible errors.

Possible source of error	Uncertainty
1. Reading density ρ from the hydrometer	± 1.0 kg/m^3
2. Reading length s and c	± 0.01 mm
3. Reading time from a stopwatch	± 0.01 s
4. Measurement of distance travelled by trolley using a rule	± 1.0 mm
5. Velocity measurement using tape and stopwatch (0.26 m/s)	± 0.0043 m/s
6. Calibration chart error for ρ	± 1.85 kg/m^3
7. Calibration chart error for U	± 0.00117 m/s
8. Calibration chart error for drag, D	± 0.00158 N
9. Calibration chart error for lift, L	± 0.00402 N

Table 4.3 Possible measurement errors.

It is very difficult to quantify the errors associated from source of error 1, 2, 3 and 4. For example, error 3 depends on the user's response time and error 1 may depend on the float staying parallel to the fluid level and not too near the surface of the container. Error 5 is the result of error 3 and 4. These are random errors and the effects could probably cancel out. Errors 6 to 9 are obtained statistically and therefore should cover the random errors associated with each parameter.

Assuming D = 0.05 N, ρ = 1123 kg/m^3, c = 0.09 m, s = 0.153 m, U = 0.33 m/s. The equation for calculating the absolute limits on the overall error, E_a, is given by

$$E_a = \left| \Delta D \frac{\partial C_D}{\partial D} \right| + \left| \Delta U \frac{\partial C_D}{\partial U} \right| + \left| \Delta \rho \frac{\partial C_D}{\partial \rho} \right| + \left| \Delta s \frac{\partial C_D}{\partial s} \right| + \left| \Delta c \frac{\partial C_D}{\partial c} \right|$$

where ΔD is the sum of uncertainties for drag force, ΔU for velocity, Δρ for density, Δs for span and Δc for chord of the wing. Given $C_D = \frac{2D}{\rho U^2 sc}$,

$$E_a = \left|(0.00158)\left(\frac{2}{(1123)(0.33)^2(0.153)(0.09)}\right)\right|$$

$$+\left|(0.00117)\frac{-4(0.05)}{(1123)(0.33)^3(0.153)(0.09)}\right|$$

$$+\left|(1.85)\frac{-2(0.05)}{(1123)^2(0.33)^2(0.153)(0.09)}\right|+\left|(0.00001)\frac{-2(0.05)}{(1123)(0.33)^2(0.153)^2(0.09)}\right|$$

$$+\left|(0.00001)\frac{-2(0.05)}{(1123)(0.33)^2(0.153)(0.09)^2}\right|,$$

$$E_a = (0.00188)+(0.000421)+(0.0000978)+(0.00000388)+(0.0000066)$$

and $E_a = 0.0024$.

The method of finding the probable errors, $E_{a_{rss}}$, is according to the root-sum square (rss) as given by the following equation,

$$E_{a_{rss}} = \sqrt{\left(\Delta D\frac{\partial C_D}{\partial D}\right)^2+\left(\Delta U\frac{\partial C_D}{\partial U}\right)^2+\left(\Delta\rho\frac{\partial C_D}{\partial \rho}\right)^2+\left(\Delta s\frac{\partial C_D}{\partial s}\right)^2+\left(\Delta c\frac{\partial C_D}{\partial c}\right)^2},$$

$$E_{a_{rss}} = \sqrt{(0.00188)^2+(0.000421)^2+(0.0000978)^2+(0.00000388)^2+(0.0000066)^2}$$

and $E_{a_{rss}} = 0.0019$.

Using similar arguments and with lift force L = 0.2 N,

$$E_a = (0.00477)+(0.00168)+(0.000391)+(0.0000155)+(0.0000264)$$

$E_a = 0.0069$ and $E_{a_{rss}} = 0.0051$.

The error for drag of 0.05 N is possibly as large as 0.0024 N (4.8%) but probably not larger than 0.0019 N (3.8%). For lift of 0.2 N, the largest possible error is 0.0069 N (3.45%) while the largest probable error is 0.0051 N (2.55%). The values of lift and drag represent highest typical forces experienced by the wing.

4.7 Signal processing

The force transducer is capable of measuring forces smaller than one hundredth of a newton as shown in the calibration charts in sections 4.5 and 4.6. The investigation of the inertia force during wing oscillation has shown that their effect is of the order of 1/100 N. Forces of this magnitude produce electrical signals that are always accompanied by noise that can come from many sources having different frequencies

which must be identified and removed. A few signal processing methods have been investigated and they will be presented here.

4.7.1 Identification of noise frequencies

The noise can come from sources such as the analogue to digital converter, the electric pickup by the wires, the movement of the trolley and the oscillatory mechanism. The different types of noise experienced so far are all high frequency and they can be eliminated by a low-pass filter. It is necessary to transform the signal into its frequency domain to see the dominant frequencies. This can be done using a 4096 points fast Fourier transform. Figure 4.32a shows a typical frequency output from a wing travelling at 0.33 m/s and oscillating at 1.2 Hz in a pycnocline with $N_c = 0.784$ Hz. The frequencies will be expressed in Hz to be consistent with the input parameters of the signal processing methods. The peak at 1.2 Hz is the oscillation frequency of the wing and the two other high peaks at 9.5 Hz can be 12.5 Hz well above the natural frequency of the fluid. No other prominent frequency can be seen near the frequency of oscillation and the signals higher than 6.0 Hz can be safely filtered off. The peak very near the 0 Hz is associated with the cycle involving the start and the end of a run.

To identify the frequency of the motor, the force transducers were mounted onto the oscillatory mechanism without the model. The motor was then switched on with the gearboxes linked by rubber belts. The voltage outputs from the strain gauges were measured over a period of 30 seconds and the frequency of the motor was found to be at 50 Hz which was well away from the range of frequencies of interest. The power spectral density associate with this frequency has been greatly reduced by the spring system and it is not a prominent frequency.

4.7.2 Noise reduction by a moving average method

A number of ways can be used to reduce the noise. The most straight forward method is a moving average. This method has the similar effect of putting a capacitor across each input channel. The computer program for data acquisition can be programmed to produce a moving average result based on any number of points and the results can be plotted directly onto the screen. However this method lacks the precision to cut-off unwanted frequencies and can be misleading if the noise frequencies are too near to the frequencies of interest. Figure 4.33 illustrates the effect of increasing the

moving average on a typical signal. The signal has been transformed to its frequency domain in order to show how frequencies are being removed. The original signal is shown in figure 4.32a. At 25 and 50 averaging points, the power spectrum at 1.2 Hz is only slightly reduced. At 75 averaging points, it is being reduced significantly and at 100 averaging points, it disappears completely. In many cases the amplitude associated with important frequencies are often reduced in order to remove the noise. This makes it difficult to compare the force measurements as the number of averaging points is now an extra factor to consider. However, this method may be applied to cases where the voltage outputs are associated with the wing moving at a fixed incidence or with outputs associated with strut drag corrections. These outputs are often steady and the only important frequency is the cycle involving the start to the end of the runs, which is very near to the 0 Hz.

4.7.3 Signal processing using Matlab version 4.2

As an alternative the raw data can be analysed using MatLab's signal processing package. The data are transformed to their frequency domains with a fast Fourier transform to identify the prominent frequencies and to determine the range of frequencies required. The next step is then to design a filter to screen off unwanted high frequency noise. Four different low-pass filters were considered, they are the Butterworth, the Elliptic and the Chebyshev type I and II filters. Figure 4.34 shows their frequency responses with a cut-off frequency of 2 Hz at two different sampling rates. All the responses have the highest possible order to minimise the transition width, beyond that limit a singularity may emerge to cause a failure of the filter. The transition width of the filters decreases with increasing order. The order determines the length of the 2 vectors used to define the filter coefficients. Figure 4.35 shows the effect of increasing the order on the transition width of the frequency response of the filters. The elliptic filter is the preferred filter because it has the smallest transition width, a low enough stopband and a flat passband. One design criteria is that the ripples in the passband must be kept to a minimum and the presence of ripples in the stopband is compromised in order to achieve this. Chebyshev type I is also acceptable but it has a larger transition width. The Butterworth filter has the advantage of being flat in both passband and stopband but it seems to act before the cut-off frequency. Both elliptic

and Chebyshev type I filters have negligible ripples in the passband and the tendency to overshoot the cut-off frequency. Chebyshev type II filter is inferior.

The original signal from a wing moving at 0.33 m/s and oscillating at 1.2 Hz in a pycnocline with N_c = 0.784 Hz is shown in figure 4.36. The results after filtering through various filters are also shown. The cut-off frequency is 1.44 Hz. In this case, all the three filters appear to work almost as well. Figures 4.37 to 4.38 show the results using different cut-off frequencies and two sampling rates. At the lower sampling rate the cut-off frequency must not be less than 2 Hz with oscillating frequency of 1.2 Hz. At the high sampling rate the signal is more tolerant to low cut-off frequencies. Figures 4.39 to 4.40 show similar results for an oscillating frequency of 0.392 Hz.

4.7.4 Using the elliptic filter

The input data is arranged in matrix form with columns separated by tabs. The number of data in each column, the Nyquist frequency, the cut-off frequency and the order number of the filter are the input parameters. Most of the tasks are done by Microsoft Excel. The Nyquist frequency is half the sampling rate, ie $f_{Ny} = \frac{1}{2\Delta t}$ where Δt is the time interval between the data points. The raw data has to be first transformed to its frequency domain using a fast Fourier transform to identify the important frequencies and to determine the cut-off frequency. The order number typically starts at 6 and increases in steps of 1 until the filter fails.

Most of the data will be processed by the elliptic filter. The superiority of the filter over the moving average method can be shown by filtering the signal shown in figure 4.32a at an order of 8 and a cut-off frequency as low as 2.4 Hz to give the results in figure 4.32b. There seems to be no reduction in the power spectral density associated with the oscillation frequency of 1.2 Hz. Corresponding figures with a higher sampling rate are shown in figures 4.32c & 4.32d.

Figures 4.41 and 4.42 show the voltage outputs using the elliptic filter and the moving average method for two sampling rates. The original signals are shown in (a) of both figures. The signal after being filtered by the elliptic filter with a cut-off frequency of 1.44 Hz is shown in figure 4.41(c). The other figures are for different moving averages.

4.7.5 Data acquisition and analysis

The data acquisition uses a Microlink 3000 12 bit analogue to digital converter. The total number of input channels required depends on the strain gauge balance used. Three channels are needed for the sting balance while six channels are used for the overhead balance. A channel is normally required for the oscillation of the model while an additional channel will be needed for the conductivity probe which detects the presence of pycnocline waves.

The digital outputs from the analogue to digital converter are fed into an Acorn RiscPC 700 computer. These results are displayed on the screen and are saved as data files. Typically an acquisition involving eight channels produces a raw data file of 280Kbytes, providing 17,500 readings per channel in 35 seconds.

4.8 Dimensional analysis

4.8.1 An oscillating wing in a constant density media.

When a wing moves in a media of constant density, the lift and drag on the body depends on the following parameters.

- Fluid properties, viscosity μ and density ρ.
- Velocity and acceleration of the wing.
- Geometry of the wing: chord c and span s together with the shape.
- The time t and the oscillation frequency ω_f in rad/s.
- The wing incidence $\propto$ and the incidence amplitude $\propto_a$.

The oscillation is sinusoidal and the circulation and distance between the vortices are probably accounted for in the lift L and drag D. If the oscillation is non-sinusoidal, then the shape of the pitch waveform will have an effect on the vortical patterns in the wake of the wing (Koochesfahani, 1989).

When the wing is moving at a constant speed U, the force coefficients $C_L = \frac{2L}{\rho U^2 sc}$ and $C_D = \frac{2D}{\rho U^2 sc}$ depend on μ, ρ, α, α_a, s, c, t, and ω_f which form the dimensionless groups:

Reynolds number $Re = \frac{\rho U c}{\mu}$

reduced frequency $K_f = \frac{\omega_f c}{2U}$

also α, α_a, s/c, and $\omega_f t$ together with the wing shape parameters. For geometrically similar comparisons, C_L and C_D are functions of Re , K_f, α and α_a only.

4.8.2 With stratification included

The extra parameters are:

- Pycnocline properties: the thickness ε, density ρ_c, and natural frequency N_c at the centre, density difference across the pycnocline, $\Delta\rho$.
- Pycnocline properties at the level of the wing at 0 degree incidence: N and ρ_{cw}.
- Distance of the wing from the centre of the pycnocline, h.
- Acceleration due to gravity, g.

Due to the large number of variables involved, it will not be possible to derive a sensible set of non-dimensional quantities without considering the physics of the problem. Eight possible numerics are $\frac{\rho_{cw}Uc}{\mu}, \frac{N_c\varepsilon}{U}, \frac{\omega_f}{N_c}, \frac{\varepsilon}{c}, \frac{h}{c}, \frac{\Delta\rho}{\rho_c}, \frac{N}{N_c}$ and $\frac{U^2}{gc}$. If ρ_c, N_c and ε are known, then $\Delta\rho$ is known from $N_c^2 \cong \frac{g\Delta\rho}{\rho_c\varepsilon}$. This means that $\frac{\Delta\rho}{\rho_c}$ can be excluded if N_c is to be retained. The distance, h, from the centre of the pycnocline can be related by $N = N_c \operatorname{sech}\left(\frac{2h}{\varepsilon}\right)$ and only one of the two numerics, $\frac{N}{N_c}$ and $\frac{h}{c}$ is retained. C_D and C_L can be a function of

$$\frac{\rho_{cw}Uc}{\mu}, \frac{N_c\varepsilon}{U}, \frac{\omega_f}{N_c}, \frac{\varepsilon}{c}, \frac{h}{c} \text{ and } \frac{U^2}{gc} \qquad (4.2)$$

or

$$\frac{\rho_{cw}Uc}{\mu}, \frac{N_c\varepsilon}{U}, \frac{\omega_f}{N_c}, \frac{\varepsilon}{c}, \frac{N}{N_c} \text{ and } \frac{U^2}{gc} \qquad (4.3)$$

where $\text{Drag} = \frac{1}{2}\rho_{cw}U^2 scC_D$, $\text{Lift} = \frac{1}{2}\rho_{cw}U^2 scC_L$ and ρ_{cw} is the density at the centre of the wing position. The Froude number $Fr = \frac{U^2}{gc}$ can be written in a number of ways,

$$Fr = \frac{2U}{\varepsilon N_c}, \qquad Fr = \frac{U}{\sqrt{(g\varepsilon/2)}} \qquad (4.4)$$

and

$$Fr = \frac{U}{\sqrt{g'h}} \quad \text{where} \quad g' = g\frac{\rho_2 - \rho_1}{\rho_2 + \rho_1}, \text{ Lamb (1932).} \qquad (4.5)$$

$Fr = \frac{U}{\sqrt{g'h}}$ includes the position of the wing in the pycnocline. If the experiments are carried out at the centre of the pycnocline, and h is not a factor, then $Fr = \frac{U}{\sqrt{(g\varepsilon/2)}}$ should be used instead. The internal Froude number is

$$Fr_i = \frac{U}{cN} \qquad \text{where N is the local natural frequency.} \qquad (4.6)$$

In chapter 3, $M = \frac{\varepsilon N_c}{U}$ and $\beta_f = \frac{U\omega_f}{\varepsilon N_c^2}$. $Re = \frac{\rho_{cw} Uc}{\mu}$ and the parameters in equation (4.3) can be written as

$$C_D = f\left(Re, M, \beta_f, \frac{\varepsilon}{c}, \frac{N}{N_c}, \frac{\varepsilon N_c^2}{2g}\right). \qquad (4.7)$$

which could relate the force measurement to the wave configurations shown in chapter 3. The last term conveniently approaches unity for interfacial waves and approaches zero for a constant density fluid. The internal Froude number in equation (4.6) can be brought in at this stage to give

$$C_D = f\left(Re, M, \beta_f, \frac{\varepsilon}{c}, \frac{U}{cN}, \frac{\varepsilon N_c^2}{2g}\right) \qquad (4.8)$$

Another function for C_D can be derived from parameters in equation (4.2).

$$C_D = f\left(Re, M, \frac{\omega_f}{N_c}, \frac{\varepsilon}{c}, \frac{h}{c}, \frac{\varepsilon N_c^2}{2g}\right) \qquad (4.9)$$

The numeric $G = \frac{\varepsilon N_c^2}{2g}$ can be written as $\frac{\varepsilon N_c^2}{2g'}$ since $g' \equiv g\frac{\Delta\rho}{2\rho}$ and $g \to g'$. $\frac{\varepsilon N_c^2}{2g'}$ can be replaced with Froude number $Fr = \frac{U}{\sqrt{g'h}}$. When the wing is moving at a speed U, the wavelength of the natural frequency waves is given by $\lambda = \frac{2\pi U}{N_c}$ and hence $M = \frac{2\pi\varepsilon}{\lambda}$ which is a ratio of the pycnocline thickness to the wavelength. Note that M has the form of an inverse Froude number where $Fr = \frac{2U}{\varepsilon N_c}$. M can be replaced by the term $\frac{cN_c}{2\pi U} = \frac{c}{\lambda}$ which is the ratio of the wing chord to the natural frequency wavelength. When the wing chord is less or equal to half the wavelength, the energy

associated with a natural frequency oscillation appeared to be stronger. This is demonstrated in many of the video clips provided in the CD-ROM, an example for a steady wing with a forward velocity is shown in clips 83, 84 and 148p. Under this condition the drag on the wing is expected to be high. Video clips 105, 124 and 163 are some other examples of an oscillating wing producing waves with wavelength about twice the chord length. The numeric $\frac{\omega_f}{N_c}$ can be replaced with $K_f = \frac{c\omega_f}{2U}$ which is the reduced frequency commonly used for experiments on wing oscillations in a constant density fluid. K_f is also related to the Strouhal number $St = \frac{c\omega_f}{2\pi U} = \frac{K_f}{\pi}$. Equation (4.9) can be written as

$$C_D = f\left(Re, \frac{c}{\lambda}, K_f, \frac{\varepsilon}{c}, \frac{h}{c}, \frac{U}{\sqrt{g'h}}\right) \qquad (4.10)$$

Peake (1996) considered the force experienced by a sphere oscillating and moving horizontally in a stratified fluid. A graph of Froude number $Fr = \frac{U}{\sqrt{g'h}}$ against frequency parameter $\sigma = \frac{U\omega_f}{g'}$ was produced which defined a region in which one component of the expression for drag decreased.

The legends in figures 4.91 to 4.98 show

$$L = \frac{c}{\lambda}, M = \frac{\varepsilon N_c}{U}, E = \frac{\varepsilon}{c}, Fr = \frac{U}{\sqrt{g'h}}, Fr_i = \frac{U}{cN}, G = \frac{\varepsilon N_c^2}{2g}.$$

These definitions will be used throughout the rest of this thesis.

4.8.3 Reynolds number

Two trip wires were used to simulate turbulent flow over the wing on both sides of the wing. The critical Reynolds number depends on the size of the trip wire. The trip wire used was 0.404 mm which should not alter the shape of the wing significantly. The wing was allowed to move at various velocities in fluid of constant density and the drag coefficients were recorded. The results indicate that the trip wire is not causing transition at velocities below 0.228 m/s or Reynolds numbers below about 22,000.

4.9 Results of the force measurements

The wing starts to oscillate, accelerates from rest, reaches a constant velocity and then decelerates to rest again. All the figures show the force coefficients just after the acceleration. As the wing decelerates to rest, the force coefficients can be seen to drop to zero. The oscillation is sinusoidal. Force measurements were recorded with various frequencies at several velocities. In order to ensure that the boundary layer is turbulent, only those with high enough Reynolds numbers are presented.

4.9.1 Force measurements in constant density fluid

Figures 4.43 to 4.64 show the force coefficients of an oscillating wing in a constant density fluid. The figures are grouped together according to their velocities or Reynolds numbers. Within each group with the same Reynolds number, the figures are arranged in increasing oscillatory frequencies. The sinusoidal green lines show the position of the wing at any instance, the red and blue lines are for the lift and drag measurements of an oscillating wing. Force measurements associated with the wing at fixed incidences of 0 and 4.8 degrees are shown as pink and pale blue lines. There is a phase shift between the force and the position of the wing. The non-dimensional group in equation (4.10) will be used, since the reduced frequency K_f is commonly used for experiments involving oscillating wings in constant density fluid. Figures 4.43 and 4.44 show the force measurements of an oscillating wing with U = 0 m/s. In this case, the reduced frequency K_f is infinite, and the drag can be seen reducing at higher ω_f. There is a very small average lift. When the wing is moving forward, at lower K_f, the lift coefficients of the oscillating wing fall within the lift coefficients of the wing fixed at 0 and 4.8 degrees. This is expected since the incidence angles were well away from the stalling angle. However, at K_f = 1.49 and K_f = 1.32 as shown in figures 4.49a and 4.54a, the maximum lift coefficients from the oscillating wing were seen to exceed that of the C_L with a fixed incidence of 4.8 degrees. The minimum lift coefficients were also seen to be lower at higher K_f. These observations are consistent with the stronger vortices being generated at higher K_f as also seen from the experiments by Koochesfahani (1989) and McAlister (1978). From the figures, there is no apparent decrease in the mean drag across the range of K_f. Koochesfahani has also shown that there is little change in drag at K_f under 4.4 and around K_f = 6.8, a wing oscillating

between ±2 degrees will have no drag. These results, in a constant density fluid, will be compared with those where the wing is in a stratified fluid.

4.9.2 Force measurements in stratified fluid

Figures 4.65 to 4.90 show the force coefficients of a wing in a stratified fluid. In figure 4.75, the vertical green lines show the position of the wing at 4.8 degrees. This is due to the inconsistency in the frequency of oscillation between the first and second cycle. There are 5 sets of figures grouped together such that each group has fixed values of the parameters $\mathrm{Re}, \frac{c}{\lambda}, \frac{\varepsilon}{c}, \frac{h}{c}, \frac{U}{\sqrt{g'h}}$ (see equation 4.10). The figures within each group have increasing K_f. Similarly the parameters $\mathrm{Re}, M, \frac{\varepsilon}{c}, \frac{U}{cN}, \frac{\varepsilon N_c^2}{2g}$ are fixed (see equation 4.8) but have increasing β_f. These figures are arranged in such a manner that the information can be conveniently used to plot C_D and C_L against K_f or β_f later.

It was necessary to allow at least a 15 minute interval between each of the fixed incidence and oscillatory runs. The pycnocline properties changed with time as a result of the disturbances as well as from diffusion, and the time needed for the waves to settle down before the next run make it impossible to make too many runs in a given time. The lift coefficients for the wing moving in a stratified fluid are significantly lower and the drag coefficients are seen to be slightly higher than in a constant density fluid.

It appears that both C_D and C_L are complicated by the distance of the wing from the centre of the pycnocline, h. Without h, parameters in equation (4.10) will be

$$C_D = f\left(\mathrm{Re}, \frac{c}{\lambda}, K_f, \frac{\varepsilon}{c}\right)$$

$\frac{\varepsilon}{c}$ is constant for a particular pycnocline and Reynolds numbers would have little effect if the boundary layers were turbulent. C_D can then be plotted against K_f with several values of $\frac{c}{\lambda}$. The extra numeric h has added an extra parameter to equation (4.8) and appears in two parameters in equation (4.10).

The summary of the results for both stratified and constant density fluid are plotted in figures 4.91 to 4.96 showing the variation of force coefficients with K_f. Figure 4.91 shows the graph of mean C_D against K_f, the curves associated with a constant density fluid have smaller C_D than those in pycnoclines. The variation among

the constant density curves indicates the slight Reynolds number effect on C_D and it shows C_D to be lower at high Reynolds numbers. Among the pycnocline curves, it appears that the dominant factor is Fr where higher Fr corresponds to lower C_D. However, at L = 0.52, and Fr = 1.09, the mean drag is seen to be much higher. This corresponds to the case where the wavelength is twice the chord length of the wing. The wave energy associated with this flow is higher as demonstrated in some of the video clips 83, 84 and 148p. Even if the wing is oscillating, there will still be a steady wave system in addition to the oscillatory wave system. Under this condition the drag associated with the steady system will be high.

The graphs of mean C_L against K_f are shown in figure 4.92. The C_L for the constant density fluid for different Reynolds numbers is around 0.13 to 0.14 which is much higher than those for the pycnocline. A higher Froude number appears to yield higher C_L, except for L = 0.48 and 0.52.

Figure 4.93 shows the graph of maximum C_D against K_f. The sudden increase in C_D for L = 0.24, K_f = 1.31 is due to the increase in C_D at time = 6s shown in figure 4.85, else the value should be around 0.06. The reason for this jump in C_D is unclear. The results for maximum C_L against K_f are shown in figure 4.94 which indicates an increase with K_f for both the stratified and constant density cases. The results for the constant density are close together showing that the force coefficients are insensitive to the non-dimensional terms other than K_f. However the curves for the pycnocline cases have indicated the differences that arise in terms of the various parameters.

The minimum C_D and C_L tend to decrease with increase of K_f and this is reflected in figures 4.95 and 4.96. The graphs for C_D vs K_f are more volatile due to the variations between different peaks and troughs associated with the drag output. It is therefore more appropriate to put the emphasis on the trend rather than each individual point during a comparison.

4.10 Other possible explanation for results

The lift coefficient is affected by the freestream velocity, the local fluid density and the incidence angle. The results attained have shown that the lift coefficients are lower when the wing is in a stratified fluid in both steady and dynamic cases. In cases of lower Reynolds numbers or wing velocities, the lift coefficients can be negative during parts of the oscillation. There are few explanations for the observation.

Consider a two-dimensional aerofoil at constant incidence in a stratified fluid at low Reynolds numbers, there will be an upstream wake producing a high drag. With the range of Reynolds numbers considered, this upstream influence is unlikely to be a complete blocking. Nevertheless, at lower Reynolds numbers, the flow is expected to slow down considerably ahead of the aerofoil. This results in lower lift compared with a wing in an unstratified fluid. Hurdis & Pao (1976) showed that with a vertical plate moving horizontally in the centre of a pycnocline, there is an internal solitary wave in front of the upstream disturbance. This wave could be caused by the impulsive start of the plate. The upstream influence becomes weaker as the Reynolds numbers or Froude numbers increase.

For a finite wing this reduction in lift and increase in drag would still be present to a smaller degree but flow can now move around the sides of the wing rather than over the top or below the wing. This will have the effect of reducing the lift and the form drag. But the form drag can still be higher than in the non-stratified case. The induced drag will probably be lower, and internal waves are produced so that there is now a wave drag contribution. The experimental results show that the total drag is higher than in the non-stratified case. At higher Froude numbers, the stratified fluid is more likely to be displaced over the wing hence generating more lift and less drag. This is clearly shown in figures 4.91 and 4.92.

A velocity deficit is expected in the downstream flow close to the trailing edge of the wing, unless the frequency of oscillation is high enough to generate a reverse jet in the wake. However, with a non-oscillating vertical plate, Hurdis & Pao (1976) had also observed a reverse jet further downstream. This lee jet appears to exist between the wake of the wing and the lee waves. When the fluid is displaced vertically, the streamlines were constricted between the obstacle and the adjacent stratified fluid strata, which is reluctant to move upward. This constricted fluid accelerated over the obstacle and returned to its equilibrium position with enough momentum to create the reverse jet. The jet is replaced by lee waves further downstream. It is unclear how this jet will change the forces on the wing. The lift distribution is likely to be different from that of the constant density case due to the accelerated flow over the surface of the wing.

The maximum lift coefficients are shown to increase as the frequencies of oscillation increase. McAlister et al (1978) have shown that the vortices associated with the dynamic increase in incidence angle of an oscillating aerofoil moving in a constant density media is more dominant than the steady case, and there will be a dynamic

increase in lift. The figures of lift outputs for a wing moving in constant density media indicate that the lift coefficients in part of the cycle can be more than that for the steady cases if $K_f > 1.103$ for $U = 0.228$ m/s, figure 4.48. Similarly the minimum lift coefficients become lower than the steady cases for the respective values of K_f. In stratified fluid, the vortex does not roll-up as readily as the constant density case. The upward movement of the vortex lines parallel to the trailing edge are restricted by the stratification and the vortices quickly collapse before the fluid returns to its equilibrium position. This may be an indication that the lift will be lower in the stratified fluid. Clips 93 to 100 in the enclosed CD-ROM show the vortex roll-up in the wake of an oscillating wing moving in a pycnocline. Clips 95 and 99 are cases with higher frequency of oscillation where several vortices can be seen and the lift is expected to be higher. The schlieren images are shown in clips 164s, 165s and 166s where the vortices can be seen to collapse and internal waves are generated.

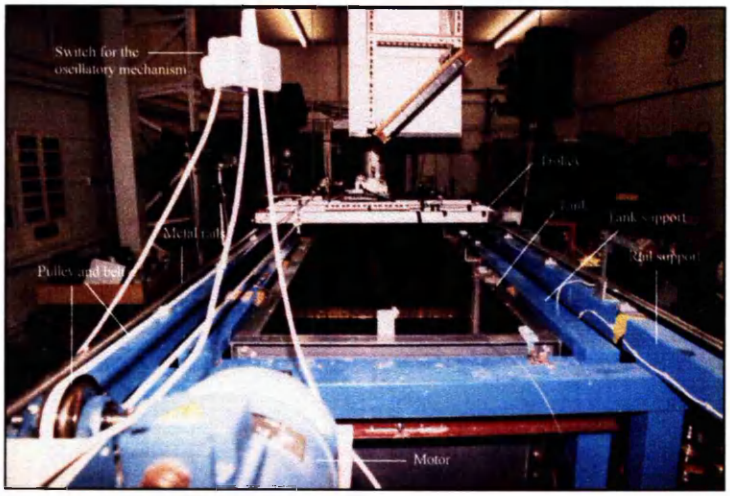

Figure 4.1 The towing tank.

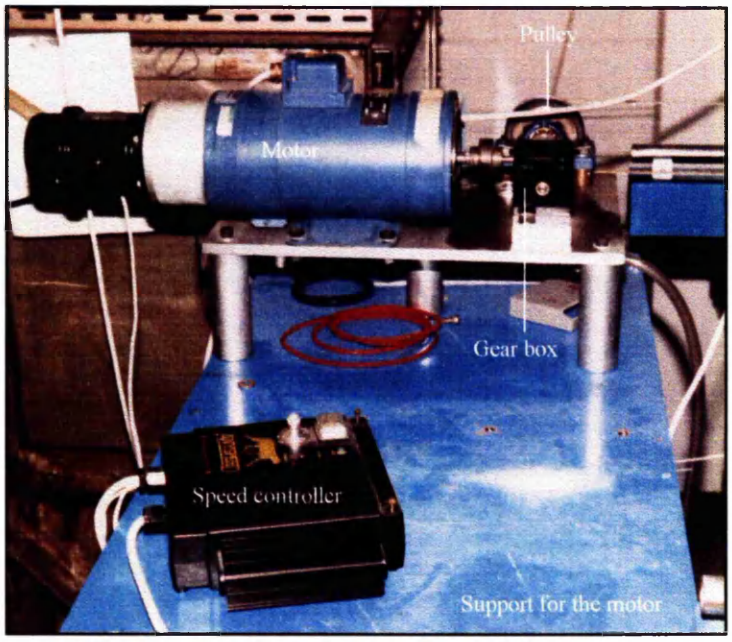

Figure 4.2 Speed controller and the motor.

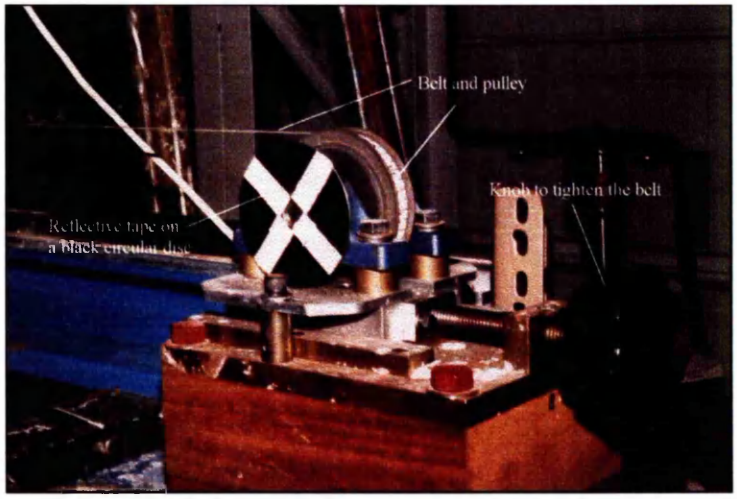

Figure 4.3 The belt and pulley system used to drive the trolley.

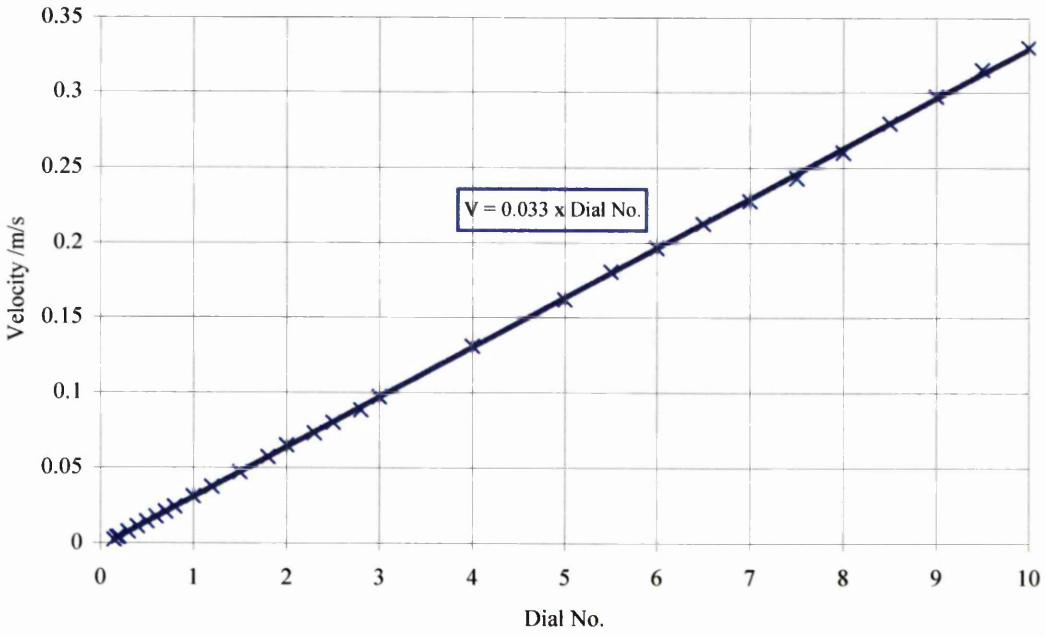

FIGURE 4.4 CALIBRATION CHART FOR TROLLEY VELOCITY

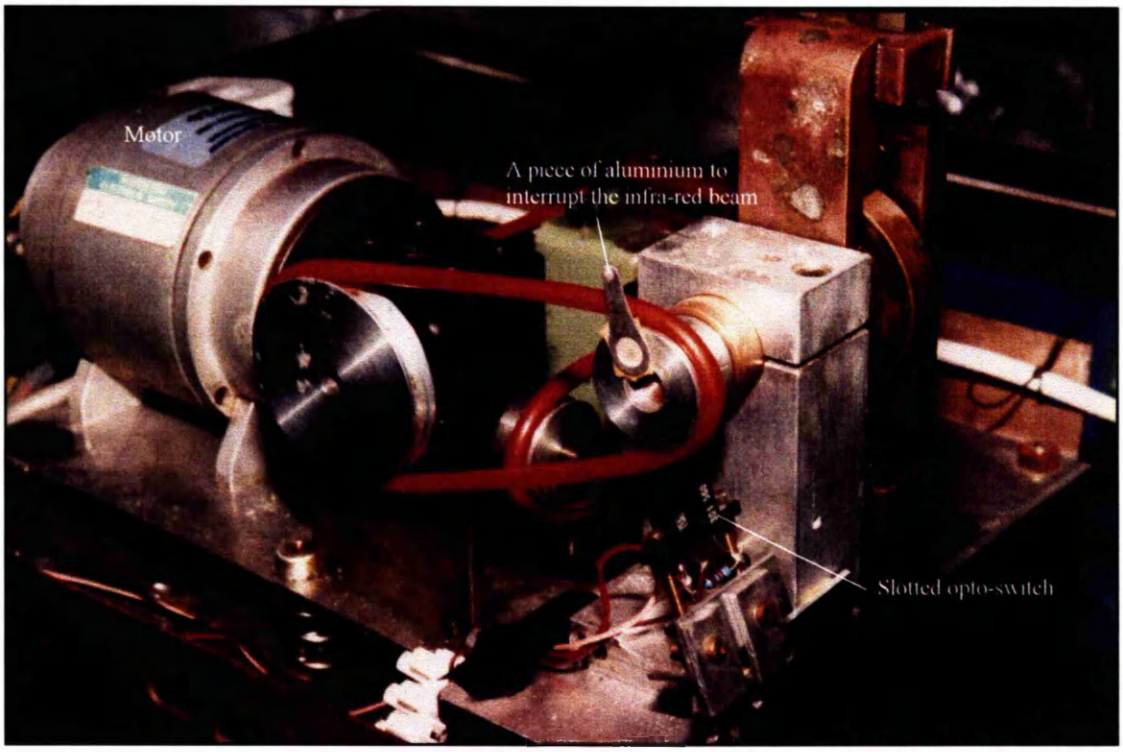

Figure 4.5 The oscillatory mechanism for the pitching motion of the wing.

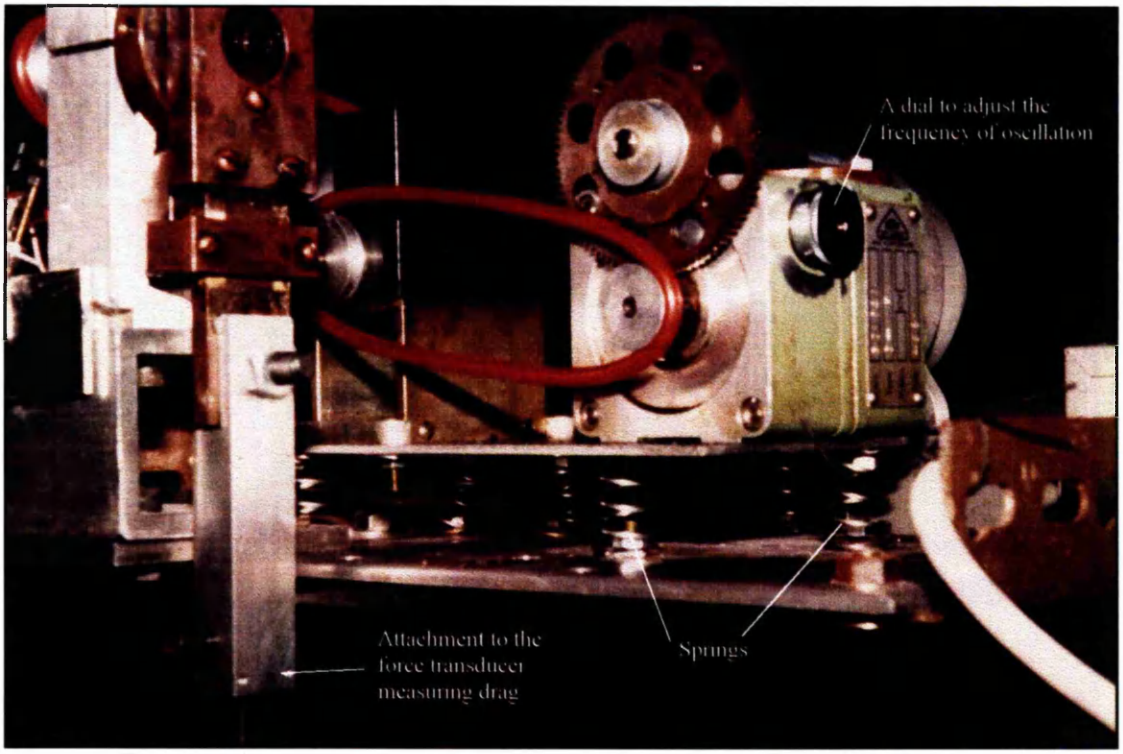

Figure 4.6 The spring system supporting the oscillatory mechanism.

Figure 4.7 The two tanks used to contain fluid before filling the towing tank.

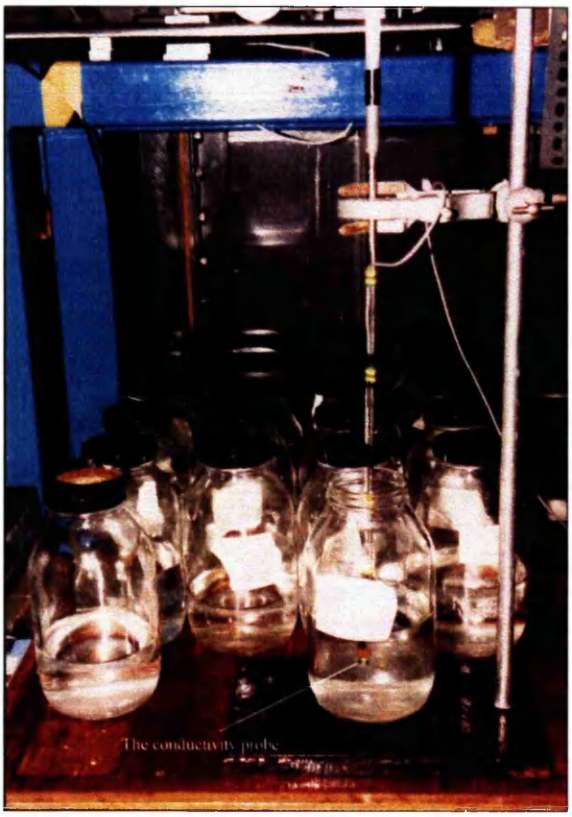

Figure 4.8 The conductivity probe is dipped into the bottles containing salt solutions of different densities to obtain the voltage output for each density.

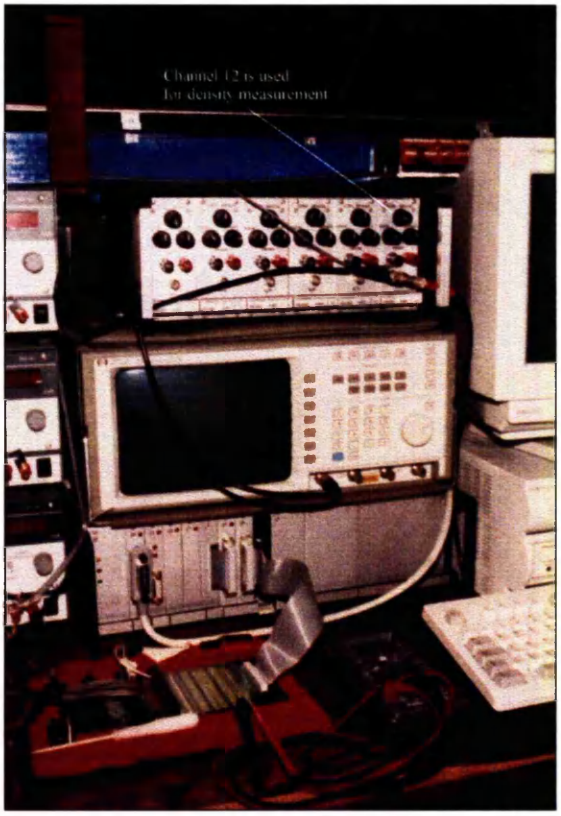

Figure 4.9 Equipment for density measurement.

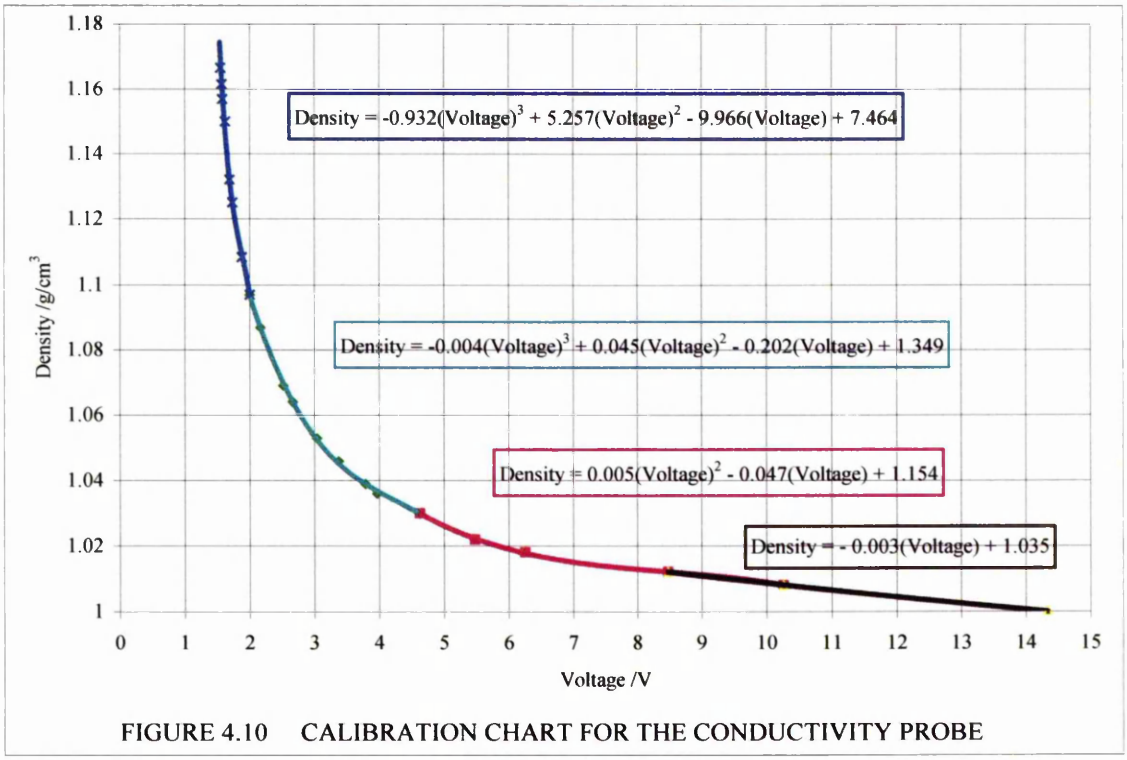

FIGURE 4.10 CALIBRATION CHART FOR THE CONDUCTIVITY PROBE

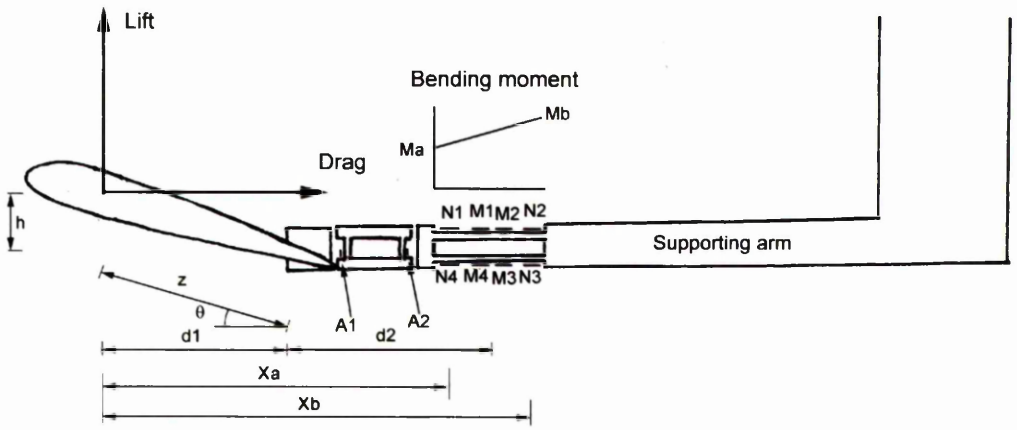

Figure 4.11 Positions of strain gauges relative to the forces.

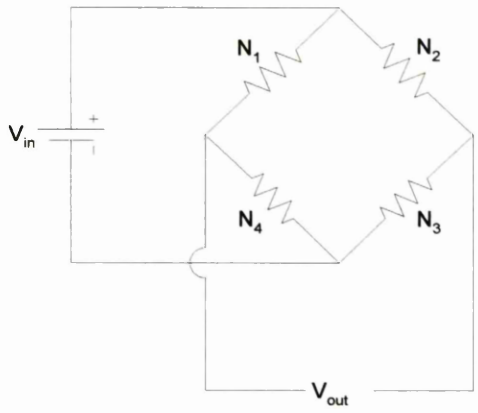

Figure 4.12 Wheatstone bridge circuit for normal force measurement.

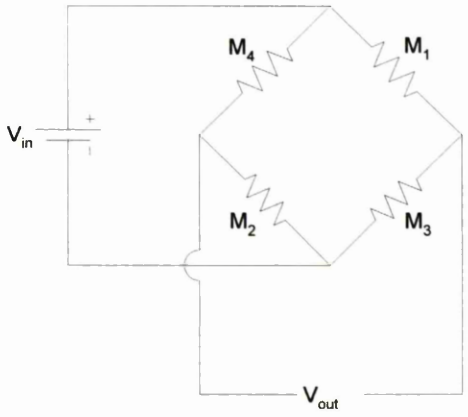

Figure 4.13 Wheatstone bridge circuit for moment measurement.

4. Measurement of forces on an oscillating wing moving in a pycnocline

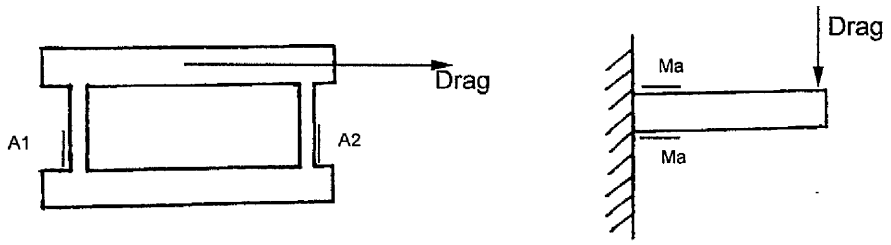

Figure 4.14 Positions of strain gauges measuring drag.

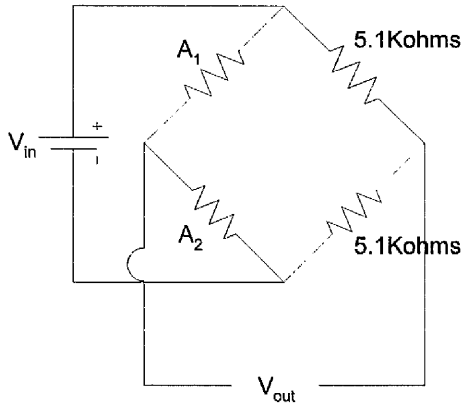

Figure 4.15 Wheatstone bridge circuit for drag measurement.

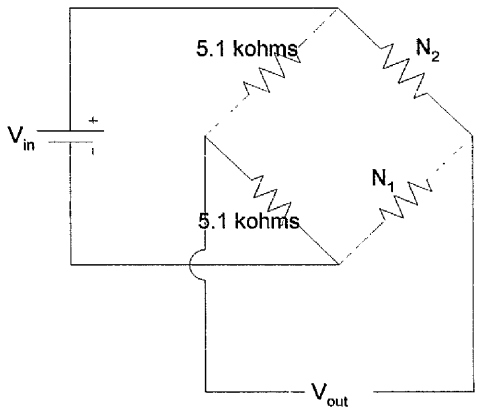

Figure 4.16 Half bridge circuit for normal force measurement.

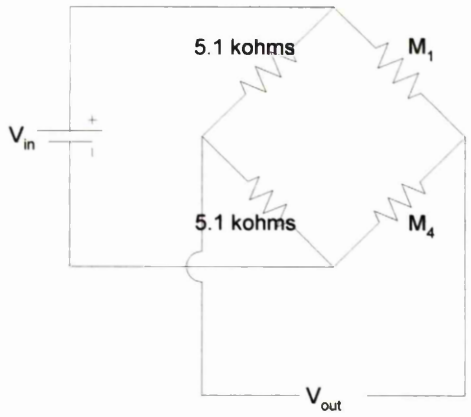

Figure 4.17a

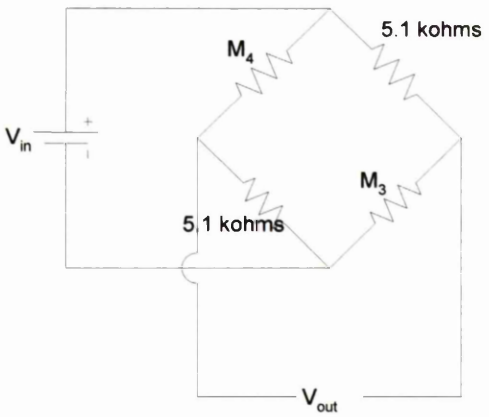

Figure 4.17b

Half bridge circuits for moment measurement.

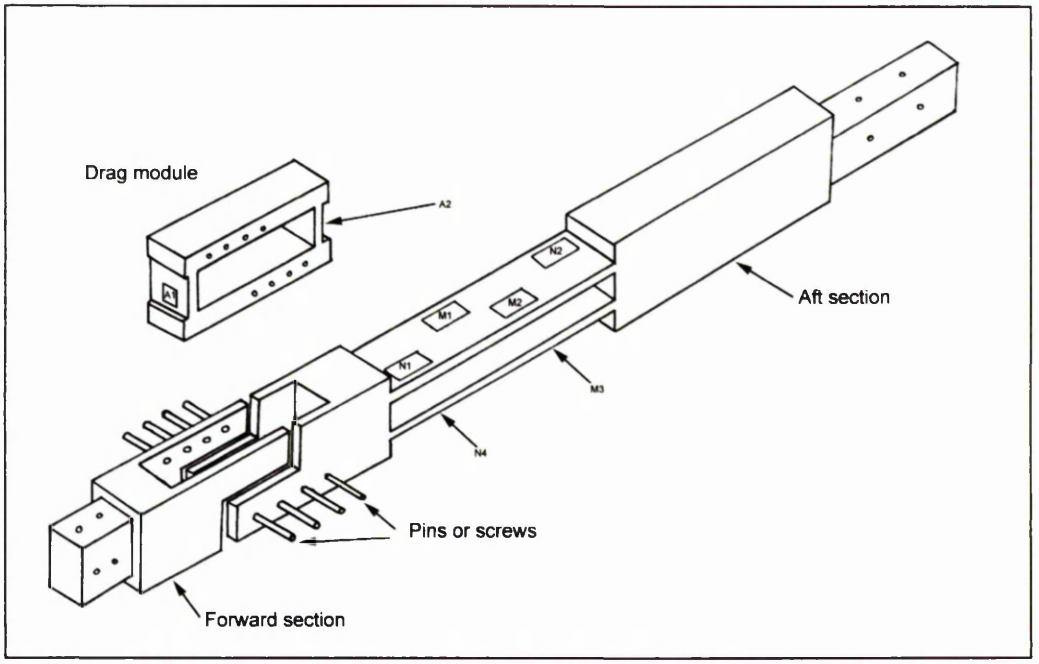

Figure 4.18 Force transducer module.

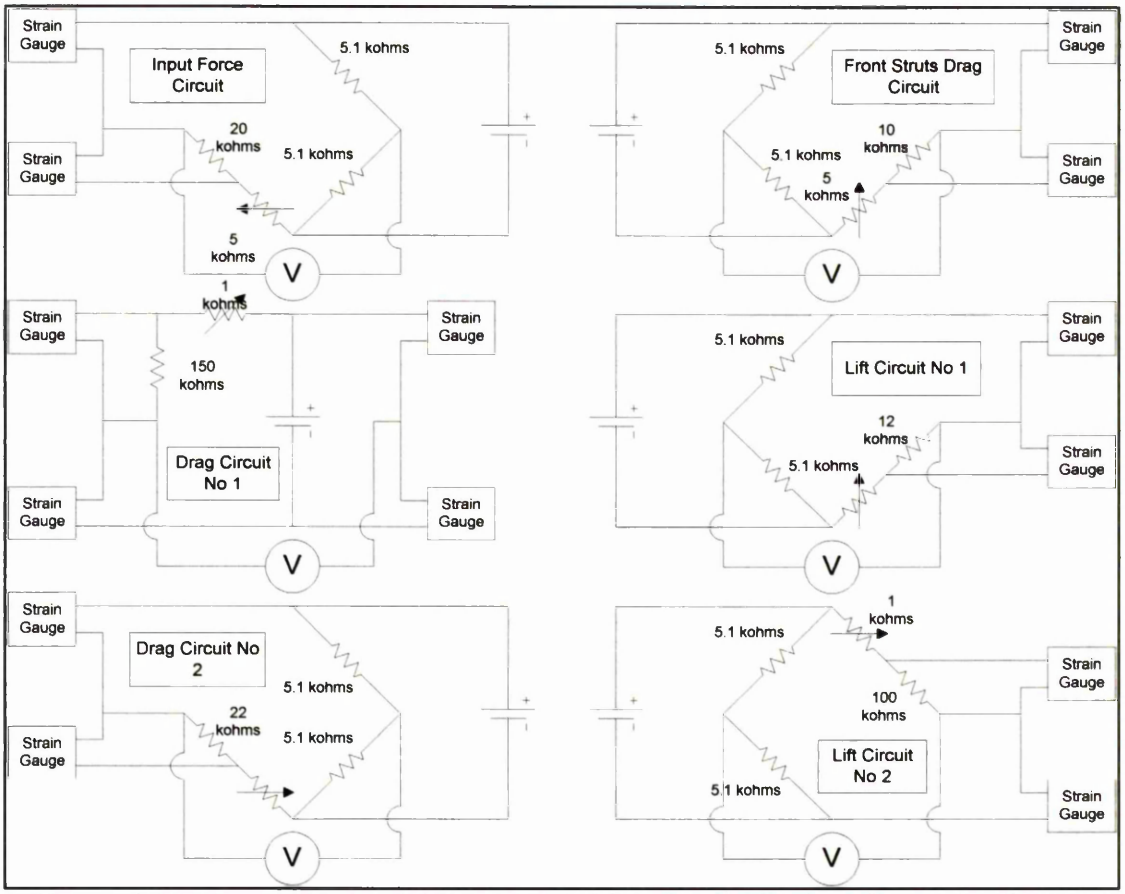

Figure 4.19 Arrangement of Wheatstone bridge circuits for the 2 force transducers.

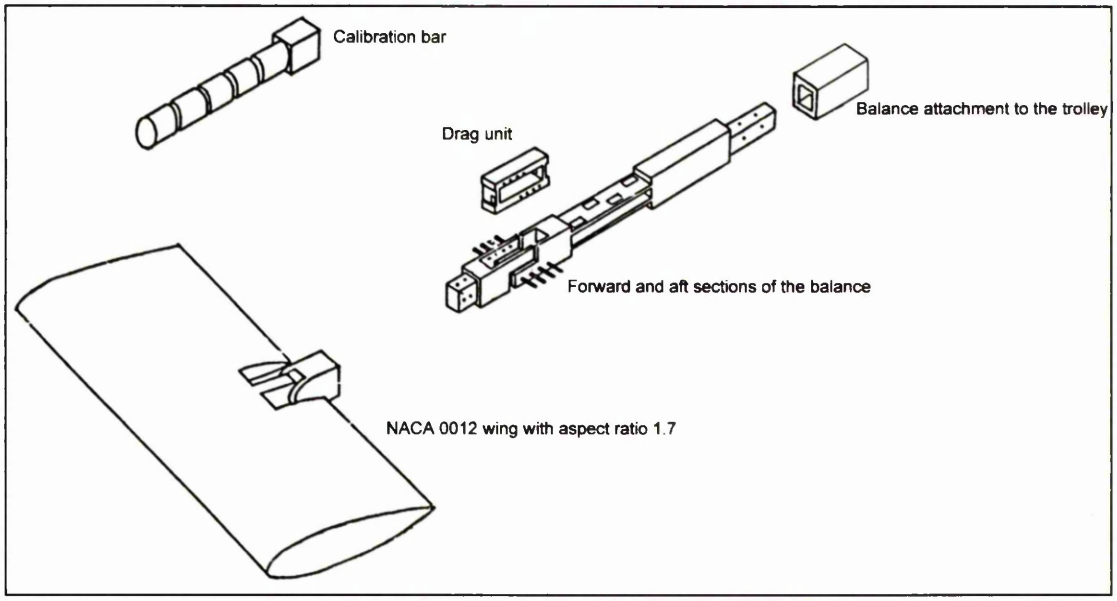

Figure 4.20a

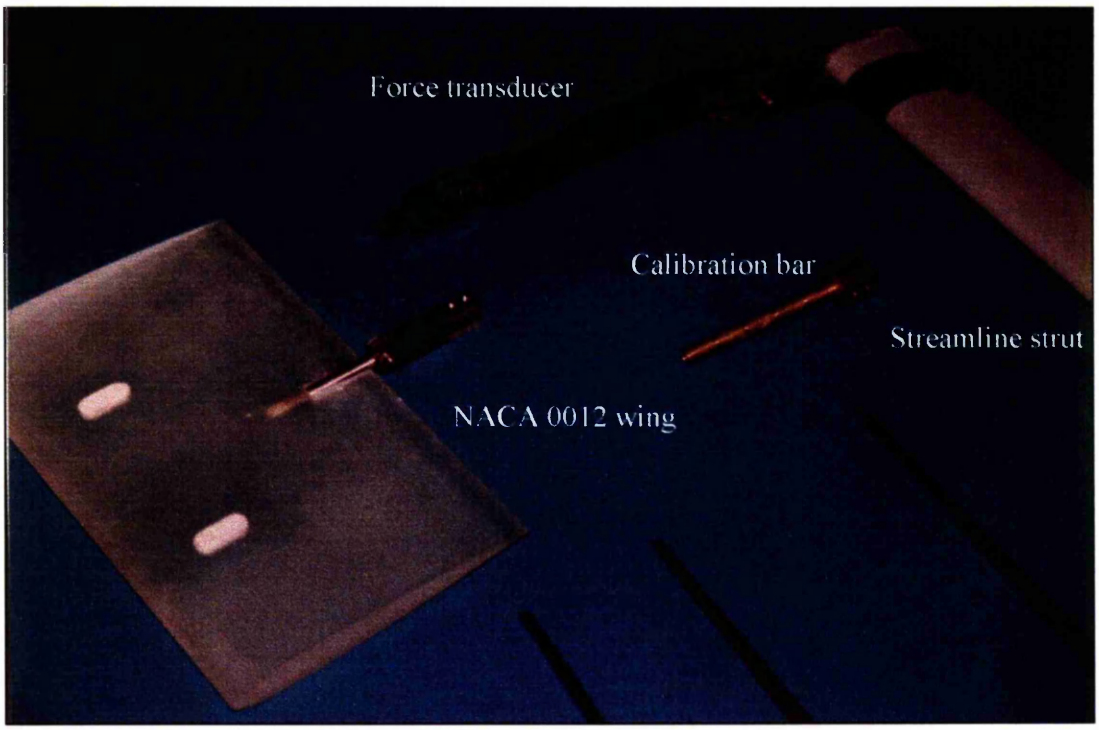

Figure 4.20b

Components of balance 1.

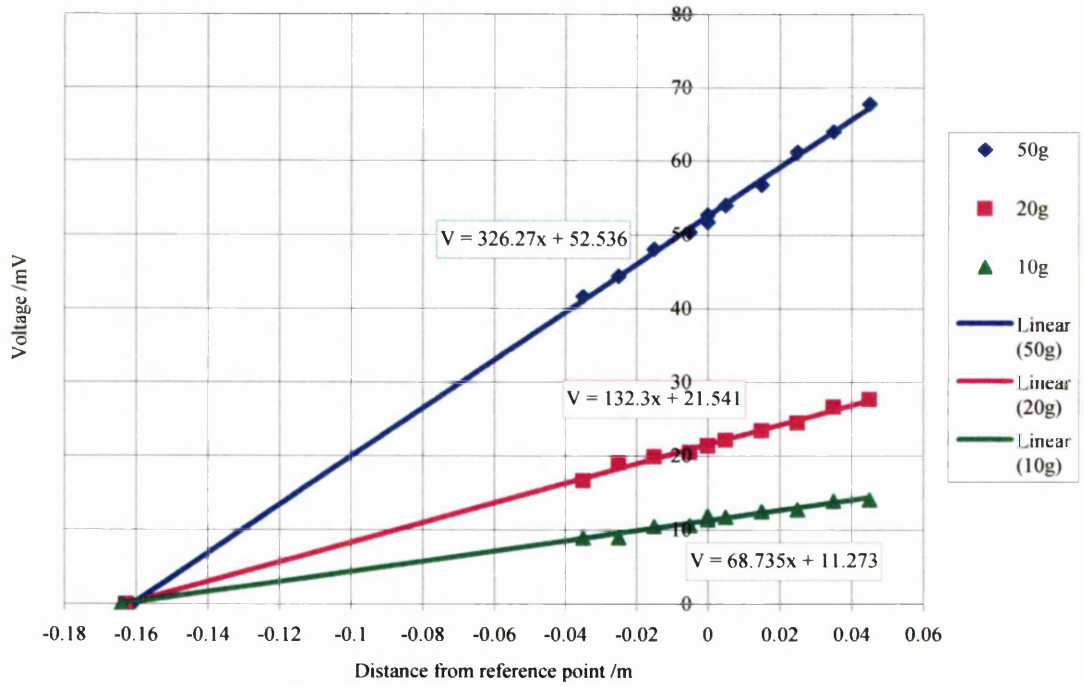

Figure 4.22a Moment circuit output due to normal force loadings at several positions from the reference point.

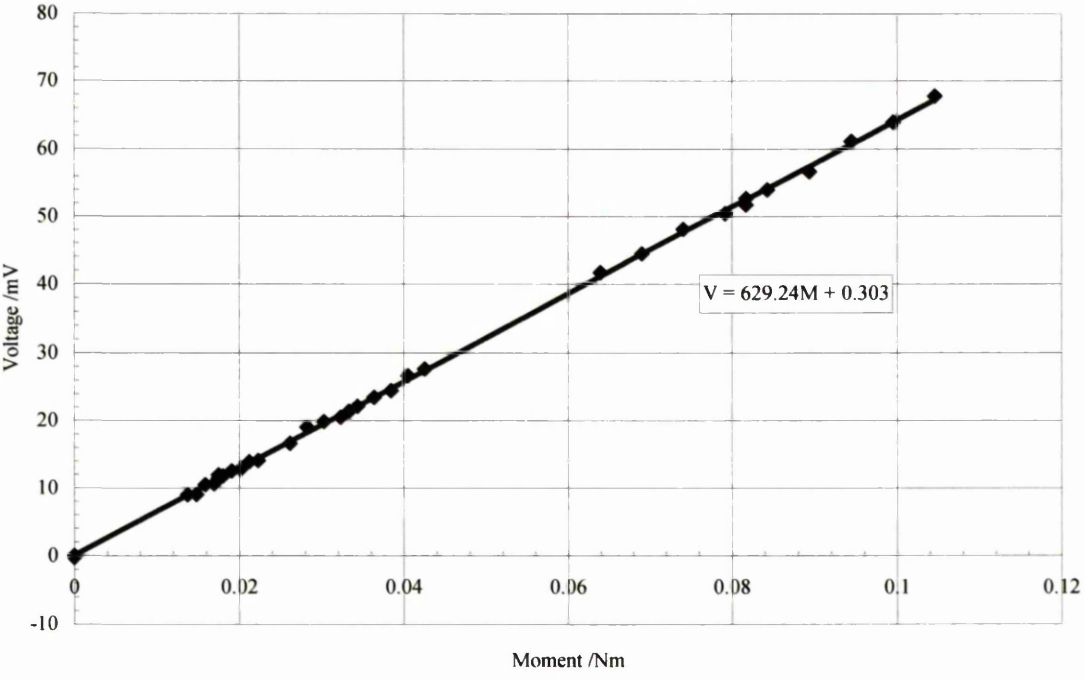

Figure 4.22b Moment circuit output due to moment about the zero voltage point.

The top graph shows the variation of voltage output from the moment circuit by varying the positions of the normal force. The reference point is 0.163m from the zero voltage point. The bottom figure represents the result in terms of the moment about the zero voltage point.

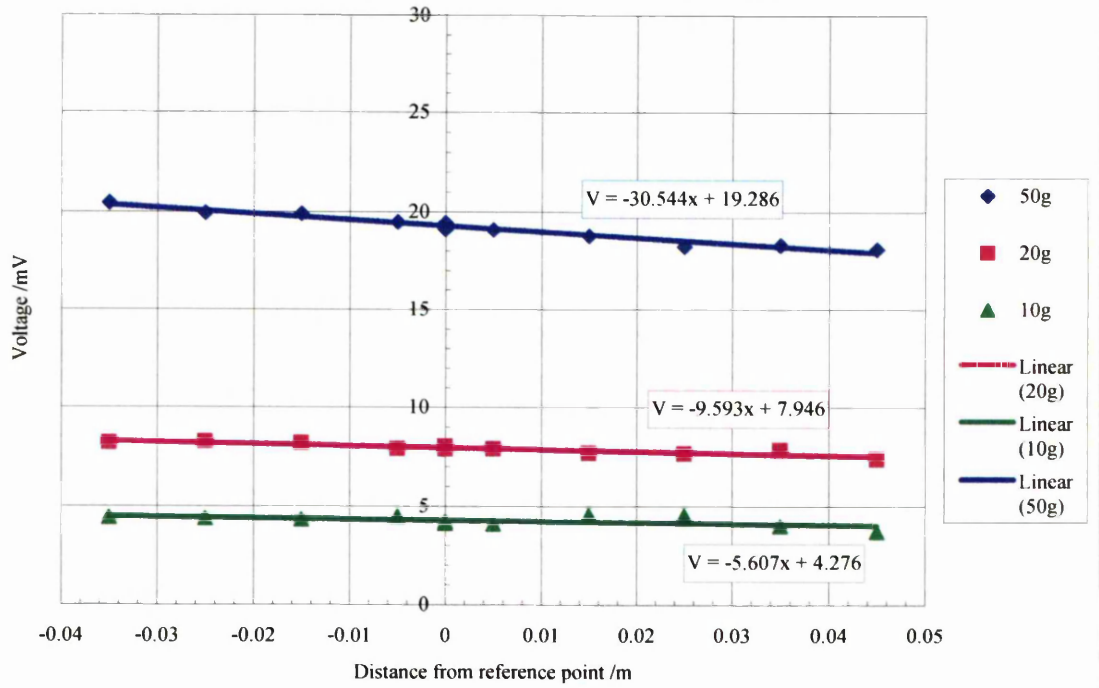

Figure 4.23a Normal circuit output due to normal force loadings at several positions from the reference point.

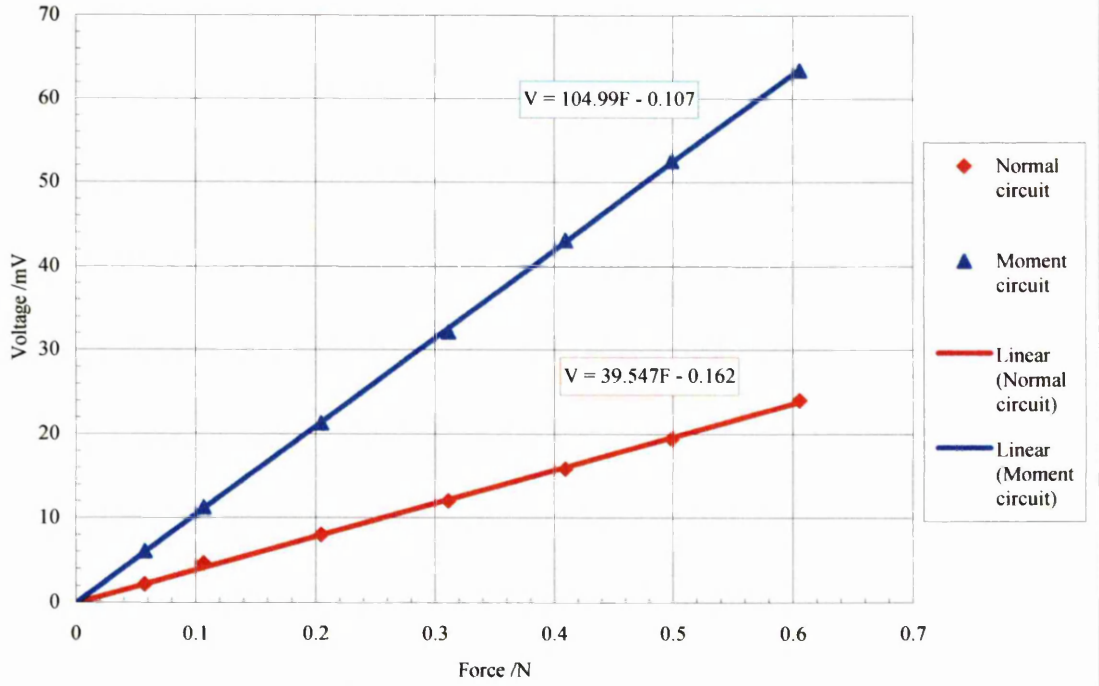

Figure 4.23b Voltage outputs due to normal force loadings at the reference point.

The top graph shows the voltage outputs from the lift circuit by varying the position of the normal force. The bottom graph shows the outputs from the lift and moment circuits due to normal force loadings at the reference point.
The reference point is 0.163m from the zero voltage point.

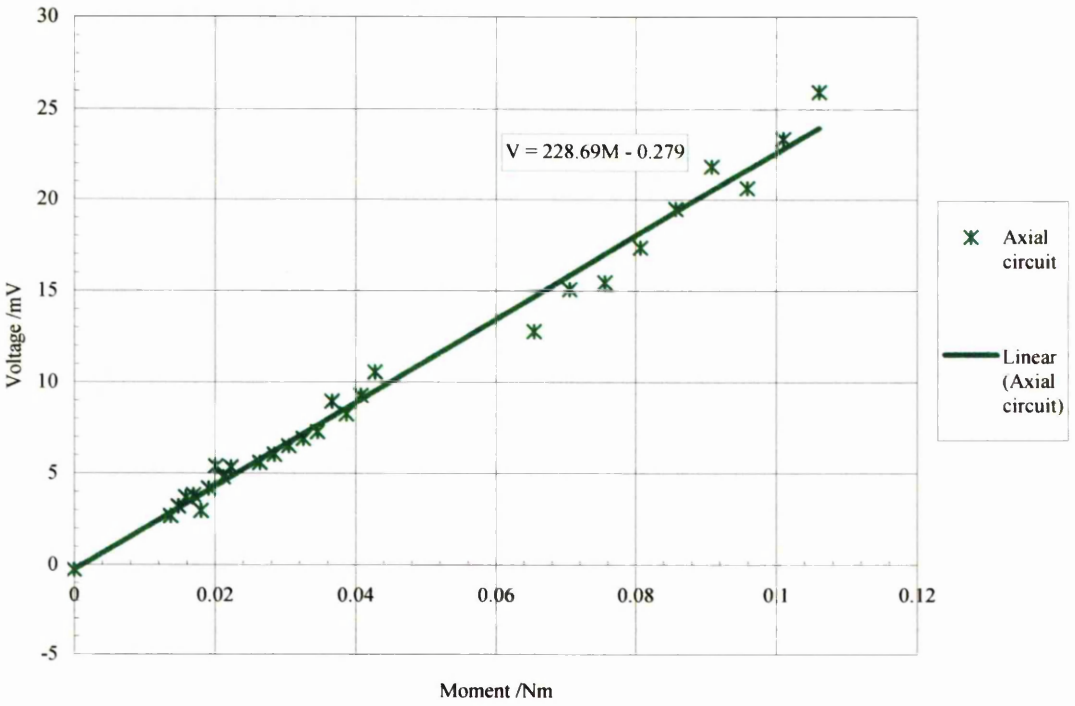

Figure 4.24a Axial circuit output due to applied moment.

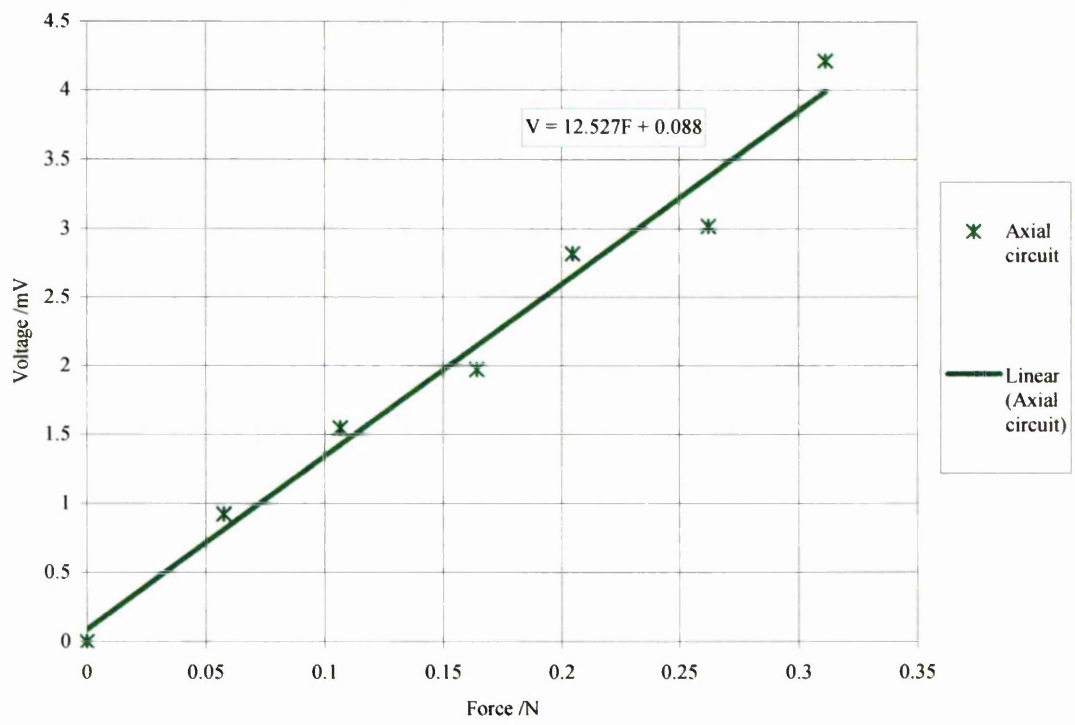

Figure 4.24b Axial circuit output due to axial force loadings.

The top graph shows the voltage outputs from the axial circuit by varying the position of the normal force. The reference point is 0.163m from the zero voltage point.
The bottom graph shows the outputs from the axial circuit due to axial force loadings.

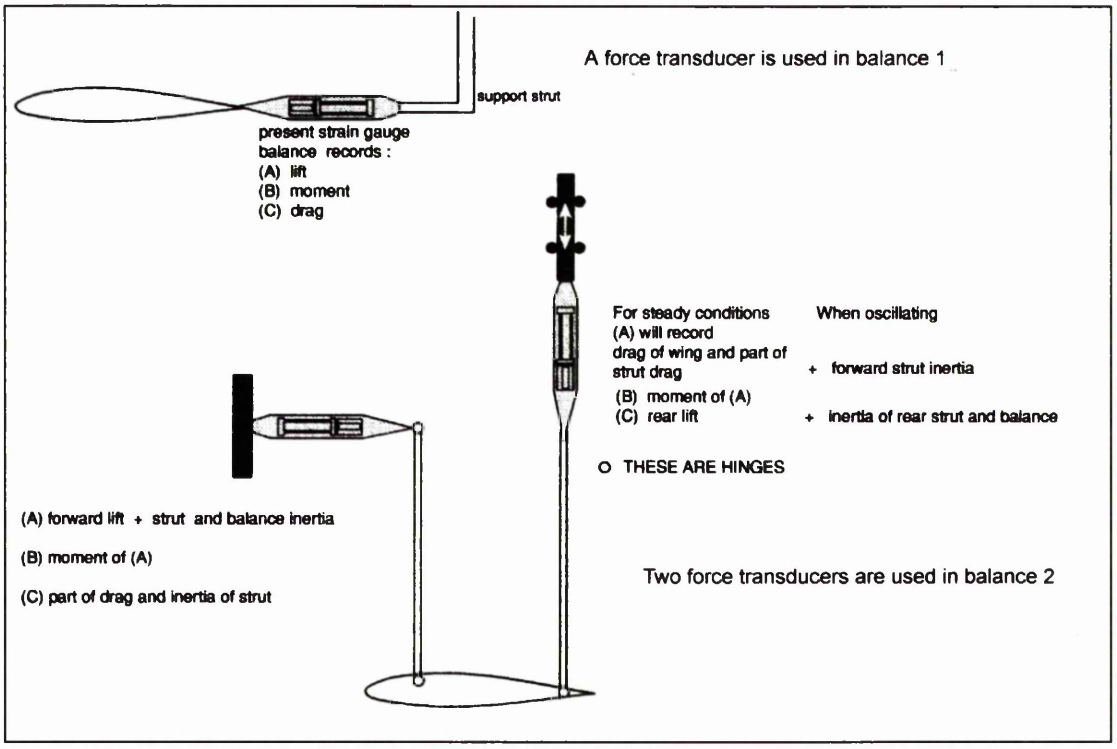

Figure 4.25a

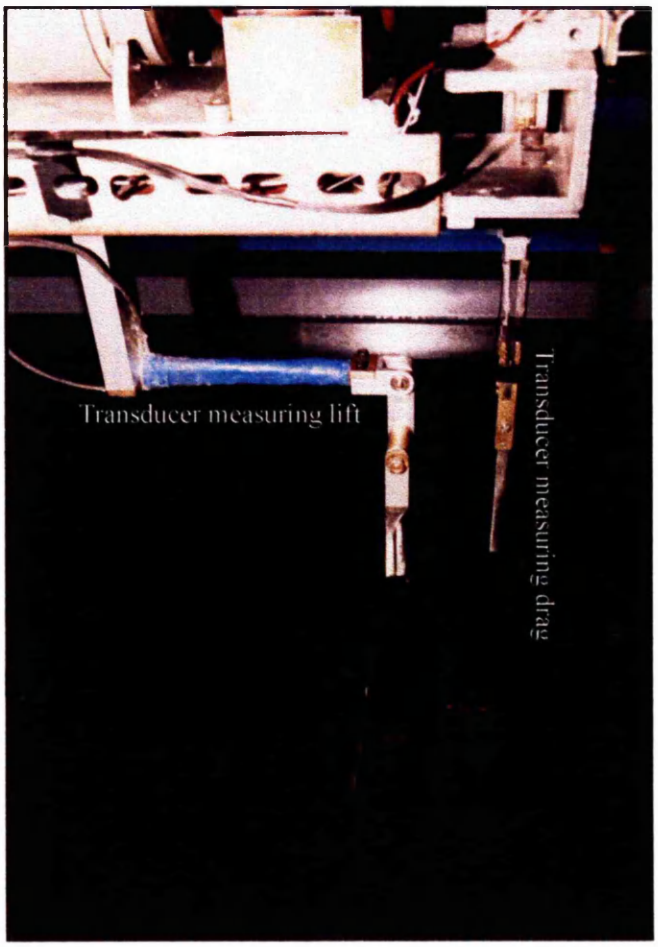

Figure 4.25b

Components of balance 2.

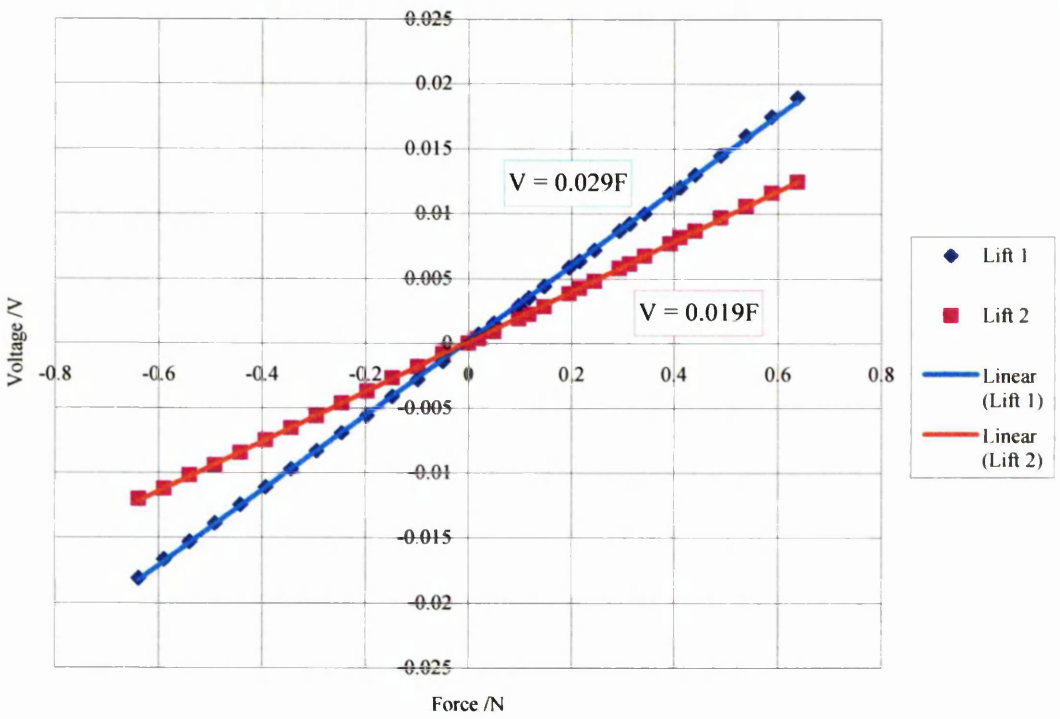

Figure 4.26a Calibration chart for normal force loadings.

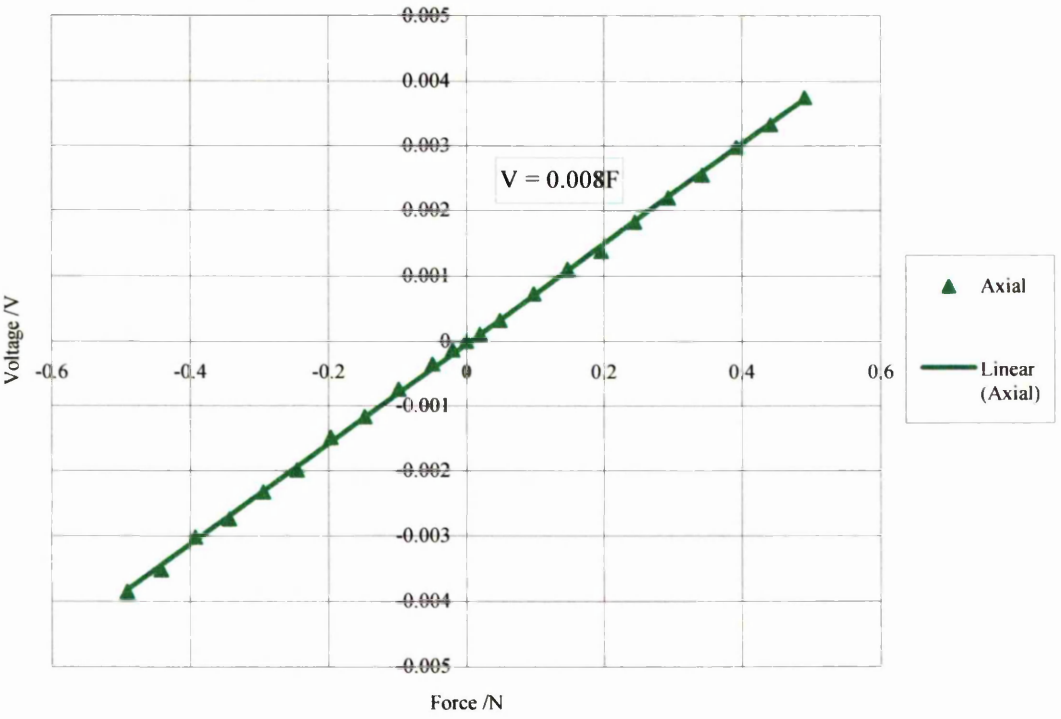

Figure 4.26b Calibration chart for axial force loadings.

Calibration charts for the force tranducer measuring lift.

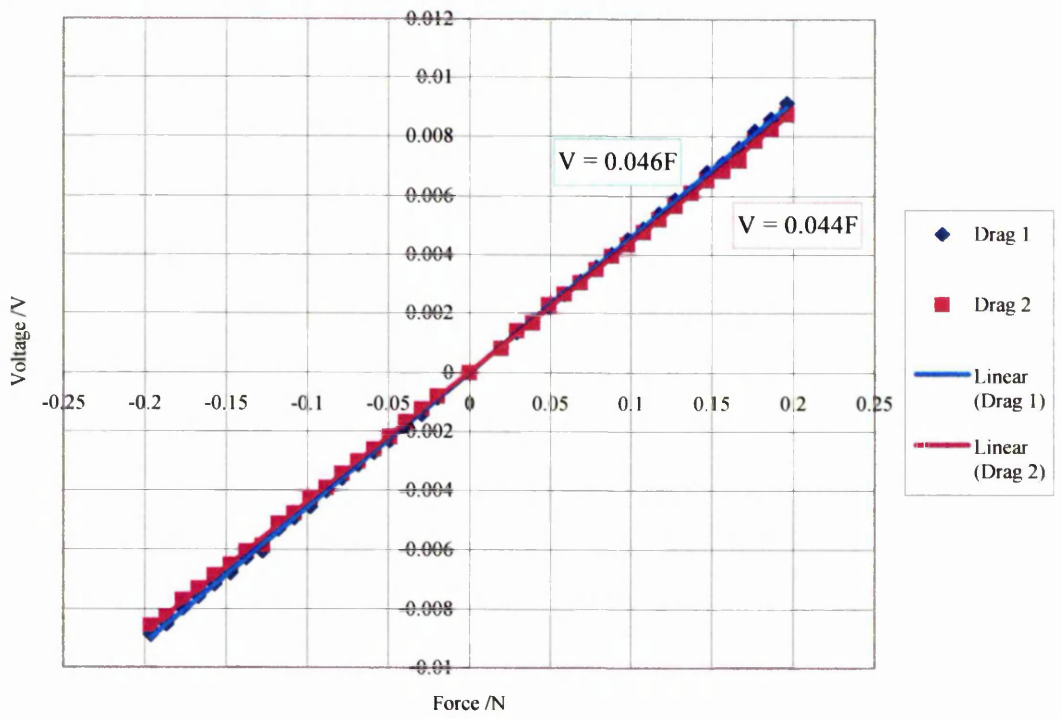

Figure 4.27a Calibration chart for normal force loadings.

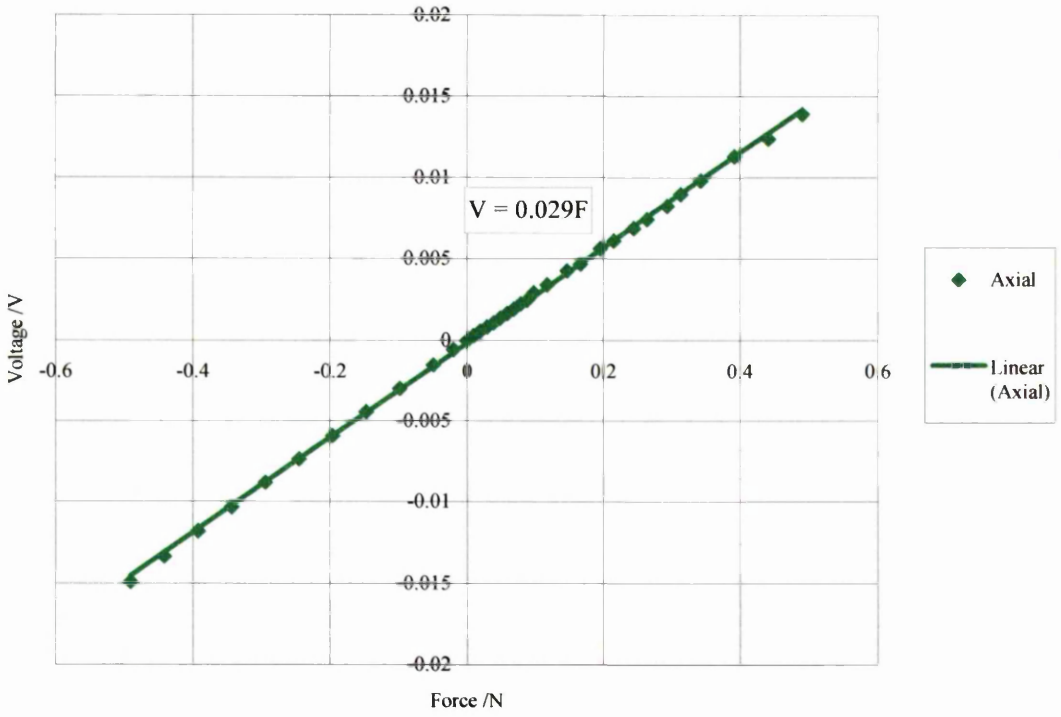

Figure 4.27b Calibration chart for axial force loadings.

Calibration charts for the force tranducer measuring drag.

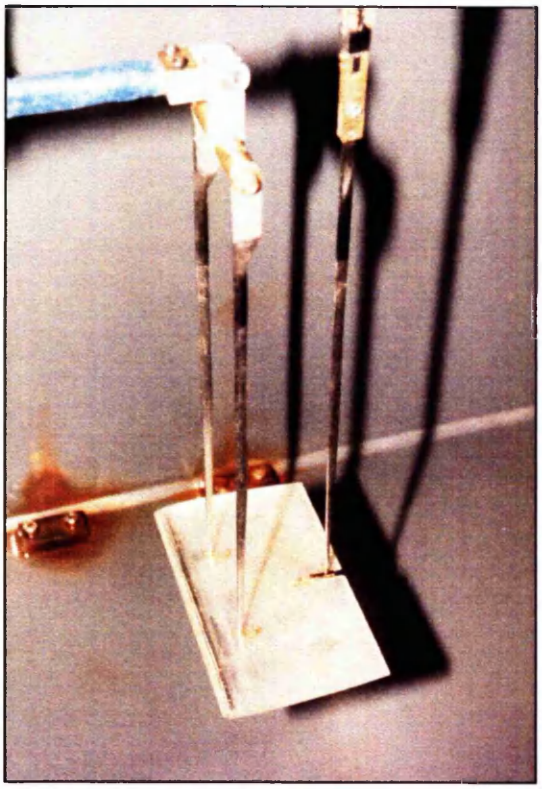

Figure 4.29a

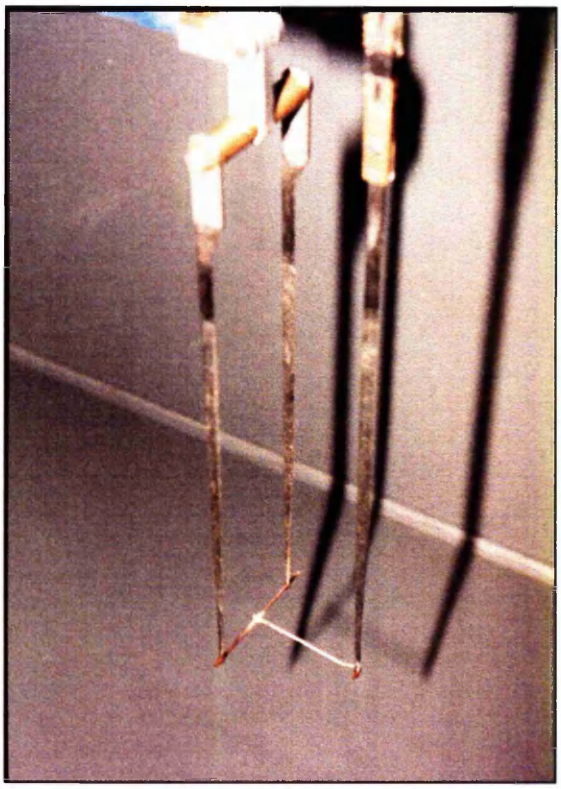

Figure 4.29b

The 3 struts holding the wing and the T-structure.

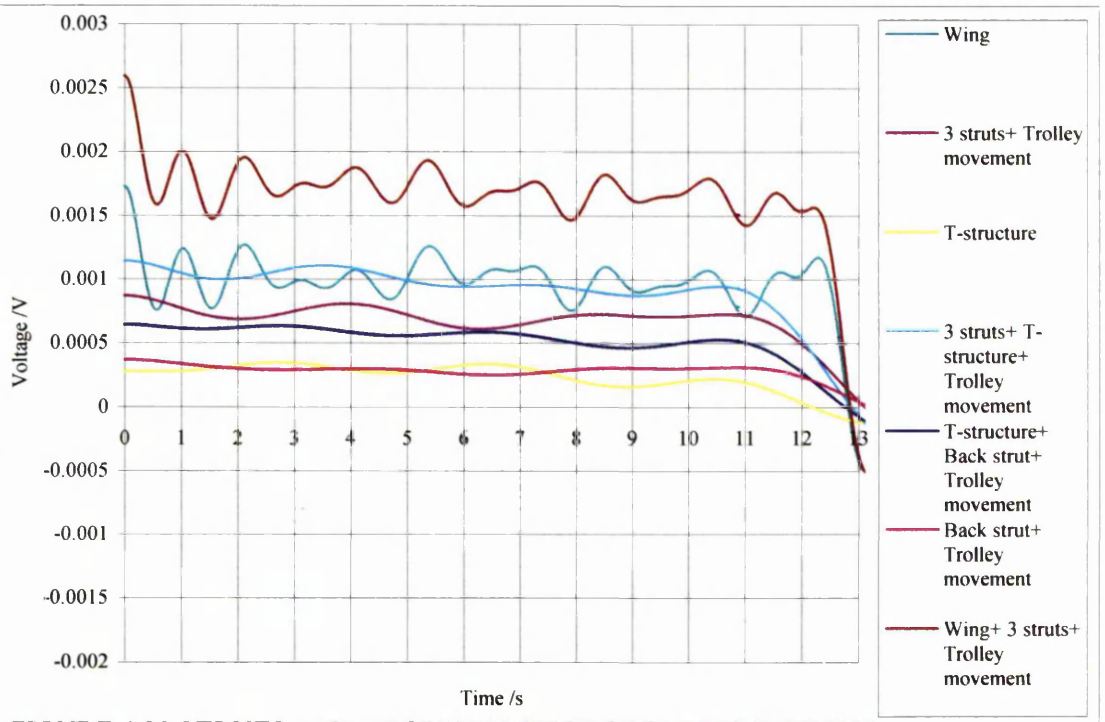

FIGURE 4.30 STRUTS AND TROLLEY MOVEMENT CORRECTIONS

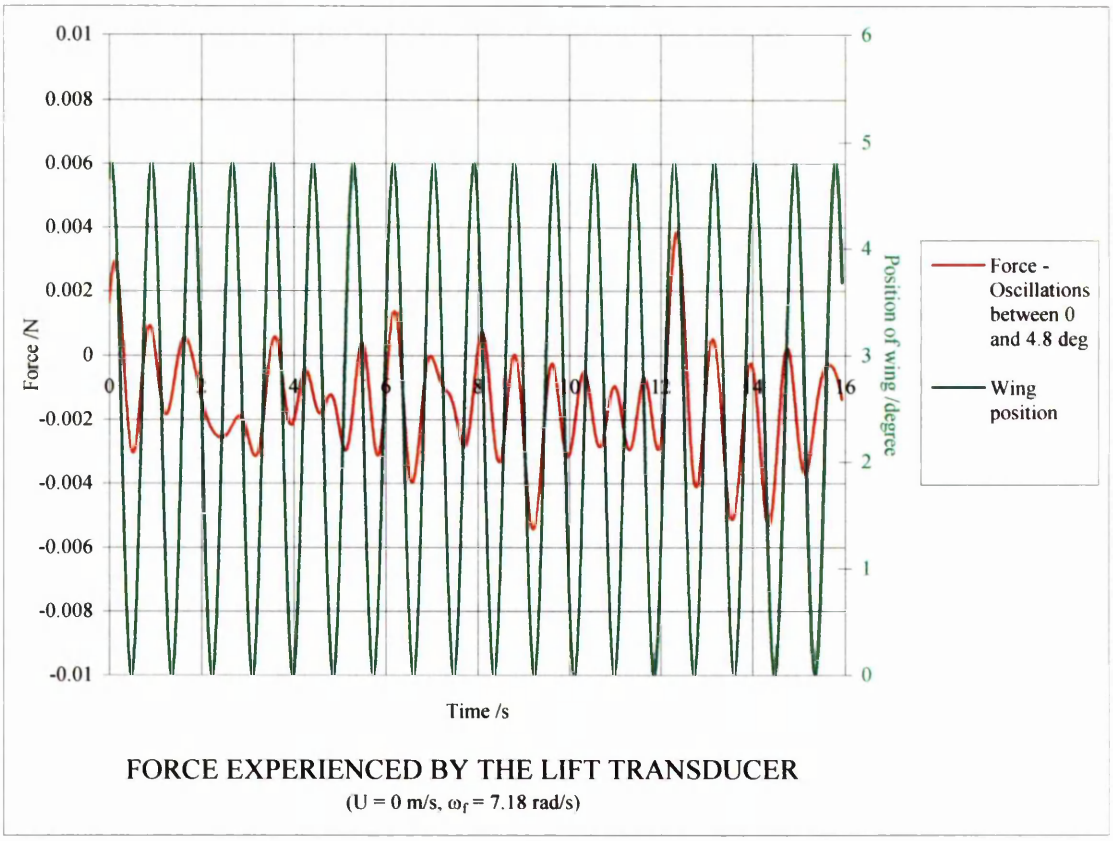

FORCE EXPERIENCED BY THE LIFT TRANSDUCER

(U = 0 m/s, ω_f = 7.18 rad/s)

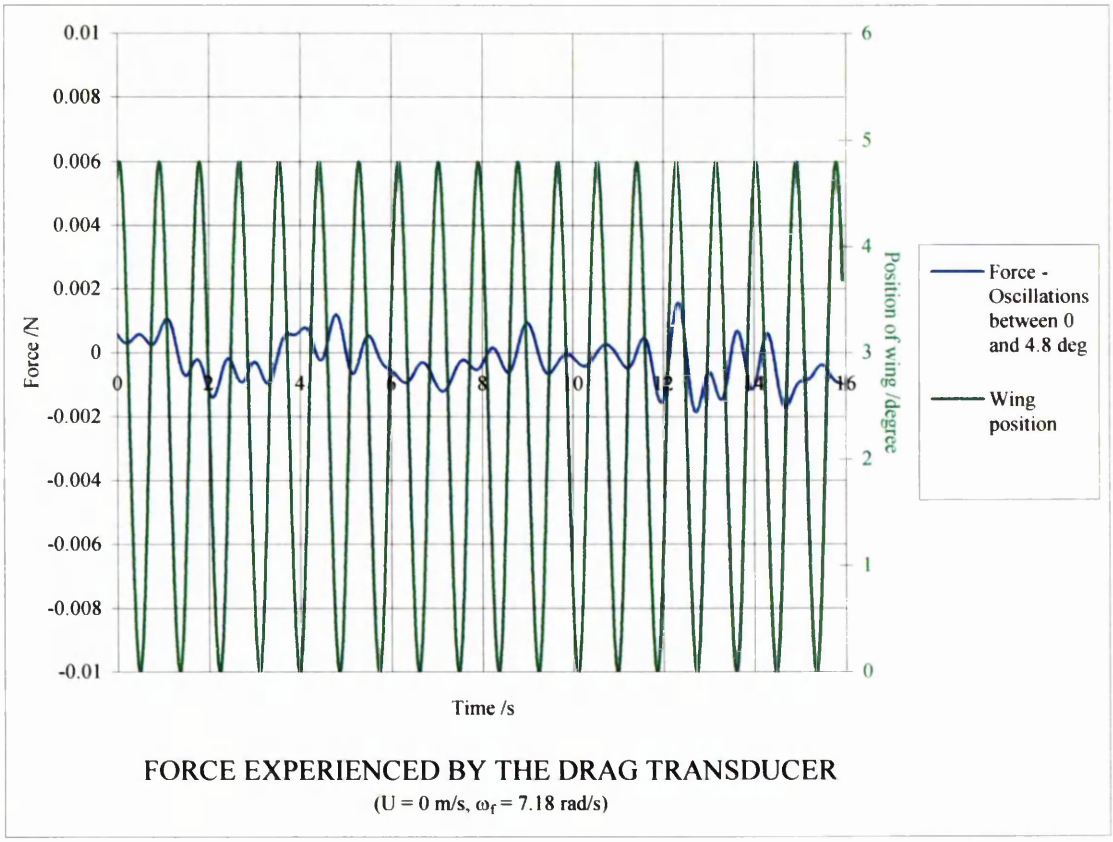

FORCE EXPERIENCED BY THE DRAG TRANSDUCER

(U = 0 m/s, ω_f = 7.18 rad/s)

Figures 4.31a & b The lift and drag of the T-structure oscillating in water.

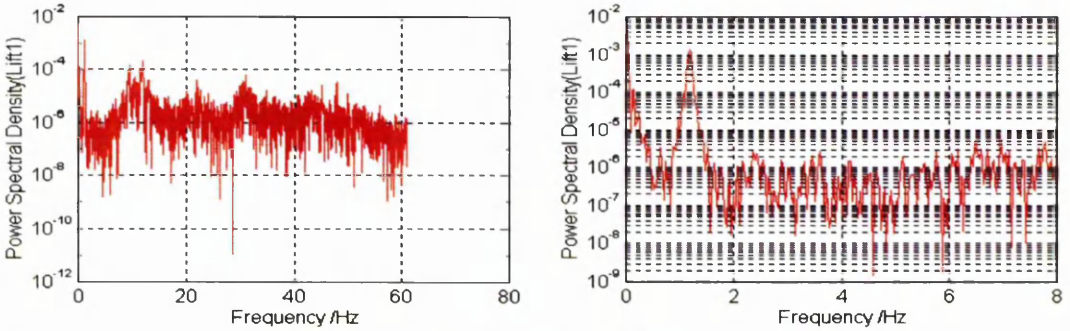

(a) Original data with sampling frequency of 122.1Hz.

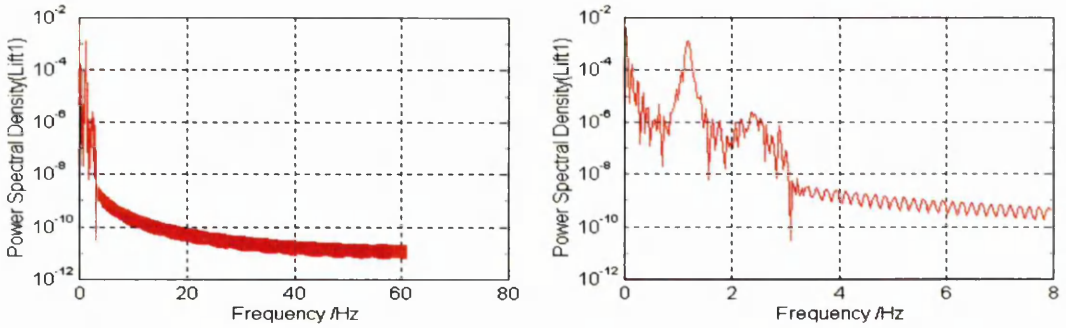

(b) Sampling frequency of 122.1 Hz and filtered with a cut-off frequency of 2.4 Hz.

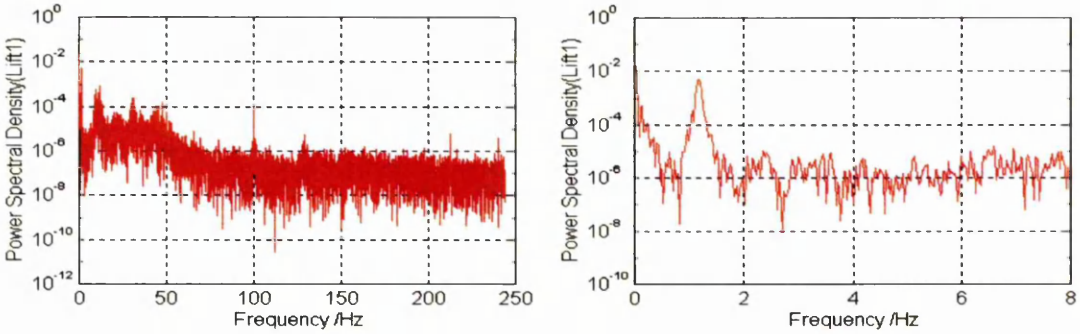

(c) Original data with sampling frequency of 488.3 Hz.

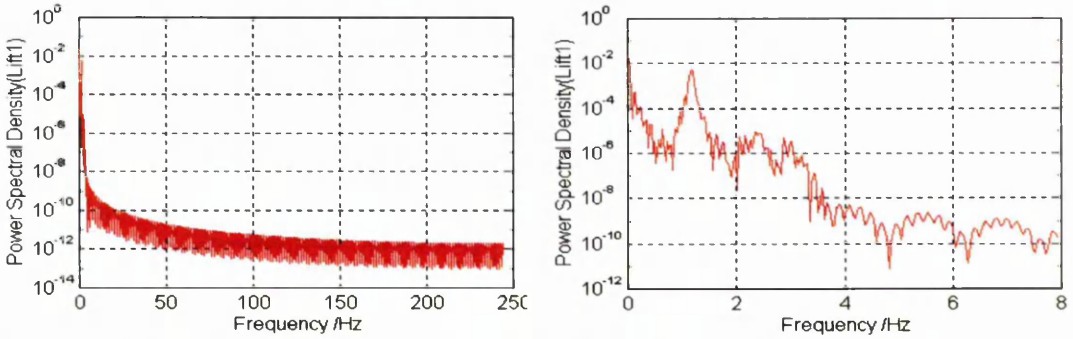

(d) Sampling frequency of 488.3 Hz and filtered with a cut-off frequency of 2.4 Hz.

Figure 4.32 The power spectral density of a typical signal from an oscillating wing moving in a pycnocline. The data was sampled at 2 different frequencies and an elliptic filter was used to reduce the high frequency noise. Figures from the right column are the close-up of the figures on the left.

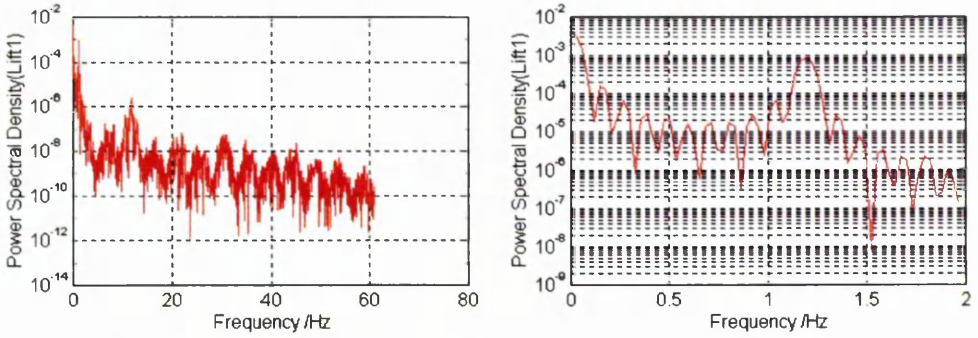

(a) Moving averaging with 25 points.

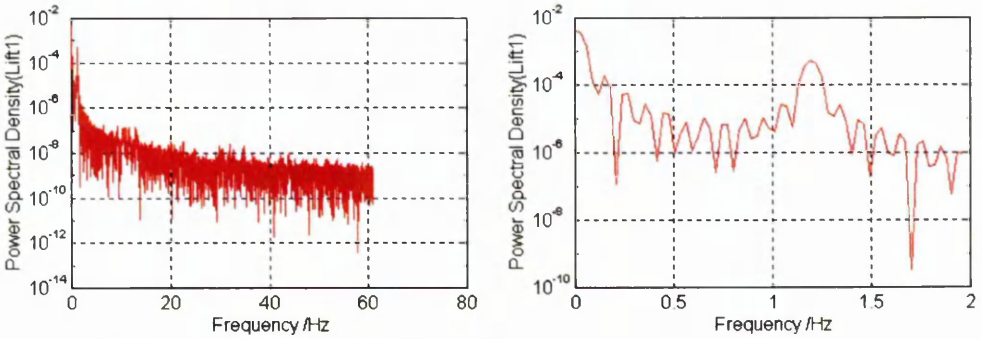

(b) Moving averaging with 50 points.

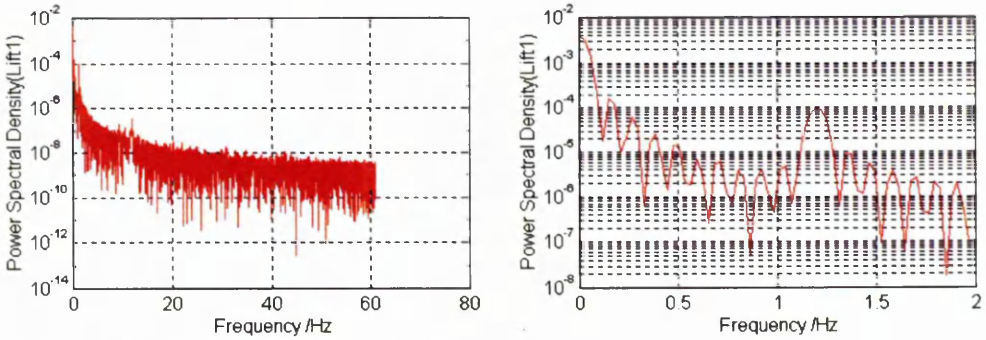

(c) Moving averaging with 75 points.

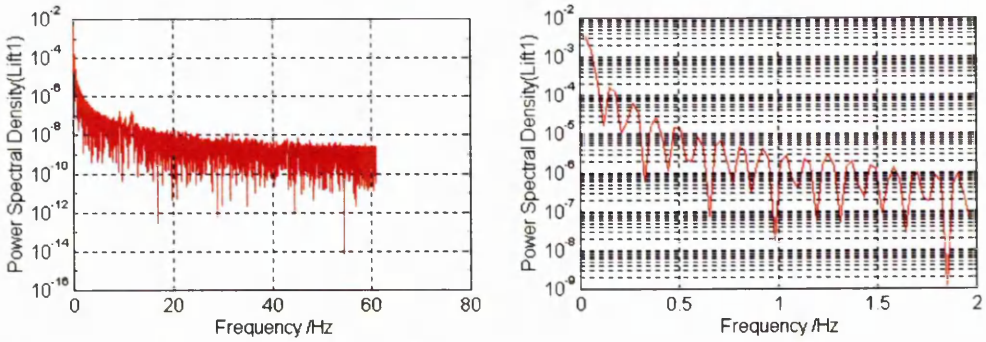

(d) Moving averaging with 100 points.

Figure 4.33 The effect of averaging points on frequencies associated with a typical signal from an oscillating wing moving in a pycnocline. Figures from the right column are the close-up of the figures on the left. The sampling rate for the data is 122.1 Hz.

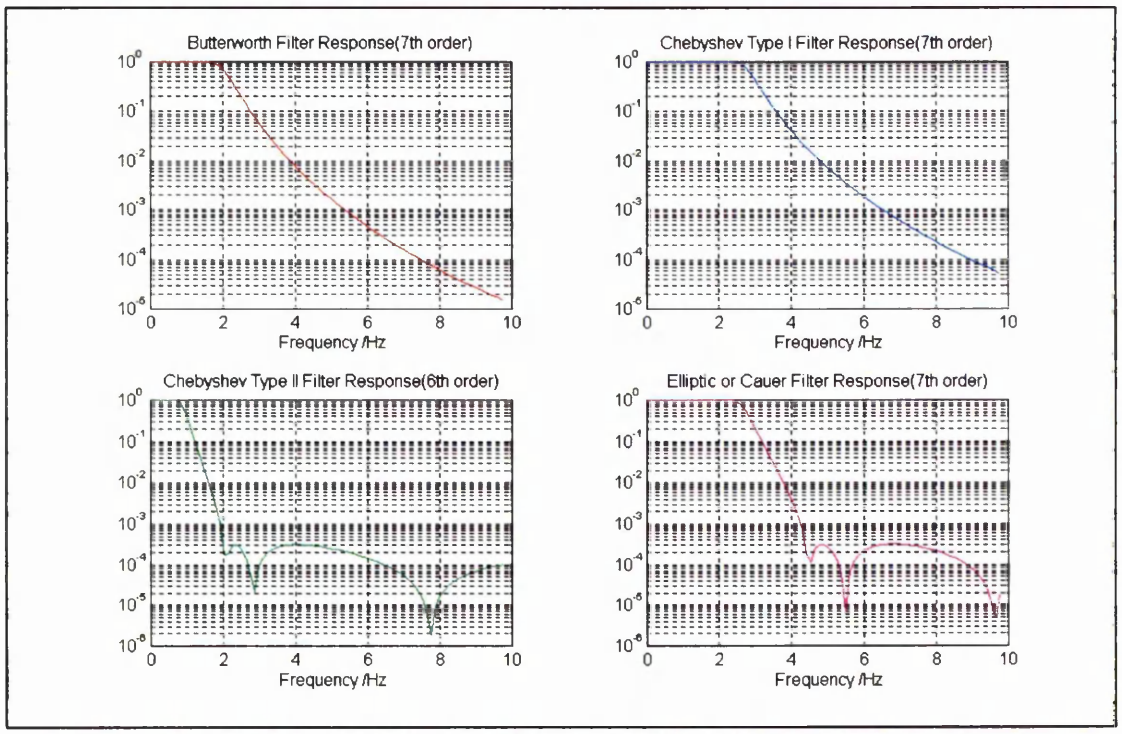

(a) Sampling rate = 488.3 Hz.

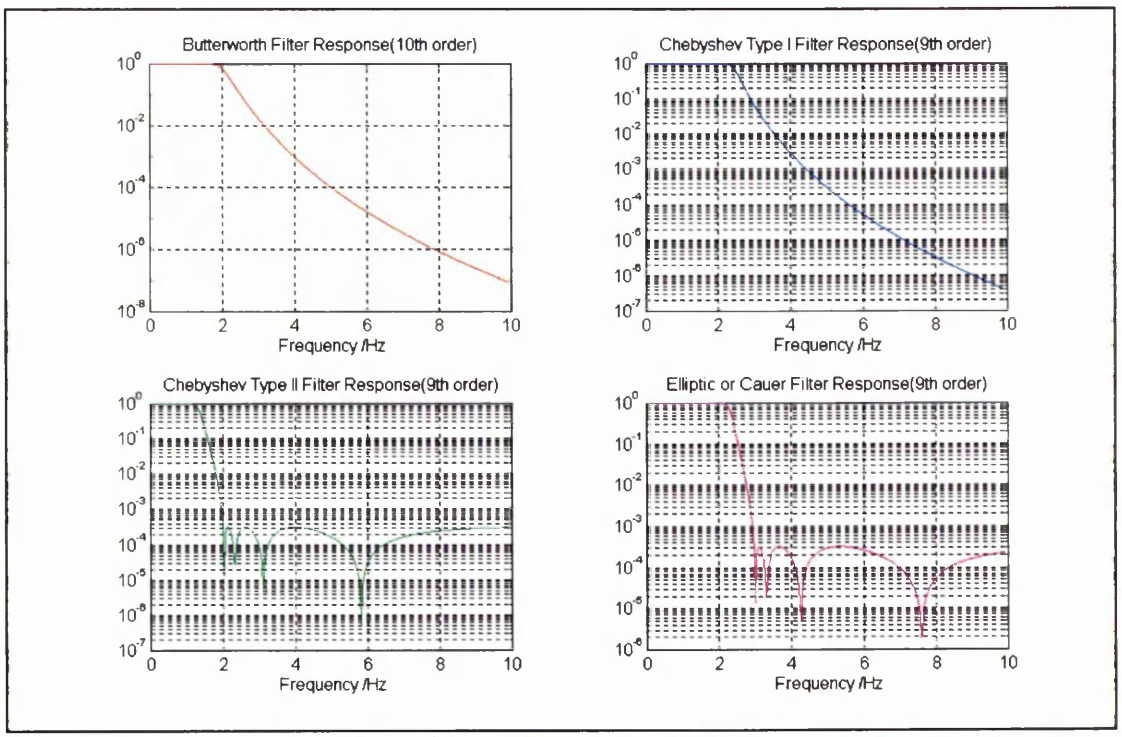

(b) Sampling rate = 122.1 Hz.

Figure 4.34a & b The frequency responses of the various filters at two different sampling rates.

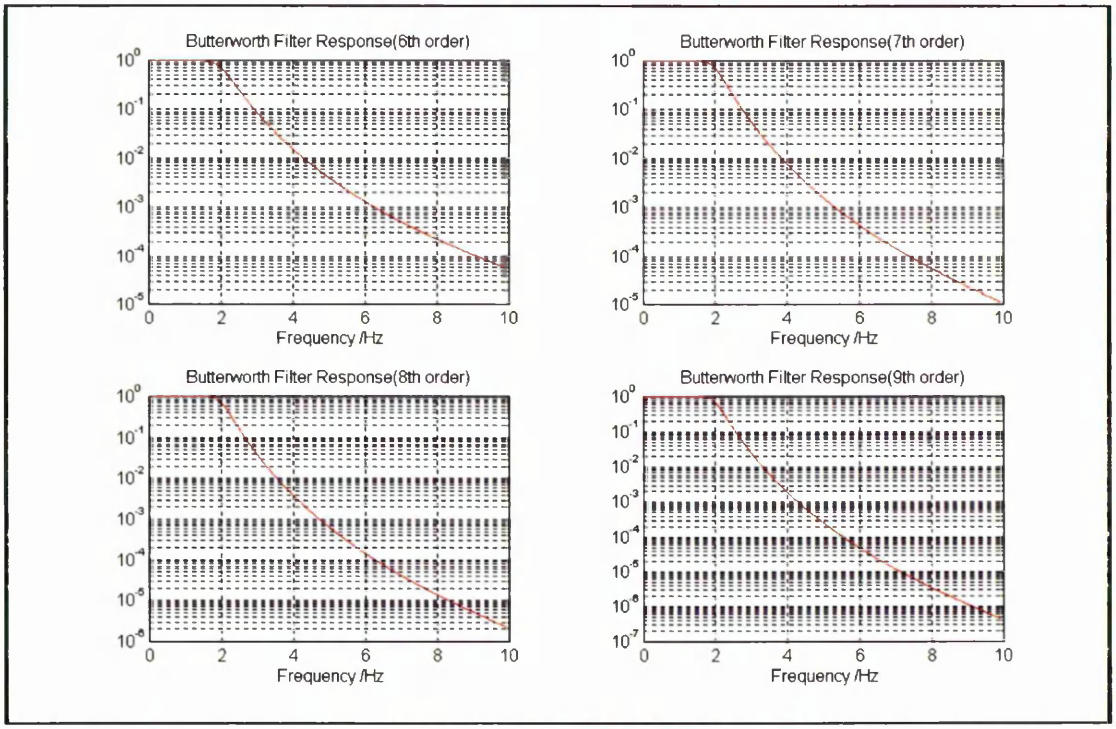

(a) Butterworth filter

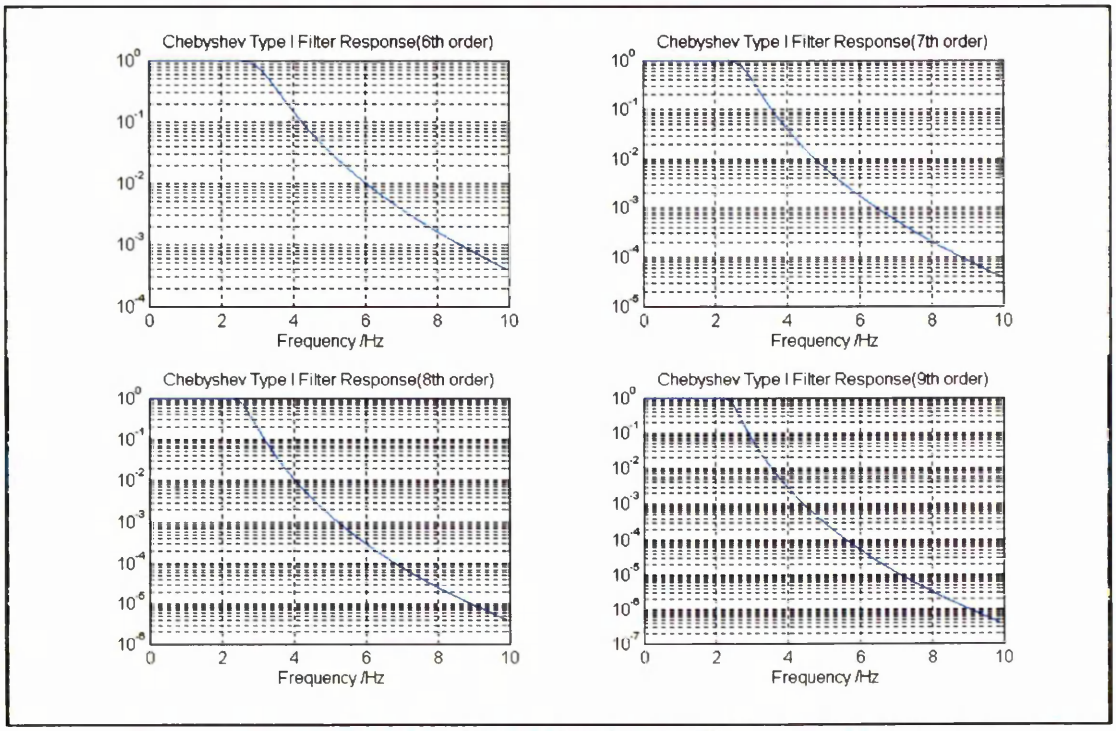

(b) Chebyshev type 1 filter

Figure 4.35a & b The effects of increasing the order on the transition width of the filters. The sampling rate is 122.1 Hz.

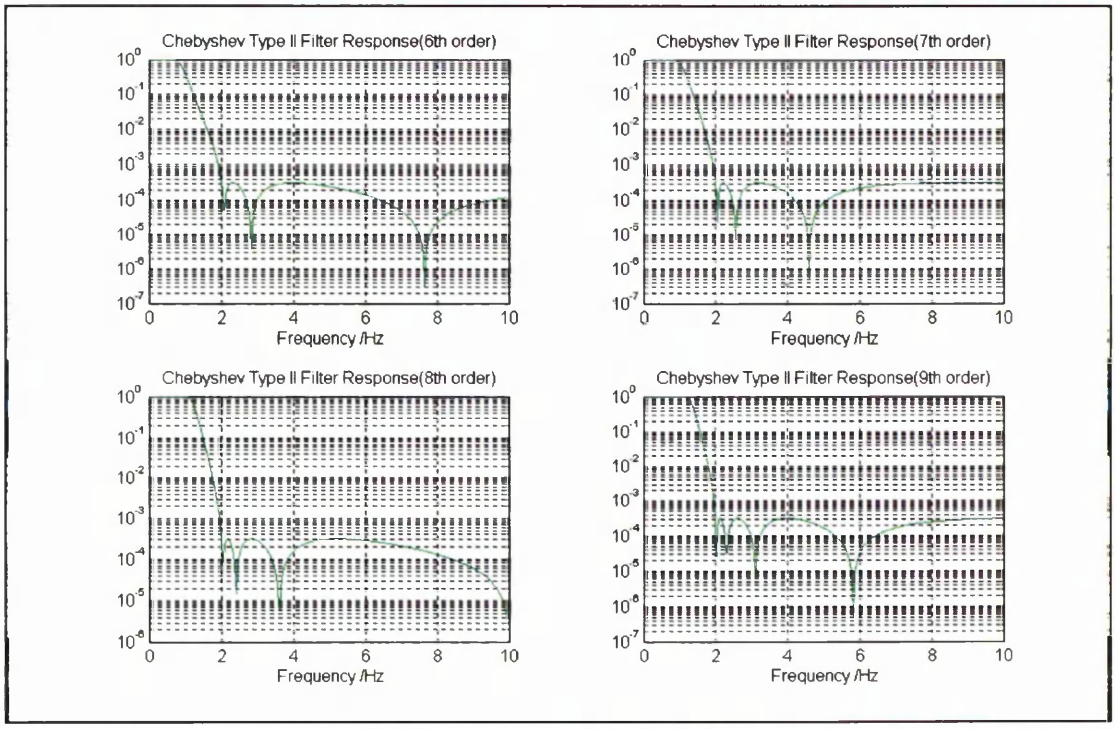

(c) Chebyshev type 2 filter

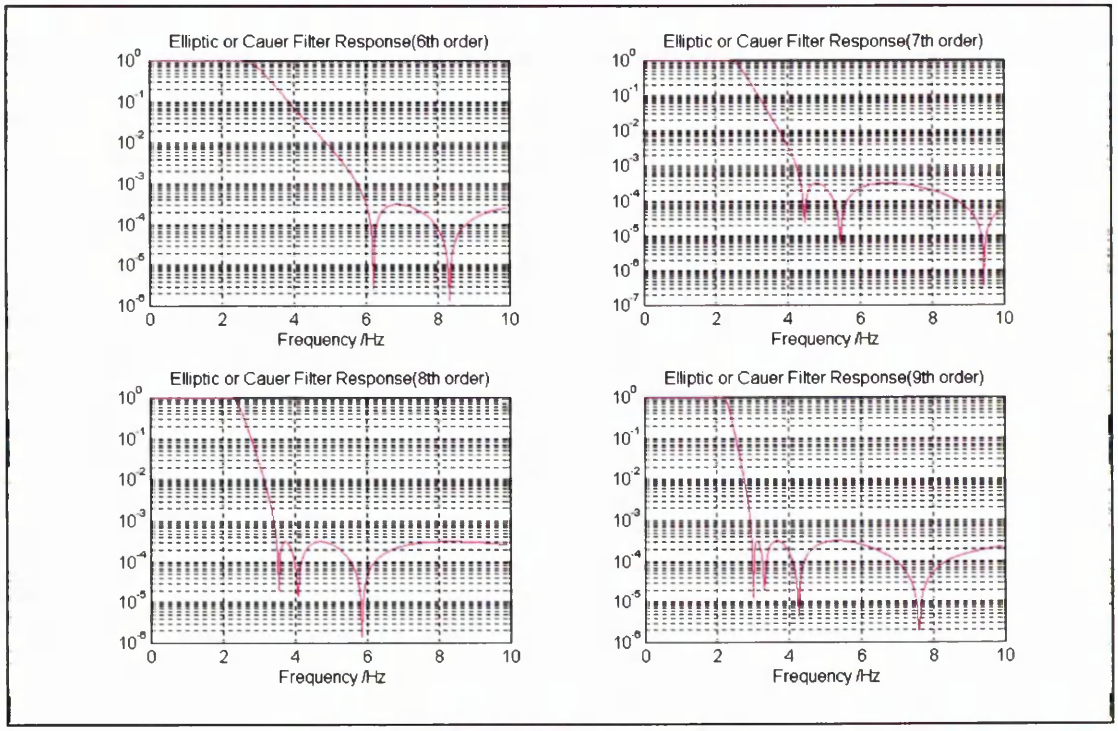

(d) Elliptic or Cauer filter.

Figure 4.35c & d The effects of increasing the order on the transition width of the filters. The sampling rate is 122.1 Hz.

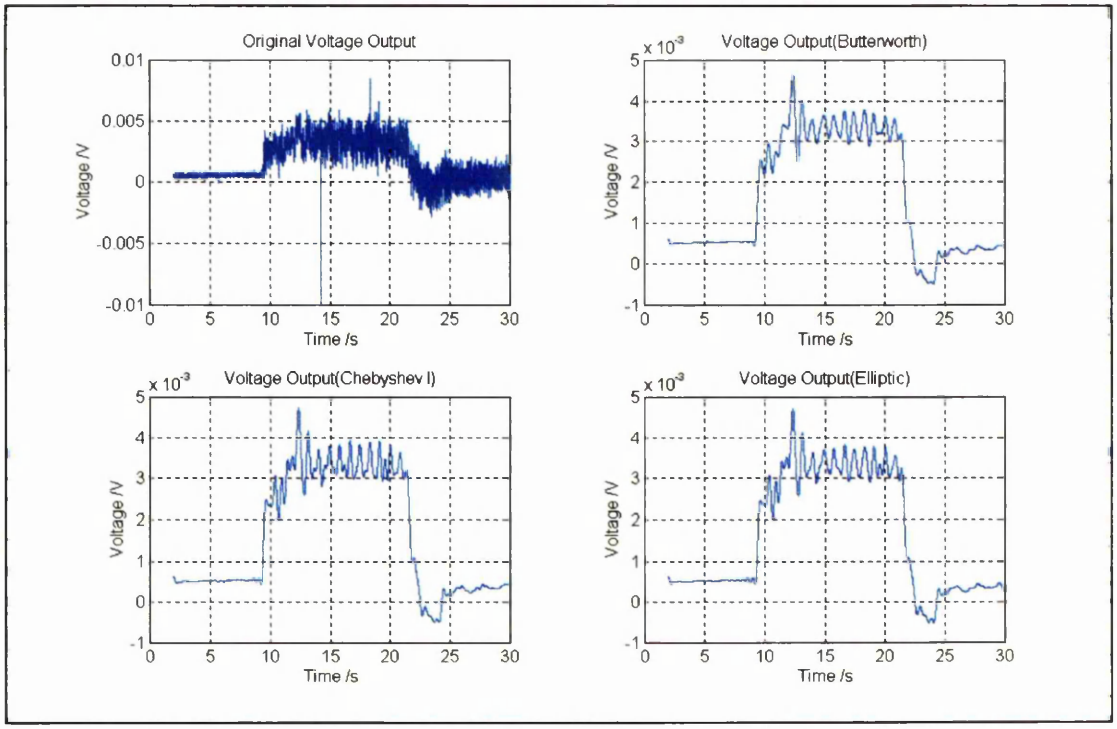

(a) Drag outputs.

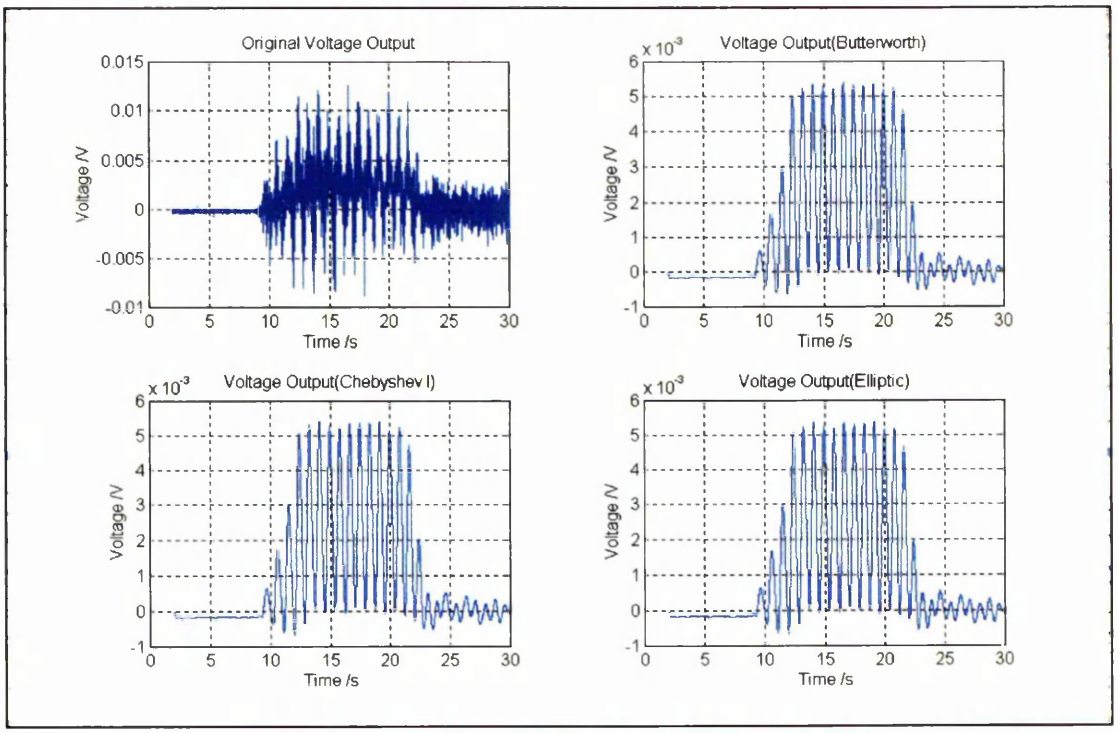

(b) Lift outputs.

Figure 4.36a & b The voltage outputs using various filters for a wing moving at 0.33 m/s and oscillating at 1.2 Hz in a pycnocline with $N_c = 0.784$ Hz.

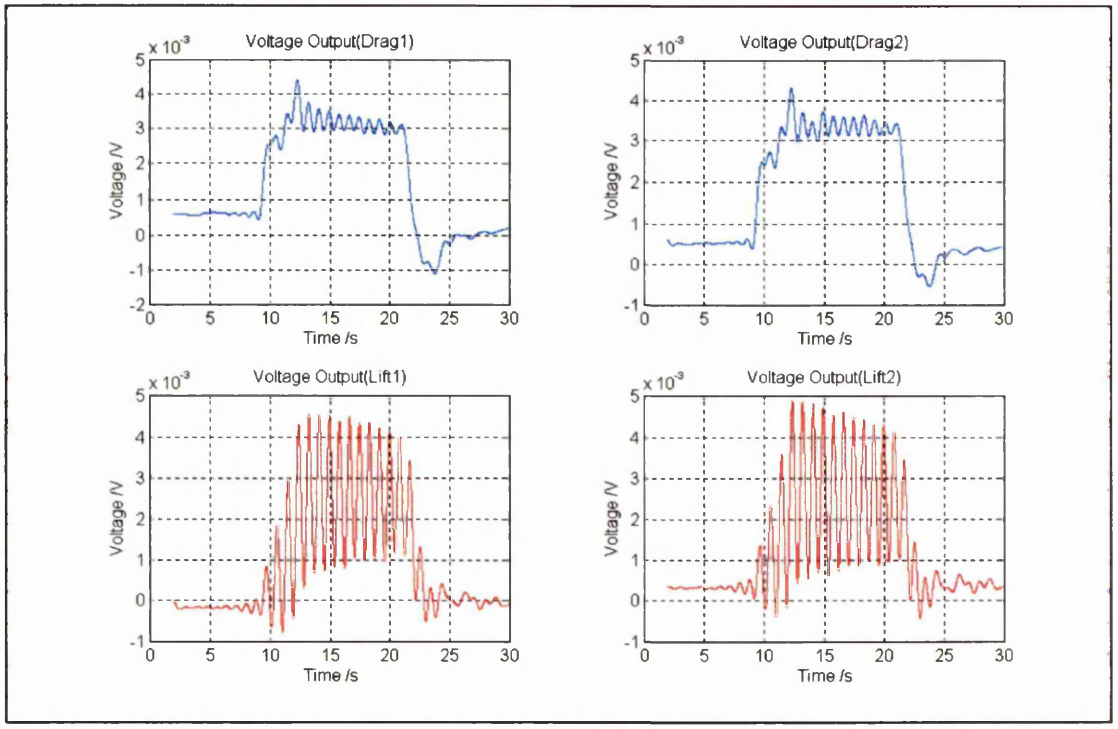

(a) Cut-off frequency = 1 Hz.

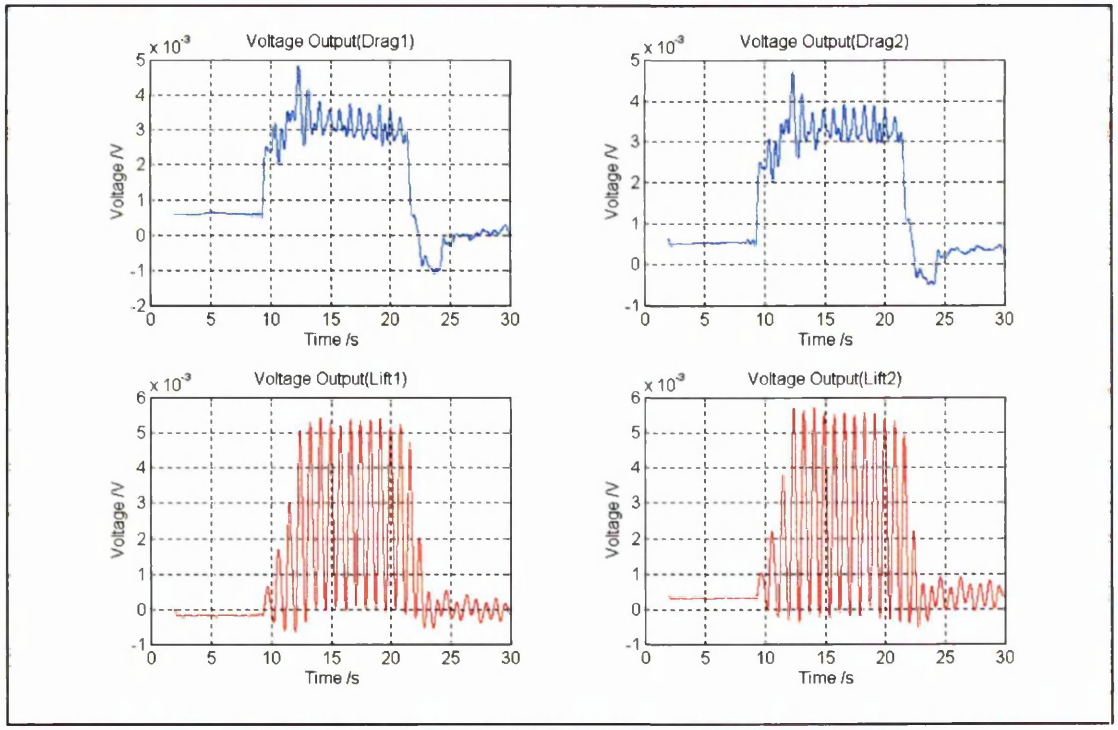

(b) Cut-off frequency = 2 Hz.

Figure 4.37a & b The voltage outputs from a wing moving at 0.33 m/s and oscillating at 1.2 Hz in a pycnocline with N_c = 0.784 Hz. The outputs were filtered with the elliptic filter at various cut-off frequencies. The sampling frequency is 122.1 Hz.

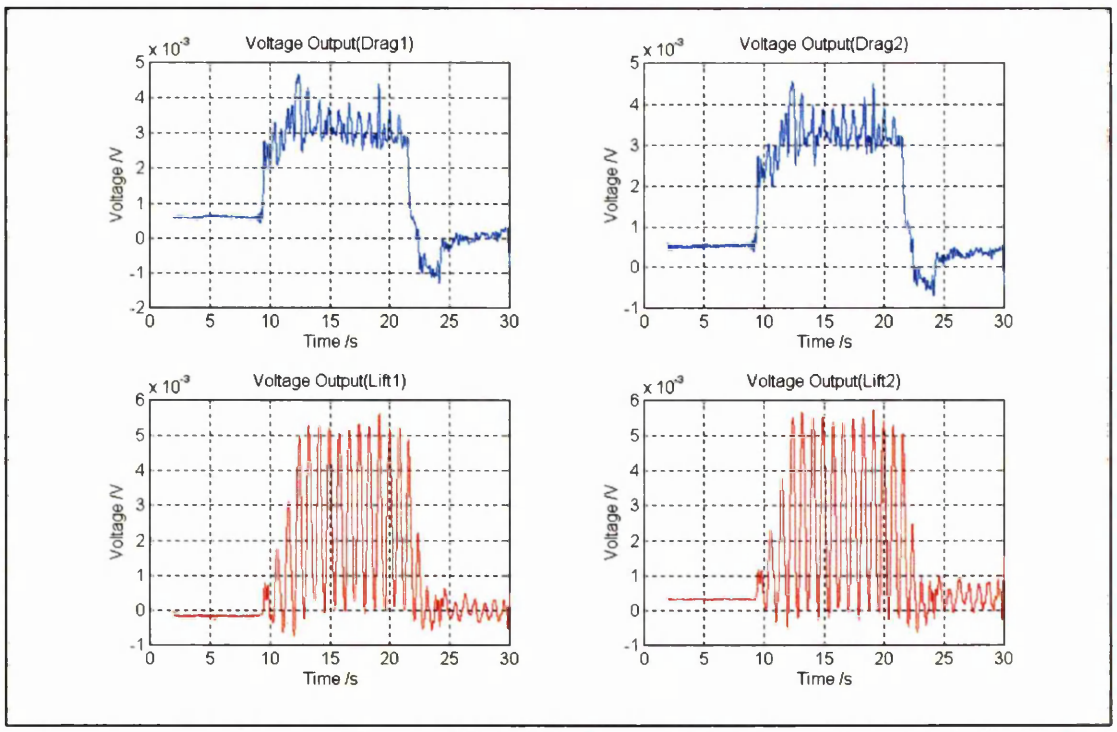

(c) Cut-off frequency = 4 Hz.

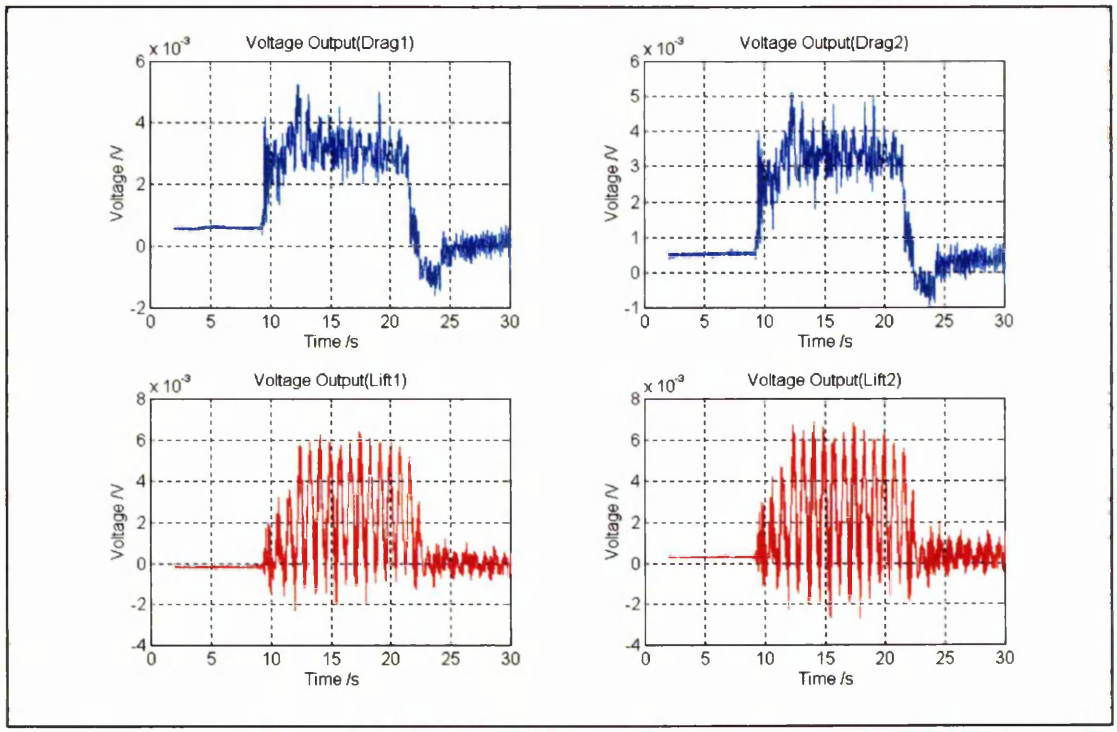

(d) Cut-off frequency = 8 Hz.

Figure 4.37c & d The voltage outputs from a wing moving at 0.33 m/s and oscillating at 1.2 Hz in a pycnocline with N_c = 0.784 Hz. The outputs were filtered with the elliptic filter at various cut-off frequencies. The sampling frequency is 122.1 Hz.

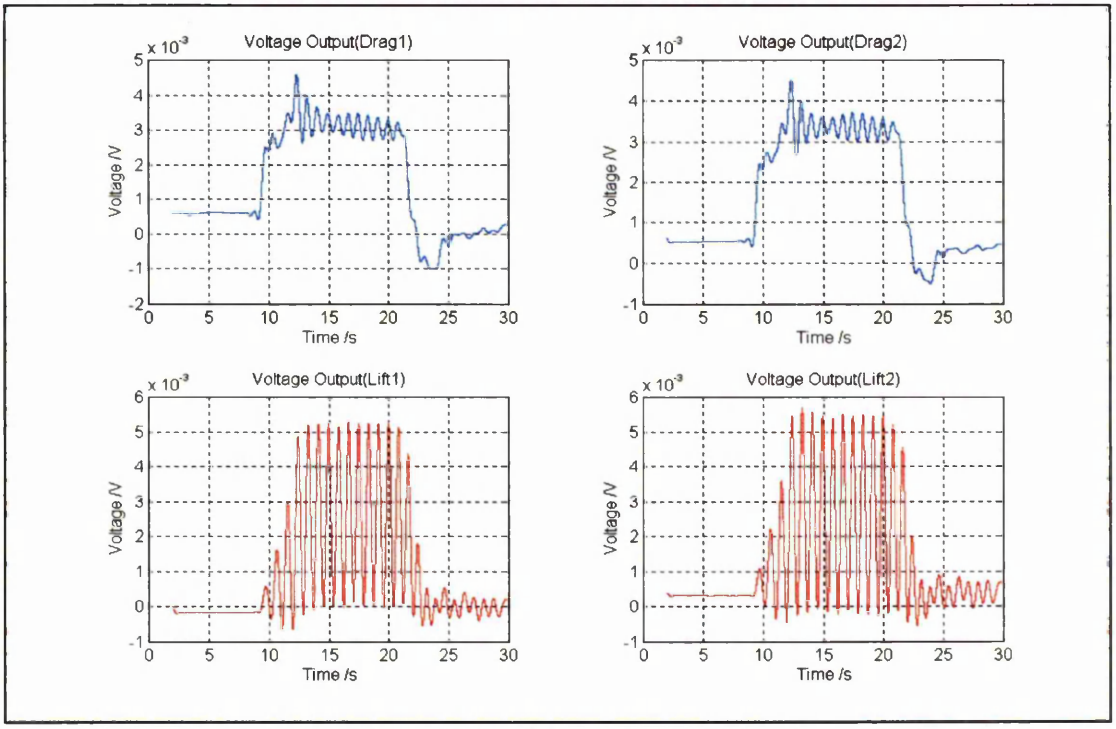

(a) Cut-off frequency = 1 Hz.

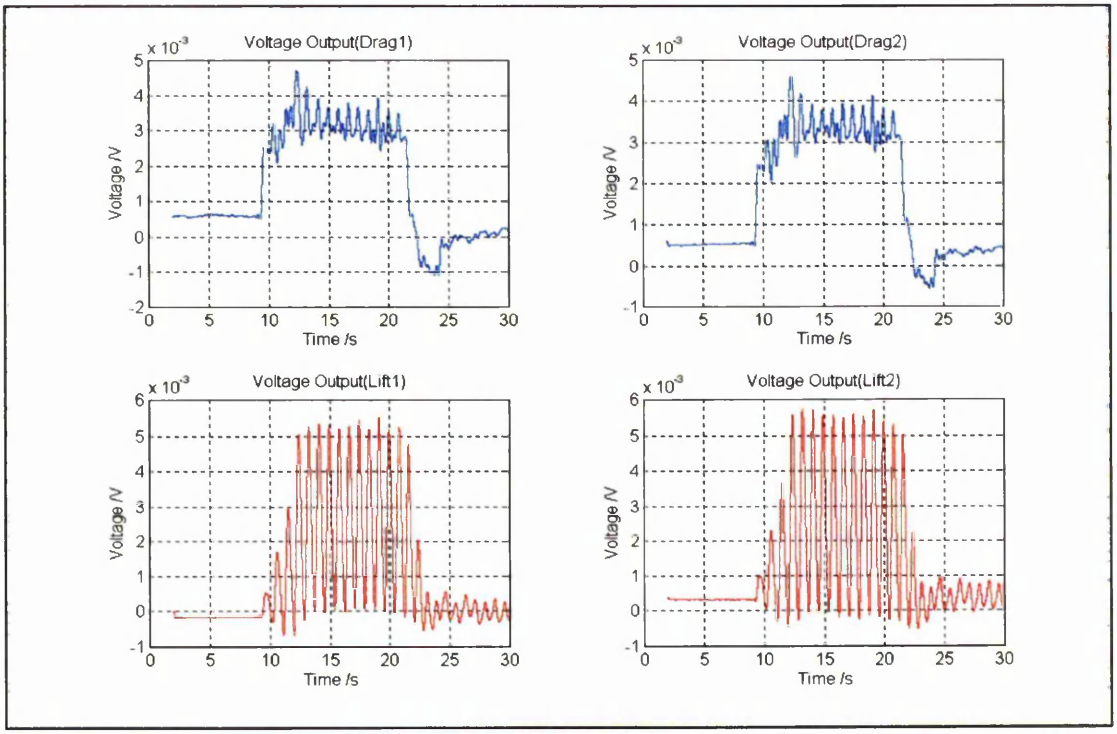

(b) Cut-off frequency = 2 Hz.

Figure 4.38a & b The voltage outputs from a wing moving at 0.33 m/s and oscillating at 1.2 Hz in a pycnocline with N_c = 0.784 Hz. The outputs were filtered with the elliptic filter at various cut-off frequencies. The sampling frequency is 488.3 Hz.

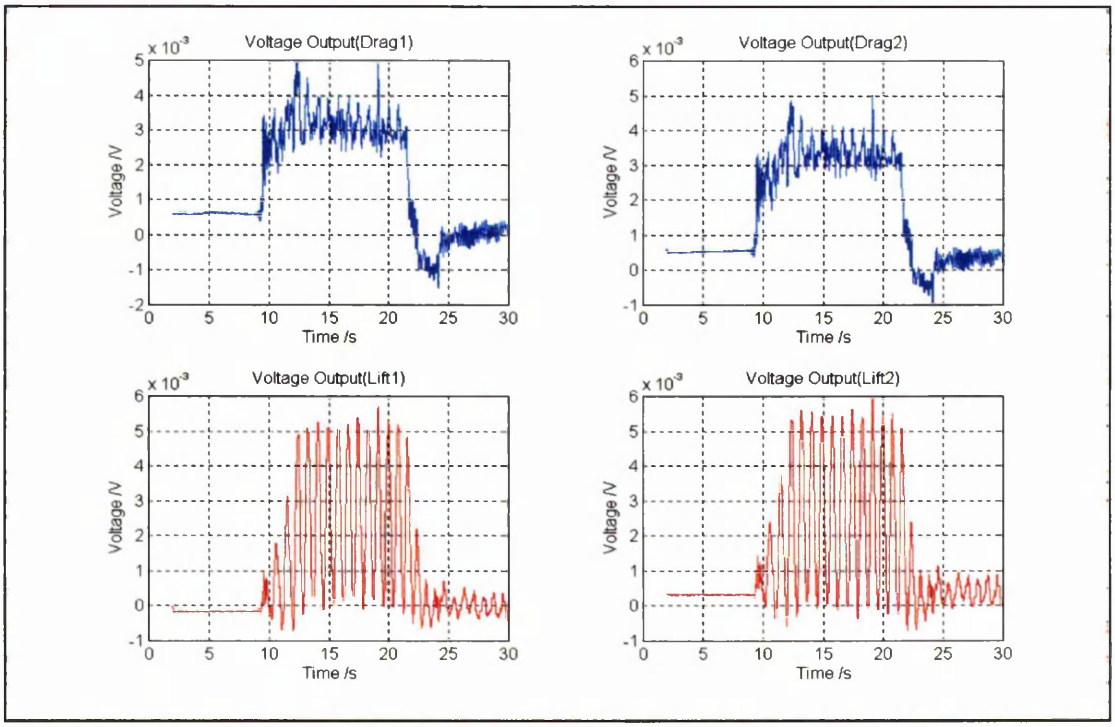

(c) Cut-off frequency = 4 Hz.

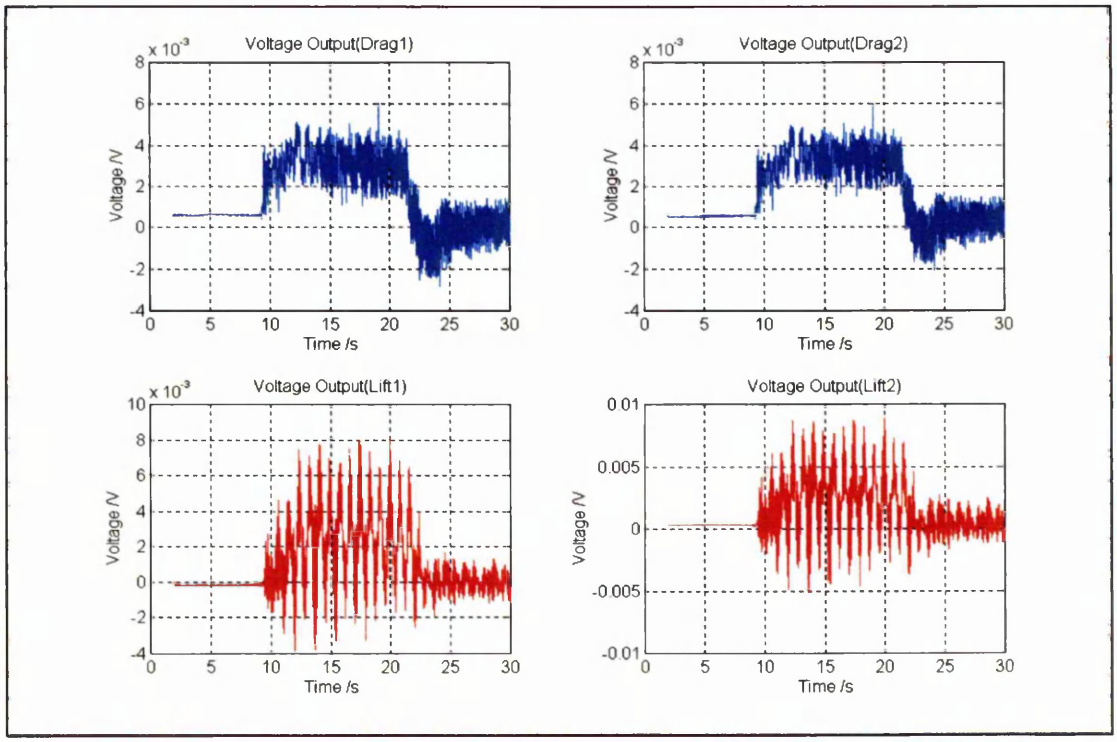

(d) Cut-off frequency = 8 Hz.

Figure 4.38c & d The voltage outputs from a wing moving at 0.33 m/s and oscillating at 1.2 Hz in a pycnocline with N_c = 0.784 Hz. The outputs were filtered with the elliptic filter at various cut-off frequencies. The sampling frequency is 488.3 Hz.

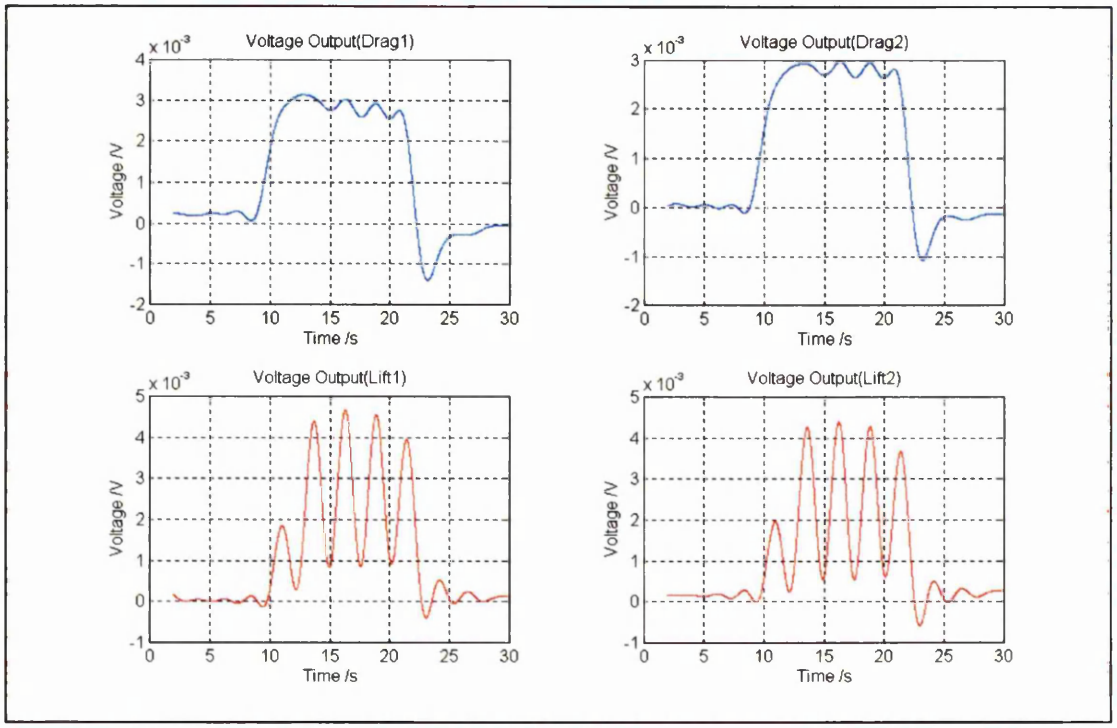

(a) Cut-off frequency = 0.3 Hz.

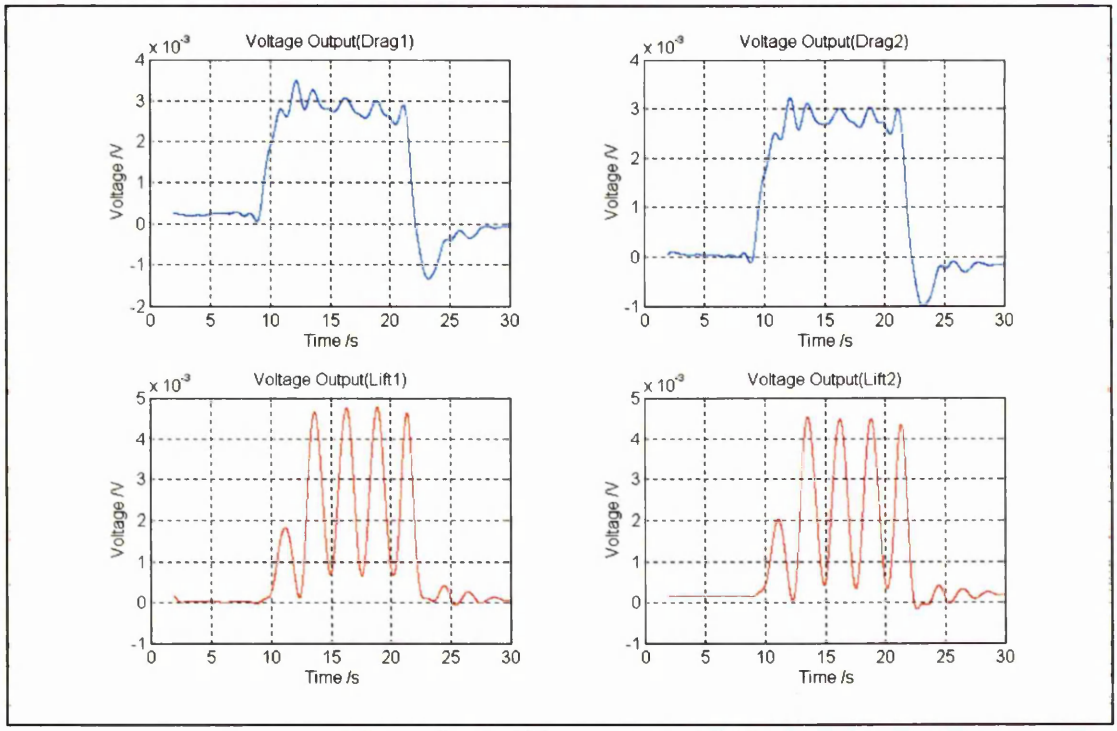

(b) Cut-off frequency = 0.6 Hz.

Figure 4.39a & b The voltage outputs from a wing moving at 0.33 m/s and oscillating at 0.392 Hz in a pycnocline with N_c = 0.784 Hz. The outputs were filtered with the elliptic filter at various cut-off frequencies. The sampling frequency is 122.1 Hz.

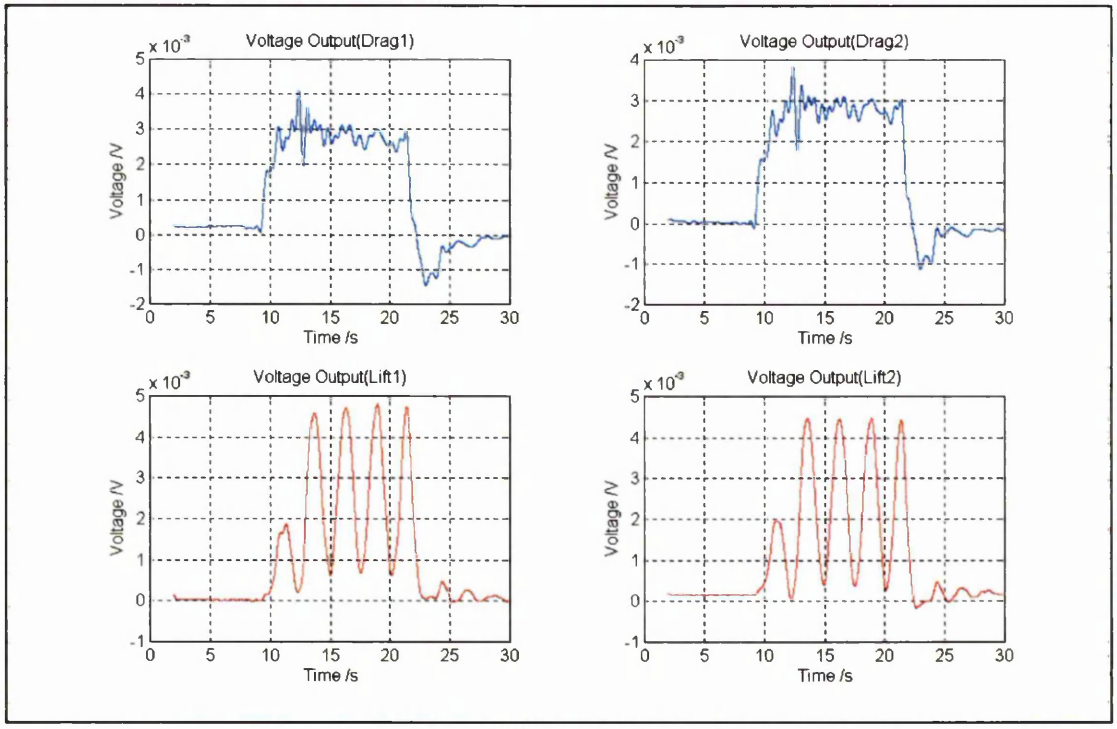

(c) Cut-off frequency = 1.2 Hz.

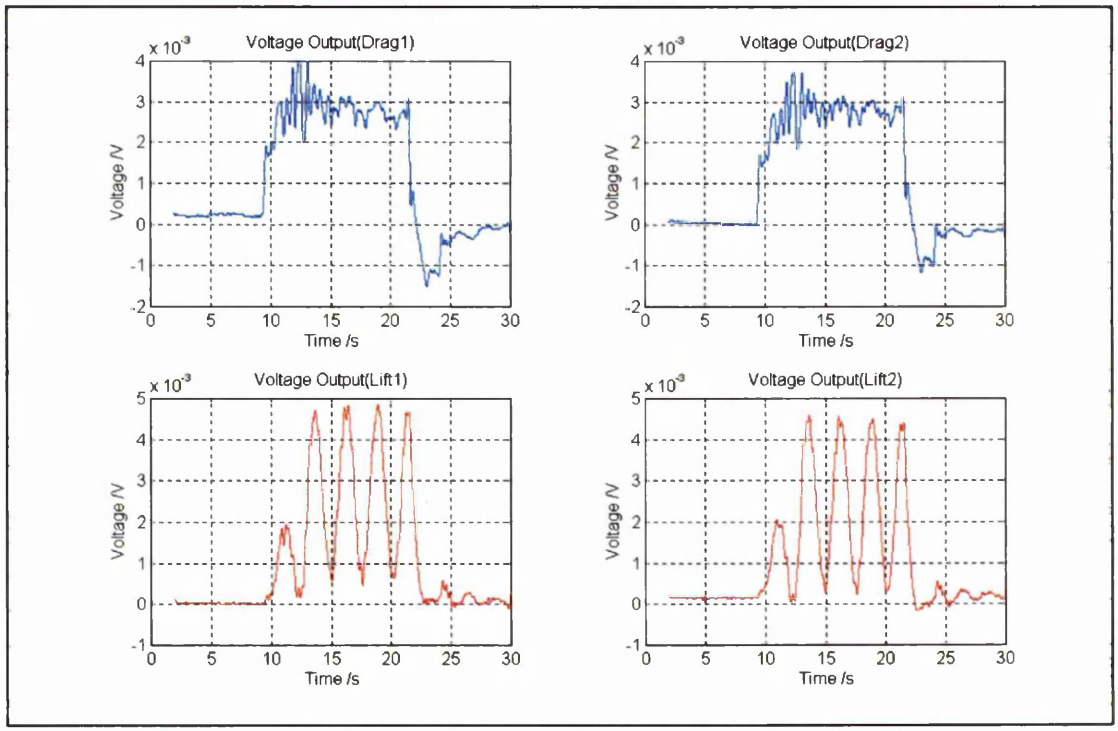

(d) Cut-off frequency = 2.4 Hz.

Figure 4.39c & d The voltage outputs from a wing moving at 0.33 m/s and oscillating at 0.392 Hz in a pycnocline with N_c = 0.784 Hz. The outputs were filtered with the elliptic filter at various cut-off frequencies. The sampling frequency is 122.1 Hz.

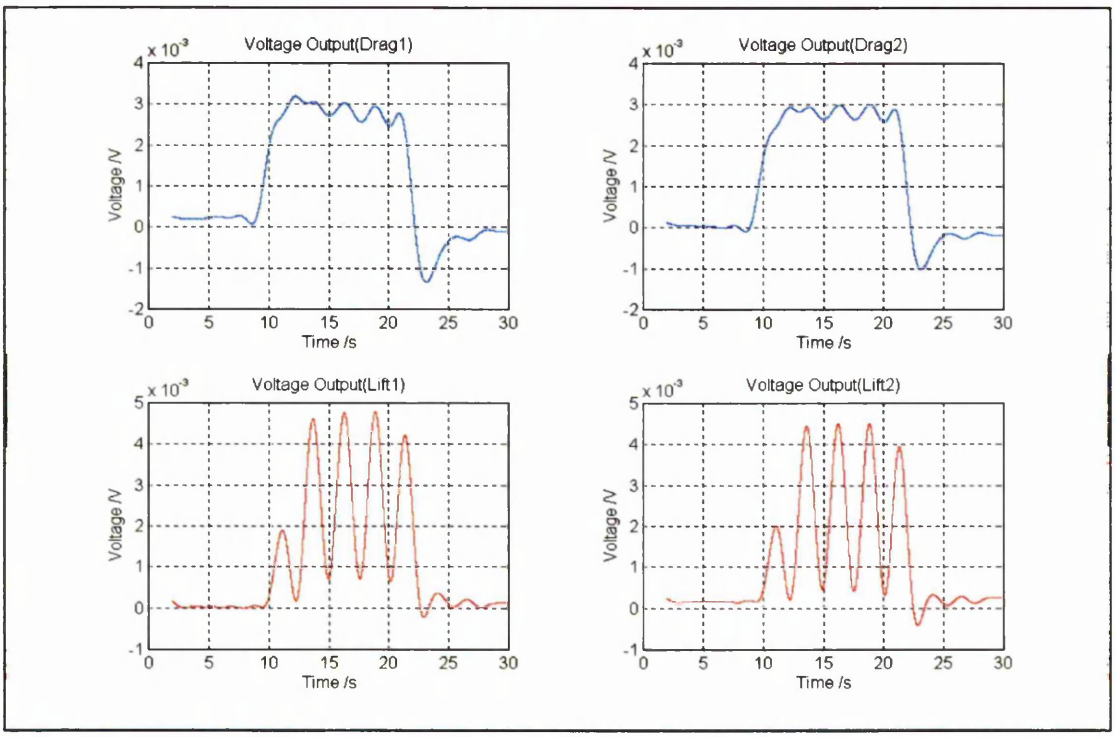

(a) Cut-off frequency = 0.3 Hz.

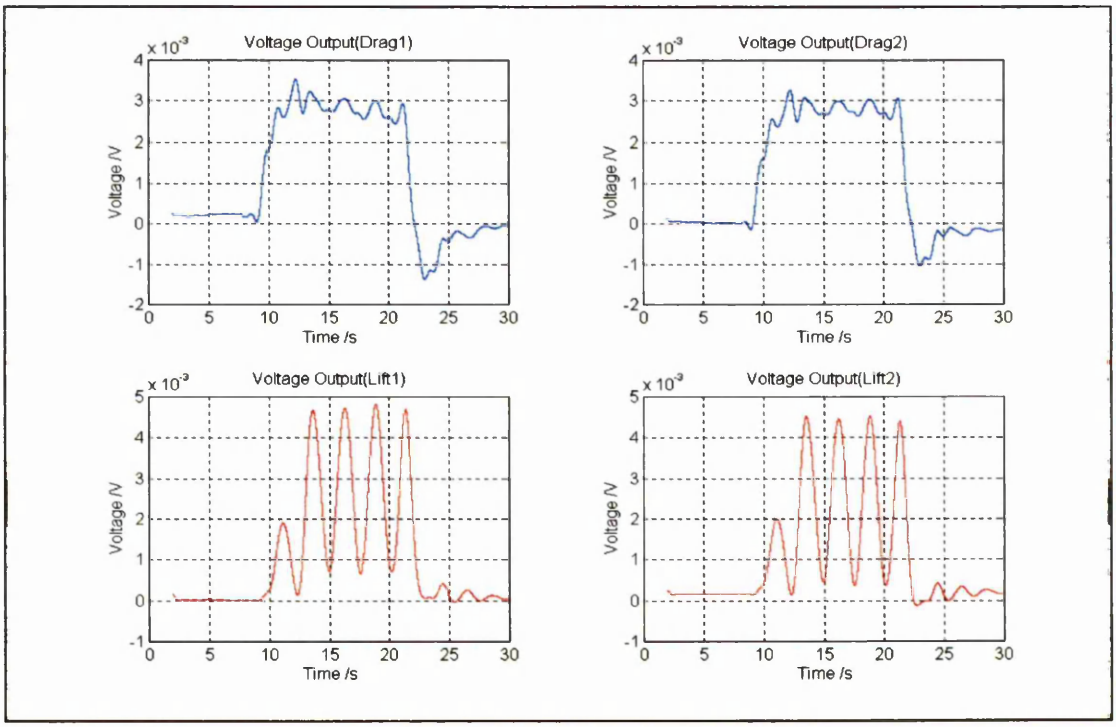

(b) Cut-off frequency = 0.6 Hz.

Figure 4.40a & b The voltage outputs from a wing moving at 0.33 m/s and oscillating at 0.392 Hz in a pycnocline with N_c = 0.784 Hz. The outputs were filtered with the elliptic filter at various cut-off frequencies. The sampling frequency is 488.3 Hz.

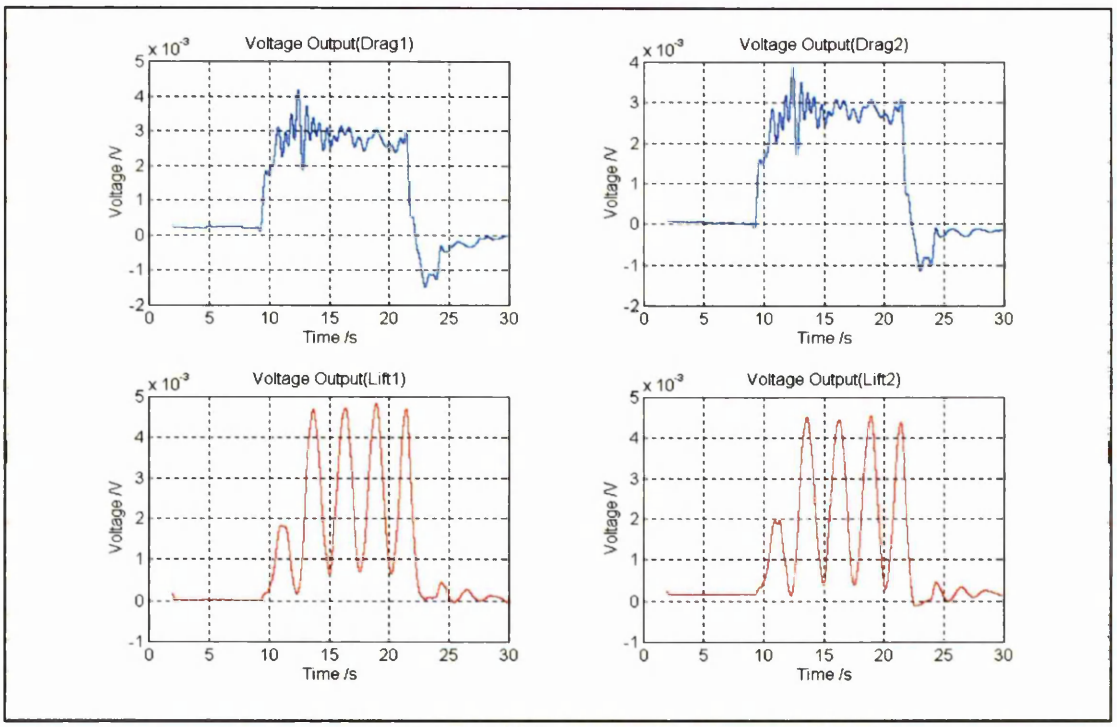

(c) Cut-off frequency = 1.2 Hz.

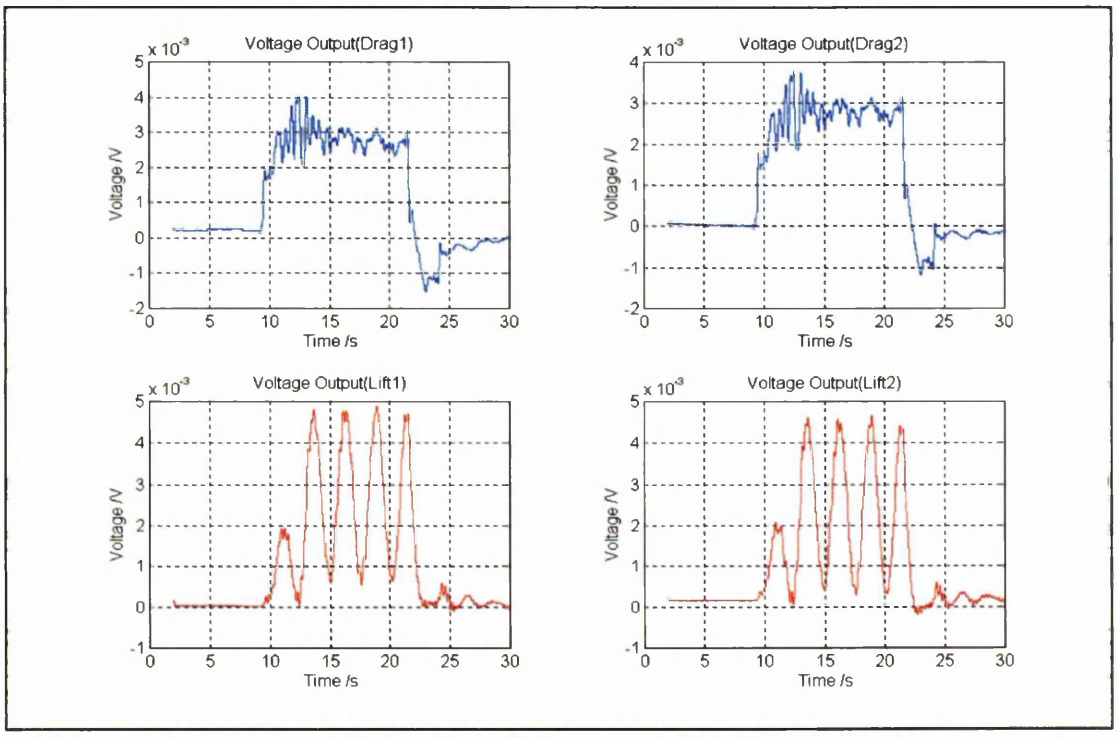

(d) Cut-off frequency = 2.4 Hz.

Figure 4.40c & d The voltage outputs from a wing moving at 0.33 m/s and oscillating at 0.392 Hz in a pycnocline with N_c = 0.784 Hz. The outputs were filtered with the elliptic filter at various cut-off frequencies. The sampling frequency is 488.3 Hz.

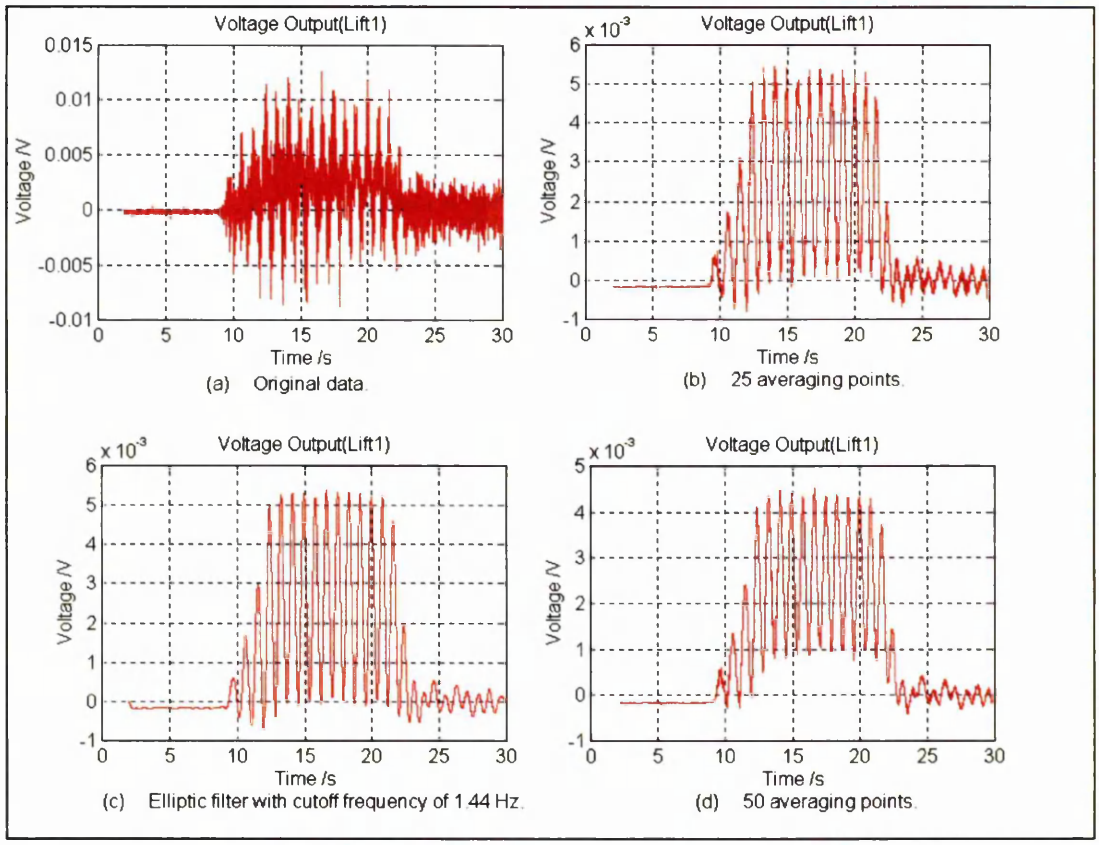

Figure 4.41a to d The voltage outputs for the lift of a wing moving at 0.33 m/s and oscillating at 1.2 Hz in a pycnocline with N_c = 0.784 Hz. The graphs on the right column were filtered using a moving average and the sampling rate was 122.1 Hz.

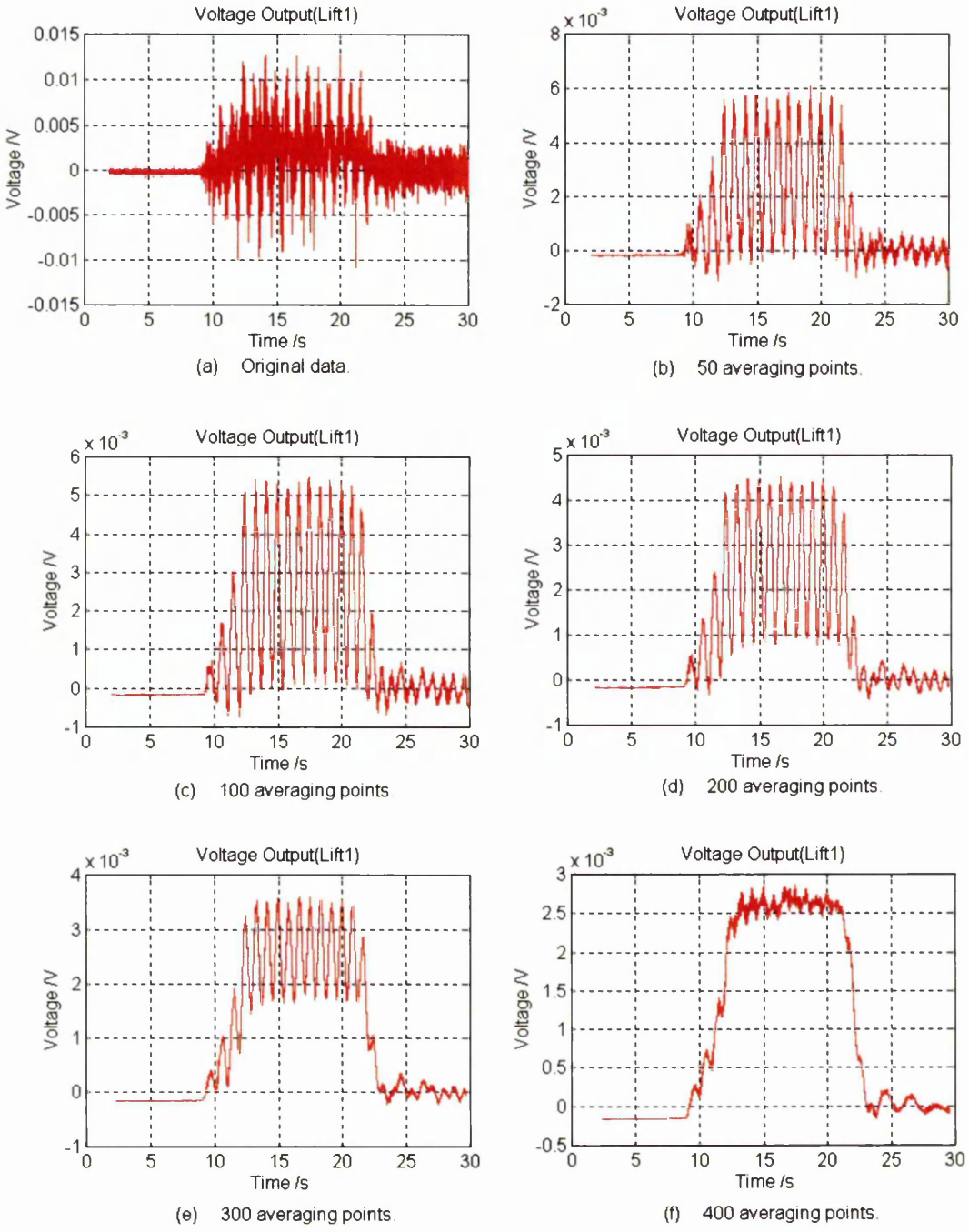

Figure 4.42a to f The voltage outputs for the lift of a wing moving at 0.33 m/s and oscillating at 1.2 Hz in a pycnocline with N_c = 0.784 Hz. The data were filtered with the moving average and the sampling rate was 488.3 Hz.

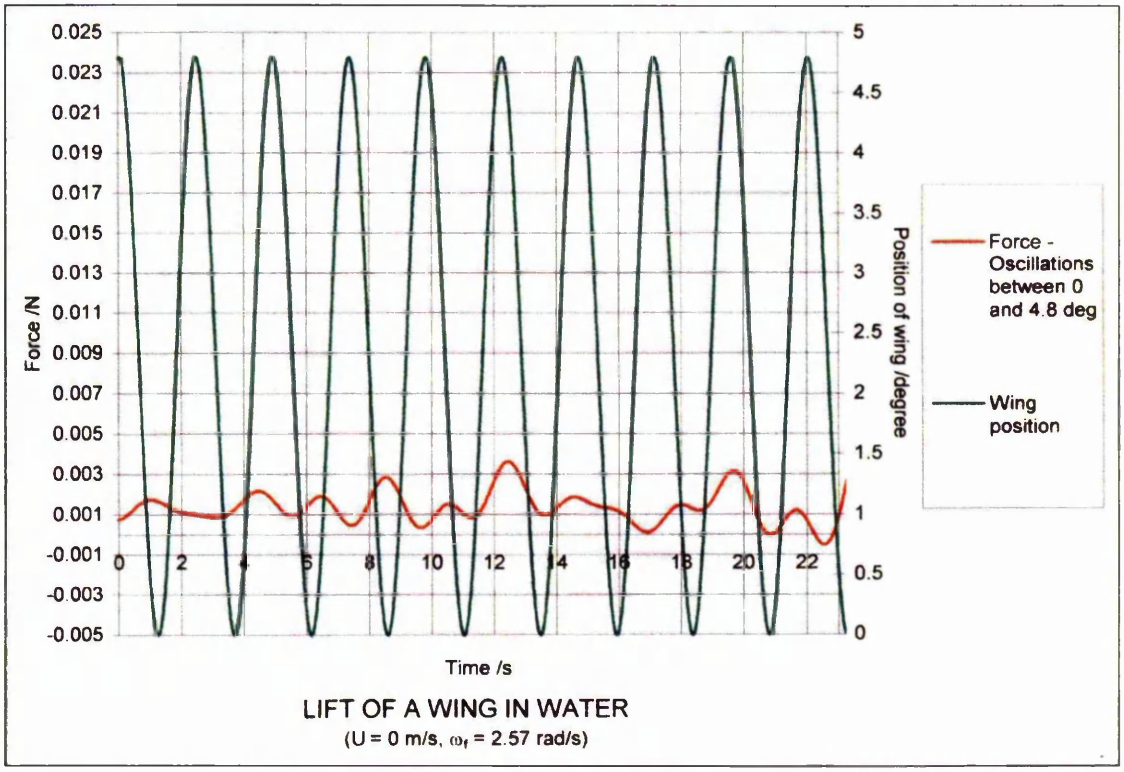

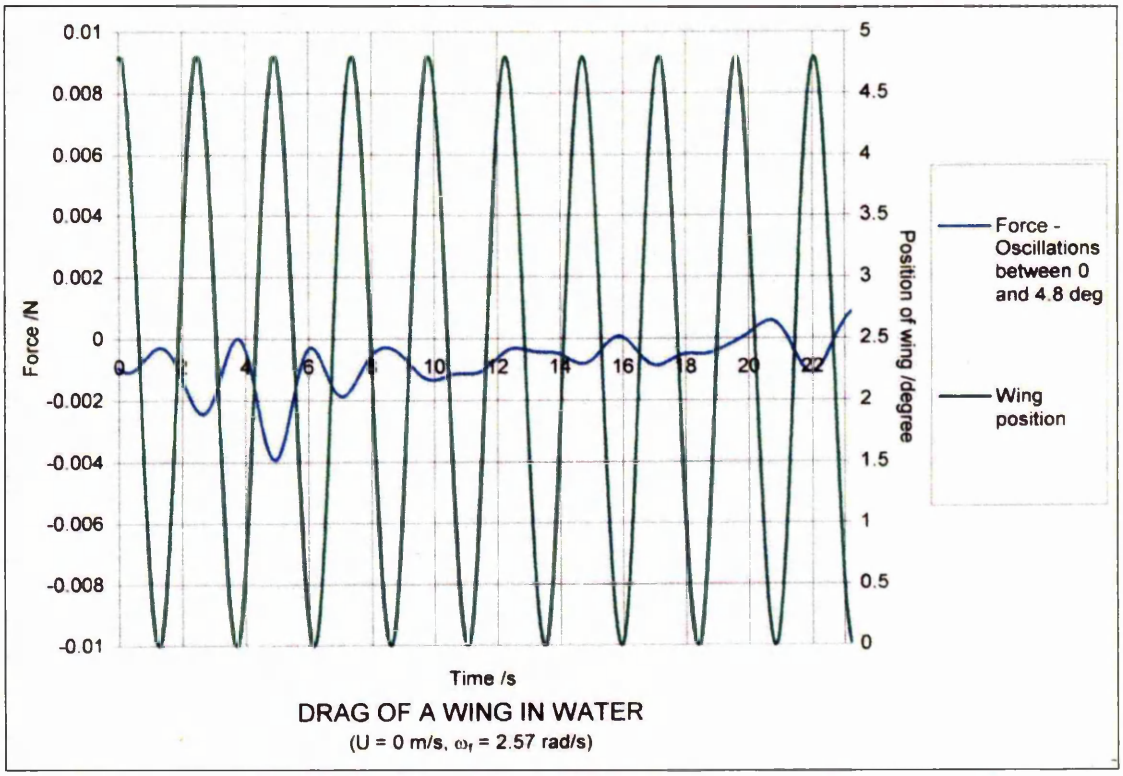

Figures 4.43a & b The lift and drag of a NACA 0012 wing with aspect ratio 1.7 oscillating in a constant density fluid.

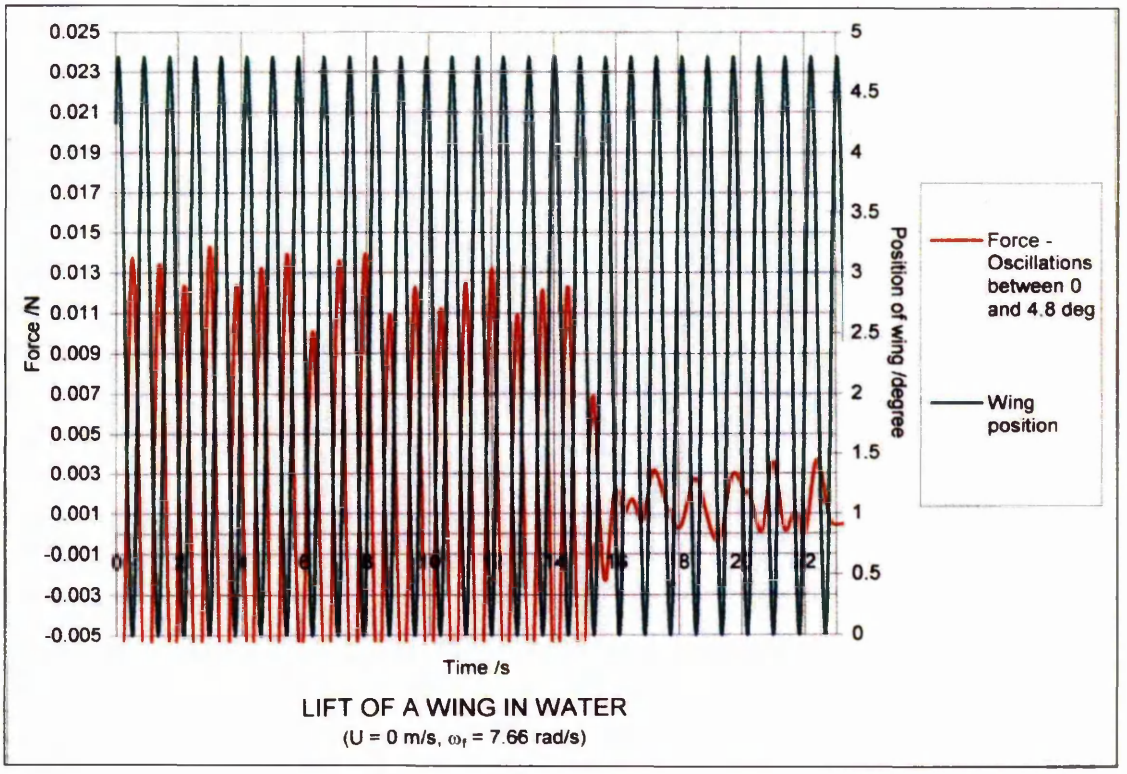

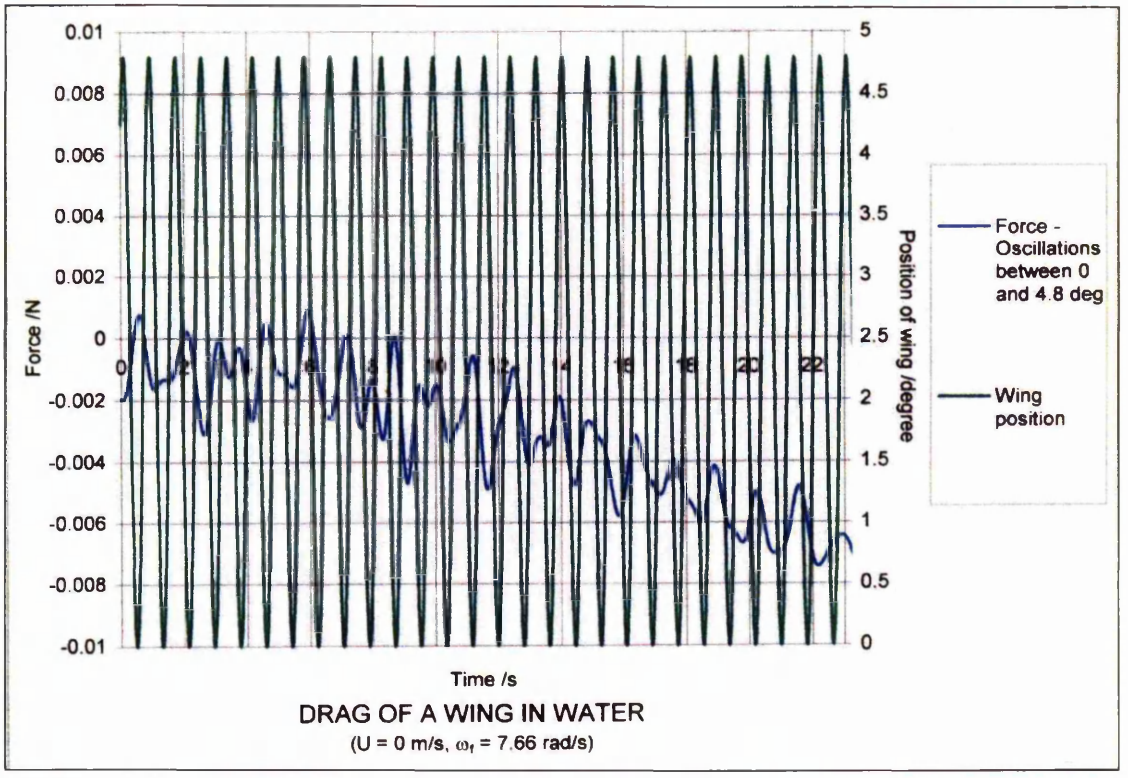

Figures 4.44a & b The lift and drag coefficients of a NACA 0012 wing with aspect ratio 1.7 oscillating in a constant density fluid.

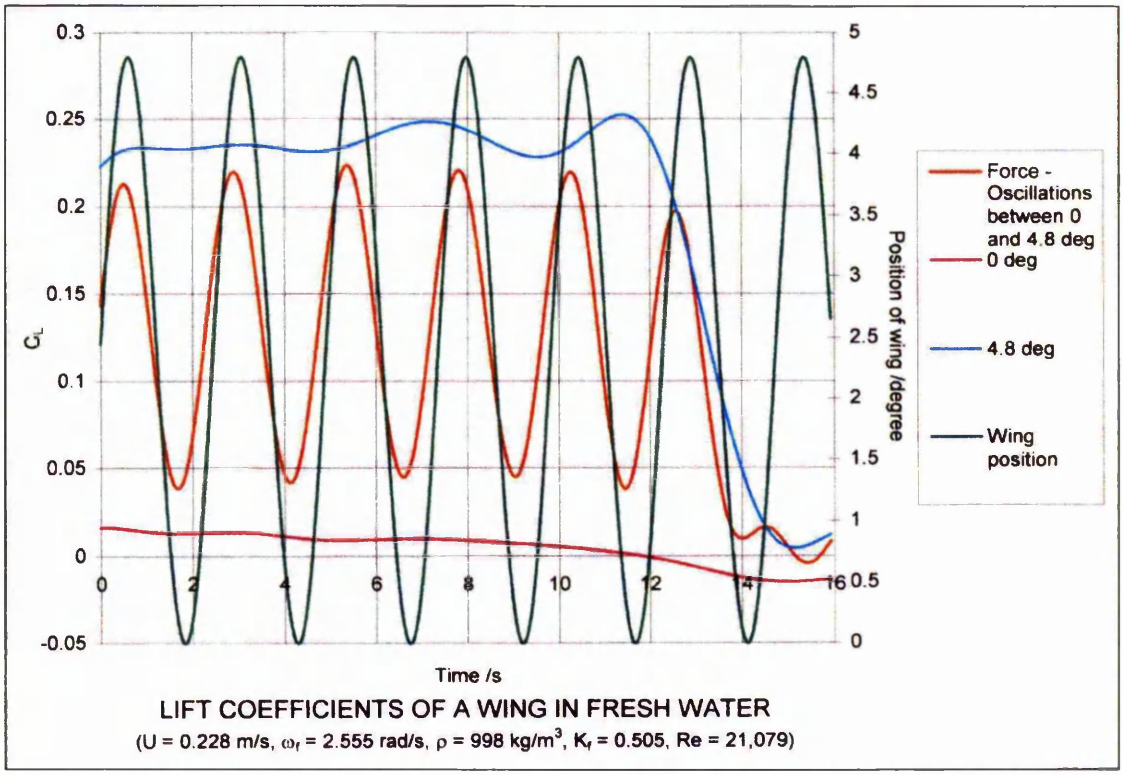

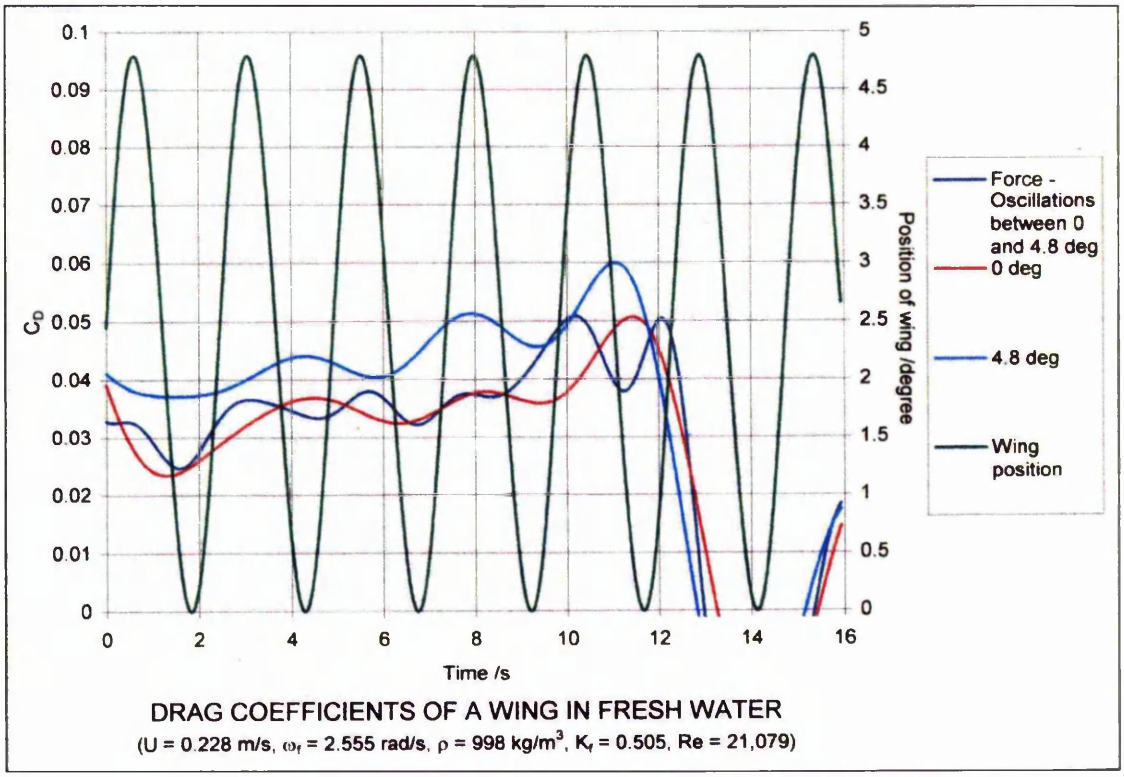

Figures 4.45a & b The lift and drag coefficients of a NACA 0012 wing with aspect ratio 1.7 moving in a constant density fluid.

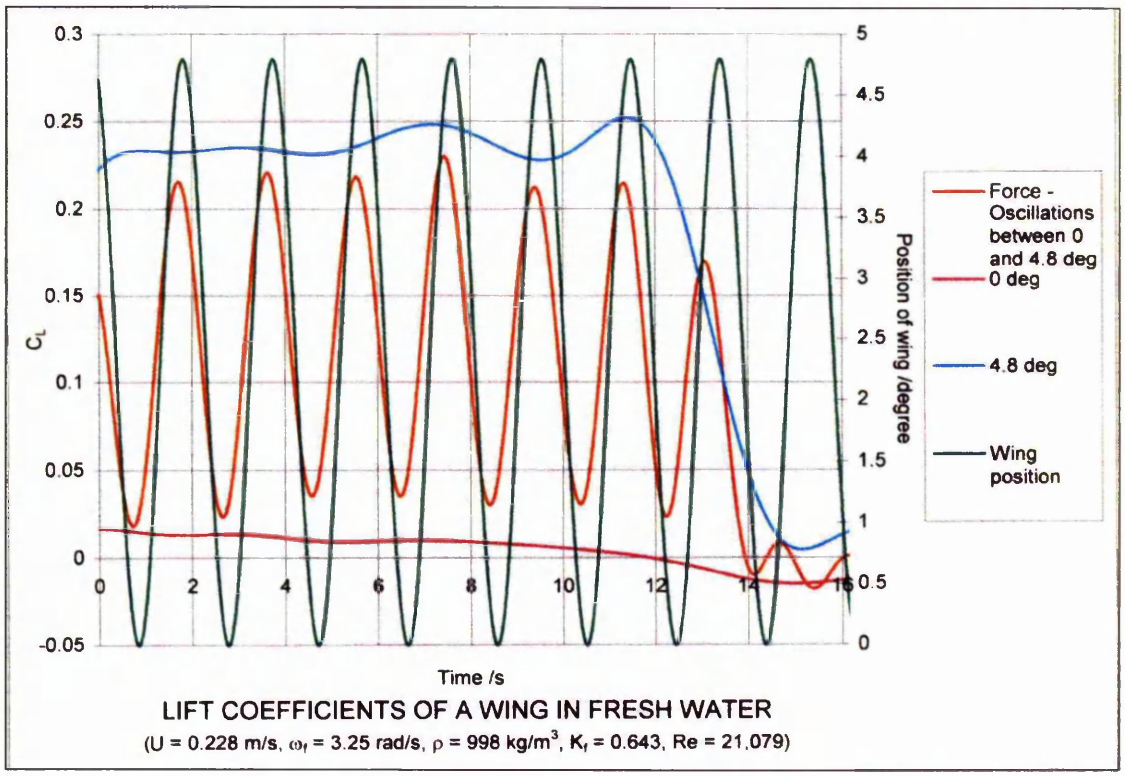

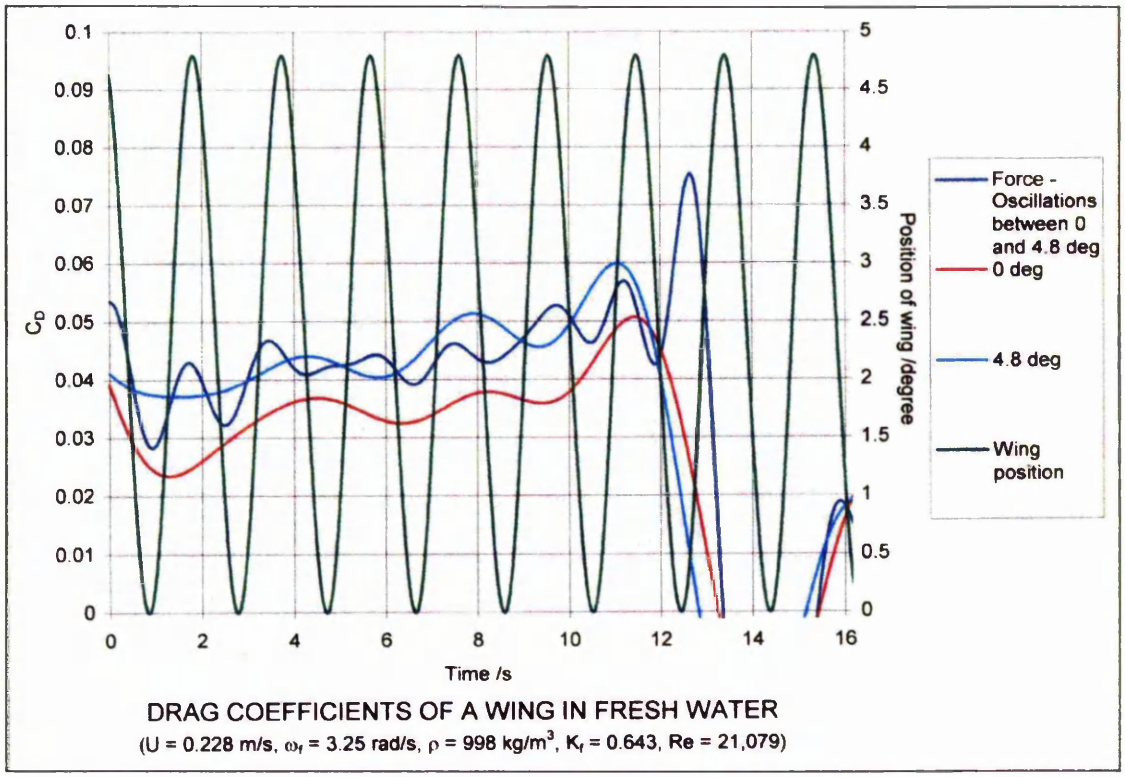

Figures 4.46a & b The lift and drag coefficients of a NACA 0012 wing with aspect ratio 1.7 moving in a constant density fluid.

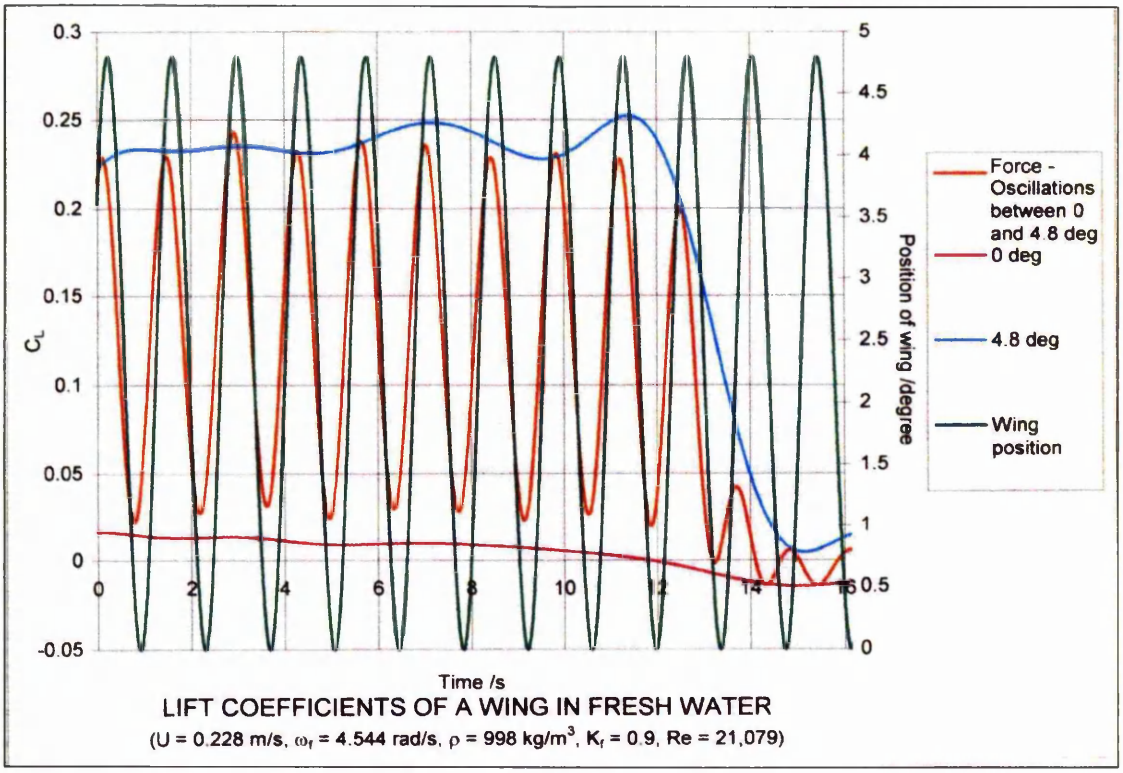

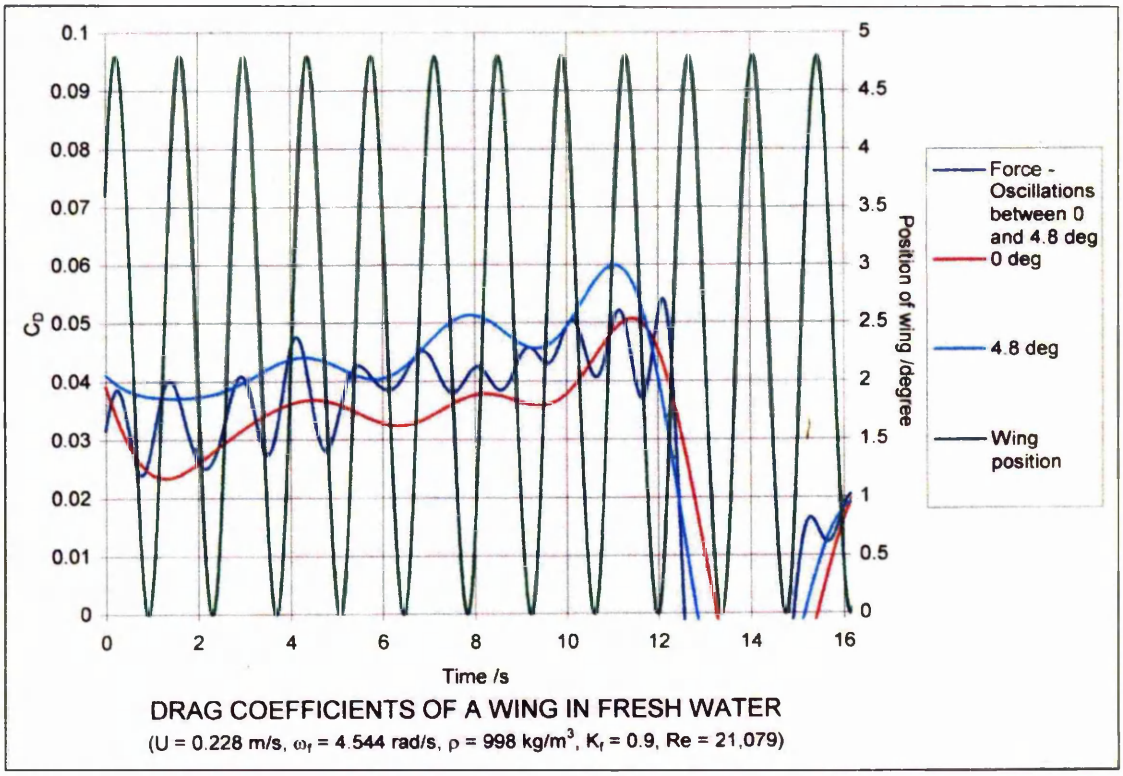

Figures 4.47a & b The lift and drag coefficients of a NACA 0012 wing with aspect ratio 1.7 moving in a constant density fluid.

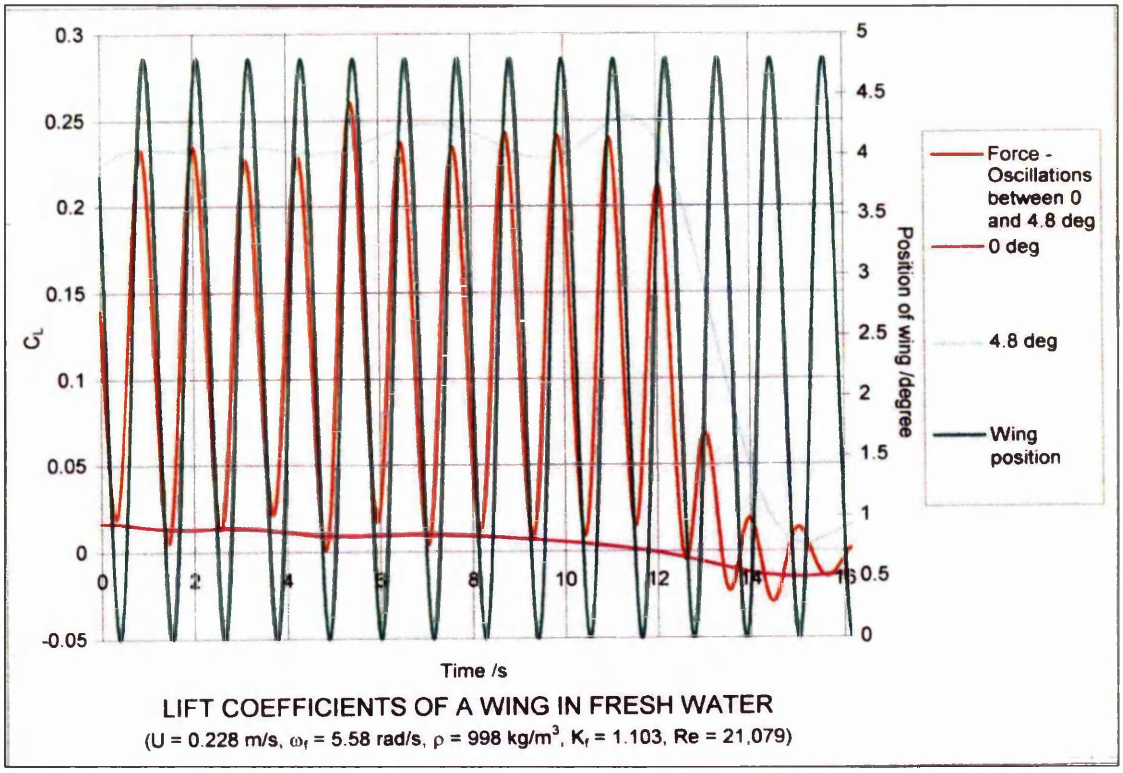

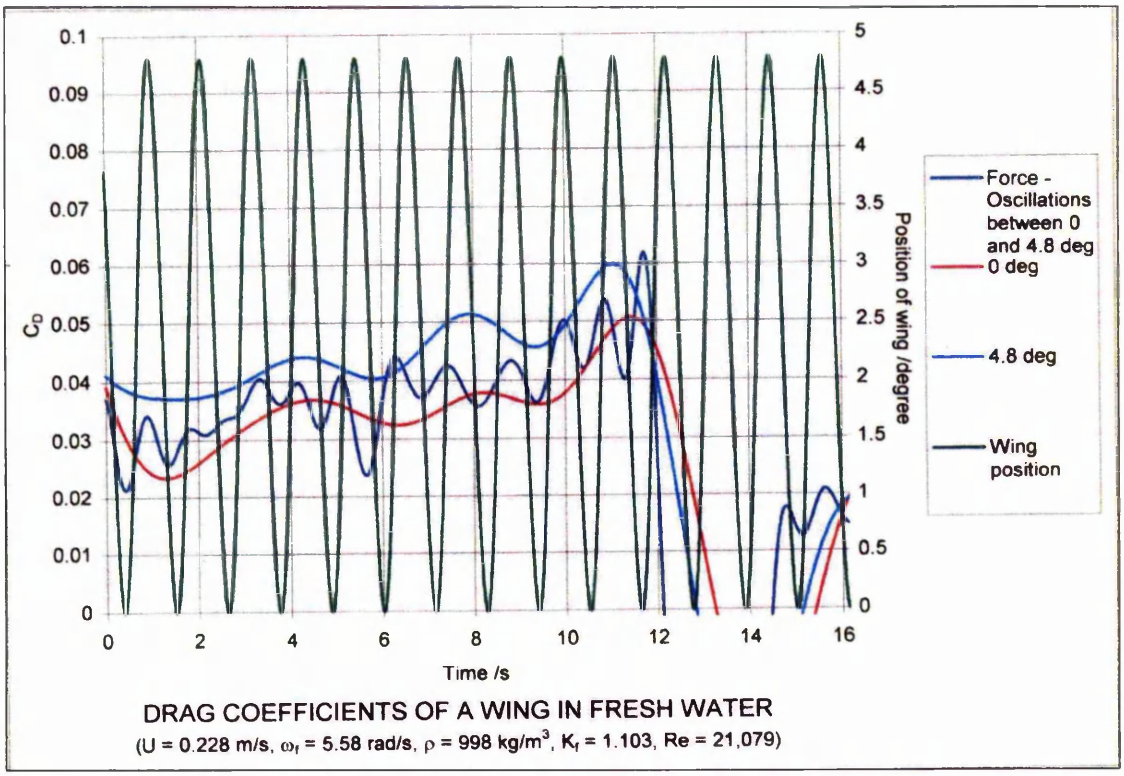

Figures 4.48a & b The lift and drag coefficients of a NACA 0012 wing with aspect ratio 1.7 moving in a constant density fluid.

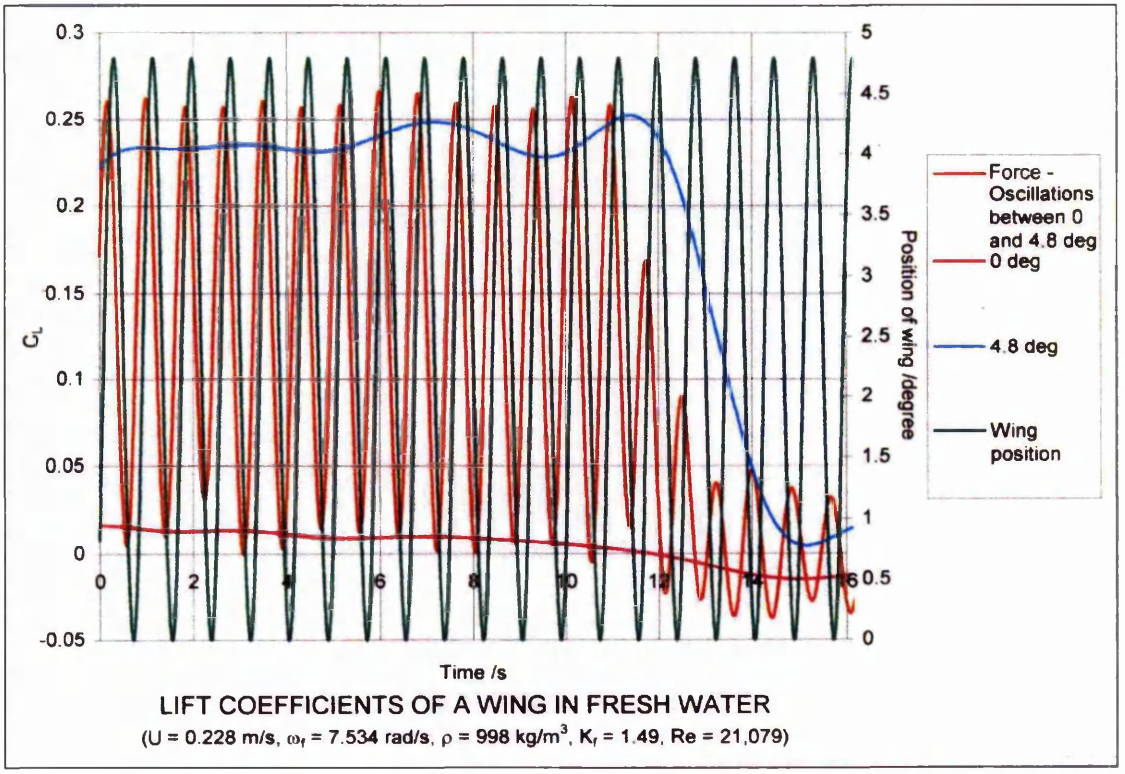

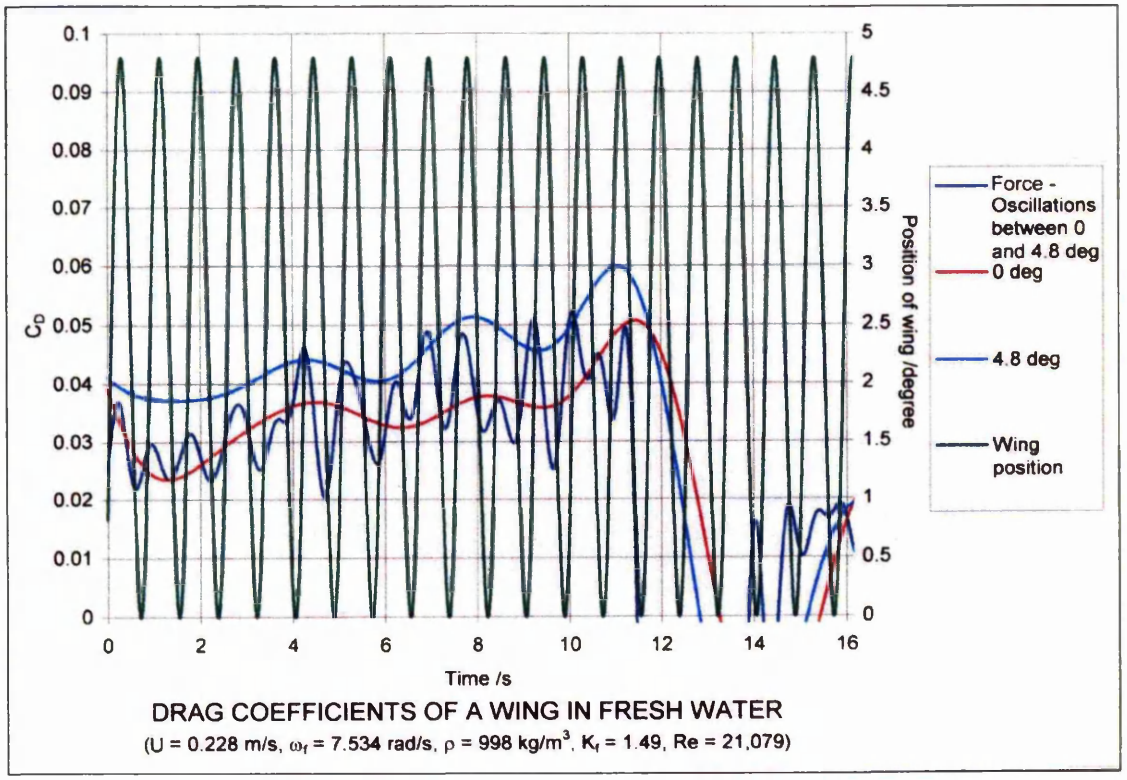

Figures 4.49a & b The lift and drag coefficients of a NACA 0012 wing with aspect ratio 1.7 moving in a constant density fluid.

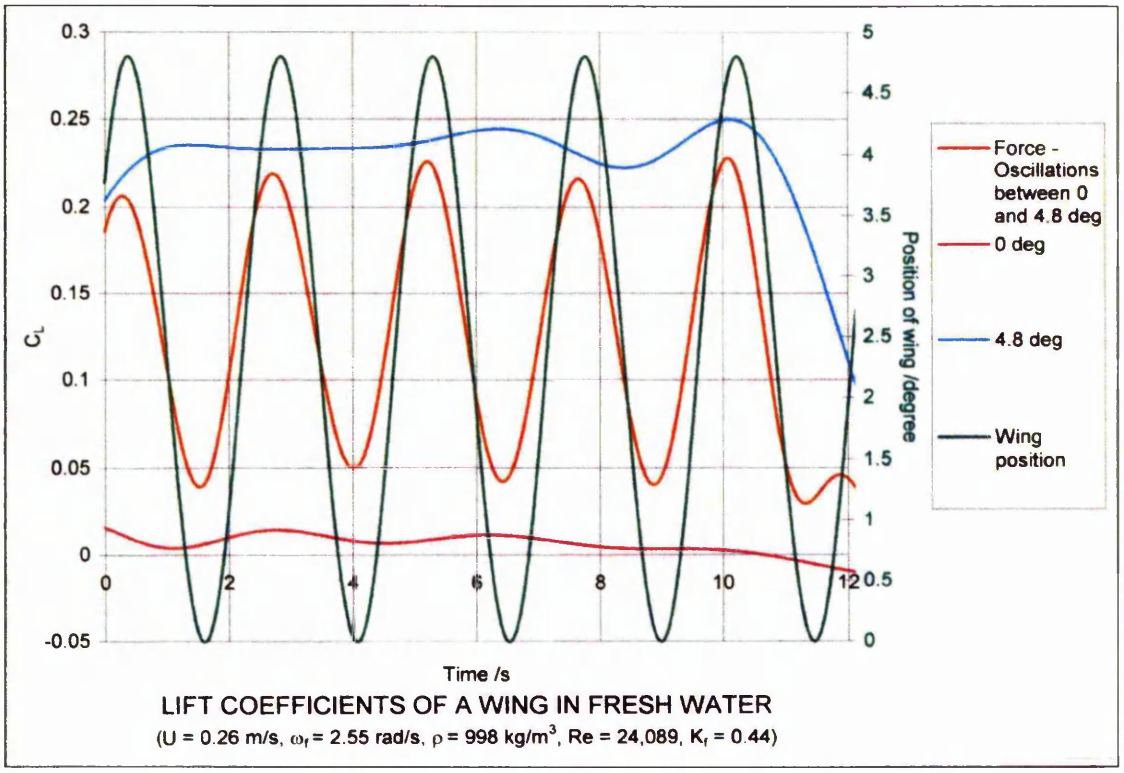

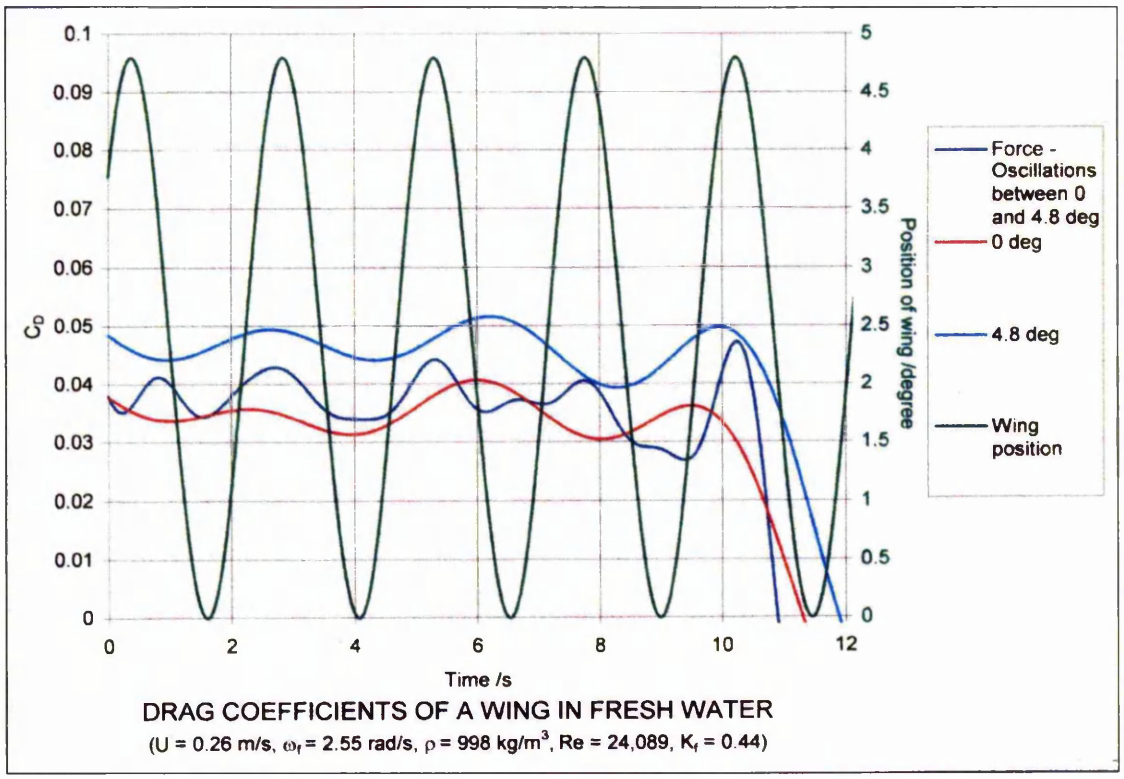

Figures 4.50a & b The lift and drag coefficients of a NACA 0012 wing with aspect ratio 1.7 moving in a constant density fluid.

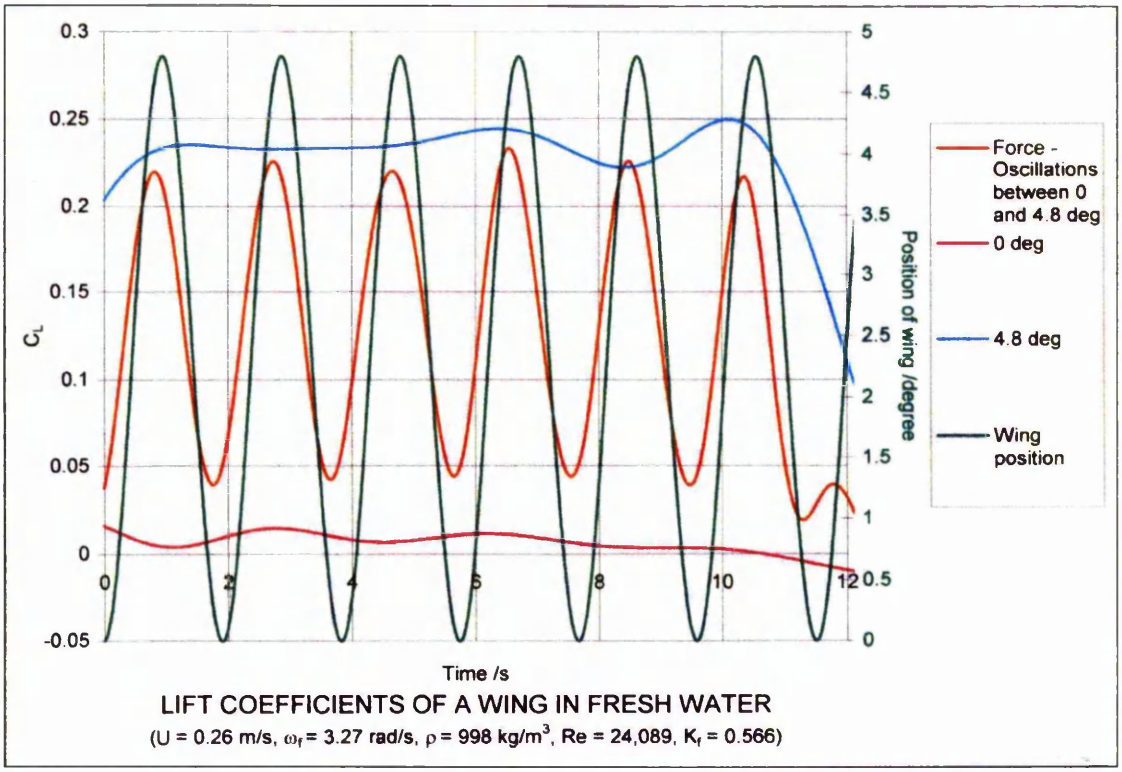

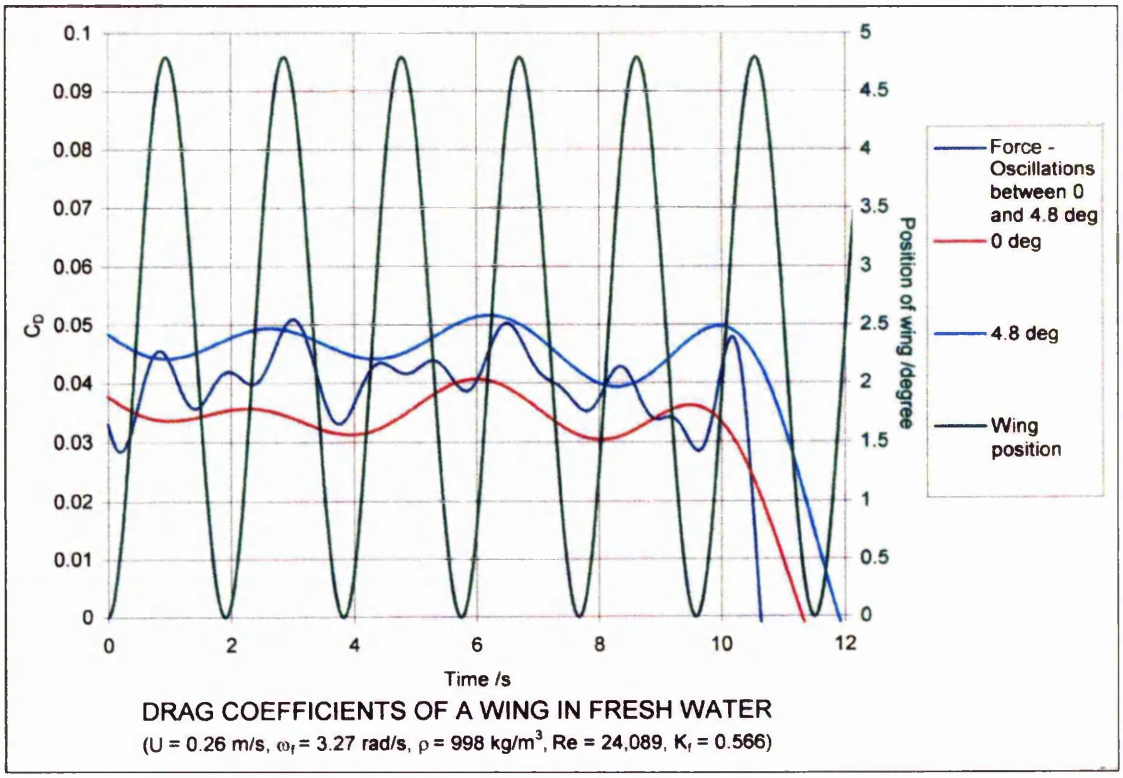

Figures 4.51a & b The lift and drag coefficients of a NACA 0012 wing with aspect ratio 1.7 moving in a constant density fluid.

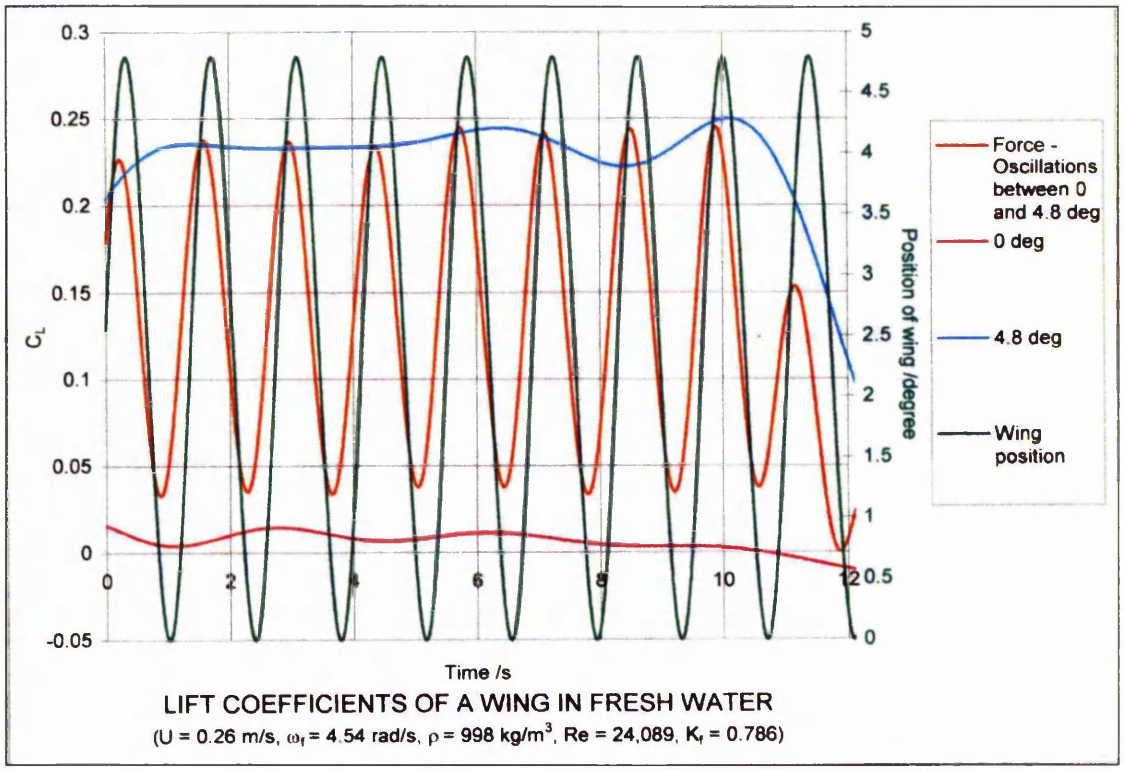

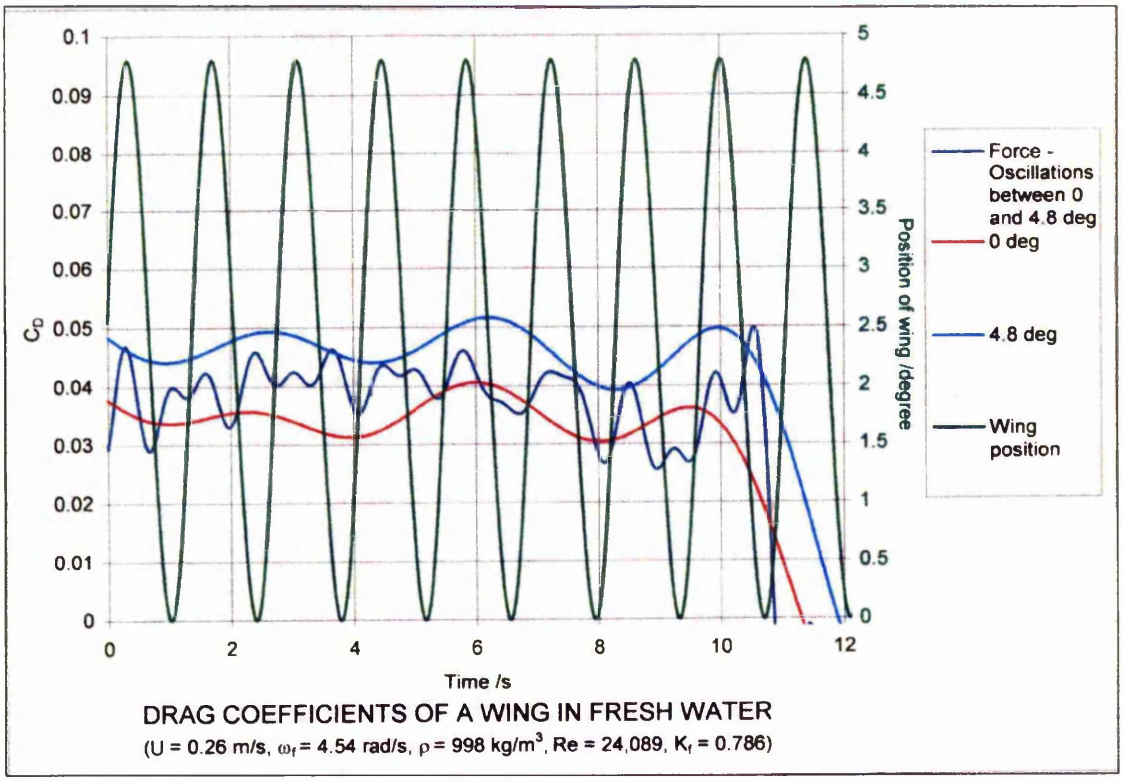

Figures 4.52a & b The lift and drag coefficients of a NACA 0012 wing with aspect ratio 1.7 moving in a constant density fluid.

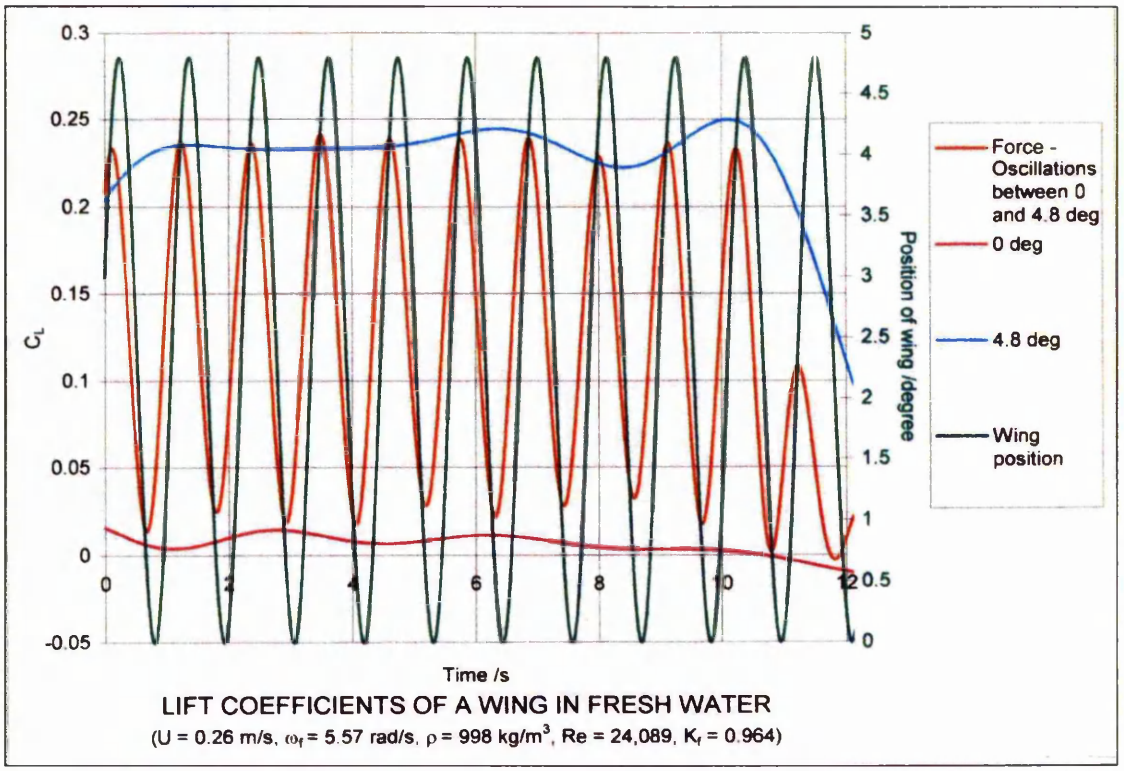

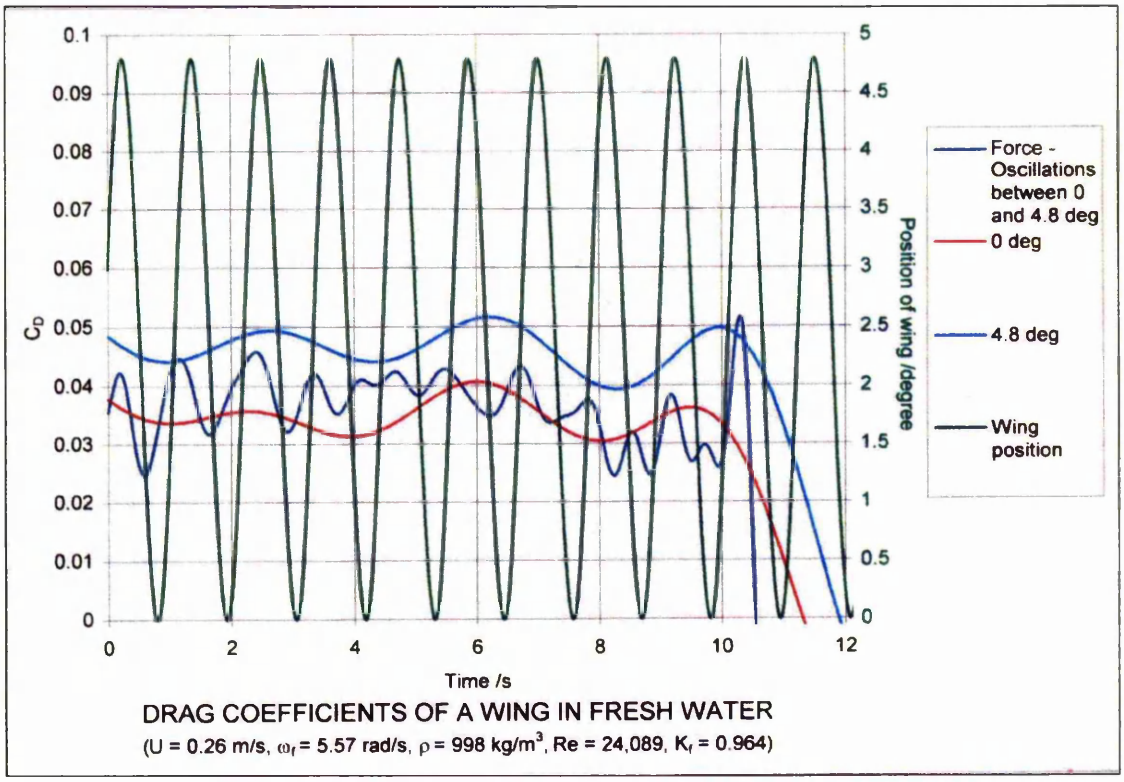

Figures 4.53a & b The lift and drag coefficients of a NACA 0012 wing with aspect ratio 1.7 moving in a constant density fluid.

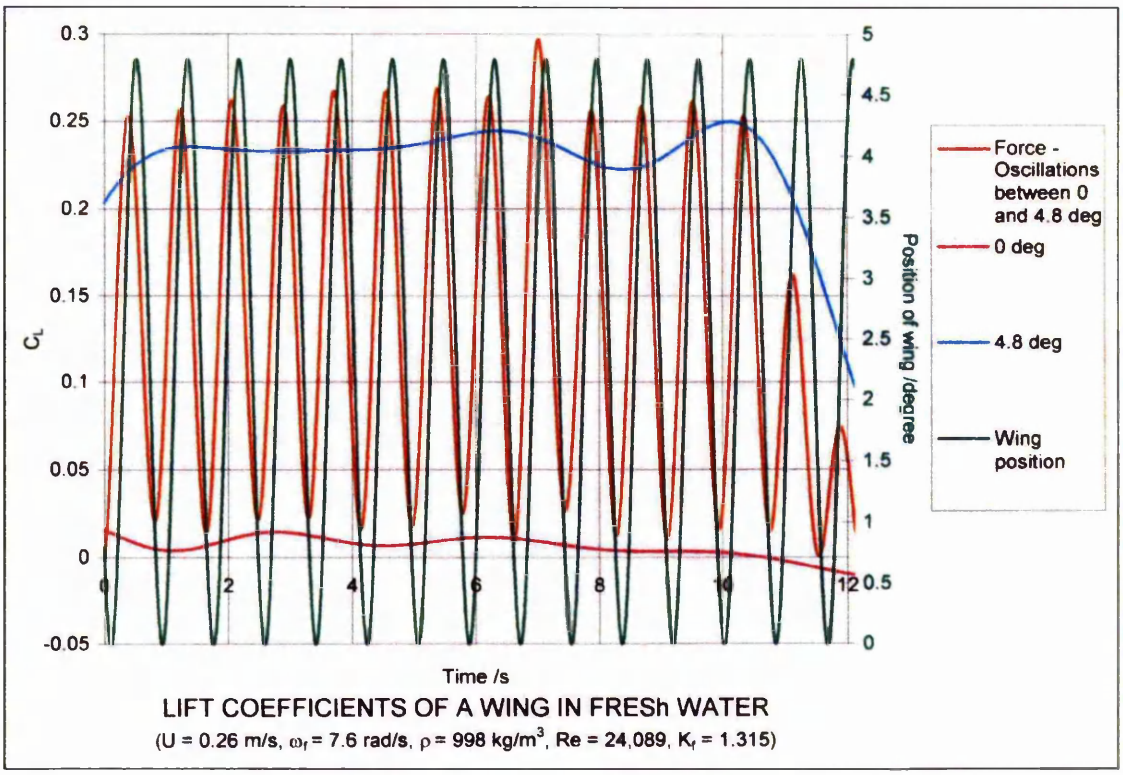

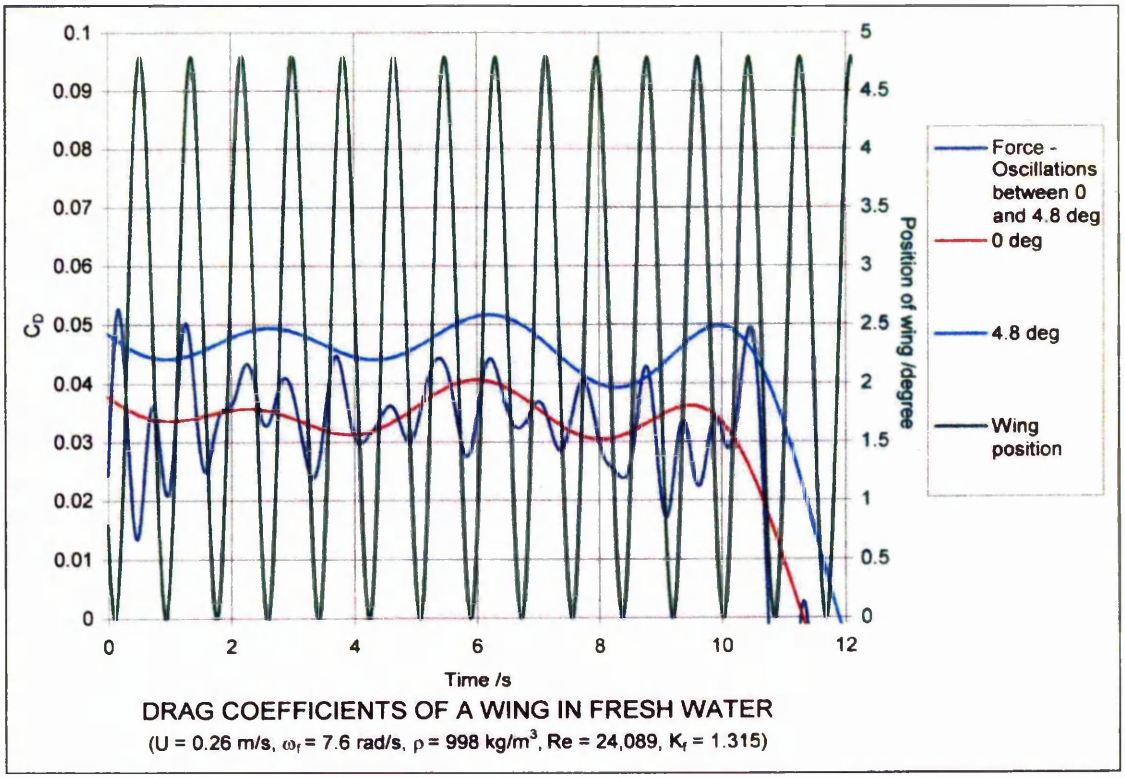

Figures 4.54a & b The lift and drag coefficients of a NACA 0012 wing with aspect ratio 1.7 moving in a constant density fluid.

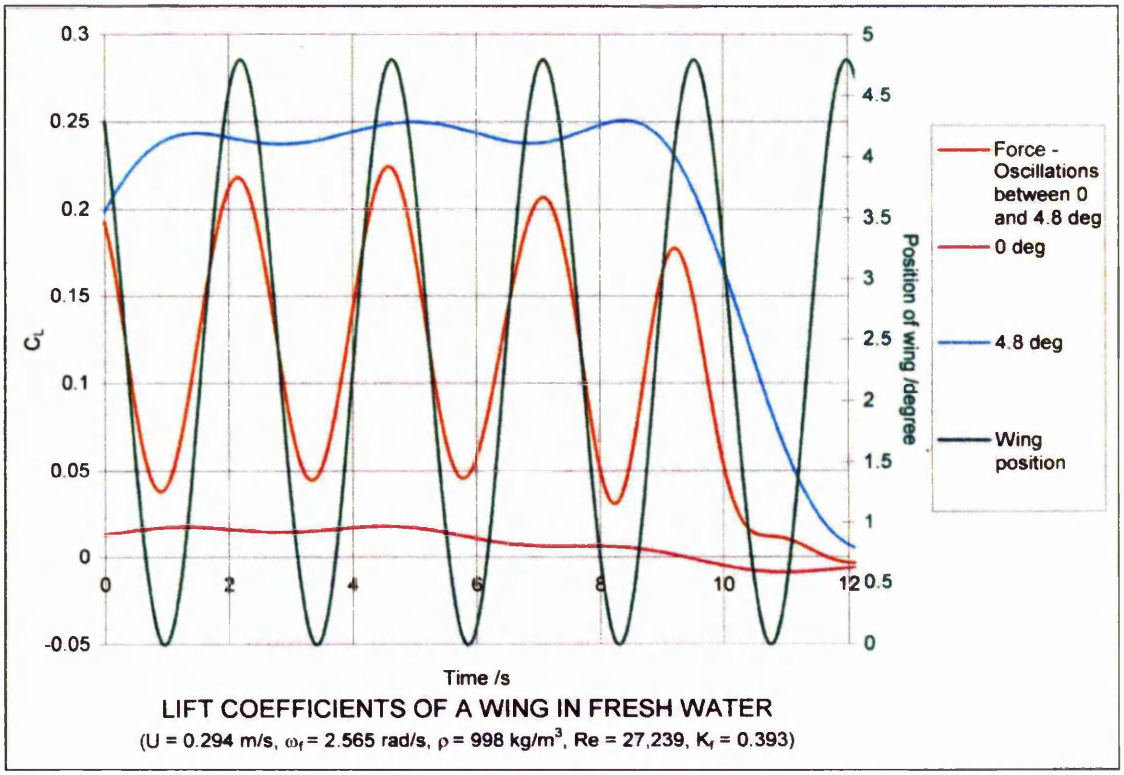

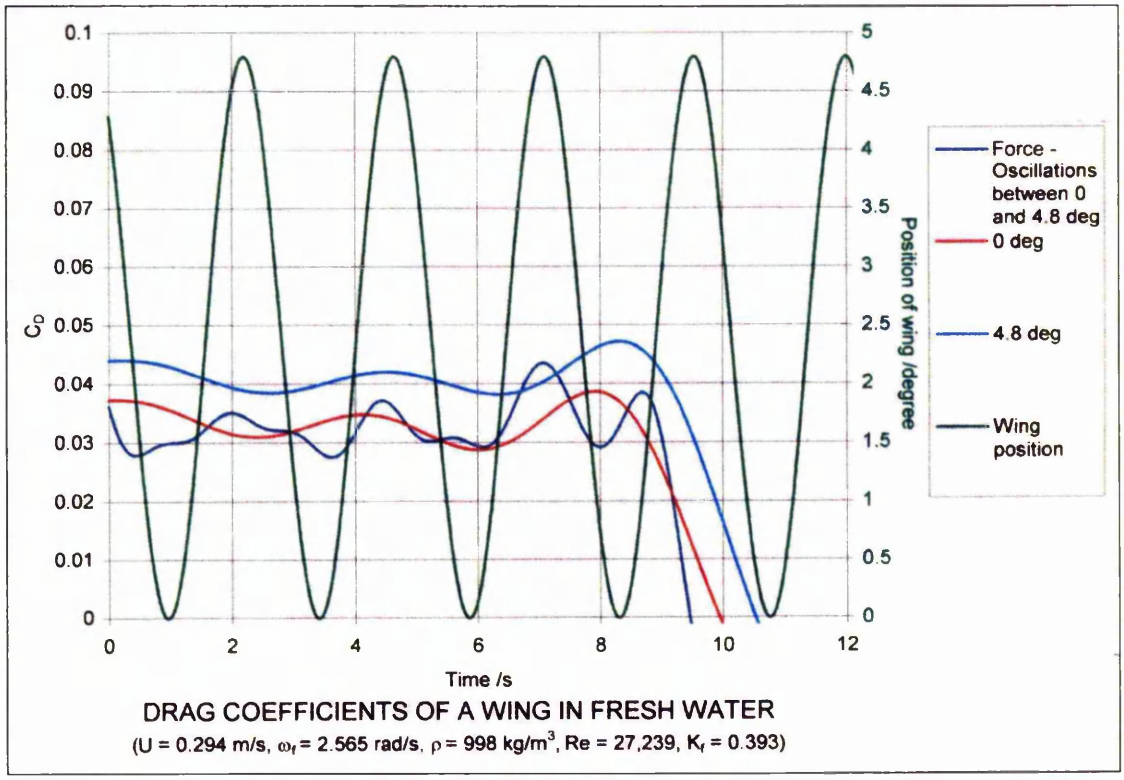

Figures 4.55a & b The lift and drag coefficients of a NACA 0012 wing with aspect ratio 1.7 moving in a constant density fluid.

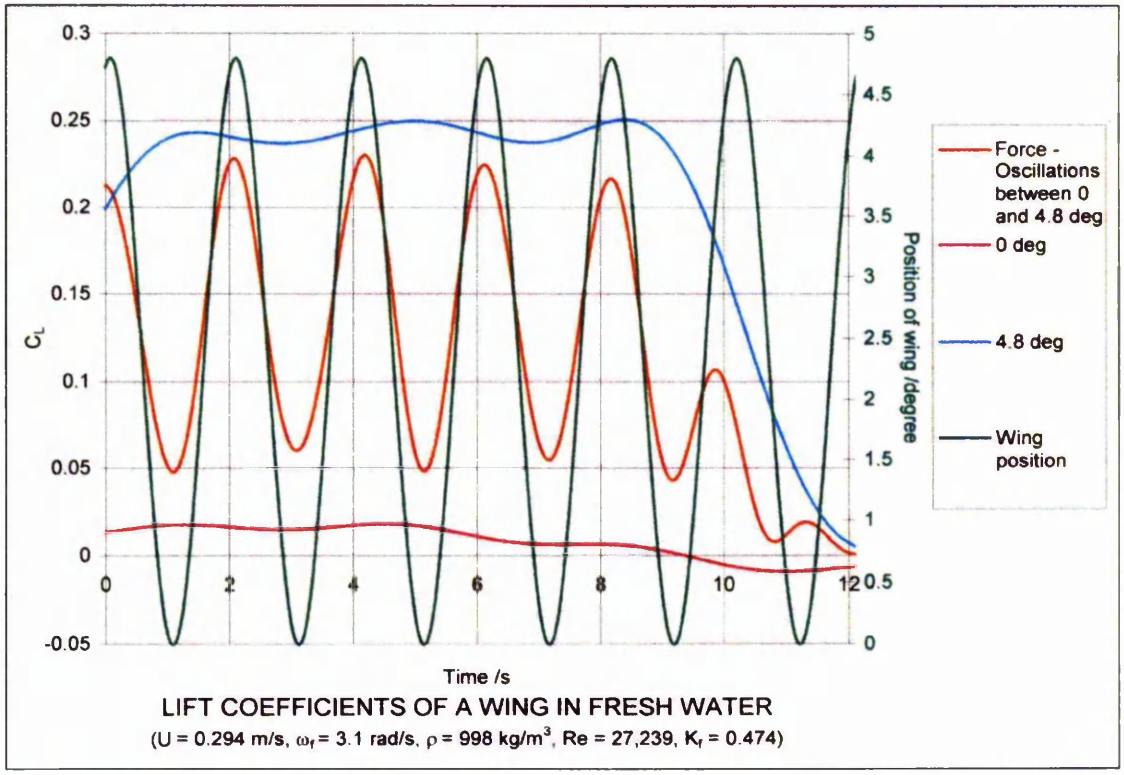

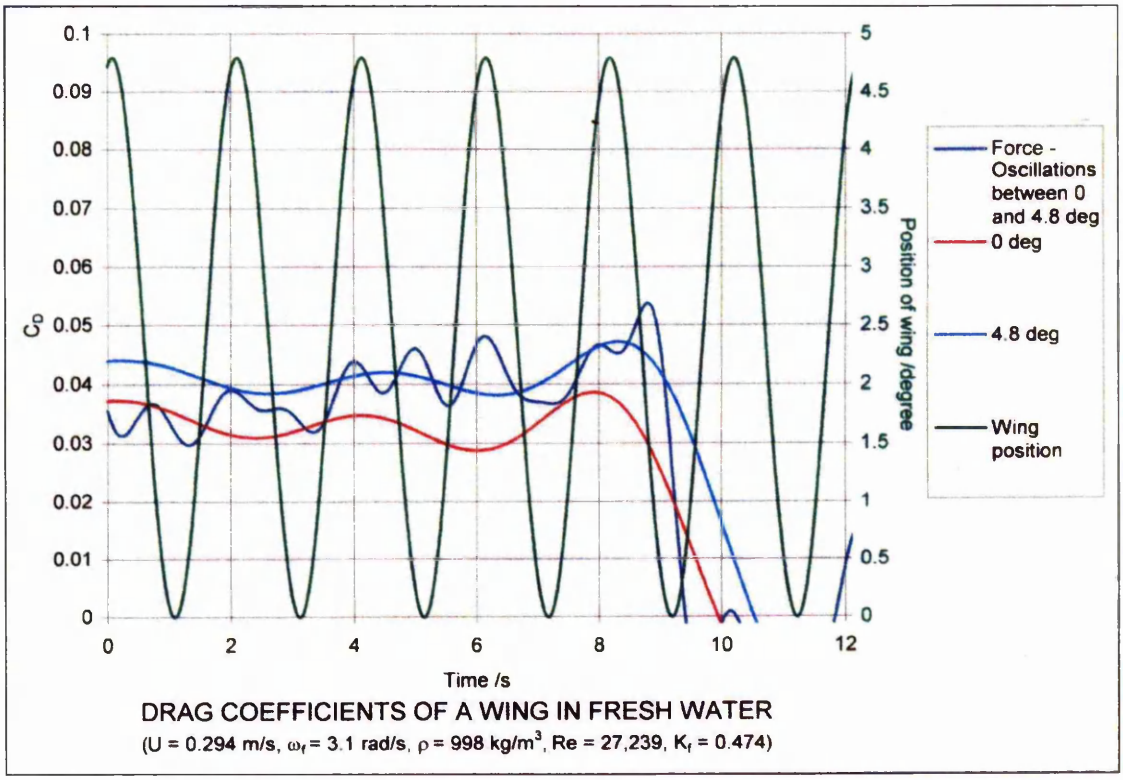

Figures 4.56a & b The lift and drag coefficients of a NACA 0012 wing with aspect ratio 1.7 moving in a constant density fluid.

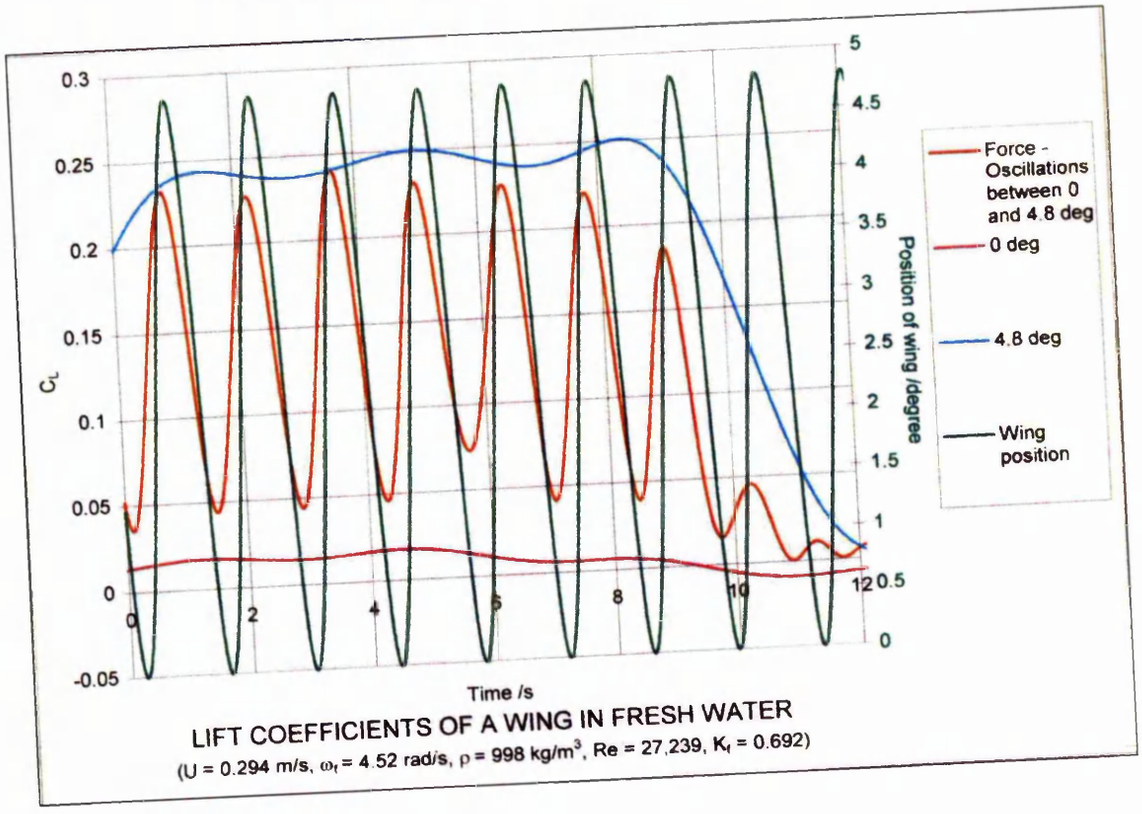

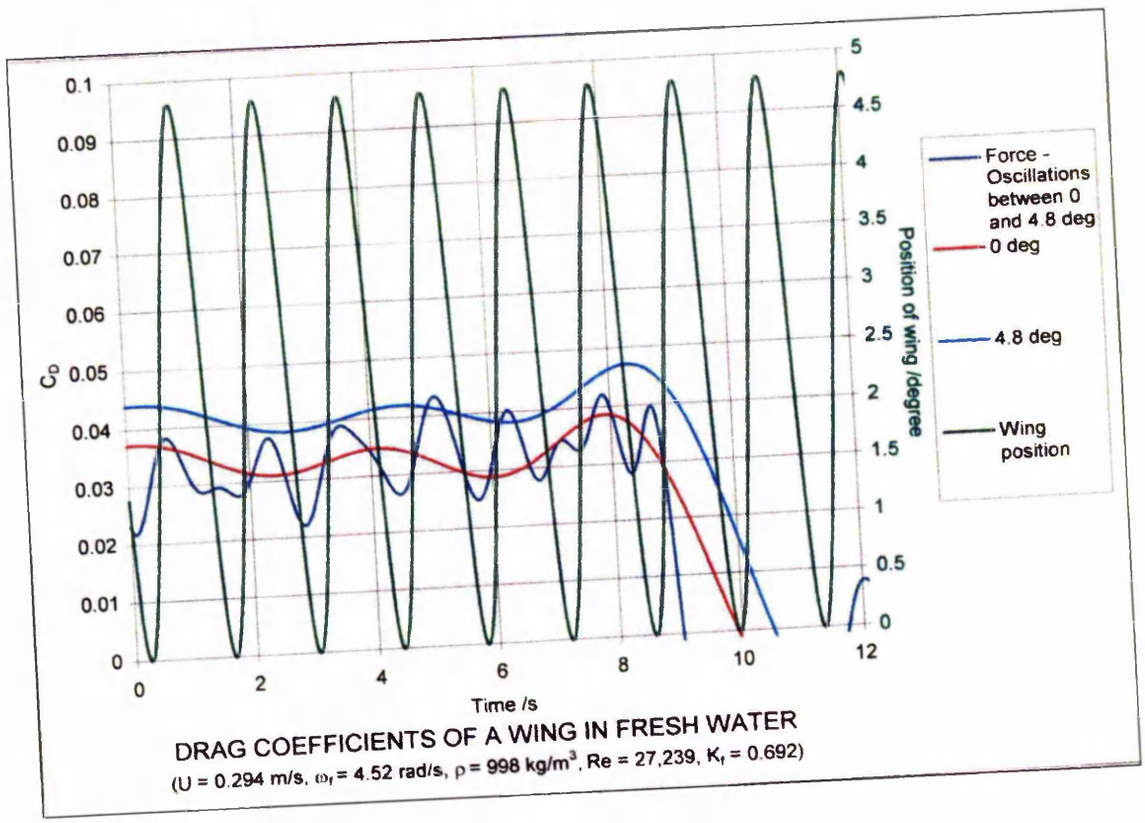

Figures 4.57a & b The lift and drag coefficients of a NACA 0012 wing with aspect ratio 1.7 moving in a constant density fluid.

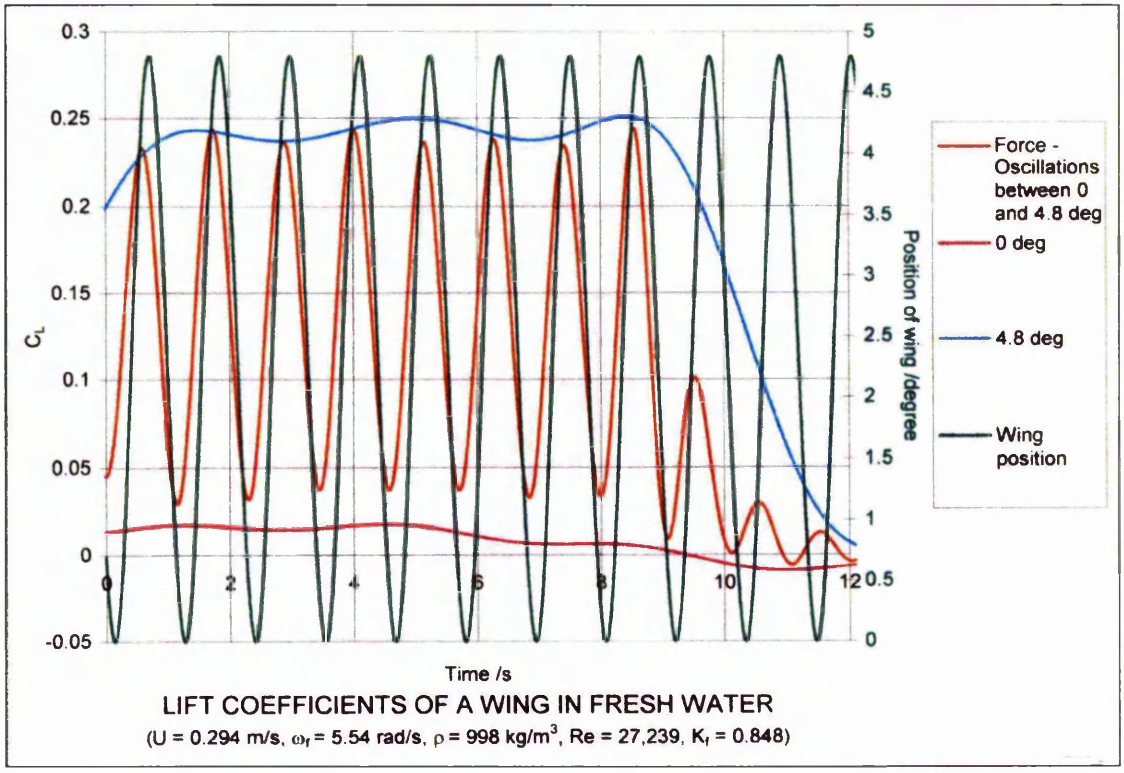

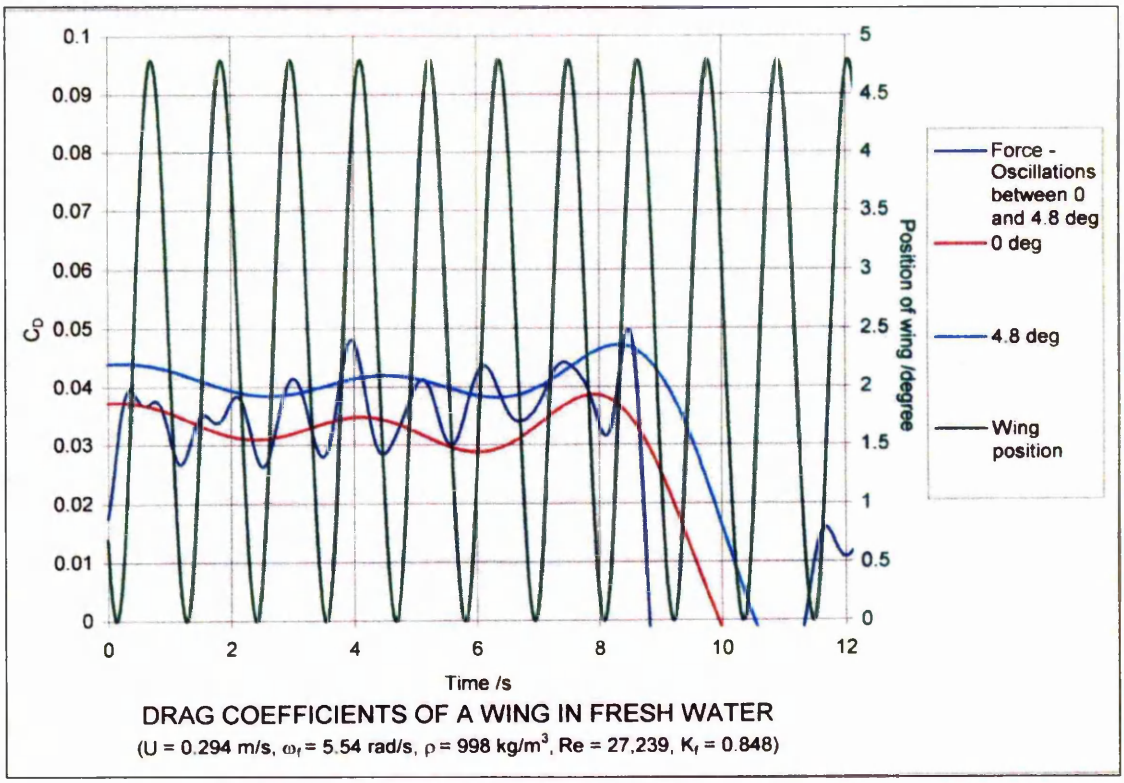

Figures 4.58a & b The lift and drag coefficients of a NACA 0012 wing with aspect ratio 1.7 moving in a constant density fluid.

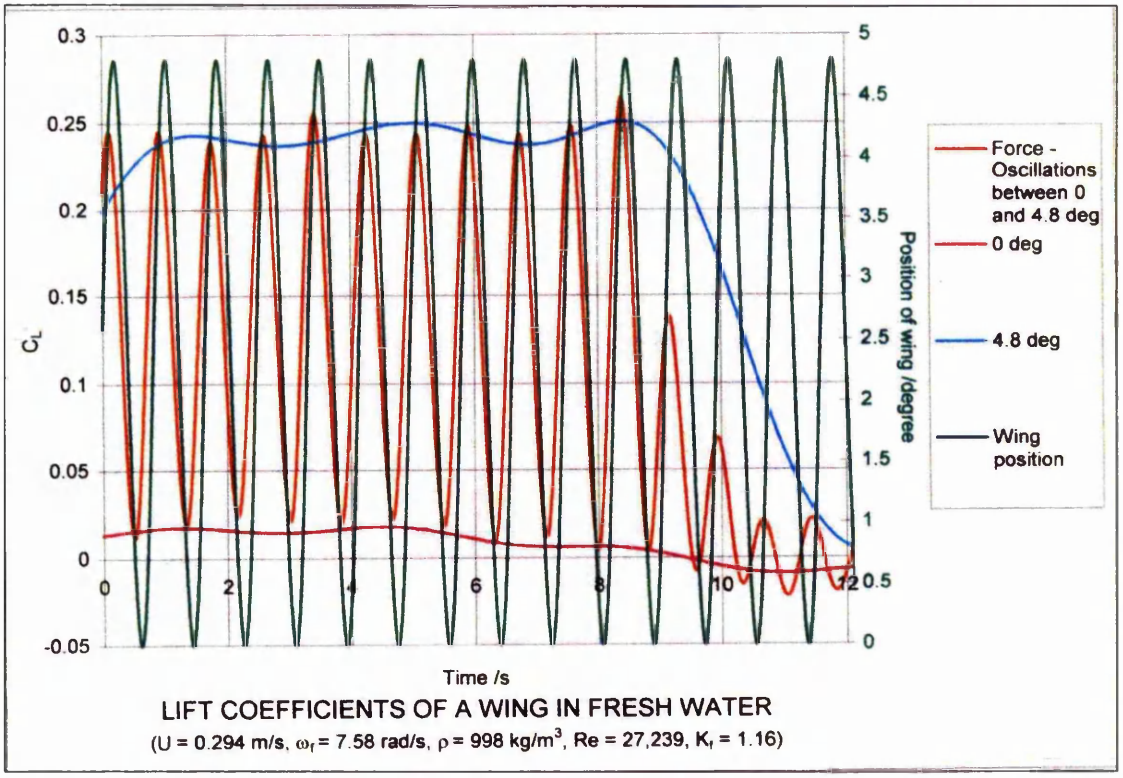

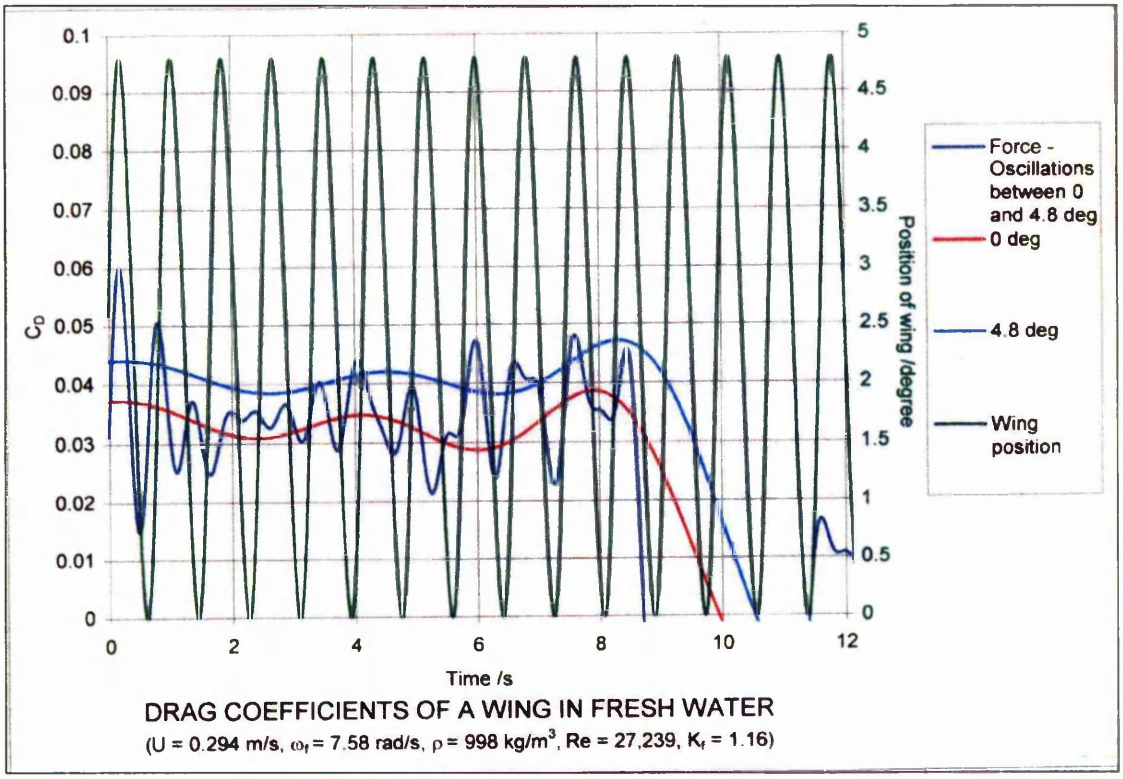

Figures 4.59a & b The lift and drag coefficients of a NACA 0012 wing with aspect ratio 1.7 moving in a constant density fluid.

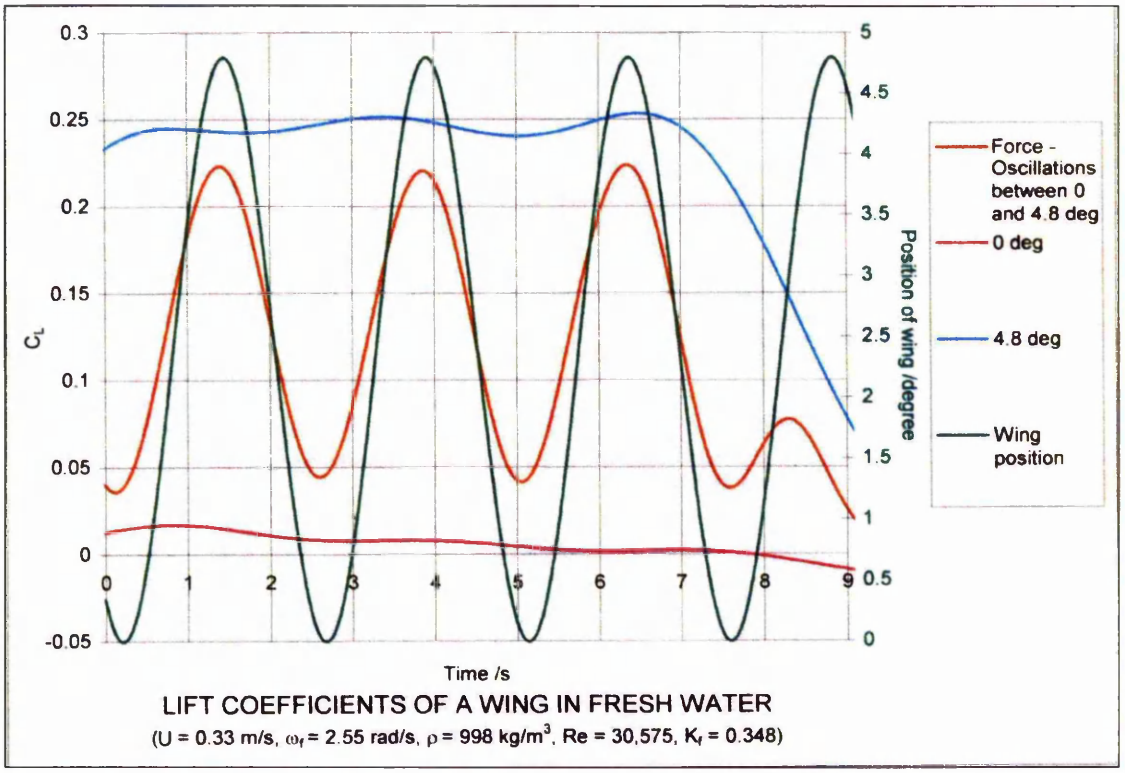

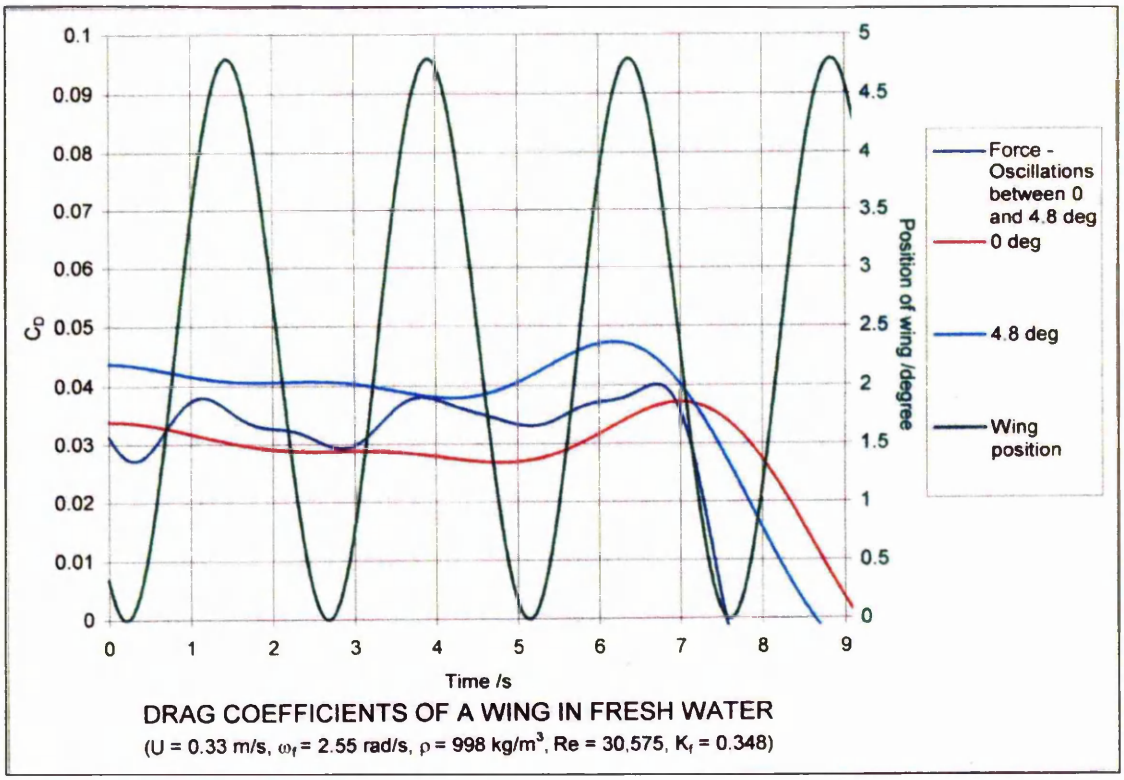

Figures 4.60a & b The lift and drag coefficients of a NACA 0012 wing with aspect ratio 1.7 moving in a constant density fluid.

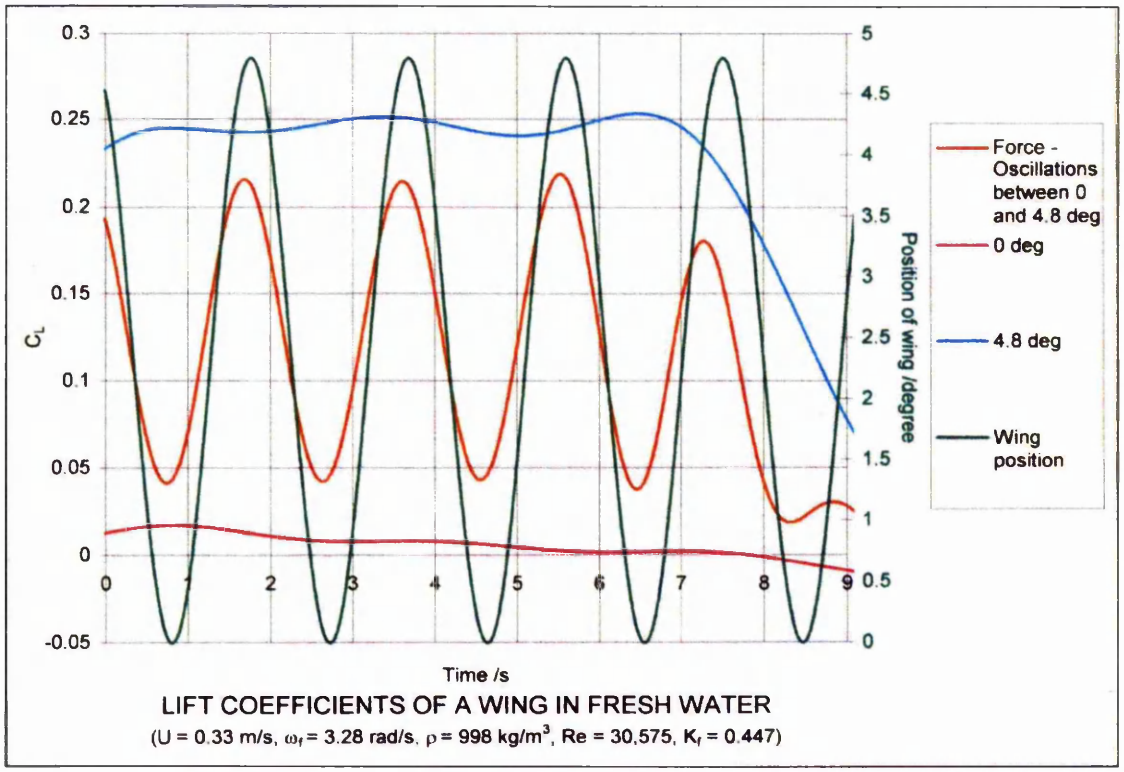

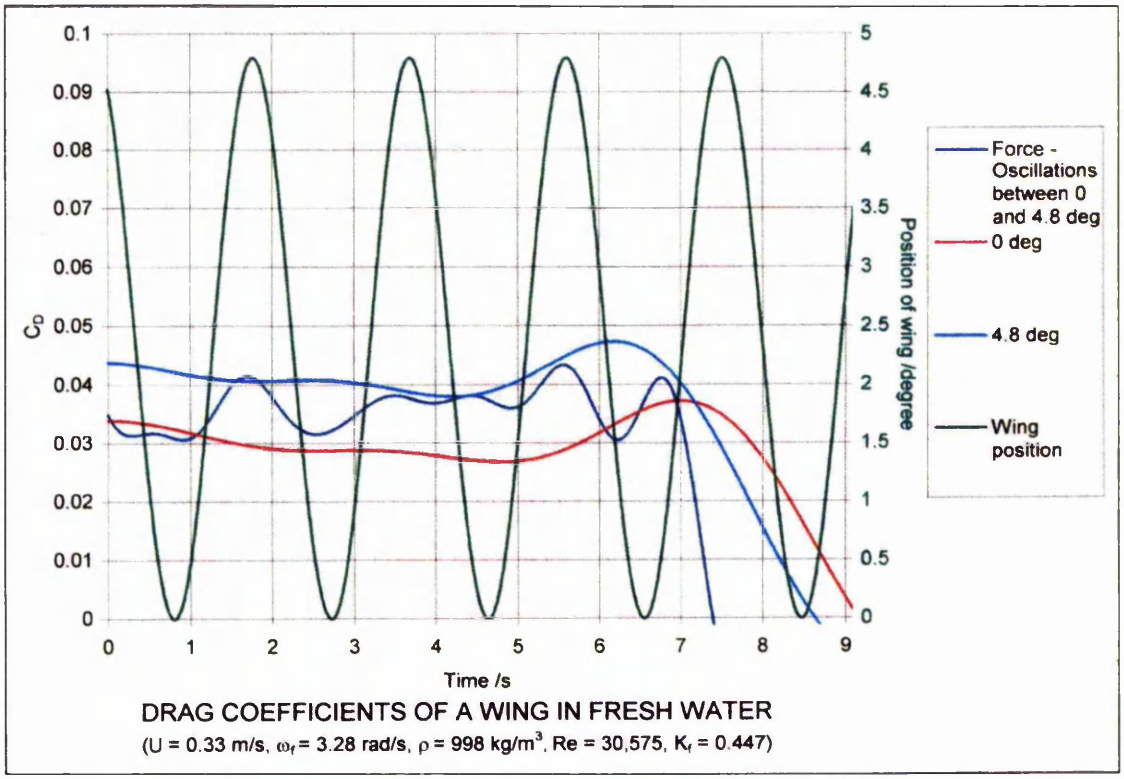

Figures 4.61a & b The lift and drag coefficients of a NACA 0012 wing with aspect ratio 1.7 moving in a constant density fluid.

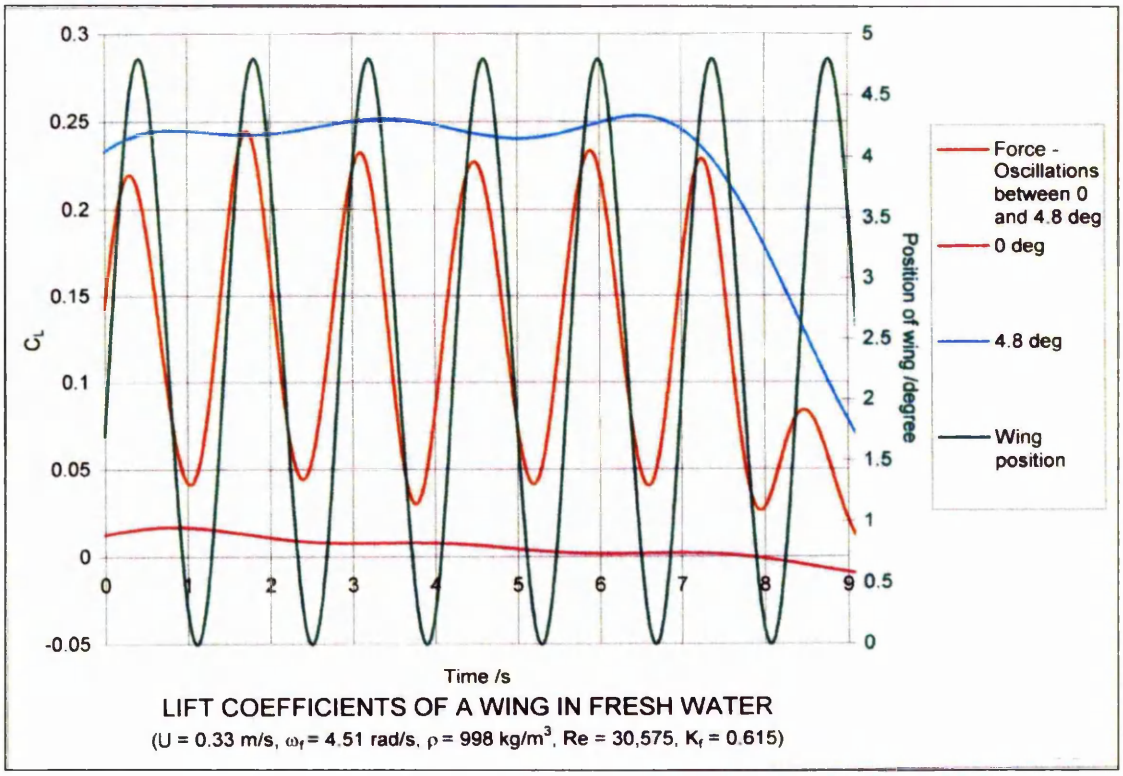

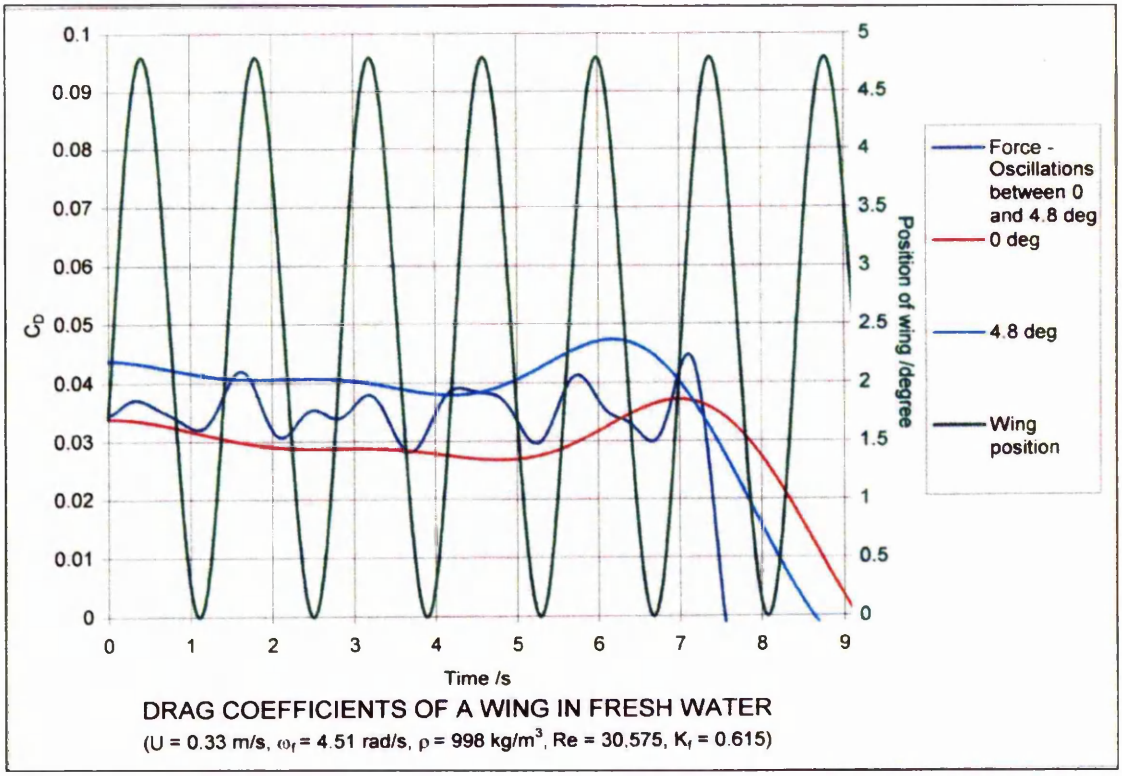

Figures 4.62a & b The lift and drag coefficients of a NACA 0012 wing with aspect ratio 1.7 moving in a constant density fluid.

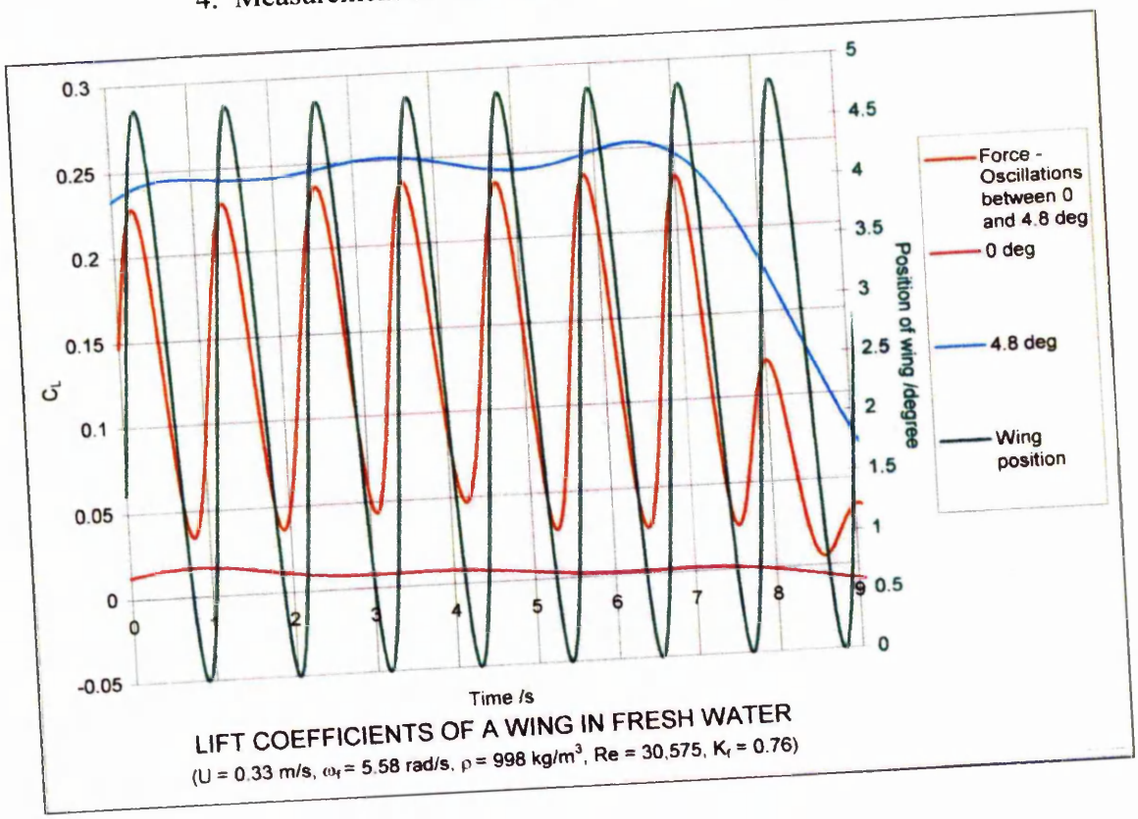

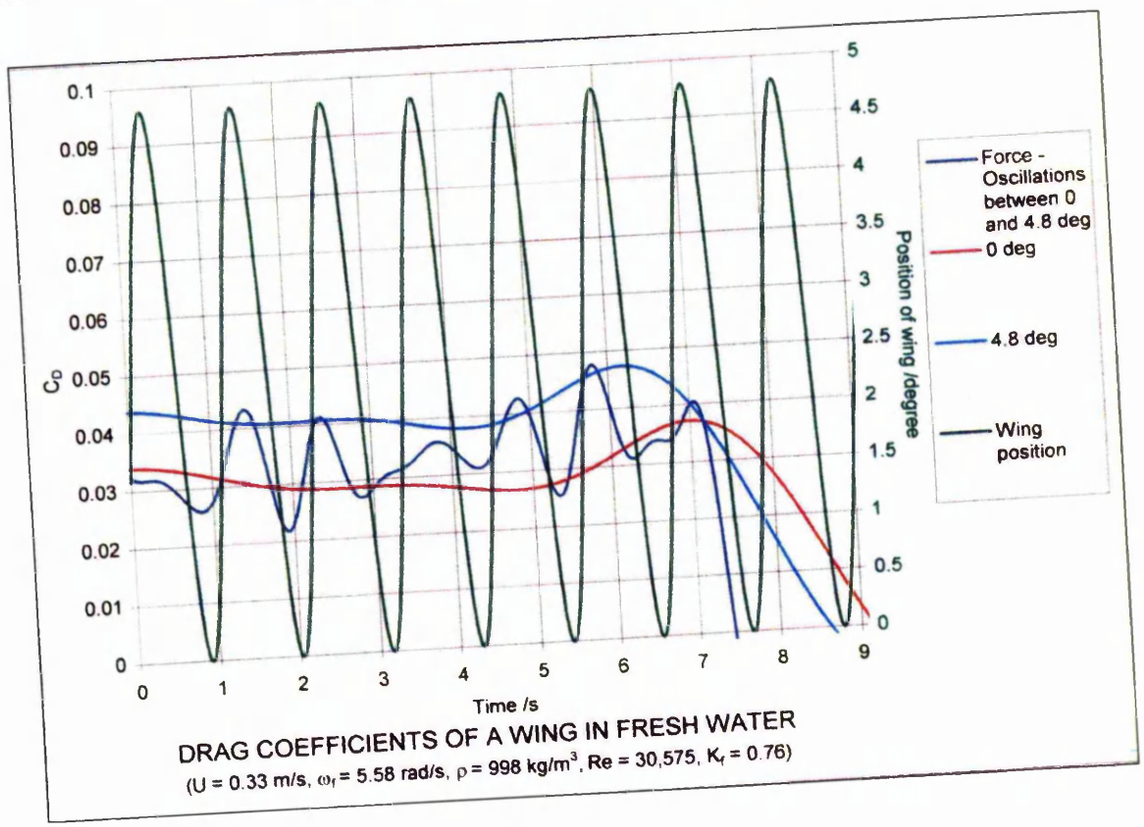

Figures 4.63a & b The lift and drag coefficients of a NACA 0012 wing with aspect ratio 1.7 moving in a constant density fluid.

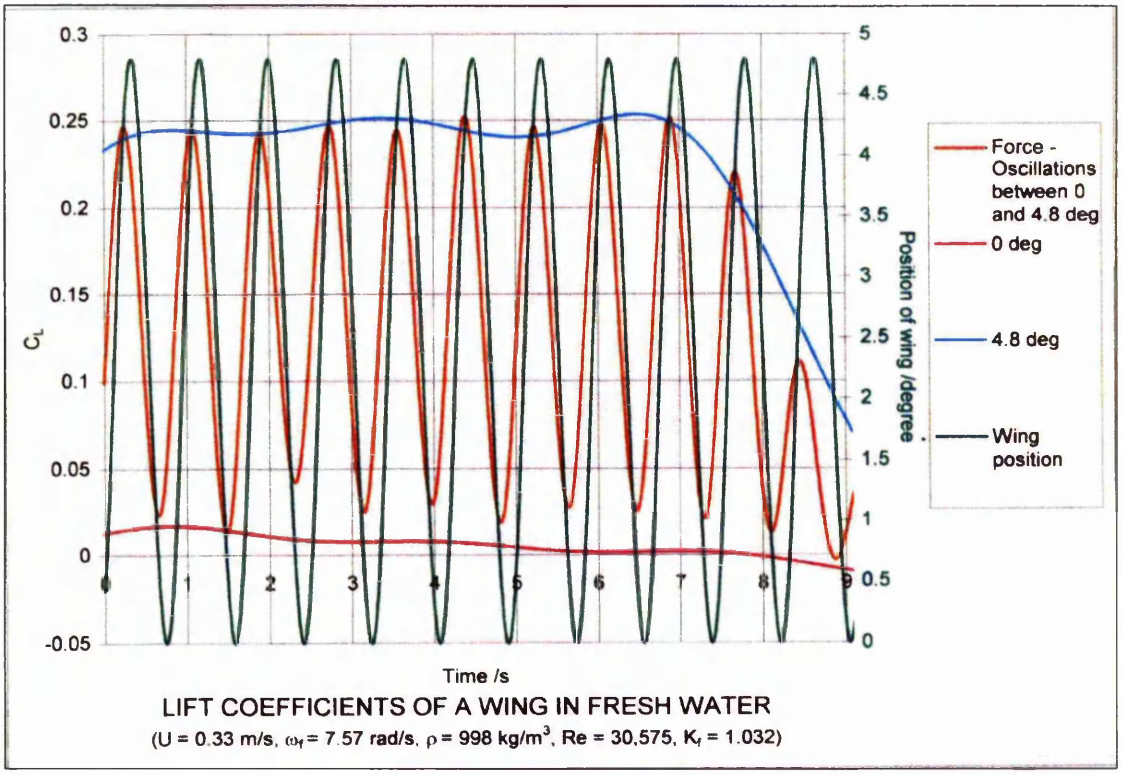

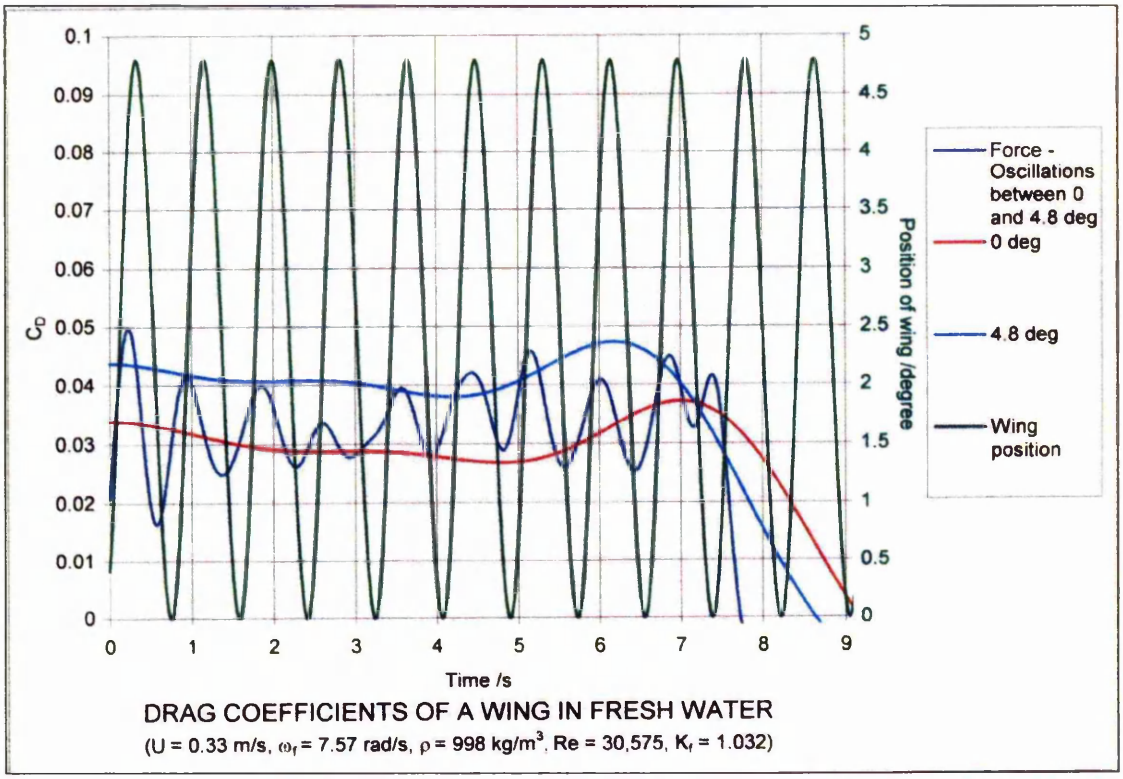

Figures 4.64a & b The lift and drag coefficients of a NACA 0012 wing with aspect ratio 1.7 moving in a constant density fluid.

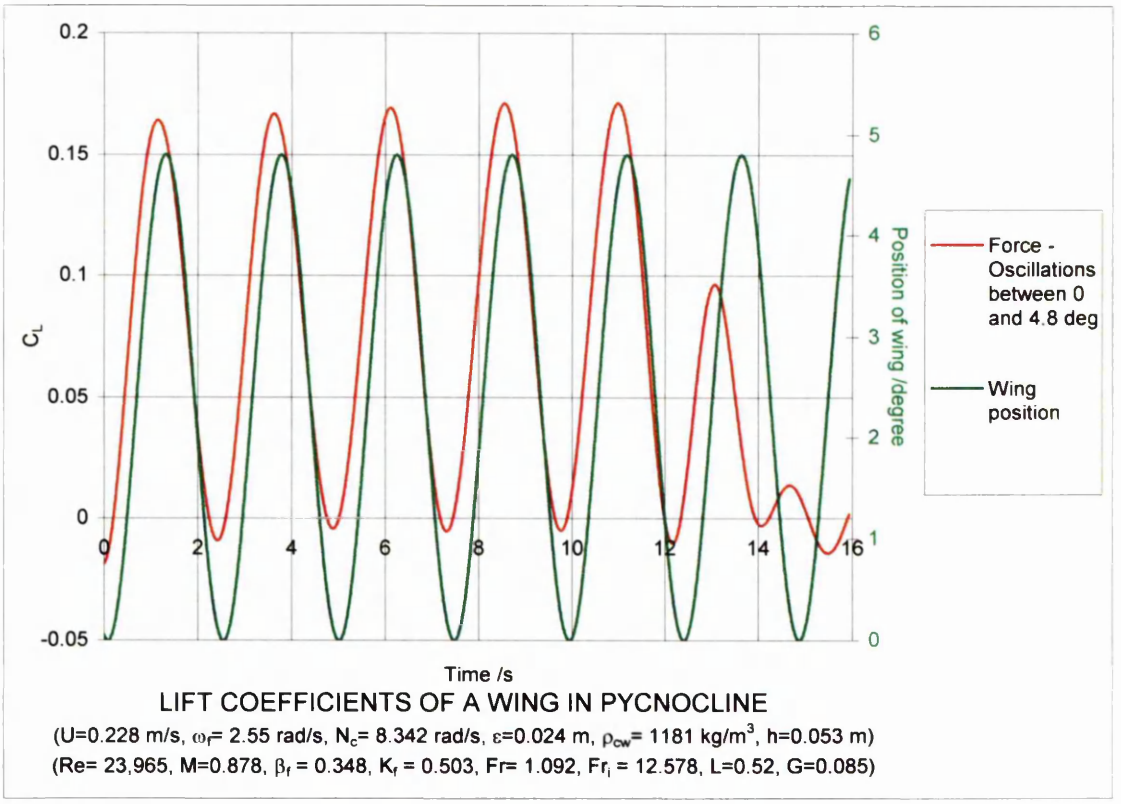

LIFT COEFFICIENTS OF A WING IN PYCNOCLINE

(U=0.228 m/s, ω_f= 2.55 rad/s, N_c= 8.342 rad/s, ε=0.024 m, ρ_{cw}= 1181 kg/m^3, h=0.053 m)

(Re= 23,965, M=0.878, β_f = 0.348, K_f = 0.503, Fr= 1.092, Fr_i = 12.578, L=0.52, G=0.085)

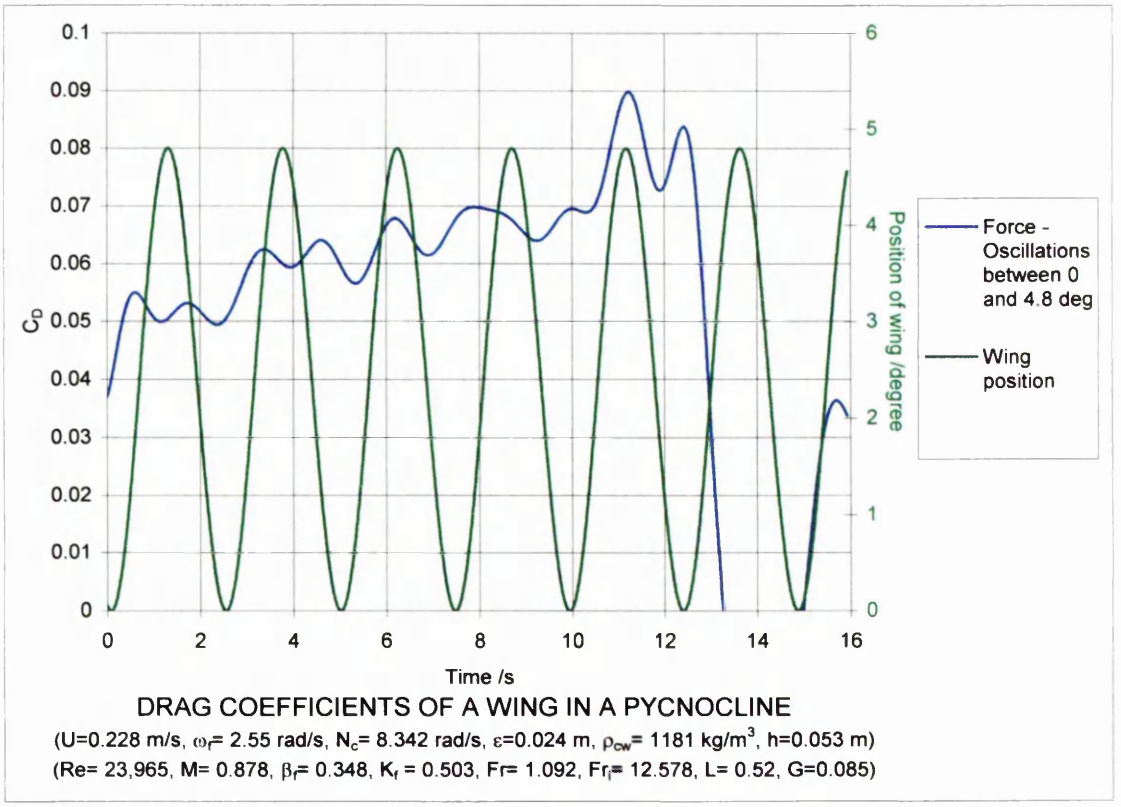

DRAG COEFFICIENTS OF A WING IN A PYCNOCLINE

(U=0.228 m/s, ω_f= 2.55 rad/s, N_c= 8.342 rad/s, ε=0.024 m, ρ_{cw}= 1181 kg/m^3, h=0.053 m)

(Re= 23,965, M= 0.878, β_f= 0.348, K_f = 0.503, Fr= 1.092, Fr_i= 12.578, L= 0.52, G=0.085)

Figures 4.65a & b The lift and drag coefficients of a NACA 0012 wing with aspect ratio 1.7 moving in a pycnocline. The density distribution of the pycnocline is shown in figure 4.99.

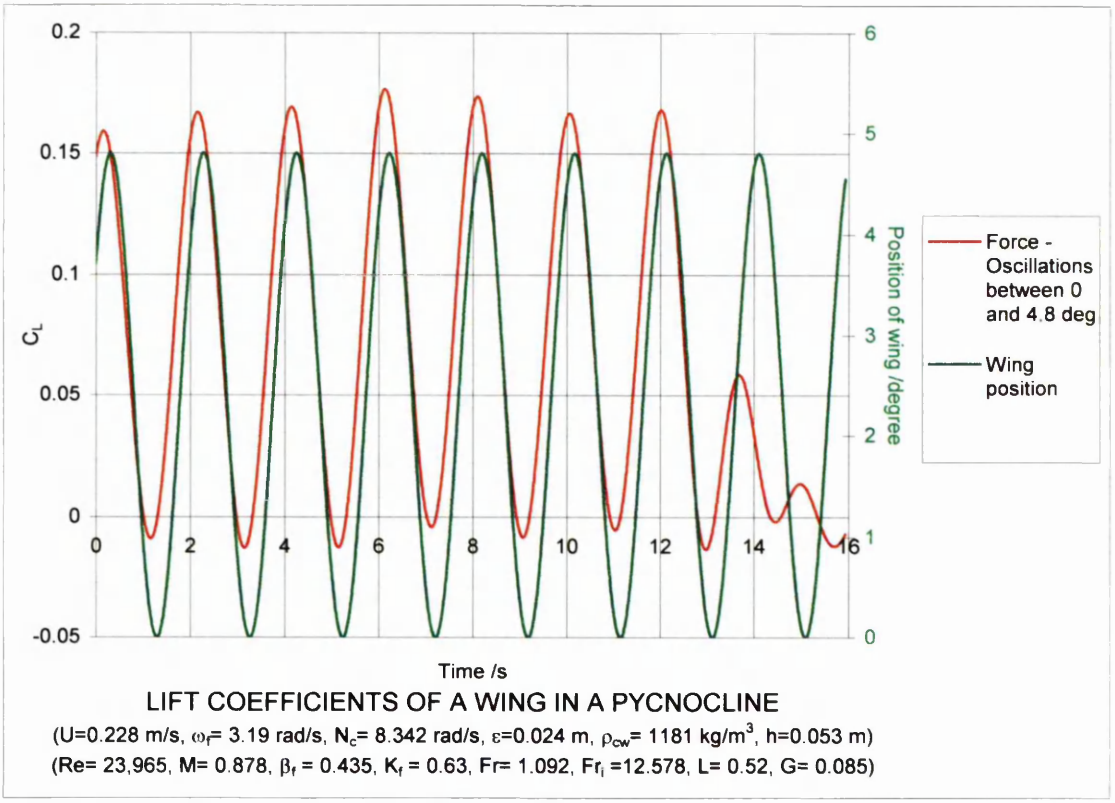

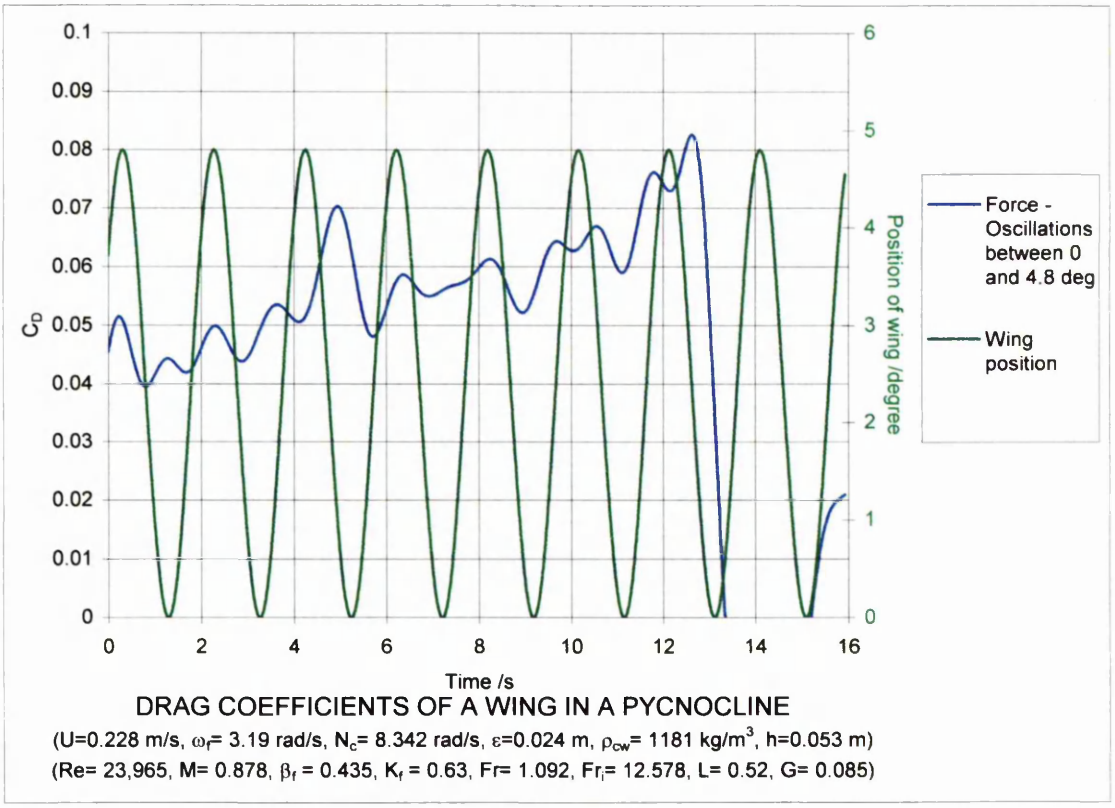

Figures 4.66a & b The lift and drag coefficients of a NACA 0012 wing with aspect ratio 1.7 moving in a pycnocline. The density distribution of the pycnocline is shown in figure 4.99.

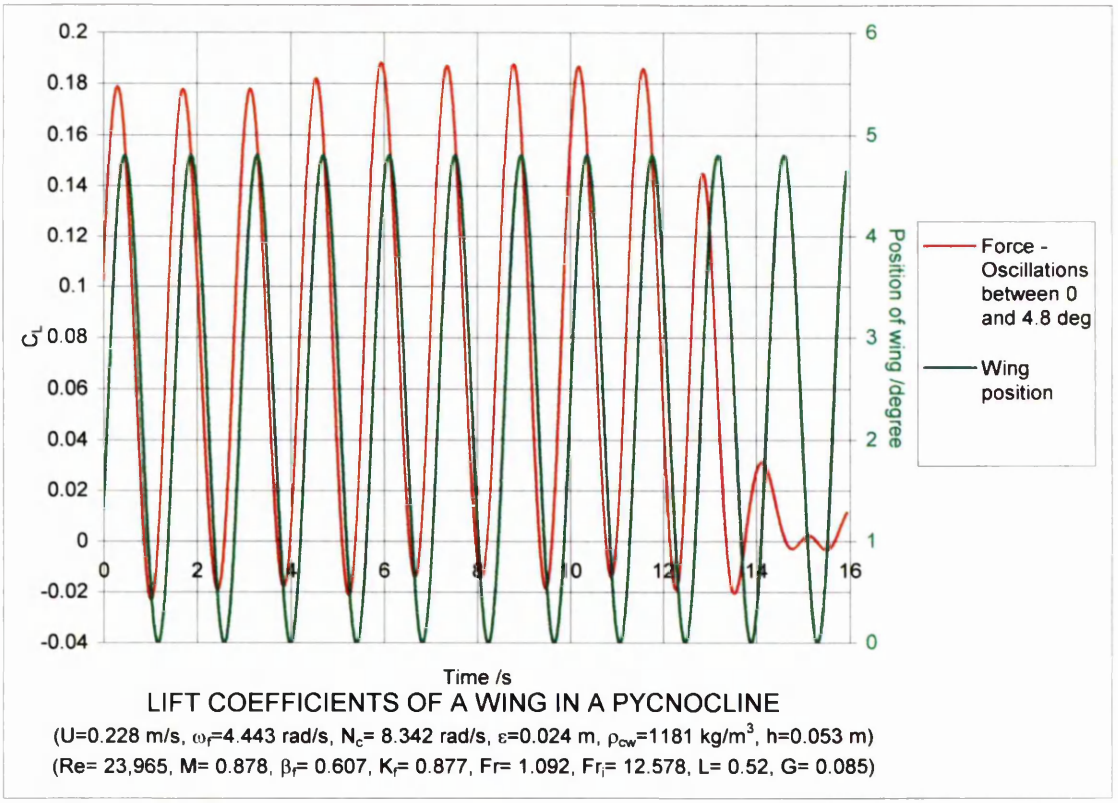

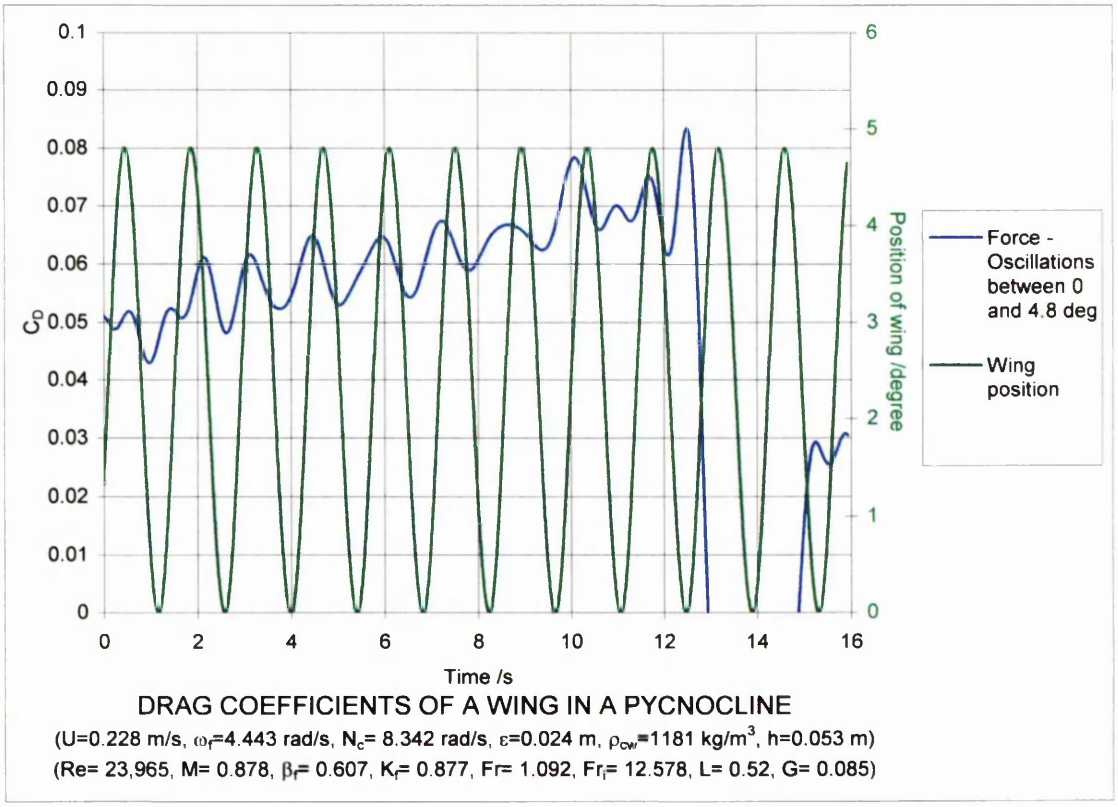

Figures 4.67a & b The lift and drag coefficients of a NACA 0012 wing with aspect ratio 1.7 moving in a pycnocline. The density distribution of the pycnocline is shown in figure 4.99.

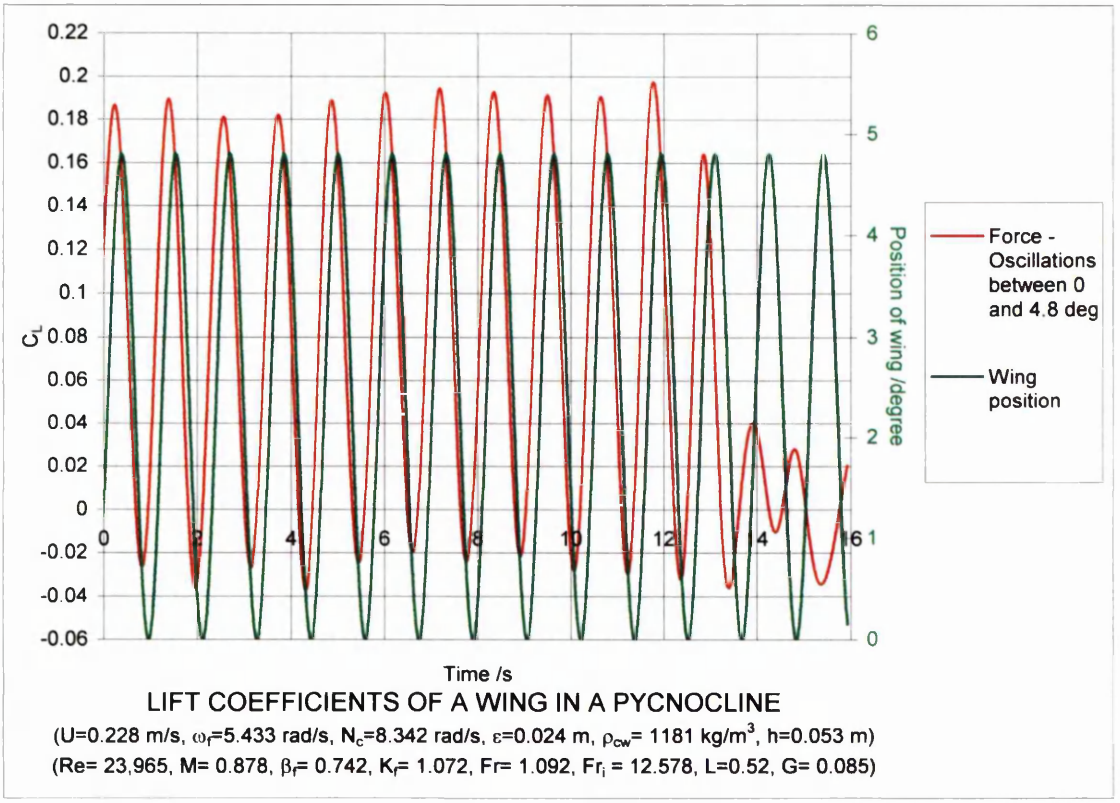

LIFT COEFFICIENTS OF A WING IN A PYCNOCLINE

(U=0.228 m/s, ω_f=5.433 rad/s, N_c=8.342 rad/s, ε=0.024 m, ρ_{cw}= 1181 kg/m^3, h=0.053 m)

(Re= 23,965, M= 0.878, β_f= 0.742, K_f= 1.072, Fr= 1.092, Fr_i = 12.578, L=0.52, G= 0.085)

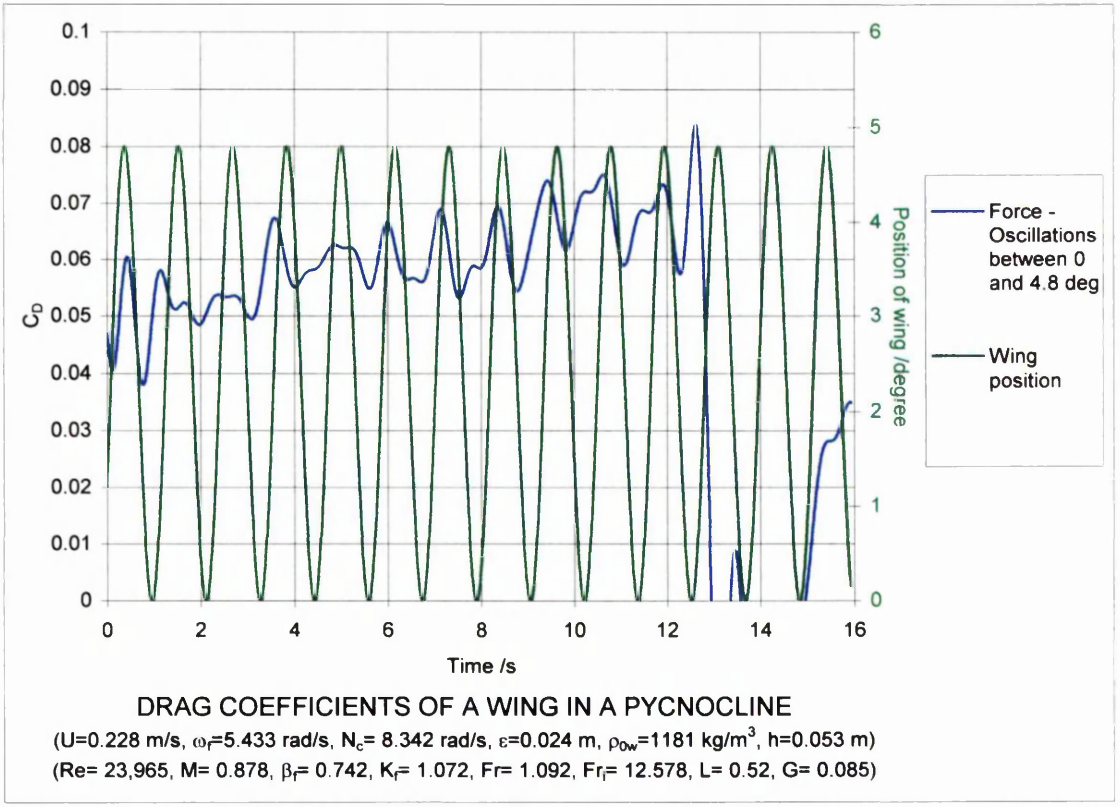

DRAG COEFFICIENTS OF A WING IN A PYCNOCLINE

(U=0.228 m/s, ω_f=5.433 rad/s, N_c= 8.342 rad/s, ε=0.024 m, ρ_{ow}=1181 kg/m^3, h=0.053 m)

(Re= 23,965, M= 0.878, β_f= 0.742, K_f= 1.072, Fr= 1.092, Fr_i= 12.578, L= 0.52, G= 0.085)

Figures 4.68a & b The lift and drag coefficients of a NACA 0012 wing with aspect ratio 1.7 moving in a pycnocline. The density distribution of the pycnocline is shown in figure 4.99.

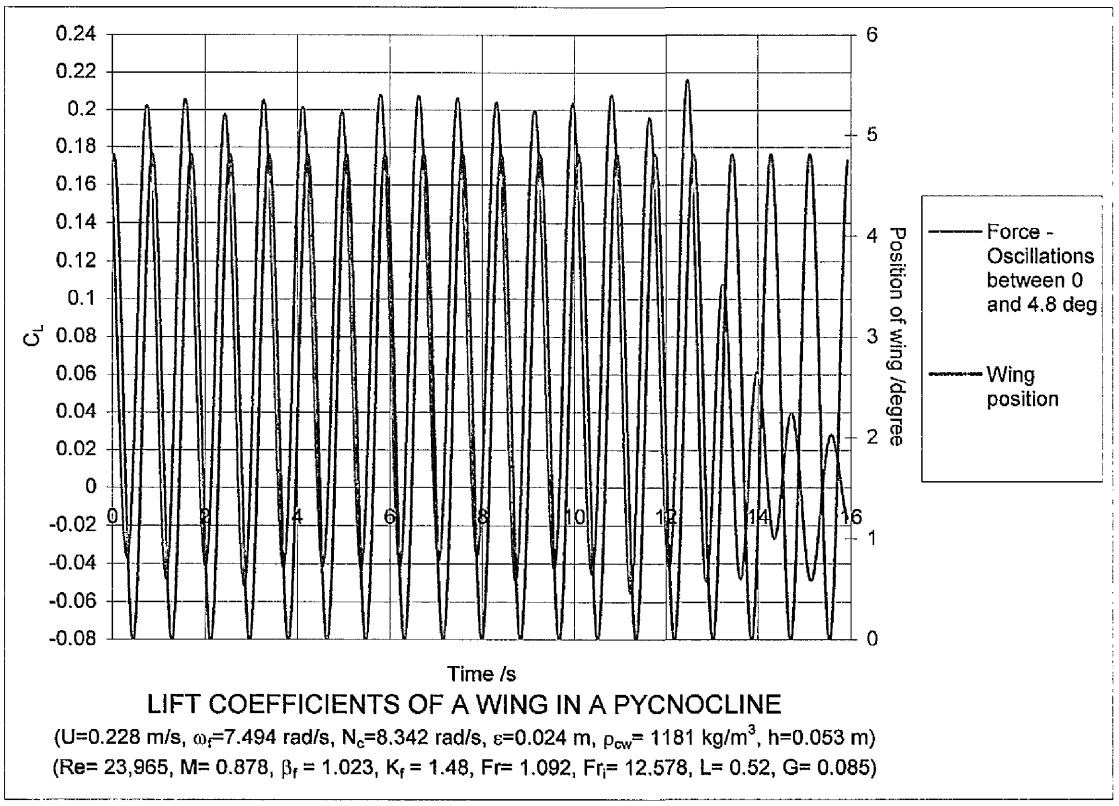

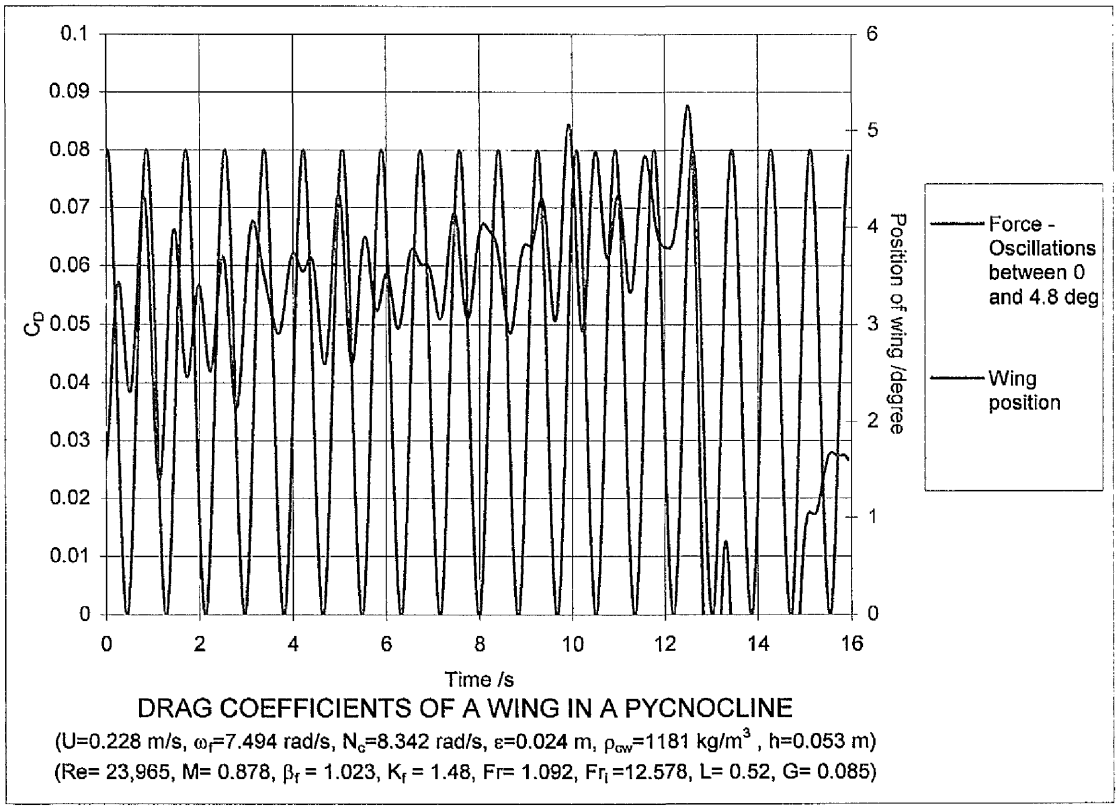

Figures 4.69a & b The lift and drag coefficients of a NACA 0012 wing with aspect ratio 1.7 moving in a pycnocline. The density distribution of the pycnocline is shown in figure 4.99.

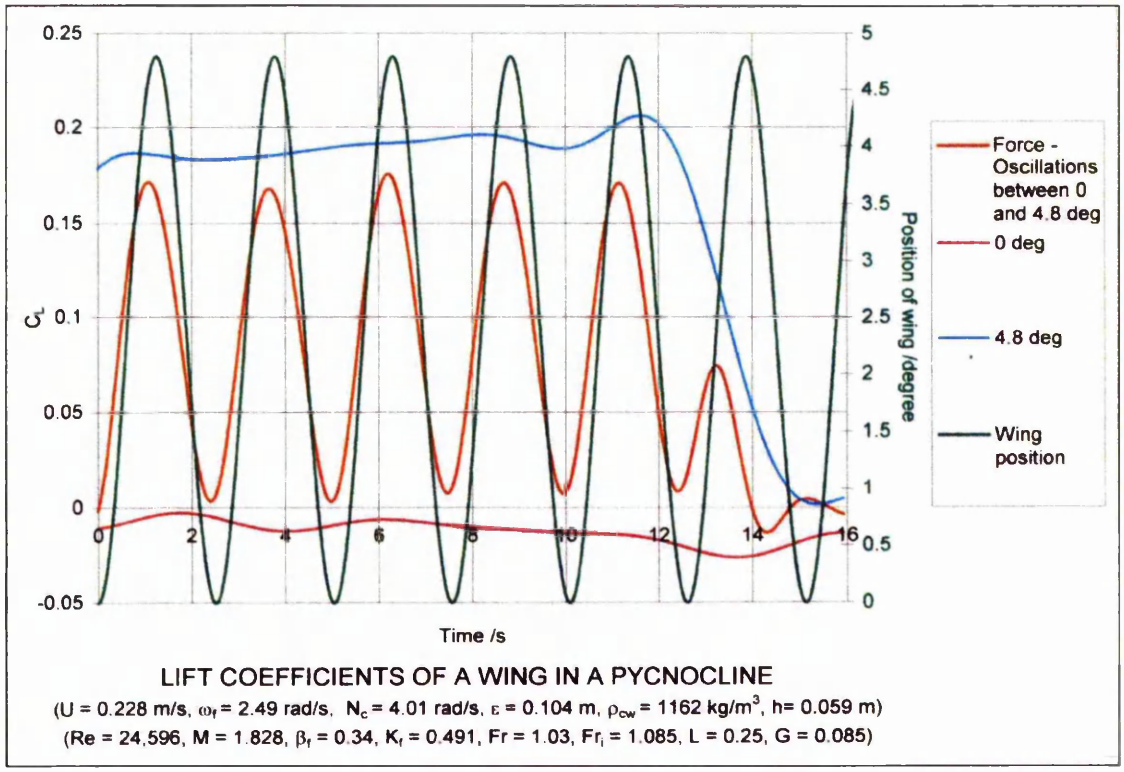

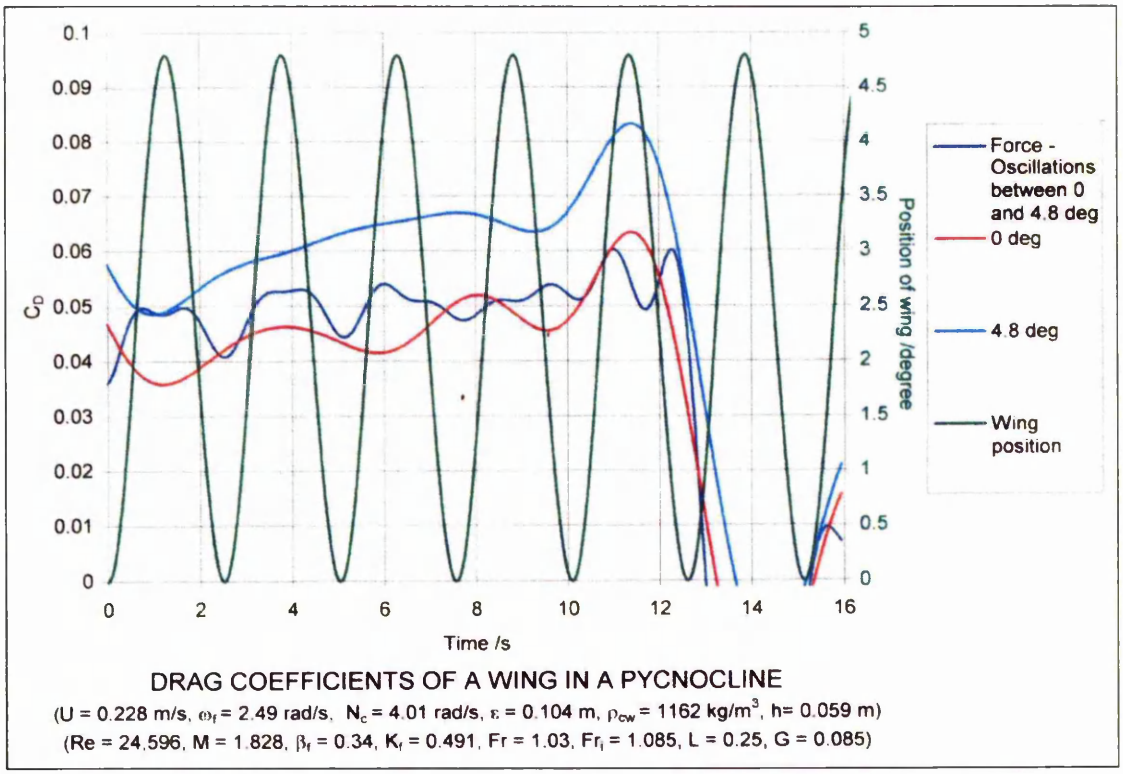

Figures 4.70a & b The lift and drag coefficients of a NACA 0012 wing with aspect ratio 1.7 moving in a pycnocline. The density distribution of the pycnocline is shown in figure 4.100.

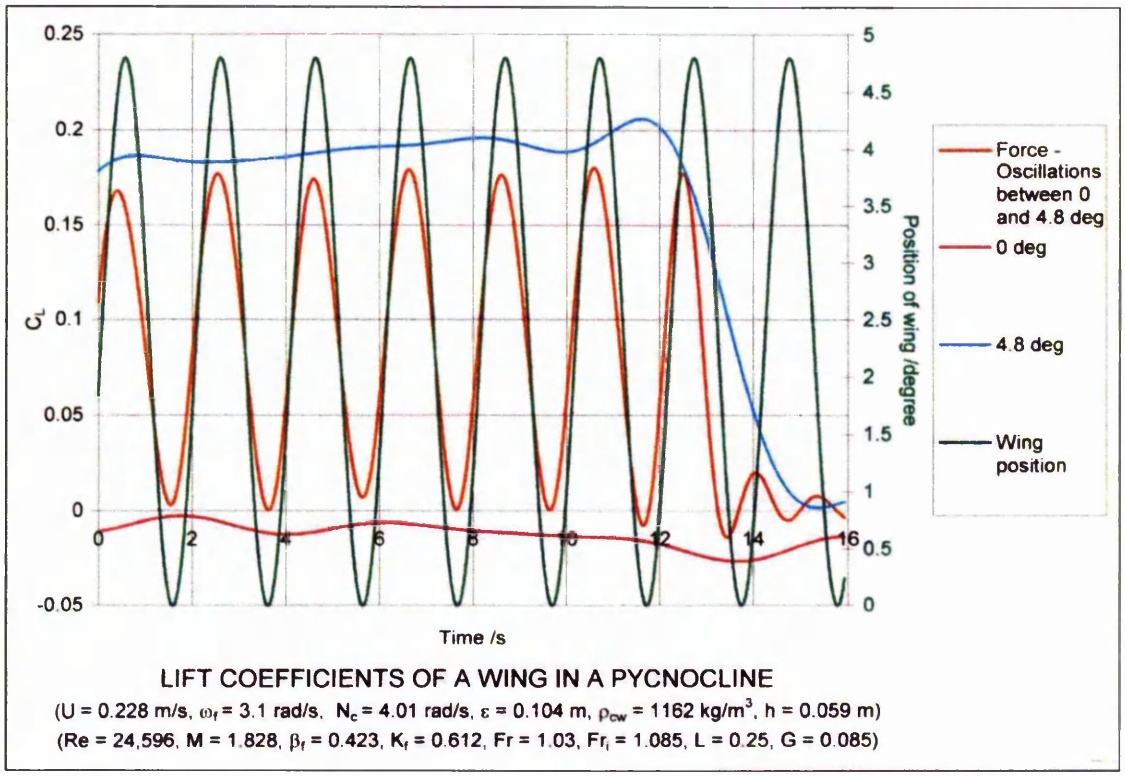

LIFT COEFFICIENTS OF A WING IN A PYCNOCLINE

(U = 0.228 m/s, ω_f = 3.1 rad/s, N_c = 4.01 rad/s, ε = 0.104 m, ρ_{cw} = 1162 kg/m^3, h = 0.059 m)
(Re = 24,596, M = 1.828, β_f = 0.423, K_f = 0.612, Fr = 1.03, Fr_i = 1.085, L = 0.25, G = 0.085)

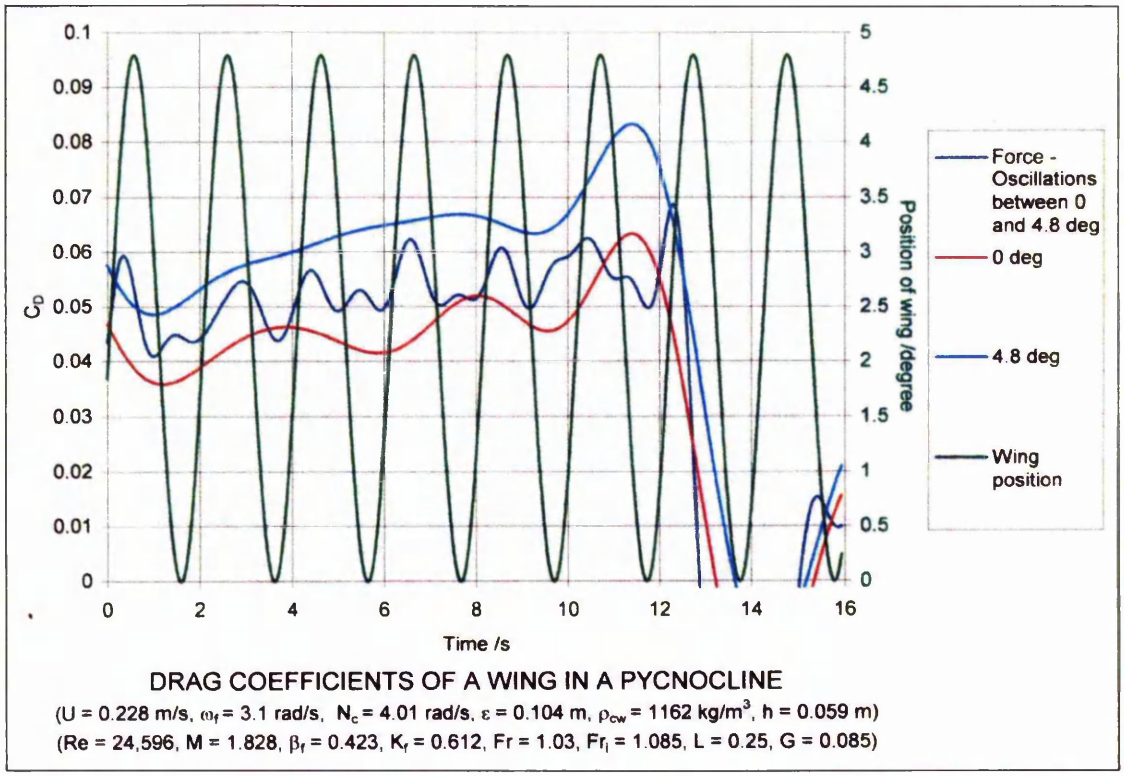

DRAG COEFFICIENTS OF A WING IN A PYCNOCLINE

(U = 0.228 m/s, ω_f = 3.1 rad/s, N_c = 4.01 rad/s, ε = 0.104 m, ρ_{cw} = 1162 kg/m^3, h = 0.059 m)
(Re = 24,596, M = 1.828, β_f = 0.423, K_f = 0.612, Fr = 1.03, Fr_i = 1.085, L = 0.25, G = 0.085)

Figures 4.71a & b The lift and drag coefficients of a NACA 0012 wing with aspect ratio 1.7 moving in a pycnocline. The density distribution of the pycnocline is shown in figure 4.100.

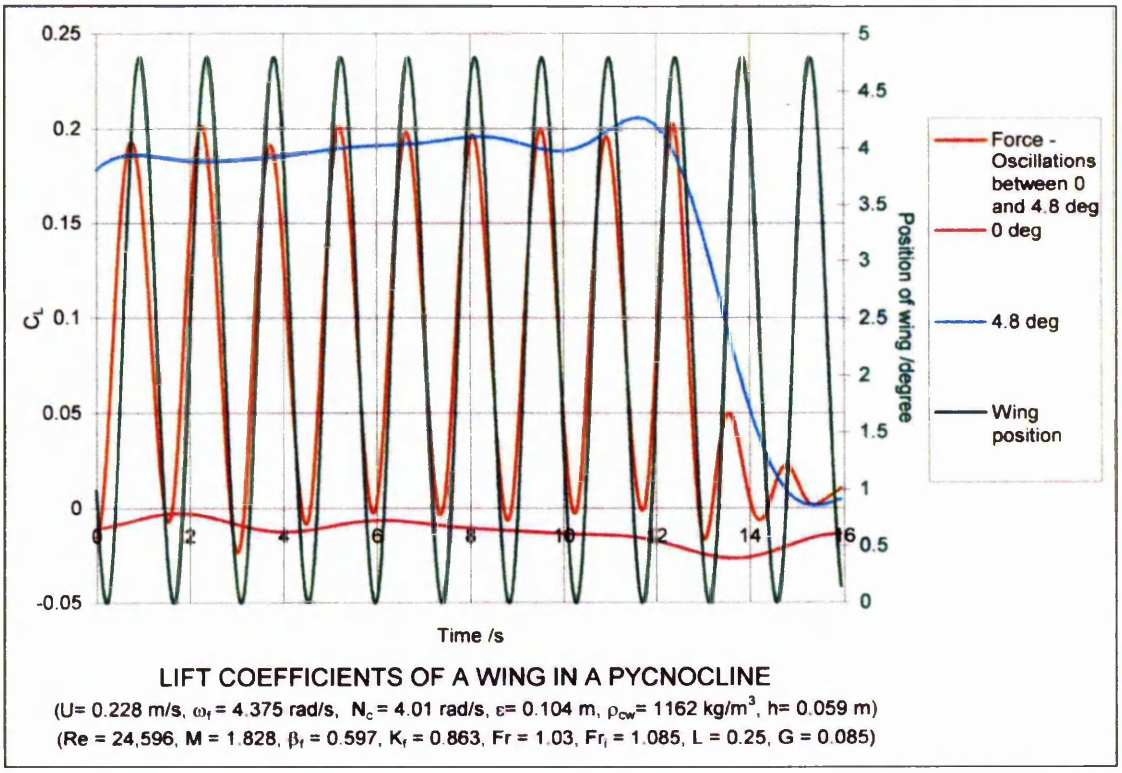

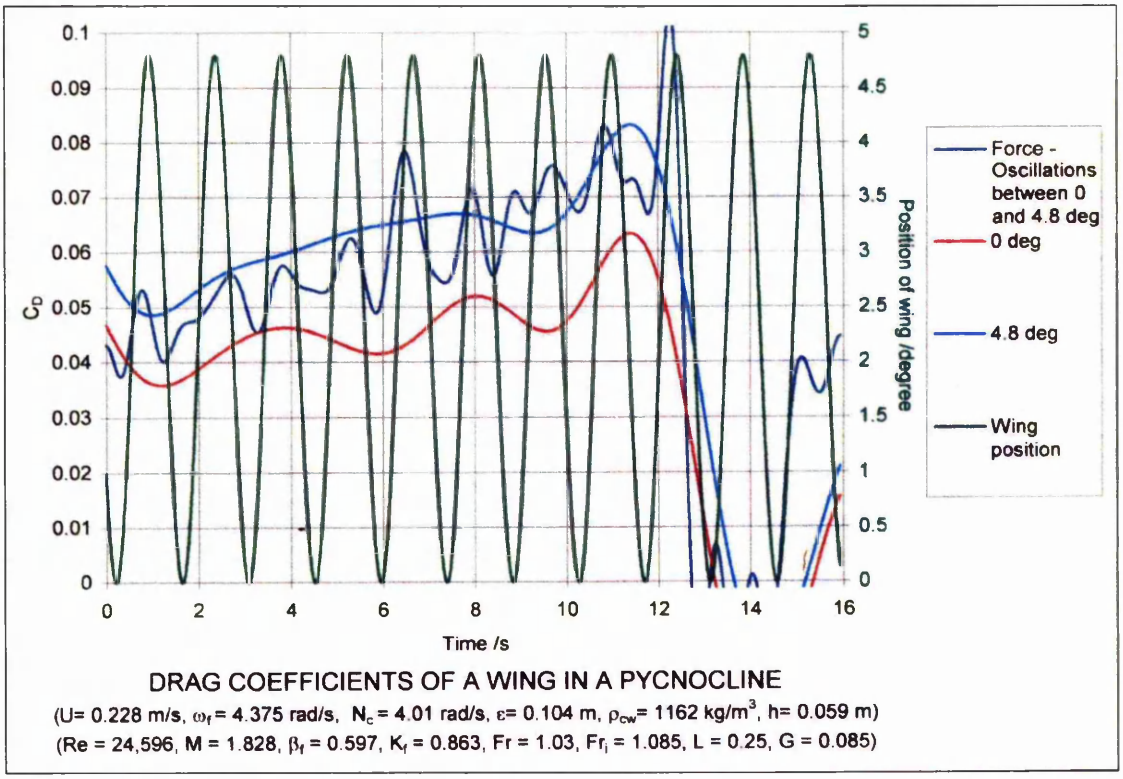

Figures 4.72a & b The lift and drag coefficients of a NACA 0012 wing with aspect ratio 1.7 moving in a pycnocline. The density distribution of the pycnocline is shown in figure 4.100.

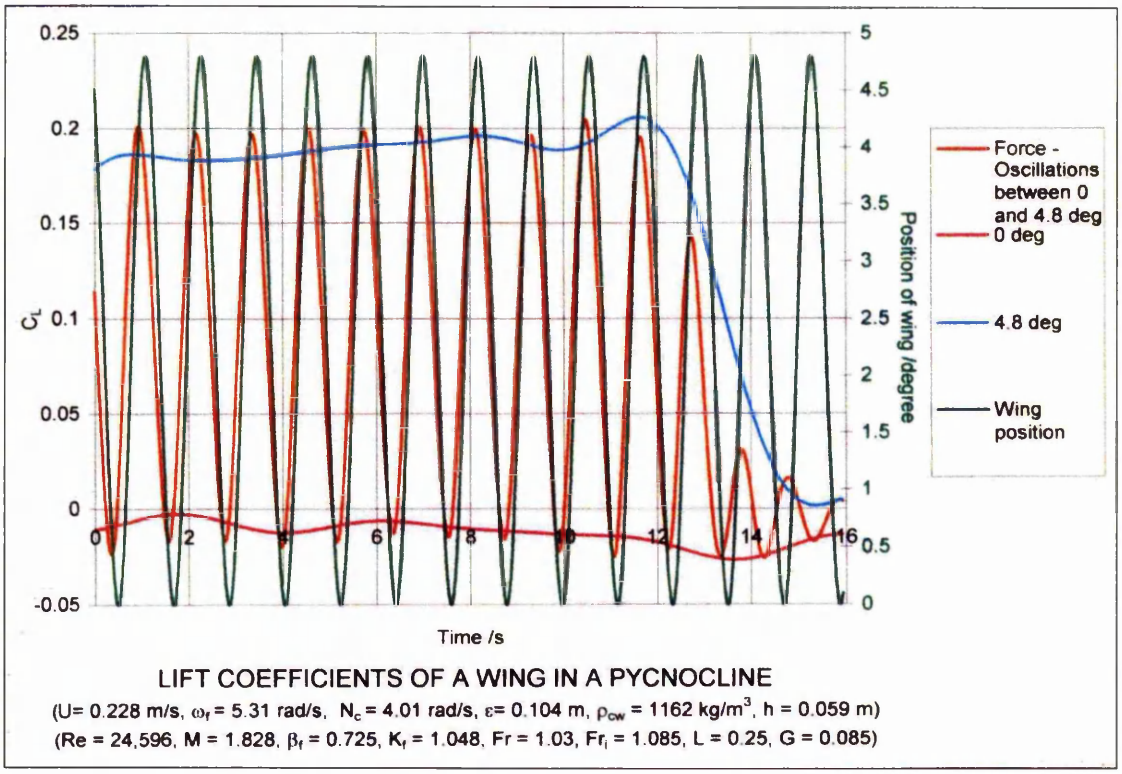

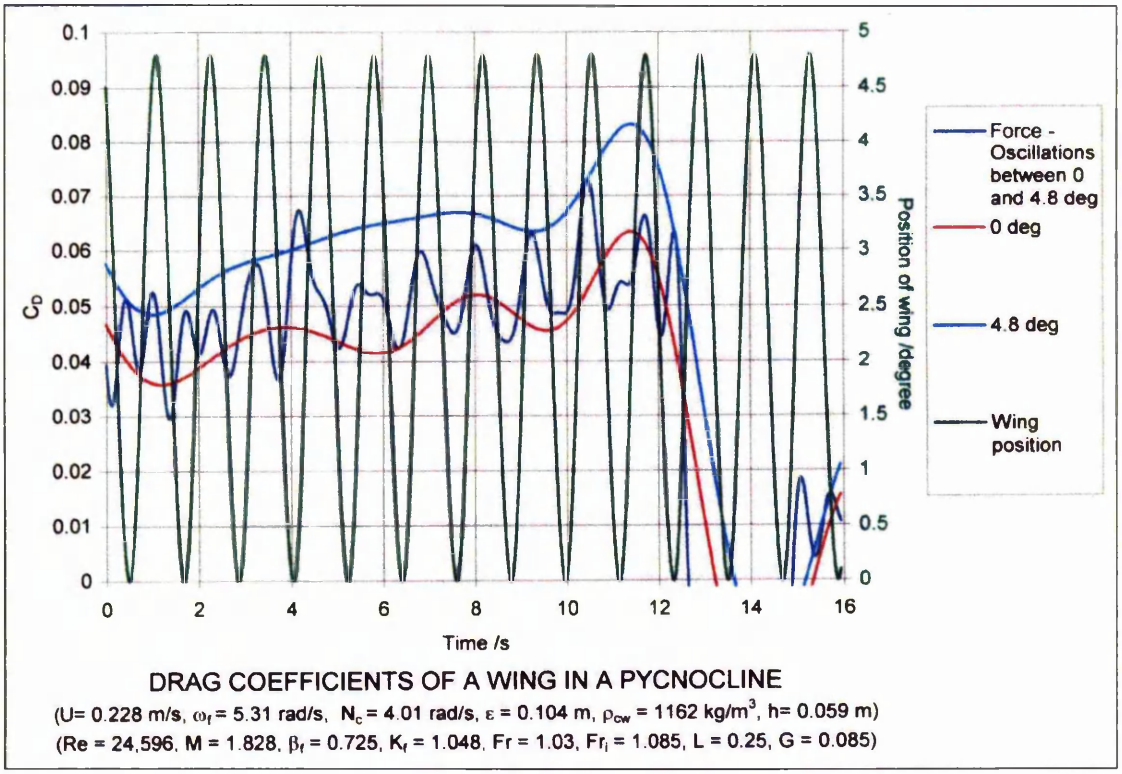

Figures 4.73a & b The lift and drag coefficients of a NACA 0012 wing with aspect ratio 1.7 moving in a pycnocline. The density distribution of the pycnocline is shown in figure 4.100.

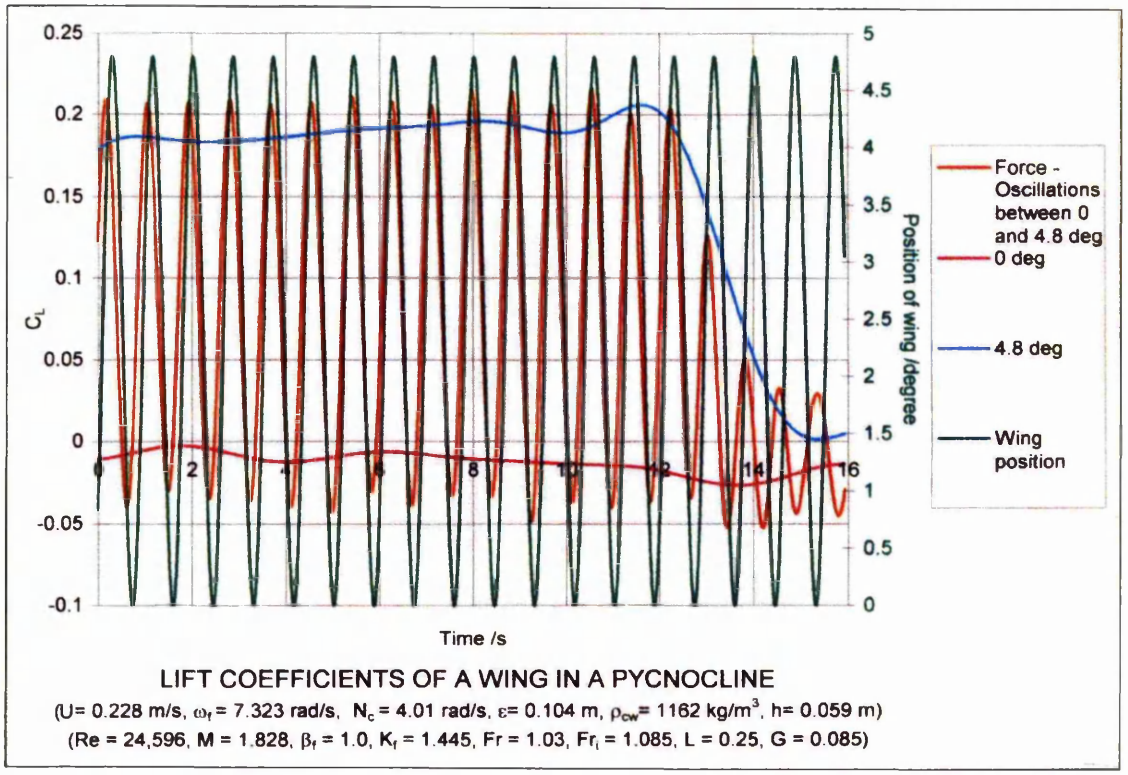

LIFT COEFFICIENTS OF A WING IN A PYCNOCLINE

(U= 0.228 m/s, ω_f = 7.323 rad/s, N_c = 4.01 rad/s, ε= 0.104 m, ρ_{cw}= 1162 kg/m^3, h= 0.059 m)

(Re = 24,596, M = 1.828, β_f = 1.0, K_f = 1.445, Fr = 1.03, Fr_i = 1.085, L = 0.25, G = 0.085)

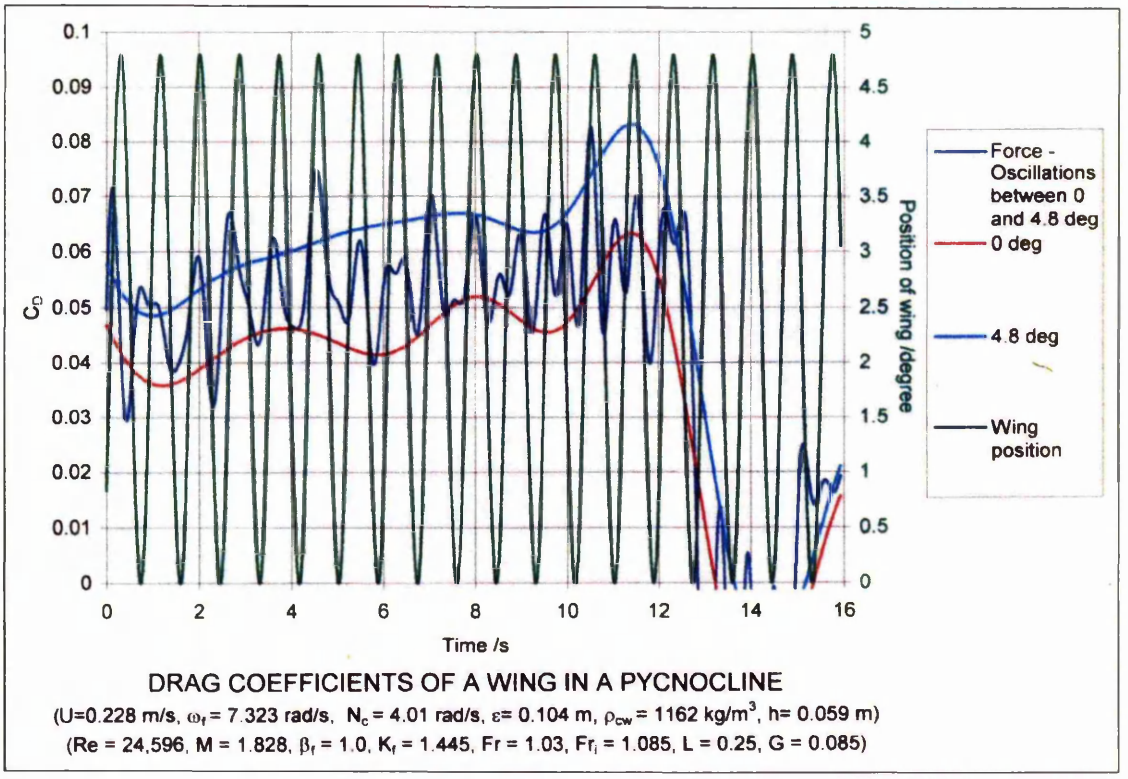

DRAG COEFFICIENTS OF A WING IN A PYCNOCLINE

(U=0.228 m/s, ω_f = 7.323 rad/s, N_c = 4.01 rad/s, ε= 0.104 m, ρ_{cw} = 1162 kg/m^3, h= 0.059 m)

(Re = 24,596, M = 1.828, β_f = 1.0, K_f = 1.445, Fr = 1.03, Fr_i = 1.085, L = 0.25, G = 0.085)

Figures 4.74a & b The lift and drag coefficients of a NACA 0012 wing with aspect ratio 1.7 moving in a pycnocline. The density distribution of the pycnocline is shown in figure 4.100.

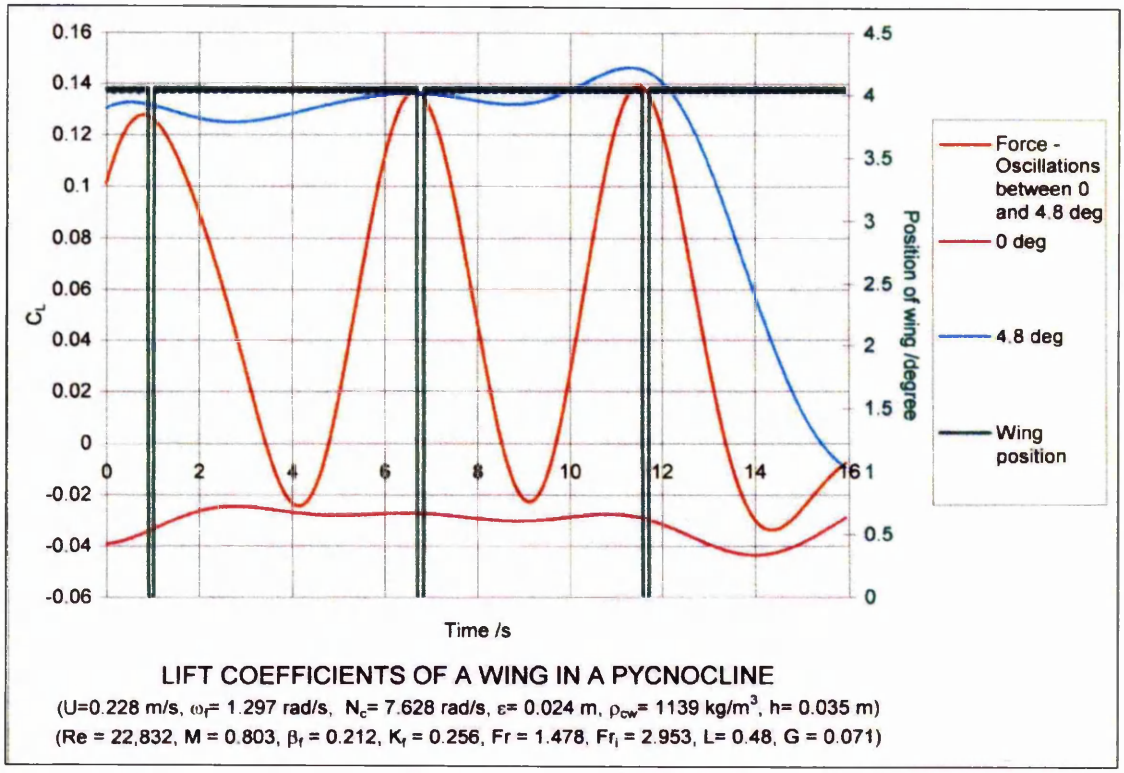

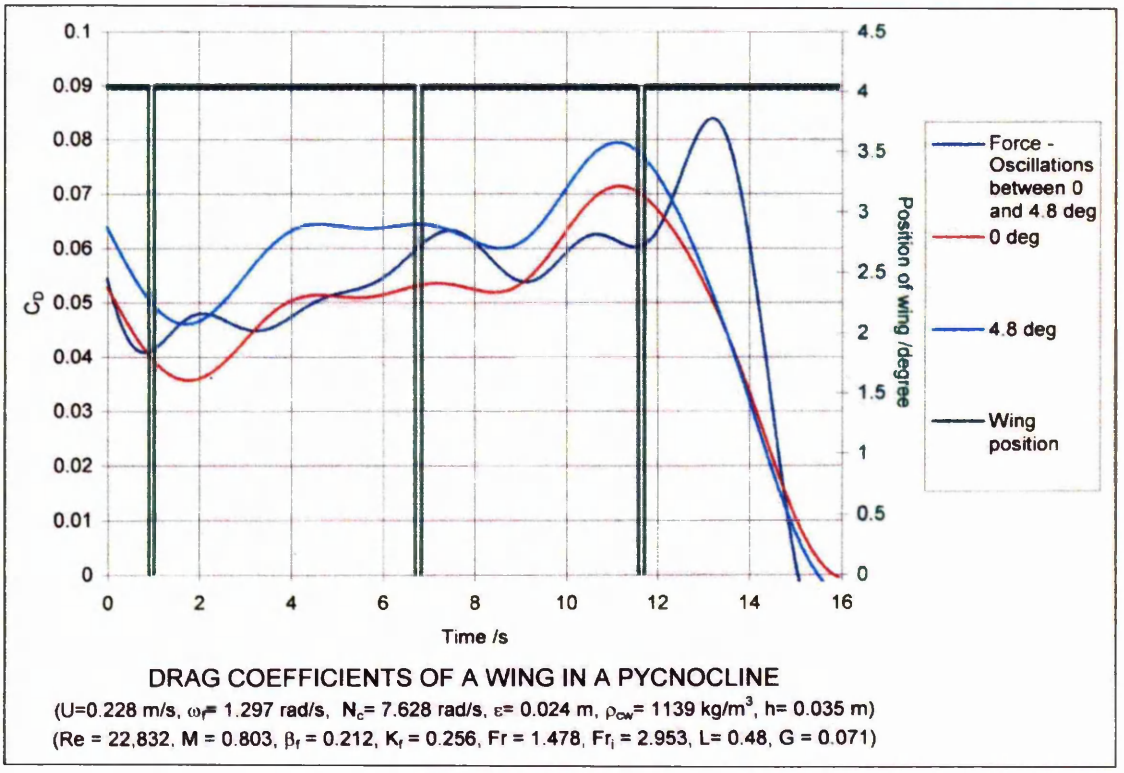

Figures 4.75a & b The lift and drag coefficients of a NACA 0012 wing with aspect ratio 1.7 moving in a pycnocline. The density distribution of the pycnocline is shown in figure 4.101.

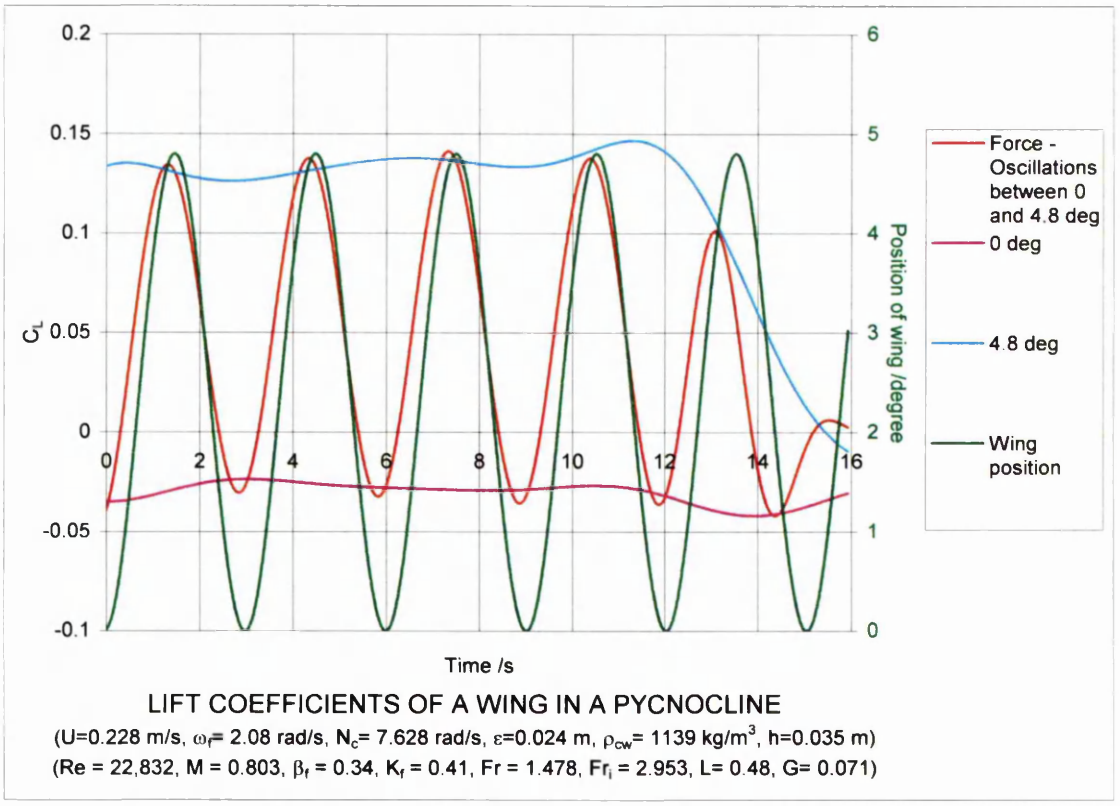

LIFT COEFFICIENTS OF A WING IN A PYCNOCLINE

(U=0.228 m/s, ω_f= 2.08 rad/s, N_c= 7.628 rad/s, ε=0.024 m, ρ_{cw}= 1139 kg/m^3, h=0.035 m)

(Re = 22,832, M = 0.803, β_f = 0.34, K_f = 0.41, Fr = 1.478, Fr_i = 2.953, L= 0.48, G= 0.071)

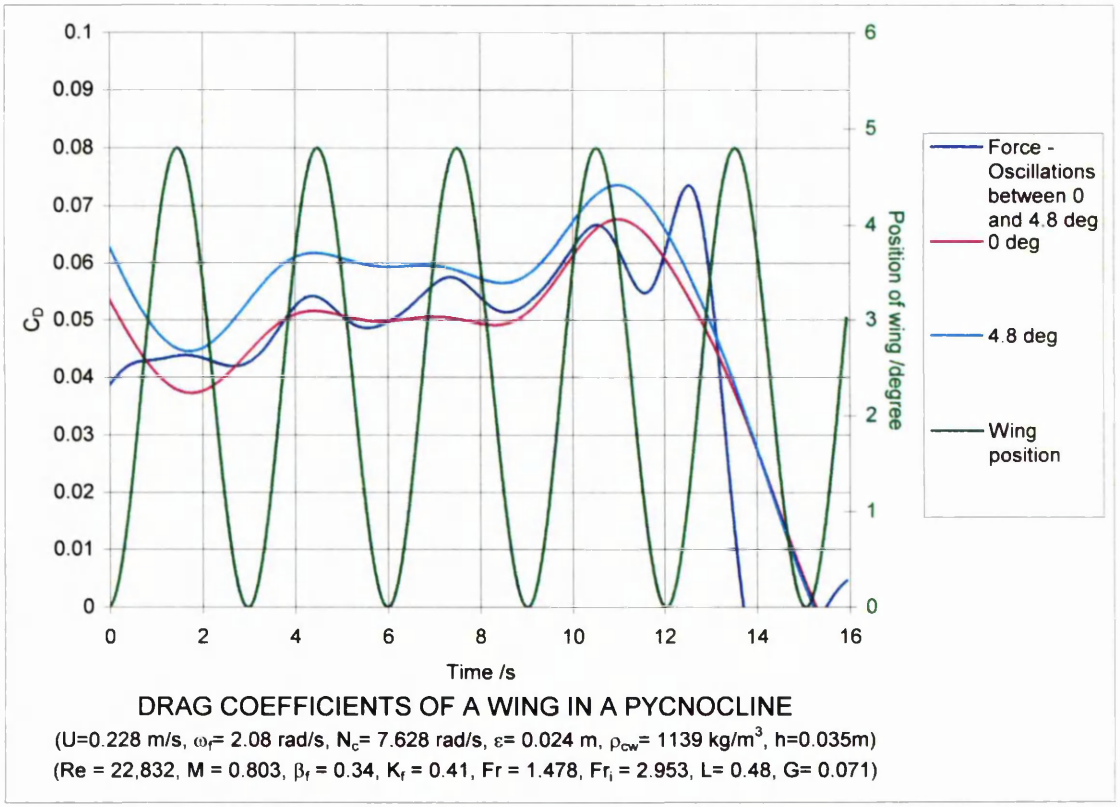

DRAG COEFFICIENTS OF A WING IN A PYCNOCLINE

(U=0.228 m/s, ω_f= 2.08 rad/s, N_c= 7.628 rad/s, ε= 0.024 m, ρ_{cw}= 1139 kg/m^3, h=0.035m)

(Re = 22,832, M = 0.803, β_f = 0.34, K_f = 0.41, Fr = 1.478, Fr_i = 2.953, L= 0.48, G= 0.071)

Figures 4.76a & b The lift and drag coefficients of a NACA 0012 wing with aspect ratio 1.7 moving in a pycnocline. The density distribution of the pycnocline is shown in figure 4.101.

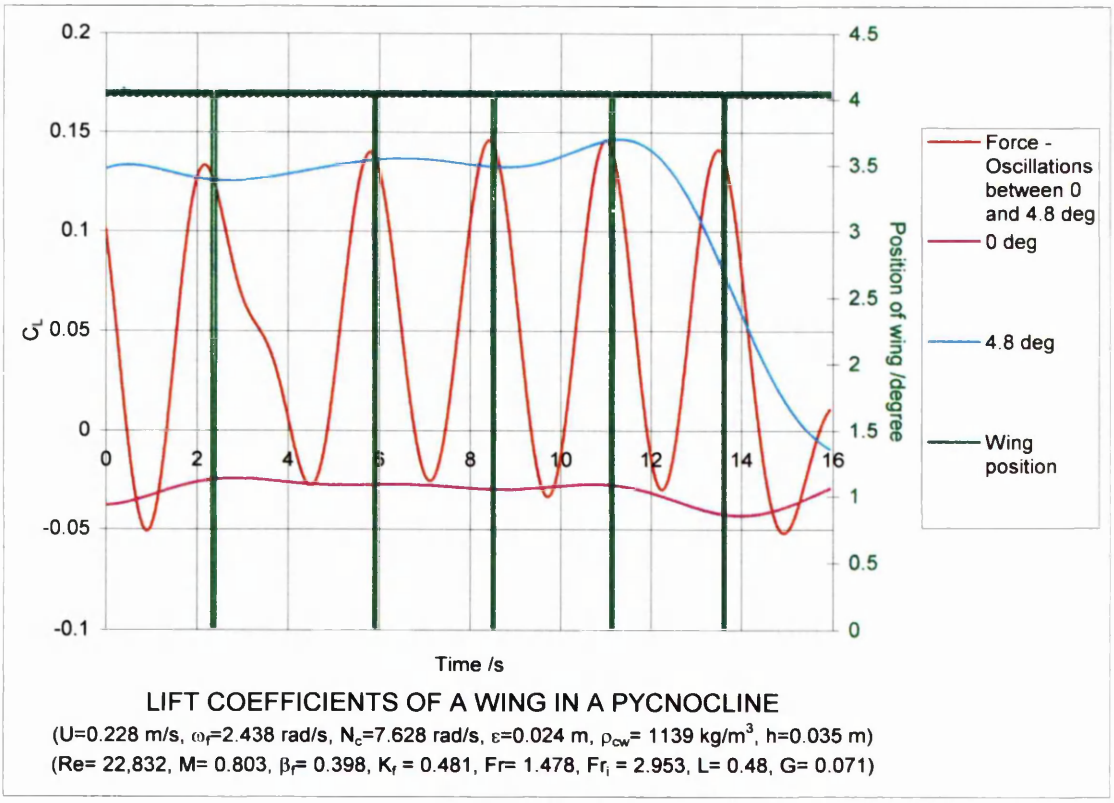

LIFT COEFFICIENTS OF A WING IN A PYCNOCLINE

(U=0.228 m/s, ω_f=2.438 rad/s, N_c=7.628 rad/s, ε=0.024 m, ρ_{cw}= 1139 kg/m^3, h=0.035 m)

(Re= 22,832, M= 0.803, β_f= 0.398, K_f = 0.481, Fr= 1.478, Fr_i = 2.953, L= 0.48, G= 0.071)

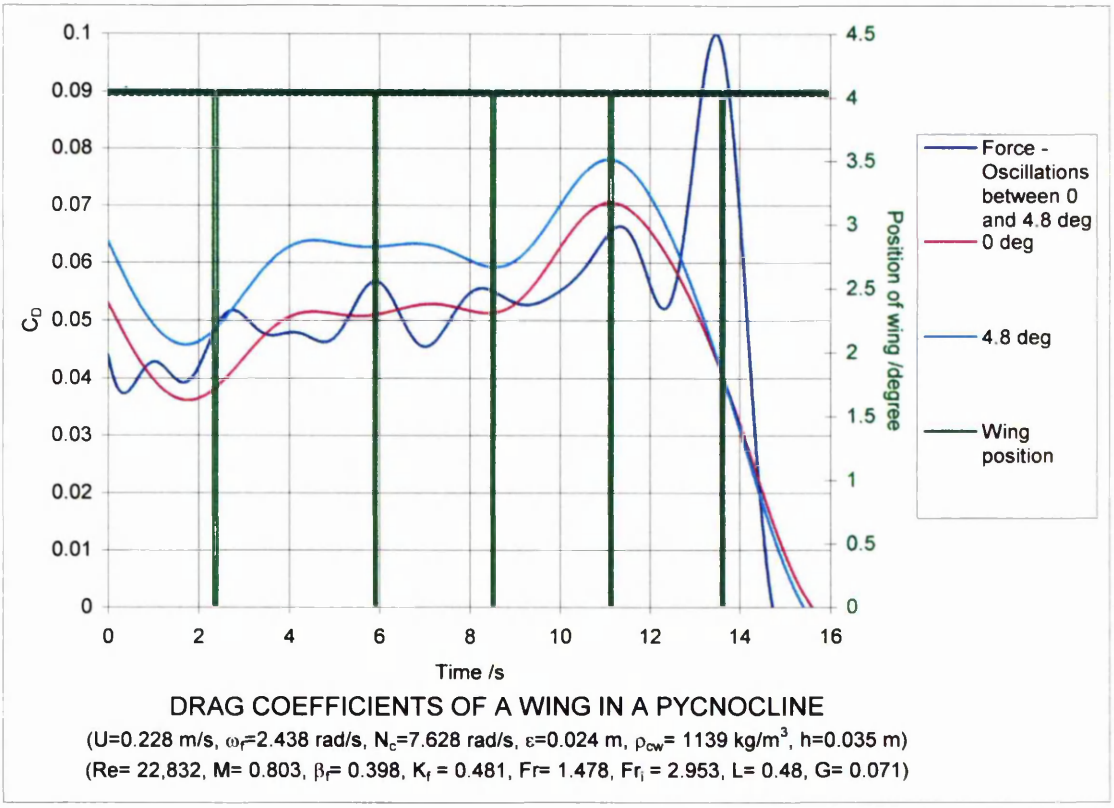

DRAG COEFFICIENTS OF A WING IN A PYCNOCLINE

(U=0.228 m/s, ω_f=2.438 rad/s, N_c=7.628 rad/s, ε=0.024 m, ρ_{cw}= 1139 kg/m^3, h=0.035 m)

(Re= 22,832, M= 0.803, β_f= 0.398, K_f = 0.481, Fr= 1.478, Fr_i = 2.953, L= 0.48, G= 0.071)

Figures 4.77a & b The lift and drag coefficients of a NACA 0012 wing with aspect ratio 1.7 moving in a pycnocline. The density distribution of the pycnocline is shown in figure 4.101.

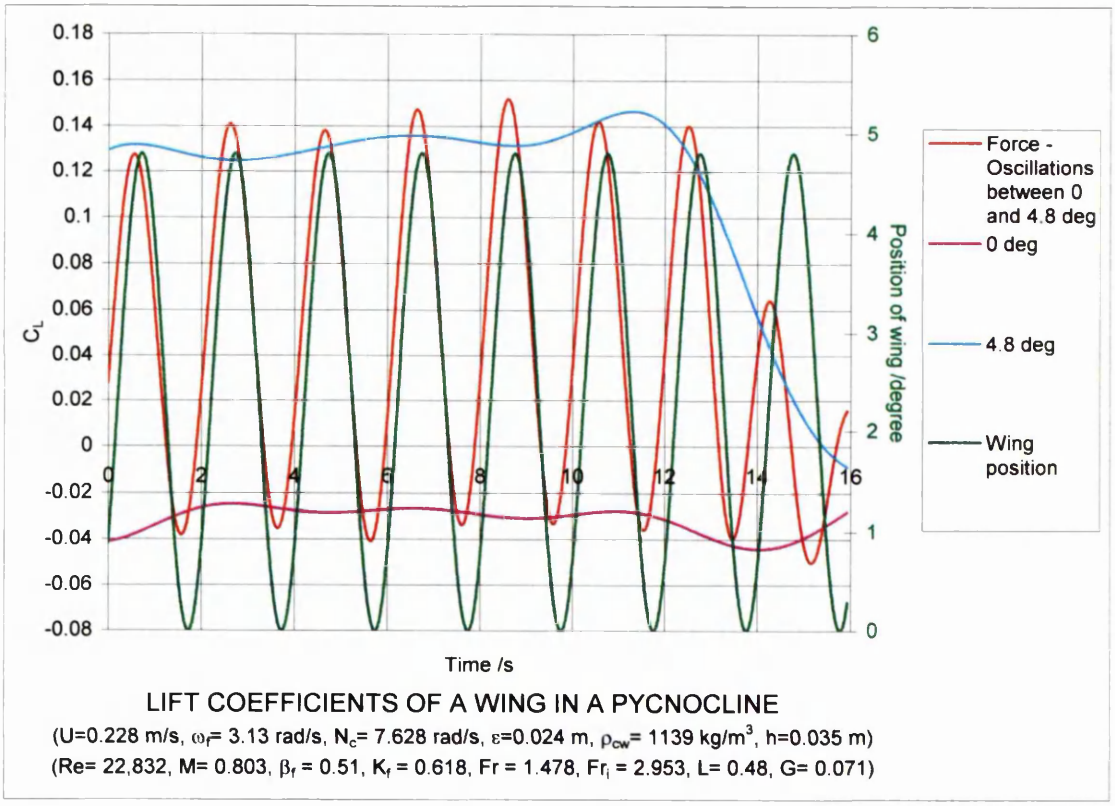

LIFT COEFFICIENTS OF A WING IN A PYCNOCLINE

(U=0.228 m/s, ω_f= 3.13 rad/s, N_c= 7.628 rad/s, ε=0.024 m, ρ_{cw}= 1139 kg/m^3, h=0.035 m)

(Re= 22,832, M= 0.803, β_f = 0.51, K_f = 0.618, Fr = 1.478, Fr_i = 2.953, L= 0.48, G= 0.071)

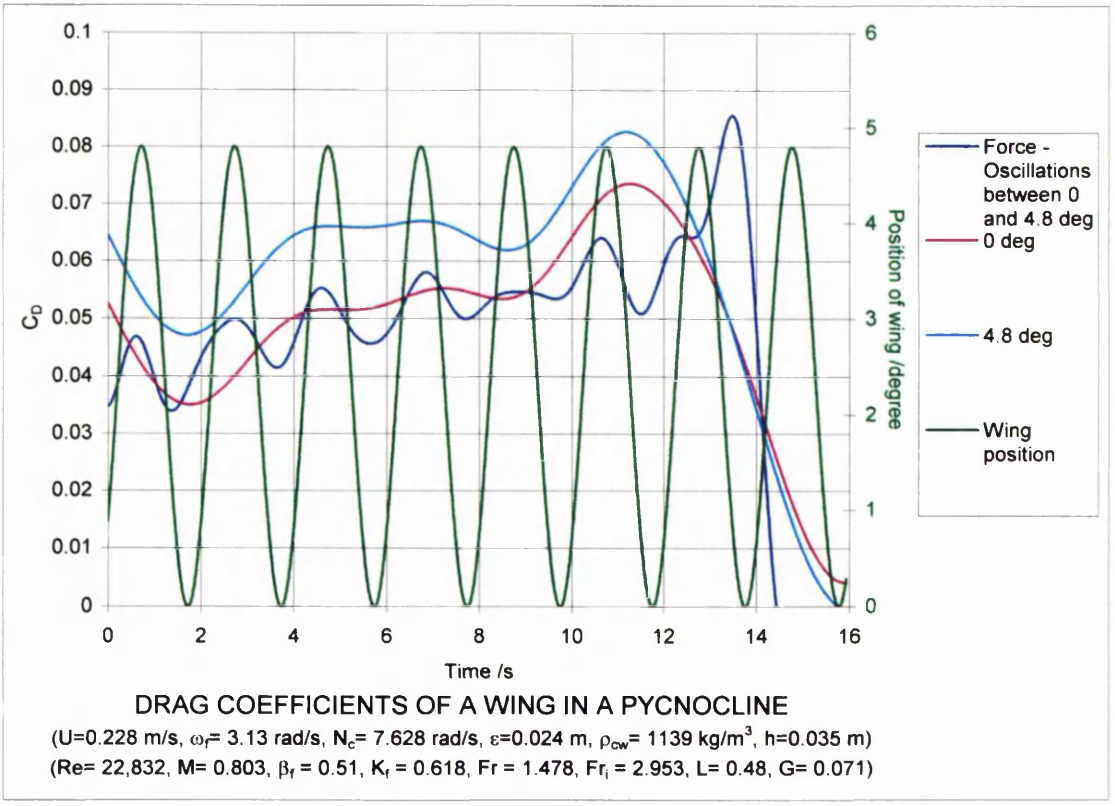

DRAG COEFFICIENTS OF A WING IN A PYCNOCLINE

(U=0.228 m/s, ω_f= 3.13 rad/s, N_c= 7.628 rad/s, ε=0.024 m, ρ_{cw}= 1139 kg/m^3, h=0.035 m)

(Re= 22,832, M= 0.803, β_f = 0.51, K_f = 0.618, Fr = 1.478, Fr_i = 2.953, L= 0.48, G= 0.071)

Figures 4.78a & b The lift and drag coefficients of a NACA 0012 wing with aspect ratio 1.7 moving in a pycnocline. The density distribution of the pycnocline properties is shown in figure 4.101.

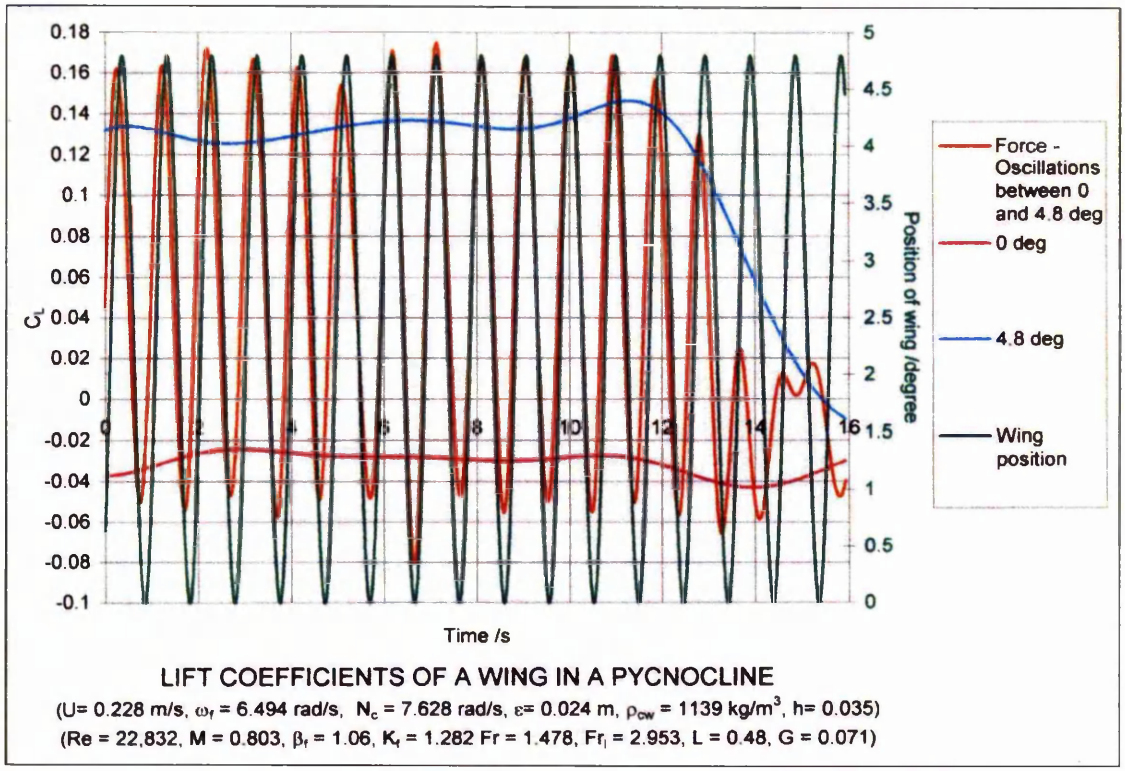

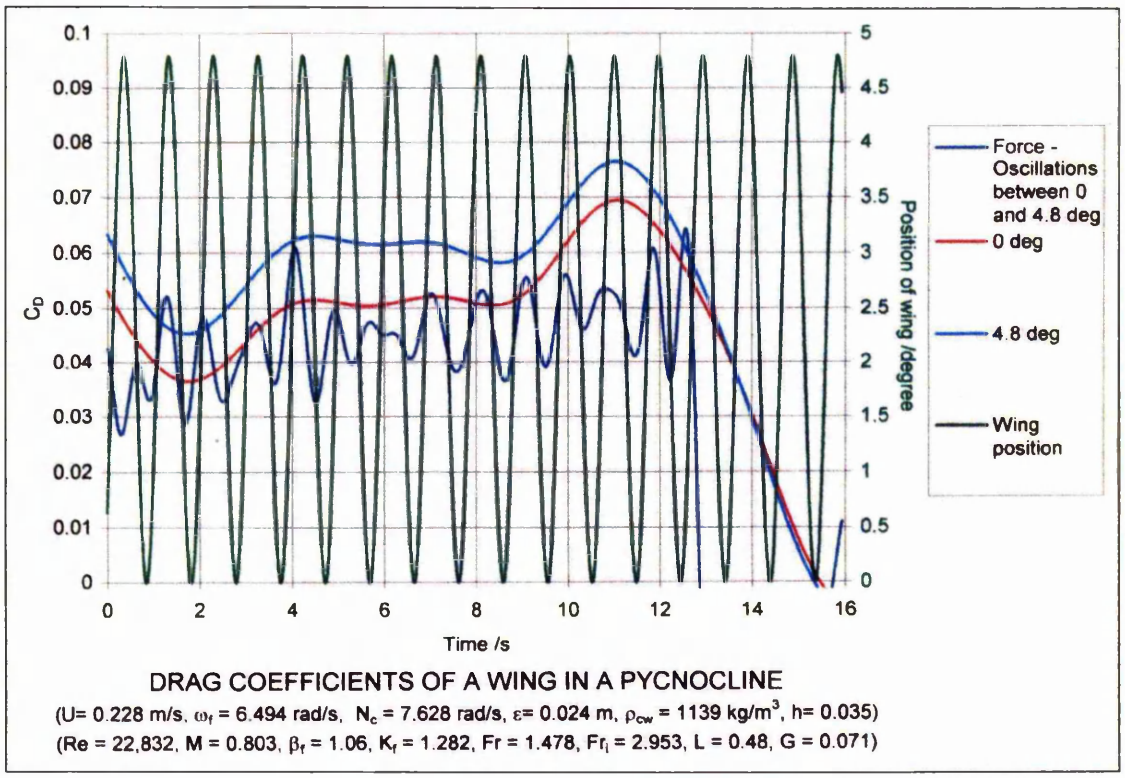

Figures 4.79a & b The lift and drag coefficients of a NACA 0012 wing with aspect ratio 1.7 moving in a pycnocline. The density distribution of the pycnocline is shown in figure 4.101.

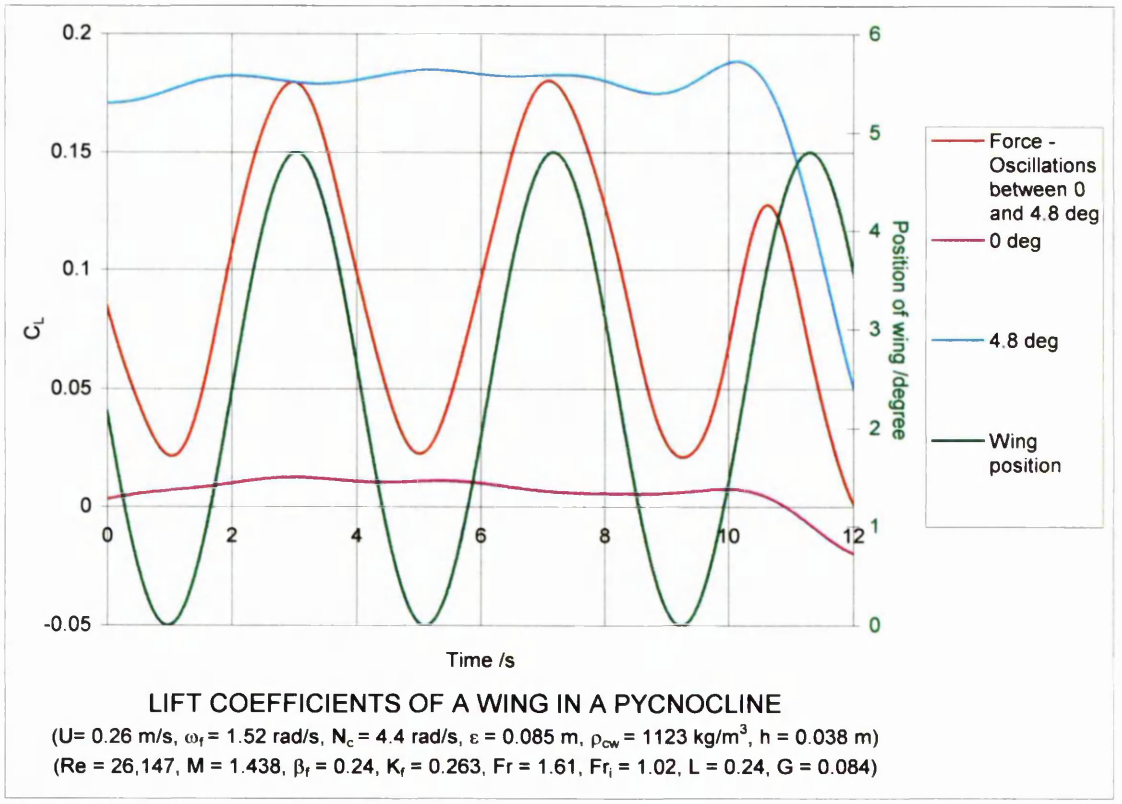

LIFT COEFFICIENTS OF A WING IN A PYCNOCLINE

(U= 0.26 m/s, ω_f = 1.52 rad/s, N_c = 4.4 rad/s, ε = 0.085 m, ρ_{cw} = 1123 kg/m^3, h = 0.038 m)
(Re = 26,147, M = 1.438, β_f = 0.24, K_f = 0.263, Fr = 1.61, Fr_i = 1.02, L = 0.24, G = 0.084)

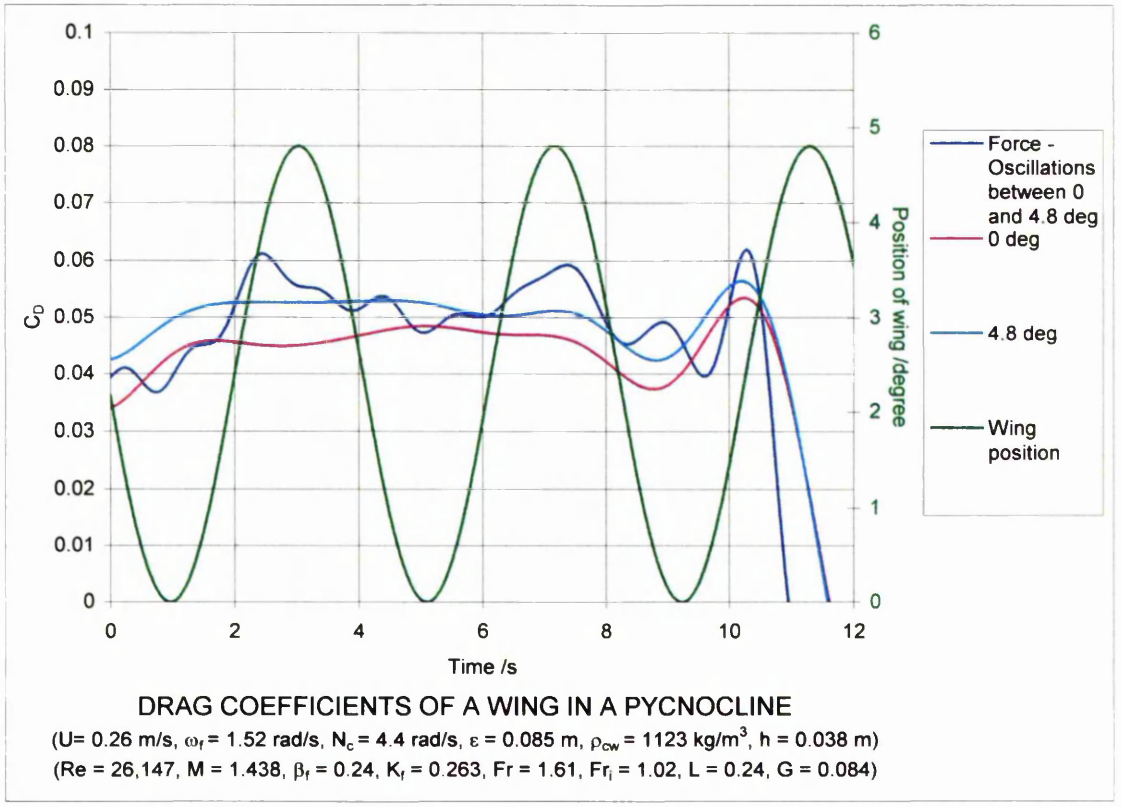

DRAG COEFFICIENTS OF A WING IN A PYCNOCLINE

(U= 0.26 m/s, ω_f = 1.52 rad/s, N_c = 4.4 rad/s, ε = 0.085 m, ρ_{cw} = 1123 kg/m^3, h = 0.038 m)
(Re = 26,147, M = 1.438, β_f = 0.24, K_f = 0.263, Fr = 1.61, Fr_i = 1.02, L = 0.24, G = 0.084)

Figures 4.80a & b The lift and drag coefficients of a NACA 0012 wing with aspect ratio 1.7 moving in a pycnocline. The density distribution of the pycnocline is shown in figure 4.102.

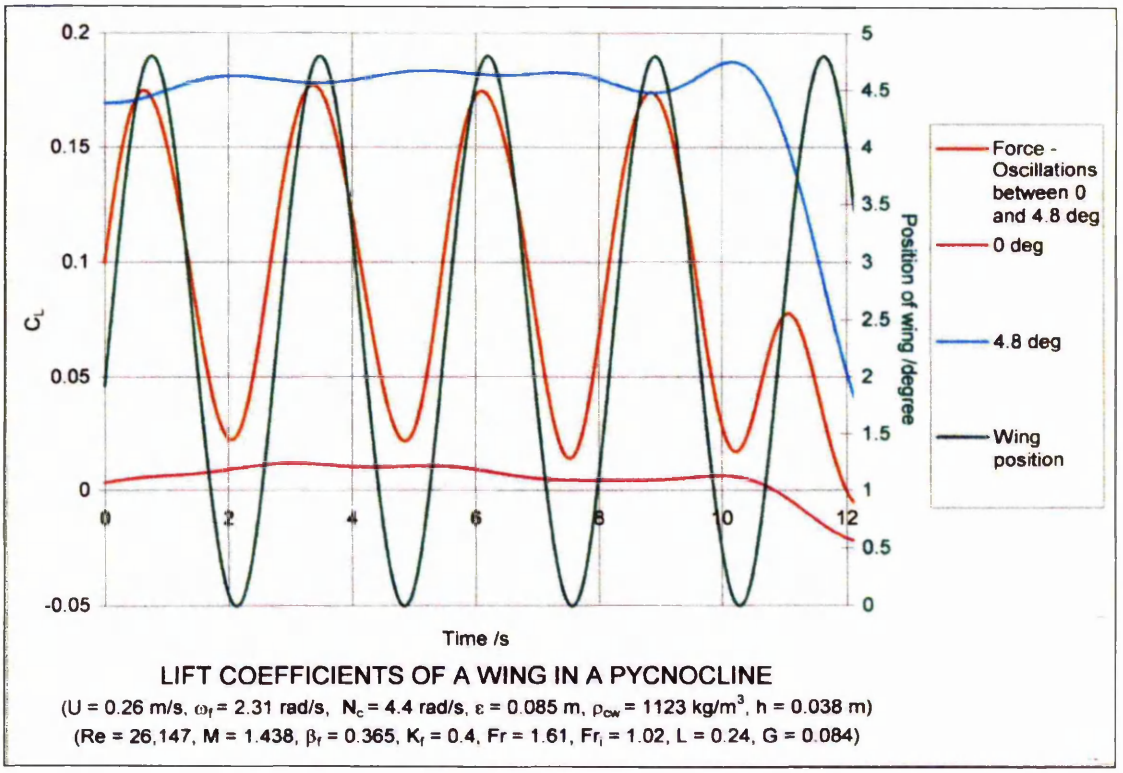

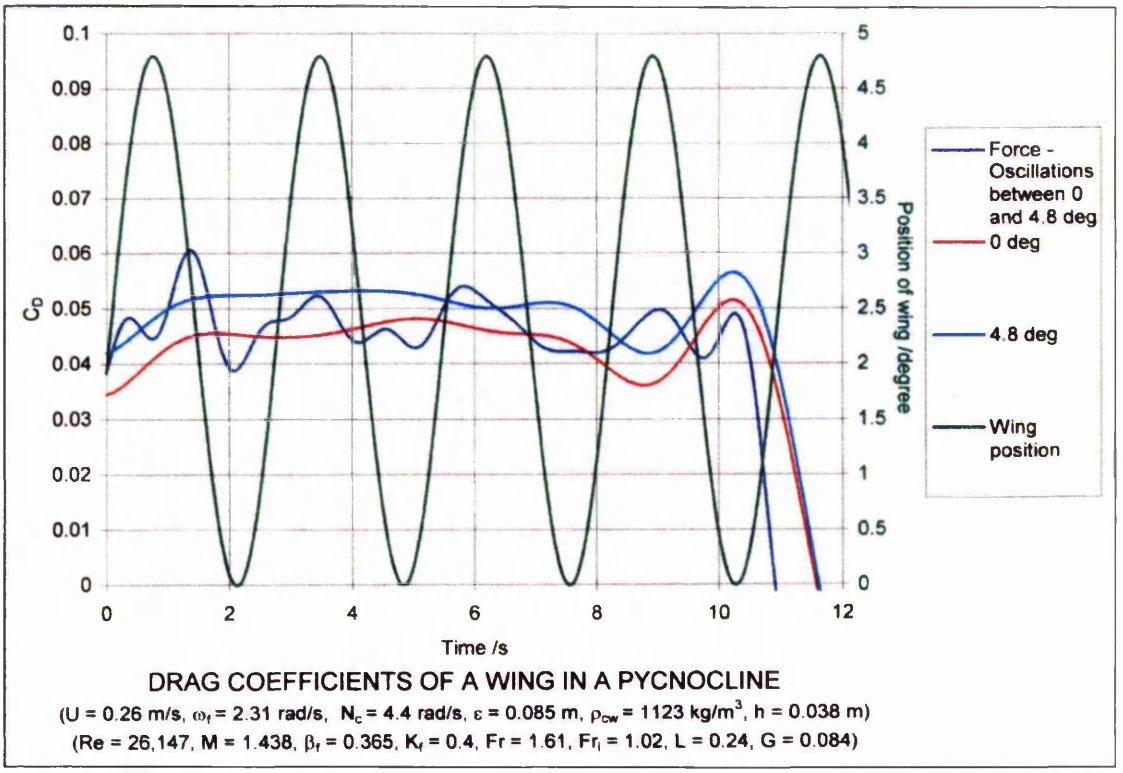

Figures 4.81a & b The lift and drag coefficients of a NACA 0012 wing with aspect ratio 1.7 moving in a pycnocline. The density distribution of the pycnocline is shown in figure 4.102.

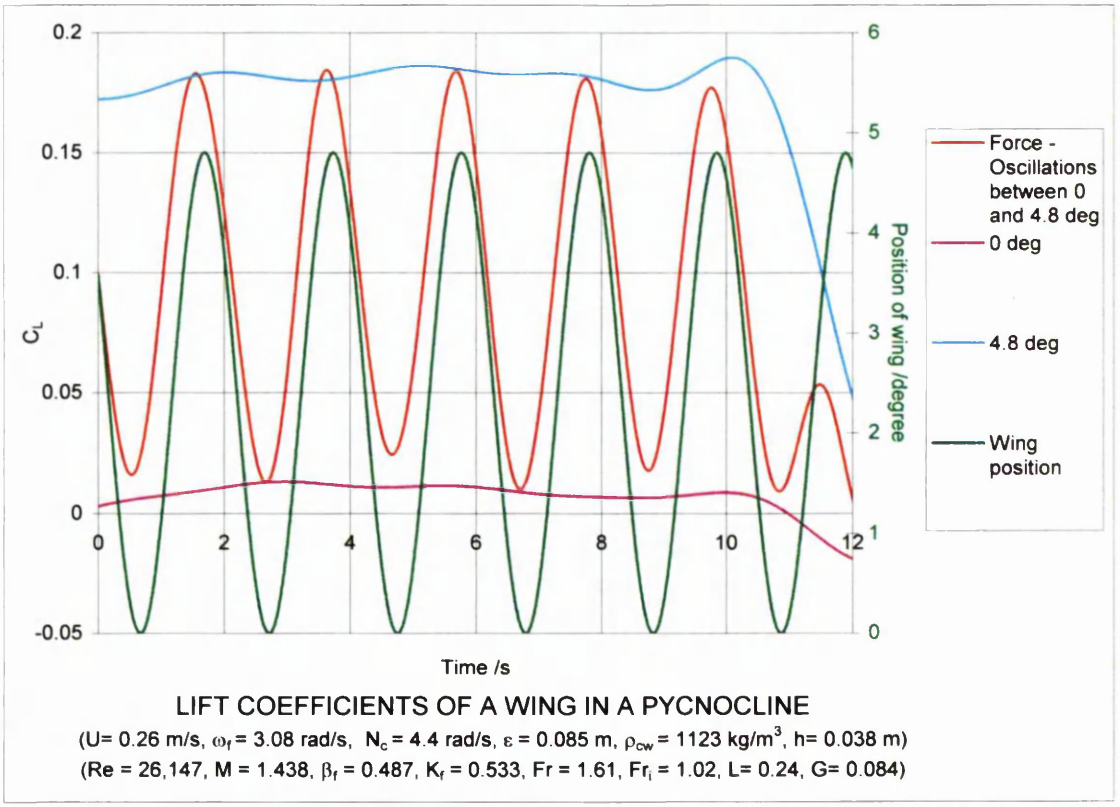

LIFT COEFFICIENTS OF A WING IN A PYCNOCLINE

(U= 0.26 m/s, ω_f = 3.08 rad/s, N_c = 4.4 rad/s, ε = 0.085 m, ρ_{cw} = 1123 kg/m^3, h= 0.038 m)
(Re = 26,147, M = 1.438, β_f = 0.487, K_f = 0.533, Fr = 1.61, Fr_i = 1.02, L= 0.24, G= 0.084)

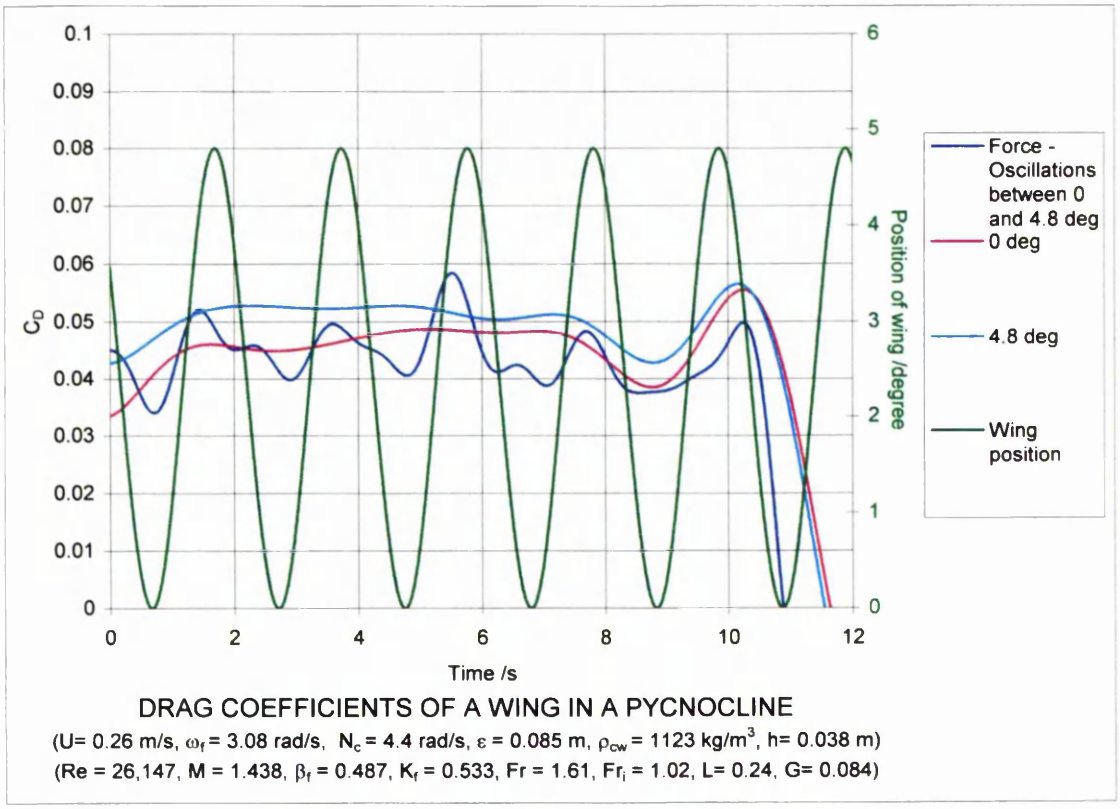

DRAG COEFFICIENTS OF A WING IN A PYCNOCLINE

(U= 0.26 m/s, ω_f = 3.08 rad/s, N_c = 4.4 rad/s, ε = 0.085 m, ρ_{cw} = 1123 kg/m^3, h= 0.038 m)
(Re = 26,147, M = 1.438, β_f = 0.487, K_f = 0.533, Fr = 1.61, Fr_i = 1.02, L= 0.24, G= 0.084)

Figures 4.82a & b The lift and drag coefficients of a NACA 0012 wing with aspect ratio 1.7 moving in a pycnocline. The density distribution of the pycnocline is shown in figure 4.102.

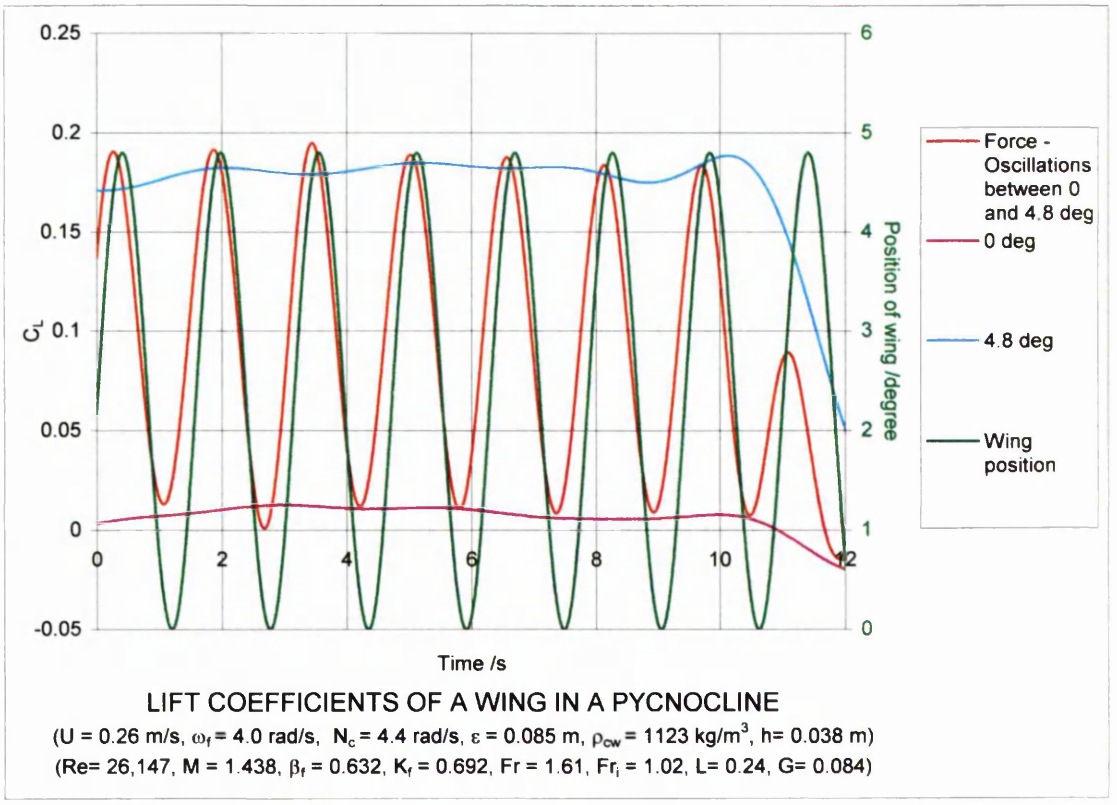

LIFT COEFFICIENTS OF A WING IN A PYCNOCLINE

(U = 0.26 m/s, ω_f = 4.0 rad/s, N_c = 4.4 rad/s, ε = 0.085 m, ρ_{cw} = 1123 kg/m^3, h= 0.038 m)
(Re= 26,147, M = 1.438, β_f = 0.632, K_f = 0.692, Fr = 1.61, Fr_i = 1.02, L= 0.24, G= 0.084)

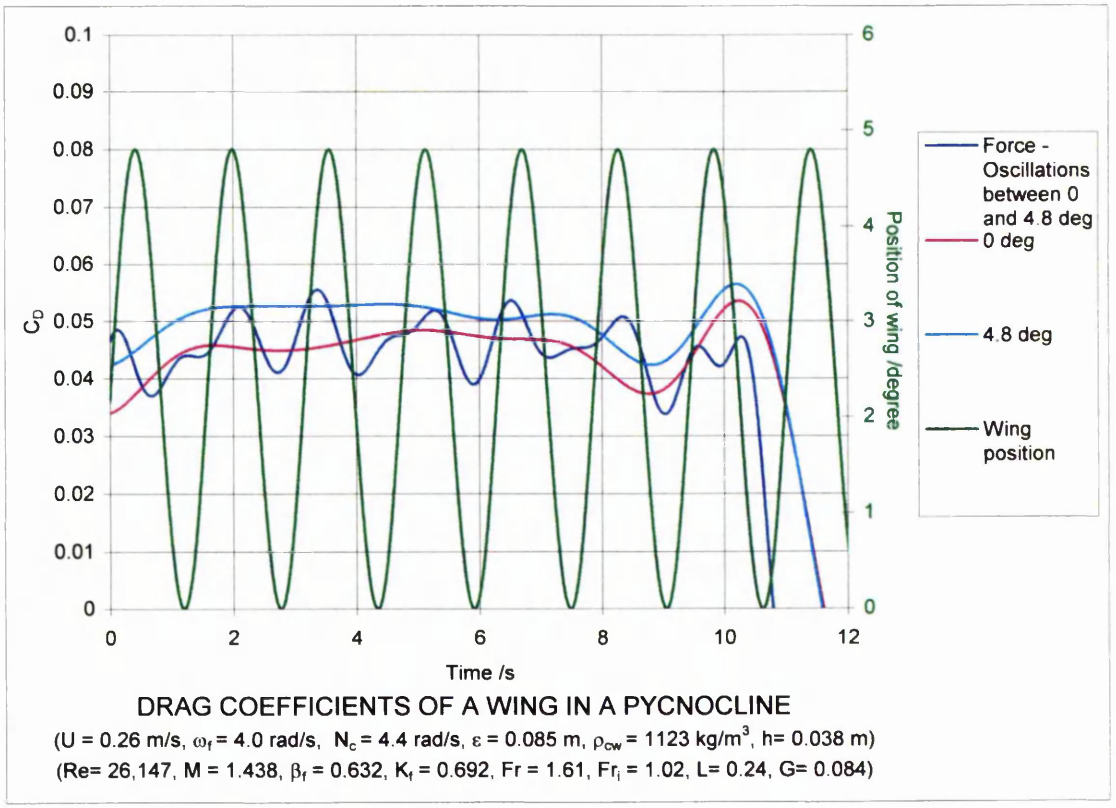

DRAG COEFFICIENTS OF A WING IN A PYCNOCLINE

(U = 0.26 m/s, ω_f = 4.0 rad/s, N_c = 4.4 rad/s, ε = 0.085 m, ρ_{cw} = 1123 kg/m^3, h= 0.038 m)
(Re= 26,147, M = 1.438, β_f = 0.632, K_f = 0.692, Fr = 1.61, Fr_i = 1.02, L= 0.24, G= 0.084)

Figures 4.83a & b The lift and drag coefficients of a NACA 0012 wing aspect ratio 1.7 moving in a pycnocline. The density distribution of the pycnocline is shown in figure 4.102.

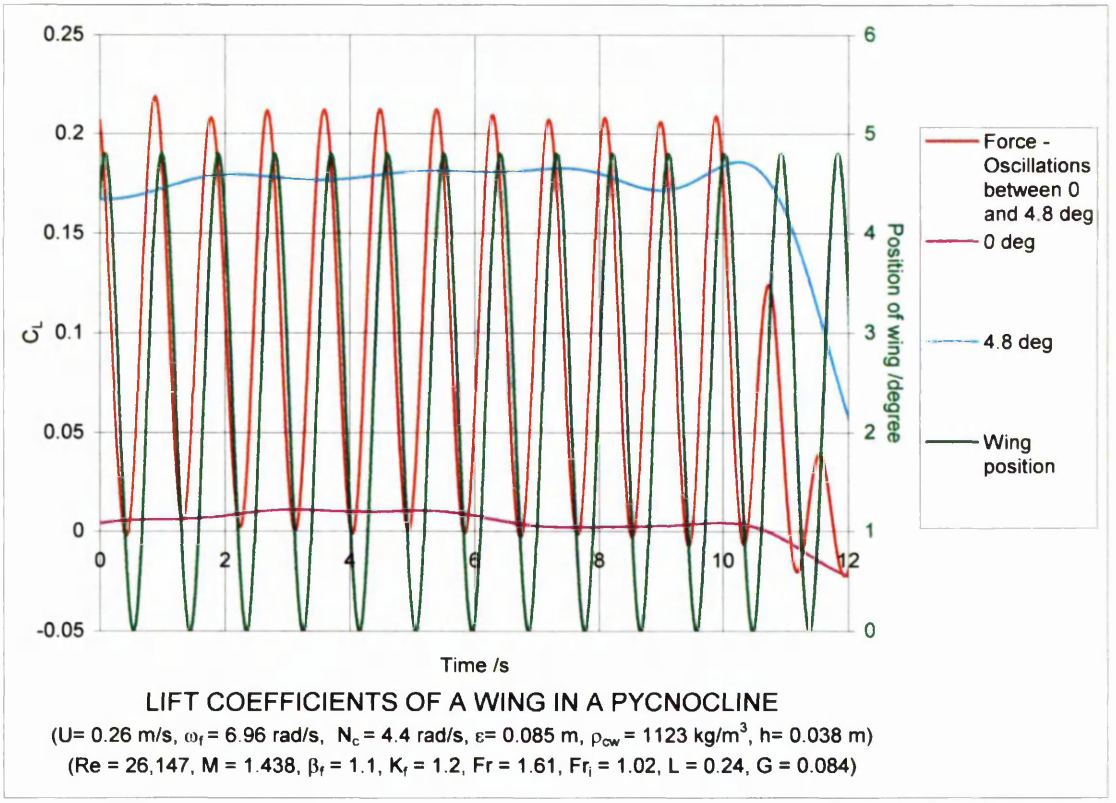

LIFT COEFFICIENTS OF A WING IN A PYCNOCLINE

(U= 0.26 m/s, ω_f = 6.96 rad/s, N_c = 4.4 rad/s, ε= 0.085 m, ρ_{cw} = 1123 kg/m^3, h= 0.038 m)
(Re = 26,147, M = 1.438, β_f = 1.1, K_f = 1.2, Fr = 1.61, Fr_i = 1.02, L = 0.24, G = 0.084)

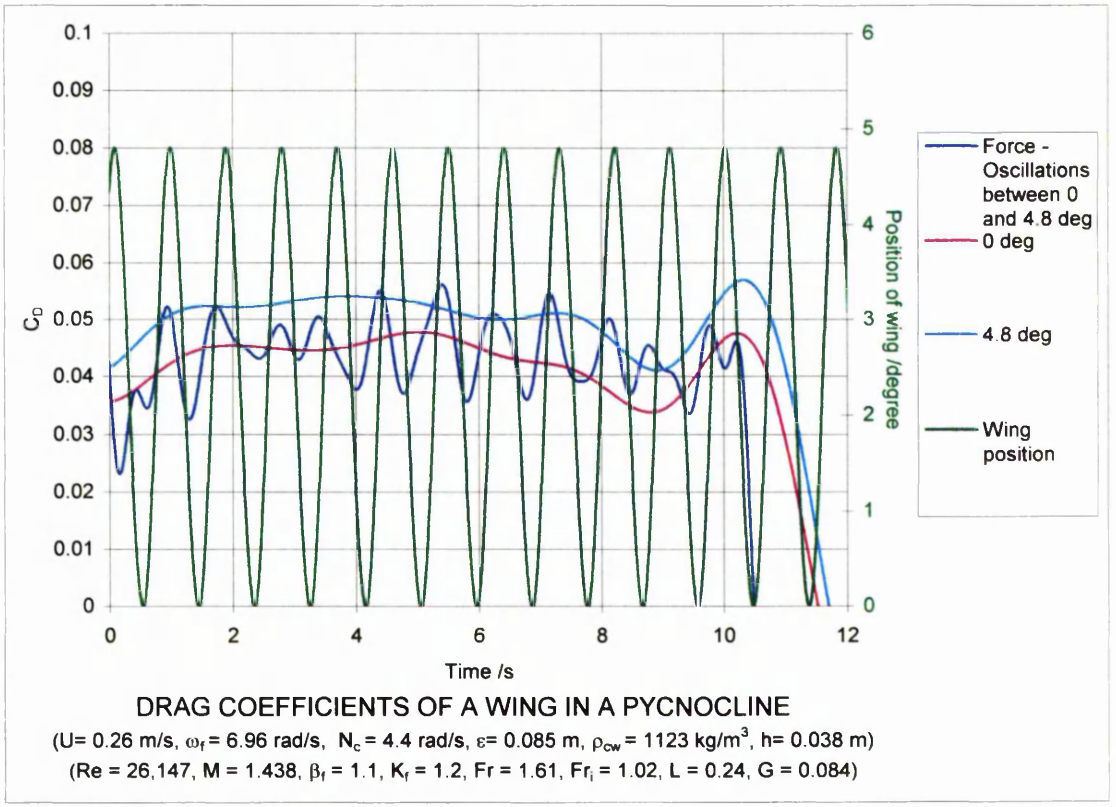

DRAG COEFFICIENTS OF A WING IN A PYCNOCLINE

(U= 0.26 m/s, ω_f = 6.96 rad/s, N_c = 4.4 rad/s, ε= 0.085 m, ρ_{cw} = 1123 kg/m^3, h= 0.038 m)
(Re = 26,147, M = 1.438, β_f = 1.1, K_f = 1.2, Fr = 1.61, Fr_i = 1.02, L = 0.24, G = 0.084)

Figures 4.84a & b The lift and drag coefficients of a NACA 0012 wing with aspect ratio 1.7 moving in a pycnocline. The density distribution of the pycnocline is shown in figure 4.102.

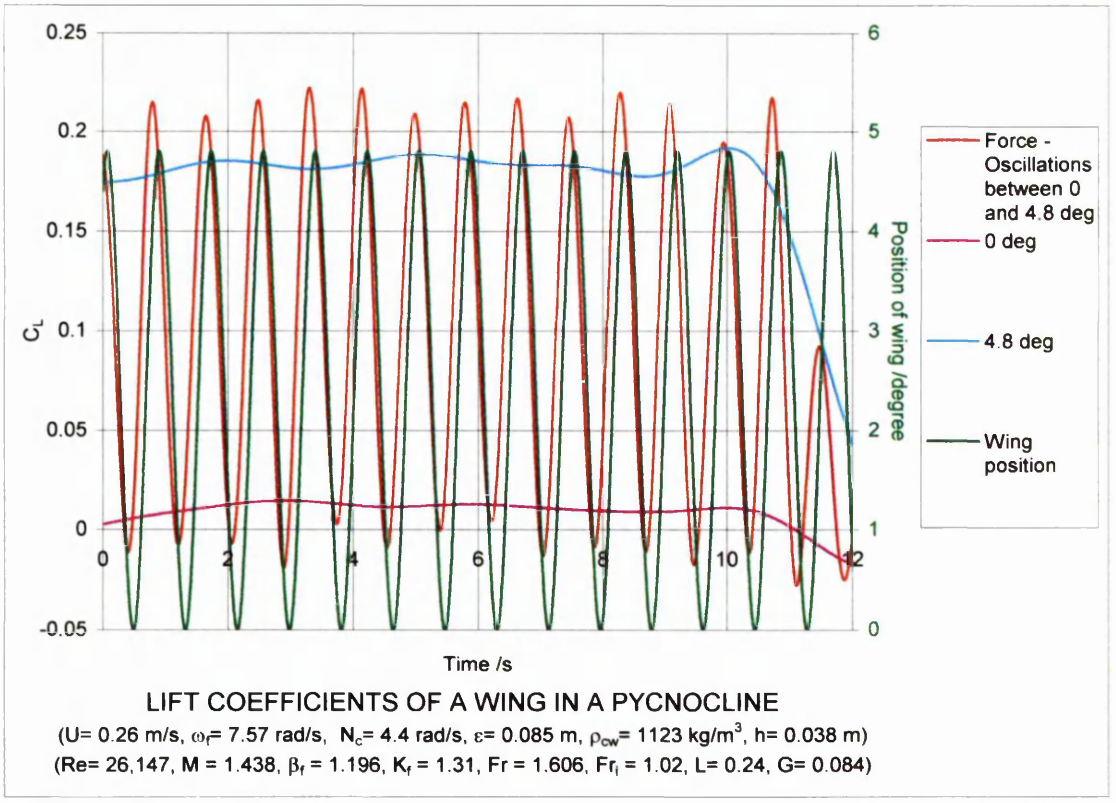

LIFT COEFFICIENTS OF A WING IN A PYCNOCLINE

(U= 0.26 m/s, ω_f= 7.57 rad/s, N_c= 4.4 rad/s, ε= 0.085 m, ρ_{cw}= 1123 kg/m^3, h= 0.038 m)

(Re= 26,147, M = 1.438, β_f = 1.196, K_f = 1.31, Fr = 1.606, Fr_i = 1.02, L= 0.24, G= 0.084)

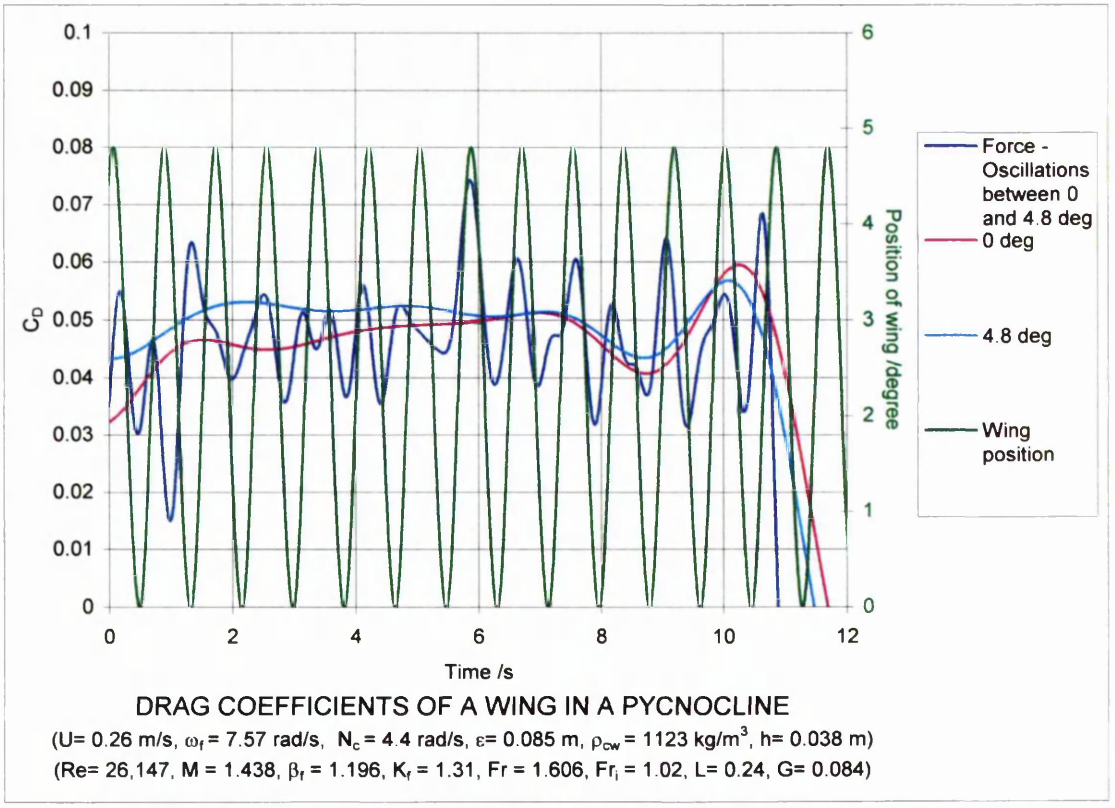

DRAG COEFFICIENTS OF A WING IN A PYCNOCLINE

(U= 0.26 m/s, ω_f = 7.57 rad/s, N_c = 4.4 rad/s, ε= 0.085 m, ρ_{cw} = 1123 kg/m^3, h= 0.038 m)

(Re= 26,147, M = 1.438, β_f = 1.196, K_f = 1.31, Fr = 1.606, Fr_i = 1.02, L= 0.24, G= 0.084)

Figures 4.85a & b The lift and drag coefficients of a NACA 0012 wing with aspect ratio 1.7 moving in a pycnocline. The density distribution of the pycnocline is shown in figure 4.102.

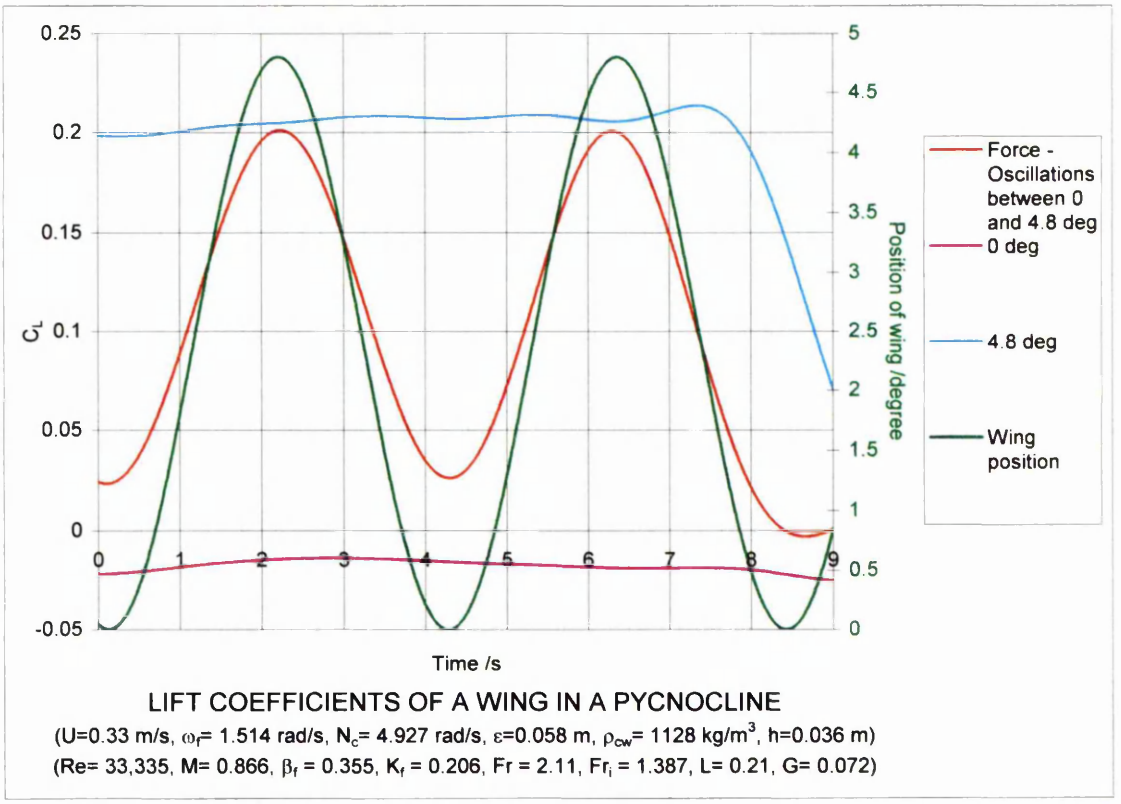

LIFT COEFFICIENTS OF A WING IN A PYCNOCLINE

(U=0.33 m/s, ω_f= 1.514 rad/s, N_c= 4.927 rad/s, ε=0.058 m, ρ_{cw}= 1128 kg/m^3, h=0.036 m)

(Re= 33,335, M= 0.866, β_f = 0.355, K_f = 0.206, Fr = 2.11, Fr_i = 1.387, L= 0.21, G= 0.072)

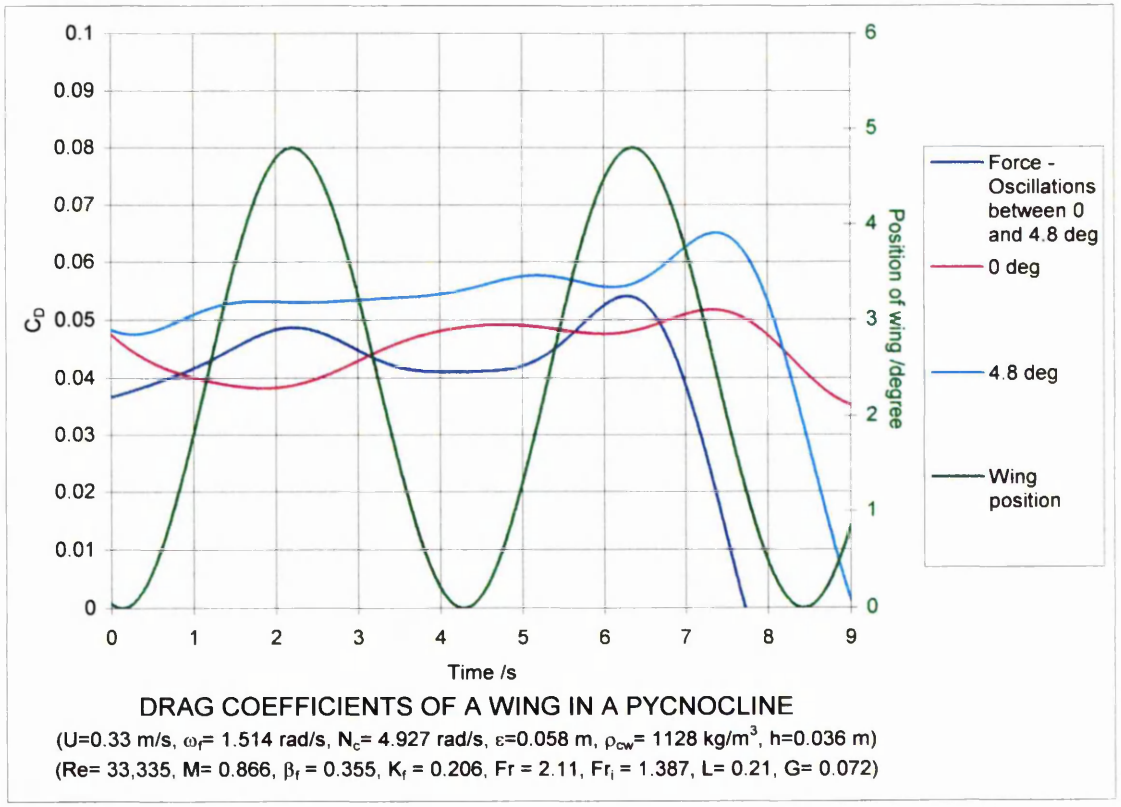

DRAG COEFFICIENTS OF A WING IN A PYCNOCLINE

(U=0.33 m/s, ω_f= 1.514 rad/s, N_c= 4.927 rad/s, ε=0.058 m, ρ_{cw}= 1128 kg/m^3, h=0.036 m)

(Re= 33,335, M= 0.866, β_f = 0.355, K_f = 0.206, Fr = 2.11, Fr_i = 1.387, L= 0.21, G= 0.072)

Figures 4.86a & b The lift and drag coefficients of a NACA 0012 wing with aspect ratio 1.7 moving in a pycnocline. The density distribution of the pycnocline is shown in figure 4.103.

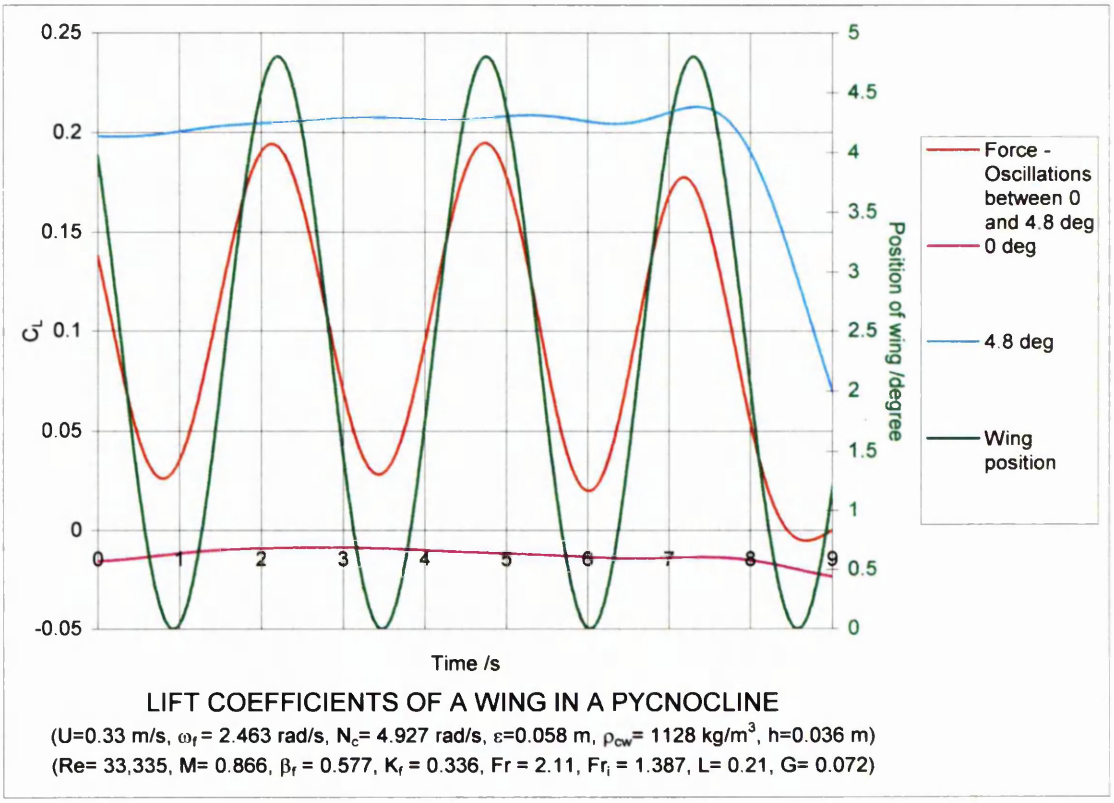

LIFT COEFFICIENTS OF A WING IN A PYCNOCLINE

(U=0.33 m/s, ω_f = 2.463 rad/s, N_c= 4.927 rad/s, ε=0.058 m, ρ_{cw}= 1128 kg/m^3, h=0.036 m)

(Re= 33,335, M= 0.866, β_f = 0.577, K_f = 0.336, Fr = 2.11, Fr_i = 1.387, L= 0.21, G= 0.072)

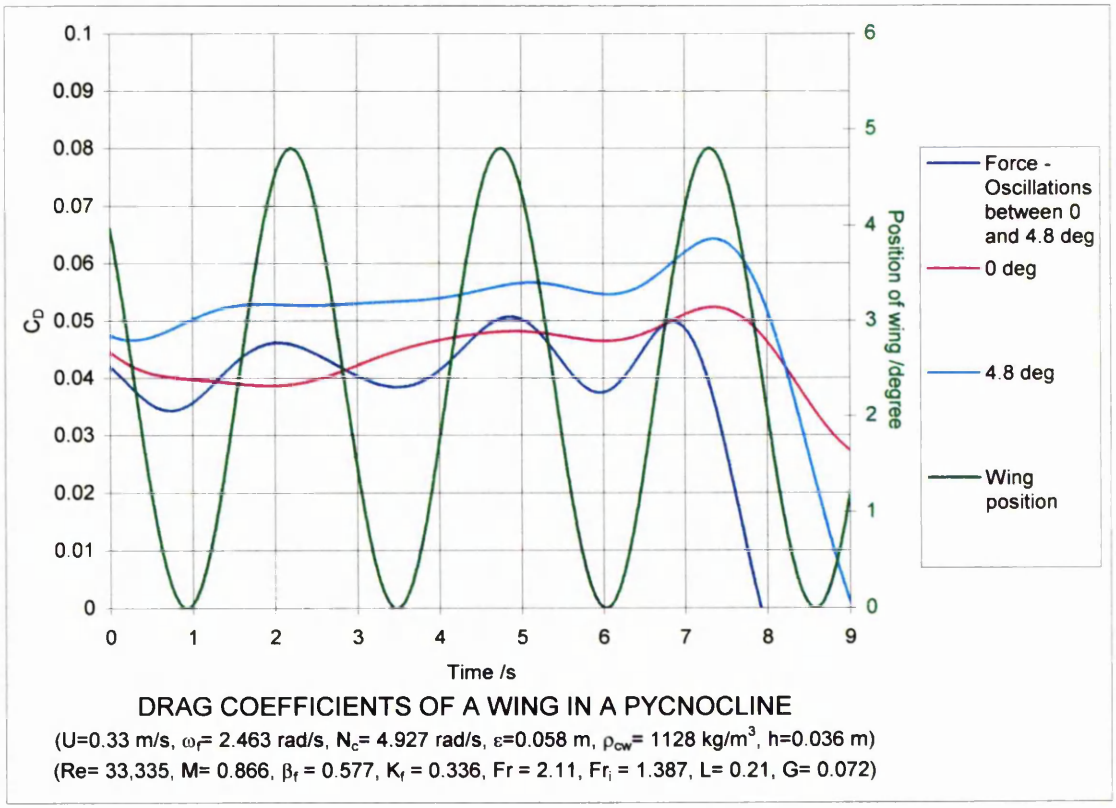

DRAG COEFFICIENTS OF A WING IN A PYCNOCLINE

(U=0.33 m/s, ω_f= 2.463 rad/s, N_c= 4.927 rad/s, ε=0.058 m, ρ_{cw}= 1128 kg/m^3, h=0.036 m)

(Re= 33,335, M= 0.866, β_f = 0.577, K_f = 0.336, Fr = 2.11, Fr_i = 1.387, L= 0.21, G= 0.072)

Figures 4.87a & b The lift and drag coefficients of a NACA 0012 wing with aspect ratio 1.7 moving in a pycnocline. The density distribution of the pycnocline is shown in figure 4.103.

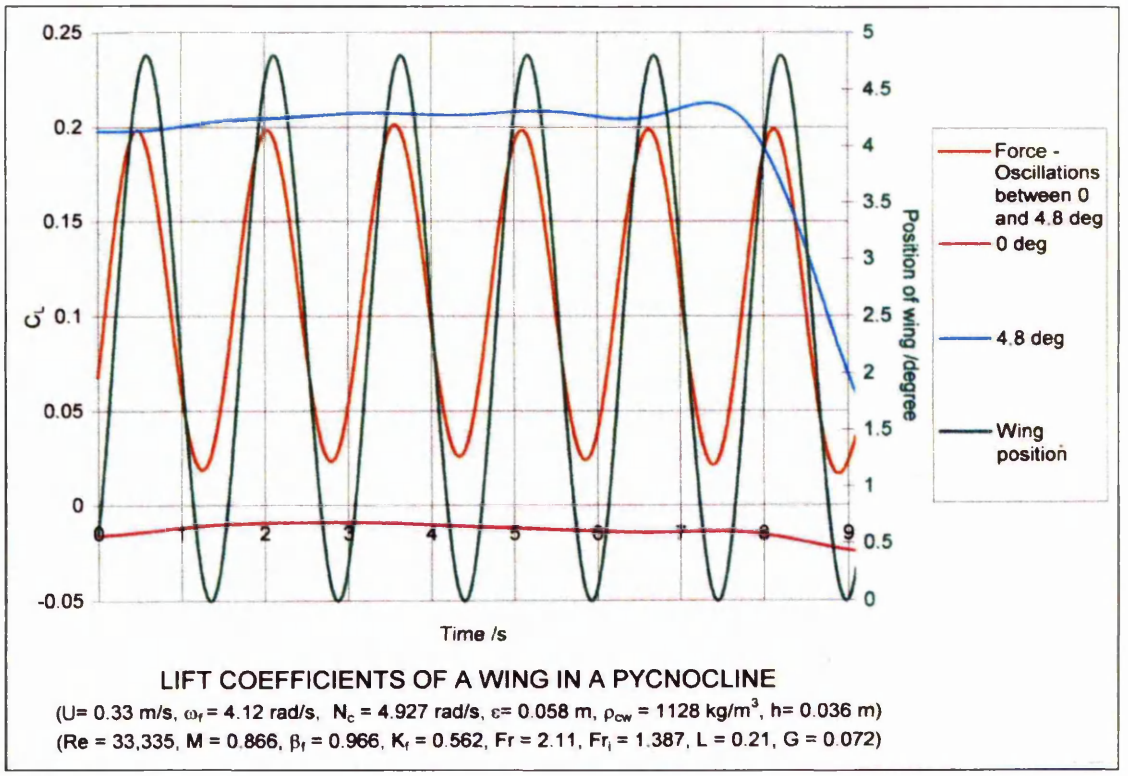

LIFT COEFFICIENTS OF A WING IN A PYCNOCLINE

(U= 0.33 m/s, ω_f = 4.12 rad/s, N_c = 4.927 rad/s, ε= 0.058 m, ρ_{cw} = 1128 kg/m^3, h= 0.036 m)
(Re = 33,335, M = 0.866, β_f = 0.966, K_f = 0.562, Fr = 2.11, Fr_i = 1.387, L = 0.21, G = 0.072)

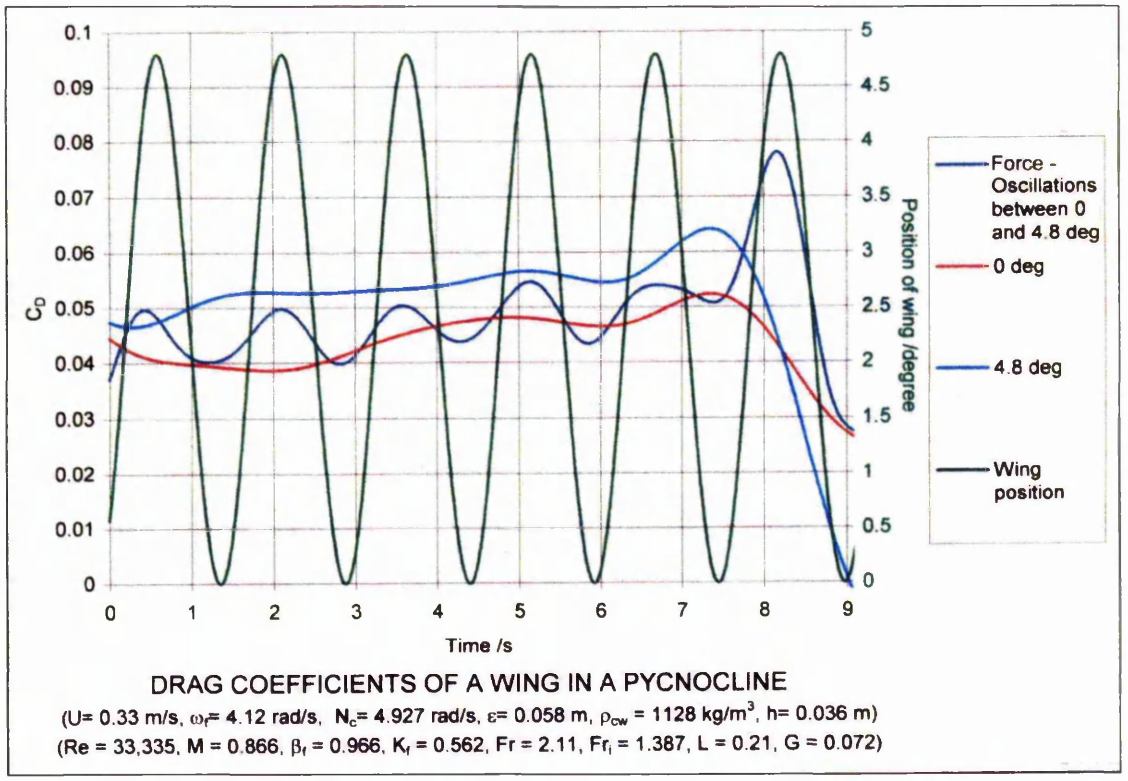

DRAG COEFFICIENTS OF A WING IN A PYCNOCLINE

(U= 0.33 m/s, ω_f= 4.12 rad/s, N_c= 4.927 rad/s, ε= 0.058 m, ρ_{cw} = 1128 kg/m^3, h= 0.036 m)
(Re = 33,335, M = 0.866, β_f = 0.966, K_f = 0.562, Fr = 2.11, Fr_i = 1.387, L = 0.21, G = 0.072)

Figures 4.88a & b The lift and drag coefficients of a NACA 0012 wing with aspect ratio 1.7 moving in a pycnocline. The density distribution of the pycnocline is shown in figure 4.103.

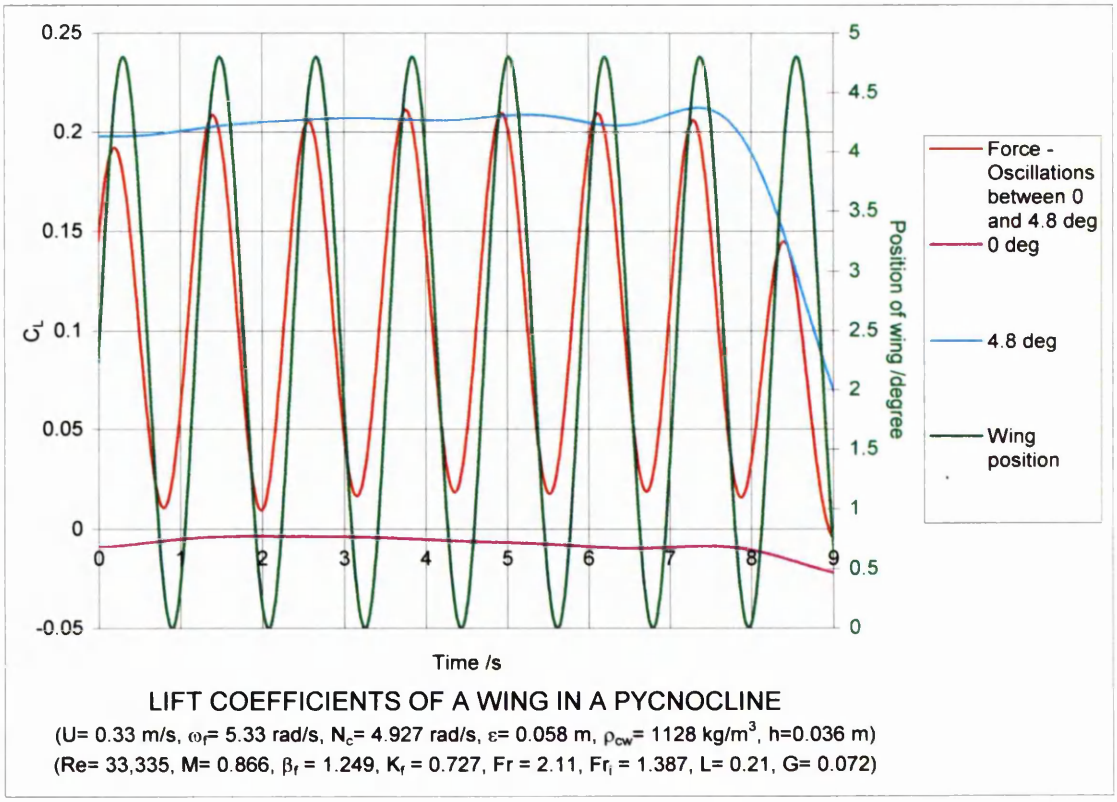

LIFT COEFFICIENTS OF A WING IN A PYCNOCLINE

(U= 0.33 m/s, ω_f= 5.33 rad/s, N_c= 4.927 rad/s, ε= 0.058 m, ρ_{cw}= 1128 kg/m^3, h=0.036 m)

(Re= 33,335, M= 0.866, β_f = 1.249, K_f = 0.727, Fr = 2.11, Fr_i = 1.387, L= 0.21, G= 0.072)

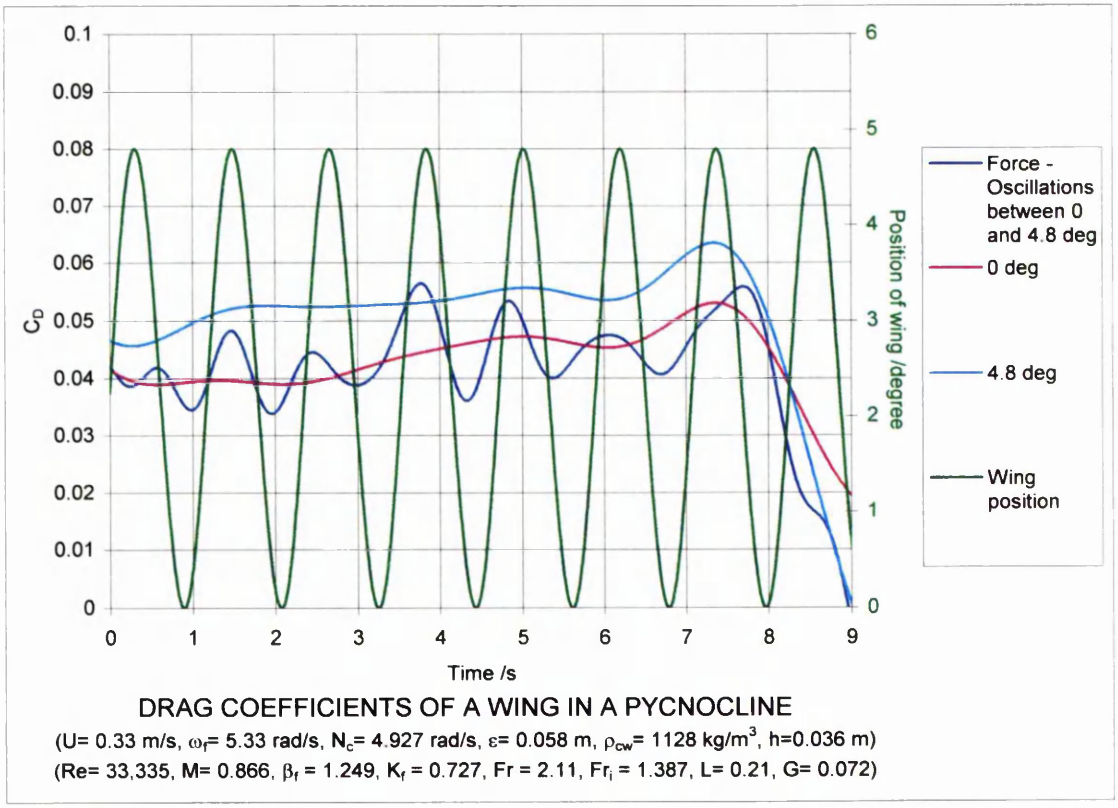

DRAG COEFFICIENTS OF A WING IN A PYCNOCLINE

(U= 0.33 m/s, ω_f= 5.33 rad/s, N_c= 4.927 rad/s, ε= 0.058 m, ρ_{cw}= 1128 kg/m^3, h=0.036 m)

(Re= 33,335, M= 0.866, β_f = 1.249, K_f = 0.727, Fr = 2.11, Fr_i = 1.387, L= 0.21, G= 0.072)

Figures 4.89a & b The lift and drag coefficients of a NACA 0012 wing with aspect ratio 1.7 moving in a pycnocline. The density distribution of the pycnocline is shown in figure 4.103.

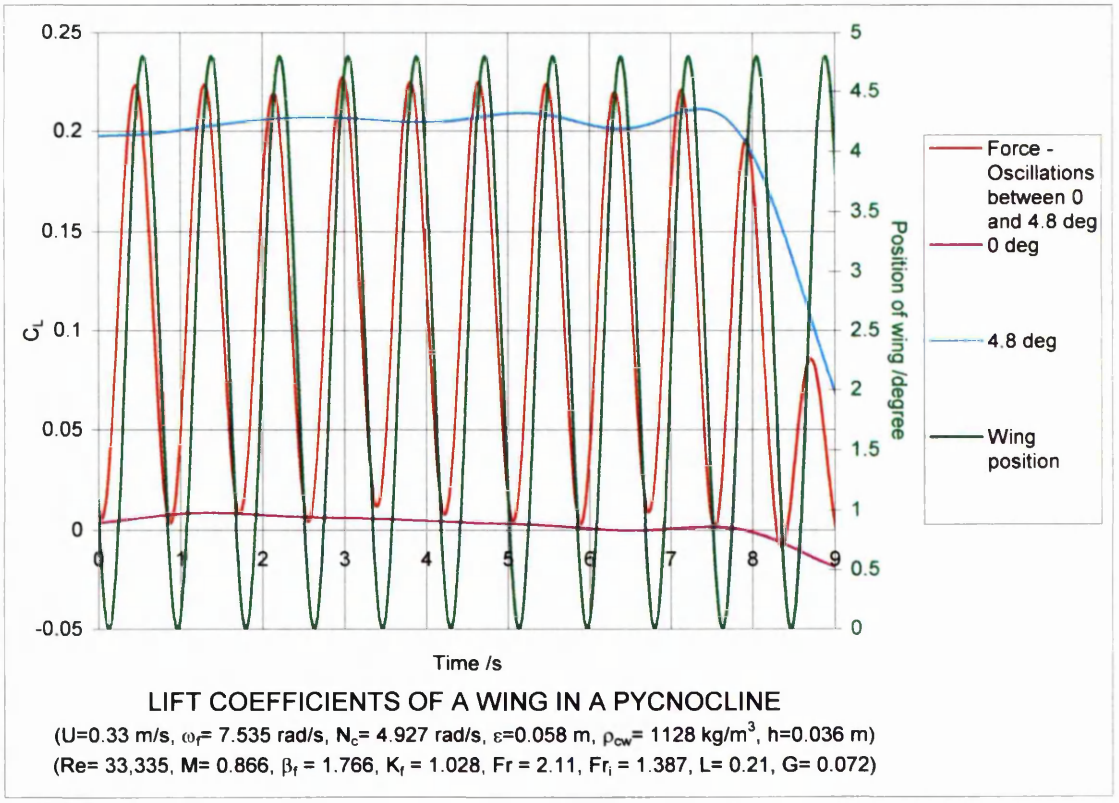

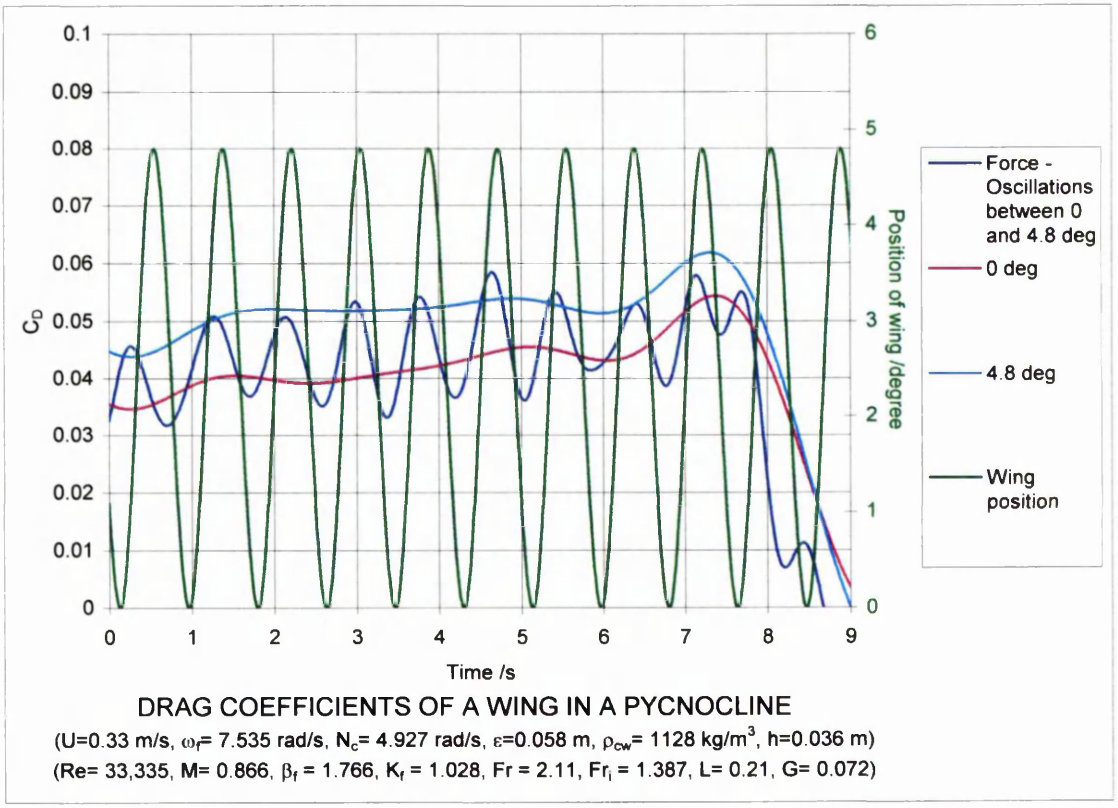

Figures 4.90a & b The lift and drag coefficients of a NACA 0012 wing with aspect ratio 1.7 moving in a pycnocline. The density distribution of the pycnocline is shown in figure 4.103.

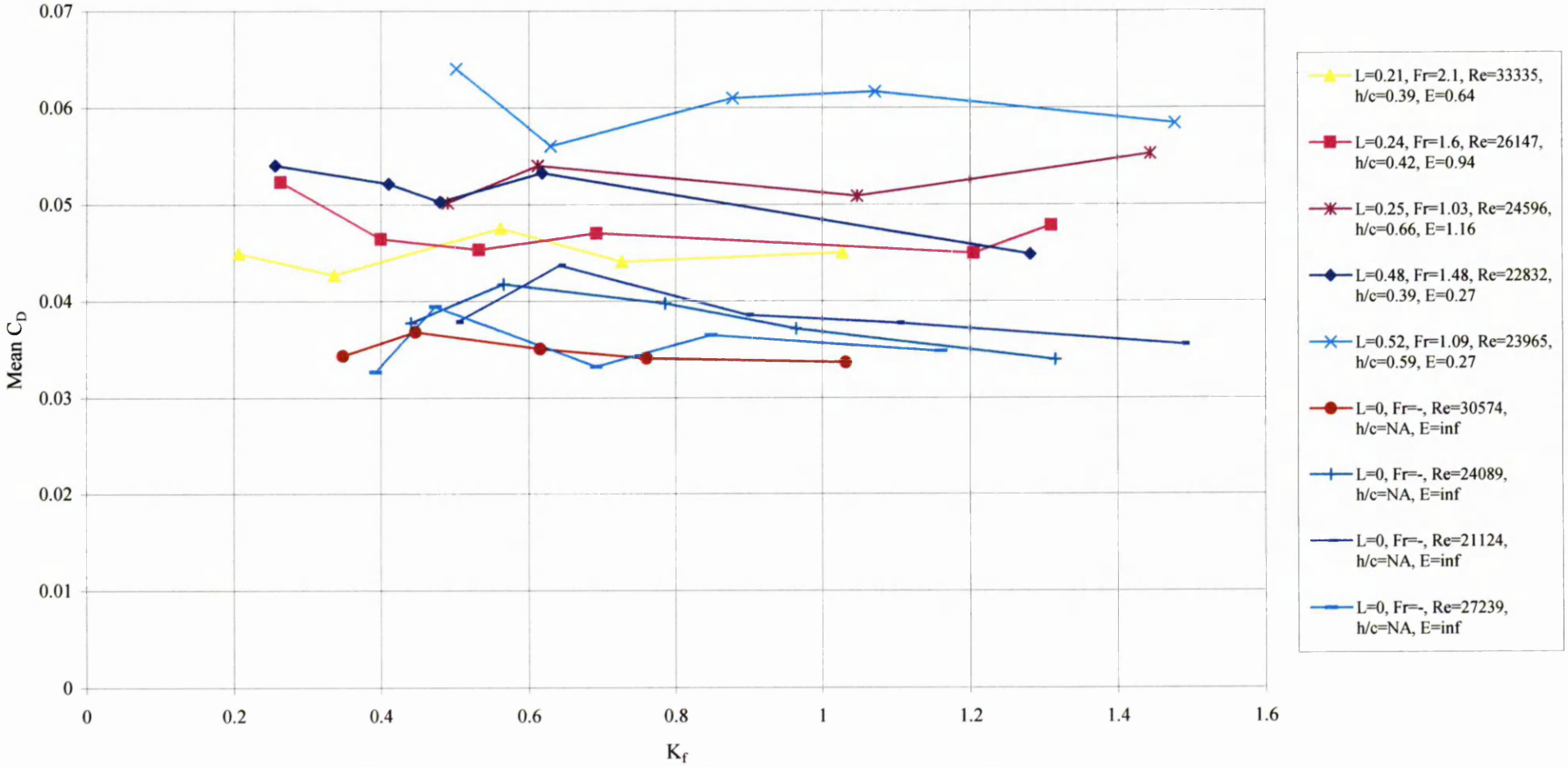

Figure 4.91 Variation of mean C_D with reduced frequency K_f

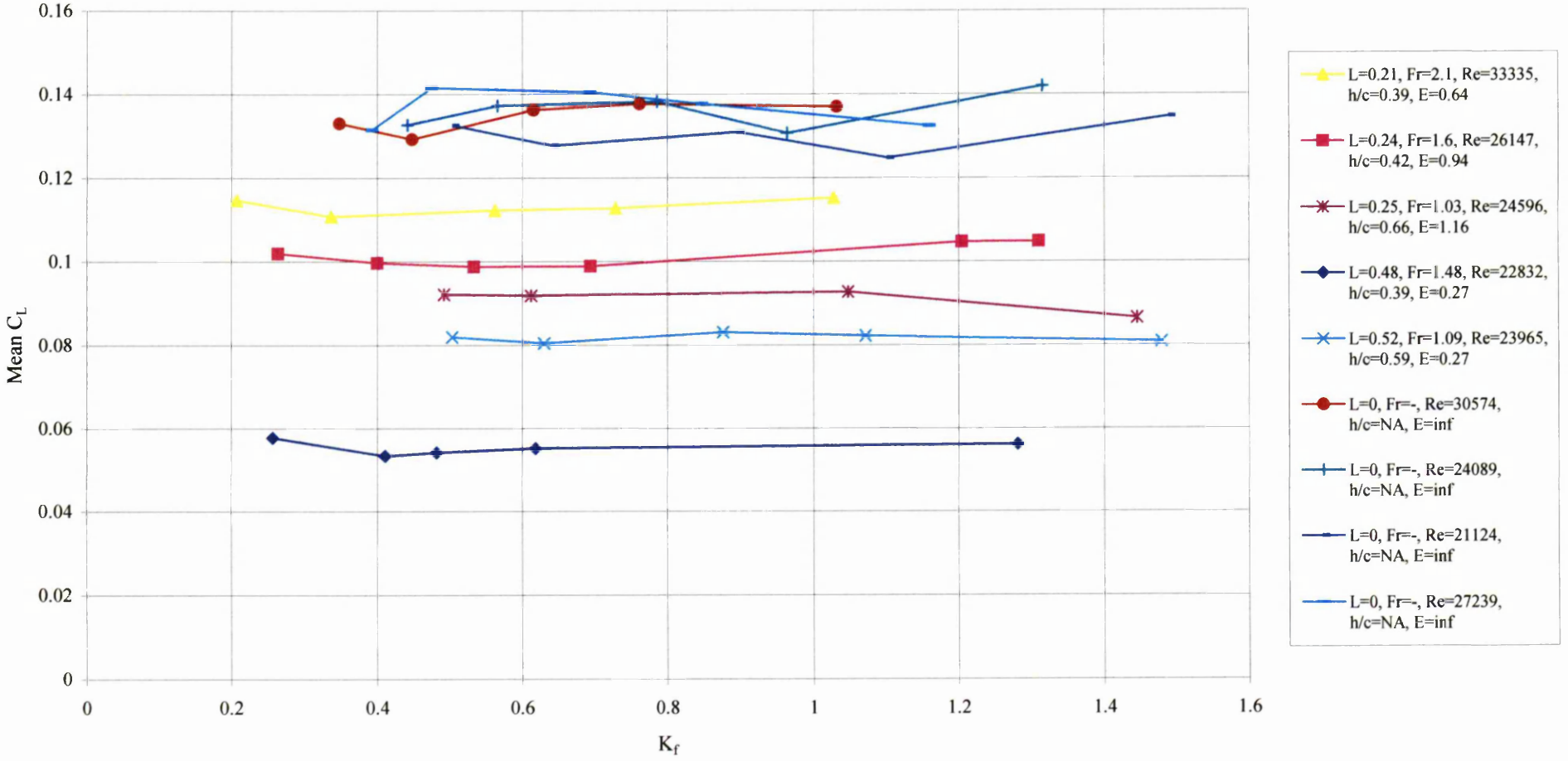

Figure 4.92 Variation of mean C_L with reduced frequency K_f

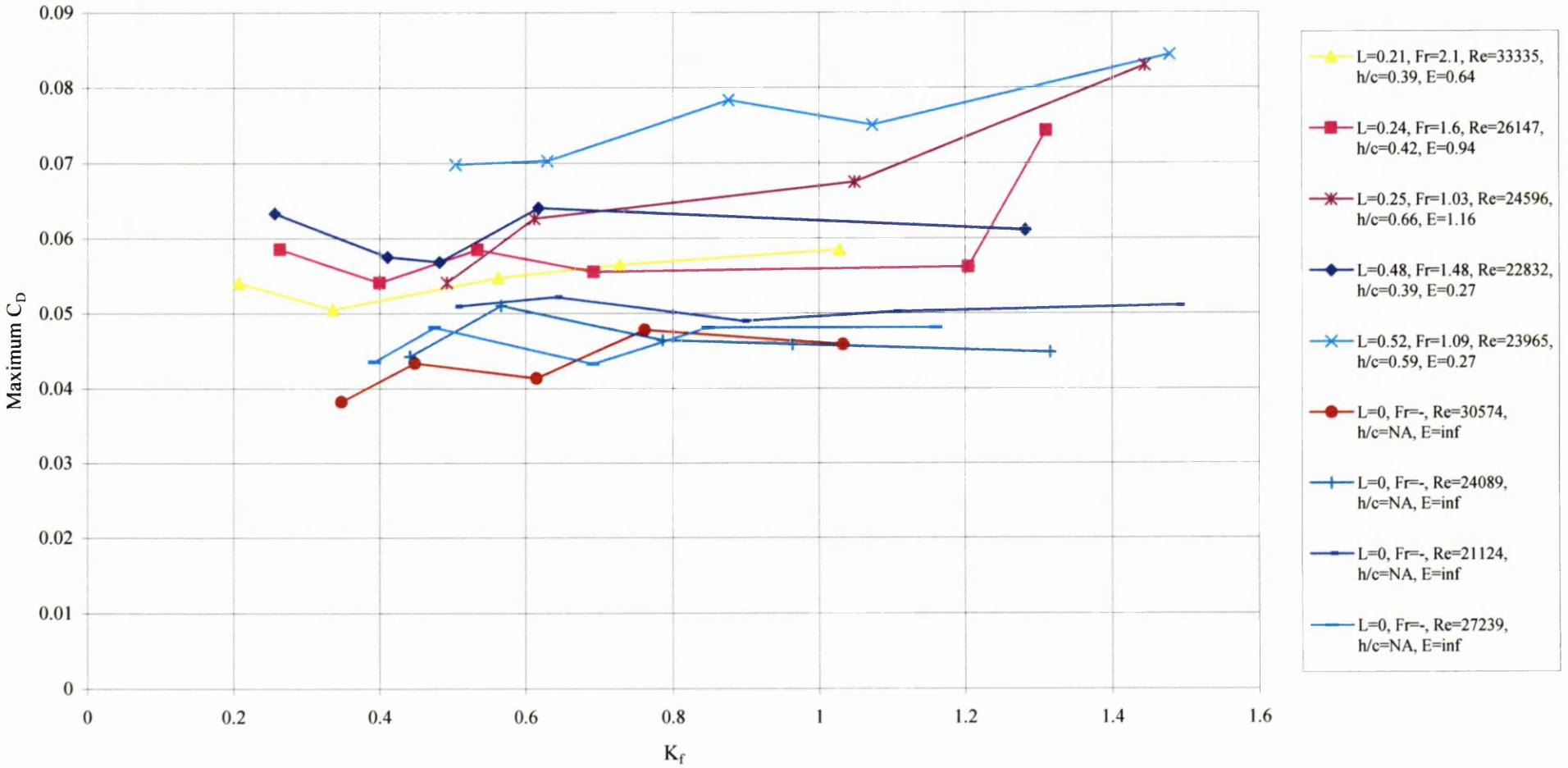

Figure 4.93 Variation of maximum C_D with reduced frequency K_f

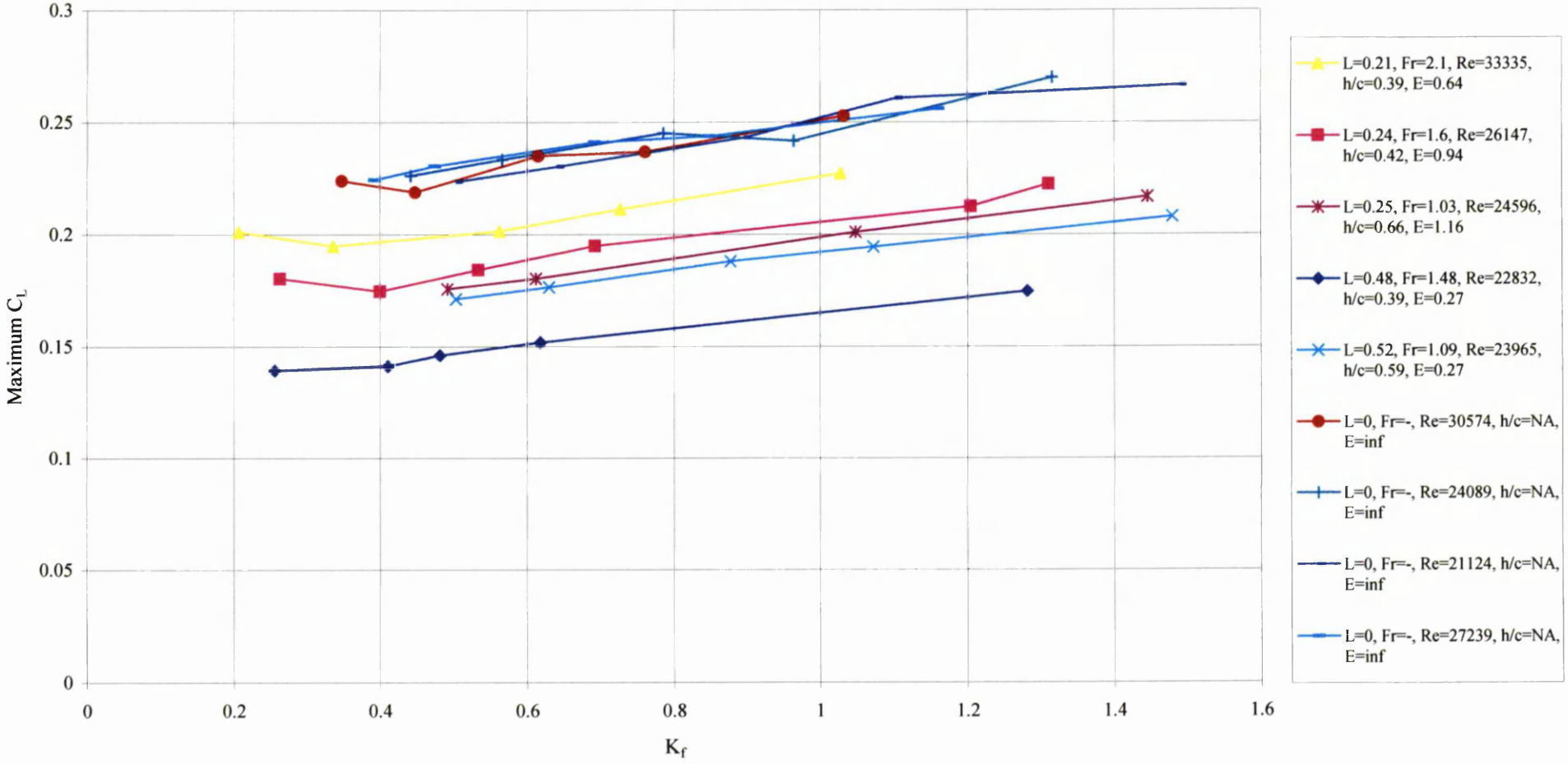

Figure 4.94 Variation of maximum C_L with reduced frequency K_f

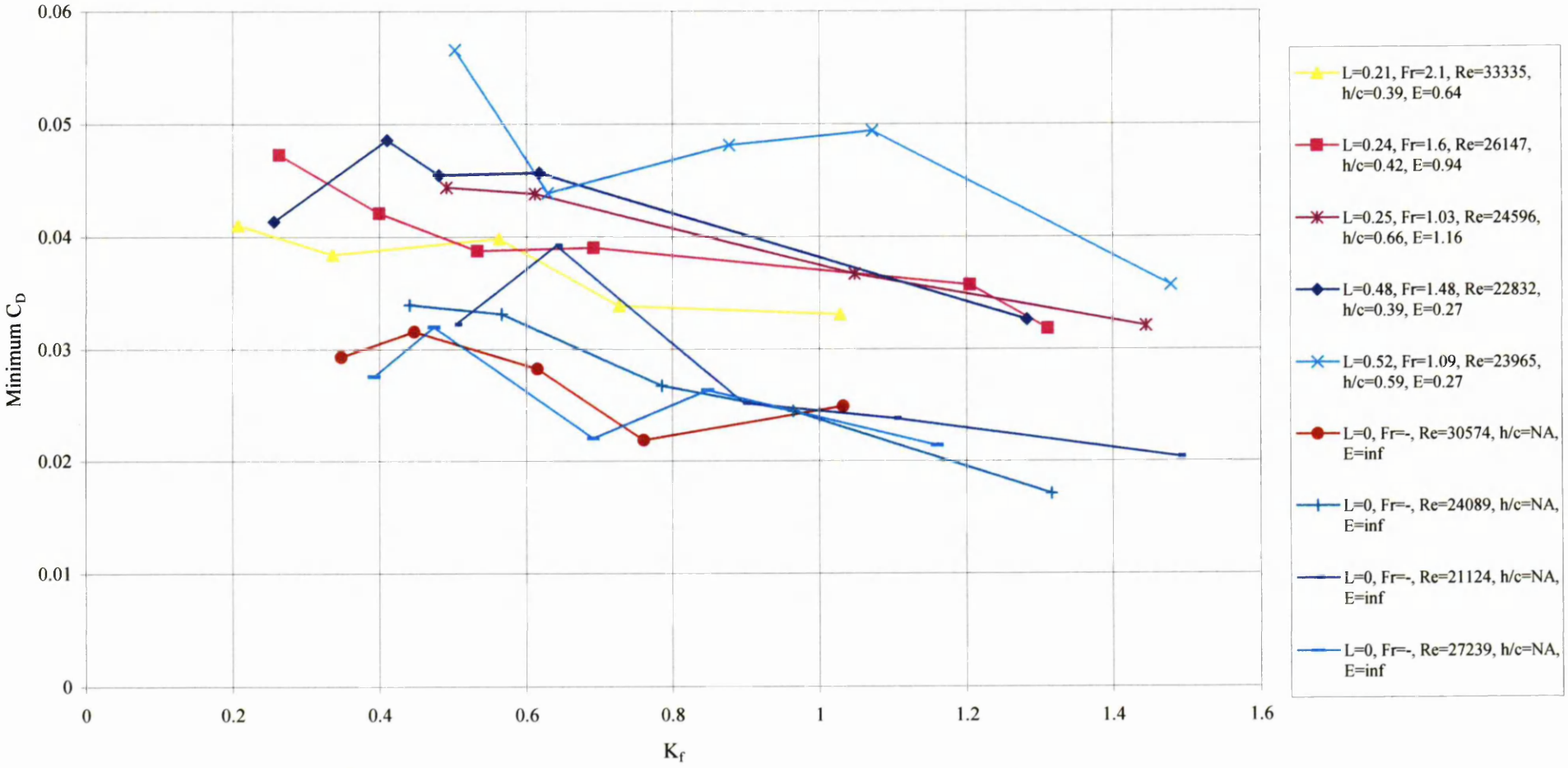

Figure 4.95 Variation of minimum C_D with reduced frequency K_f

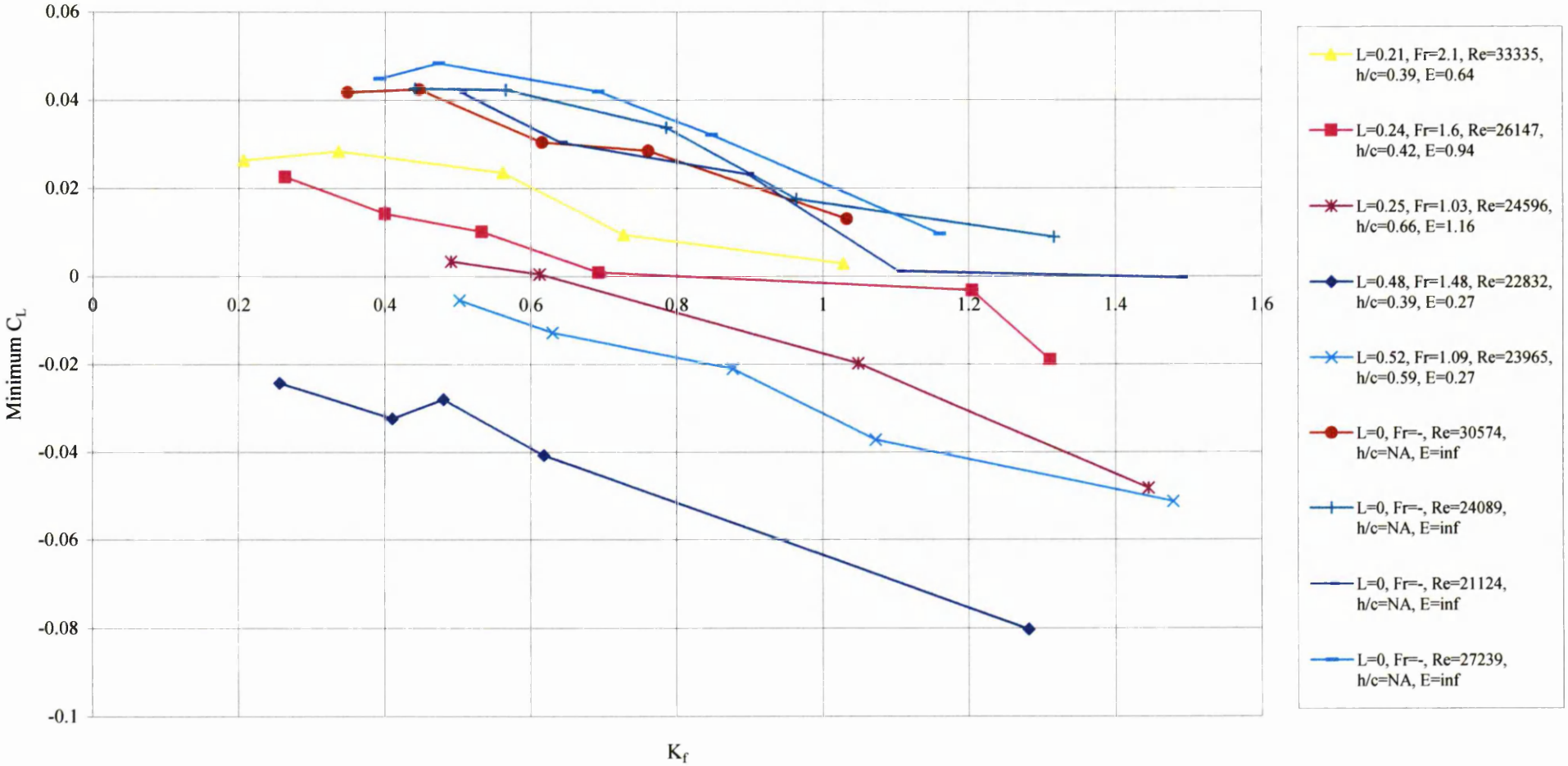

Figure 4.96 Variation of minimum C_L with reduced frequency K_f

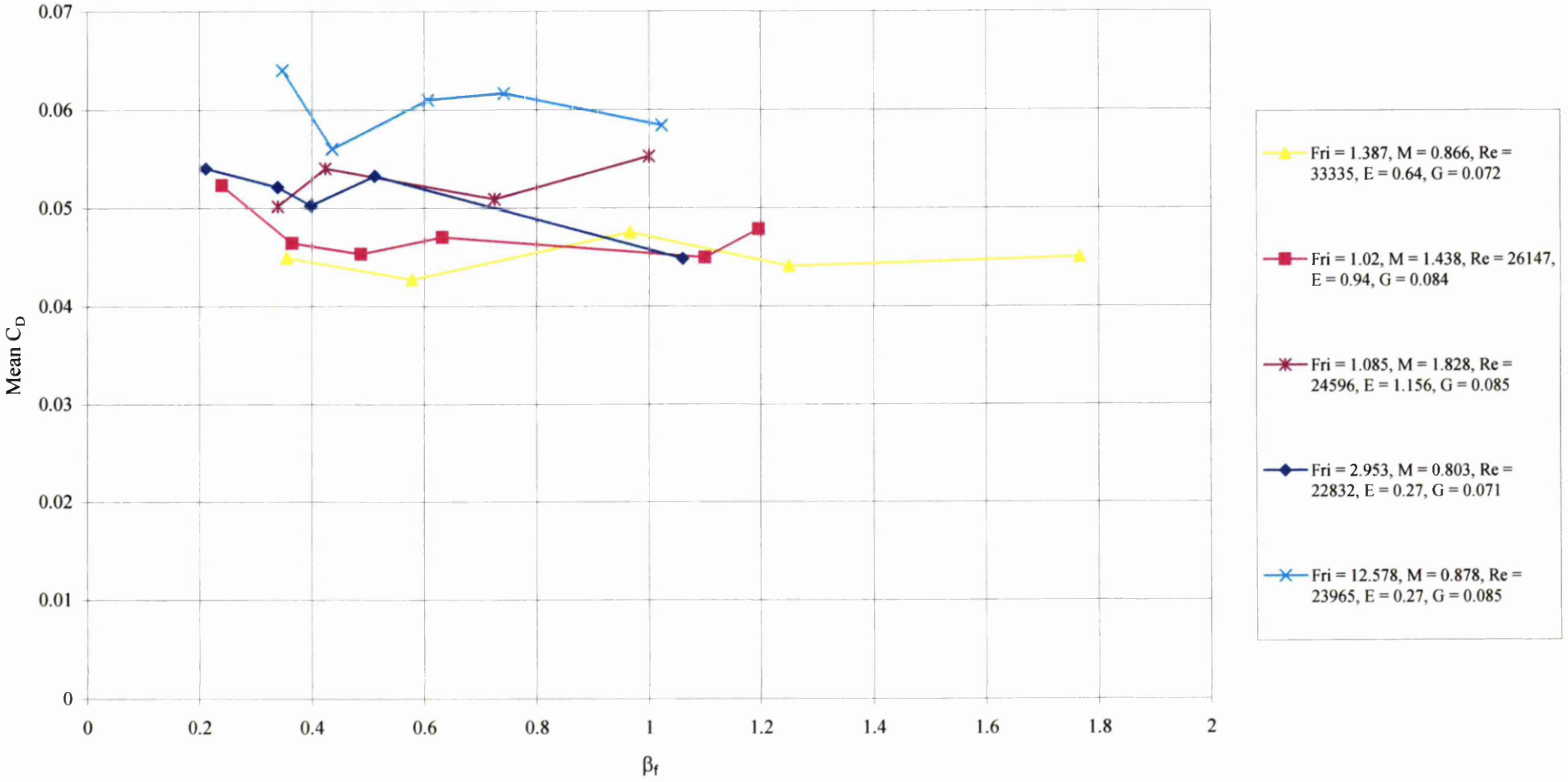

Figure 4.97 Variation of mean C_D with β_f

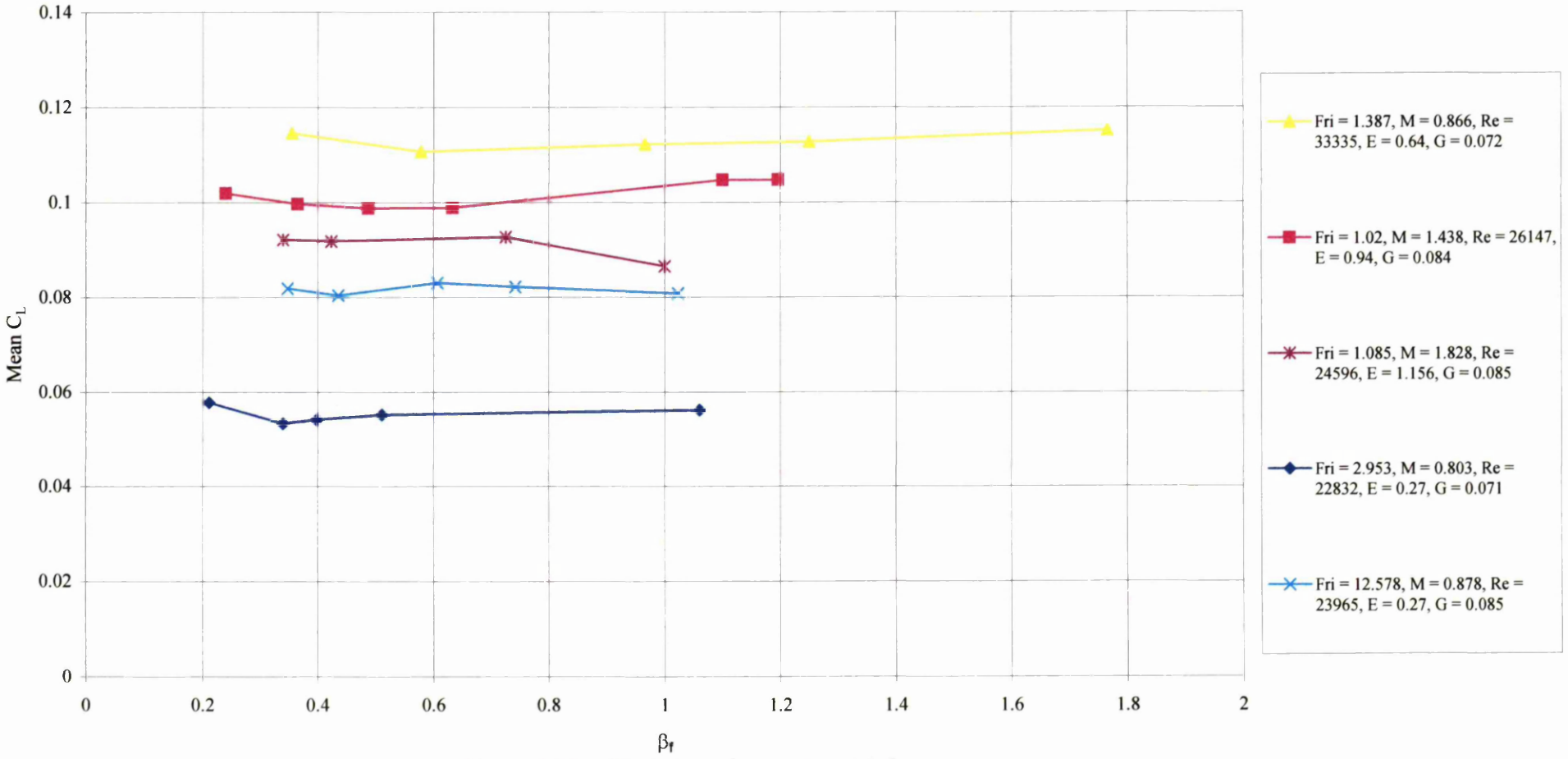

Figure 4.98 Variation of mean C_L with β_f

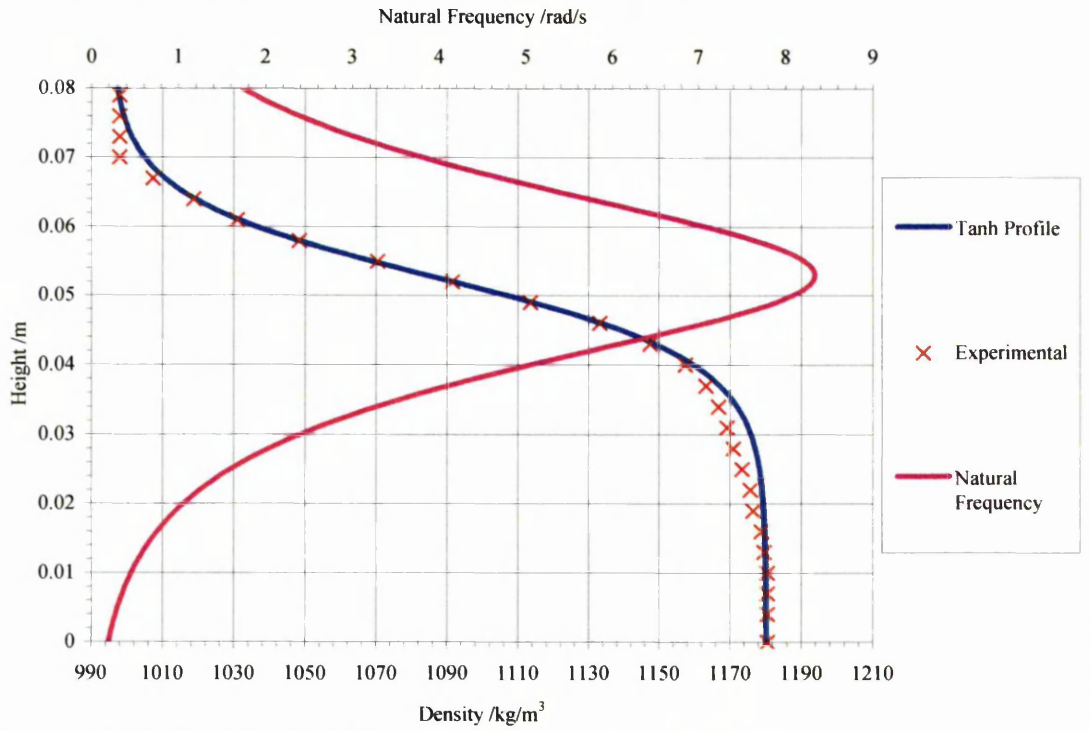

FIGURE 4.99 DENSITY AND FREQUENCY DISTRIBUTIONS

N_c = 8.342 rad/s, ε = 0.024 m, $\Delta\rho$ = 184.5 kg/m^3, ρ_c = 1084 kg/m^3, h = 0.053 m

Wing's position, height = 0 m, ρ_{cw} = 1181 kg/m^3

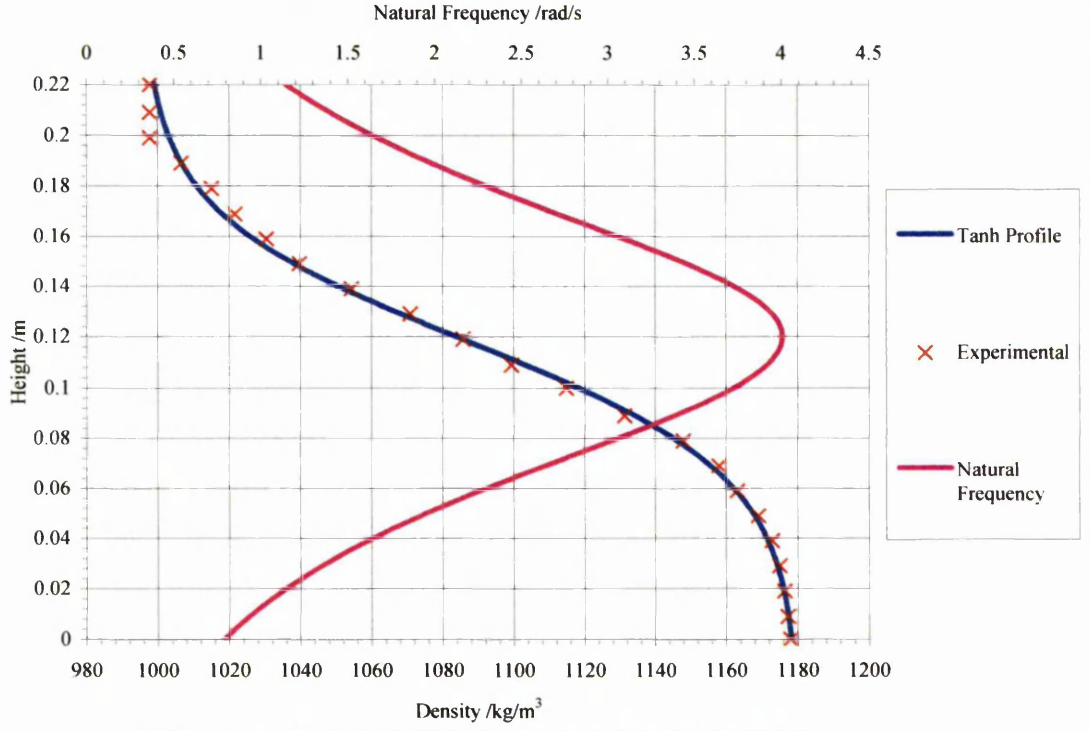

FIGURE 4.100 DENSITY AND FREQUENCY DISTRIBUTIONS

N_c = 4.01 rad/s, ε = 0.104 m, $\Delta\rho$ = 184.5 kg/m^3, ρ_c = 1084 kg/m^3, h = 0.059 m

Wing's position, height = 0.061 m, ρ_{cw} = 1162 kg/m^3

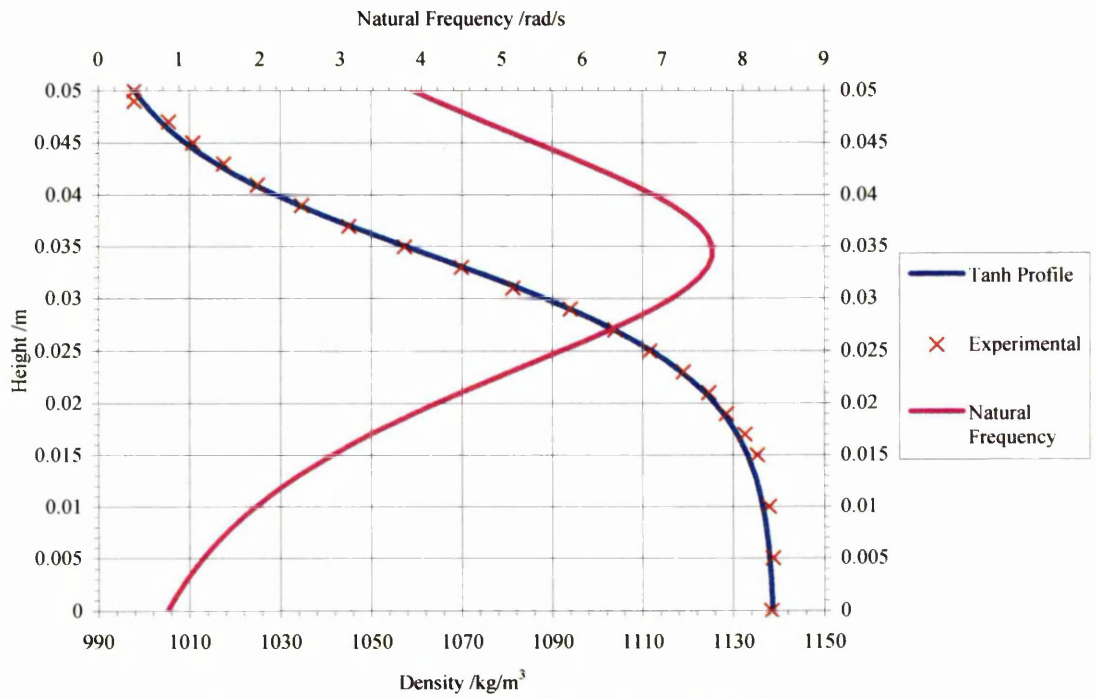

FIGURE 4.101 DENSITY AND FREQUENCY DISTRIBUTIONS

N_c = 7.628 rad/s, ε = 0.024 m, $\Delta\rho$ = 151 kg/m^3, ρ_c = 1061 kg/m^2, h = 0.035 m

Wing's position, height = 0 m, ρ_{cw} = 1139 kg/m^2

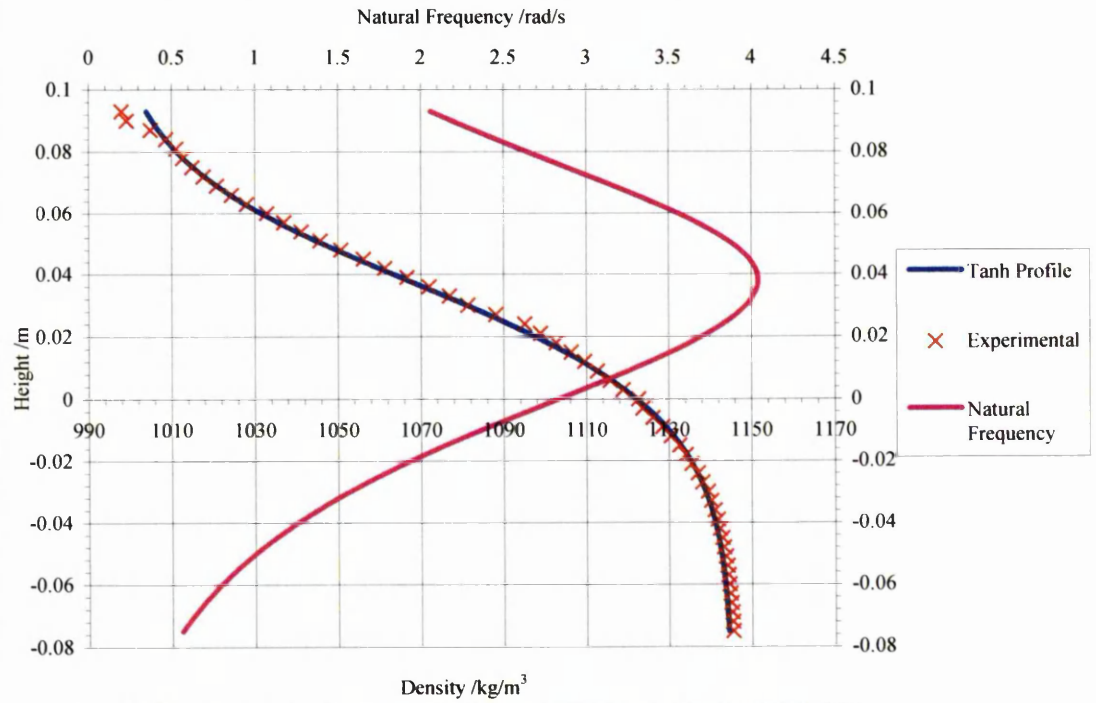

FIGURE 4.102 DENSITY AND FREQUENCY DISTRIBUTIONS

N_c = 4.4 rad/s, ε = 0.085 m, $\Delta\rho$ = 151 kg/m^3, ρ_c = 1067 kg/m^2, h = 0.038 m

Wing's position, height = 0 m, ρ_{cw} = 1123 kg/m^2

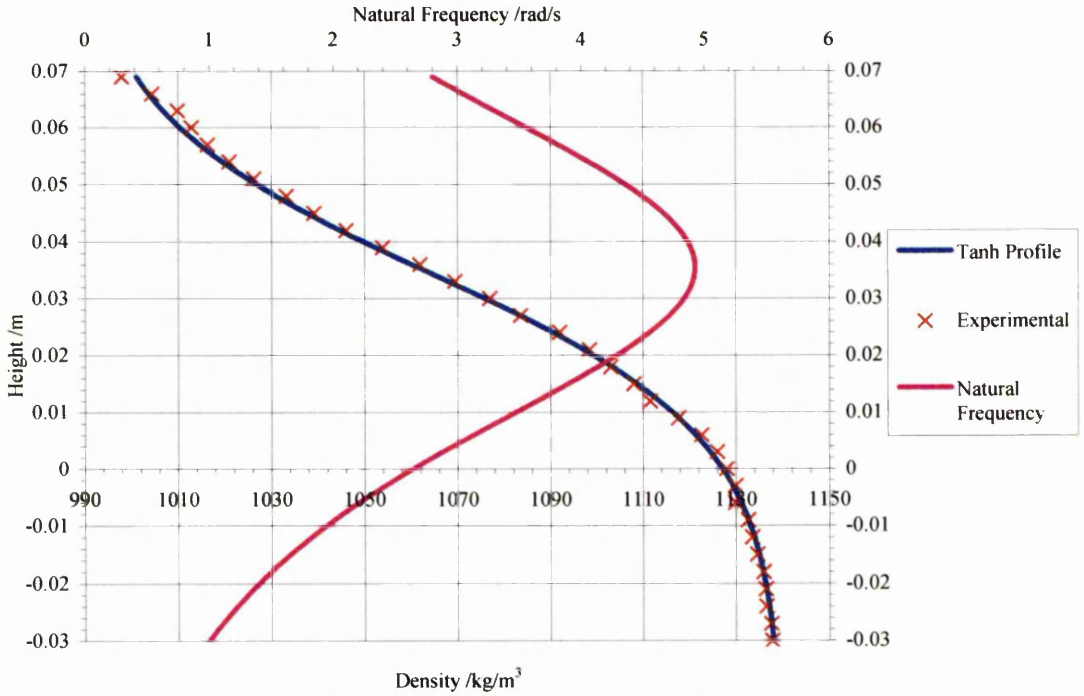

FIGURE 4.103 DENSITY AND FREQUENCY DISTRIBUTIONS

N_c = 4.927 rad/s, ε = 0.058 m, $\Delta\rho$ = 151 kg/m^3, ρ_c = 1062 kg/m^2, h = 0.036 m

Wing's position, height = 0 m, ρ_{cw} = 1128 kg/m^2

CHAPTER 5

GENERATION OF INTERNAL WAVES BY A LOW ASPECT RATIO WING

5.1 Introduction

The measurement of the forces on an oscillating wing in a pycnocline has been studied in chapter 4. The results reflect the presence of internal waves and vortices on the low aspect ratio NACA 0012 wing. In order to improve the understanding of the force readings, it is necessary to see the behaviour of fluid motion induced by the wing. Several wings of different scales but with the same section and aspect ratio will be used to study the flow.

Section 5.2 describes the experiments involving visualisations of both the plan-view and the side-view waves. The vertical and horizontal schlieren systems, as described in section 3.3, are used. Some modification to the experimental set-up as described in chapter 4 will be necessary to allow the smaller wing to oscillate about its quarter chord.

Stevenson et al (1986) have produced theory and experiments involving a cylinder moving in a pycnocline. Nicolaou & Stevenson (1997) have the theory for an oscillating source moving in a fluid with arbitrary stratification and background shear flow and presented some theoretical side-view phase configurations of an oscillating and moving point source in a constant natural frequency fluid. Section 5.3 will discuss the theory for side-view internal waves around a wing moving horizontally in a pycnocline. This theory is that produced by Stevenson et al (1986) and Nicolaou & Stevenson

(1997).

In section 5.4, the steady wave system in a wide pycnocline is studied. The side-view waves produced resemble those produced by a cylinder, Stevenson et al (1986). The plan-views show lee waves near to the wing. Away from the wing where the geometry of the source has less influence on the wave shapes, there is a gradual transformation to the 'herring bone' waves. The velocity deficit in the wake is an important consideration if the wing is travelling at high velocity.

The oscillatory waves in a wide pycnocline with and without the wing moving are studied in section 5.5. When the wing is not moving forward, the side-view waves produced look like those produced by an oscillating cylinder (Nicolaou et al 1993). There are two sources, the primary source will be the vertical displacement at the trailing edge while the movement at the leading edge will be a weaker source. With the wing moving, near the source the waves look like those theoretical phase configurations for constant N produced by Nicolaou & Stevenson (1997). These stratified waves soon become pycnocline waves away from the wing. The theory for pycnocline waves has been discussed in section 3.4.

Section 5.6 discusses the waves in a thin pycnocline. Any background flow due to the movement and the oscillatory motion of the wing will affect the whole pycnocline. The transition from stratified to pycnocline waves will be very near the source and hence it is sufficient to apply the pycnocline dispersion relation alone. As in section 3.6, the oscillatory waves were not steady relative to the source. Some of these waves are natural frequency waves and they have zero group velocity. Together with the experimental results, their phase velocities will be deduced.

In section 5.7, there is a description of some experiments on wing tip vortices produced in a pycnocline. The vortices produced during an impulsive start and those from the wing travelling for a long time are studied. There are some general comparisons with the case for a constant density fluid.

When there is a change of incidence, vortices are shed downstream of the wing. McAlister and Carr (1978) have studied the vortices from an oscillating wing, with the wing in a constant density fluid. The behaviour of the vortices depends on the frequency of oscillation and the velocity of the wing. Koochesfahani (1989) has investigated the velocity in the wake of the wing at several frequencies and the formation of the corresponding vortices. The video clips in section 5.8 will show some

trailing edge vortices from the oscillating wing in a stratified fluid. The vortices in the stratified fluid were seen to collapse quickly compared to the constant density case. Both the dye method and schlieren systems will be used to visualise the vortices.

The behaviour of a vortex dipole in a horizontal plane produced by a horizontal jet in a stratified fluid has been studied extensively by Voropayev & Afanasyev (1994). In a stratified fluid, a vortex dipole is almost two-dimensional since any vertical fluid motion will be impeded by gravity. As a result, the vortex dipole can spread to many times the size of the source. The velocity in the wake of the wing has a profile similar to those produced by a horizontal jet. The resulting dipole varies according to how the wing moves. In section 5.9, a vortex pattern produced by a move-stop-move movement of the wing will be demonstrated. The visualisation was done using colour dye.

Section 5.10 gives a summary of the important parameters for most of the video clips in the enclosed CD-ROM.

5.2 The experiments

The wing is attached to the same oscillatory mechanism as described in section 4.2.1. The model is a NACA 0012 wing with a chord length of 0.02 m and an aspect ratio of 1.7. The vertical displacement at the trailing edge remains at 5 mm and it causes the wing to oscillate through incidence angles of plus and minus 10 degrees. This range of incidence angles is well away from stall and is apparently necessary to cause enough disturbance for the pycnocline waves to be visible through the schlieren systems. The amplitude of the oscillation will not change the wave pattern in the far field. However it will increase the size of the mixing region dominated by non-linear and viscous effects. A smaller amplitude of oscillation would cause less disturbance and produce better agreement with the ray theory nearer to the body.

The wing is pin jointed at its quarter chord to a bent strut and a second similar strut oscillates the wing through another pin joint near the trailing edge. Both struts are hinged at the mid-span of the wing. The plan and side-view image of the waves can be visualized by having the vertical and horizontal schlieren systems operating simultaneously. These two systems have been described in sections 3.3.1 and 3.3.2. The knife edge was vertical so that the systems were sensitive to change of density in the horizontal direction. All the pictures are stills from the video and they are taken through the perspex sides of a tank of stratified brine. Looking from the top of the tank,

the two dark lines at the bottom of the pictures are the bent portion of the struts holding the wing. From the side views, the struts can be seen as dark columns from the top edge of the pictures.

Some of the images in this report were recorded a day after the tank had first been filled with two layers of fluid with a density difference of 168 kg/m^3. The pycnocline density and natural frequency distribution are shown in figure 5.1. The profile of the pycnocline a month later is shown in figure 5.2. More videos were also produced with this profile. There is still some light distortion but it does not affect the results significantly.

5.3 Theory

The stratified wave theory for the side-view phase configuration of a steady wave system from a body moving in a pycnocline has been presented by Stevenson et al (1986). Nicolaou & Stevenson (1997) have extended the theory to an oscillating moving disturbance in a flow with arbitrary stratification and background shear. The natural frequency and the shear flow velocity are functions of the vertical co-ordinate z. Their experimental results include two-dimensional schlieren images for steady waves from a moving source in an arbitrary stratification with background shear. The theory is capable of producing a three-dimensional wave system, but only two-dimensional results comparable with the experimental images were produced. In this section, a simplified two-dimensional version of the theory which is applicable to the current experimental results will be discussed.

When a wing moves horizontally in a pycnocline, the fluid in the wake of the wing will move in the direction of the wing motion. If the wing oscillates about its quarter chord, the fluid near the trailing edge is being pushed in the opposite direction away from the wing. The net direction of the fluid movement in the wake of the wing depends on the frequency of oscillation and the velocity of the wing. This background flow velocity of the fluid relative to space that exists only in the wake of the wing is termed U_{bg}. U_{bg} should be a function of x, z, and t, but in the theory discussed in this section, U_{bg} is a function of z only.

Near to the wing, the side-view wave patterns can be compared with the two-dimensional theoretical phase configurations of an oscillating point source moving in a constant buoyancy frequency fluid, Nicolaou & Stevenson (1997). The ray tracing

method described in section 2.6 and implemented in section 3.4 can be adopted to find the phase configurations of waves moving in a vertical plane. Instead of the pycnocline dispersion relation (equation 2.6), the stratified dispersion relation (equation 2.4) for two-dimensional inviscid incompressible waves in a vertical plane [x , z] will be used. The dispersion relation with natural frequency, N(z), and velocity $U_{bg}(z)$ near to the trailing edge of the wing is given by

$$\omega = kU_{bg}(z) + \gamma(N(z))\sqrt{\frac{k^2}{k^2 + (m(z))^2}} = kU_{bg}(z) + \omega_r \qquad (5.1)$$

where [k, m(z)] are the x and z components of wavenumber **k**, $\gamma = \pm 1$ and ω_r is the frequency of the fluid relative to the background. The horizontal wavenumber, k, and ω, remain constant along a ray path but ω_r varies along the path. U_{bg} is the background velocity of the fluid in the positive x-direction and is a function of the vertical coordinate z.

If $$\sin(\theta(z)) = \frac{k}{\sqrt{k^2 + (m(z))^2}}$$

and $$\cos(\theta(z)) = \frac{-m(z)}{\sqrt{k^2 + (m(z))^2}}$$

then $$\omega = kU_{bg}(z) + \gamma(N(z))|\sin(\theta(z))| \qquad (5.2)$$

where $\theta(z)$ is the angle between the phase velocity vector and the vertical. $\theta(z)$ is also the angle the ray path makes with the horizontal and is measured anticlockwise from the positive x-direction. N(z), $\theta(z)$ and the vertical wavenumber component m(z), are functions of z only. If the source were travelling horizontally with velocity, U, in the positive x-direction as shown in figure 5.3 then the frequency of the energy as it leaves the source satisfies the Doppler relation,

$$\omega = \omega_f + Uk \qquad (5.3)$$

where ω_f is the frequency of oscillation.

Equations (5.2) and (5.3) give

$$\omega_r = \gamma(N(z))|\sin(\theta(z))| = \omega_f + (U - U_{bg}(z))k. \qquad (5.4)$$

The group velocity relative to the background flow is given by

$$\mathbf{u}_{gr} = \left[\frac{\partial\omega_r}{\partial k}, \frac{\partial\omega_r}{\partial m}\right] = [u_{gr}, w_{gr}] = \frac{N(z)^2 km}{\omega_r(k^2 + m^2)^2}[m, -k]$$

or $$\left[u_{gr}, w_{gr}\right] = U_{gr}\left[\cos\theta, \sin\theta\right] = \frac{\omega_r}{k}\left[\cos^2\theta, \sin\theta\cos\theta\right]. \qquad (5.5)$$

where $U_{gr} = \left(u_{gr}^2 + w_{gr}^2\right)^{1/2}$. The group velocity relative to space is then

$$\left[u_g, w_g\right] = \left[u_{gr}, w_{gr}\right] + \left[U_{bg}, 0\right]. \qquad (5.6)$$

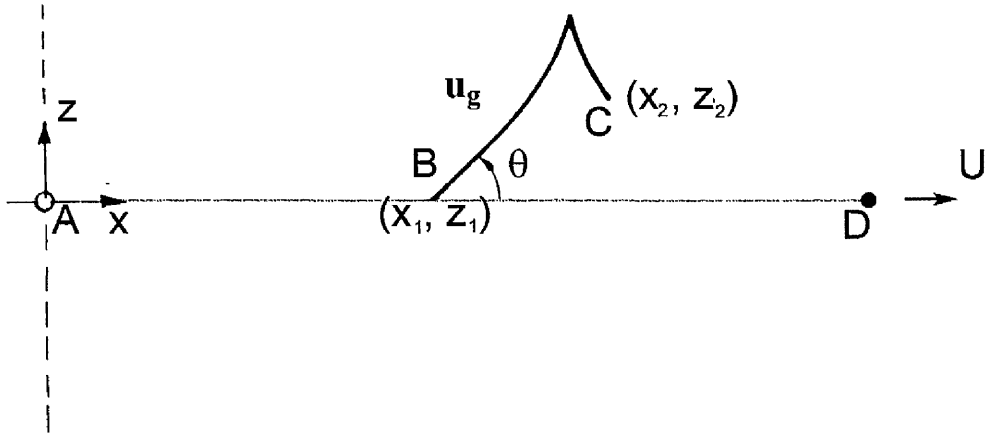

Figure 5.3 The side view co-ordinate system for stratified waves

Referring to figure 5.3, at time t_0, the body moves with speed U from the origin to position D in $(t_2 - t_0)$ seconds. At any time t_1, such that $t_0 < t_1 < t_2$, energy of frequency ω leaves the source at B and reaches point C at t_2 with its phase given by

$$\phi_2 = \phi_0 - \omega_f\left(t_1 - t_0\right) + \int_{t_1}^{t_2} \frac{D\phi}{Dt} dt + \phi_r \qquad (5.7)$$

where $\phi_0 - \omega_f\left(t_1 - t_0\right)$ is the phase at t_1 and ϕ_r is the total of the phase shift that occur each time the energy reaches the caustics. $\frac{D\phi}{Dt} = \frac{\partial\phi}{\partial t} + u_g\frac{\partial\phi}{\partial x} + w_g\frac{\partial\phi}{\partial z}$ is the rate of change of phase of the energy in the x-z plane as it propagates along its ray. The phase at any instant is $\phi = \left(kx + mz - \omega t\right)$ and hence

$$\omega = -\frac{\partial\phi}{\partial t}, \qquad k = \frac{\partial\phi}{\partial x}, \qquad m = \frac{\partial\phi}{\partial z}. \qquad (5.8)$$

Equations 5.6 and 5.8 give

$$\frac{D\phi}{Dt} = -\omega + \left(u_{gr} + U_{bg}\right)k + w_{gr}m. \qquad (5.9)$$

The relative group velocity vector and the wavenumber vector are mutually

perpendicular, i.e. $\mathbf{u_{gr}}\cdot\mathbf{k} = 0$. From equation (5.1), equation (5.9) can be written as

$$\frac{D\phi}{Dt} = -\omega + U_{bg}k = -\omega_r . \tag{5.10}$$

Hence from equation (5.7), the phase at t_2 is given by

$$\phi_2 = \phi_0 - \omega_f(t_1 - t_0) + \int_{t_1}^{t_2}(-\omega_r)dt + \phi_r , \tag{5.11}$$

where $\int_{t_1}^{t_2}(-\omega_r)dt = -\int_{t_1}^{t_2}(\omega_f + k(U - U_{bg}))dt$ is the phase shift that occurs as the energy moves along the ray path in time $t_2 - t_1$. The shape of the ray path depends on U_{bg}. The phase equation can be re-arranged to give

$$\phi_2 = \phi_0 + \phi_r - \omega_f(t_2 - t_0) - \int_{t_1}^{t_2} k(U - U_{bg})dt . \tag{5.12}$$

Each value of horizontal wavenumber k remains unchanged along a ray path,

$$dx = u_g\,dt = (u_{gr}+U_{bg})dt, \qquad dz = w_g\,dt = w_{gr}\,dt \tag{5.13}$$

and

$$\frac{dx}{dz} = \frac{u_{gr} + U_{bg}}{w_{gr}} . \tag{5.14}$$

Now

$$t_2 - t_1 = \int_{z_1}^{z_2}\frac{k}{\omega_r \sin\theta\cos\theta}dz \tag{5.15}$$

and

$$x_2 - x_1 = \int_{z_1}^{z_2}\left(\cot\theta + \frac{U_{bg}k}{\omega_r \sin\theta\cos\theta}\right)dz . \tag{5.16}$$

To integrate the phase equation with z, from equations (5.12) and (5.15),

$$\phi_2 = \phi_0 + \phi_r - \omega_f(t_2 - t_0) - \gamma k^2 \int_{z_1}^{z_2}\frac{U - U_{bg}}{N|\sin\theta|\sin\theta\cos\theta}dz \tag{5.17}$$

or

$$\phi_2 = \phi_0 + \phi_r - \omega_f(t_2 - t_0) - k\int_{z_1}^{z_2}\frac{J}{\cos\theta\sin\theta}dz \tag{5.18}$$

where

$$J = 1 - \frac{\gamma\omega_f}{N|\sin\theta|} . \tag{5.19}$$

The position of the energy relative to the body, x_b, can be found from equation (5.16)

$$x_b = \int_{z_1}^{z_2}\cot\theta dz - \gamma k\int_{z_1}^{z_2}\frac{U - U_{bg}}{N|\sin\theta|\sin\theta\cos\theta}dz . \tag{5.20}$$

Any energy that leaves the body will have to satisfy the two conditions, the magnitude of $k > 0$ and $dt > 0$. From equation (5.4), the first condition becomes

$$k = \frac{\gamma N|\sin\theta| - \omega_f}{U - U_{bg}} > 0 .$$

In terms of J,

$$k = \frac{\gamma N|\sin\theta|}{U - U_{bg}} J > 0 \qquad (5.21)$$

and since $N|\sin\theta| > 0$, the first condition simplifies to $\pm \frac{J}{U - U_{bg}} > 0$.

and since $N|\sin\theta| > 0$, the first condition simplifies to $\pm$

From equations (5.4) and (5.13), the second condition, $dt > 0$ gives

$$dt = \frac{dz}{w_{gr}} = \frac{\omega_r - \omega_f}{(U - U_{bg})\omega_r \sin\theta\cos\theta} dz > 0$$

and

$$dt = \frac{J}{(U - U_{bg})\sin\theta\cos\theta} dz > 0. \qquad (5.22)$$

Along a ray, $\frac{dz}{\sin\theta} > 0$ and the second condition becomes $\frac{J}{(U - U_{bg})\cos\theta} > 0$.

Equation (5.18) gives the time taken for the energy to move along the ray and equation (5.20) gives the x-position of that energy. These equations will be used when looking at the side view pictures of the waves around an oscillating wing. The energy travels into a background flow induced by the moving wing.

Nicolaou et al (1995) have also shown how the plan-view phase configurations can be obtained from the stratified dispersion relation (5.1) by evaluating average group velocities in a horizontal plane at the centre of the pycnocline when there is no shear.

When an oscillating body moves horizontally very slowly the side view of the oscillatory waves are slightly modified arms of the St. Andrew's cross-wave. The initial width of the arms depends on the amplitude of oscillation and the size of the body. Away from the source, the arms curve due to the change in background natural frequency and widen because of viscous effects. Eventually, the energy will fill the whole pycnocline in the form of pycnocline waves. This transition is a combined result of viscosity, wave path curvature and the superposition of waves, and the details have been discussed by Nicolaou et al (1993). Far away from the source, the plan-view waves can be obtained by the method used in section 3.4.

5.4 Steady waves in a wide pycnocline, $\omega_f = 0$

Figures 5.4 to 5.7 show plan and side-views of the steady waves produced by a wing, with an incidence angle fixed at 10 degrees, moving from left to right at various velocities. The narrow wake from the wing can be seen in all figures showing the side-view waves. Notice that the side-view steady wave system is not exactly symmetrical about the centre of the pycnocline which may suggest that the wing was slightly above the centre of the pycnocline. However, the positive incidence angle could have contributed to this effect. Figure 5.4 shows the side-view waves with the wing travelling at U = 4.03 mm/s, the steady waves are hardly visible. Above U = 7.57 mm/s, the side-view wave shapes have many of the features found in the waves around a moving horizontal cylinder (Stevenson et al 1986). For a horizontal cylinder which is very small compared with the thickness of the pycnocline, the waves close to the cylinder are almost semicircular as predicted by theory. However, in the wake region the semi-circle is dented towards the body. The size of the dent increases as the ratio of body diameter to wave diameter increases. This effect is particularly noticeable in the wing side-view photographs where the wake from the wing at 10 degrees incidence is fairly strong at speed of U = 7.57 mm/s and above. Looking at the plan-view waves, it appears that the struts are modifying the waves slightly. The plan-view images also show how the lee waves near the wing finally transform into far field waves having the 'herring bone' shape. This is shown clearly in figures 5.6a and 5.7a. This transformation can complicate the side-view waves as each span-wise cross sectional vertical plane is no longer the same. If the wing has a higher aspect ratio, then the lee waves should continue for a longer distance after the wing and the side-view waves will look closer to those produced by Stevenson et al (1986). The plan-view images also show that the lee waves are very much confined within the span of the wing.

The still images in figures 5.6 and 5.7 are also presented in video clips as listed in table 5.1.

Figure number	Video clip number	Velocity of wing (m/s)
5.6	150	1.44×10^{-2}
5.7	148	0.021

Table 5.1 Video clips in the CD-ROM corresponding to figures 5.6 and 5.7.

5.5 Oscillatory waves in the wide pycnocline of figure 5.2

5.5.1 Without forward velocity

The wing was made to oscillate at 2.29 rad/s about its quarter chord. Figure 5.8a & b show the top and side-views. The figures described in this section are collections of still images, some of which are available in video clips 138p, 138s, 141p, 141s, 142p, 142s. The 'p' indicates plan-view and 's' indicates side-view. The motion represents vertical oscillations at the leading and trailing edges. The top-views show circular waves of slightly longer wavelength near to the wing and constant wavelength further away. If the vertical disturbance was at the centre of the pycnocline, the mode of oscillation should be even. The cross-wave from the trailing edge was stronger than the one from the leading edge because of its larger amplitude. Initially the leading edge cross waves could just be seen but they soon appeared to be overwhelmed by the widening of the trailing edge cross-waves. This can be clearly seen in video clips 138s and 142s. The inviscid theory described in section 5.3 with U = 0 cannot account for the width of the cross-wave. The figures show that the arms tend to widen away from the source as explained by the viscous theory provided by Thomas & Stevenson (1972) for a St Andrew's cross-wave. In a pycnocline, the natural frequency N varies with height so that the beams are curved. The angle of the beam to the horizontal is given by

$$\theta(z) = \pm \sin^{-1}\left(\frac{\omega_f}{N}\right)$$

from equation (5.2) with $\omega = \omega_f$ and a negligible U_{bg}. $\theta(z)$ is measured anticlockwise from the positive x-direction. Near the caustics, the beams bend towards the vertical. At the caustics, where the reflection of the waves occurs, ω_f is equal to the local background natural frequency. There will be a phase shift in time of $\pi/2$ lag in the vertical velocity component and a $\pi/2$ lead in the horizontal velocity component, Lighthill (1978). For each frequency of oscillation, the horizontal wavenumber k and the frequency of the fluid oscillations ω remain constant along the arms. Figure 5.11, which is from figure 5.8b, shows the directions of the phase velocities as indicated by the red arrows. The intermediate region consists of a transition to pycnocline waves which can be treated with ray theory. The far field can also be dealt with by either the ray theory or the simplified dispersion relation discussed in section 3.4.

The distance between the successive crests or troughs are slightly larger near to

the wing and transition to pycnocline waves took place about 3 to 4 chord lengths away. Nicolaou et al (1993) have shown in detail how stratified waves produced by an oscillating cylinder develop into pycnocline waves.

Figures 5.9 and 5.10 show the side-views of the wing oscillating at 1.56 rad/s and 2.48 rad/s. The angle θ between the arms of the cross-waves and the horizontal increases with the frequency of oscillation ω_f. Video clips 151 to 156 show the plan-view and side-view waves produced at several different frequencies of oscillation.

Clip number	Frequency of oscillation (rad/s)
151p &s	2.82
152p & s	2.63
153p & s	2.44
154p & s	2.29
155p & s	1.87
156p & s	5.66

Table 5.2 Frequencies of oscillations for video clips 151 to 156.

Video clip 151s shows an oscillation very near to the background natural frequency where θ is seen to be almost π/2. The theory for a stationary oscillating source tell us that there is no solution with frequency higher than the background natural frequency. However due to the nature of the wing oscillation about its quarter chord, there was a small negative background velocity, $-U_{bg}$, at the trailing edge of the wing. For a constant density fluid, the velocity profile of U_{bg} can be described by a sech function, but with stratified fluid there will be an extra vertical velocity component due to gravity. With U = 0, the arms make an angle θ measured anti-clockwise from positive x-direction and is given by equation (5.4),

$$\theta(z) = \pm \sin^{-1}\left\{\frac{\omega_f - U_{bg}k}{N}\right\}.$$

The background velocity effectively reduces the value of the numerator such that it is less than N. However, since this oscillation induced background flow is only confined to a narrow region approximately equal to the vertical displacement of the trailing edge, the waves cannot travel far above this region. Away from the wing, the magnitude of U_{bg} also tends to fall off rapidly and the wavelength of the train of waves will decrease

before disappearing completely when $\left|\frac{\omega_f - U_{bg}k}{N}\right| \geq 1$. Video clip 151p shows the plan-view image which gives a clearer indication of the waves vanishing as the magnitude of U_{bg} is reduced.

Video clip 156p & s shows a train of waves confined within a thin wake behind an oscillating wing at a frequency well above the background natural frequency. These waves appear to be present because of $-U_{bg}$, but were further complicated by the effects of turbulence. The net background flow remains a function of the frequency of oscillation and the properties of the pycnocline.

5.5.2 With forward wing velocity, $U \neq 0$

The experiments were repeated with an oscillating wing moving in the direction shown by the black arrows in figures 5.12 to 5.17. The plan-view figures show waves that have many features similar to those found in section 3.6. However the transition to pycnocline waves took place over a larger distance due to the wider pycnocline and also the near field waves were modified by the geometry of the wing. Within the frame of observation, there will be transitions from stratified waves to pycnocline waves near to the source. This transition normally takes place over 3 to 5 body lengths away from the source depending on the thickness of the pycnocline, the velocity and the oscillation frequency of the source. The pycnocline wave theory should show good agreement in the far field.

Figures 5.12 shows the side-view of the waves produced by an oscillating wing when the velocity was 2.16 mm/s. Both the plan-view and side-view images are shown together in figures 5.13a and b. There are forward moving waves and this is verified by the plan-view wavenumber surfaces shown in figure 5.18 with M = 234 and $\beta_f = 3.48 \times 10^{-3}$. The surfaces are produced by the same approach as described in section 3.7. There are two surfaces for each value of β_f, the left surface has $-\beta$ while the right branch has $+\beta$. Figure 5.18 plots only the branch with $+\beta$ since this is where the solutions for the waves observed in the image are found. With this relatively large value of M, the waves associate with $-\beta$ will be extremely tiny. The effect of increasing M on the size of the waves with $-\beta$ can be seen by comparing figures 3.26b and 3.27b. The forward moving waves all around the source belong to the oval near to the origin. These

waves have very small wavenumbers and large wavelengths with high group velocities and cannot be easily identified from the still image and are best seen in motion from video clip 144p and 144s.

The positions of the energy relative to the source at any one time can also be deduced from the two conditions stated in section 5.3, equations (5.21 and 5.22). The two conditions are that the magnitude of the horizontal wavenumber is greater than zero, hence $\pm\frac{J}{(U-U_{bg})\cos\theta} > 0$, and the radiation condition must be satisfied, and $(U-U_{bg})>0$ for a body moving in positive x-direction. The results in the form of radiation diagrams have been presented by Nicolaou & Stevenson (1997) for a constant N fluid. All the experimental images in figures 5.12 to 5.17 correspond to the case for γ = +1 and $\frac{\omega_f}{N} < 1$ where γ is the $\pm$ sign in equation (5.19). The side-view phase configurations were also provided by Nicolaou & Stevenson (1997) for constant N. Very near to the source, before the energy is reflected at the caustics, the general positions of the energy for the pycnocline case should resemble those of the constant N case. However each ray of energy does bend according to the background natural frequency.

Figure 5.13a and b have $\frac{\omega_f}{N_c} = 0.815$ and most of the energy seen has a positive relative frequency. From the stratified wave theory, these waves have $\gamma = +1$, and away from the body they become pycnocline waves with $+\beta$. The waves with $\gamma = -1$ near the narrow wake of the source are either destroyed by turbulent mixing or simply are too weak to be seen. These are waves with negative relative frequency, corresponding to the pycnocline waves with $-\beta$. Figure 5.12 illustrates the directions in which the energy radiated for the case when U = 2.16 mm/s and ω_f = 2.29 rad/s. The energy with phase velocities indicated by the green arrows have J > 0 and cosθ > 0, whereas those shown by the red arrows have J < 0 and cosθ < 0. All the energy shown here has U > 0, γ = +1 and $\frac{\omega_f}{N} < 1$. Further to the left of figure 5.12 is the transition to pycnocline waves where the theory in section 3.4 can be applied. The steady wave system is too weak to be seen.

At U = 4.03 mm/s, again forward moving waves could be seen, figure 5.14a and b. The corresponding video clips are 143p and 143s. This observation is verified by the wavenumber surface corresponding to $\beta_f = 6.5\times10^{-3}$ shown in figure 5.19. The directions in which the energy radiates remain the same as the case in figure 5.12.

Figures 5.15 to 5.17 show the oscillating wing travelling at U = 7.60 mm/s, 11.0 mm/s and 14.4 mm/s. These figures show strong steady waves but no forward moving oscillatory waves. The side-view transverse waves fail to move ahead of the wing. Figures 5.20 and 5.21 show the wavenumber surface for U = 7.60 mm/s and 14.4 mm/s. The waves in figure 5.15 correspond to the branch with $\beta_f = 1.22\times10^{-2}$ in figure 5.20 and those in figure 5.17 have $\beta_f = 2.32\times10^{-2}$ in figure 5.21. Unlike the first two cases with $\beta_f = 3.48\times10^{-3}$ in figure 5.18 and $\beta_f = 6.5\times10^{-3}$ in figure 5.19, where one of the wave number surfaces for the appropriate value of β_f was cylindrical, no such surface occurs for the conditions of figures 5.15 and 5.17. Again the experimental wave system is in agreement with the theoretical wave number surfaces.

Table 5.3 lists all the figures in this section corresponding to their video clips and velocities. The frequency of oscillation, ω_f is 2.29 rad/s, N_c = 2.81 rad/s and ε = 0.18 m for all cases.

Figure number	Video clip number	Velocity of wing (mm/s)
5.13a & b	144p & s	2.16
5.14a & b	143p & s	4.03
5.15a & b	145p & s	7.57
5.16a & b	146p & s	11.0
5.17a & b	147p & s	14.4

Table 5.3 Video clips in the CD-ROM corresponding to figures 5.13 to 5.17.

The directions in which the energy radiates for constant N and high frequency of oscillation, such that $\frac{\omega_f}{N}>1$, are given by Nicolaou & Stevenson (1997). However, there can be no waves if, from equation (5.4),

$$|\sin\theta| \quad \text{or} \quad \left|\frac{\omega_f + (U - U_{bg})k}{\gamma(N)}\right| \; > \; 1.$$

Near to 1, the waves will be confined to a narrow wake similar to those shown in video clips 151s and 156s. This is because the waves cannot extend outside the region where there is no background flow.

5.6 Oscillatory waves in the thin pycnocline of figure 5.1

If the pycnocline thickness is thin, the transition to pycnocline waves can be very near to the source and pycnocline theory as discussed in section (3.4) can be applied. The dispersion relation is given by

$$\omega = U_{bg} K \cos\psi + \omega_{rh} \qquad (5.23)$$

where U_{bg} is the background velocity in the positive x-direction at the trailing edge of the wing and it is a function of y. ψ is the angle made by the horizontal group velocity and the positive x-direction as defined in figure 3.3 and ω_{rh} is the frequency of the fluid relative to the background fluid. From equation (3.1),

$$\omega_{rh} = \frac{\gamma(\varepsilon N_c K)}{\sqrt{(\varepsilon K)^2 + 2m\varepsilon K + (m^2 - 1)}} \qquad (5.24)$$

where $\gamma = \pm 1$ and K is the magnitude of the horizontal wavenumber. m is equal to 2n+1 where n is the mode of the pycnocline oscillation, ε is the pycnocline thickness and N_c the natural frequency at the centre of the pycnocline. The Doppler relation is $\omega = \omega_f + UK\cos\psi$ where ω_f is the oscillatory frequency of the wing, and U is the velocity of the source. Hence the two equations yield

$$\omega_{rh} = \omega_f + (U - U_{bg})K\cos\psi . \qquad (5.25)$$

Taking $\cos\psi = 1$ for waves travelling parallel to the path of the source and as $K = \frac{2\pi}{\lambda}$, the wavelength λ is given by

$$\lambda = \frac{2\pi(U - U_{bg})}{\omega_{rh} - \omega_f} . \qquad (5.26)$$

The phase velocity relative to the background fluid is

$$\frac{\lambda\omega_{rh}}{2\pi} = V_{Pr} = \frac{U - U_{bg}}{1 - \frac{\omega_f}{\omega_{rh}}} \qquad (5.27)$$

and relative to space, the phase velocity is

$$(V_P)_{space} = V_{Pr} + U_{bg} = \frac{1}{\left(1 - \frac{\omega_f}{\omega_{rh}}\right)}\left[U - \left(\frac{\omega_f}{\omega_{rh}}\right)U_{bg}\right] . \qquad (5.28)$$

For natural frequency oscillations relative to the background fluid, $\omega_{rh} = N_c$ and λ and V_{Pr} from equations (5.26), (5.27) and (5.28) become

$$(\lambda)_{\omega_{rh}=N_c} = \frac{2\pi(U - U_{bg})}{N_c - \omega_f}, \tag{5.29}$$

$$(V_{Pr})_{\omega_{rh}=N_c} = \frac{U - U_{bg}}{1 - \frac{\omega_f}{N_c}} \tag{5.30}$$

and

$$(V_P)_{space,\omega_{rh}=N_c} = V_{Pr} + U_{bg} = \frac{1}{\left(1 - \frac{\omega_f}{N_c}\right)}\left[U - \left(\frac{\omega_f}{N_c}\right)U_{bg}\right]. \tag{5.31}$$

When the wing is moving without oscillation, $\omega_f = 0$ and U_{bg} is the velocity deficit in the wake of the wing. In stratified fluid, the presence of U_{bg} when $\omega_f = 0$ is only confined to a horizontal plane with a width equivalent to the span of the wing. Any vertical motion of the fluid will be limited by the effect of gravity. Other than in the wake of the wing, the majority of the flow field is not affected by the presence of U_{bg} and hence from equation (5.30), V_{Pr} is equal to the wing velocity U. In the wake, the phase velocity relative to space is given by $(V_p)_{space} = V_{Pr} + U_{bg}$. With $\omega_f = 0$, $(V_p)_{space} =$ U and the wave crests move at the same speed as the wing. This analysis is verified by video clip 83.

If $\omega_f \neq 0$ and $\frac{\omega_f}{N_c} < 1$, the mean magnitude of U_{bg} relative to U depends on factors such as ω_f, and its distance away from the wing, but is certainly less than U. Hence it can be shown from equation (5.31) that $(V_p)_{space} >$ U and the wave crests move toward the wing. Examples of these phenomena are shown in video clips 121 and 122. The group velocity relative to the background fluid is zero so these natural frequency waves do not appear in front of the wing. The waves moving ahead of the wing are part of the oscillatory wave system at frequencies other than N_c and the directions in which the energy travels can be determined by the wavenumber surface approach as discussed in section 3.7.

For high ω_f such that $\frac{\omega_f}{N_c} > 1$, then U_{bg} can be in the direction opposite to U. $(V_p)_{space}$ is negative and hence the wave crests can move away from the wing in the opposite direction to U. Two very good examples are video clip 164p and 165p, where $\frac{\omega_f}{N_c} = 1.3$. Video clip 166 has the same value of $\frac{\omega_f}{N_c}$, but the wave system is complicated

by the presence of the steady wave system.

If $\omega_f = N_c$ both V_p and λ are infinite so that the schlieren system will not show the waves. Note that the existence of U_{bg} is only confined to a narrow wake approximately the span of the wing with an initial height equal to the vertical displacement of the trailing edge during oscillation. Outside this region the phase velocity is only sensitive to the velocity of the wing, U. However with a thin pycnocline, the disturbance will produce a background flow which is significant compared to the pycnocline thickness.

5.6.1 Without forward wing velocity

Figure 5.22a to h show a series of images with increasing frequency of oscillation when the wing is not moving forward. The wing was made to oscillate at each frequency for a short while for the waves to develop. Figures 5.22a to 5.22f have ω_f below N_c and figure 5.22f has $\omega_f = 8.13$ rad/s which is just below N_c at 8.19 rad/s. Note that only those with oscillation frequencies less than 6.3 rad/s have waves in front of the wing. For a stationary oscillating streamline body there are waves all around the source. Video clips 31 and 48 show plan-view images. For a thin pycnocline these waves can be described by the dispersion relation in equation (5.24) and no waves appear when $\omega_f > N_c$.

In the case of a wing the waves are affected by the geometry. The circular oscillatory wave system appears to become weaker as $\omega_f \rightarrow N_c$ and the wavelength as predicted by theory approaches zero. However the schlieren system is less sensitive to very small wavelengths. As the circular waves become weaker a different wave system dominates. If these waves are natural frequency waves then the wavelength from equation (5.29) is

$$\lambda = \left| \frac{2\pi U_{bg}}{\omega_f - N_c} \right| \qquad (5.32)$$

and from equation (5.31),

$$(V_P)_{space,\omega_{rh}=N_c} = \frac{-U_{bg}}{\left(\frac{N_c}{\omega_f} - 1\right)}. \qquad (5.33)$$

Waves are also present when the oscillatory frequency is above N_c. Small

amplitude theory tells us that no wave energy will leave the source and therefore no waves will be visible when $\omega_f > N_c$. What is happening is that the wing oscillation about its quarter chord is producing a small flow of velocity U_{bg} from the trailing edge from right to left in the pictures. An example of this is in video clip 156p with $N_c = 2.7$ rad/s and $\omega_f = 5.66$ rad/s. $\frac{\omega_f}{N_c} > 1$, U_{bg} is negative and V_p in this case is also negative which indicates a velocity from right to left. Observation from the clip suggests that the phase velocity, $(V_p)_{space}$, a chord length to the left of the wing's trailing edge is about 10.3 mm/s. From equation (5.33), $U_{bg} = 5.4$ mm/s and the wavelength $\lambda = 11.5$ mm from equation (5.32). By direct measurement from the still of the video clip, the wavelength is 12.3 mm. Further away from the trailing edge, U_{bg} becomes smaller and the wavelength decreases accordingly. There are no waves when U_{bg} becomes zero.

Figure 5.22i to 5.22o show stills from a run in which there was a continuous decrease in the frequency of oscillation, except at $\omega_f = 13.14$ rad/s, 6.64 rad/s and 6.14 rad/s where the wing was allowed to oscillate at a fixed frequency for a short while.

5.6.2 With forward wing velocity

When the body is moving with a forward velocity U, the natural frequency waves have their wavelength and phase velocity described by equations (5.29) and (5.31). There will be a velocity deficit in the wake of the wing, unless the frequency of oscillation is so high as to cause a flow in the opposite direction. When this happens, the wing will have a thrust rather than a drag. Regardless of the flow direction, waves in the wake of the source will be subjected to a background flow which will modify their shape from those which are outside the wake. The background flow velocity is relative to the free stream velocity. Near to the trailing edge, the background flow will be the strongest and away from the wing, will weaken until it virtually disappears altogether. There will be shear due to the velocity gradient between fluid in the wake and that outside the wake. Near to the wing, there will be wing tip vortices and turbulence in the wake which will eventually disappear by viscous dissipation, however the net velocity flow remains dependent on the frequency of oscillation and the velocity of the source. A good example of the wave pattern produced is video clip 104. Near to the wing, there are lee waves in the wake which are subjected to the background flow. There is a discontinuity between the waves in the wake near to the wing and the 'herring bone'

wave structure outside the wake. The theoretical herring bone system is produced by a point source. At this velocity, it appears that the pressure difference is too weak to cause the roll-up of the wing tip vortices. Further away from the wing where the velocity deficit is reduced significantly, the waves in the wake join with those outside the wake. There are still some other waves in the path of the source and they appear to come from the struts supporting the wing.

Other examples of the waves in and outside the wake of the wing are shown in video clips 77 to 88. Video clips 77, 81 and 82 show a stalled wing with the vortex shedding at the trailing edge of a wing travelling at 29 mm/s. The frequency of the vortex shedding appears to be higher than the natural frequency, hence producing oscillatory waves moving away from the wing. Similar evidence can also be found at higher velocities of 47 mm/s, 65 mm/s and 87 mm/s, video clips 78, 79 and 80 respectively are similar cases with the wing moving at higher velocities. In video clips 83 to 88, the wing was in a slightly wider pycnocline.

In figure 5.23a to c, the wing is moving at 7.8 mm/s with 3 different frequencies of oscillation ranging from 3.58 to 7.88 rad/s. Forward moving waves can be seen in figure 5.23a but they are not obvious in figure 5.23b. The waves in figure 5.23c are moving left relative to the wing. Figures 5.25a and b show the wave number surfaces for mode 0 and mode 1 oscillations for U = 7.8 mm/s. The branches which correspond to each value of β_f can be found in the legend box. Both the experiments in figure 5.23 and 5.24 were in the pycnocline as shown in figure 5.1. The wing is slightly above the centre of the pycnocline, but since the disturbance is large relative to the pycnocline thickness, the mode of oscillation is predominantly mode zero.

In figure 5.24a to c, the wing travels from left to right at 14.4 mm/s with 3 different frequencies. In the video, the case as shown in figure 5.24a as a still, will show some signs of forward moving waves. In figure 5.24c, the waves are clearly travelling to the left. The wave number surfaces for this velocity are shown in figures 5.26a and b.

The small amplitude theory cannot be expected to produce good results for the phase configuration when the amplitude of oscillation is large and the frequency is high unless the background flow is included in the evaluation. As soon as there is a small local background flow the phase configuration of internal waves is obviously changed. What must be remembered is that the wave pattern developed by a moving body depends on the relative velocity between the body and the background flow.

5.7 Wing tip vortices

Figures 5.27a & b show the impulsive start of a wing. The wing was accelerating from left to right reaching a maximum velocity of 0.33 m/s. The wing tip vortices can clearly be seen. The image of vortex shedding from the struts holding the wing is superimposed vertically. The effect of the vortex shedding from the struts was greatly reduced in experiments involving lower velocities.

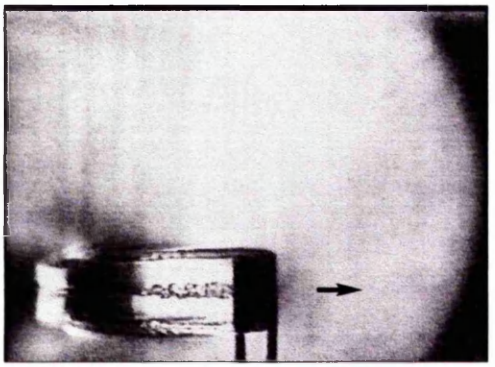

Figure 5.27a

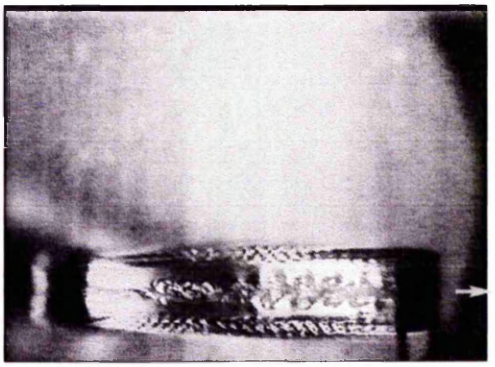

Figure 5.27b

Figures 5.27a and b were stills from the video clip 132. A closer view of the plan-view vortices around the wing can be seen in the video clips as listed in table 5.4. The pycnocline properties are shown in figure 5.34.

It is not easy to generate wing tip vortices in stratified fluid as the vertical motion of the fluid will be impeded by the force of gravity. Even if the vortices are generated they can collapse quickly, producing internal waves. The distance between the wing and the position where the vortex rotation ceases increases as N_c decreases.

Video clips 89 to 91 show some wing tip vortices from a NACA 0012 wing travelling in a constant density fluid. The wing chord length is 45 mm and the velocity was 18 mm/s in video clip 89, 34 mm/s for 90 and 91. The dye used was an emulsion of milk and methanol. Methanol is used to adjust the specific weight of the dye to that of the background density. The emulsion was released from two small holes near the wing tip. The exit velocity of the emulsion was controlled by a dye supply system similar in principle to the one used by Voropayev & Afanasyev (1994). This system consists of a constant reservoir level container with an overflow outlet. The volume flow rate can be controlled accurately by varying the difference between the water level in the towing

tank and that of the reservoir. The light source was a 100W photo floodlight and the flow field was illuminated vertically from below by a 0.01 m wide plane light sheet. The axis of the camera was perpendicular to the illuminated plane. The light source and the camera were fixed to the towing tank. The background was blackened with cardboard to eliminate any shadows in the flow field. Heat transfer from the light source to the perspex surface of the working section must be kept to a minimum.

This system is limited to a small range of Reynolds number up to 1500 based on the chord of the wing to prevent the dye lines from becoming turbulent. The difficulty with this system is ensuring that the emulsion is of the same density as the background fluid. While the video clips show that it is sufficiently accurate for constant density fluid, it proved very difficult for stratified fluid.

Video clip	Maximum U (m/s)	ω_f (rad/s)	N_c (rad/s)	ε (m)
101	0.0078	3.02	7.01	0.02
102	0.0144	3.02	7.01	0.02
103	0.031	0	7.01	0.02
104	0.031	0	7.01	0.02
105	0.047	3.02	7.01	0.02
106	0.031	3.02	7.01	0.02
107	0.064	0	7.01	0.02
108	0.064	0	7.01	0.02
109	0.080	3.02	7.01	0.02
110	0.080	0	7.01	0.02
111	0.097	0	7.01	0.02
112	0.097	0	7.01	0.02
113	0.163	0	7.01	0.02
114	0.33	0	7.01	0.02
117	0.0076	5.87	7.01	0.02
118	0	5.87	7.01	0.02
162p	0.08	3.023	7.01	0.02
163p	0.047	3.023	7.01	0.02

Table 5.4 Video clips showing plan-view vortices around the wing.

5.8 Vortical patterns in the wake of a wing in a pycnocline

The general magnitude of the circulation around a wing in an unstratified fluid is determined by the strength of the vortices which are shed in the initial stages of the motion or at any time when the speed or incidence angle is changed. In addition this is subject to a small fluctuation due to the vorticity of the boundary layer which passes down stream in a vortex wake and develops into a Karman vortex street, McAlister & Carr (1978). Presumably there will be a resonance when the Strouhal frequency coincides with the oscillatory frequency of the wing. When the flow is stratified the vortices eventually cease to rotate and go into a wave motion. Yet another frequency is then present, the Brunt-Vaisala frequency.

5.8.1 Visualisation using dye

Some visualisations were made of the vortices produced by a wing in a pycnocline. The wing was painted with coloured dye and was then allowed to dry overnight. It was then lowered into the pycnocline when the solid dye started to dissolve. The rate at which the solid dye dissolves depends very much on the density of the fluid; the denser the surrounding fluid the slower it dissolves. When the disturbance had settled down after about fifteen minutes, the wing was then set into motion. By now the wing was surrounded by coloured fluid. In these experiments, the quality of the video clips were not good due to the difficulties in controlling the density but the vortices can be seen. Video clips 92 to 100 show the wing oscillating at various frequencies. The wing in the clips has a chord length of 90 mm.

The wake patterns of a wing in a pycnocline were observed. Only at 0^{o} fixed incidence was there no vortex shedding. There is evidence of a small upstream wake which will reduce the velocities on the upper surface of the wing close to the leading edge. This possibly accounts for the lower lifts achieved with the stratified fluid (see chapter 4). Usually the vortex street collapses quickly but its character depends on the frequency of oscillation. The strength and the distance between the vortices depend on both frequency and velocity.

The wing was set to oscillate at various frequencies with a fixed amplitude of 0 to 4.8 degrees and different forward velocities were used. The flow could be divided into 4 different basic patterns. At a very low frequency of oscillation a succession of

vortices with weak circulation are produced but they quickly settle to their equilibrium level and collapse, video clip 92.

If the frequency of oscillation is increased, a stronger vortex with positive circulation was produced. The vortex with negative circulation can barely be seen. The pair of vortices soon collapsed before the next vortex was produced. See video clips 93, 94, 96, 97, 98 and 100.

Video clips 95 and 99 show the wing with a further increase in frequency of oscillation. It was observed that the vortex with positive circulation tends to swirl downward. As the incidence angle decreases the vortex of opposite circulation was also produced. The next vortex with positive circulation was soon formed as the incidence angle was increased again and the process is repeated. The vortices were later seen to return to their equilibrium position before collapsing. The vorticity was clearly much stronger than before

The frequency of oscillation was again increased. Both the vortices with positive and negative circulation were very close together. The mean velocity in the wake was clearly seen to move away from the aerofoil which means that the wing will have thrust instead of drag. Koochesfahani (1989) studied a similar problem in a uniform fluid.

5.8.2 Visualisation using the schlieren system

Visualisation of the vortices was also done with the horizontal schlieren system. The optical lens was changed from a 135mm to 300mm lens to get a closer side-view of the vortices. The vertical schlieren system was also available to visualise the plan-view of the vortices. The optical lens was changed from a 105 to 200 mm. The wing was set to oscillate at 4.08 rad/s, travelling at 3 different velocities. The roll-up of the vortices can be seen to be limited by the stratification and the fluid quickly returned to the equilibrium position. The following table lists the video clips and their parameters.

Video clip	Velocity (mm/s)	ω_f (rad/s)	N_c (rad/s)	ε (m)
164	4.03	4.083	3.143	0.105
165	11.1	4.083	3.143	0.105
166	21	4.083	3.143	0.105

Table 5.5 Video clips showing roll-up of the vortices.

5.9 Vortex dipole produced by a wing

The fluid behind a stationary wing at an incidence angle of 2.5 degrees was made visible with potassium permanganate. Figures 5.28a to i show the plan-views of the wing and the coloured fluid. The wing was allowed to travel at a constant velocity of 8.3 mm/s for a long time before it was brought to rest as shown in figure 5.28a. The dyed fluid, which followed behind the wing, could be seen hitting the wing. The incidence angle was then changed to 0 degree (figure 5.28b). The wing started to move again 30 seconds later at 2.7 mm/s. Figure 5.28d to i show the formation of the vortex dipole for the next 60 seconds.

The dipole is essentially two-dimensional since the vertical motion of the fluid is prevented by gravity. The dipole behaviour is sensitive to the way in which the wing is moved. For example, if the wing remains at rest without change of incidence angle in figure 5.28b, the jet following the wing will collide with the wing, forming a dipole in the opposite direction. These phenomena have been shown by Voropayev & Afanasyev (1994) in chapters on collision of a dipole with a small body and on the symmetric collision of a dipole with a wall. They used a jet from a thin horizontal nozzle in a stratified fluid. This produces a horizontal vortex pair similar to that from the wing. The mean velocity profile in the wake of a fixed incidence NACA 0012 wing and also in the wake of a sinusoidally pitching aerofoil in a homogeneous media are given by Koochesfahani (1989). The velocity profile for the fixed incidence is like a jet flowing in the direction of the wing velocity but with a mean velocity slower than the wing velocity. This shows the usual momentum defect. As the frequency increases, the velocity in the wake changes until the velocity of the fluid in the wake is the same as the free stream velocity which means the wing will have no drag at all. A further increase in the frequency of the oscillation will yield a jet in the reverse direction, that is, the wing will propel itself forward. When the wing oscillates in a pycnocline, the velocity profile of the fluid in the wake will behave in the same manner, but will be modified by the presence of internal waves and the vertical velocities will be suppressed. This is like a thin horizontal nozzle sending a jet in a direction depending on the frequency of oscillation, hence acting as a source for producing a vortex dipole.

5.10 Summary of video clips in the CD-ROM

Video clip information regarding the pycnocline and the positions of the wing are given in the table 5.6. The pycnocline properties for the experiments seen in clips 1 to 31 are not available. However they were all done in thin pycnoclines with thickness of around 20 mm and a natural frequency at the centre of the pycnocline of about 7 to 8 rad/s.

Two optical lenses were used for the vertical schlieren systems providing the plan-view images. The lens with a focal length of 105 mm gives a view of 222 mm horizontally across each frame in the video clip. The enlarged view given by the 200mm lens has 117 mm across each frame and was used for video clips 101 to 114, 117, 118, 162p to 166p. The horizontal schlieren system has 135 mm and 300 mm lenses, which give 173 mm and 78 mm respectively across the frames. Only video clips 164s to 166s have the 78 mm view across the frames. Video clips 92 to 100 have a zoom lens, so that the distance across the frames is variable. However the chord length of the perspex wing is 90 mm. The chord length of the wing in clips 89 to 91 is 45 mm. Clips 77 to 88 show the waves produced by a stalling wing.

Video Cilp	U	ω_f	N_c	ε	Pycnocline properties
32	0.0041	5.96	8.7	0.017	Figure 5.29
33	0.0075	5.96	8.7	0.017	Figure 5.29
34	0.0111	5.96	8.7	0.017	Figure 5.29
35	0.0144	5.96	8.7	0.017	Figure 5.29
36	0.0075	8.96	8.7	0.017	Figure 5.29
37	0.0111	8.96	8.7	0.017	Figure 5.29
38	0.0176	8.96	8.7	0.017	Figure 5.29
39	0.0245	12.85	8.7	0.017	Figure 5.29
40	0.0471	12.85	8.7	0.017	Figure 5.29
41	0.0144	3.85	8.7	0.017	Figure 5.29
42	0.0176	3.85	8.7	0.017	Figure 5.29
43	0.00216	6.33	8.7	0.017	Figure 5.29
44	0.0041	5.11	8.7	0.017	Figure 5.29
45	0.0111	5.11	8.7	0.017	Figure 5.29
46	-	-	-	-	Plan-view grid
47	NA	NA	NA	NA	NA
48	0	6.33	7.97	0.019	Figure 5.30
49	0.0041	6.33	7.97	0.019	Figure 5.30
50	0.0075	6.33	7.97	0.019	Figure 5.30
51	0.0111	6.33	7.97	0.019	Figure 5.30
52	0.0144	6.33	7.97	0.019	Figure 5.30

Video Cilp	U	ω_f	N_c	ε	Pycnocline properties
53	0.0176	6.33	7.97	0.019	Figure 5.30
54	start & stop				Figure 5.30
55	0.0572	0	7.97	0.019	Figure 5.30
56	0.0652	0	7.97	0.019	Figure 5.30
57	0.0802	0	7.97	0.019	Figure 5.30
58	0	4.398	7.97	0.019	Figure 5.30
59	0.0075	4.57	7.97	0.019	Figure 5.30
60	0.0111	4.833	7.97	0.019	Figure 5.30
61	0.0041	6.378	7.23	0.022	Figure 3.17
62	0.0075	6.378	7.23	0.022	Figure 3.17
63	0.0144	6.378	7.23	0.022	Figure 3.17
64	0.0374	6.378	7.23	0.022	Figure 3.17
65	0	6.378	7.23	0.022	Figure 3.17
66	0.0021	6.378	7.23	0.022	Figure 3.17
67	0.0038	6.378	7.23	0.022	Figure 3.17
68	0.0021	5.67	7.23	0.022	Figure 3.17
69	0.0038	5.67	7.23	0.022	Figure 3.17
70	0.0041	5.67	7.23	0.022	Figure 3.17
71	0.0075	5.67	7.23	0.022	Figure 3.17
72	0.0243	0	7.23	0.022	Figure 3.17
73	0.0374	0	7.23	0.022	Figure 3.17
74	0.0652	0	7.23	0.022	Figure 3.17
75	0.0041	4.75	7.23	0.022	Figure 3.17
76	0.0075	4.75	7.23	0.022	Figure 3.17
77	0.029	Stalled wing	NA	NA	NA
78	0.047	Stalled wing	NA	NA	NA
79	0.065	Stalled wing	NA	NA	NA
80	0.087	Stalled wing	NA	NA	NA
81	0.029	Stalled wing	NA	NA	NA
82	0.029	Stalled wing	NA	NA	NA
83	0.029	Stalled wing	NA	NA	NA
84	0.047	Stalled wing	NA	NA	NA
85	0.065	Stalled wing	NA	NA	NA
86	0.074	Stalled wing	NA	NA	NA
87	0.089	Stalled wing	NA	NA	NA
88	0.131	Stalled wing	NA	NA	NA
89	0.018	0	0	-	Constant density
90	0.034	0	0	-	Constant density
91	0.034	0	0	-	Constant density
92	0.006	2.1	NA	NA	NA
93	0.0098	3.38	NA	NA	NA
94	0.0098	3.45	NA	NA	NA
95	0.031	12.57	NA	NA	NA
96	0.013	3.43	NA	NA	NA
97	NA	3.38	NA	NA	NA

Video Cilp	U	ω_f	N_c	ε	Pycnocline properties
98	NA	3.49	NA	NA	NA
99	0.031	13.61	NA	NA	NA
100	0.013	3.77	NA	NA	NA
101	0.0078	3.02	7.01	0.02	Figure 5.34
102	0.0144	3.02	7.01	0.02	Figure 5.34
103	0.031	0	7.01	0.02	Figure 5.34
104	0.031	0	7.01	0.02	Figure 5.34
105	0.047	3.02	7.01	0.02	Figure 5.34
106	0.031	3.02	7.01	0.02	Figure 5.34
107	0.064	0	7.01	0.02	Figure 5.34
108	0.064	0	7.01	0.02	Figure 5.34
109	0.080	3.02	7.01	0.02	Figure 5.34
110	0.080	0	7.01	0.02	Figure 5.34
111	0.097	0	7.01	0.02	Figure 5.34
112	0.097	0	7.01	0.02	Figure 5.34
113	0.163	0	7.01	0.02	Figure 5.34
114	0.33	0	7.01	0.02	Figure 5.34
115	1.10×10^{-2}	0	2.81	0.18	Figure 5.2
116	0	2.29	2.81	0.18	Figure 5.2
117	0.0076	5.87	7.01	0.02	Figure 5.31
118	0	5.87	7.01	0.02	Figure 5.31
119	7.57×10^{-3}	4.5	7.15	0.032	Figure 5.31
120	7.57×10^{-3}	4.5	7.15	0.032	Figure 5.31
121	1.10×10^{-2}	4.5	7.15	0.032	Figure 5.31
122	1.10×10^{-2}	4.5	7.15	0.032	Figure 5.31
123	1.10×10^{-2}	4.5	7.15	0.032	Figure 5.31
124	1.44×10^{-3}	4.5	7.15	0.032	Figure 5.31
125	1.44×10^{-3}	4.5	7.15	0.032	Figure 5.31
126	2.1×10^{-2}	4.5	7.15	0.032	Figure 5.31
127	0.034	4.5	7.15	0.032	Figure 5.31
128	0.064	4.5	7.15	0.032	Figure 5.31
129	0.064	0	7.15	0.032	Figure 5.31
130	0.080	0	7.15	0.032	Figure 5.31
131	0.080	0	7.15	0.032	Figure 5.31
132	0.080	0	7.15	0.032	Figure 5.31
133	0.097	4.5	7.15	0.032	Figure 5.31
134	0.097	0	7.15	0.032	Figure 5.31
135	0.0	4.5	7.15	0.032	Figure 5.31
136	0.163		7.15	0.032	Figure 5.31
137	0.064	4.5	7.15	0.032	Figure 5.31
138p & s	0	2.29	2.81	0.18	Figure 5.2
139p & s	0.011	0	2.81	0.18	Figure 5.2
140	-	-	-	-	Figure 5.2
141p & s	0	2.29	2.81	0.18	Figure 5.2
142p & s	0	2.29	2.81	0.18	Figure 5.2

Video Cilp	U	ω_f	N_c	ε	Pycnocline properties
143p & s	4.03×10^{-3}	2.29	2.81	0.18	Figure 5.2
144p & s	2.16×10^{-3}	2.29	2.81	0.18	Figure 5.2
145p & s	7.57×10^{-3}	2.29	2.81	0.18	Figure 5.2
146p & s	1.10×10^{-2}	2.29	2.81	0.18	Figure 5.2
147p & s	1.44×10^{-2}	2.29	2.81	0.18	Figure 5.2
148	0.021	0	2.81	0.18	Figure 5.2
149	0.031	0	2.81	0.18	Figure 5.2
150	1.44×10^{-3}	0	2.81	0.18	Figure 5.2
151p & s	0	2.82	2.7	0.18	Figure 5.36
152p & s	0	2.63	2.7	0.18	Figure 5.36
153p & s	0	2.44	2.7	0.18	Figure 5.36
154p & s	0	2.29	2.7	0.18	Figure 5.36
155p & s	0	1.87	2.7	0.18	Figure 5.36
156p & s	0	5.66	2.7	0.18	Figure 5.36
157p & s	4.03×10^{-3}	2.57	2.54	0.196	Figure 5.32
158p & s	0.0144	2.57	2.54	0.196	Figure 5.32
159p & s	0.021	2.57	2.54	0.196	Figure 5.32
160p & s	2.16×10^{-3}	1.9	2.13	0.277	Figure 5.33
162p	0.08	3.023	7.01	0.02	Figure 5.34
163p	0.047	3.023	7.01	0.02	Figure 5.34
164	4.03×10^{-3}	4.083	3.143	0.105	Figure 5.35
165	1.11×10^{-2}	4.083	3.143	0.105	Figure 5.35
166	2.1×10^{-2}	4.083	3.143	0.105	Figure 5.35

p - plan-view, s - side-view and NA - Information not available.

Table 5.6 Parameters concerning video clips in the CD-ROM.

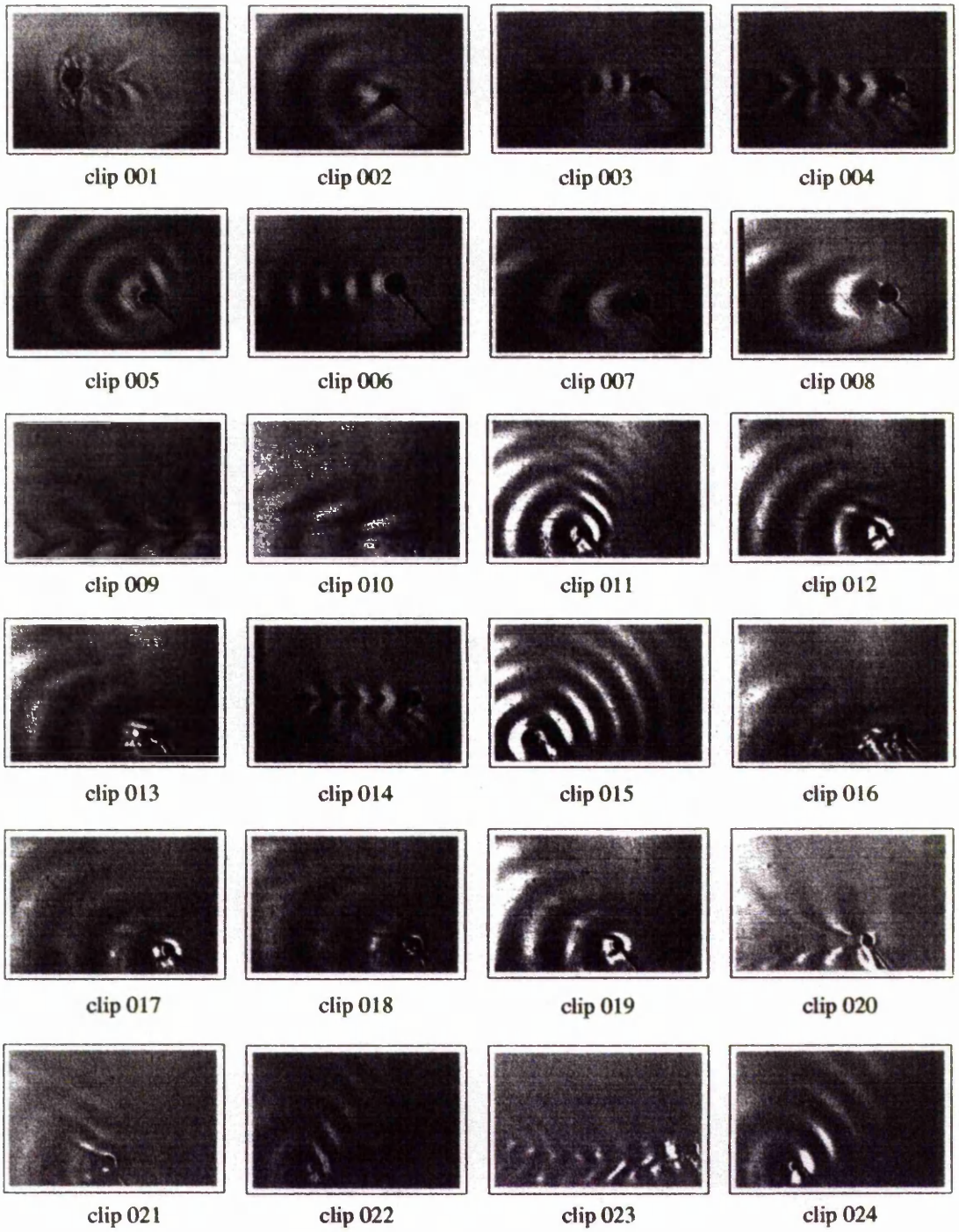

Stills from the video clips 1 to 24 on the enclosed CD-ROM

All are plan views

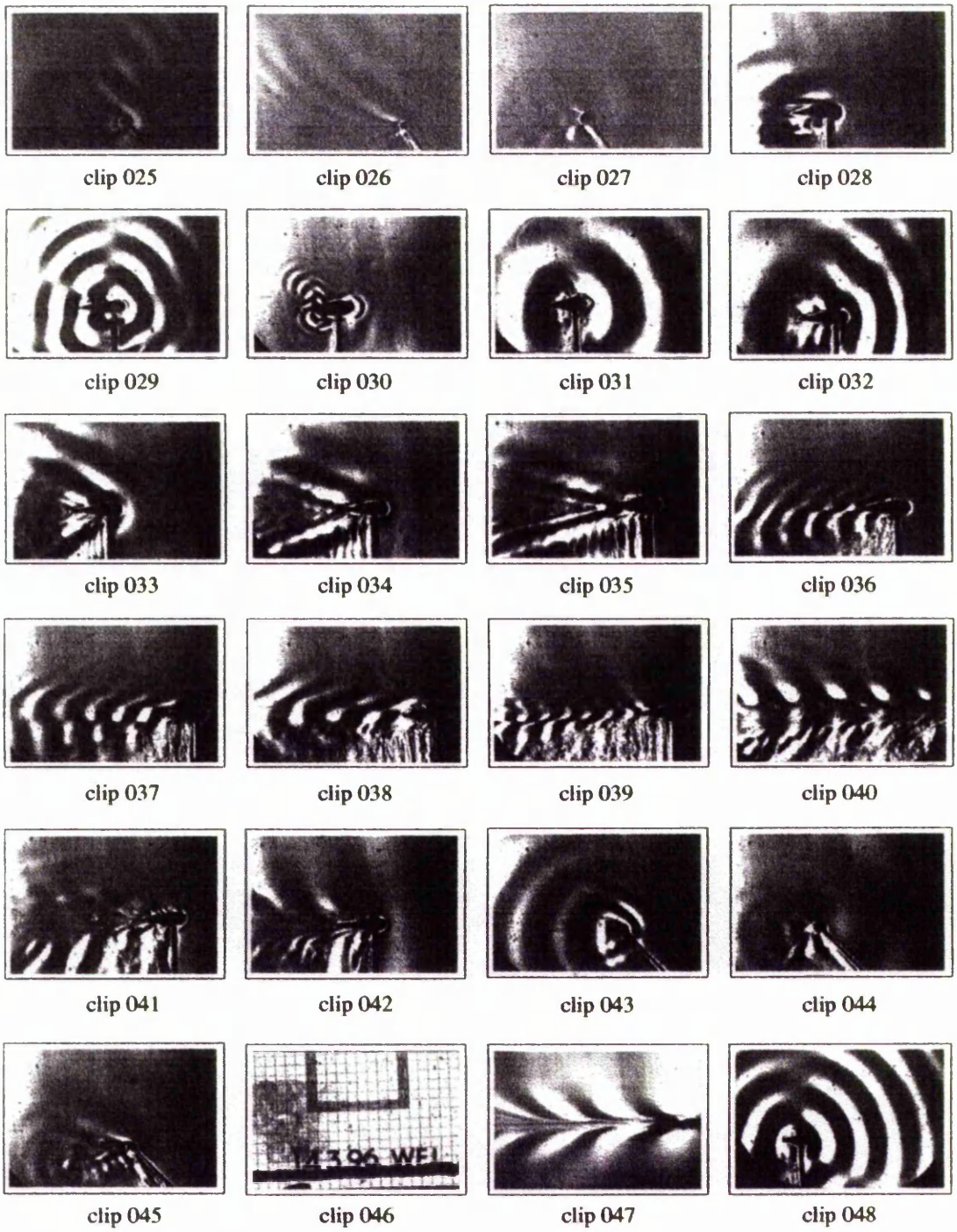

Stills from the video clips 25 to 48 on the enclosed CD-ROM

All are plan views

Stills from the video clips 49 to 72 on the enclosed CD-ROM

All are plan views

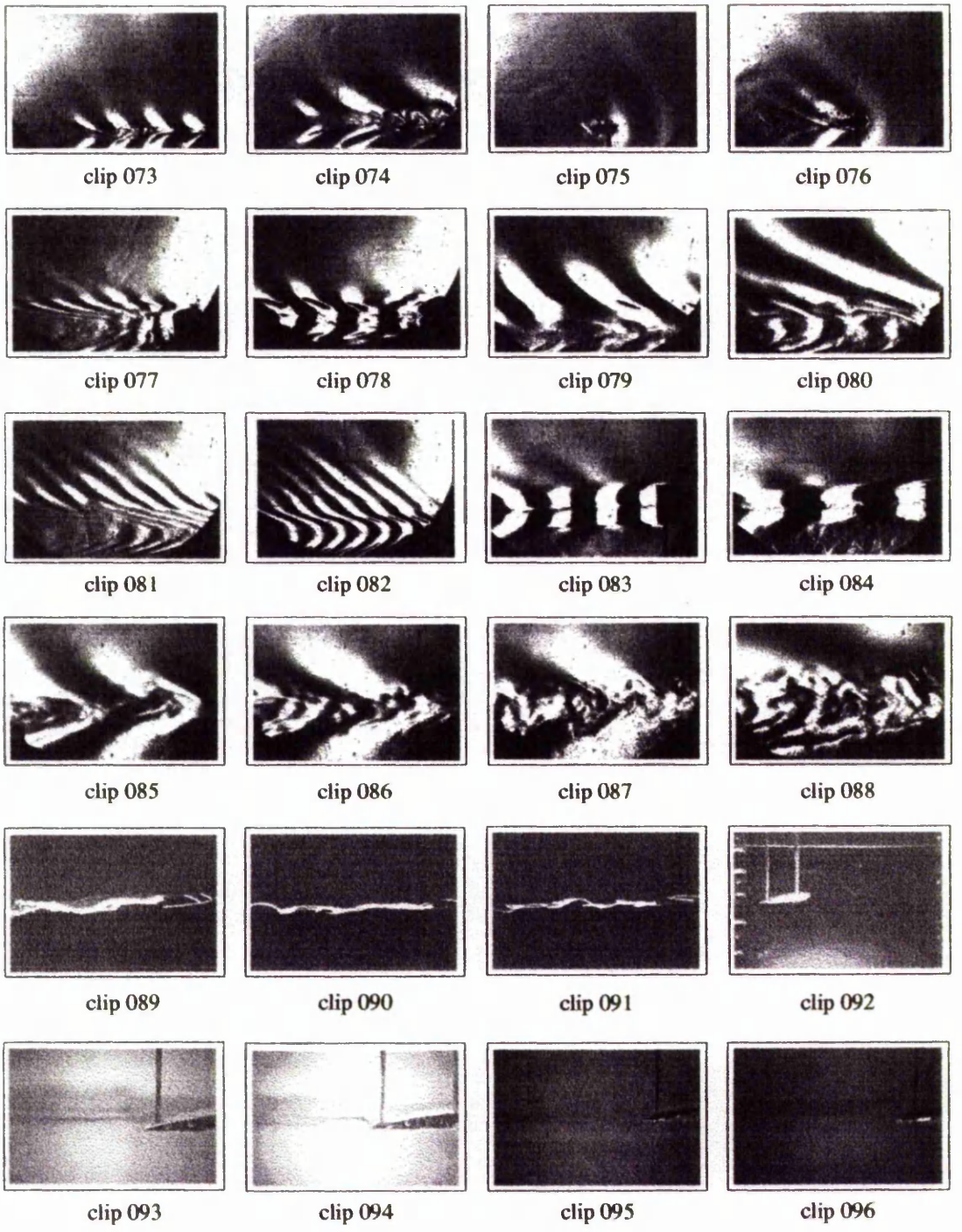

Stills from the video clips 73 to 96 on the enclosed CD-ROM

Up to clip 88 are plan views. Clips 89 to 96 are side views.

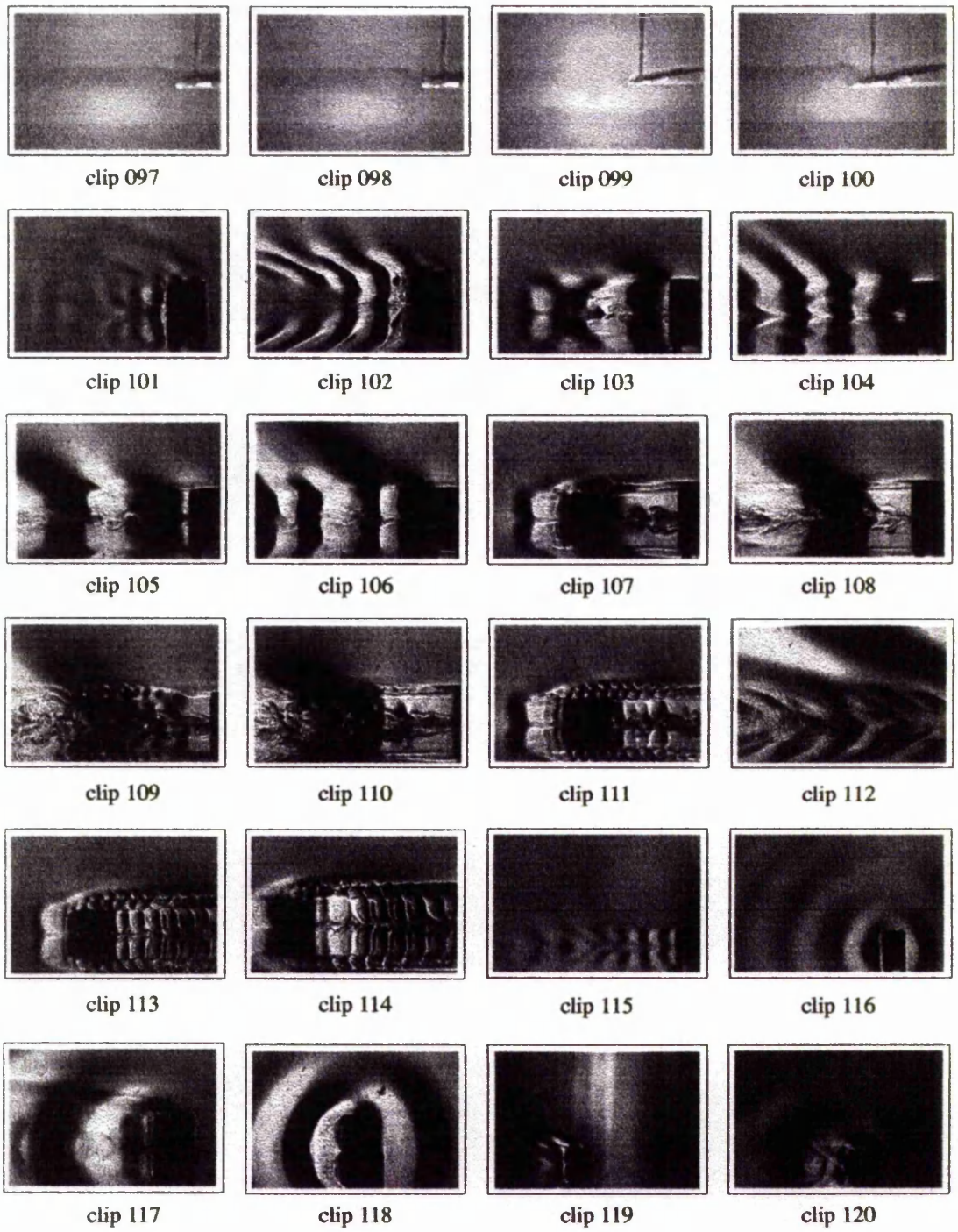

clip 097 clip 098 clip 099 clip 100

clip 101 clip 102 clip 103 clip 104

clip 105 clip 106 clip 107 clip 108

clip 109 clip 110 clip 111 clip 112

clip 113 clip 114 clip 115 clip 116

clip 117 clip 118 clip 119 clip 120

Stills from the video clips 97 to 120 on the enclosed CD-ROM

Clips 97 to 100 are side views, the rest are plan views.

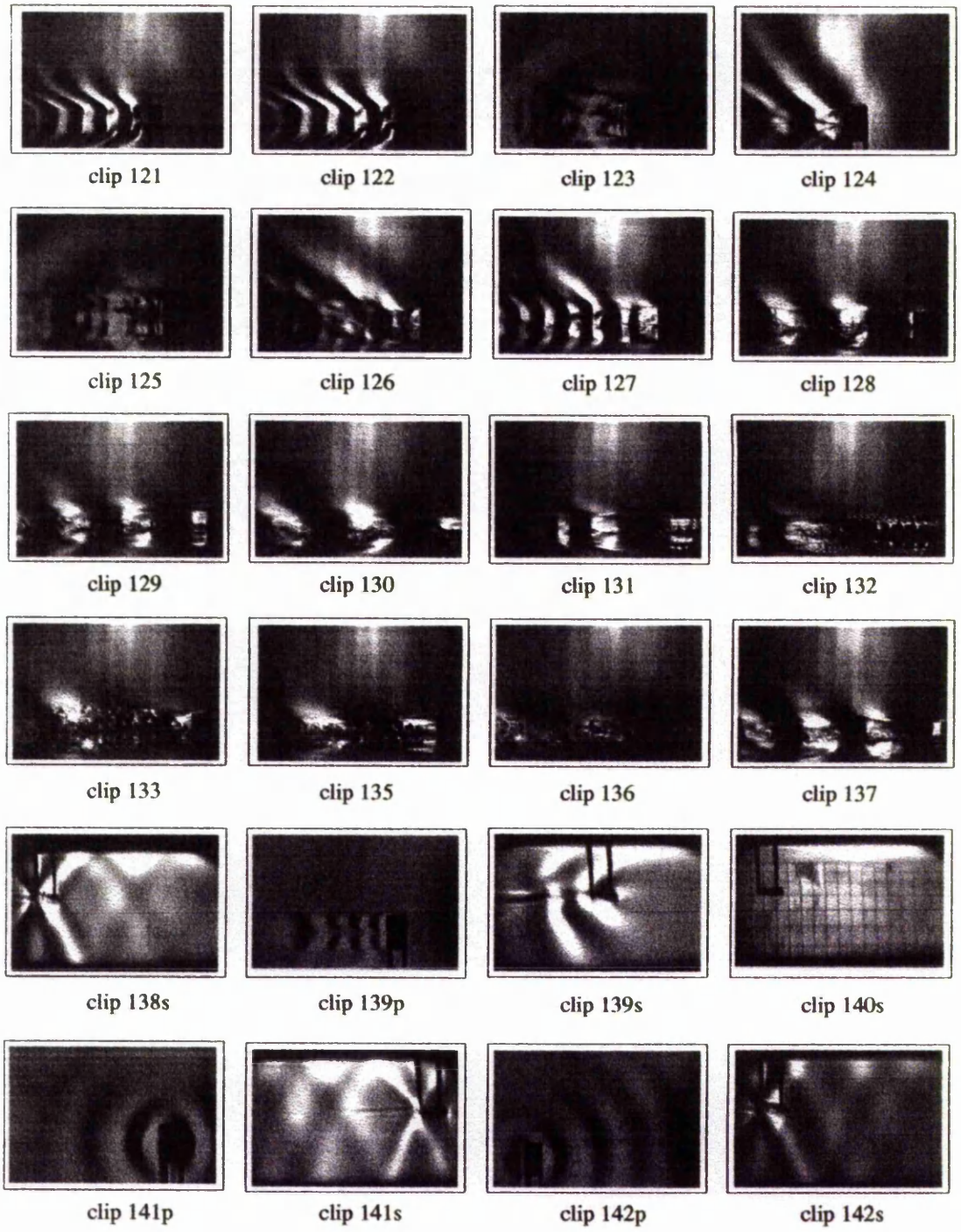

Stills from the video clips 121 to 142 on the enclosed CD-ROM

All are plan views except those with a 's' which are side views.

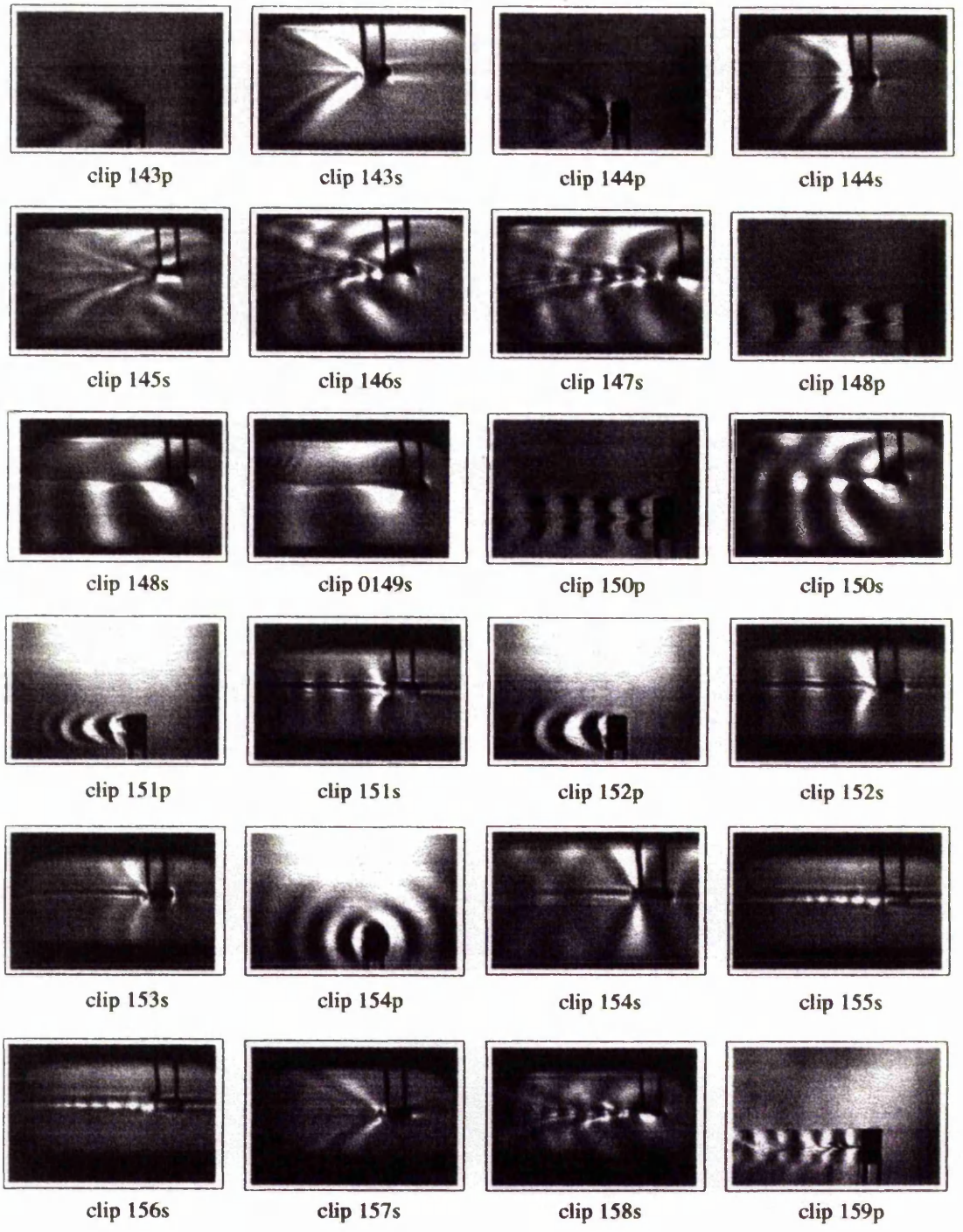

Stills from the video clips 143 to 159 on the enclosed CD-ROM

'p' refers to plan view and 's' indicates a side view.

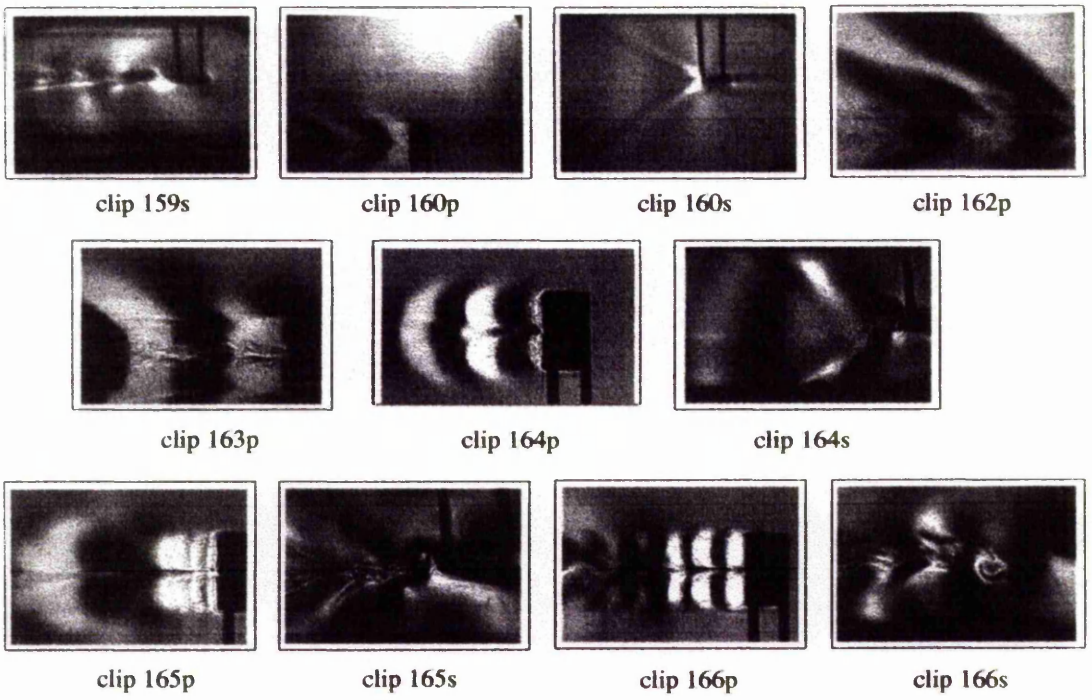

Stills from the video clips 159s to 166 on the enclosed CD-ROM

'p' refers to plan view and 's' indicates a side view.

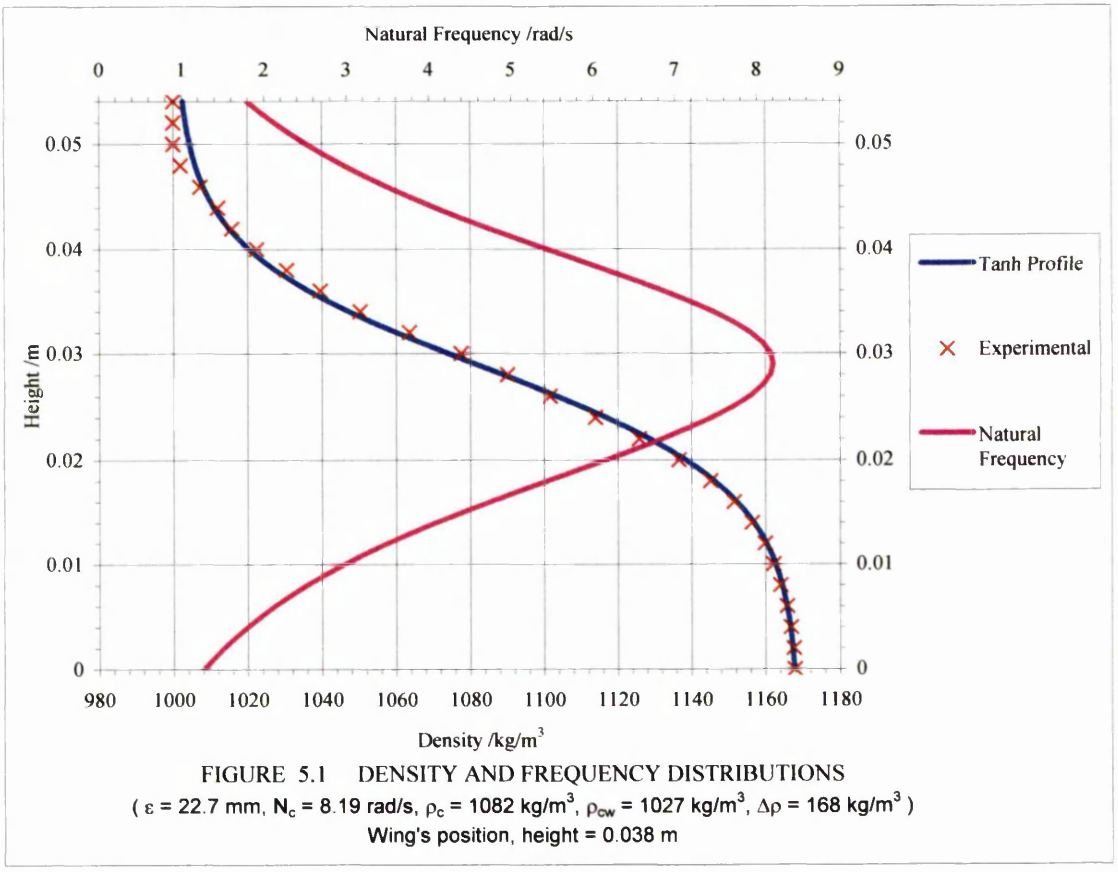

FIGURE 5.1 DENSITY AND FREQUENCY DISTRIBUTIONS

(ε = 22.7 mm, N_c = 8.19 rad/s, ρ_c = 1082 kg/m^3, ρ_{cw} = 1027 kg/m^3, $\Delta\rho$ = 168 kg/m^3)

Wing's position, height = 0.038 m

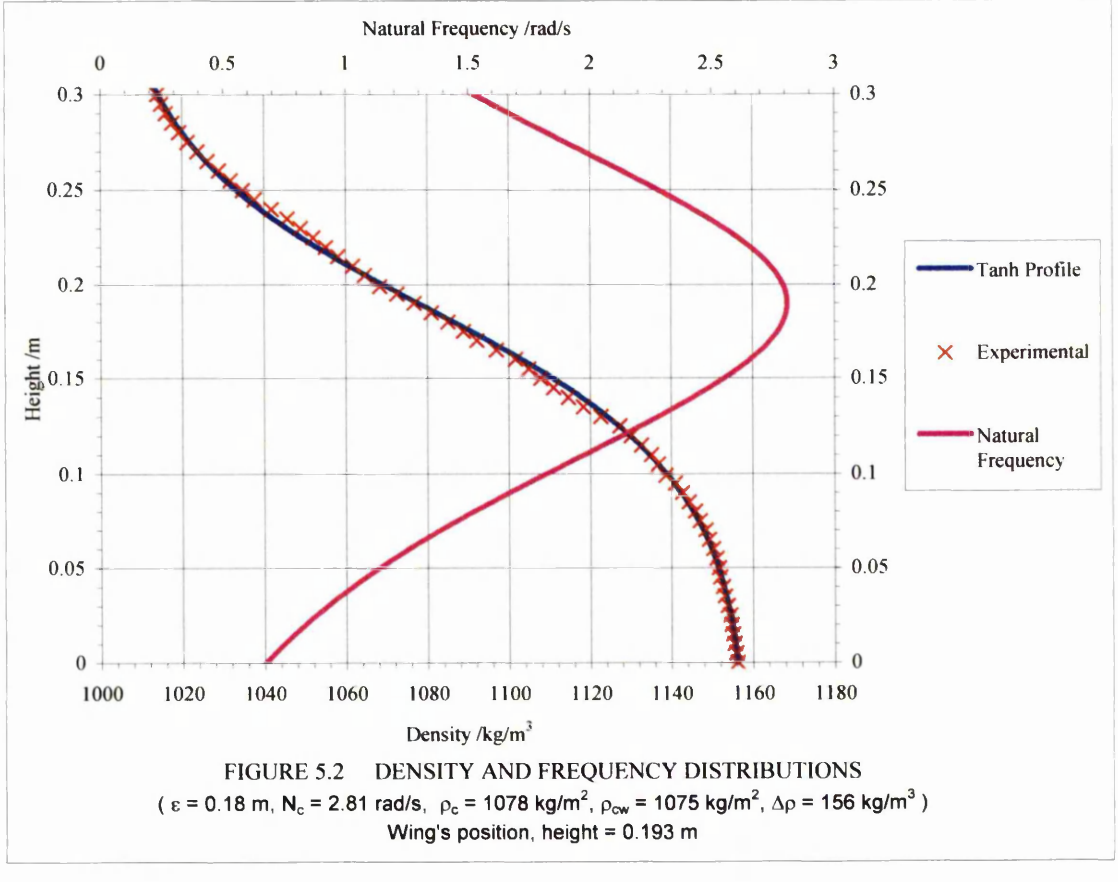

FIGURE 5.2 DENSITY AND FREQUENCY DISTRIBUTIONS

(ε = 0.18 m, N_c = 2.81 rad/s, ρ_c = 1078 kg/m^2, ρ_{cw} = 1075 kg/m^2, $\Delta\rho$ = 156 kg/m^3)

Wing's position, height = 0.193 m

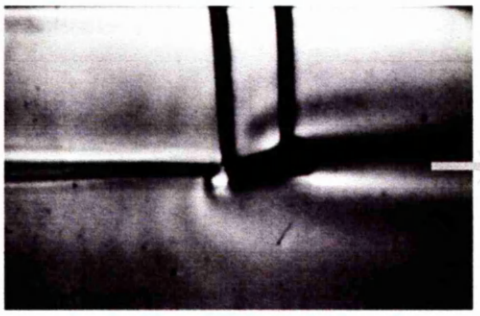

Figure 5.4 Steady wave system from a wing at 10 degrees incidence travelling horizontally in a pycnocline.

U = 4.03 mm/s, N_c = 2.81 rad/s and ε = 0.18 m. At this velocity, the side-view steady waves are just about visible with the horizontal schlieren system while the vertical schlieren system was not sensitive enough to record any waves. The density distribution of the pycnocline is shown in figure 5.2. The grey arrow shows the direction of travel. The two vertical lines are the struts holding the wing.

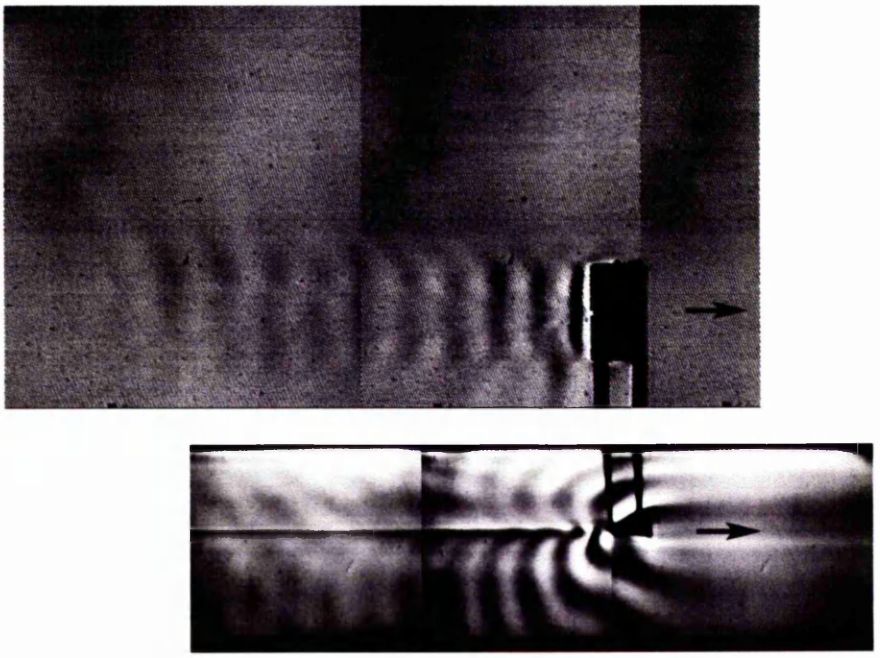

Figures 5.5a and b The top figure shows the plan-view and the bottom figure shows the side-view wave system from a wing at 10 degrees incidence travelling horizontally in a pycnocline.

U = 7.57 mm/s, N_c = 2.81 rad/s and ε = 0.18 m. Both the plan and side-view steady waves are clearly visible under the two schlieren systems. The density distribution of the pycnocline is shown in figure 5.2. The black arrows show the directions of travel.

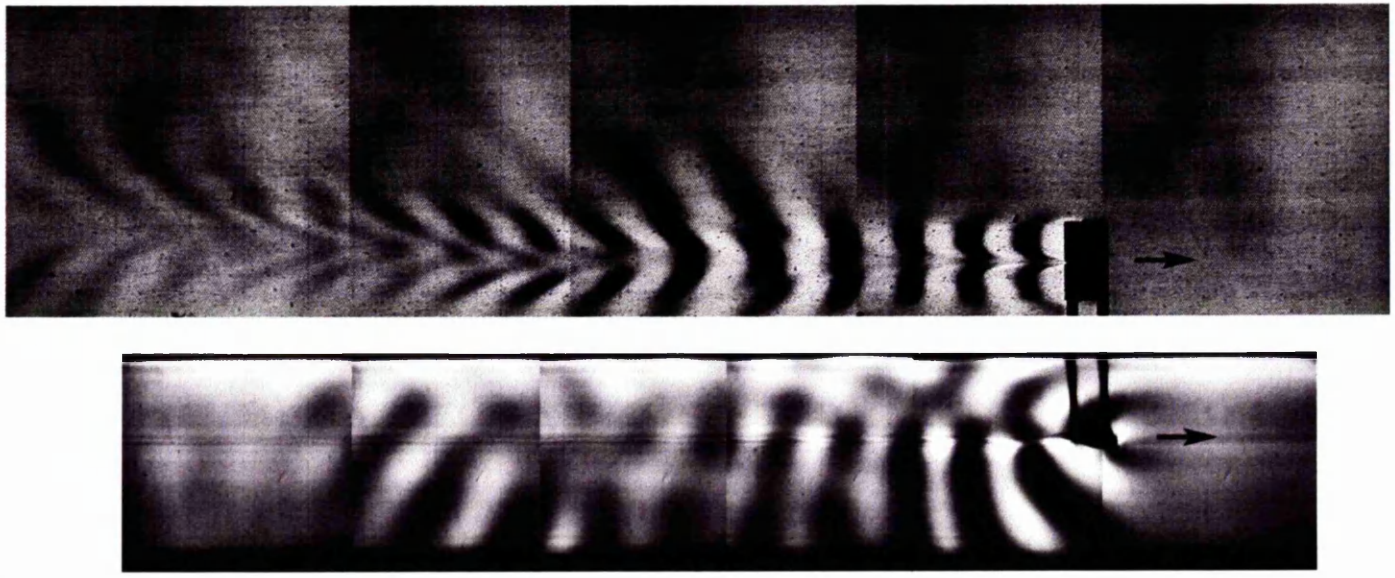

Figures 5.6a and b The top figure shows the plan-view and the bottom figure shows the side-view wave system from a wing at 10 degrees incidence travelling horizontally in a pycnocline.

$U = 1.44\times10^{-2}$ m/s, $N_c = 2.81$ rad/s and $\varepsilon = 0.18$ m. The plan-view image shows how the wave system is affected by the geometry of the wing in the near field, and slowly transforms to the 'herring bone' structure away from the wing. The effect of the struts holding the wing can clearly be seen in the near field. The density distribution of the pycnocline is shown in figure 5.2. The black arrows show the directions of travel.

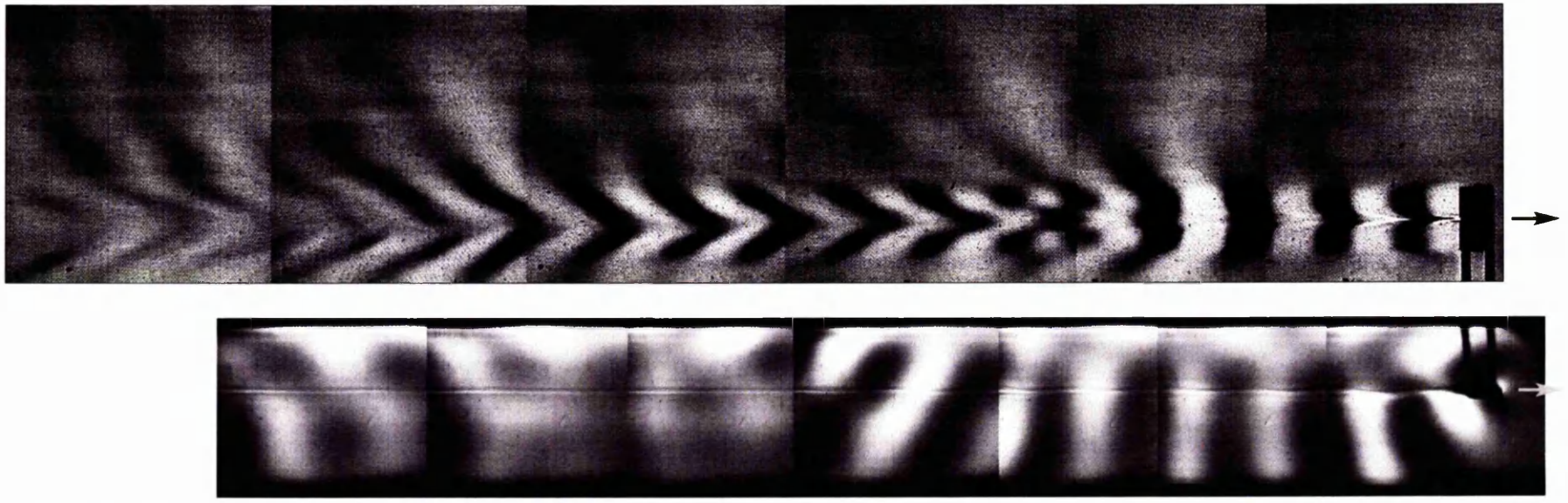

Figures 5.7a and b The top figure shows the plan-view and the bottom figure shows the side-view wave system from a wing at 10 degrees incidence travelling horizontally in a pycnocline.

$U = 2.1\times10^{-2}$ m/s, $N_c = 2.81$ rad/s and $\varepsilon = 0.18$ m. The plan-view image indicates that the wave system is affected by the geometry of the wing in the near field, and in the far field the lee waves are transformed to the 'herring bone' structure. The effect of the struts holding the wing can clearly be seen. The density distribution of the pycnocline is shown in figure 5.2. The arrows show the directions of travel.

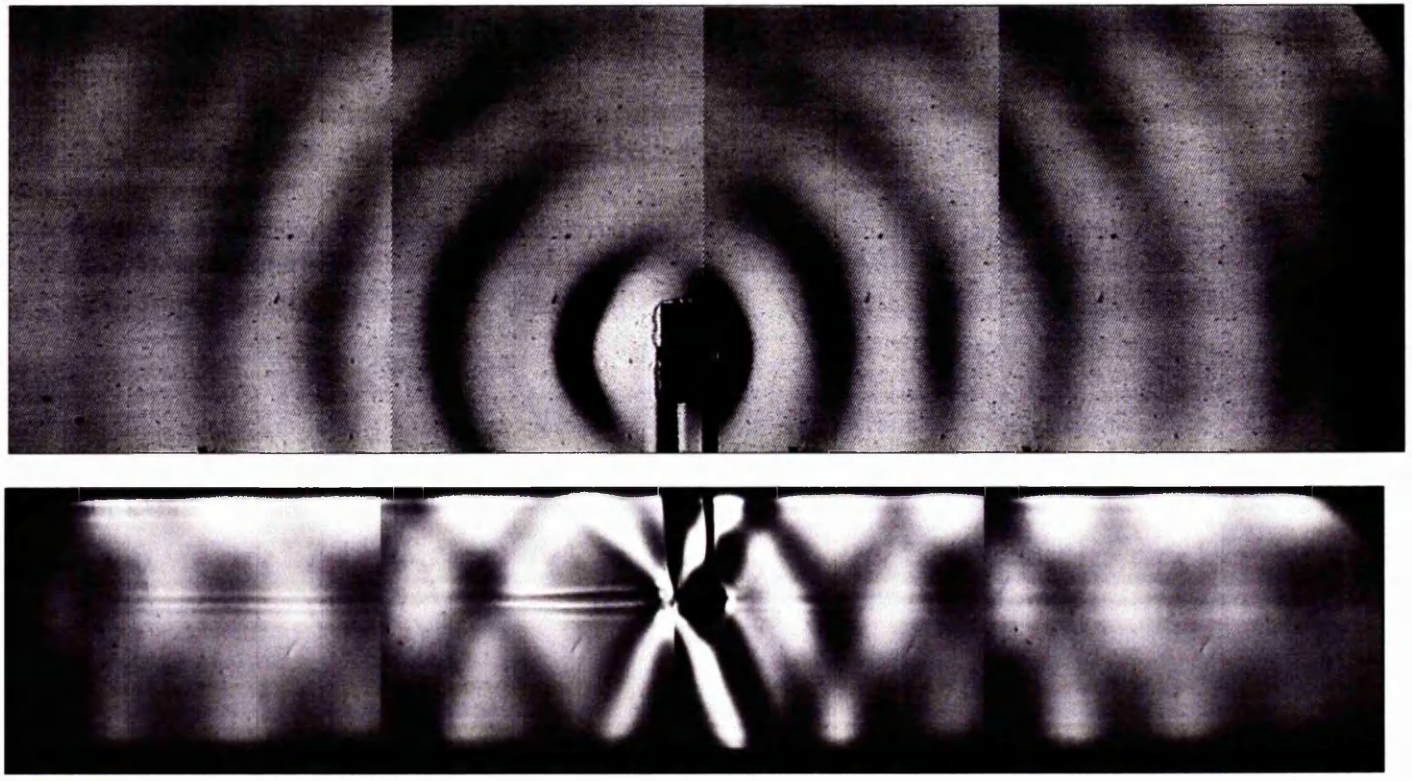

Figures 5.8a and b The top figure shows the plan-view and the bottom figure shows the side-view wave system from a wing oscillating from 0 to 10 degrees in a pycnocline.

U = 0 m/s, ω_f = 2.29 rad/s, N_c = 2.81 rad/s and ε = 0.18 m. The transition to pycnocline waves took place about 6 chord lengths away from the wing. The density distribution of the pycnocline is shown in figure 5.2. The leading edge of the wing is to the right.

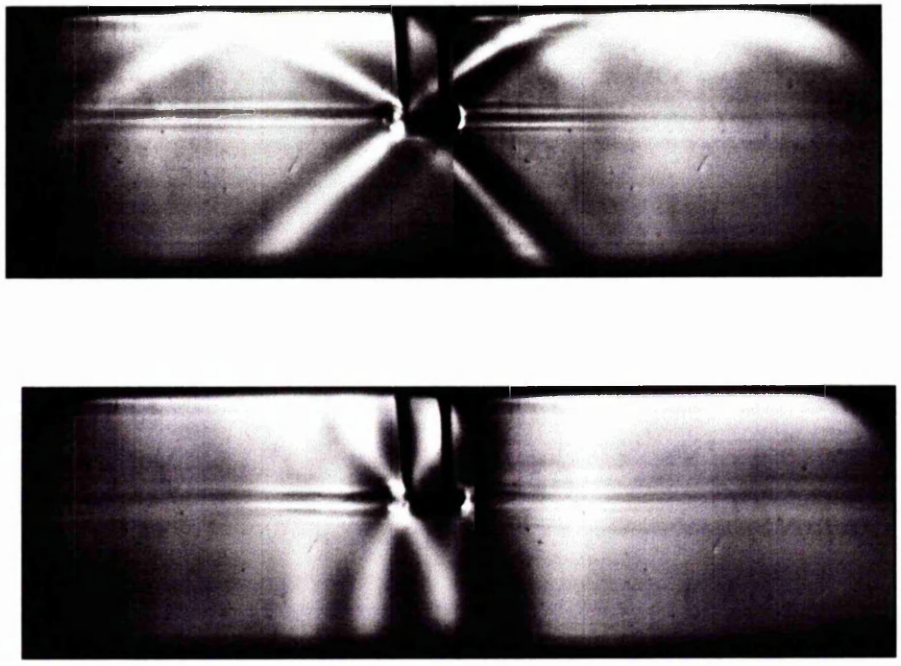

Figures 5.9 and 5.10 The top figure shows the side-view schlieren image of a wing oscillating at a lower frequency of $\omega_f = 1.56$ rad/s and the bottom figure has the wing oscillating at a higher frequency of $\omega_f = 2.48$ rad/s. The range of incidence angle is 0 to 10 degrees.

$U = 0$ m/s, $N_c = 2.81$ rad/s and $\varepsilon = 0.18$ m. The transition to pycnocline waves took place nearer to the wing at the higher frequency. The density distribution of the pycnocline is shown in figure 5.2.

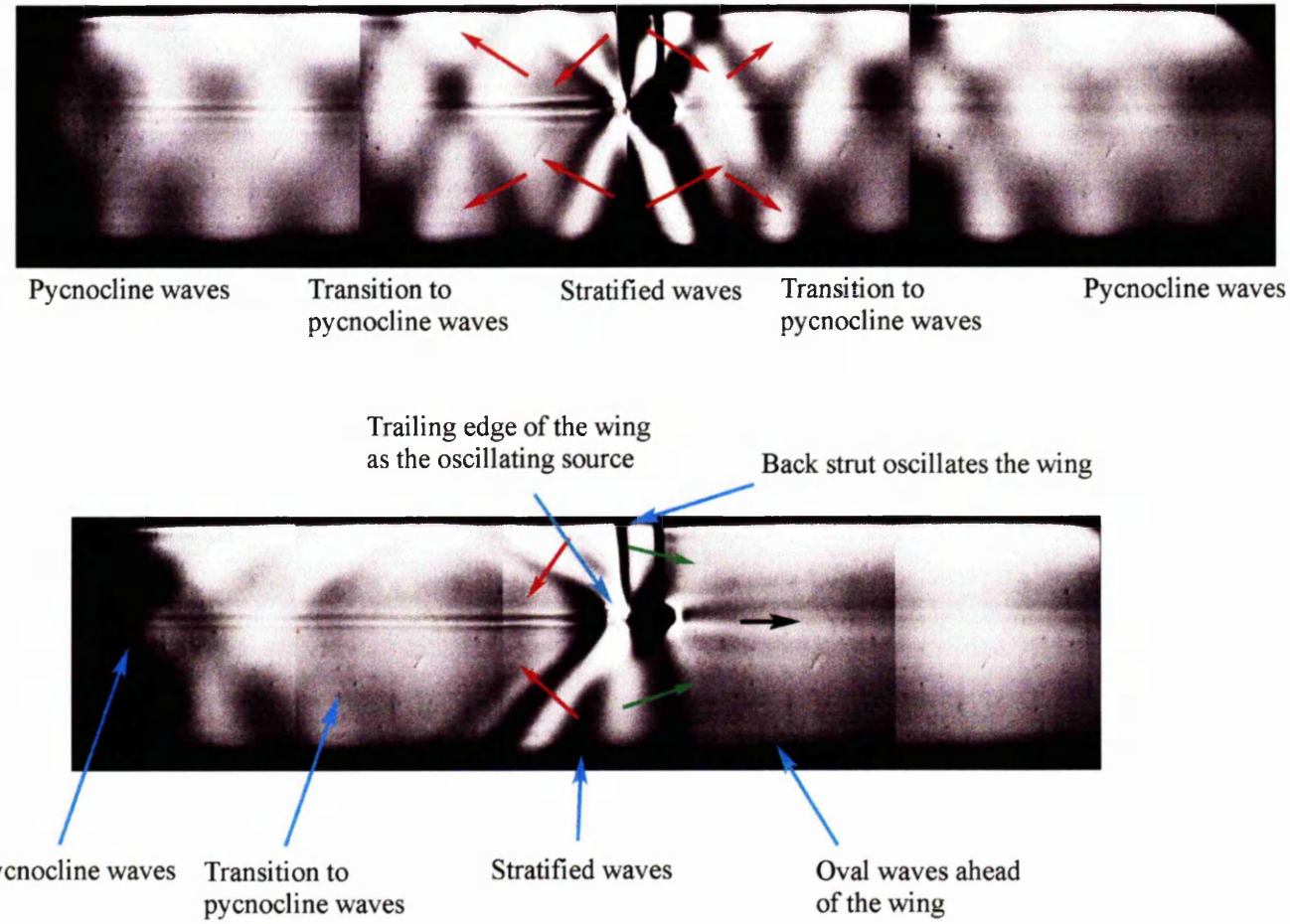

Figures 5.11 and 5.12 The side-view schlieren images showing the directions of the phase velocities as indicated by the red and green arrows. The top figure is the same as figure 5.8b and the bottom figure is from figure 5.13b. Direction of travel is shown by the black arrow.

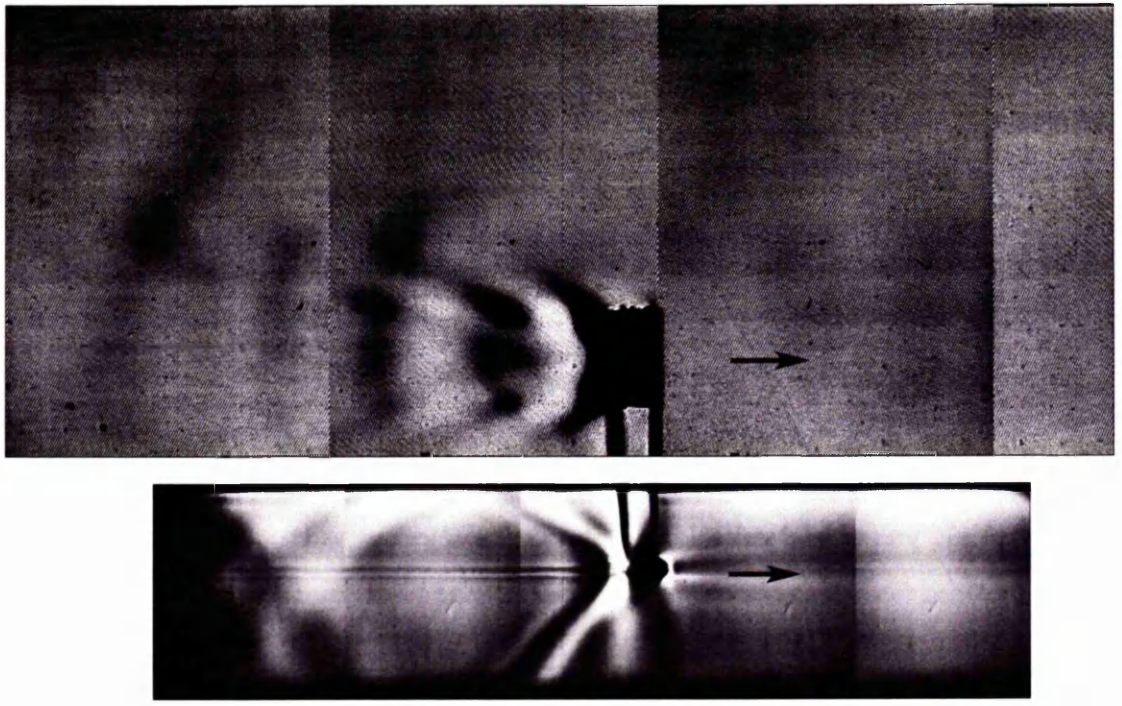

Figures 5.13a and 5.13b The top figure shows the plan-view and the bottom figure shows the side-view schlieren image of an oscillating wing travelling horizontally in a pycnocline. The range of incidence angle is 0 to 10 degrees.

$U = 2.16$ mm/s, $\omega_f = 2.29$ rad/s, $N_c = 2.81$ rad/s, $\varepsilon = 0.18$ m, $M = 234$, $\beta_f = 3.48\times10^{-3}$. The wave number surface is shown in figure 5.18. The density distribution of the pycnocline is shown in figure 5.2. The black arrows show the direction of travel.

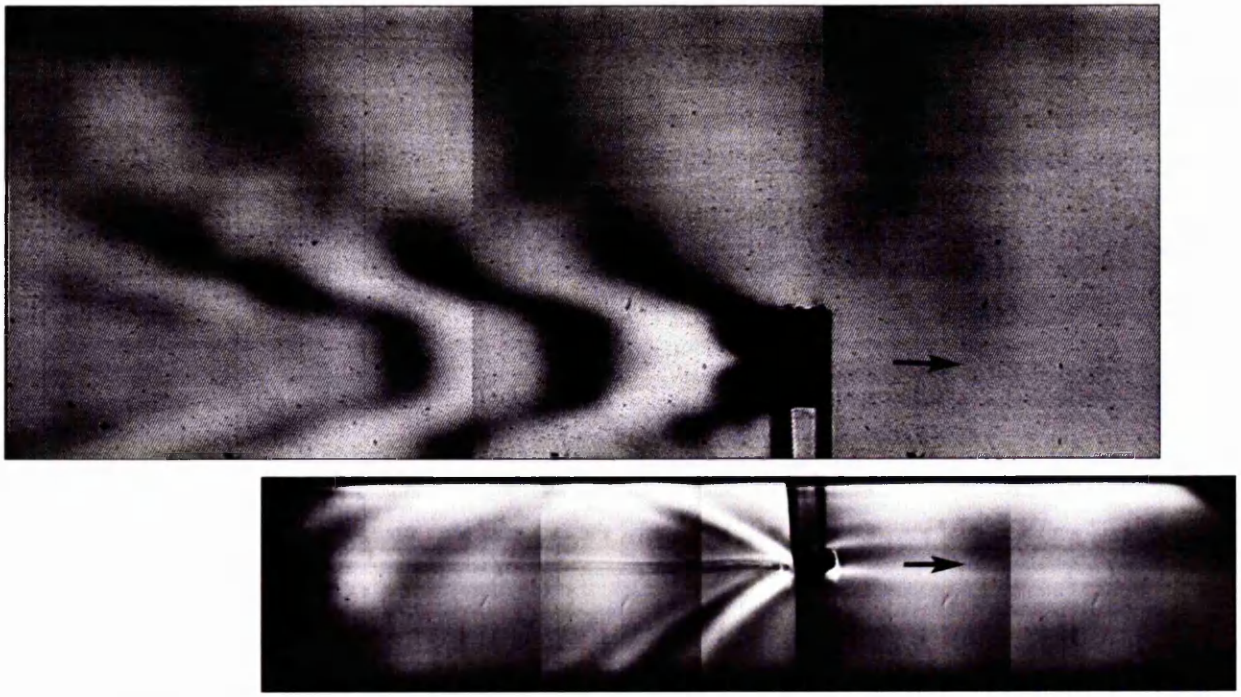

Figures 5.14a and 5.14b The top figure shows the plan-view and the bottom figure shows the side-view schlieren image of an oscillating wing travelling horizontally in a pycnocline. The range of incidence angle is 0 to 10 degrees.

$U = 4.03$ mm/s, $\omega_f = 2.29$ rad/s, $N_c = 2.81$ rad/s, $\varepsilon = 0.18$ m, $M = 125$, $\beta_f = 6.50\times10^{-3}$. The wave number surface is shown in figure 5.19. The density distribution of the pycnocline is shown in figure 5.2. The black arrows show the direction of travel.

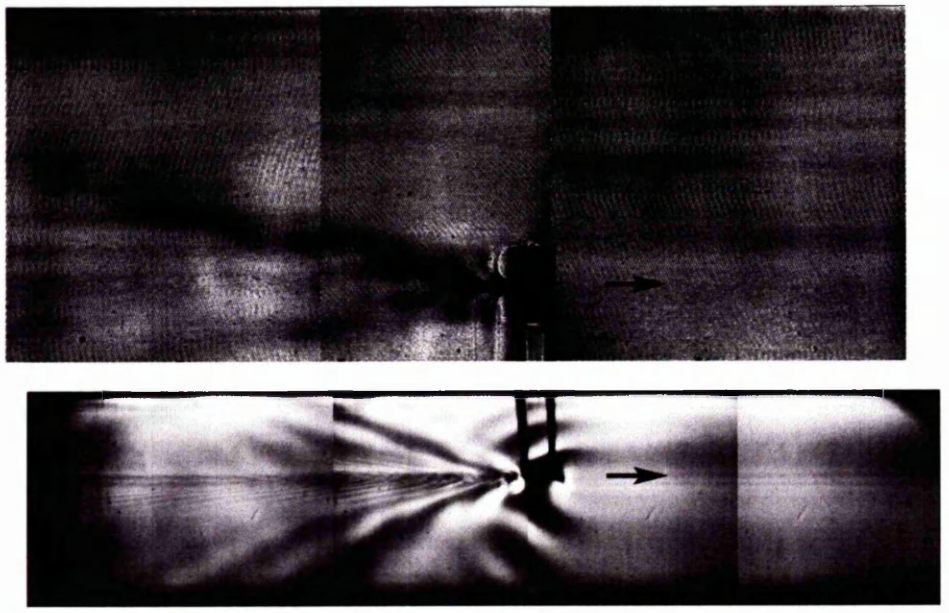

Figures 5.15a and 5.15b The top figure shows the plan-view and the bottom figure shows the side-view schlieren image of an oscillating wing travelling horizontally in a pycnocline. The range of incidence angle is 0 to 10 degrees.

U = 7.57 mm/s, ω_f = 2.29 rad/s, N_c = 2.81 rad/s, ε = 0.18 m, M = 67 and $\beta_f = 1.22\times10^{-2}$. The steady wave system can be seen superimposed onto the oscillatory wave system. The wave number surface is shown in figure 5.20. The density distribution of the pycnocline is shown in figure 5.2. The black arrows show the direction of travel.

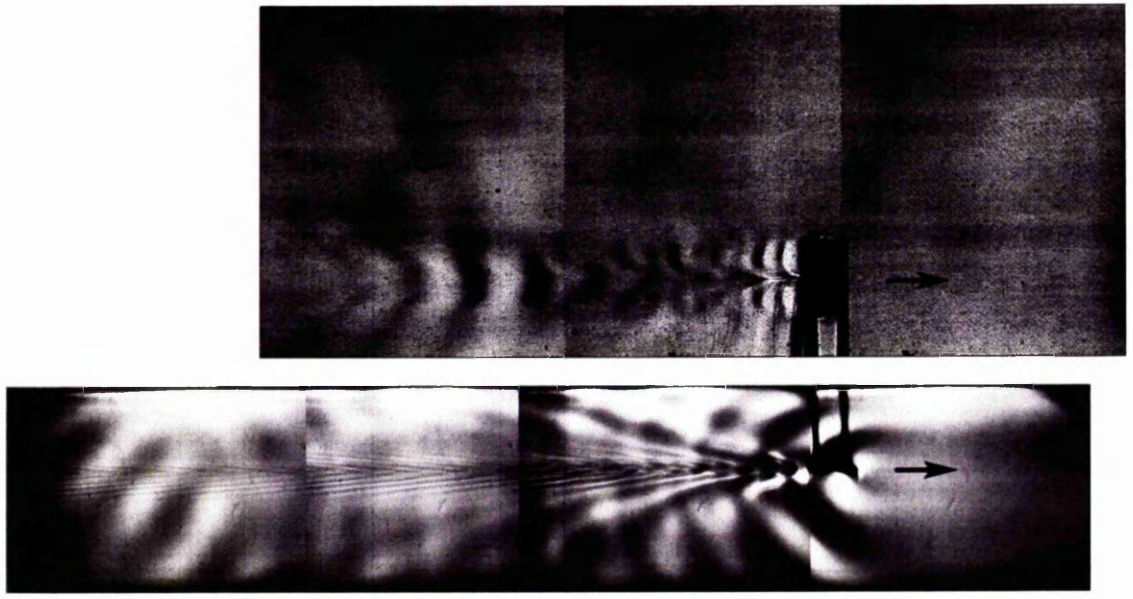

Figures 5.16a and 5.16b The top figure shows the plan-view and the bottom figure shows the side-view schlieren image of an oscillating wing travelling horizontally in a pycnocline. The range of incidence angle is 0 to 10 degrees.

$U = 1.10\times10^{-2}$ m/s, $\omega_f = 2.29$ rad/s, $N_c = 2.81$ rad/s, $\varepsilon = 0.18$ m, $M = 46$ and $\beta_f = 1.77\times10^{-2}$. The steady wave system can be seen superimposed onto the oscillatory wave system. Density distribution of the pycnocline is shown in figure 5.2. The black arrows show the direction of travel.

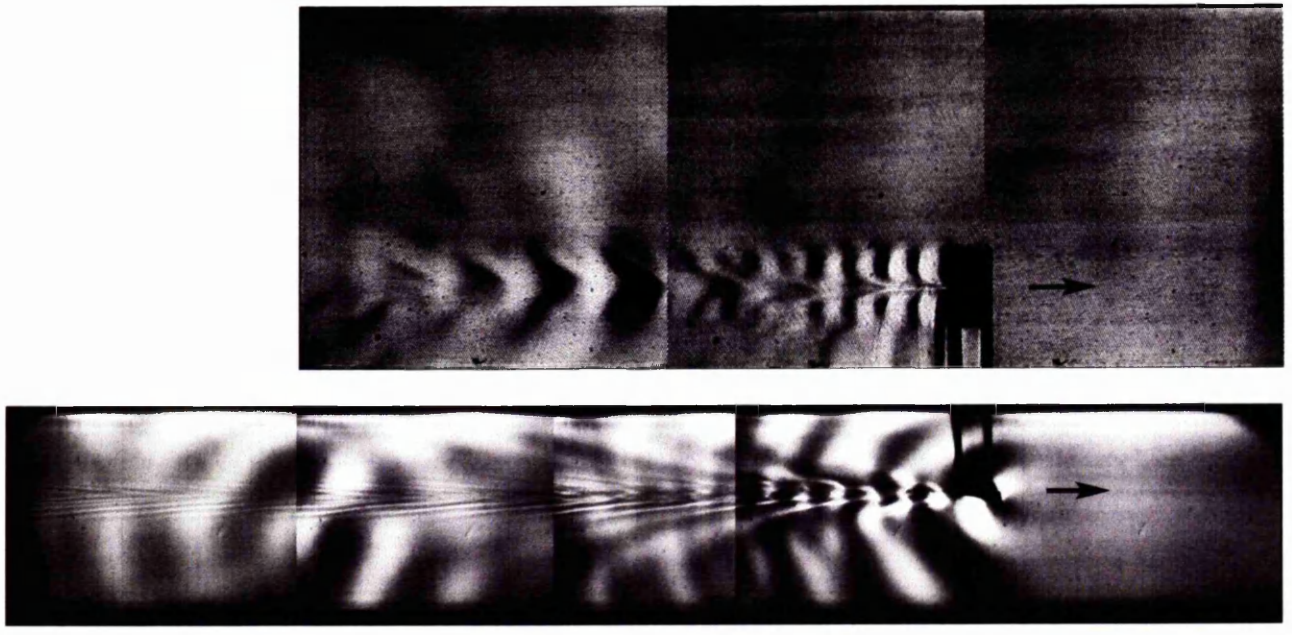

Figures 5.17a and 5.17b The top figure shows the plan-view and the bottom figure shows the side-view schlieren image of an oscillating wing travelling horizontally in a pycnocline. The range of incidence angle is 0 to 10 degrees.

$U = 1.44\times10^{-2}$ m/s, $\omega_f = 2.29$ rad/s, $N_c = 2.81$ rad/s, $\varepsilon = 0.18$ m, $M = 35$ and $\beta_f = 2.32\times10^{-2}$. The steady wave system can be seen superimposed onto the oscillatory wave system. The wave number surface is shown in figure 5.21. Density distribution of the pycnocline is shown in figure 5.2. The black arrows show the direction of travel.

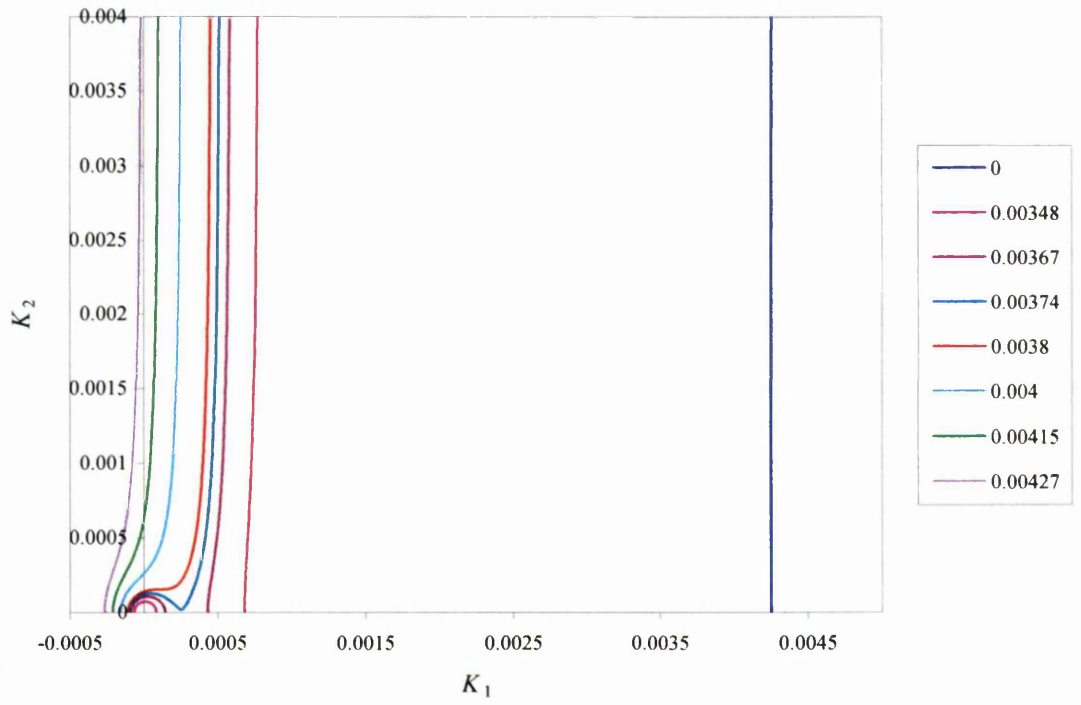

FIGURE 5.18 WAVENUMBER SURFACES FOR PYCNOCLINE WAVES

M = 234, n = 0, ε = 0.18 m, N_c = 2.81 rad/s and U = 2.16 x 10^{-3} m/s.

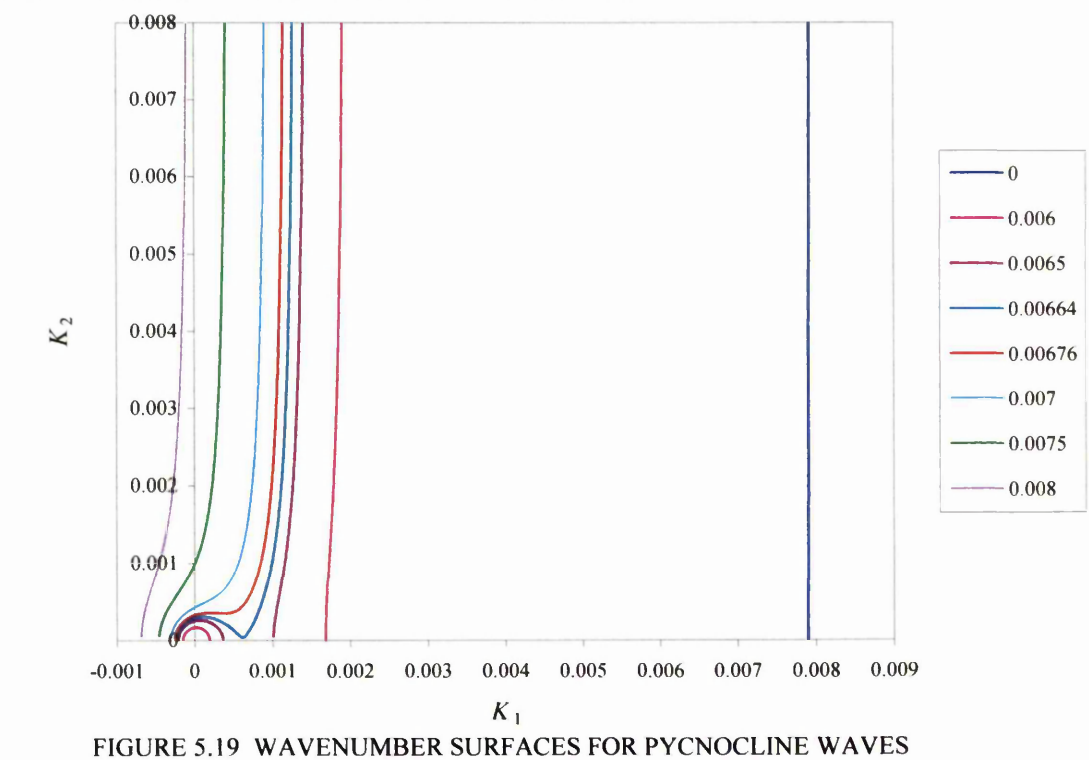

FIGURE 5.19 WAVENUMBER SURFACES FOR PYCNOCLINE WAVES

M = 125, n = 0, ε = 0.18 m, N_c = 2.81 rad/s and U = 4.03 x 10^{-3} m/s.

The legend shows the values of β_f.

Each value of β_f produces two curves, only the right curve with $+\beta$ is shown.

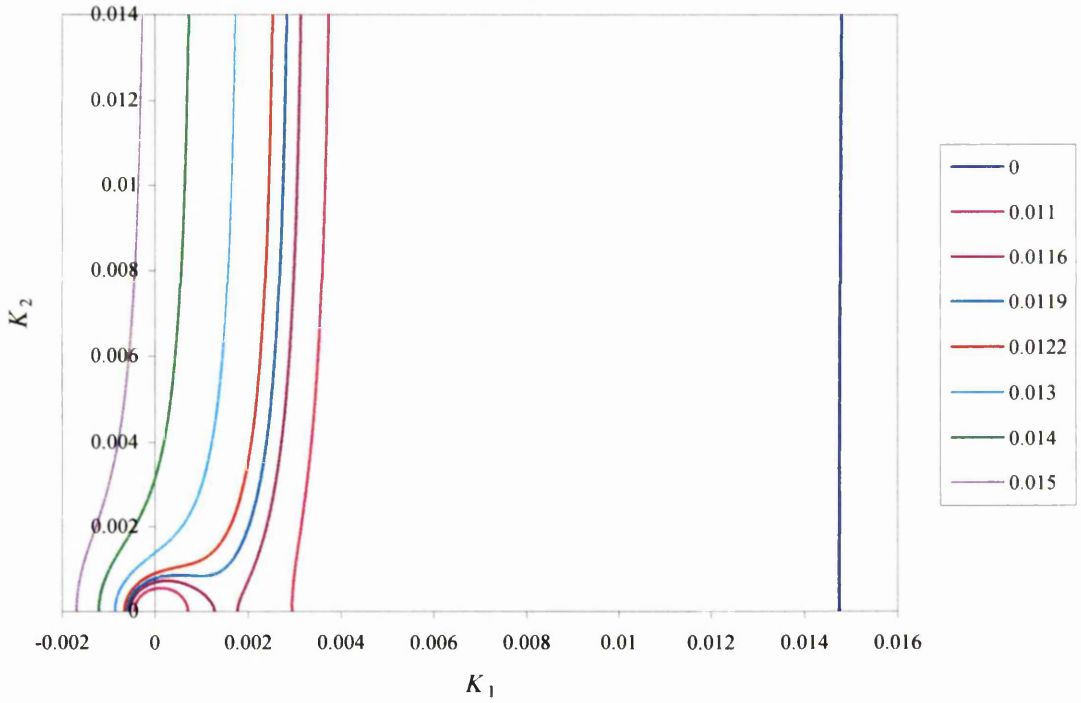

FIGURE 5.20 WAVENUMBER SURFACES FOR PYCNOCLINE WAVES

M = 67, n = 0, ε = 0.18 m, N_c = 2.81 rad/s and U = 7.57 x 10^{-3} m/s.

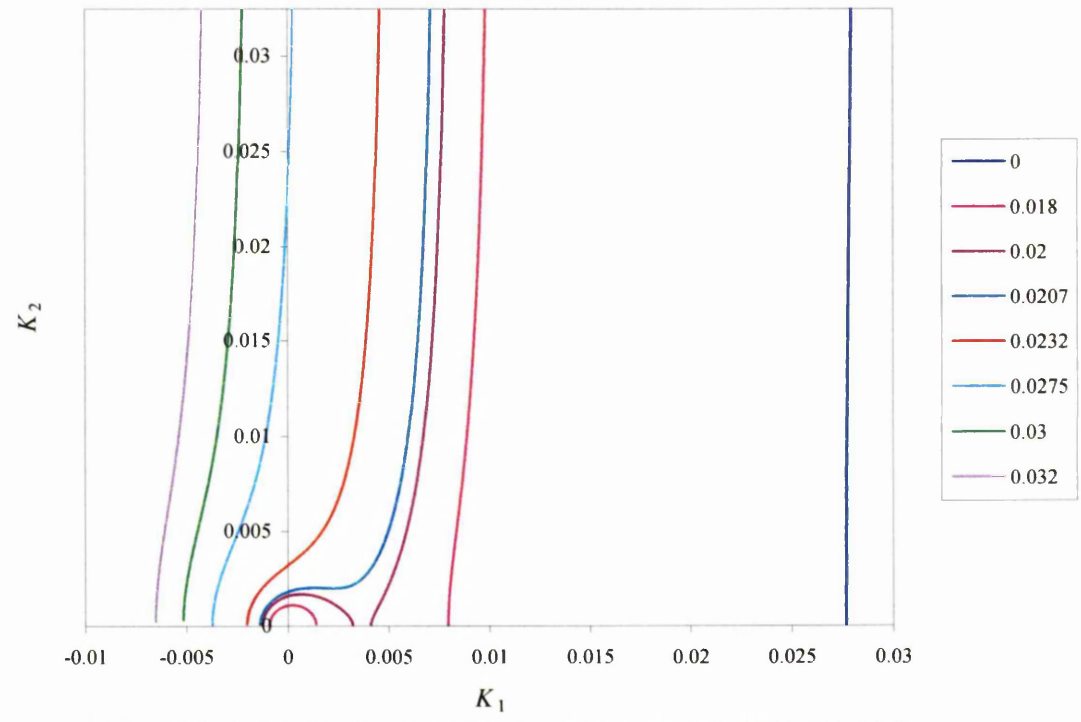

FIGURE 5.21 WAVENUMBER SURFACES FOR PYCNOCLINE WAVES

M = 35, n = 0, ε = 0.18 m, N_c = 2.81 rad/s and U = 1.44 x 10^{-3} m/s.

The legend shows the values of β_f.

Each value of β_f produces two curves, only the right curve with +β is shown.

Figure 5.22a. $\omega_f = 3.58$ rad/s.

Figure 5.22b. $\omega_f = 6.0$ rad/s.

Figure 5.22c. $\omega_f = 6.3$ rad/s.

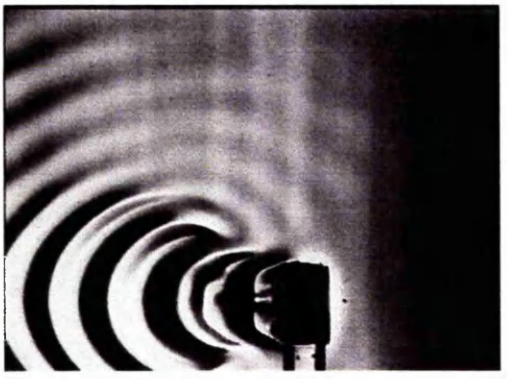

Figure 5.22d. $\omega_f = 6.73$ rad/s.

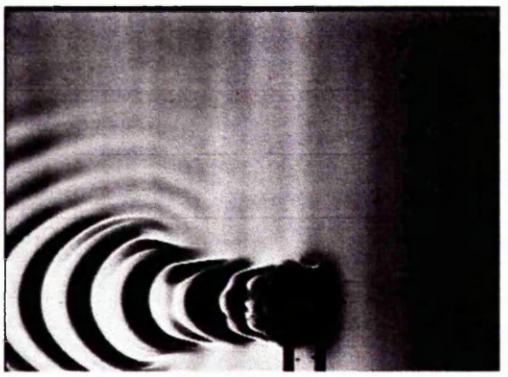

Figure 5.22e. $\omega_f = 7.04$ rad/s.

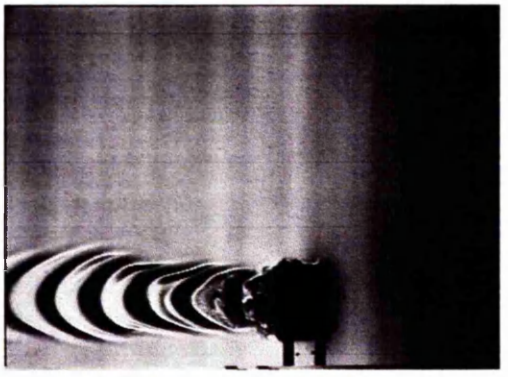

Figure 5.22f. $\omega_f = 8.13$ rad/s.

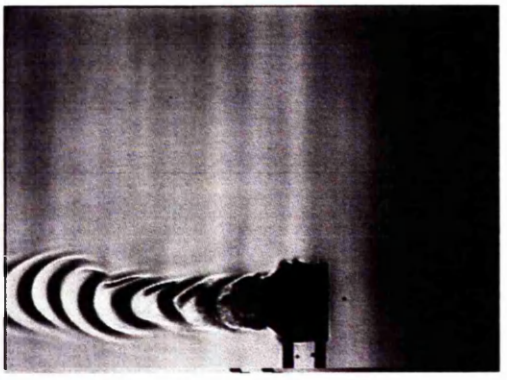

Figure 5.22g. $\omega_f = 9.42$ rad/s.

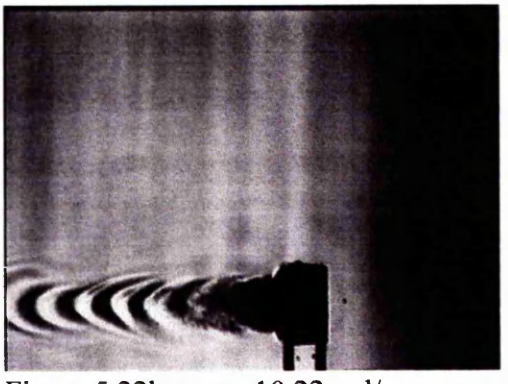

Figure 5.22h. $\omega_f = 10.22$ rad/s.

Figure 5.22 continues on the next page.

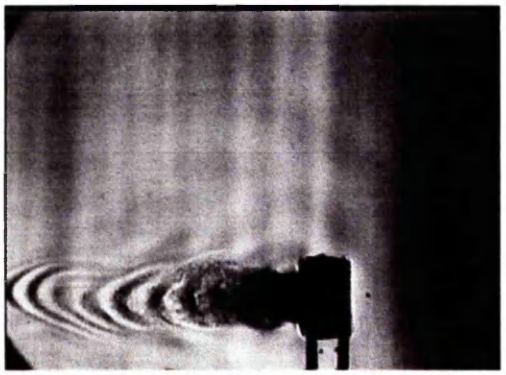

Figure 5.22i. $\omega_f = 13.14$ rad/s.

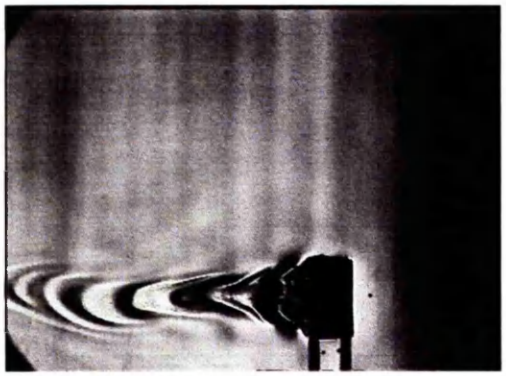

Figure 5.22j. Decreasing ω_f.

Figure 5.22k. Decreasing ω_f further.

Figure 5.22l. $\omega_f = 6.64$ rad/s.

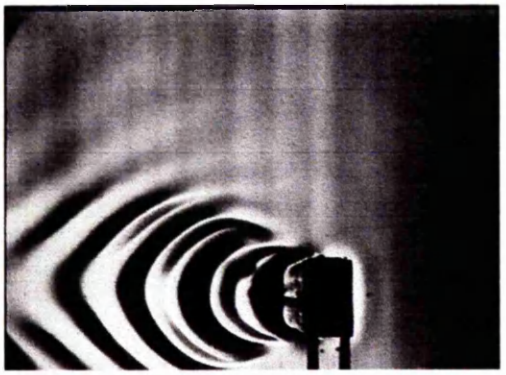

Figure 5.22m. Decreasing ω_f.

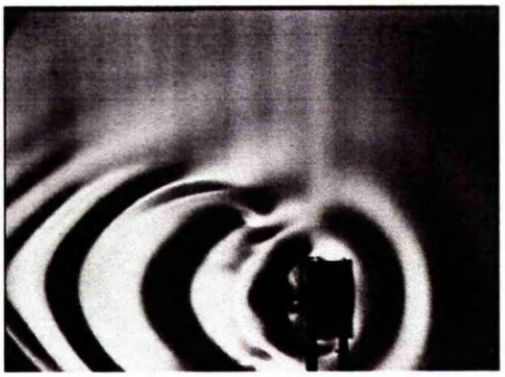

Figure 5.22n. Decreasing ω_f further.

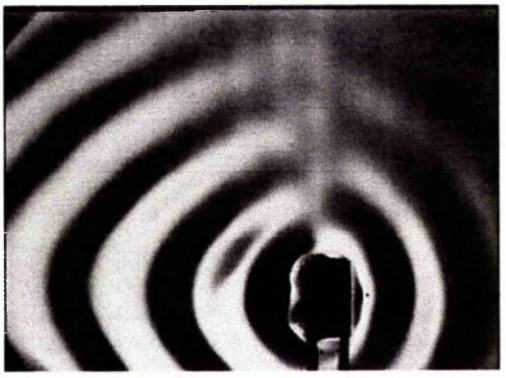

Figure 5.22o. $\omega_f = 6.14$ rad/s.

Figure 5.22 A wing at U = 0 m/s oscillating with increasing to decreasing ω_f. The profile of the pycnocline is shown in figure 5.1.

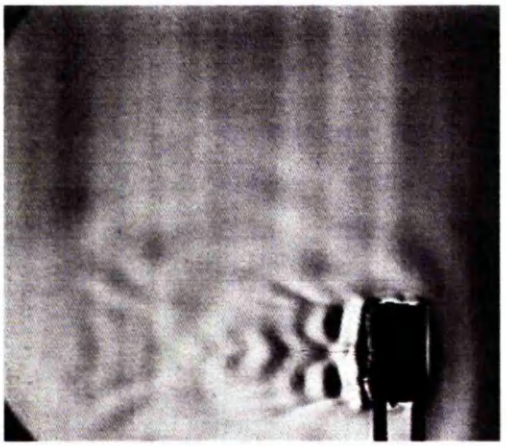

Figure 5.23a.
$\omega_f = 3.58$ rad/s, $\beta_f = 0.0183$.

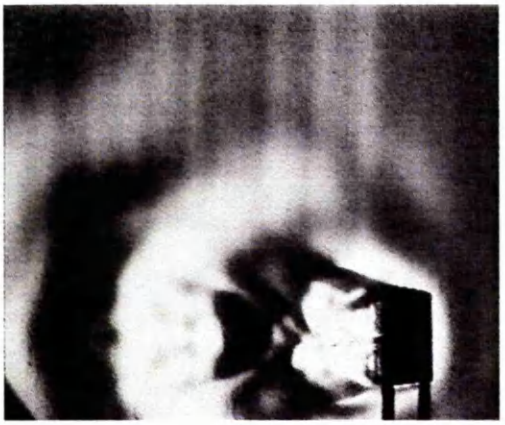

Figure 5.23b.
$\omega_f = 6.04$ rad/s, $\beta_f = 0.0309$.

Figure 5.23c.
$\omega_f = 7.88$ rad/s, $\beta_f = 0.0403$.

A wing oscillating and moving from left to right at $U = 7.8\times10^{-3}$ m/s. M = 24.

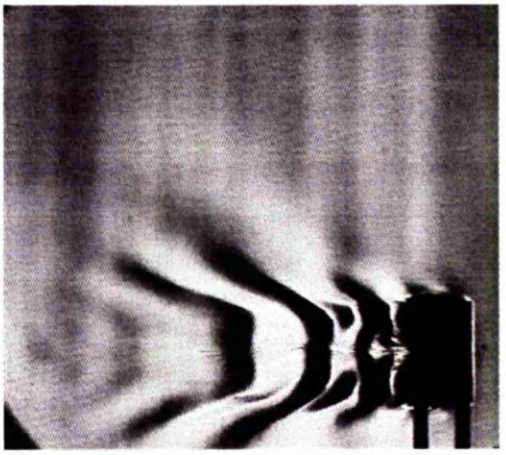

Figure 5.24a.
$\omega_f = 3.58$ rad/s, $\beta_f = 0.0339$.

Figure 5.24b.
$\omega_f = 6.04$ rad/s, $\beta_f = 0.057$.

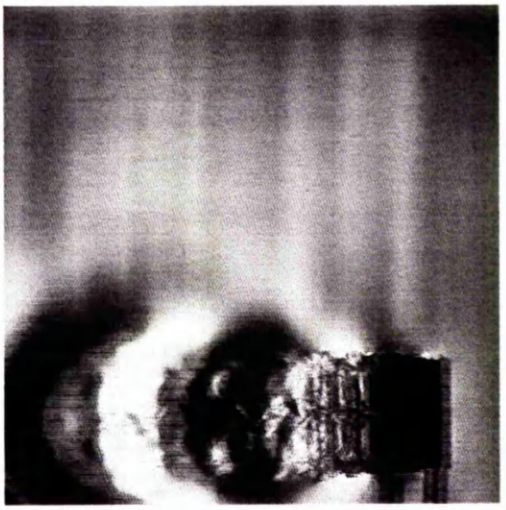

Figure 5.24c.
$\omega_f = 7.88$ rad/s, $\beta_f = 0.075$.

A wing oscillating and moving from left to right at $U = 1.44\times10^{-2}$ m/s. M = 13.

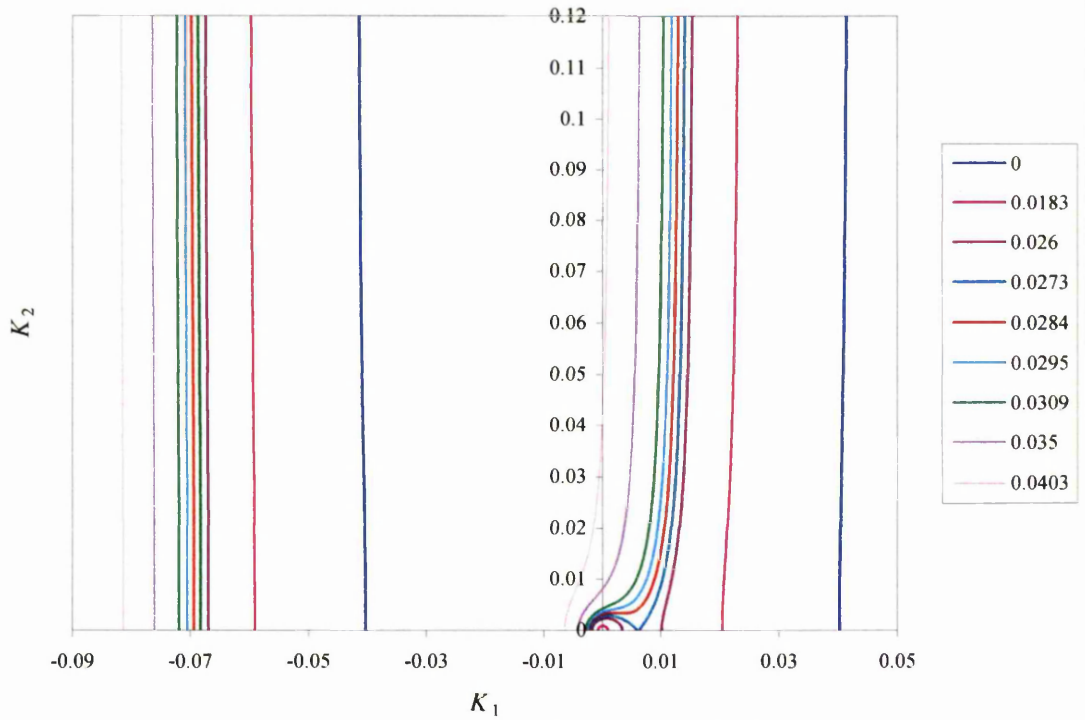

FIGURE 5.25a WAVENUMBER SURFACES

M = 24, n = 0, ε = 22.7 mm, N_c = 8.19 rad/s and U = 7.8 x 10^{-3} m/s.

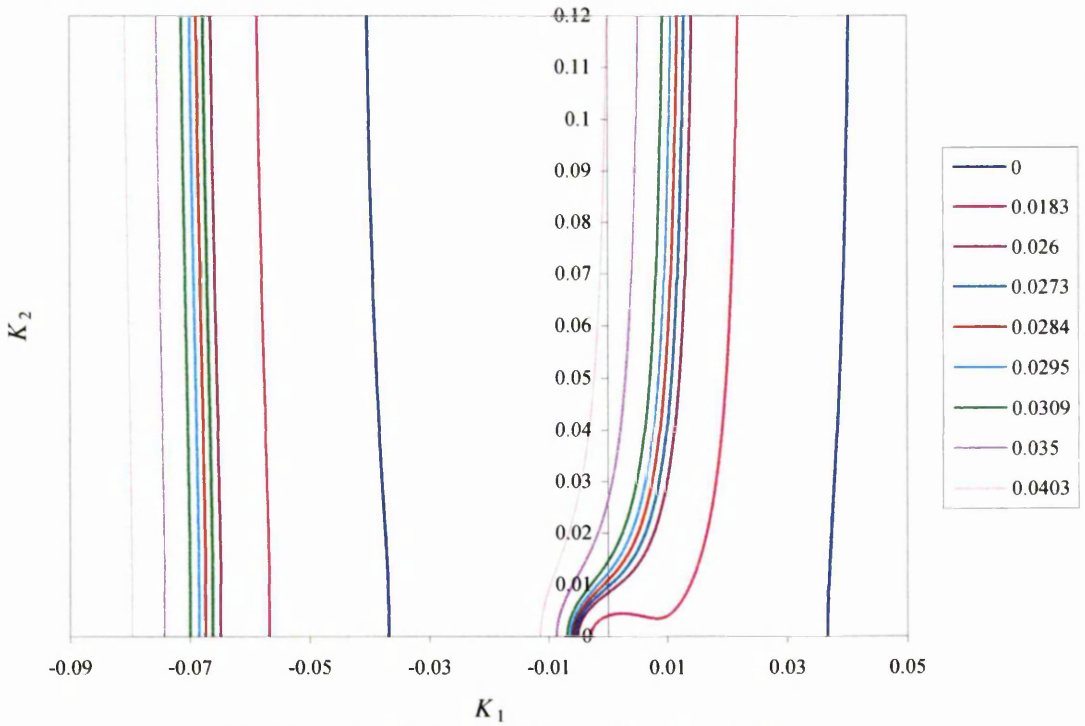

FIGURE 5.25b WAVENUMBER SURFACES

M = 24, n = 1, ε = 22.7 mm, N_c = 8.19 rad/s and U = 7.8 x 10^{-3} m/s.

Wavenumber surfaces for figures 5.23a to c. The legend shows the values of β_f.

Each value of β_f produces two curves, the right curve has +β while the left curve has -β.

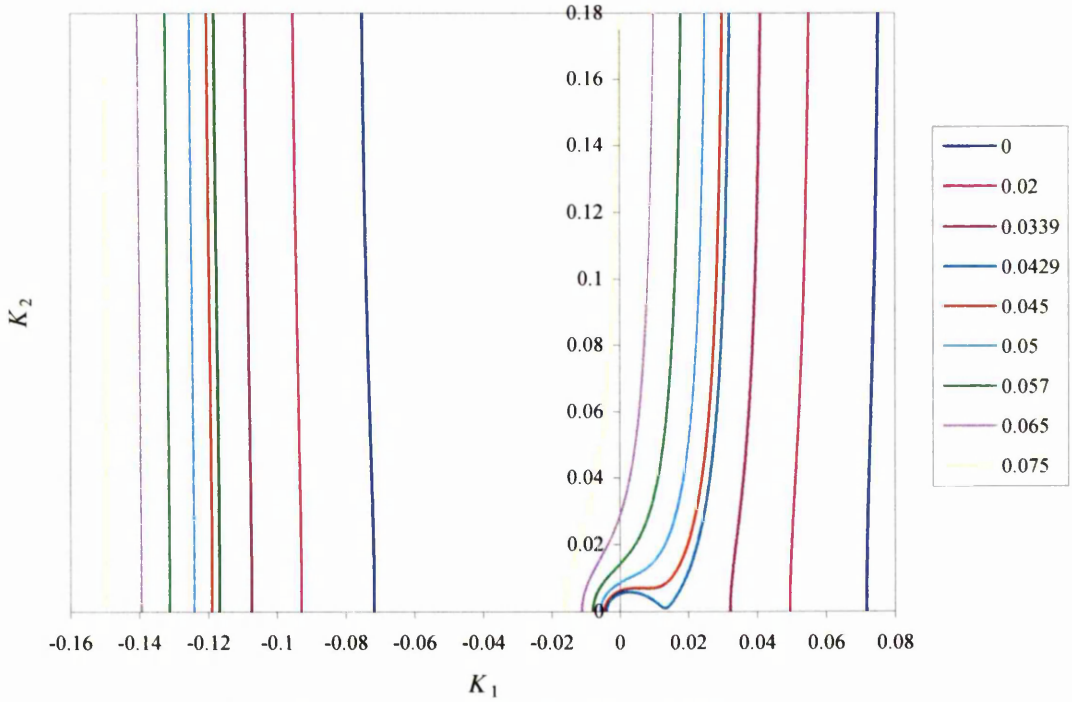

FIGURE 5.26a WAVENUMBER SURFACES

M = 13, n = 0, ε = 22.7 mm, N_c = 8.19 rad/s and U = 1.44 x 10^{-3} m/s.

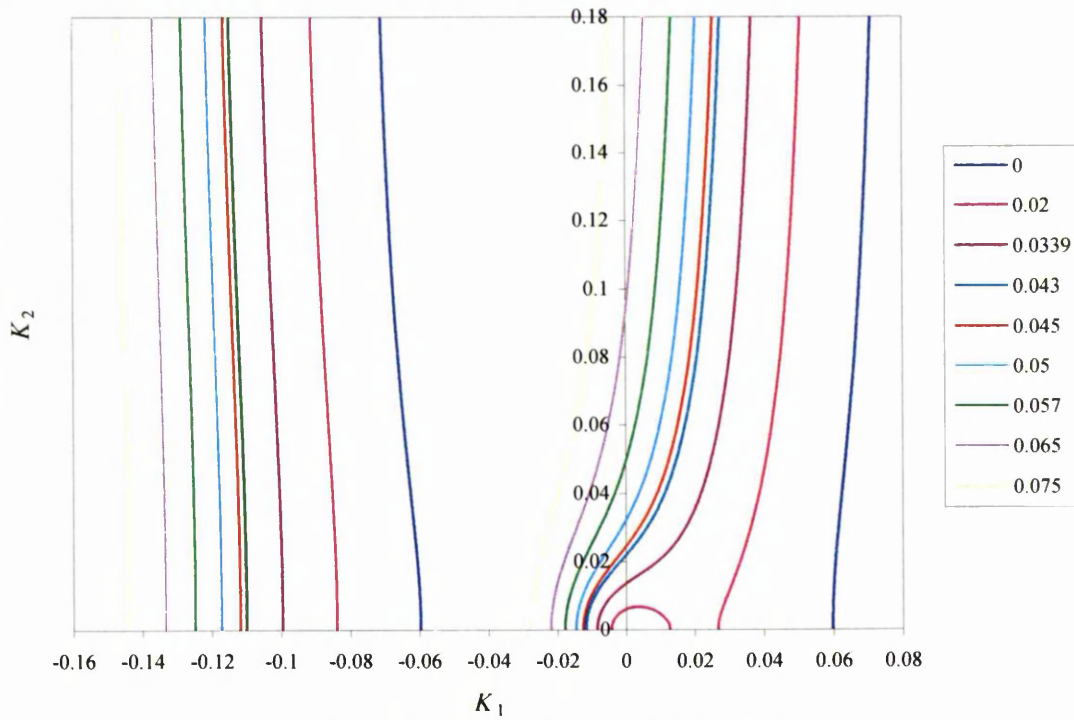

FIGURE 5.26b WAVENUMBER SURFACES

M = 13, n = 1, ε = 22.7 mm, N_c = 8.19 rad/s and U = 1.44 x 10^{-3} m/s.

Wavenumber surfaces for figures 5.24a to c. The legend shows the values of β_f. Each value of β_f produces two curves, the right curve has $+\beta$ while the left curve has $-\beta$.

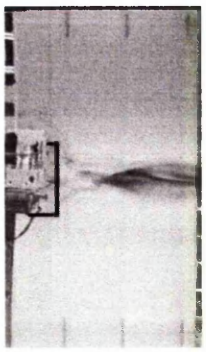

(a) The wing comes to a halt after travelling for a long time at a constant velocity of 8.3 mm/s. The angle of incidence is 2.5 degrees .

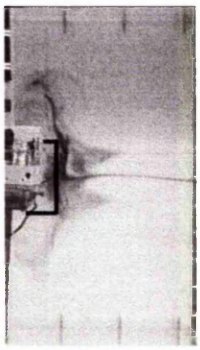

(b) 20s later, the incidence angle is changed to 0 degree.

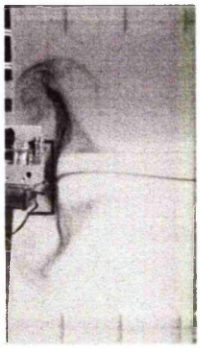

(c) 30s later and the wing starts to move to the left again at 2.7 mm/s.

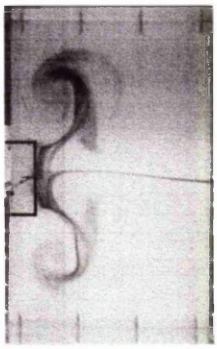

(d) 40s later.

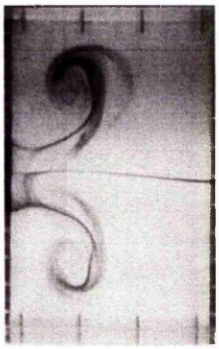

(e) 50s later.

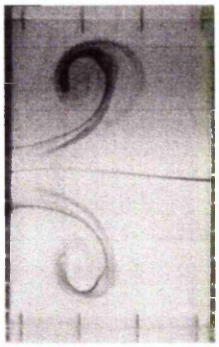

(f) 60s later.

(g) 70s later.

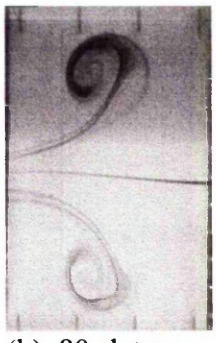

(h) 80s later.

(i) 90s later.

Figure 5.28.
The evolution of a vortex dipole.
Wing travelling from right to left.

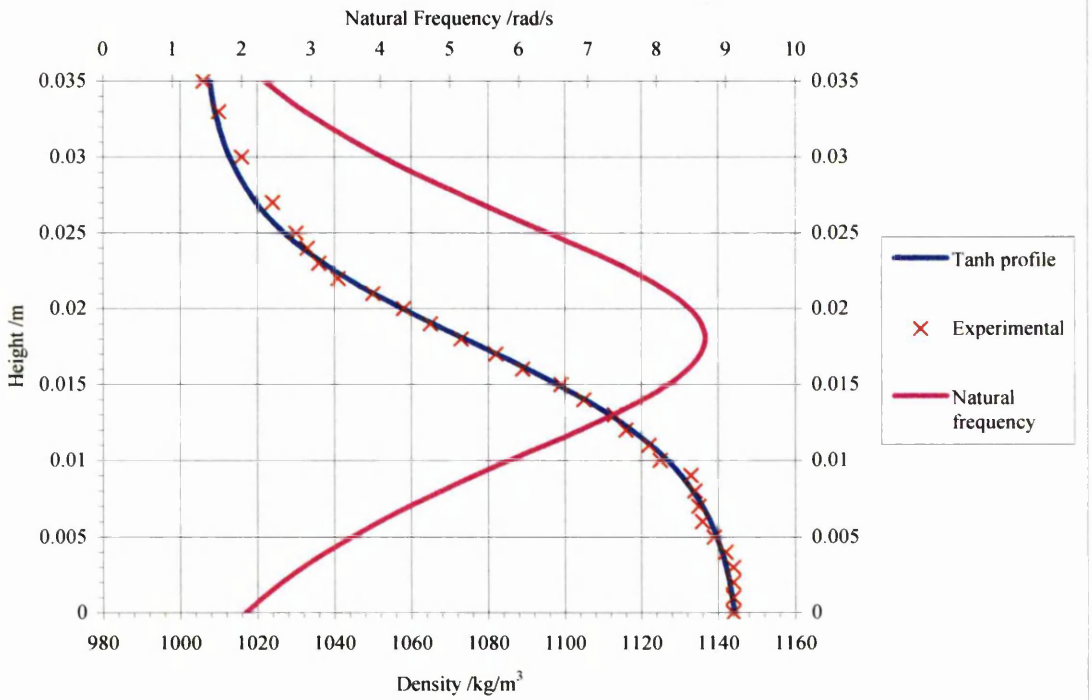

FIGURE 5.29 DENSITY AND FREQUENCY DISTRIBUTIONS

(ε = 17 mm, N_c = 8.7 rad/s, ρ_c = 1074 kg/m^3, $\Delta\rho$ = 141 kg/m^3, ρ_{cw} = 1073 kg/m^3)

Wing's position, height = 0.018 m

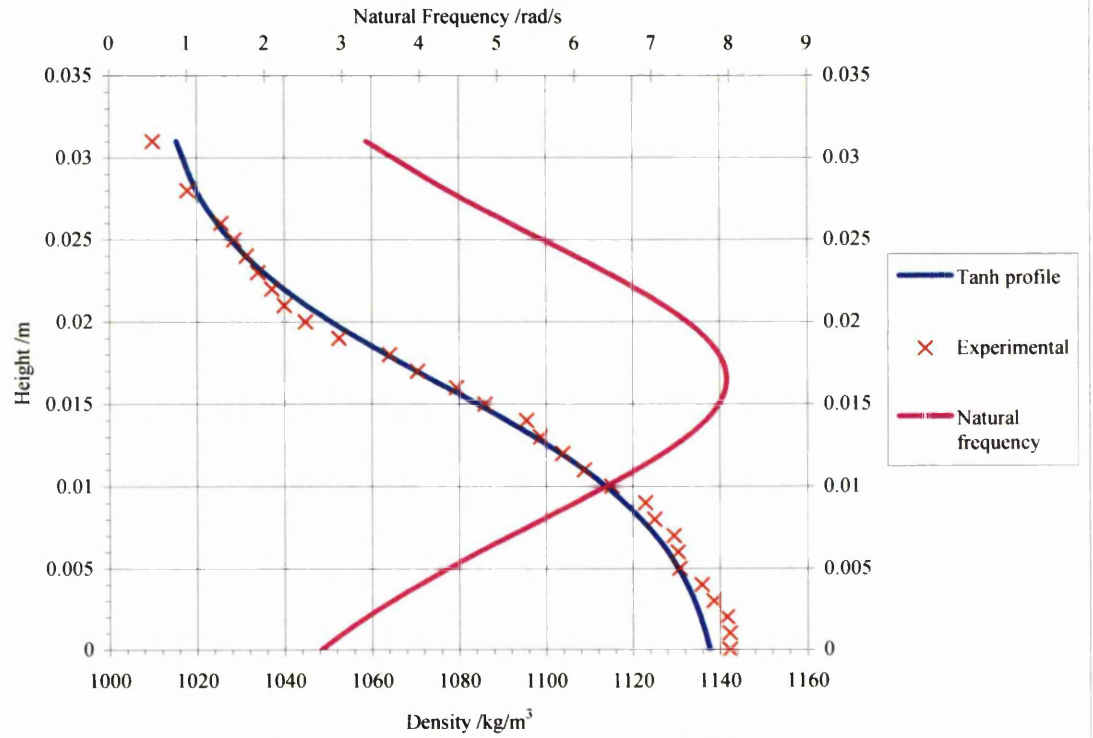

FIGURE 5.30 DENSITY AND FREQUENCY DISTRIBUTIONS

(ε = 19 mm, N_c = 7.97 rad/s, ρ_c = 1072 kg/m^3, $\Delta\rho$ = 132 kg/m^3, ρ_{cw} = 1072 kg/m^3)

Wing's position, height = 0.017 m

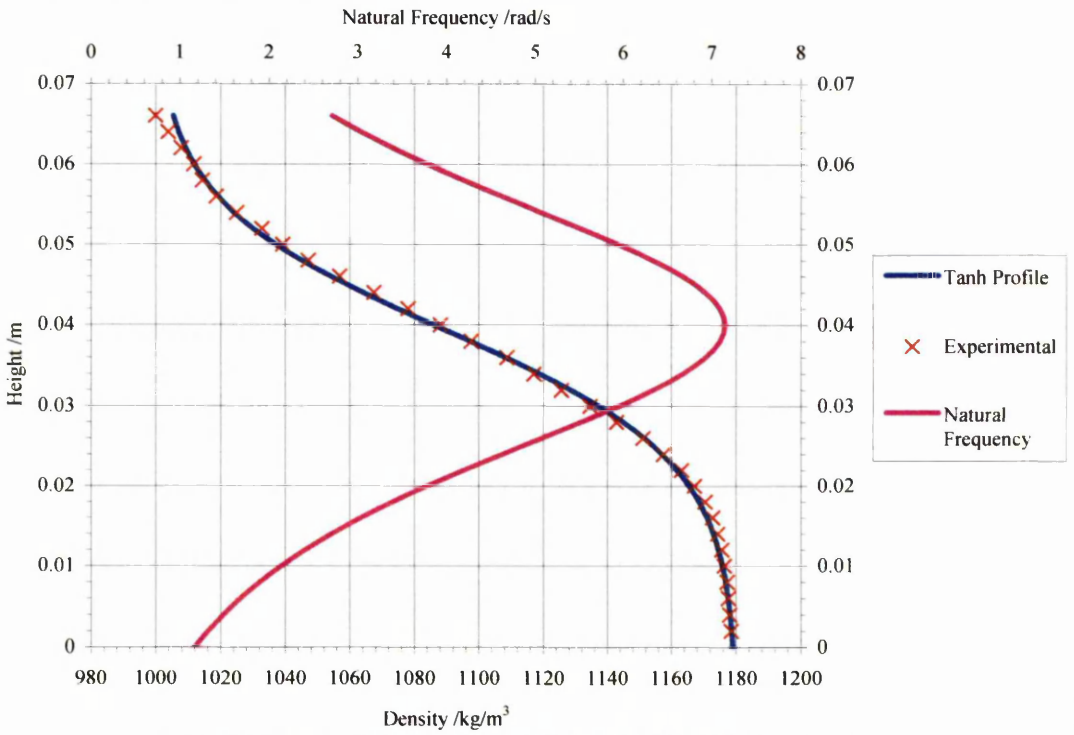

FIGURE 5.31 DENSITY AND FREQUENCY DISTRIBUTIONS

(N_c = 7.15 rad/s, ε = 0.032 m, $\Delta\rho$ = 181 kg/m^3, ρ_c = 1086 kg/m^2, ρ_{cw} = 1075 kg/m^2)

Wing's position, height = 0.043 m

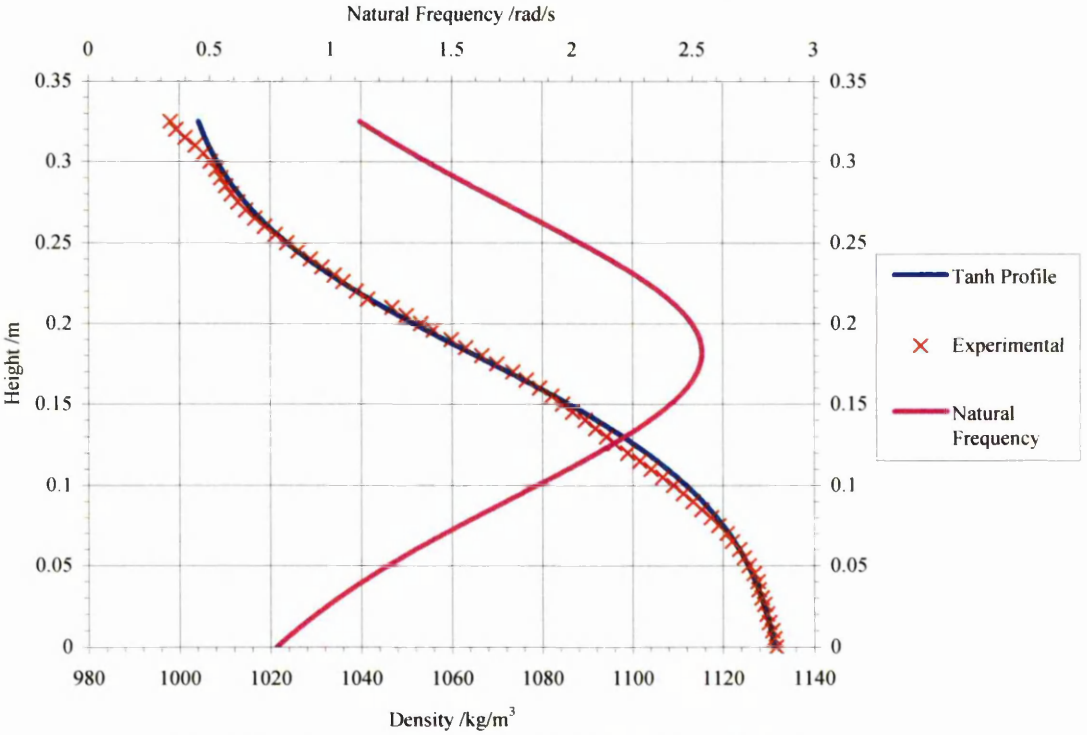

FIGURE 5.32 DENSITY AND FREQUENCY DISTRIBUTIONS

(N_c = 2.54 rad/s, ε = 0.196 m, $\Delta\rho$ = 137 kg/m^3, ρ_c = 1064 kg/m^2, ρ_{cw} = 1065 kg/m^2)

Wing's position, height = 0.18 m

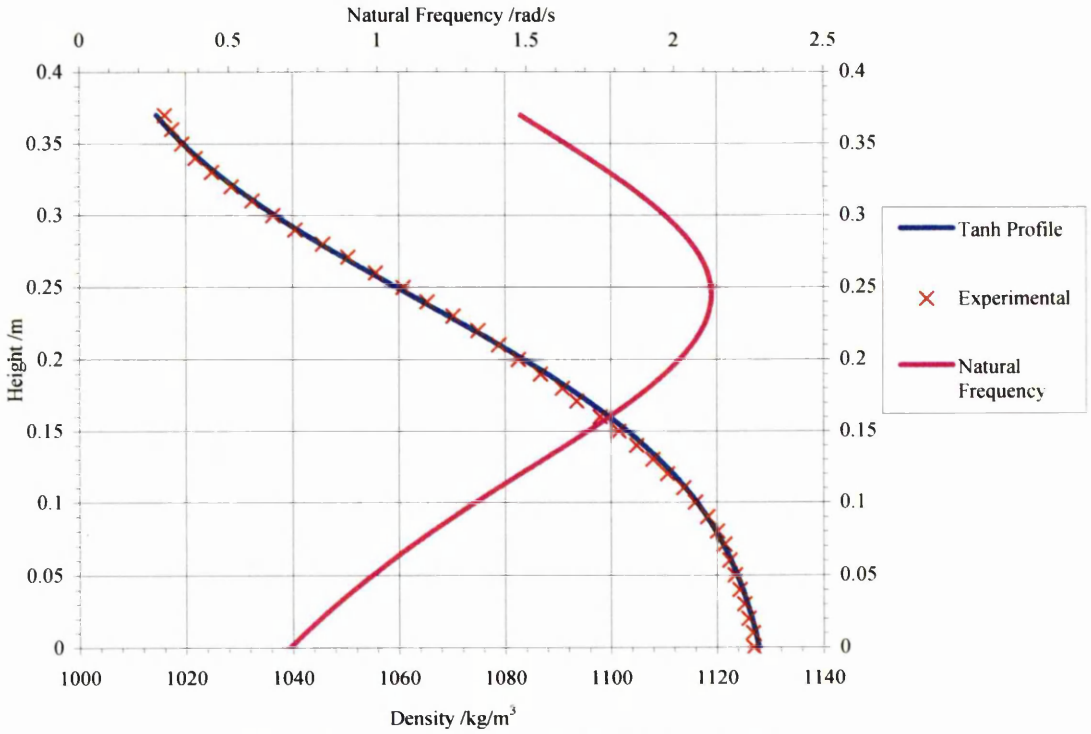

FIGURE 5.33 DENSITY AND FREQUENCY DISTRIBUTIONS

(N_c = 2.13 rad/s, ε = 0.277 m, $\Delta\rho$ = 136 kg/m^3, ρ_c = 1062 kg/m^2, ρ_{cw} = 1072 kg/m^2)

Wing's position, height = 0.225 m

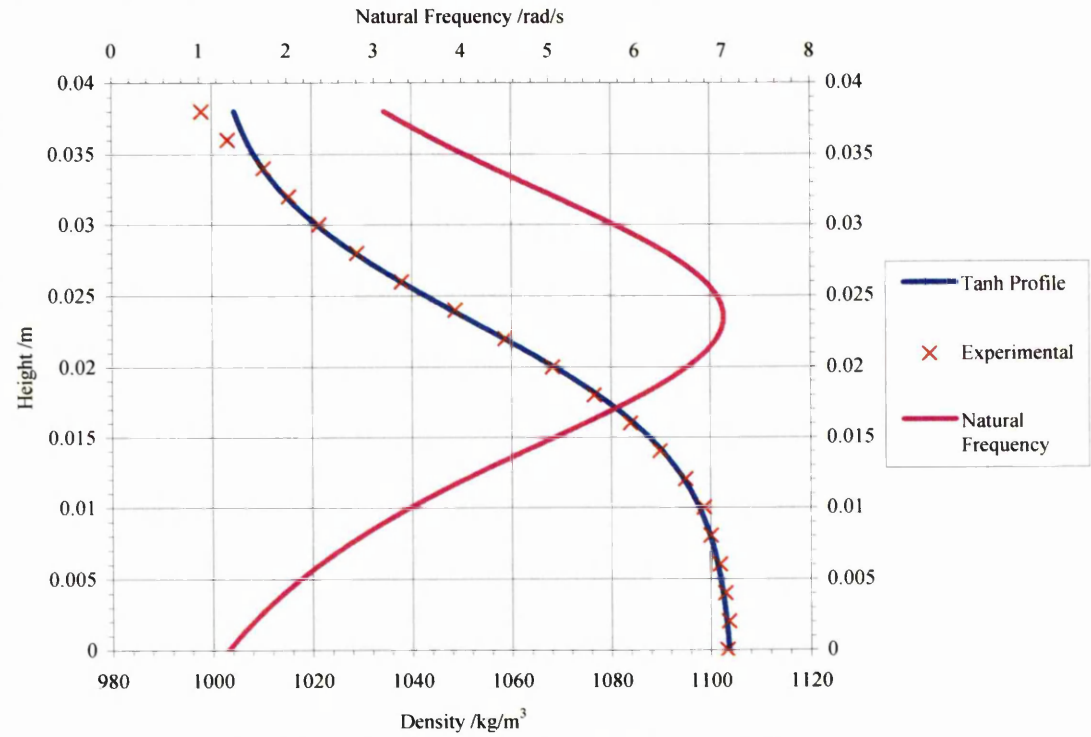

FIGURE 5.34 DENSITY AND FREQUENCY DISTRIBUTIONS

(N_c = 7.01 rad/s, ε = 0.02 m, $\Delta\rho$ = 105 kg/m^3, ρ_c = 1051 kg/m^2, ρ_{cw} = 1051 kg/m^2)

Wing's position, height = 0.024 m

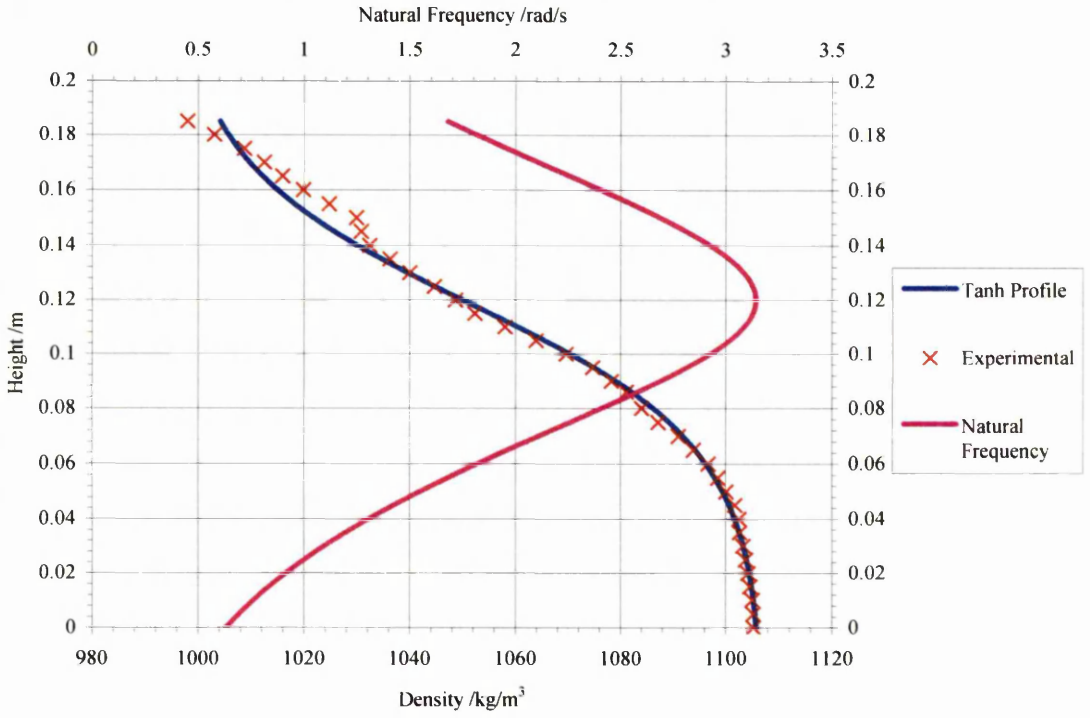

FIGURE 5.35 DENSITY AND FREQUENCY DISTRIBUTIONS

(N_c = 3.14 rad/s, ε = 0.105 m, $\Delta\rho$ = 111 kg/m^3, ρ_c = 1050 kg/m^2, ρ_{cw} = 1029 kg/m^2)

Wing's position, height = 0.141 m

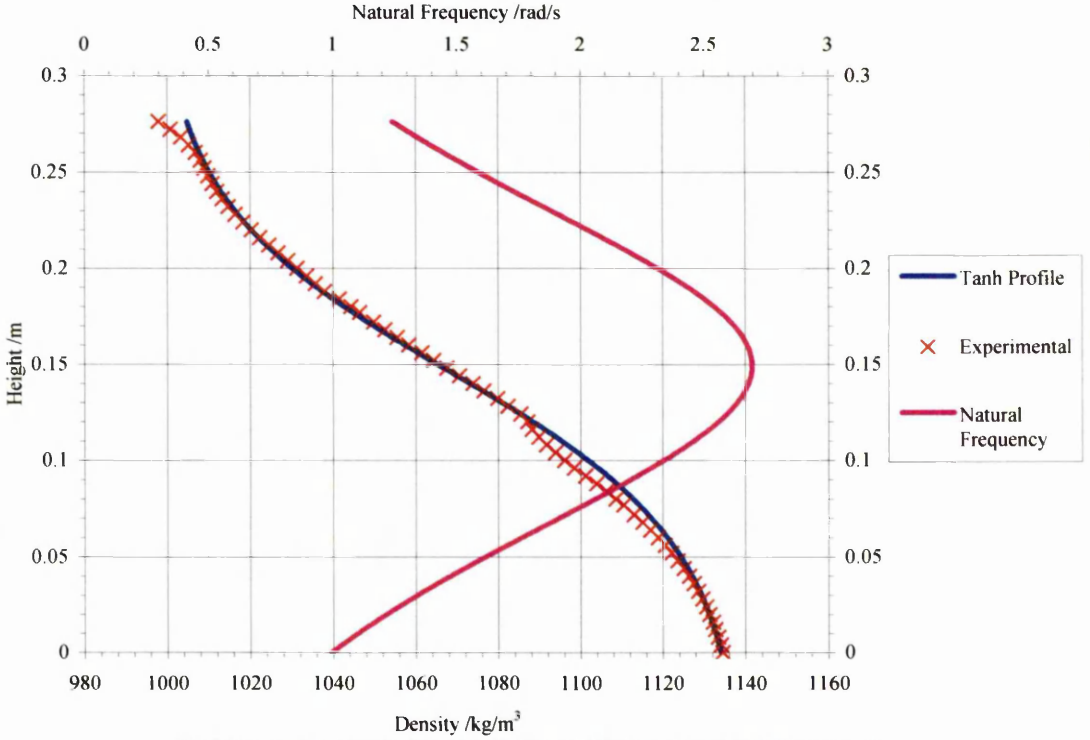

FIGURE 5.36 DENSITY AND FREQUENCY DISTRIBUTIONS

(N_c = 2.7 rad/s, ε = 0.18 m, $\Delta\rho$ = 142 kg/m^3, ρ_c = ρ_{cw} = 1066 kg/m^2)

Wing's position, height = 0.149 m

CHAPTER 6

CONCLUSION AND FUTURE WORK

6.1 General conclusions and suggestions for future work

Wave systems from moving oscillating streamlined bodies have been studied experimentally and by small amplitude wave theory. The flow around a moving oscillating finite aerofoil has been studied experimentally.

The first experiment involved oscillating a small streamlined body which was at a fixed position in the tank. The body could slide along a stretched wire fastened to both ends of the tank. The body was attached to another wire which spanned the length of the tank and was moved so that the body oscillated backwards and forwards on the stretched wire. The body was at the centre of a pycnocline. At some frequencies this produces circular waves propagating away from the body along the pycnocline. A vertical schlieren system was used to view the waves. The circular waves were expected because a pycnocline behaves in some way like a free surface. However at other frequencies interspersed with those producing circular waves, the wave pattern was very different, with waves moving away from the body on the pycnocline in particular directions. The body oscillation was far from simple harmonic. Later experiments have shown that these waves exist on jets of fluid moving horizontally and were obviously due to peculiar body oscillations. These waves are shown in several of the video sequences on the CD-ROM presented with this thesis.

The shape of oscillatory pycnocline waves has been derived using Krauss's dispersion relation and Stevenson's ray theory for a moving oscillating body. The

theory for the zeroth mode reduces to surface waves or interfacial waves when the thickness of the pycnocline approaches zero and the centreline natural frequency approaches infinity in such a way that $\varepsilon N_c^2 \rightarrow 2g$.

Lighthill (1978) looked at surface waves from a moving oscillating body and plotted the wavenumber surfaces, showing that under certain circumstances waves could move ahead of the body, unlike the steady Kelvin ship waves which are always behind the body. However he did not calculate the shape of the waves. The present analysis in the thin pycnocline limit confirms Lighthill's results and the wave shapes are analysed.

In order to confirm the theory the vertical schlieren system was used to observe waves from a streamlined body oscillating as it moved, accelerating to a constant speed. The agreement between theory and experiment is good. When the body moved steadily the waves were the same as those studied by Paonessa (1992)

The small amplitude theory has been used to show the phase configuration for an accelerating or decelerating oscillating body. Other than the few accelerating cases seen so far, there appear to be no published experimental results available. To fully verify the theory with experiment, a mechanism that can accurately vary the acceleration and deceleration will be required as part of the future work.

Interesting experimental images of surface waves dominated by surface tension were observed with the vertical schlieren system. A vibrating thin wire just touching the water surface was used as the point source. A theoretical study uses the dispersion relation of surface waves with surface tension effects included. The comparison between experiment and theory shows reasonable agreement. Lighthill (1978) discussed the transition between capillary waves and gravity waves, however no phase configurations were provided. The theory and experiments in this thesis demonstrate that at low source velocities, the surface waves cannot be realistically produced by either the surface gravity wave or the capillary wave dispersion relation alone. At higher velocities, the wavelengths for surface tension waves become smaller and those for surface gravity waves become longer. This allows the surface tension waves to be differentiated from the gravity waves.

The DERA Agreement was to measure the forces on an oscillating finite wing. The forces involved were small and of the order of 0.01 N. Two strain gauge balances were designed by the author and constructed by the technicians in the department workshop.

The NACA 0012 wing with an aspect ratio of 1.7 could oscillate about its quarter chord position. These were specified by DERA. The frequency of interest is much lower than the frequencies of the noise associated with the oscillatory mechanism. These unwanted frequencies are removed in two ways. Firstly, the whole oscillatory mechanism was mounted on a spring and damper system so that the magnitude of the noise was reduced. Secondly, signal processing employed a low pass filter to eliminate the higher frequency noise.

In a pycnocline, the drag of a wing is made up from profile drag, wave drag, induced drag and viscous drag. The profile drag can be less if the flow over the surface is attached longer at the rear of the wing. Law (1999) has shown that separation occurs later for flow over a cylinder in a stratified fluid. This reduces the base drag of the cylinder causing the overall drag to be less than that in a homogeneous fluid even though internal waves were radiating from the cylinder. Thus the reduction in profile drag was greater than the wave drag. For a NACA 0012 wing at a low incidence angle, the reduction in profile drag is probably not as much as the increase in viscous drag if the flow remains attached for a longer distance. Wave drag is expected to have a positive contribution to the overall drag.

Peake (1996) gave an analysis of the anomalous behaviour whereby the wave drag of a sphere due to oscillatory waves can reduce at certain Froude numbers. The sphere is moving and oscillating horizontally. However the analysis has a condition that the wavelengths are much greater than the amplitude of the sphere oscillation this cannot be satisfied using the current experimental set-up. For steady waves, when the wavelength of the wave is twice the length of the wing chord, the wave energy is seen to be strongest and the wave drag will be high. Even if the oscillatory waves produce a wave thrust, it may not be sufficient to overcome the wave drag due to the steady waves. Induced drag can be less than in a homogeneous fluid as the fluid is reluctant to move upward over the wing tips and the lift is also less than in a homogeneous fluid. The net result is that the overall drag is unlikely to reduce when the wing is oscillating from 0 to 5 degrees incidence. However this analysis may change if the incidence angle is high.

A later paper by Peake (1998) for the case of a continuous density stratification suggests that the radiation instability of a plunging sphere occurs when $\frac{U}{N} > 0.3D$ where D is the cylinder diameter and is independent of the frequency of oscillation. The

present experiments span this condition with D equivalent to either the wing chord or thickness. In the experiments the wing oscillates about its quarter chord. The result will probably be closer to the theoretical analysis of Peake if a plunging wing was used instead. No instabilities or reductions in drag were observed.

The results from the force measurements indicate that the mean drag coefficients during the oscillations are higher in a pycnocline than in the homogeneous fluid. The mean lift coefficients are lower in a pycnocline than in the homogeneous fluid. These results vindicate the analysis above, however it is not conclusive enough. The forces can vary when any of the parameters are changed thereby making comparisons difficult. Future experiments can be improved by varying only one parameter at a time and while keeping the rest constant. This too may prove to be difficult as the pycnocline properties can change with time.

Visualisation of both the side-view and plan-view internal waves around a low aspect ratio wing used the vertical and horizontal schlieren systems. The theory which is used to explain the wave shapes is a two-dimensional version of that given by Nicolaou & Stevenson (1997). When the wing moves at a high enough velocity, the velocity deficit along the path of the wing becomes an important consideration. This is clearly demonstrated in figure 5.7a where a discontinuity can be seen in the 'herring bone' structure of the steady wave systems further away from the wing. Nearer to the wing, there is a transformation from the lee waves close to the wing to the 'herring bone' waves. When the wing oscillates without forward velocity the side-view resembles that of the even mode pycnocline waves shown by Nicolaou et al (1993), except that the primary source is the trailing edge of the wing and the ratio of the frequency of oscillation to the background natural frequency is smaller. At higher velocities, the steady wave systems can be seen superimposed onto the oscillatory systems. The observations of the experimental results agree with the wavenumber surface predictions.

The transition from trapped stratified waves to pycnocline waves take place closer to the source as the ratio of the wavelength to the pycnocline thickness increases. In a thin pycnocline, the velocity deficit or surplus at the trailing edge of the wing can cover the whole pycnocline. With no forward velocity, small amplitude theory states that no waves will be produced at oscillatory frequencies higher than the background frequency. However when the wing is oscillating at above the background natural

frequency, waves are produced due to the background velocity produced at the trailing edge. These waves disappear away from the wing as the velocity decreases. When the wing is moving at a constant velocity, then both Doppler relation and the background velocity are applicable.

Some visualisation of the trailing edge and wing tip vortices were made using dye and the schlieren system. These vortices tend to collapse rapidly forming internal waves. A horizontal dipole was also produced by the velocity deficit in the wake of the wing.

Reference

Aksenov, A. V., Kirillov, V. I., Mozhaev, V. V., Skorovarov, V. E (1985) Structure of internal waves in a channel. *Fluid Dyn.* **20**. 92-96.

Aksenov, A. V., Mozhaev, V. V., Skorovarov, V. E. and Sheronov, A. A. (1987) Internal wave structure in a three-layer fluid with a stratified middle layer. *Fluid Dyn.* **22**. 437-441.

Aksenov, A. V., Mozhaev, V. V., Skorovarov, V. E. and Sheronov, A. A. (1989) Structure of internal ship waves in a three-layer liquid with a stratified middle layer. *J. Appl. Mech. Phys*. **30**. 101-105.

Arshanaya, N. I. and Stetsenko, A. G. (1988) Internal waves from a powered source travelling under a layer of a stratified liquid. *Fluid Mechanics – Soviet Research* 17(2). 119-127.

Bradshaw, P. (1970) Experimental Fluid Mechanics. Pergamon Press, Oxford. UK. 127-131.

Bretherton, F. P. (1966) The propagation of groups of internal waves in a shear flow. *Q. J. R. Met. Soc.* **92**, 466.

Crapper, G. D. (1967) Ship waves in a stratified ocean. *J. Fluid. Mech.* **29**, part 4, 667-672.

DeLaurier, J. D. and Harris, J. M. (1982) Experimental study of oscillating-wing propulsion. *J. Aircraft*. **19**, No 5. 368-373.

Doebelin, E. O. (1990) Measurement systems. McGraw-Hill, Inc. USA.

Dokuchaev, V. P. and Dolina, I. S. (1977) Radiation of internal waves by sources in an exponentially stratified fluid. *Izv. Atmos. Ocean. Physc.* **13**, 444-449.

Dupont, P. and Voisin, B. (1994) Internal waves generated by translating and oscillating sphere. *Dyn. Atmos. Oceans.* **23**. 289-298.

Dysthe, K. B. and Trulsen, J. (1989) Internal waves from moving point sources. *John Hopkins APL Tech. Dig.* 10(4). 307-317.

Ekman, V. W. (1904) On dead water. Scientific Results of the Norwegian North Polar Expedition, 1893-1896 5(15), 1, Christiana 1-152.

Gad-el-Hak, M. (1986) The use of the dye-layer technique for unsteady flow visualization. *J. Fluids Eng*. **108**. 34-38.

Gad-el-Hak, M. and Ho, C. M. (1986) Unsteady vortical flow around three-dimensional lifting surfaces. *AIAA J.*. **24**, No 5. 713-721.

Gapanov-Grekhov, A. P., Dolina, I. S. and Ostrovskii, L. A. (1983) The anomalous Doppler effect and radiation instability of the motion of oscillators in hydrodynamics. *Dokl. Akad. Nauk SSSR* **268**, 827-831.

Gilreath, H. E. (1983) The establishment and control of density microstructure in stratified flow experiments. *Experiments in Fluids.* 210-212

Groen, P. (1948) Contributions to the theory of internal waves. *Konin. Neder. Met. Inst. Bilt. Med-en-Verhand.* Ser. B2(11).

Holliday, D. (1981) Internal wave wake of a ship. RDA-TR-118100-001, R&D Associates, California.

Hudimac, A. A. (1961) Ship waves in a stratified ocean. *J. Fluid. Mech.* **11**, 229-243.

Hurdis, D. A. and Pao, H. P. (1976) Observations of wave motion and upstream influence in a stratified fluid. *J. Appl. Mech.* June, 222-226.

Hurley, D. G. (1969) The emission of internal waves by vibrating cylinders. *J. Fluid. Mech.* **36**, 657-672.

Keller, J. B. and Munk, W. H. (1970) Internal wave wakes of a body moving in a stratified fluid. *Phy. Fluid.* **13**, No 6. 1425-1431.

Kim, J. S. and Park, S. O. (1988) Smoke wire visualization of unsteady separation over an oscillating airfoil. *AIAA J.* **26**, No 11. 1408-1410

Koochesfahani, M. M. (1989) Vortical patterns in the wake of an oscillating airfoil. *AIAA J.* **27**, No 9. 1200-1205.

Krauss, W. (1966) Methoden und Ergebnisse der Theoretischen Ozeanographie. *Interne Wellen* **2**, 32.

Laha, M. K. (1993) A vortex lattice method for thin wings oscillating in ideal flow. *Aero. J.*, Nov. 314-320.

Lamb, H (1932) Hydrodynamics. Cambridge University Press. UK. 377.

Law, A.K.O. (1999) Numerical simulations of internal waves in stratified fluids. PhD Thesis. Univ. of Manchester.

Lighthill, M. J. (1967) On waves generated in dispersive systems by travelling forcing effects, with applications to the dynamics of rotating fluids. *J. Fluid Mech.* **27**. 725-752

Lighthill, M. J. (1978) Waves in fluids. Cambridge University Press. UK.

McAlister, K. W. and Carr, L. W. (1978) Water-tunnel experiments on an oscillating airfoil at Re = 21,000. *NASA TM78446.*

McAlister, K. W. and Carr, L. W. (1979) Water tunnel visualization of dynamic stall. *J. Fluids Eng.* **101**. 376-380.

McCroskey, W. J (1982) Unsteady airfoils. *Ann. Rev. Fluid Mech.* **14**. 285-311.

McCroskey, W. J and Pucci, S. L. (1982) Viscous-inviscid interaction on oscillating airfoils in subsonic flow. *AIAA J.* **20**, No 2. 167-174.

McCroskey, W. J., McAlister, K. W., Carr, L. W., Pucci, S. L., Lambert, O. and Indergrand, R. F. (1981) Dynamic stall on advanced airfoil sections. *J. Amer. Heli.* Soc. July, 40-50.

Miles, J. W. (1971) Internal waves generated by a horizontally moving source. *Geophys. Fluid Dyn.* **2**, 63-87.

Mook, D. T. and Dong, B. (1994) Perspective: Numerical simulations of wakes and blade-vortex interaction. *J. Fluids Eng.* **116**. 5-21.

Mowbray, D. E. (1967) The use of schlieren and shadowgraph technique in the study of flow patterns in density stratified liquids. *J. Fluid Mech.* **27**. 595.

Mowbray, D. E. and Rarity, B. S. H. (1967) The internal wave pattern produced by a sphere moving vertically in a density stratified liquid. *J. Fluid Mech.* **30**, 489-496.

Mowbray, D. E. and Rarity, B. S. H. (1967) A theoretical and experimental investigation of phase configuration of internal waves of small amplitude in a density stratified liquid. *J. Fluid Mech.* **28**, 1-16.

Nicolaou, D (1987) Internal waves around a moving body. PhD Thesis. Univ. of Manchester.

Nicolaou, D. and Stevenson, T. N. (1997) Internal waves around a disturbance in a fluid with arbitrary stratification and background shear flow. *Appl. Sci. Res.* **57**, 95-117.

Nicolaou, D., Garman, J. F. R. and Stevenson, T. N. (1995) Internal waves from a body accelerating in a thermocline. *Appl. Sci. Res.* **55**, 171-186.

Nicolaou, D., Liu, R. & Stevenson, T. N. (1993) The evolution of thermocline waves from an oscillatory disturbance. *J. Fluid Mech.* **254**, 401-416.

Paonessa, F. A. (1992) Thermocline waves from bodies near a free surface. Ph.D Thesis. Univ. of Manchester.

Park, S. O., Kim, J. S. and Lee, B. I. (1990) Hot-wire measurements of near wakes behind an oscillating airfoil. *AIAA J.* **28** No 1. 22-28.

Peake (1996) A report on "The anomalous Doppler effect and radiative instability of the motion of oscillators in hydrodynamics" by A. V. Gaponov-Grekhov et al. *Dokl. Akad. Nauk SSSR* **268**, 827-831 (February 1983). Univ. of Cambridge.

Peake (1998) Non-linear development of radiative instabilities in stratified flow. University Agreement SSDH300032. Univ. of Cambridge.

Pope, A. (1965) High-speed Wind tunnel testing. John Wiley & Sons. 257-259.

Pope, A. (1984) Low-speed Wind tunnel testing. John Wiley & Sons. 177-223.

Ringel, M. and Levin, D. (1985) Improved drag element for wind tunnel sting balances. *J. Aircraft.* **22**, No. 11, 979-982.

Sarpkaya, T. (1983) Trailing vortices in homogeneous and density-stratified media. *J. Fluid Mech.* **136**. 85-109.

Soviero, P. A. O., Bortolus, M. V. (1992) Generalized vortex lattice method for oscillating lifting surfaces in subsonic flow. *AIAA J.* **30**, No 11. 2723-2729.

Stevenson, T. N. (1968) Some two-dimensional internal waves in a stratified fluid. *J. Fluid. Mech.* **33**, 715-720.

Stevenson, T. N. (1969) Axisymmetric internal waves generated by a travelling oscillating body. *J. Fluid. Mech.* **35**, part 2, 219-224.

Stevenson, T. N. (1973) The phase configuration of internal waves around a body moving in a density stratified fluid. *J. Fluid. Mech.* **60**, 759-767.

Stevenson, T. N. and Thomas, N. H.(1969) Two-dimensional internal waves generated by a travelling oscillating cylinder. *J. Fluid. Mech.* **36**, part 3, 505-511.

Stevenson, T. N., Kanellopulos, D. & Constantinides, M. (1986) The phase configuration of trapped internal waves from a body moving in a thermocline. *Appl. Sci. Res.* **43**, 91-105.

Sturova, I. V. (1978) Internal waves generated by local disturbances in a linearly stratified liquid of finite depth. *J. Appl. Mech. Phys.* **19**, 330-336.

Sturova, I. V. and Sukharev, V. A. (1981) Generation of internal waves by local disturtbances in a fluid with a specified vertical density profile. *Izv. Atmos. Ocean Phys.* 17(6). 457-461.

Sturova, I. V. and Sukharev, V. A. (1983) Generation of internal waves in a thermocline. *Fluid Mech. – Soviet Research* 12(1). 131-139.

Thomas, N. H. (1971) Linear internal waves and viscous effects in stably stratified fluids. Ph.D. Thesis, University of Manchester.

Thomas, N. H. and Stevenson, T. N. (1973) An internal wave in a viscous ocean stratified by both salt and heat. *J. Fluid Mech.* **61**. 301-304.

Thorpe, S. A. (1971) Experiments on the instability of stratified shear flows: miscible fluids. *J. Fluid Mech.* **46**. 299-319.

Voisin, B. (1994) Internal wave generation in uniformly stratified fluids. Part 2. Moving point sources. *J. Fluid Mech.* **261**. 333-374.

Voropayev, S. I. and Afanasyev, Y. D. (1994) Vortex structures in a stratified fluid. Chapman & Hall, London. UK.

Wilder, M. C., Mathioulakis, D. S., Poling, D. R. and Telionis, D. P. (1996) The formation and internal structure of coherent vortices in the wake of a pitching airfoil. *J. Fluid Struct.* **10**. 3-20.

Woodhead, T. J. (1983) The phase configuration of the waves around an accelerating disturbance in a rotating stratified fluid. *Wave Motion.* **5**, 157-165.

Bibliography

Avital, E. and Miloh, T. (1994) On the determination of density profiles in stratified seas from kinematical patterns of ship-induced internal waves. *J. Ship Research.* **38**, No 4. 308-318.

Barber, B. C. (1993) On the dispersion relation for trapped internal waves. *J. Fluid Mech.* **252**. 31-49.

Clayton, B. R. and Massey, B. S. (1967) Flow visualization in water: a review of techniques. *J. Sci. Instrum.* **44**.2-11.

Gilreath, H. E. (1991) Stratified flow around an axisymmetric body at small angle of attack. *AIAA J.* **29**, No 12. 2259-2262,

Gilreath, H. E. and Brandt, A. (1985) Experiments on the generation of internal waves in a stratified fluid. *AIAA J.* **23**, No 5. 693-700.

Gordon, D., Klement, U. R. and Stevenson, T. N. (1975) A viscous internal wave in a stratified fluid whose buoyancy frequency varies with altitude. *J. Fluid Mech.* **69**, part 3. 615-624.

Hoerner. S. (1958) Fluid Dynamic Drag. Published by the author, Midland Park, NJ.

Hopfinger, E. J., Flor, J. -B., Chomaz, J. -M. and Bonneton, P. (1991) Internal waves generated by a moving sphere and its wake in a stratified fluid. *Experiments in Fluids.* **11**. 255-261.

Jessen, C. and Grönig, H. (1989) A new principle for a short-duration six component balance. *Experiments in Fluids.* **8**. 231-233.

Johari, H and Fang, H (1997) Horizontal vortex ring motion in linearly stratified media. *Phys. Fluids.* **9**, No 9. 2605-2615.

Joshi, P. N. (1992) Strain-Gauge Applications in Wind Tunnel Balances. *IETE Tech. Review.* **9**, No. 2, 161-167.

Kulite (1997) Semiconductor Strain Gauge Manual.

Law, A.K.O., Nicolaou, D. and Stevenson, T. N. (2000) 15th progress report under Farnborough DERA agreement No 2052/131.

Law, A.K.O., Nicolaou, D. and Stevenson, T. N. (2000) 16th progress report under Farnborough DERA agreement No 2052/131.

McCroskey, W. J., Carr, L. W. and McAlister, K. W. (1976) Dynamic stall experiments on oscillating airfoils. *AIAA J.* **14**, No 1. 57-63.

Micro Measurements instruction bulletin B-130-14.

Micro Measurements instruction bulletin B-134-3.

Micro Measurements instruction bulletin B-147-4.

Mole, P. J. (1990) Strain-gage applications in wind tunnel balances. *Experimental Techniques.* **14**. 39-42.

Panda, J. and Zaman, K. B. M. Q. (1994) Experimental investigation of the flow field of an oscillating airfoil and estimation of lift from wake surveys. *J. Fluid Mech.* **265**. 65-95.

Tse, F. S. & Morse, I. E. (1989) Measurement and instrumentation in engineering. Marcel Dekker, INC, New York. USA.

Voisin, B. (1991) Internal wave generation in uniformly stratified fluids. Part 1. Green's function and point source. *J. Fluid Mech.* **231**. 439-480.

CD-ROM

This CD-ROM is a standard ISO-9660 disc formatted with Joliet extension and can be used on any system that supports this format, including Windows 95, Windows 98 and Windows NT. It is packed with MPEG video clips of schlieren images and dye visualisations. Some of the stills of these clips can be found in this thesis.